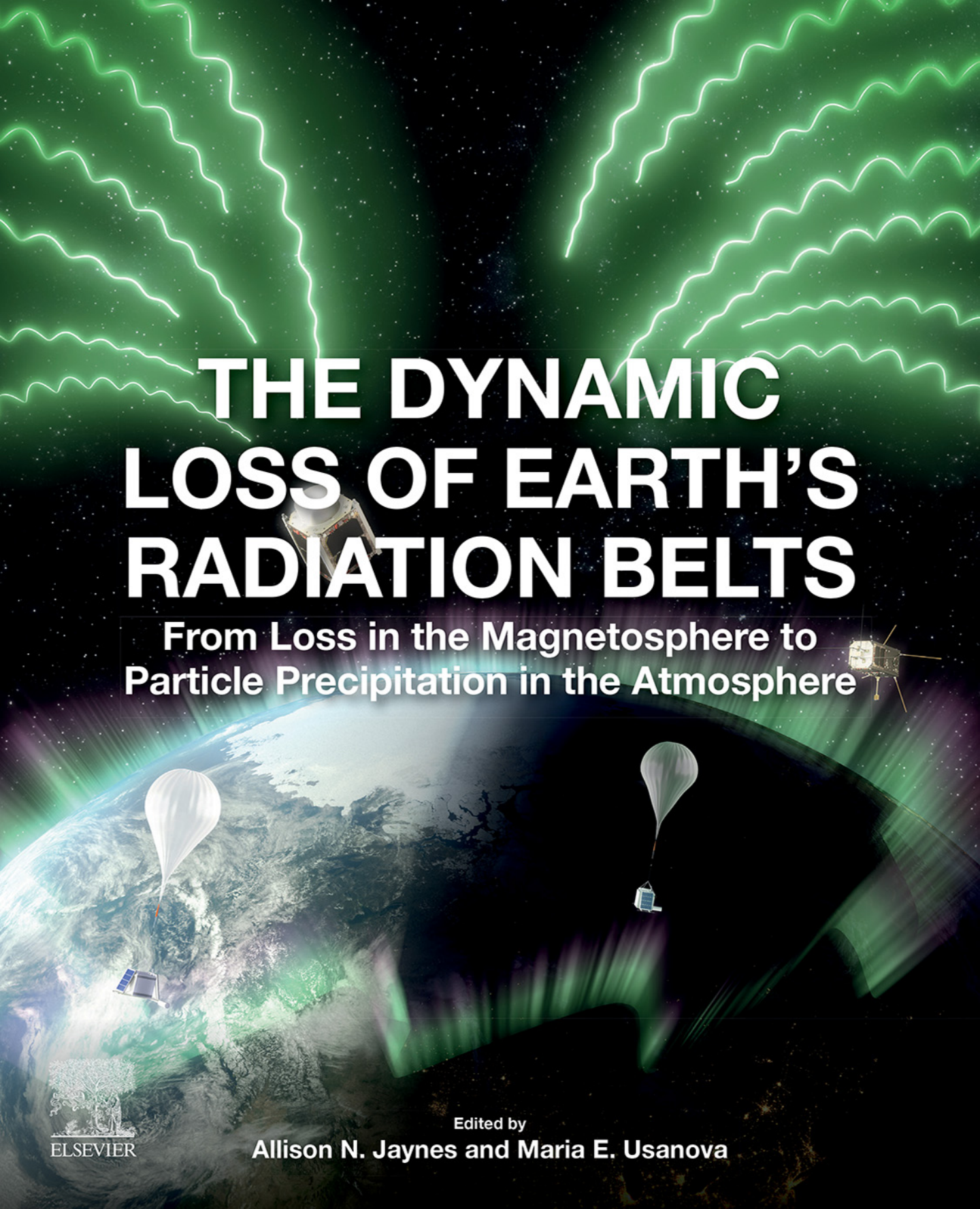
THE DYNAMIC LOSS OF EARTH'S RADIATION BELTS
From Loss in the Magnetosphere to Particle Precipitation in the Atmosphere
Edited by
Allison N. Jaynes and Maria E. Usanova
ELSEVIER

The Dynamic Loss of Earth's Radiation Belts

This page intentionally left blank

The Dynamic Loss of Earth's Radiation Belts

From Loss in the Magnetosphere to Particle Precipitation in the Atmosphere

Edited by

ALLISON N. JAYNES

Department of Physics & Astronomy, University of Iowa, Iowa, United States

MARIA E. USANOVA

Laboratory for Atmospheric and Space Physics, University of Colorado Boulder, Colorado, United States

ELSEVIER

Elsevier
Radarweg 29, PO Box 211, 1000 AE Amsterdam, Netherlands
The Boulevard, Langford Lane, Kidlington, Oxford OX5 1GB, United Kingdom
50 Hampshire Street, 5th Floor, Cambridge, MA 02139, United States

Notices

Knowledge and best practice in this field are constantly changing. As new research and experience broaden our understanding, changes in research methods, professional practices, or medical treatment may become necessary.

Practitioners and researchers must always rely on their own experience and knowledge in evaluating and using any information, methods, compounds, or experiments described herein. In using such information or methods they should be mindful of their own safety and the safety of others, including parties for whom they have a professional responsibility.

To the fullest extent of the law, neither the Publisher nor the authors, contributors, or editors, assume any liability for any injury and/or damage to persons or property as a matter of products liability, negligence or otherwise, or from any use or operation of any methods, products, instructions, or ideas contained in the material herein.

British Library Cataloguing-in-Publication Data
A catalogue record for this book is available from the British Library

Library of Congress Cataloging-in-Publication Data
A catalog record for this book is available from the Library of Congress

ISBN: 978-0-12-813371-2

For Information on all Elsevier publications
visit our website at https://www.elsevier.com/books-and-journals

Publisher: Candice Janco
Acquisition Editor: Marisa Lafleur
Editorial Project Manager: Katerina Zaliva
Production Project Manager: Omer Mukthar
Cover Designer: Miles Hitchen

Typeset by MPS Limited, Chennai, India

Contents

This page intentionally left blank

List of contributors

Lauren W. Blum
NASA Goddard Space Flight Center, Greenbelt, MD, United States

Jacob Bortnik
Department of Atmospheric and Oceanic Sciences, University of California at Los Angeles, Los Angeles, CA, United States

Aaron W. Breneman
School of Physics and Astronomy, University of Minnesota, Twin Cities, Minneapolis, MN, United States

Thiago V. Brito
Department of Physics, University of Helsinki, Helsinki, Finland

Lunjin Chen
Department of Physics, University of Texas at Dallas, Richardson, TX, United States

Mark A. Clilverd
British Antarctic Survey (NERC), Cambridge, United Kingdom

Chris M. Cully
Department of Physics and Astronomy, University of Calgary, Calgary, AB, Canada

Scot R. Elkington
Laboratory for Atmospheric and Space Physics, University of Colorado, Boulder, CO, United States

Mark J. Engebretson
Augsburg University, Minneapolis, MN, United States

Bernd Funke
Institute of Astrophysics of Andalusia, CSIC, Granada, Spain

Alexa J. Halford
Space Sciences Department, Aerospace Corporation, Chantilly, VA, United States

Aaron T. Hendry
Department of Space Physics, Institute of Atmospheric Physics, Prague, Czechia

Robert J. Irvin
SRI International, Menlo Park, CA, United States; Department of Electrical and Computer Engineering, University of Illinois at Urbana-Champaign, Urbana, IL, United States

Stephen R. Kaeppler
Department of Physics and Astronomy, Clemson University, Clemson, SC, United States

Robert A. Marshall
Ann and H. J. Smead Department of Aerospace Engineering Sciences, University of Colorado, Boulder, CO, United States

Robyn M. Millan
Department of Physics and Astronomy, Dartmouth College, Hanover, New Hampshire, United States

Ashton S. Reimer
SRI International, Menlo Park, CA, United States

Pablo M. Reyes
SRI International, Menlo Park, CA, United States

Craig J. Rodger
Department of Physics, University of Otago, Dunedin, New Zealand

John G. Sample
Department of Physics, Montana State University, Bozeman MT, United States

Ennio Sanchez
SRI International, Menlo Park, CA, United States

Miriam Sinnhuber
Institute of Meteorology and Climate Research, Karlsruhe Institute of Technology, Karlsruhe, Germany

Drew L. Turner
Space Sciences Department, The Aerospace Corporation, El Segundo, CA, United States

Aleksandr Y. Ukhorskiy
Johns Hopkins University Applied Physics Laboratory, Laurel, MD, United States

Roger H. Varney
SRI International, Menlo Park, CA, United States

Leslie A. Woodger
Department of Physics and Astronomy, Dartmouth College, Hanover, New Hampshire, United States

Preface

Loss of radiation belt electrons is one of the important outstanding questions of modern space physics. Although significant progress has been made in understanding radiation belt acceleration processes and radial transport, loss processes have yet to be fully understood. This is the first book in the area to focus exclusively on loss and not target acceleration by local processes or radial transport.

This book presents a timely review of precipitation and magnetospheric loss data from various explorative missions, including the NASA Van Allen Probes and Magnetospheric Multiscale (MMS) missions, several current CubeSat missions, the completion of four BARREL stratospheric balloon campaigns, very low frequency (VLF) receiver networks, and incoherent scatter radars.

Nine chapters cover the following topics: outward transport and magnetopause shadowing, radiation belt losses due to wave-particle interactions, CubeSat- and balloon-based studies of radiation belt loss, ground-based VLF-network and radar observations of energetic particle loss, ionospheric effects of energetic particle precipitation, and finally, effects of energetic particle precipitation on atmospheric chemistry and potential impact on climate.

Each chapter was reviewed by a leading expert in the field and by one of the editors. We would like to acknowledge our reviewers for their insightful comments, time, and dedication to improve the quality of this volume (in alphabetical order): Jay Albert, Lauren Blum, Chris Cully, Aaron Hendry, Stephen Kaeppler, Robert Marshall, Annika Seppala, Drew Turner, Aleksandr Ukhorskiy. We would also like to thank our friend and colleague, Andy Kale, for the design of the cover artwork and Elsevier editors, Katerina Zaliva and Redding Morse, and production project manager, Omer Mukthar for their help in preparing this manuscript for publication.

Allison N. Jaynes
University of Iowa, Iowa City, USA

Maria E. Usanova
University of Colorado, Boulder, USA

May 2019

This page intentionally left blank

CHAPTER 1

Outer radiation belt losses by magnetopause incursions and outward radial transport: new insight and outstanding questions from the Van Allen Probes era

Drew L. Turner[1] **and Aleksandr Y. Ukhorskiy**[2]
[1]Space Sciences Department, The Aerospace Corporation, El Segundo, CA, United States
[2]Johns Hopkins University Applied Physics Laboratory, Laurel, MD, United States

Contents

1.1 Introduction

Earth's electron radiation belts consist of two toroidal zones in near-Earth space characterized by very high intensities of relativistic electrons that are quasi-stably trapped in the geomagnetic field. Electrons in the inner radiation belt (e.g., Selesnick, 2015; Fennell et al., 2015; Li et al., 2017), located inside of ~2 Earth radii (R_E), are most often stable over time scales of days to months, with only intermittent sudden enhancements observed during some of the most geomagnetically active periods (e.g., Blake et al., 1992, 2004; Su et al., 2016; Turner et al., 2016; Zhao et al., 2017).

The Dynamic Loss of Earth's Radiation Belts
DOI: https://doi.org/10.1016/B978-0-12-813371-2.00001-9

The inner and outer electron radiation belts are separated by a slot region, which is generally devoid of high intensities of electrons and located at *L*-shells (or where any particular magnetic equipotential field line intersects the magnetic equatorial plane in R_E) between ~2 and 4 R_E. The location and width of the slot region is energy-dependent (e.g., Reeves et al., 2016) and forms from the interplay between inward radial diffusion from a source of electrons in the outer belt and energy-dependent atmospheric scattering loss from interactions between radiation belt electrons and plasmaspheric hiss (e.g., Lyons and Thorne, 1973; Ripoll et al., 2016). Earth's outer radiation belt is located at $\sim 3 < L < \sim 7$ and consists of electrons ranging from 100s keV to >5 MeV. The intensity of outer belt electrons varies drastically, by many orders of magnitude, over a range of timescales from as long as decades (e.g., solar cycles) to as short as just a few hours (e.g., Friedel et al., 2002). Such variability results from the combined effects of outer belt source and loss mechanisms, with the efficiencies of each mechanism being the complex product of solar wind and geomagnetic conditions during any particular event.

We focus in detail on one particular set of loss mechanisms that is considered important for some of the most intense losses of outer belt electrons. Processes that result in depletions of electron intensity in the outer radiation belt can be grouped into four categories: (1) nonadiabatic transport toward and loss to the outer boundary of the greater system, which is ultimately the magnetopause; (2) nonadiabatic transport and loss to the inner boundary of the system, which is ultimately Earth's atmosphere; (3) nonadiabatic (i.e., irreversible) energy loss; and (4) some adiabatic changes. Our focus here is on the first and fourth categories of depletion processes, those to the outer boundary of the system via outward radial transport (both adiabatic and nonadiabatic), but we will also discuss some aspects of atmospheric losses when relevant. Nonadiabatic energy loss may occur from nonlinear wave-particle interactions with whistler-mode chorus waves (e.g., Bortnik et al., 2008), but we do not focus on such processes here. For reviews of outer radiation belt loss processes and modeling prior to the Van Allen Probes era, see Millan and Thorne (2007) and Shprits et al. (2008a,b).

By definition, radiation belt electrons are (quasi-)stably trapped on fully closed drift trajectories within Earth's magnetosphere. Therefore, conceptually, losses of outer radiation belt electrons to the magnetopause must occur via either inward motion (global or localized) of the magnetopause, outward motion of electron drift shells, or some combination of those two processes; for examples, see the conceptual scenarios in Fig. 1.1. Note that Fig. 1.1 is a highly simplified two-dimensional version of a very complicated three-dimensional system that does not account for some physical processes—for example drift orbit bifurcation (e.g., Ukhorskiy et al., 2011). Inward motion of the magnetopause results from pressure enhancements in the solar wind and erosion of the dayside magnetosphere by reconnection under the southward interplanetary magnetic field (IMF). For pressure enhancements, if the inward magnetopause

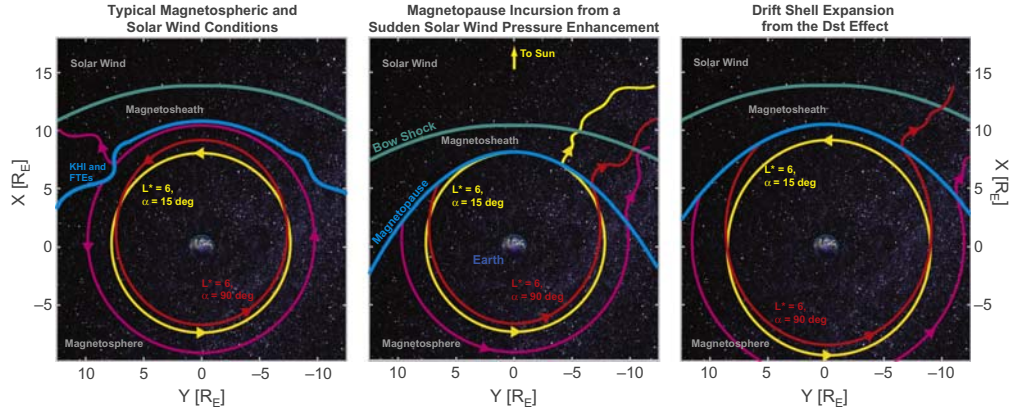

Figure 1.1 Simplified schematics illustrating outer radiation belt drift shells and losses through the magnetopause. In the panel on the left, three drift trajectories are shown in *magenta*, *red*, and *yellow*. The *red* and *yellow* drift shells are closed, representing electrons that are stably trapped within the inner magnetosphere; these two curves also illustrate the effect of drift shell splitting, in which electrons with different equatorial pitch angles (90 degrees in *red*; 15 degrees in *yellow*) have different drift trajectories owing to the day–night asymmetry in Earth's magnetosphere. The *magenta* curve shows an electron drift trajectory at the edge of the trapping region on which some electrons might be lost to the magnetopause via waves [e.g., Kelvin–Helmholtz instability (KHI)] and transient phenomena [e.g., flux transfer events (FTEs)] along the magnetopause (e.g., Kavosi et al., 2018). The center panel illustrates how magnetopause incursions can result in sudden losses on drift trajectories that end up intersecting the compressed magnetopause. The panel on the right illustrates how drift shell expansion from the disturbance storm time (Dst) effect can also result in losses of electrons on any drift shells that expand through the magnetopause. L^* = adiabatic invariant.

motion is slow relative to electron drift periods, then the electrons will respond adiabatically to the enhanced magnetic fields in the compressed magnetosphere (e.g., Borovsky and Denton, 2016) and move radially inward to conserve their third adiabatic invariant [Φ or L^* (Roederer, 1970)], which will reduce the extent of outer belt losses to the magnetopause. However, if the solar wind pressure enhancement is fast compared to the electrons' drift periods, then electrons do not have time to respond adiabatically and can be lost from the system very rapidly (within a fraction of their drift period) when their drift trajectory intersects the magnetopause. Such sudden inward magnetopause motion may result from transient pressure pulses in the solar wind (e.g., Sibeck et al., 1989; Sibeck, 1990), the compression regions at the downstream edges of high-speed–stream interaction regions in the solar wind (e.g., Borovsky and Denton, 2009), or the sudden jump in solar wind density and velocity from an interplanetary shock (e.g., Lugaz et al., 2015).

Here, we refer to sudden magnetospheric compression events that result in enhanced losses of outer belt electrons as "magnetopause incursions." In the literature, the term commonly used for outer belt electron losses to the magnetopause is *magnetopause shadowing*. However, in general, this term is not accurate for all types of magnetopause loss. Magnetopause shadowing implies that all electrons are lost along the dawnside magnetopause and at the subsolar point. However, some studies (e.g., Cohen et al., 2016) have shown that electron magnetopause losses also occur along the duskside magnetopause and that the region there within the magnetosphere is also not void of energetic electrons, as magnetopause shadowing would imply. The term *magnetopause shadowing* is more accurate to describe the void remaining on previously populated electron drift shells that have intersected the magnetopause owing to magnetopause incursion and/or drift shell expansion.

Magnetopause losses from outward radial transport can result from either adiabatic or nonadiabatic processes (e.g., Kim et al., 2008; Ukhorskiy and Sitnov, 2008). Adiabatic outward radial transport involves electron drift shells expanding outward to conserve the third adiabatic invariant. When Earth's ring current is enhanced during geomagnetically active periods, the magnetic field within the ring current is depressed, and since the ring current's development is slow compared to relativistic electron drift periods in the outer radiation belt, electron drift shells should expand to conserve the third invariant. This process is referred to as the "Dst effect," after the disturbance storm time geomagnetic index. The Dst effect was considered the mechanism responsible for outer belt flux "dropout" events during geomagnetic storms (e.g., Dessler and Karplus, 1961; McIlwain, 1966), but since the late 1990s (e.g., Kim and Chan, 1997; Li et al., 1997), observations have revealed that flux "dropouts" actually involve true (i.e., nonadiabatic and irreversible) losses of outer belt electrons and cannot be fully accounted for by variations in Dst alone. Regardless, purely adiabatic drift shell expansion from the Dst effect or a slowly (∼hours) decompressed magnetosphere can result in electron losses to the magnetopause, particularly during geomagnetic storms (e.g., Kim et al., 2010). The Dst effect can also result in strong depletions of flux in the heart of the outer belt even though the electrons might not be permanently lost from the system. Also, the Dst effect may not be fully adiabatic, particularly during large geomagnetic storms, when ring current growth is substantial over electron drift timescales (Ukhorskiy et al., 2015, 2016). Note that for this chapter, we follow the definition of a flux dropout event defined by Turner et al. (2012a): a flux dropout is a decrease of trapped electron flux by a factor of 50 or more (unless the instrument hits background levels) at a particular L-shell, equatorial pitch angle, and magnetic local time (MLT) over a period of 24 hours or less.

Nonadiabatic outward radial transport is itself a true loss process for outer belt electrons. When the third adiabatic invariant is broken and electrons are transported

radially outward to regions of lower magnetic field strength, their energy drops owing to conservation of the first and second adiabatic invariants. Outward radial transport itself can result from radial diffusion (e.g., Shprits et al., 2006, 2017a), enabled by ultralow frequency (ULF) waves (e.g., Loto'aniu et al., 2010) or drift-bounce resonance on timescales less than the drift orbit (e.g., Chaston et al., 2018), and rapid cascades of electrons across sharp negative gradients in radial distributions (e.g., Turner et al., 2013, 2014a). Another mechanism that can lead to loss of electrons by outward transport is the loss of adiabaticity in bifurcated drift orbits that form in the compressed magnetic fields at higher radial distance on the dayside of Earth's magnetosphere (e.g., Kim et al., 2008; Ukhorskiy et al., 2011, 2014). Provided that there is some source of electron phase space density within the heart of the outer radiation belt (i.e., phase space density distributions that have a peak somewhere in the heart of the outer belt), as is typically the case (e.g., Turner et al., 2012b; Boyd et al., 2014, 2016), any nonadiabatic outward radial transport should eventually lead to loss of electrons to the outer boundary of the system, which is ultimately the magnetopause.

It is important to understand the nature and relative importance of outer radiation belt losses by magnetopause incursions and outward radial transport because of the potential role these mechanisms play in outer belt flux dropout events. As reviewed by Turner et al. (2012a), flux dropouts are one of the most extreme types of outer radiation belt variability. In a dropout event, intensities of outer belt electrons can drop by over three orders of magnitude in only a few hours over a range of energies, pitch angles, and *L*-shells that encompass the majority of the outer radiation belt. A classic example of a flux dropout event is shown in Figs. 1.2 and 1.3, drawn from data from NASA's Van Allen Probes mission (Mauk et al., 2012), which will be discussed further later in this chapter. Losses from a combination of magnetopause incursions and rapid outward radial transport may play a major role in outer belt dropouts (e.g., Turner et al., 2012c), but the relative amount of loss from those as compared with other loss processes (e.g., precipitation loss to Earth's atmosphere) remains an outstanding question and point of ongoing debate (e.g., Shprits et al., 2013, 2017b; Mann et al., 2018).

Many important advances have been made on this topic in just the few years since the launch of Van Allen Probes in late 2012. This review is limited to the recent results from only the Van Allen Probes era concerning the loss of outer radiation belt electrons to the magnetopause and outward radial transport. For reviews of outer belt losses and dynamics prior to the Van Allen Probes era, we refer readers to Friedel et al. (2002), Millan and Thorne (2007), Shprits et al. (2008a,b), Turner et al. (2012a), and Ukhorskiy and Sitnov (2012). This chapter is structured with major sections focusing on observational results, modeling efforts and challenges, and outstanding questions; we conclude with an overarching summary and some suggestions for future efforts.

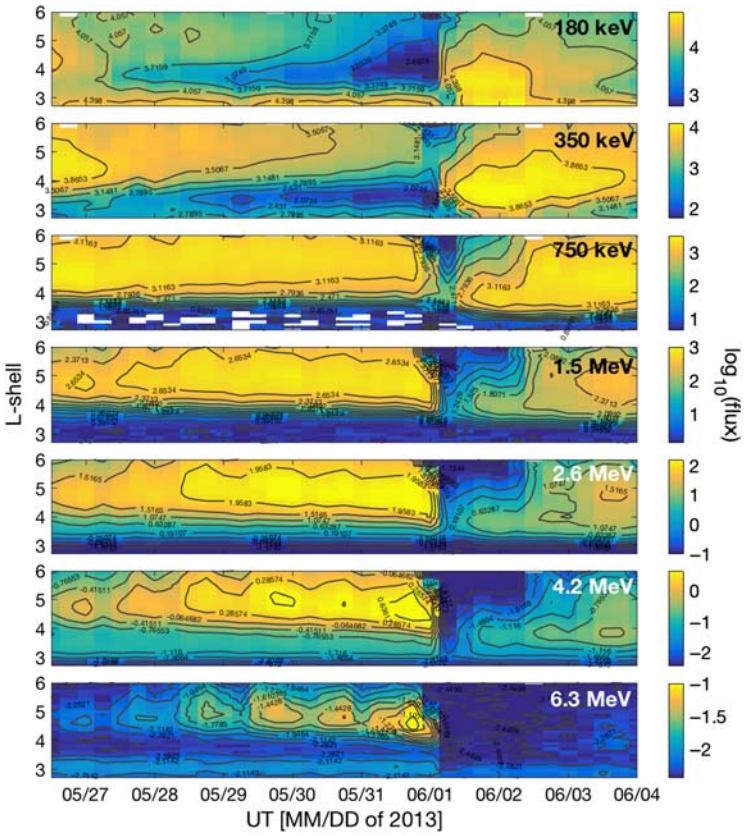

Figure 1.2 *L*-sorted electron fluxes from Van Allen Probes MagEIS and REPT instruments binned in time ($\Delta t = 6$ h) and *L*-shell ($\Delta L = 0.1$). Each panel corresponds to a different energy channel, with each channel's equivalent energy listed in the upper right of each plot. Average fluxes in each bin are plotted in color on a logarithmic scale. The period from May–June 2013 included a pronounced dropout event on June 1, 2013, during the main phase of a geomagnetic storm. *REPT*, Relativistic Electron and Proton Telescope.

1.2 Observational results during the Van Allen Probes era

Since the launch of Van Allen Probes in 2012, a series of observational studies have shown evidence of rapid and drastic losses of outer radiation belt electrons due to magnetopause incursions and outward radial transport. Those studies used data from several different missions, including, but not limited to, the Van Allen Probes. In this section, we review those studies and their results, starting first with recent statistical results before focusing on the latest results from detailed case studies.

1.2.1 Statistical studies

With statistical studies, correlations between radiation belt loss events and quantities related to magnetopause incursions or outward radial transport can be tested, and

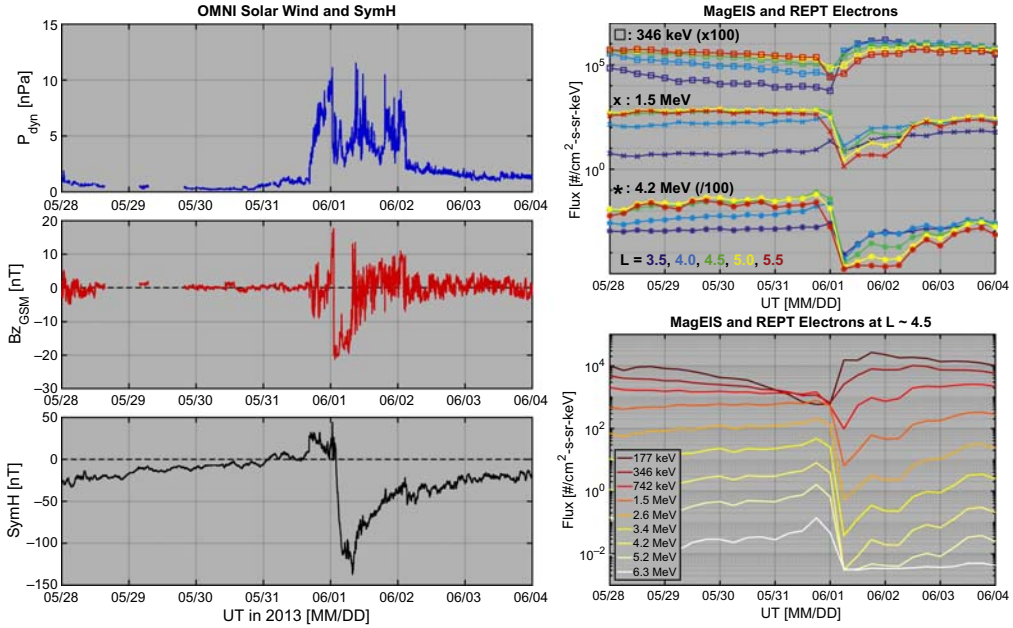

Figure 1.3 Solar wind, geomagnetic index, and Van Allen Probes electron data from the example dropout event on June 1, 2013. All plots show the same time range from May 28, 2004 to June 1, 2013. In the leftmost panels, from top to bottom are solar wind dynamic pressure, IMF Bz, and the SymH index, respectively. In the panels on the right, the top panel shows electron fluxes from MagEIS and REPT for three different energies at five different *L*-shells over the course of the event. Electrons of 346 keV, 1.5 MeV, and 4.2 MeV are shown with square, x, and star symbols, respectively, with the 346 keV and 4.2 MeV curves shifted by factors of 100 × for clarity. Different colors represent the time history of the fluxes at different *L*-shells, with $L = 3.5$, 4.0, 4.5, 5.0, and 5.5 represented in dark blue, light blue, green, yellow, and red, respectively. The bottom panel on the right shows the history of electrons at nine different energies (in colors listed in the legend) at $L = 4.5$. *IMF*, interplanetary magnetic field; *MagEIS*, Magnetic Electron and Ion Spectrometer; *UT*, universal time.

multiple recent statistical studies have found evidence of the importance of these loss processes to the outer radiation belt electrons. Hietala et al. (2014) studied the outer radiation belt response to 31 interplanetary coronal mass ejection (ICME) sheaths that impact the magnetosphere. They tested the hypothesis that the high dynamic pressure and enhanced ULF wave activity associated with ICME sheaths would result in enhanced outward radial transport and dropouts of radiation belt electrons. Using a superposed epoch analysis with solar wind data and relativistic electron fluxes from the National Oceanic and Atmospheric Administration - Geostationary Operational Environmental Satellites (NOAA-GOES) satellites in geosynchronous orbit, they found that ICME sheaths were especially effective at driving outer belt losses, particularly in storm events in which the Dst effect is expected to act in concert with magnetopause incursions and outward radial transport. Kilpua et al. (2015) conducted a similar study with more events and organized the results by particular solar wind drivers. They found that the distinct characteristics associated with the different solar wind drivers corresponded to distinct responses by outer belt electrons. In particular, they found that the high pressure and strong magnetic fluctuations associated with stream interfaces and ICME sheaths and ejecta corresponded well to sudden losses of electrons observed by GOES. Those results are consistent with those of Ni et al. (2016), who used data from the GOES and Polar Operational Environmental Satellites (POES) satellites to study the outer belt response during 40 solar wind dynamic pressure pulse events. They found that electron losses are strongly correlated with sudden solar wind dynamic pressure increases, but that the losses were further enhanced when the Z-component of the IMF was also considered: southward Bz resulted in enhanced losses compared to northward Bz. Using observations from Solar, Anomalous, and Magnetospheric Particle Explorer (SAMPEX) during 110 ICME-driven storms, Yuan and Zong (2013) found consistent results: electron dropouts are strongest for events with enhanced solar wind dynamic pressure and southward IMF.

Using 193 dropout events and superposed epoch analysis with POES, GOES, and OMNI solar wind data, Gao et al. (2015) found the same result: either large solar wind dynamic pressure or southward IMF Bz is capable of driving dropouts. However, they argued that there were two different loss processes in action: the dynamic pressure resulted in loss by magnetopause incursions and outward radial transport while southward IMF Bz resulted in loss to Earth's atmosphere from interactions with electromagnetic ion cyclotron (EMIC) waves in the dusk MLT sector. Others have also found statistical evidence supporting the role of EMIC waves in dropout events. For example, Boynton et al. (2017) found that dropouts at $L \sim 4.2$ are more pronounced and frequent for >1 MeV electrons than for <1 MeV electrons. Despite EMIC waves also being an important cause of outer belt electron losses, there is additional evidence supporting the importance of outward radial transport and magnetopause losses. For example, Borovsky and Denton (2011) concluded that enhancements of energetic electrons in the near-Earth plasma sheet during high-speed–stream

driven storms were evidence of outer belt loss by outward radial transport, and Cohen et al. (2017) presented magnetospheric multiscale (MMS) observations of very energetic electrons streaming away from the magnetopause in the magnetosheath, including many events on the duskside of the system, which they concluded were direct evidence of magnetopause losses of outer belt electrons. From studies of outer belt electron response to 52 geomagnetic storms using Van Allen Probes data, Turner et al. (2015) and Moya et al. (2017) reported that often, loss of electrons started at higher *L*-shells and then moved in, consistent with losses by magnetopause incursions and outward radial transport.

After some dropout events, the outer radiation belt will redevelop such that it has two distinct peaks in intensity as a function of the *L*-shell (e.g., Baker et al., 2013). Turner et al. (2013) studied 53 geomagnetic storms and found such double outer belts during the recovery phase of 13 of those events. Using data from NASA's SAMPEX mission, Yuan and Zong (2013) found eight storms with double outer belts. From the observational evidence, Turner et al. (2013) presented a scenario to explain such double outer belt structures, in which outward radial transport plays a critical role. They showed evidence from Time History of Events and Macroscale Interactions during Substorms (THEMIS) of how a "remnant" belt can form at low *L*-shells ($L^* \sim 4$ or less) after strong dropout events. As the plasmasphere expands after the peak activity period, this remnant belt can be relatively shielded while a new outer radiation belt forms at *L*-shells beyond the plasmapause. The result of such a scenario is two outer radiation belts with distinct peaks in intensity (and phase space density). This scenario is consistent with the results of Goldstein et al. (2016), who studied a double outer belt case in January 2013. They found that the innermost belt was relatively stable inside the plasmasphere over several days around $L^* \sim 3.3$. The outermost belt formed outside the plasmasphere after a dropout event and was relatively dynamic. To summarize, remnant outer belts can form at lower *L*-shells as a result of magnetopause incursions and enhanced outward radial transport during dropout events, and the plasmasphere can play a critical role in sheltering those remnant belts and the formation of double outer belt structures. The plasmasphere can suppress loss by outward radial transport, likely owing to decreased ULF wave power within the plasmasphere, and can serve as a boundary separating remnant belts from any new outer radiation belts that form from acceleration processes active outside the plasmapause (e.g., Thorne et al., 2013).

1.2.2 Case studies

As discussed in the previous section, dropouts of outer radiation belt electrons are correlated with southward (i.e., negative Bz) IMF and sudden dynamic pressure increases in the solar wind (e.g., Ni et al., 2013, 2016), such as those that occur in interplanetary shocks and coronal-mass ejections (e.g., Hietala et al., 2014;

Kilpua et al, 2015; Lugaz et al., 2015) and high-pressure regions at the boundaries of high-speed solar wind streams (e.g., Borovsky and Denton, 2009). When the solar wind dynamic pressure increases suddenly, the magnetopause responds by rapidly compressing inward in an incursion on the inner magnetosphere. Southward IMF also contributes to magnetopause erosion on the dayside owing to active reconnection along the equatorial, dayside magnetopause. A telltale signature of loss by magnetopause incursions is a sharp negative gradient in the radial distribution of electrons accompanied by the very sudden decrease of electrons at any *L*-shells expected to be directly affected by a sudden inward motion of the magnetopause. A schematic of this loss scenario is shown in Fig. 1.4. A good way to examine this is in the time history of radial distributions (i.e., as a function of the third invariant, L^*) of electron phase space density for fixed values of the first and second adiabatic invariants, M and K, respectively (e.g., Turner and Angelopoulos, 2016).

Several case studies have now shown observational evidence consistent with this loss process. Using THEMIS data, Turner et al. (2013) examined in detail two cases with outer belt dropouts. From the case in April 2010, NASA's THEMIS mission (Angelopoulos, 2008) observed sharp negative gradients (sudden dropoffs over a very short range of L^*) in radial distributions of phase space density on April 11 (around $L^* = 6$) and again on April 14 (at $L^* \sim 6.7$); both periods were characterized by magnetopause incursions from enhanced solar wind dynamic pressure. One of the first studies of radiation belt dropouts using data from Van Allen Probes was conducted

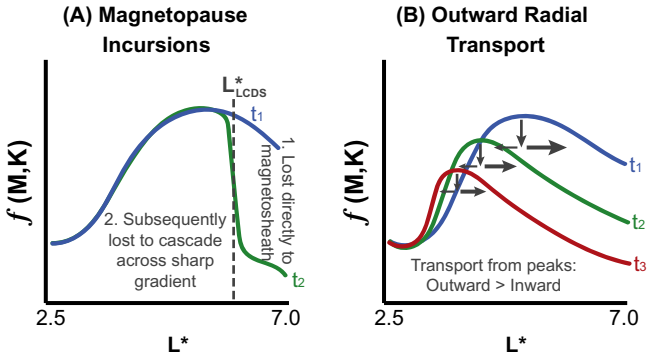

Figure 1.4 Schematics illustrating telltale signatures of loss by (A) magnetopause incursions and (B) outward radial transport. With radial (i.e., L^*) distributions of electron phase space density for fixed first and second adiabatic invariants, *f*(*M*,*K*), magnetopause incursions result in sudden loss of electrons at higher *L*-shells above the last closed drift shell (L^*_{LCDS}), as shown with the evolution of *f*(*M*,*K*) from some time, t_1, to subsequent time, t_2, illustrated with the *blue* and *red* curves. All those particles in region 1 are lost directly to the magnetosheath, while those in region 2 at $L^* < L^*_{LCDS}$ can be subsequently lost due to enhanced outward radial transport across the sharp gradient in *f*(*M*,*K*). In (B), outward radial transport affecting the initial distribution shown in the blue curve at some time, t_1, will result in the peak in *f*(*M*,*K*) moving to lower L^* and *f* over time, as illustrated with the *green* and *red* curves at two subsequent times.

by Turner et al. (2014a). They studied a dropout event on September 30, 2012, just after the launch of Van Allen Probes, which involved the loss of >90% of the entire preevent outer belt population of relativistic electrons. Again, sharp negative gradients were observed by both Van Allen Probes and THEMIS around the start of the dropout on September 30. From the multipoint capability with those two missions, Turner et al. (2014a) showed that these dropoffs in the radial distributions followed sudden enhancements of the solar wind dynamic pressure and moved inward from higher L^* to lower over time during the dropout, consistent with the magnetopause motion during that event. Zhang et al. (2016) and Su et al. (2017) studied another radiation belt dropout event on February 27, 2014. Sharp negative gradients in L^* distributions of relativistic electron phase space density were observed moving inward from L^* ~4.8 to ~4.5 by both Van Allen Probes during the magnetopause incursion from an interplanetary shock that impacted the magnetosphere. A very strong dropout was observed throughout the entire outer belt during the next 4 hours of that event and the investigators showed how drift shell splitting contributed to the dropout and evolution of observed pitch angle distributions. Su et al. (2016) used Van Allen Probes to study a dropout event from September 2013. In this event, Van Allen Probes directly observed the dropout of MeV electrons starting at apogee around $L\sim6$ and moving very rapidly inward to $L\sim5.5$ just after a magnetopause incursion. Xiang et al. (2017) examined a dropout event from June 2015, and also observed sharp negative gradients in relativistic electron phase space density immediately following a magnetopause incursion from a sudden enhancement of solar wind dynamic pressure; they concluded that magnetopause shadowing can be effective to very low L-shells ($L^*<4$) during some events. For those storm-time cases, it is important to note that these sharp negative gradients are often observed during the sudden storm commencement, when the magnetosphere is compressed and the Dst effect should not yet be resulting in the outward motion of drift shells. Thus, they represent indirect evidence of the magnetopause incursions alone, and they establish an important condition for enhanced outward radial transport to occur owing to a cascade of electrons across such a sharp gradient in the distribution.

Losses by outward radial transport also results in telltale signatures in L^* distributions of outer belt electron phase space density. If the outward radial transport is effectively diffusive in nature (e.g., Shprits et al., 2006), then for it to be effective as a loss process, there must be a negative gradient in the L^* distribution of phase space density at higher L-shells. If that is the case, then outward radial transport, which may be enhanced by ULF wave activity during active conditions, should result in a peak in outer belt distributions moving downward in magnitude and inward in L^* over time. Such an evolution in electron phase space density for fixed first and second adiabatic invariants was reported for a number of dropout events by Turner et al. (2013, 2014a), Li et al. (2014, 2016), Tu et al. (2014), Alves et al. (2016), Yu et al. (2015), Mann et al. (2016), Turner and Angelopoulos (2016), and Ozeke et al. (2017). Several

of these case studies also showed another telltale signature of losses by outward radial transport: consistent evolution of the L^* distribution of phase space density for a broad range of energies and equatorial pitch angles. For example, Boyd et al. (2014) showed that the main phase dropout was effective for all electrons with first adiabatic invariant values greater than $\sim$300 MeV/G down to $L^* = 4$. When coupled with sudden losses at higher L^* from magnetopause incursions (as was true for many of the cases referenced here) outward radial transport can be especially effective. As discussed in several of these papers and in the modeling results below, magnetopause incursions naturally result in a peaked distribution of outer belt electrons and a very sharp negative gradient in that distribution, both important criteria for enabling enhanced outward radial transport. At the sharp gradient in the radial distribution, there are very many more electrons (orders of magnitude) at lower L^* than there are at higher L^* on the other side of the gradient. If any radial transport of those electrons is enabled by ULF wave activity and/or drift orbit bifurcations, the abundance of electrons at lower L^* will cascade rapidly outward in L^* across the sharp gradient, since many, many more electrons are available to be transported outward than inward. This results in effective losses of electrons at L^* below that initially affected by the magnetopause incursion. It is this combination of magnetopause incursions and rapid outward radial transport that many have used to explain losses of outer belt electrons during dropout events.

While particularly effective at higher L-shells, magnetopause losses and outward radial transport cannot explain all losses observed during dropout events. Several studies have shown loss signatures that are inconsistent with losses by magnetopause incursions and/or outward radial transport. EMIC waves can theoretically result in very rapid loss of outer radiation belt electrons due to gyroresonant scattering in pitch angle and diffusion toward the atmospheric loss cone (e.g., Thorne, 2010; Ukhorskiy et al., 2010). Unlike losses from magnetopause incursions, losses by interactions with EMIC waves should be highly dependent on electron energy and pitch angle, as was confirmed observationally by Usanova et al. (2014) in a series of events observed by Van Allen Probes in October and November 2012. Using a combination of NOAA-POES and space- and ground-based observations of EMIC waves, Rodger et al. (2015) and Hendry et al. (2016) observed simultaneous relativistic electron precipitation and EMIC waves, further supporting their importance as outer belt loss mechanisms. Yu et al. (2015) examined a case from October 31 to November 1, 2012, with Van Allen Probes and NOAA-POES data and found that losses during sudden storm commencement revealed a pitch-angle dependency, with more field-aligned $>$2 MeV electrons being lost at all $L^* > 5$, but electrons with pitch angles between 30 and 150 degrees were lost predominantly at higher L-shells. Alongside supporting wave data from Van Allen Probes, they interpreted this as the result of EMIC waves scattering the field-aligned electrons while magnetopause incursions and outward transport affected the bulk of the trapped population at pitch angles closer to 90 degrees. Essentially, EMIC waves are most efficient for losses of highly relativistic (several MeV; high-M) electrons that have mirror points further off

the magnetic equator (high-K); outer belt electrons with lower energies ($< \sim$1 MeV) and equatorial pitch angles near 90 degrees (low-K) are largely unaffected by EMIC waves under most conditions.

Again, examining the history of L^* distributions of electron phase space density for fixed M and K can distinguish signatures of EMIC losses. Shprits et al. (2017a) and Aseev et al. (2017) presented multiple cases of strong outer radiation belt losses in Van Allen Probes data that were consistent with scattering from EMIC waves: the losses were only for multi-MeV (M of several 1000 MeV/G) electrons at high-K and with L^* distributions that showed losses resulting in deepening localized minima. In their study of the February 2014 dropout event, Su et al. (2017) argued that a depletion of outer belt phase space density (PSD) across the entire preevent outer belt could result in the observed monotonically increasing distribution only if EMIC waves also contributed to the loss process, since outward radial transport should result in an enhancement of phase space density at lower L^*. Turner et al. (2014a,b) reported that, while the majority of losses observed from the September 30, 2012, dropout case were consistent with magnetopause incursion and rapid outward transport, the highest energy electrons observed (several MeV) displayed rapid loss that was both energy and pitch angle dependent; they concluded that the losses were consistent with rapid scattering of several MeV electrons with higher second invariant values (i.e., mirroring farther off the magnetic equator) by EMIC waves. Using data from seven spacecraft during a geomagnetic storm on November 12−14, 2012, Sigsbee et al. (2016) observed evidence that both magnetopause losses and scattering by EMIC waves were responsible for electron losses from the outer radiation belt. From a dropout event in February 2014, Xiang et al. (2017) found that EMIC waves were likely the dominant loss mechanism during the dropout and that the waves were effective for losses over a broad range of L^*; they also concluded, by studying three different dropout events in detail, that dropouts can result from a combination of loss processes dominated by either magnetopause losses and outward radial transport or EMIC losses.

From both the recent statistical evidence and this series of new observational results from in-depth case studies, it is apparent that the community is still somewhat divided on exactly how and why losses in some outer belt dropout events are dominated by magnetopause incursions and enhanced outer radial transport while others are dominated by losses from interactions with EMIC waves. Furthermore, there are interesting aspects of and questions concerning just how outer belt electrons are lost through the thermal ion scale boundary that is the magnetopause. Interesting aspects and outstanding questions also concern various mechanisms that result in outward radial transport and how it can also serve as an effective loss mechanism during nondropout events. These aspects and questions can best be addressed with advances in modeling of the outer electron radiation belt system, and in the next section, we review some of the most recent advances in outer belt modeling and simulations.

1.3 New modeling approaches and results

In this section, we briefly review recent developments of radiation belt models and the results produced from simulations with these models. In particular, we focus on the models that attempt to capture various aspects of magnetopause losses and outward radial transport and the relative levels of loss by those processes compared with loss by interactions with EMIC waves.

1.3.1 Losses of electrons to the magnetopause

Earth's magnetopause is an ion scale boundary, with a thickness on the order of 100s to $\sim$1000 km or several thermal ion gyroradii (e.g., Le and Russell, 1994). In an ideal state under northward IMF, the magnetopause is a current sheet allowing no magnetic connectivity on the dayside of the system. Given a boundary that is much thicker than electron gyroradii and ideally with no magnetic connectivity under northward IMF, one may ask how exactly outer belt electrons escape through the magnetopause, which is a topic that was investigated in two recent studies that are discussed next.

Kim and Lee (2014) developed simplified models of the magnetopause and used test-particle simulations with those models to test how relativistic electrons from the outer radiation belt can escape through the magnetopause. They tested two different magnetopause models: one with no normal component of—but including a finite gradient in—the magnetic field across the boundary (as in an ideal tangential discontinuity under northward IMF) and another with a finite normal component across the boundary (simulating an "open" magnetopause boundary that has undergone reconnection with sheath plasma under southward IMF). In the first case, they found that electrons could be lost by gradient drifting through the boundary. However, for that case, they also found that the loss process was energy dependent, with only higher energy electrons being able to escape through a magnetopause with larger scale-lengths of the magnetic gradient. With the second simulation, they found electron loss to be much more efficient and relatively independent of energy, allowing electrons to escape at energies at least as low as 500 keV. With those simulations, they also showed that even a very small normal component ($<$1 nT) was sufficient to enable loss across the boundary. In both cases, they showed that the loss also depended on the electrons' pitch angle and the direction of the magnetic field in the sheath. They concluded that a normal component of the magnetic field across the magnetopause (say, during ongoing reconnection in southward IMF) can enable substantial loss of outer radiation belt electrons.

Mauk et al. (2016) also used test particles with a simplified model of the magnetopause to study how energetic particles are lost across that boundary. Their model assumes a small but finite normal component of the magnetic field across the magnetopause. These investigators were careful to use only analytical functions for their model; in order to handle the magnetic connectivity between arbitrary field orientations on the

magnetosphere and magnetosheath sides; they employed the error function, which resulted in smooth rotations between the field lines on either side of the boundary. They found that test particles (50-keV electrons and protons over a range of pitch angles) escaped effectively from the magnetosphere side without invoking any additional perturbations to the system (e.g., waves, temporal structures) for both northern and southern orientations of the magnetosheath field. Depending on their initial conditions, test particles escaped in a variety of ways, both very suddenly with little motion along the boundary or slowly and gradually over time via a prolonged drift or meandering motion along the boundary. They also found a pitch-angle dependence to the loss process, which was consistent with the observational findings of Cohen et al. (2016).

Sorathia et al. (2017) investigated energetic particle interaction and escape through the magnetopause boundary with the use of three-dimensional test particle simulations in a high-resolution global magnetohydrodynamic (MHD) magnetospheric model. In agreement with the Cohen et al. (2016) results, Sorathia et al., showed that electrons can be lost on the either side of the noon−midnight meridian. An important part in the loss process is the Kelvin−Helmholtz instabilities, since vortices that form along the flanks of the magnetopause can trap particles and redistribute them, facilitating magnetopause loss.

1.3.2 Losses by outward radial transport

Nonadiabatic outward radial transport, which naturally results in loss of radiation belt electrons due to deceleration (if nothing else), can be enabled by any process that invalidates the third adiabatic invariant, provided that there is a negative gradient in the electron radial distribution. One such process was investigated by Ukhorskiy et al. (2011). Using three-dimensional, relativistic test-particle simulations in realistic global models of Earth's magnetosphere, these authors studied the effect of drift orbit bifurcations on electrons in Earth's outer radiation belt. Unlike throughout the rest of the magnetosphere, field lines at higher L-shells ($L > \sim 6$) on Earth's dayside magnetosphere often have two localized magnetic minima that do not fall on the magnetic equatorial plane. Such field geometries result from the compression of the dayside magnetosphere from solar wind driving, and when electrons in a particular range of pitch-angle space encounter such field geometries, their drift orbits can bifurcate such that they mirror around one of the two off-equatorial magnetic minima. Ukhorskiy et al. (2011) showed that while most electrons stay quasi-trapped on bifurcated drift shells for long periods, these drift orbit bifurcations resulted in outward radial transport and ultimately loss through the magnetopause for a significant subset of the test electrons. Ukhorskiy et al. (2014) followed up with a more detailed study that showed how the radial transport rates of electrons on bifurcated drift orbits were an order of magnitude higher and exhibited strong deviations compared to the diffusion approximation, particularly for electrons with larger equatorial pitch angles (i.e., closer to 90 degrees).

Hudson et al. (2014) also used test particle simulations in global magnetospheric fields generated with the Lyon–Fedder–Mobarry MHD model coupled to the Rice Convection Model. They studied three dropouts observed by Van Allen Probes during the period September–October 2012. They found that all three dropouts could be explained by losses from magnetopause incursions and outward radial diffusion enhanced by ULF wave activity and drift shell splitting. Hudson et al. (2015) conducted similar simulations of the March 17 and October 8, 2013, storms, both driven by ICMEs, and found consistent results. Furthermore, they provided additional detail on the complex role of ULF waves in enabling outward radial transport during dropout events. Test-particle simulations in realistic global magnetospheric fields were also employed by Ukhorskiy et al. (2015) to examine outer radiation belt depletions during geomagnetic storms. They simulated the March 17, 2013, storm and found that the majority of electrons were lost to the magnetopause owing to outward radial transport during the main phase of the storm. The losses were further enabled by drift shell expansion due to the enhanced storm-time ring current (i.e., the Dst effect). From comparisons between the simulations and data from NASA's Van Allen Probes mission, they found that the losses to the magnetopause could account for most of the observed depletions at $L > 5$, but the observed variations were mostly adiabatic at lower L-shells.

Sorathia et al. (2018) developed a new global three-dimensional test-particle model of the outer radiation belt and used it to simulate the 2013 St. Patrick's Day Storm. Similarly to earlier studies (e.g., Hudson et al., 2014) test-particle motion was computed in the electromagnetic fields from the coupled MHD-ring-current model. However, the only boundary conditions used by Sorathia et al. (2018) were the L1 solar wind data; the information of electron phase space densities was inferred directly from the MHD simulations. The model well reproduced evolution of the outer belt during the storm: the cycle of depletion, enhancement, and eventual saturation to final poststorm levels. They showed that the overwhelming majority of the prestorm electron population was permanently lost from the belt via escape through the magnetopause boundary. This suggests that the poststorm outer belt is largely independent of the prestorm population and is created through a series of injection and acceleration events during storm recovery.

Outward radial transport can also result from radial diffusion (e.g., Shprits et al., 2006; Loto'aniu et al., 2010), and many recent studies have focused on that mechanism for radiation belt loss. Yu et al. (2013) also employed a one-dimensional radial diffusion model to study radiation belt dropouts. They found that during events driven by high-speed solar wind streams, magnetopause losses and outward radial transport could account for 60%–99% of losses during corresponding dropout events near geosynchronous orbit, but that some additional loss process was required to explain dropout losses at $L^* < 5$. Herrera et al. (2016) added magnetopause losses to the Salammbo

code developed and maintained by ONERA. With that addition, their simulations showed that magnetopause incursions and outward radial transport are the dominant loss mechanism during dropout events, which they also supported using a superposed epoch analysis of NOAA-POES electron fluxes.

Using the three-dimensional DREAM3D diffusion model developed at Los Alamos National Lab, Tu et al. (2014) studied the large, double-dip geomagnetic storm of October 8–9, 2012. Using data-driven boundary conditions and event-specific inputs, they found that the main phase dropout was due to outward radial transport and magnetopause losses. They also stressed that event-specific inputs and boundary conditions were necessary to simulate the event; simulations using statistical and parameterized inputs failed to reproduce the evolution of the outer radiation belt electrons during the storm. Schiller et al. (2017) came to the same conclusions with regard to event-specific inputs for radiation belt simulations when using diffusion models. They simulated the January 13–15, 2013, event and isolated transport, loss, and source processes in a one-dimensional radial diffusion model with data-assimilative capability employing a Kalman filter. When compared to models driven by terms parameterized by geomagnetic indices, the event-specific model far outperformed (by several orders of magnitude) the parameterized models. Kang et al. (2018) used the 4D Comprehensive Inner Magnetosphere-Ionosphere model, which is also driven by event-specific inputs via the Tsyganenko and Sitnov (2005) model. Simulating the dropout event from June 1, 2013 (i.e., the example event from Figs. 1.2, 1.3, and 1.5), they concluded that the dropout

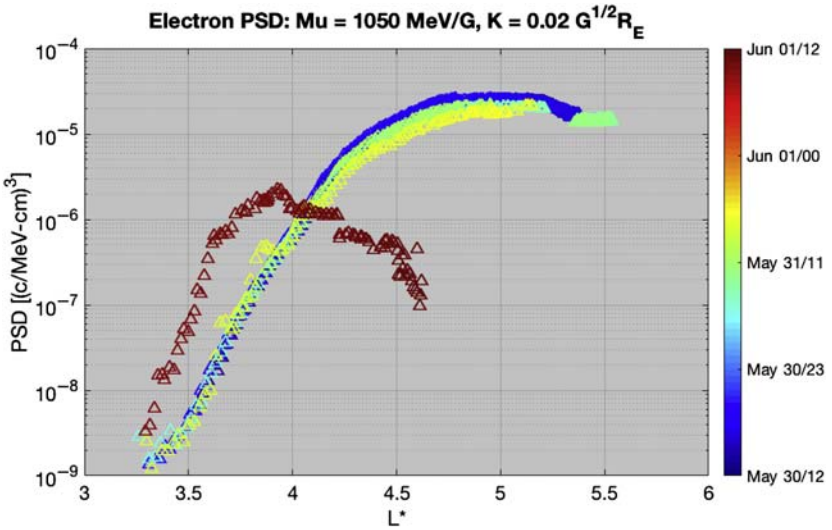

Figure 1.5 Evolution of $f(M,K)$ for $M = 1050$ MeV/G and $K = 0.02$ G1/2RE during the dropout event from June 1, 2013. Distributions at different colors represent different times throughout the event as labeled on the color bar. This dropout event was most likely dominated by losses from magnetopause incursion and enhanced outward radial transport.

occurred owing to the combination of immediate losses at high L-shells from the magnetopause incursion and subsequent losses extending to $L < 8$ via outward radial transport and further drift loss to the magnetopause.

Mann et al. (2016) used a one-dimensional radial diffusion model with a data-driven outer boundary condition and diffusion coefficients derived from ground-based magnetometer observations. They simulated the dropout and subsequent enhancement of the outer radiation belt that resulted in the remnant belt period of early September 2012 reported by Baker et al. (2013) and Thorne et al. (2013). They showed that with the data-driven and time-dependent diffusion coefficients representing radial transport of electrons from interactions with ULF waves, the dropout of several MeV electrons on September 2, 2012, could be effectively simulated with only magnetopause losses at the outer boundary and subsequent rapid outward radial transport. Ozeke et al. (2017) studied a prolonged dropout event in September 2014 using the same model as that used by Mann et al. (2016), and they too found that outward radial diffusion driven by ULF waves was critical to maintaining losses of outer belt electrons throughout the >10-day period. Both Mann et al. (2016) and Ozeke et al. (2017) used event-specific inputs for the model boundary conditions and radial diffusion coefficients, which they stressed were critical to accurately simulating the events.

1.3.3 Quantifying the relative importance of different loss mechanisms during dropouts

There is still an ongoing debate in the community concerning the relative importance of various loss processes during dropout events. As discussed throughout this chapter, there is much evidence in the most recent literature to support how magnetopause incursions and outward radial transport are the dominant loss mechanism during dropouts. However, other recent studies during the Van Allen Probes era have concluded that outer belt electron losses to the atmosphere from interactions with EMIC waves can also be dominant during dropouts. For example, Shprits et al. (2013) simulated the same remnant belt event from September 2012 that was simulated by Mann et al. (2016). Shprits et al. (2013) used the VERB three-dimensional diffusion model developed at UCLA, which did not include magnetopause losses or incursion into the simulation domain. To simulate the dropout of several MeV electrons observed by Van Allen Probes, they had to include strong losses by EMIC waves, and they stressed the importance of considering energy dependencies of various outer radiation belt processes. Drozdov et al. (2015) used the VERB model, including magnetopause losses, to simulate 1 year of outer radiation belt dynamics and compared the results to Van Allen Probes data. They too stressed the energy dependence of the results: 0.5–1 MeV electrons were well captured by the model, but additional losses from EMIC waves were needed to get good agreement for the multi-MeV electrons. Recent theory and modeling efforts, such as Pham et al. (2017), Mourenas et al. (2016),

Kubota and Omura (2016), and Kang et al. (2016), further stress the importance of losses of several MeV electrons from interactions with EMIC waves during dropout events.

From the evidence reported in the literature, it is most likely that losses from both magnetopause incursions and outward transport and atmospheric precipitation from EMIC waves are important for MeV electrons in Earth's outer radiation belt, as stressed in Xiang et al. (2017), who studied three dropout events and found evidence that some dropout events are dominated by magnetopause losses and outward radial transport, which, they reported, can also affect very low L-shells ($L^* < 4$), while others are dominated by losses to the atmosphere from scattering by EMIC waves. This leads to one of many outstanding questions concerning the importance of various loss processes of outer radiation belt electrons: what solar wind and magnetospheric conditions are most important for strong losses dominated by magnetopause incursions and outward radial transport versus by EMIC waves? In the next section, we further detail this and several other important outstanding questions.

1.4 Outstanding questions and suggestions for future studies

As discussed in this chapter, many case studies have been conducted showing that both magnetopause incursions and outward radial transport and precipitation losses from interactions with EMIC waves can dominate outer belt losses for electrons at particular invariant coordinates, M, K, and L^*. However, it remains unclear just which solar wind and geomagnetic conditions favor events in which one particular loss mechanism dominates another. Furthermore, with regard to the relative importance of losses from magnetopause incursions and outward radial transport compared to those from EMIC waves, it is important to next address this from a statistical approach. In particular, what is the statistical relevance of each loss process as a function of M, K, and L^*? That is, for electrons at any particular set of M, K, and L^*, what fraction of that population of electrons is lost by each process in the average dropout event, and what are the interquartile and 5%–95% confidence ranges of relative loss ratios (i.e., fraction of preevent population lost to the magnetopause and outward transport vs. the fraction lost to EMIC waves) based on a statistically relevant set of events? With Van Allen Probes plus THEMIS and/or MMS, there is now a large enough set of dropout events and data coverage (in M, K, and L^*) to address these questions with statistical studies.

Multiple mechanisms have been identified as being potentially important for driving outward radial transport of outer radiation belt electrons. However, an important question remains concerning the relative importance of each with respect to one another. Outward radial transport may be enabled by drift-resonant interactions with ULF waves, drift-bounce resonance with ULF waves, and nonadiabatic transport in

bifurcated drift orbits, but which of those mechanisms is the dominant contributor to outward radial transport of radiation belt electrons? This question may be addressed using a combination of test-particle simulations in dynamic global magnetospheric fields that capture the necessary ULF waves and dayside field geometries and multipoint observations from a combination of spacecraft such as Van Allen Probes (to capture the core outer belt population and evolution), geosynchronous satellites (good local time coverage), and MMS and THEMIS (to capture electron distributions and wave activity beyond geosynchronous orbit).

Based on the modeling work of Kim and Lee (2014) and Mauk et al. (2016) and the observational evidence reported in Cohen et al. (2016, 2017), there are still many outstanding questions concerning the nature of electron loss at the magnetopause. In particular, THEMIS and/or MMS data can be used to further test more of the predictions made by Kim and Lee (2014) and Mauk et al. (2016). Comparing the relative intensities of THEMIS and/or MMS observations of energetic electron streaming in the magnetosheath during dropout periods when magnetopause losses are known to be occurring (e.g., the June 1, 2013, case presented here) and during normal, nondropout periods will provide a measure of how many outer belt electrons may be lost to the outer boundary during dropouts. It is also important to study the relative importance and nature of outer belt electron losses through the magnetopause under average and quiet solar wind conditions. Kavosi et al. (2018) concluded that Kelvin–Helmholtz vortices and FTEs may be important for losses of electrons along the dayside flanks of the magnetopause, which, they argued, are responsible for the distinct field-aligned nature and repetitive timing of electron microinjection signatures reported in the premidnight MLT sector at high L-shells ($L \sim 9$ to 12) reported by Fennell et al. (2016).

Finally, it is also important to consider the role of outward radial transport as a mechanism that can balance active sources of relativistic electrons within the heart of the outer radiation belt. Internal sources of relativistic electrons, such as local acceleration by whistler-mode chorus (e.g., Thorne et al., 2013), result in growing peaks of phase space density somewhere near the heart of the belt (L^* from 4 to 5) as reported by many during the Van Allen Probes era (e.g., Turner et al., 2013; Reeves et al., 2013; Boyd et al., 2014; Schiller et al., 2014; Li et al., 2016). Once such a peak in the radial distribution of electron phase space density forms, outward radial diffusion from the peak location to higher L^* should act to balance any ongoing source activity and redistribute accelerated electrons at affected M and K to higher L^* (albeit at lower energies). Such outward radial transport should result in the flattening over time of initially peaked phase space density distributions in L^*, as has been reported previously (e.g., Turner et al., 2013). However, just how much an active internal source might be balanced—or overcome—by outward radial transport remains an important outstanding question that can now be addressed with a combination of modeling efforts and observational studies.

1.5 Conclusion

This chapter has focused on the most recent results concerning the loss of outer radiation belt electrons via magnetopause incursions and outward radial transport. We have use the term *magnetopause incursion* instead of the traditional term *magnetopause shadowing* because shadowing implies that all electrons are lost at the subsolar point or along the magnetopause at earlier MLT, which has been shown to not be the case in general. Many cases have been presented showing that magnetopause incursions and outward radial transport can serve as the dominant loss process during sudden dropouts of the outer radiation belt, and these results have been backed up with statistical studies and magnetopause loss models stressing the importance of sudden enhancements of solar wind dynamic pressure and southward IMF in enabling losses of outer belt electrons. However, a debate is ongoing concerning the relative importance of magnetopause incursions and outward radial transport versus precipitation losses to Earth's atmosphere from interactions with EMIC waves as the dominant loss mechanism active during dropout events—let alone as loss processes for nondropout periods. Both mechanisms are clearly important, but statistical studies are now needed to address the many outstanding questions concerning their relative importance, in particular for electrons as a function of invariant coordinates (M, K, and L^*). Other outstanding questions and areas for future study include which physical mechanism is most important for driving outward radial transport, the nature of electron losses across the magnetopause itself, and how outward radial transport and magnetopause losses can act to balance or overcome an active source of relativistic electrons within the outer radiation belt.

Many of the outstanding questions can be addressed with simulations using advanced models of the magnetosphere and outer radiation belt electron dynamics. More comprehensive models should be developed to better capture each of the important physical mechanisms discussed throughout this chapter. In particular, test-particle simulations in realistic global magnetospheric fields are ideal for capturing outward radial transport driven by drift resonance and drift-bounce resonance with ULF waves and bifurcated drift shells, but higher field-model resolution may be necessary to accurately capture the actual escape through the magnetopause. Also, until EMIC waves can be properly generated and captured or realistically imposed in the global models of the magnetosphere, that loss mechanism cannot be tested appropriately with test-particle simulations. Diffusion models are still ideal for simulations of long periods (months to years), and they can effectively model losses by EMIC waves in a statistical manner. However, they fail to accurately capture important effects such as magnetopause losses and transport from bifurcated drift orbits, and diffusion models are too limited by the location and treatment of the time-dependent outer radial boundary condition, which is often set very close to (far from) the heart of the outer radiation belt (the last closed drift shell).

Fortunately, we are in an unprecedented era of observations within Earth's magnetosphere. Recent missions such as NASA's THEMIS, MMS, and Van Allen Probes and JAXA's Arase add to the constellation of Los Alamos and NOAA geosynchronous and Low-Earth orbit (LEO) spacecraft plus CubeSats and high-altitude balloon campaigns, such as the Balloon Array for Radiation-belt Relativistic Electron Losses (BARREL) mission, to provide more comprehensive coverage of radiation belt electrons and relevant magnetospheric processes than has ever before been available. With such an array of observatories, many of the outstanding questions concerning the nature of outer belt electron losses via magnetopause incursions and outward radial transport and the relative importance of losses via interactions with EMIC waves can now be addressed.

Acknowledgments

The authors are thankful for support from the NASA contract for Van Allen Probes (NAS5-01072). We also thank each of the Van Allen Probes instrument teams for their respective data products, and the ACE, Wind, and OMNI teams for solar wind and geomagnetic data.

References

Alves, L.R., et al., 2016. Outer radiation belt dropout dynamics following the arrival of two interplanetary coronal mass ejections. Geophys. Res. Lett. 43. Available from: https://doi.org/10.1002/2015GL067066.

Angelopoulos, V., 2008. The THEMIS mission. Space Sci. Rev. 141, 5–34. Available from: https://doi.org/10.1007/s11214-008-9336-1.

Aseev, N.A., Shprits, Y.Y., Drozdov, A.Y., Kellerman, A.C., Usanova, M.E., Wang, D., et al., 2017. Signatures of ultrarelativistic electron loss in the heart of the outer radiation belt measured by Van Allen Probes. J. Geophys. Res. Space Phys. 122. Available from: https://doi.org/10.1002/2017JA024485. 10, 102–110, 111.

Baker, D.N., et al., 2013. A long-lived relativistic electron storage ring embedded in Earth's outer Van Allen Belt. Science 340, 186–190.

Baker, D.N., Kanekal, S.G., Li, X., Monk, S.P., Goldstein, J., Burch, J.L., 2004. An extreme distortion of the Van Allen belt arising from the 'Hallowe'en' solar storm in 2003. Nature 432, 878–881.

Blake, J.B., Kolasinski, W.A., Fillius, R.W., Mullen, E.G., 1992. Injection of electrons and protons with energies of tens of MeV into $L < 3$ on 24 March 1991. Geophys. Res. Lett. 19, 821–824.

Borovsky, J.E., Denton, M.H., 2009. Relativistic-electron dropouts and recovery: a superposed epoch study of the magnetosphere and the solar wind. J. Geophys. Res. 114, A02201. Available from: https://doi.org/10.1029/2008JA013128.

Borovsky, J.E., Denton, M.H., 2011. Evolution of the magnetotail energetic-electron population during high-speed-stream-driven storms: evidence for the leakage of the outer electron radiation belt into the Earth's magnetotail. J. Geophys. Res. 116, A12228. Available from: https://doi.org/10.1029/2011JA016713.

Borovsky, J.E., Denton, M.H., 2016. Compressional perturbations of the dayside magnetosphere during high-speed-stream-driven geomagnetic storms. J. Geophys. Res. Space Phys. 121. Available from: https://doi.org/10.1002/2015JA022136.

Bortnik, J., Thorne, R.M., Inan, U.S., 2008. Nonlinear interaction of energetic electrons with large amplitude chorus. Geophys. Res. Lett. 35, L21102. Available from: https://doi.org/10.1029/2008GL035500.

Boyd, A.J., Spence, H.E., Claudepierre, S.G., Fennell, J.F., Blake, J.B., Baker, D.N., et al., 2014. Quantifying the radiation belt seed population in the March 17, 2013 electron acceleration event. Geophys. Res. Lett. 41. Available from: https://doi.org/10.1002/2014GL059626.

Boyd, A.J., Spence, H.E., Huang, C.-L., Reeves, G.D., Baker, D.N., Turner, D.L., et al., 2016. Statistical properties of the radiation belt seed population. J. Geophys. Res. Space Phys. 121. Available from: https://doi.org/10.1002/2016JA022652.

Boynton, R.J., Mourenas, D., Balikhin, M.A., 2017. Electron flux dropouts at $L \sim 4.2$ from global positioning system satellites: occurrences, magnitudes, and main driving factors. J. Geophys. Res. Space Phys. 122. Available from: https://doi.org/10.1002/2017JA024523.

Chaston, C.C., Bonnell, J.W., Wygant, J.R., Reeves, G.D., Baker, D.N., Melrose, D.B., 2018. Radiation belt "dropouts" and drift-bounce resonances in broadband electromagnetic waves. Geophys. Res. Lett. 45. Available from: https://doi.org/10.1002/2017GL076362.

Cohen, I.J., et al., 2016. Observations of energetic particle escape at the magnetopause: early results from the MMS energetic ion spectrometer (EIS). Geophys. Res. Lett. 43. Available from: https://doi.org/10.1002/2016GL068689.

Cohen, I.J., et al., 2017. Statistical analysis of MMS observations of energetic electron escape observed at/beyond the dayside magnetopause. J. Geophys. Res. Space Phys. 122, 9440–9463. Available from: https://doi.org/10.1002/2017JA024401.

Dessler, A.J., Karplus, R., 1961. Some effects of diamagnetic ring currents on Van Allen radiation. J. Geophys. Res. 66, 2289–2295.

Drozdov, A.Y., Shprits, Y.Y., Orlova, K.G., Kellerman, A.C., Subbotin, D.A., Baker, D.N., et al., 2015. Energetic, relativistic, and ultrarelativistic electrons: comparison of long-term VERB code simulations with Van Allen Probes measurements. J. Geophys. Res. Space Phys. 120. Available from: https://doi.org/10.1002/2014JA020637.

Fennell, J.F., et al., 2016. Microinjections observed by MMS FEEPS in the dusk to midnight region. Geophys. Res. Lett. 43. Available from: https://doi.org/10.1002/2016GL069207.

Fennell, J.F., Claudepierre, S.G., Blake, J.B., O'Brien, T.P., Clemmons, J.H., Baker, D.N., et al., 2015. Van Allen Probes show that the inner radiation zone contains no MeV electrons: ECT/MagEIS data. Geophys. Res. Lett. 42. Available from: https://doi.org/10.1002/2014GL062874.

Friedel, R.H.W., Reeves, G.D., Obara, T., 2002. Relativistic electron dynamics in the inner magnetosphere—a review. J. Atmos. Sol.-Terr. Phys. 64, 265–282.

Gao, X., Li, W., Bortnik, J., Thorne, R.M., Lu, Q., Ma, Q., et al., 2015. The effect of different solar wind parameters upon significant relativistic electron flux dropouts in the magneto- sphere. J. Geophys. Res. Space Phys. 120. Available from: https://doi.org/10.1002/2015JA021182.

Goldstein, J., et al., 2016. The relationship between the plasmapause and outer belt electrons. J. Geophys. Res. Space Phys. 121, 8392–8416. Available from: https://doi.org/10.1002/2016JA023046.

Hendry, A.T., Rodger, C.J., Clilverd, M.A., Engebretson, M.J., Mann, I.R., Lessard, M.R., et al., 2016. Confirmation of EMIC wave-driven relativistic electron precipitation. J. Geophys. Res. Space Phys. 121. Available from: https://doi.org/10.1002/2015JA022224.

Herrera, D., Maget, V.F., Sicard-Piet, A., 2016. Characterizing magnetopause shadowing effects in the outer electron radiation belt during geomagnetic storms. J. Geophys. Res. Space Phys. 121, 9517–9530. Available from: https://doi.org/10.1002/2016JA022825.

Hietala, H., Kilpua, E.K.J., Turner, D.L., Angelopoulos, V., 2014. Depleting effects of ICME-driven sheath regions on the outer electron radiation belt. Geophys. Res. Lett. 41. Available from: https://doi.org/10.1002/2014GL059551.

Hudson, M.K., Baker, D.N., Goldstein, J., Kress, B.T., Paral, J., Toffoletto, F.R., et al., 2014. Simulated magnetopause losses and Van Allen Probe flux dropouts. Geophys. Res. Lett. 41, 1113–1118. Available from: https://doi.org/10.1002/2014GL059222.

Hudson, M.K., Paral, J., Kress, B.T., Wiltberger, M., Baker, D.N., Foster, J.C., et al., 2015. Modeling CME-shock-driven storms in 2012–2013: MHD test particle simulations. J. Geophys. Res. Space Phys. 120, 1168–1181. Available from: https://doi.org/10.1002/2014JA020833.

Kang, S.-B., Fok, M.-C., Glocer, A., Min, K.-W., Choi, C.-R., Choi, E., et al., 2016. Simulation of a rapid dropout event for highly relativistic electrons with the RBE model. J. Geophys. Res. Space Phys. 121. Available from: https://doi.org/10.1002/2015JA021966.

Kang, S.-B., Fok, M.-C., Komar, C., Glocer, A., Li, W., Buzulukova, N., 2018. An energetic electron flux dropout due to magnetopause shadowing on 1 June 2013. J. Geophys. Res. Space Phys. 123, 1178–1190. Available from: https://doi.org/10.1002/2017JA024879.

Kavosi, S., Spence, H.E., Fennell, J.F., Turner, D.L., Connor, H.K., Raeder, J., 2018. MMS/FEEPS observations of electron microinjections due to Kelvin-Helmholtz waves and Flux Transfer Events: A case study. JGR: Space Physics 123.

Kilpua, E.K.J., Hietala, H., Turner, D.L., Koskinen, H.E.J., Pulkkinen, T.I., Rodriguez, J.V., et al., 2015. Unraveling the drivers of the storm time radiation belt response. Geophys. Res. Lett. 42. Available from: https://doi.org/10.1002/2015GL063542.

Kim, H.-J., Chan, A.A., 1997. Fully adiabatic changes in storm-time relativistic electron fluxes. J. Geophys. Res. 102, 22,107–22,116.

Kim, K.-C., Lee, D.-Y., 2014. Magnetopause structure favorable for radiation belt electron loss. J. Geophys. Res. Space Phys. 119. Available from: https://doi.org/10.1002/2014JA019880.

Kim, K.C., Lee, D.-Y., Kim, H.-J., Lyons, L.R., Lee, E.S., Ozturk, M.K., et al., 2008. Numerical calculations of relativistic electron drift loss effect. J. Geophys. Res. 113, A09212. Available from: https://doi.org/10.1029/2007JA013011.

Kim, K.C., Lee, D.-Y., Kim, H.-J., Lee, E.S., Choi, C.R., 2010. Numerical estimates of drift loss and Dst effect for outer radiation belt relativistic electrons with arbitrary pitch angle. J. Geophys. Res. 115, A03208. Available from: https://doi.org/10.1029/2009JA014523.

Kubota, Y., Omura, Y., 2016. Rapid precipitation of radiation belt electrons induced by EMIC rising tone emissions localized in longitude inside and outside the plasmapause. J. Geophys. Res. Space Phys. 122. Available from: https://doi.org/10.1002/2016JA023267.

Le, G., Russell, C.T., 1994. The thickness and structure of high beta magnetopause current layer. Geophys. Res. Lett. 21, 2451–2454.

Li, X., et al., 1997. Multisatellite observations of the outer zone electron variation during the November 3–4, 1993, magnetic storm. J. Geophys. Res. 102, 14,123–14,140.

Li, W., et al., 2014. Radiation belt electron acceleration by chorus waves during the 17 March 2013 storm. J. Geophys. Res. Space Phys. 119. Available from: https://doi.org/10.1002/2014JA019945.

Li, W., et al., 2016. Radiation belt electron acceleration during the 17 March 2015 geomagnetic storm: observations and simulations. J. Geophys. Res. Space Phys. 121. Available from: https://doi.org/10.1002/2016JA022400.

Li, X., Selesnick, R., Schiller, Q., Zhang, K., Zhao, H., Baker, D.N., et al., 2017. Measurement of electrons from albedo neutron decay and neutron density in near-Earth space. Nature. Available from: https://doi.org/10.1038/nature24642.

Loto'aniu, T.M., Singer, H.J., Waters, C.L., Angelopoulos, V., Mann, I.R., Elkington, S.R., et al., 2010. Relativistic electron loss due to ultralow frequency waves and enhanced outward radial diffusion. J. Geophys. Res. 115, A12245. Available from: https://doi.org/10.1029/2010JA015755.

Lugaz, N., Farrugia, C.J., Huang, C.-L., Spence, H.E., 2015. Extreme geomagnetic disturbances due to shocks within CMEs. Geophys. Res. Lett. 42, 4694–4701. Available from: https://doi.org/10.1002/2015GL064530.

Lyons, L.R., Thorne, R.M., 1973. Equilibrium structure of radiation belt electrons. J. Geophys. Res. 78, 2142–2149.

Mann, I.R., et al., 2016. Explaining the dynamics of the ultra-relativistic third Van Allen radiation belt. Nat. Phys. 12. Available from: https://doi.org/10.1038/NPHYS3799.

Mann, I.R., et al., 2018. Correspondence: the dynamics of Van Allen belts revisited. Nat. Phys. 14, 102–104.

Mauk, B.H., Fox, N.J., Kanekal, S.G., Kessel, R.L., Sibeck, D.G., Ukhorskiy, A., 2012. Science objectives and rationale for the Radiation Belt Storm Probes mission. Space Sci. Rev. Available from: https://doi.org/10.1007/s11214-012-9908-y.

Mauk, B.H., Cohen, I.J., Westlake, J.H., Anderson, B.J., 2016. Modeling magnetospheric energetic particle escape across Earth's magnetopause as observed by the MMS mission. Geophys. Res. Lett. 43. Available from: https://doi.org/10.1002/2016GL068856.

McIlwain, C.E., 1966. Ring current effects on trapped particles. J. Geophys. Res. 71 (15), 3623–3628.

Millan, R.M., Thorne, R.M., 2007. Review of radiation belt relativistic electron losses. J. Atmos. Sol. Terr. Phys. 69, 362–377. Available from: https://doi.org/10.1016/j.jastp.2006.06.019.

Mourenas, D., Artemyev, A.V., Ma, Q., Agapitov, O.V., Li, W., 2016. Fast dropouts of multi-MeV electrons due to combined effects of EMIC and whistler mode waves. Geophys. Res. Lett. 43. Available from: https://doi.org/10.1002/2016GL068921.

Moya, P.S., Pinto, V.A., Sibeck, D.G., Kanekal, S.G., Baker, D.N., 2017. On the effect of geomagnetic storms on relativistic electrons in the outer radiation belt: Van Allen Probes observations. J. Geophys. Res. Space Phys. 122. Available from: https://doi.org/10.1002/2017JA024735.

Ni, B., Shprits, Y.Y., Friedel, R.H.W., Thorne, R.M., Daae, M., Chen, Y., 2013. Responses of Earth's radiation belts to solar wind dynamic pressure variations in 2002 analyzed using multisatellite data and Kalman filtering. J. Geophys. Res. Space Phys. 118. Available from: https://doi.org/10.1002/jgra.50437.

Ni, B., Xiang, Z., Gu, X., Shprits, Y.Y., Zhou, C., Zhao, Z., et al., 2016. Dynamic responses of the Earth's radiation belts during periods of solar wind dynamic pressure pulse based on normalized superposed epoch analysis. J. Geophys. Res. Space Phys. 121, 8523–8536. Available from: https://doi.org/10.1002/2016JA023067.

Ozeke, L.G., Mann, I.R., Murphy, K.R., Sibeck, D.G., Baker, D.N., 2017. Ultra-relativistic radiation belt extinction and ULF wave radial diffusion: modeling the September 2014 extended dropout event. Geophys. Res. Lett. 44, 2624–2633. Available from: https://doi.org/10.1002/2017GL072811.

Pham, K.H., Tu, W., Xiang, Z., 2017. Quantifying the precipitation loss of radiation belt electrons during a rapid dropout event. J. Geophys. Res. Space Phys. 122, 10,287–10,303. Available from: https://doi.org/10.1002/2017JA024519.

Reeves, G.D., et al., 2013. Electron acceleration in the heart of the Van Allen radiation belts. Science 341, 991. Available from: https://doi.org/10.1126/science.1237743.

Reeves, G.D., et al., 2016. Energy- dependent dynamics of keV to MeV electrons in the inner zone, outer zone, and slot regions. J. Geophys. Res. Space Phys. 121, 397–412. Available from: https://doi.org/10.1002/2015JA021569.

Ripoll, J.-F., et al., 2016. Reproducing the observed energy-dependent structure of Earth's electron radiation belts during storm recovery with an event-specific diffusion model. Geophys. Res. Lett. 43. Available from: https://doi.org/10.1002/2016GL068869.

Rodger, C.J., Hendry, A.T., Clilverd, M.A., Kletzing, C.A., Brundell, J.B., Reeves, G.D., 2015. High-resolution in situ observations of electron precipitation- causing EMIC waves. Geophys. Res. Lett. 42. Available from: https://doi.org/10.1002/2015GL066581.

Roederer, J.G., 1970. Dynamics of Geomagnetically Trapped Radiation. Springer, New York.

Schiller, Q., Li, X., Blum, L., Tu, W., Turner, D.L., Blake, J.B., 2014. A nonstorm time enhancement of relativistic electrons in the outer radiation belt. Geophys. Res. Lett. 41. Available from: https://doi.org/10.1002/2013GL058485.

Schiller, Q., Tu, W., Ali, A.F., Li, X., Godinez, H.C., Turner, D.L., et al., 2017. Simultaneous event-specific estimates of transport, loss, and source rates for relativistic outer radiation belt electrons. J. Geophys. Res. Space Phys. 122. Available from: https://doi.org/10.1002/2016JA023093.

Selesnick, R.S., 2015. High-energy radiation belt electrons from CRAND. J. Geophys. Res. Space Phys. 120. Available from: https://doi.org/10.1002/2014JA020963.

Shprits, Y.Y., Thorne, R.M., Friedel, R., Reeves, G.D., Fennell, J., Baker, D.N., et al., 2006. Outward radial diffusion driven by losses at magnetopause. J. Geophys. Res. 111, A11214. Available from: https://doi.org/10.1029/2006JA011657.

Shprits, Y.Y., Elkington, S.R., Meredith, N.P., Subbotin, D., 2008a. Review of modeling losses and sources of relativistic electrons in the outer radiation belt I: radial transport. J. Atmos. Sol. Terr. Phys. 70, 1679–1693. Available from: https://doi.org/10.1016/j.jastp.2008.06.008.

Shprits, Y.Y., Subbotin, D., Meredith, N.P., Elkington, S.R., 2008b. Review of modeling of losses and sources of relativistic electrons in the outer radiation belt II: local acceleration and loss. J. Atmos. Sol. Terr. Phys. 70, 1694–1713. Available from: https://doi.org/10.1016/j.jastp.2008.06.014.

Shprits, Y.Y., Kellerman, A., Aseev, N., Drozdov, A.Y., Michaelis, I., 2017a. Multi-MeV electron loss in the heart of the radiation belts. Geophys. Res. Lett. 44, 1204–1209. Available from: https://doi.org/10.1002/2016GL072258.

Shprits, Y.Y., Horne, R.B., Kellerman, A.C., Drozdov, A.Y., 2017b. Correspondence: the dynamics of Van Allen belts revisited. Nat. Phys. 14, 102–103.

Shprits, Y.Y., et al., 2013. Unusual stable trapping of the ultrarelativistic electrons in the Van Allen radiation belts. Nat. Phys. Available from: https://doi.org/10.1038/NPHYS2760.

Sibeck, D.G., et al., 1989. The magnetospheric response to 8-minute period strong-amplitude upstream pressure variations. J. Geophys. Res. 94, 2505–2519.

Sibeck, D.G., 1990. A model for the transient magnetospheric response to sudden solar wind dynamic pressure variations. J. Geophys. Res. 95, 3755–3771.

Sigsbee, K., et al., 2016. Van Allen Probes, THEMIS, GOES, and cluster observations of EMIC waves, ULF pulsations, and an electron flux dropout. J. Geophys. Res. Space Phys. 121, 1990–2008. Available from: https://doi.org/10.1002/2014JA020877.

Sorathia, K.A., Merkin, V.G., Ukhorskiy, A.Y., Mauk, B.H., Sibeck, D.G., 2017. Energetic particle loss through the magnetopause: a combined global MHD and test-particle study. J. Geophys. Res. Space Phys. 122, 9329–9343. Available from: https://doi.org/10.1002/2017JA024268.

Sorathia, K.A., Ukhorskiy, A.Y., Merkin, V.G., Fennell, J.F., Claudepierre, S.G., 2018. Modeling the depletion and recovery of the outer radiation belt duringa geomagnetic storm: Combined MHD and test particle simulations. J. Geophys. Res. Space Phys. 123. Available from: https://doi.org/10.1029/2018JA025506.

Su, Z., et al., 2016. Nonstorm time dropout of radiation belt electron fluxes on 24 September 2013. J. Geophys. Res. Space Phys. 121. Available from: https://doi.org/10.1002/2016JA022546.

Su, Z., Gao, Z., Zheng, H., Wang, Y., Wang, S., Spence, H.E., et al., 2017. Rapid loss of radiation belt relativistic electrons by EMIC waves. J. Geophys. Res. Space Phys. 122, 9880–9897. Available from: https://doi.org/10.1002/2017JA024169.

Thorne, R.M., 2010. Radiation belt dynamics: the importance of wave-particle interactions. Geophys. Res. Lett. 37, L22107. Available from: https://doi.org/10.1029/2010GL044990.

Thorne, R.M., et al., 2013. Evolution and slow decay of an unusual narrow ring of relativistic electrons near L ~ 3.2 following the September 2012 magnetic storm. Geophys. Res. Lett. 40. Available from: https://doi.org/10.1002/grl.50627.

Tsyganenko, N.A., Sitnov, M.I., 2005. Modeling the dynamics of the inner magnetosphere during strong geomagnetic storms. J. Geophys. Res. 110, A03208. Available from: https://doi.org/10.1029/2004JA010798.

Tu, W., Cunningham, G.S., Chen, Y., Morley, S.K., Reeves, G.D., Blake, J.B., et al., 2014. Event- specific chorus wave and electron seed population models in DREAM3D using the Van Allen Probes. Geophys. Res. Lett. 41. Available from: https://doi.org/10.1002/2013GL058819.

Turner, D.L., Angelopoulos, V., 2016. Extreme variability of relativistic electrons in Earth's outer radiation belt: an overview and recent revelations. In: Balasis, G., Daglis, I.A., Mann, I.R. (Eds.), Waves, Particles, and Storms in Geospace, First ed. © Oxford University Press, 2016. Published in 2016 by Oxford University Press.

Turner, D.L., Morley, S.K., Miyoshi, Y., Ni, B., Huang, C.-L., 2012a. Outer radiation belt flux dropouts: current understanding and unresolved questions. In: Summers, D., Mann, I.R., Baker, D.N., Schulz, M. (Eds.), Dynamics of the Earth's Radiation Belts and Inner Magnetosphere, 199. Geophysical Monograph Series.

Turner, D.L., Angelopoulos, V., Shprits, Y., Kellerman, A., Cruce, P., Larson, D., 2012b. Radial distributions of equatorial phase space density for outer radiation belt electrons. Geophys. Res. Lett. 39, L09101. Available from: https://doi.org/10.1029/2012GL051722.

Turner, D.L., Shprits, Y., Hartinger, M., Angelopoulos, V., 2012c. Explaining sudden losses of outer radiation belt electrons during geomagnetic storms. Nat. Phys. 8, 208–212. Available from: https://doi.org/10.1038/nphys2185.

Turner, D.L., Angelopoulos, V., Li, W., Hartinger, M.D., Usanova, M., Mann, I.R., et al., 2013. On the storm-time evolution of relativistic electron phase space density in Earth's outer radiation belt. J. Geophys. Res. Space Phys. 118, 2196–2212. Available from: https://doi.org/10.1002/jgra.50151.

Turner, D.L., et al., 2014a. On the cause and extent of outer radiation belt losses during the 30 September 2012 dropout event. J. Geophys. Res. Space Phys. 119. Available from: https://doi.org/10.1002/2013JA019446.

Turner, D.L., et al., 2014b. Competing source and loss mechanisms due to wave-particle interactions in Earth's outer radiation belt during the 30 September to 3 October 2012 geomagnetic storm. J. Geophys. Res. Space Phys. 119. Available from: https://doi.org/10.1002/2014JA019770.

Turner, D.L., O'Brien, T.P., Fennell, J.F., Claudepierre, S.G., Blake, J.B., Kilpua, E.K.J., et al., 2015. The effects of geomagnetic storms on electrons in Earth's radiation belts. Geophys. Res. Lett. 42. Available from: https://doi.org/10.1002/2015GL064747.

Turner, D.L., et al., 2016. Investigating the source of near-relativistic and relativistic electrons in Earth's inner radiation belt. J. Geophys. Res. Space Phys. 121. Available from: https://doi.org/10.1002/2016JA023600.

Ukhorskiy, A.Y., Sitnov, M.I., 2008. Radial transport in the outer radiation belt due to global magnetospheric compressions. J. Atmos. Sol.-Terr. Phys. 70, 1714–1726.

Ukhorskiy, A.Y., Sitnov, M.I., 2012. Dynamics of radiation belt particles. Space Sci. Rev. Available from: https://doi.org/10.1007/s11214-012-9938-5.

Ukhorskiy, A.Y., Shprits, Y.Y., Anderson, B.J., Takahashi, K., Thorne, R.M., 2010. Rapid scattering of radiation belt electrons by storm-time EMIC waves. Geophys. Res. Lett. 37, L09101. Available from: https://doi.org/10.1029/2010GL042906.

Ukhorskiy, A.Y., Sitnov, M.I., Millan, R.M., Kress, B.T., 2011. The role of drift orbit bifurcations in energization and loss of electrons in the outer radiation belt. J. Geophys. Res. 116, A09208. Available from: https://doi.org/10.1029/2011JA016623.

Ukhorskiy, A.Y., Sitnov, M.I., Millan, R.M., Kress, B.T., Smith, D.C., 2014. Enhanced radial transport and energization of radiation belt electrons due to drift orbit bifurcations. J. Geophys. Res. Space Phys. 119. Available from: https://doi.org/10.1002/2013JA019315.

Ukhorskiy, A.Y., Sitnov, M.I., Millan, R.M., Kress, B.T., Fennell, J.F., Claudepierre, S.G., et al., 2015. Global storm time depletion of the outer electron belt. J. Geophys. Res. Space Phys. 120. Available from: https://doi.org/10.1002/2014JA020645.

Ukhorskiy, A.Y., Mauk, B.H., Sibeck, D.G., Kessel, R., 2016. Radiation belt processes in a declining solar cycle. EOS 97. Available from: https://doi.org/10.1029/2016EO048705.

Usanova, M.E., et al., 2014. Effect of EMIC waves on relativistic and ultrarelativistic electron populations: ground-based and Van Allen Probes observations. Geophys. Res. Lett. 41. Available from: https://doi.org/10.1002/2013GL059024.

Xiang, Z., Tu, W., Li, X., Ni, B., Morley, S.K., Baker, D.N., 2017. Understanding the mechanisms of radiation belt dropouts observed by Van Allen Probes. J. Geophys. Res. Space Phys. 122, 9858–9879. Available from: https://doi.org/10.1002/2017JA024487.

Yu, Y., Koller, J., Morley, S.K., 2013. Quantifying the effect of magnetopause shadowing on electron radiation belt dropouts. Ann. Geo . Available from: https://doi.org/10.5194/angeo-31-1929-2013.

Yu, J., Li, L.Y., Cao, J.B., Yuan, Z.G., Reeves, G.D., Baker, D.N., et al., 2015. Multiple loss processes of relativistic electrons outside the heart of outer radiation belt during a storm sudden commencement. J. Geophys. Res. Space Phys. 120. Available from: https://doi.org/10.1002/2015JA021460.

Yuan, C.J., Zong, Q.G., 2013. The double-belt outer radiation belt during CME- and CIR-driven geomagnetic storms. J. Geophys. Res. Space Phys. 118. Available from: https://doi.org/10.1002/jgra.50564.

Zhang, X.-J., et al., 2016. Physical mechanism causing rapid changes in ultrarelativistic electron pitch angle distributions right after a shock arrival: evaluation of an electron dropout event. J. Geophys. Res. Space Phys. 121. Available from: https://doi.org/10.1002/2016JA022517.

Zhao, H., Baker, D.N., Califf, S., Li, X., Jaynes, A.N., Leonard, T., et al., 2017. Van Allen probes measurements of energetic particle deep pene- tration into the low L region ($L < 4$) during the storm on 8 April 2016. J. Geophys. Res.: Space Phys. 122. Available from: https://doi.org/10.1002/2017JA024558.

Further reading

Kang, S.-B., Min, K.-W., Fok, M.-C., Hwang, J., Choi, C.-R., 2015. Estimation of pitch angle diffusion rates and precipitation time scales of electrons due to EMIC waves in a realistic field model. J. Geophys. Res. Space Phys. 120. Available from: https://doi.org/10.1002/2014JA020644.

CHAPTER 2

Ultralow frequency-wave induced losses

Thiago V. Brito[1], Alexa J. Halford[2] and Scot R. Elkington[3]
[1]Department of Physics, University of Helsinki, Helsinki, Finland
[2]Space Sciences Department, Aerospace Corporation, Chantilly, VA, United States
[3]Laboratory for Atmospheric and Space Physics, University of Colorado, Boulder, CO, United States

Contents

2.1 Introduction

Understanding radiation belt dynamics to the point of predictability is a long-term goal for the space physics community. In order to understand the dynamics of the radiation belts, it is important to understand the relative contributions of different source and loss mechanisms. Ultralow frequency (ULF) waves are found throughout the magnetosphere during many types of geomagnetic activity and are thought to contribute to both particle loss and acceleration as well as to modify the effectiveness of other loss mechanisms that may be occurring in the same location and at the same time as the ULF wave.

ULF wave dynamics, and how they affect the magnetosphere and specifically the radiation belts, have been of great interest. Many previous review articles have highlighted ULF waves (e.g., Menk, 2011) and how they contribute to radial transport (e.g., Shprits et al., 2008) and how they affect the Earth's radiation belts (e.g., Elkington, 2013). In this chapter, we will provide a brief overview of ULF waves, including their classification, general characteristics, and updates, including a few new findings with emphasis on recent modeling efforts and associated observations.

The Dynamic Loss of Earth's Radiation Belts
DOI: https://doi.org/10.1016/B978-0-12-813371-2.00002-0

2.2 Ultralow frequency waves in the magnetosphere

The outer radiation belt of the Earth's magnetosphere at around 3–6 RE consists of trapped energetic (100s keV to several MeV) electrons. This population of particles interacts with many loss and acceleration processes in the inner magnetosphere, leading to very dynamic changes in their flux of orders of magnitude and on timescales of minutes to days. Ultimately, ULF waves are able to interact with these radiation belt particles in multiple ways, as will be outlined in this chapter.

2.2.1 Definition of ultralow frequency waves

The basic definitions of ULF waves used by the magnetospheric community have been outlined previously (Jacobs et al., 1964). This first classification of ULF waves was based on ground-based measurements of magnetic field oscillations. Despite the limitations of this definition, owing to the fact that not all ULF waves propagate to the ground, it is still commonly used in the literature. Jacobs et al. (1964) stated that these geomagnetic micropulsations observed on the ground, with period ranges of 0.2–600 seconds, are based on the physical and morphological properties and are classified based on their form (continuous or irregular) and period of the geomagnetic micropulsations and not by the physical processes involved, as they were not well understood at the time (Table 2.1). Continuous waves are more common and they are subdivided into five categories based on their period from Pc1 (0.2–5 seconds) to Pc5 (150–600 seconds) (Jacobs et al., 1964). Often today when people mention ULF waves without stating a frequency range or type, they are discussing the two main standing wave modes of oscillation in the Earth's dipole geometry in the Pc4–5 frequency range, despite the existence of other modes, frequencies, and configurations. The first is the toroidal mode, in which the magnetic fields oscillate in the azimuthal direction and generate induced electric fields in the radial direction; the second is the poloidal mode, in which the magnetic fields oscillate primarily in the radial direction and generate electric fields in the azimuthal direction (see Fig. 2.1). These modes are both idealized magnetohydrodynamic (MHD) limits for the azimuthal mode

Table 2.1 Classification of geomagnetic micropulsations.

Notation	Frequency range	Period (s)
Pc1	0.2–5 Hz	0.2–5
Pc2	0.1–0.2 Hz	5–10
Pc3	22.2–100 mHz	10–45
Pc4	6.7–22.22 mHz	45–150
Pc5	1.6–6.7 mHz	150–600

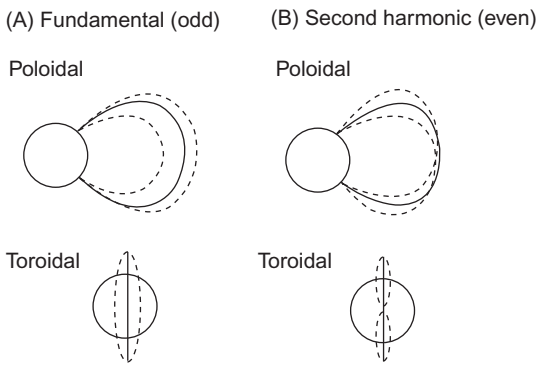

Figure 2.1 Schematic representation of ULF poloidal and toroidal modes (Hughes, 1994). (A) Fundamental (odd) and (B) second harmonic (even).

number (m), with $m \to 0$ for the toroidal mode and $m \to \infty$ for the poloidal mode. In observations, there is usually a mixed mode including a compressional component as well, which occurs off the equatorial plane in the poloidal mode.

Like all plasma waves in the magnetosphere, ULF waves act to mediate energy, momentum, and mass transfer between the different regions of the magnetosphere. The radiation belt particles interact with waves from a large range of frequencies present in the magnetosphere, from ULF waves starting at < 1 mHz to higher frequency waves like ElectroMagnetic Ion Cyclotron (EMIC) and whistler-mode waves in the Hz and kHz range, respectively. At lower L-shells and inside the plasmasphere, higher frequency waves dominate, especially the whistler-mode plasmaspheric hiss, whereas at higher L-shells, power in the Pc4–5 frequency range is found to increase. Ground-based observations of ULF pulsations often show a peak in wave power at a particular latitude, corresponding to a particular L-shell (Samson and Rostoker, 1972). Factors determining the relative importance of Pc4–5 and higher frequency waves in different regions include the source of the waves as well as the waves' propagation and damping.

Several different types of geomagnetic disturbances can produce waves in the ULF range. ULF waves are characterized as Alfvén waves and magnetosonic oscillations in the geomagnetic field. They can be either localized oscillations of the field line, divided schematically into toroidal and poloidal modes, as in Fig. 2.1, or global cavity modes standing between radial boundaries like the magnetopause and plasmapause (Goldstein et al., 1999). A large portion of the ULF waves typically observed in the inner magnetosphere are driven by variations in the solar wind; they are found to have amplitudes with peaks near the magnetopause, and the amplitude decreases as one moves further away (Mathie and Mann, 2000; Claudepierre et al., 2010). Another class of ULF waves is excited internally, for example, via mirror (Hasegawa, 1969) or

drift-bounce instabilities (Southwood et al., 1969; Chen and Hasegawa, 1991) in ring current ion populations. Both classes of waves can undergo partial reflection from the plasmapause boundary of the plasmasphere (Goldstein et al., 1999). The plasmapause boundary is located in the inner magnetosphere and changes with geomagnetic activity. Although the frequency of the Pc4–5 waves is longer than the gyromotion or bounce times for radiation belt particles, they can break the third adiabatic invariant related to the drift motion and are usually correlated with radial transport and energy diffusion.

Enhancements in electron flux at geosynchronous orbit are commonly associated with increases in wave power in the ULF range either during specific storms (Baker et al., 1998) or in statistical studies (O'Brien et al., 2003). Fig. 2.2 shows a delay that has been reported between the rise in ULF wave power and the MeV electron flux at geosynchronous orbit. This delay, and the fact that the mHz timescale is comparable to the drift period of the electrons transported from the plasmasheet into geosynchronous orbit, has fostered the idea that ULF waves play a significant role in radial diffusion (Elkington et al., 2003). The latter energizes electrons as they are transported earthward in a random walk, which violates their third but conserves their first and second adiabatic invariants (Schulz and Lanzerotti, 1974).

Radiation belt particles can also interact with Pc4–5 waves through drift resonance. An azimuthally propagating ULF wave has an $e^{i(m\phi-\omega t)}$ phase dependence. Thus for waves propagating in the direction of electron drift (eastward), drift resonance occurs when the wave frequency ω and the electron drift frequency ω_d satisfy $\omega = m\omega_d$, where m is the azimuthal mode number of the ULF wave. Under this condition the electron sees a constant phase of the wave, so a constant (poloidal mode)

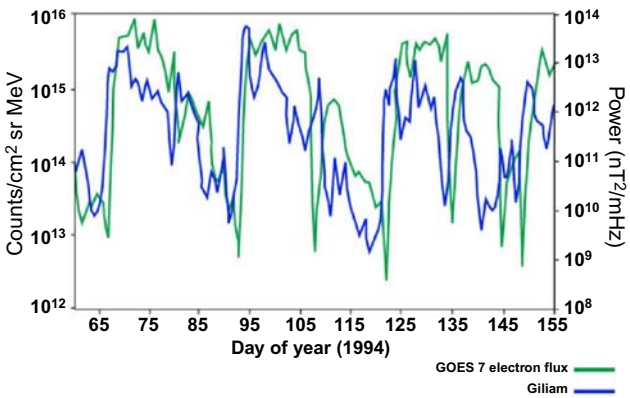

Figure 2.2 Correlation between ULF wave power and radiation belt electron flux. *From Rostoker, G., Skone, S., Baker, D.N., 1998. On the origin of relativistic electrons in the magnetosphere associated with some geomagnetic storms. Geophys. Res. Lett. 25 (19), 3701–3704, doi: 10.1029/98GL02801 (Rostoker et al., 1998).*

azimuthal electric field in the electron's frame of reference can accelerate (or decelerate) the electron, increasing (or decreasing) its perpendicular energy. Elkington et al. (2002) showed that wave power, the amount of energy available to accelerate the particle, is greatest for low m numbers in MHD simulations driven by measured solar wind input, while ring current ions not included in the MHD simulations can excite higher m number poloidal modes (10s to 100) (Southwood and Kivelson, 1981), which are thought to have a smaller effect on radiation belt electrons. For ULF waves in the mHz frequency range, a high azimuthal mode number requires a low drift frequency, so drift resonance is satisfied only for 10s of keV energy electrons (Zong et al., 2009; Claudepierre et al., 2013).

2.3 Observations and simulations of ultralow frequency wave-particle and wave-wave interactions

During the main phase of a geomagnetic storm, loss of radiation belt electrons in the outer zone is typical, even though there can be a net increase during the recovery phase of particle fluxes since a storm is also a driver for the source population (Summers et al., 2004, 2007). However, it is still unclear whether most of the loss during the main phase is due to precipitation to the atmosphere or escape through the magnetopause, since both types of loss are correlated with increased geomagnetic activity. Most of the scientific effort so far has been put into quantifying and better describing precipitation into the ionosphere rather than magnetopause loss, mostly because it is very difficult to directly measure the latter.

Among the scientific missions related to the investigation of particle precipitation is the mission of opportunity Balloon Array for Radiation belt Relativistic Electron Losses (BARREL) experiment, which consists of multiple balloons launched from the South African Antarctic Station (SANAE IV) and the British station Halley VI, forming an array of, on average, 5–8 almost static observation points during two campaigns (Woodger et al., 2015). The balloons measured bremsstrahlung X-rays produced by precipitation of radiation belt electrons. Their roughly static behavior acts as a method of observation complementary to the fast-moving in situ Van Allen Probes spacecraft. By comparing in situ observations of the particles and the waves from satellite observations during conjunctions with ground- and balloon-based platforms, which inferred precipitation data, an estimate of the total loss to the atmosphere and a comparison with loss mechanisms can be made. The multipoint semi-static configuration is ideal for the investigation of the temporal and spatial resolution of phenomena such as energetic electron precipitation. Other similar balloon missions have also been used for precipitation measurements since the beginning of the space age and throughout the modern era (Anderson and Milton, 1964; Brown et al., 1965; Kokorowski et al., 2008; Millan et al., 2007).

Global MHD simulations driven by upstream observations of the solar wind are a common way of studying the inner magnetosphere and ULF wave effects on the Earth's radiation belt population. They can be used for both analysis of the internal ULF wave and to drive test-particle simulations of trapped magnetospheric electrons. An example of the ULF wave analysis derived from these simulations is shown in Elkington et al. (2013), in order to find the wave structure and spectral peaks. Global mode structural analysis usually indicates magnetic field power confined to lower mode numbers ($m \sim 1$), but the electric field power may be more complex. This typical structure suggests the potential for drift-resonant interaction with the population of trapped energetic electrons through the resonance condition $\omega = m\omega d$. Test particles, representing packets of phase space density in the sense indicated by Liouville's theorem, are used to infer the fluxes of particles seen at the magnetic equatorial region.

2.3.1 Direct ultralow frequency generated precipitation

2.3.1.1 Observations of precipitation with ultralow frequency modulation

The BARREL campaign has inferred many precipitation events during its two Antarctic campaigns and two turnaround campaigns in Kiruna, Sweden (Millan et al., 2013; Woodger et al., 2015). An example of an inferred precipitation event with ULF timescales occurred on January 17, 2013, when a few payloads observed a clear precipitation event showing clear ULF oscillations (Fig. 2.3). Starting at 0000 UT payloads 1G and 1I observed oscillations in the X-ray counts at all energy channels in the ULF range. These oscillations are less apparent, but still present in payload 1C. This type of oscillation in the same frequency range was seen in multiple other balloon observation events, which is yet another hint about the relationship between radiation belt precipitation and ULF waves. Another feature in the Fig. 2.3 is the significant increase in precipitation counts across all energy channels also observed by payloads 1G and 1I, although these were seen at different times. Payload 1G measures the increase close to 0300 UT, while 1I does so approximately 2 hours later. Both payloads are in the dusk-to-midnight sector, but 1G, which sees the increase first, is closer to midnight. This, along with the fact that there are no oscillations in the ULF range after the peaks, is an indication that this specific event might be related to a substorm rather than to shock-induced ULF waves. The oscillations in the inferred precipitation prior to the big increase nevertheless occur immediately after the arrival of a Coronal Mass Ejection (CME) shock, which can be seen in the bottom panel of Fig. 2.3. Even though the precipitation is observed on the nightside, shock-induced ULF waves propagate from the dayside across the magnetosphere at the Alfvén speed and can reach the nightside in a matter of a couple of minutes. Therefore ULF waves could be a candidate for explaining these precipitation oscillations. Because they happen in the dusk-to-midnight sector, EMIC waves may have also contributed to the loss of radiation belt electrons. However, the EMIC waves themselves and their interaction with

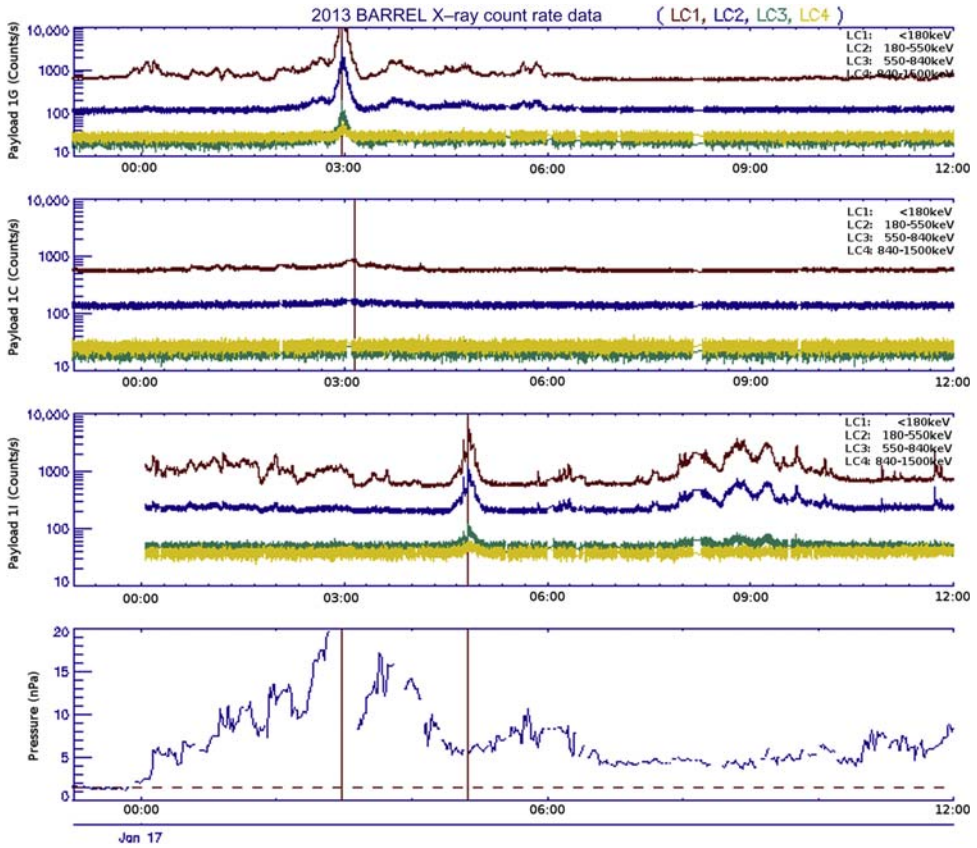

Figure 2.3 BARREL precipitation counts during the January 17, 2013, storm. The top three panels show data from payloads 1G, 1C and 1I. Each of the four lines represents a different energy channel. The bottom panels show dynamic pressure based on ACE data. *Courtesy: Leslie Woodger.*

the electrons were likely modulated by the ULF waves, which can affect ion temperature anisotropy and other local plasma characteristics, leading to changes in EMIC wave growth and their wave-particle resonance conditions.

2.3.1.2 Fermi acceleration

Another example event was observed on January 21, 2005, when a CME storm produced relativistic electron precipitation observed by the MINIature Spectrometer (MINIS) balloon campaign shortly after the shock arrival. A thorough comparison between balloon observations and simulation results was presented in Brito et al. (2012). As shown in their study, a similar pattern of precipitation into the ionospheric region can be observed in both the test-particle simulation results, shown in Fig. 2.4, and in the balloon observations, shown in Fig. 2.5. A direct comparison of the frequency observed in the precipitation counts during the simulations with the inferred

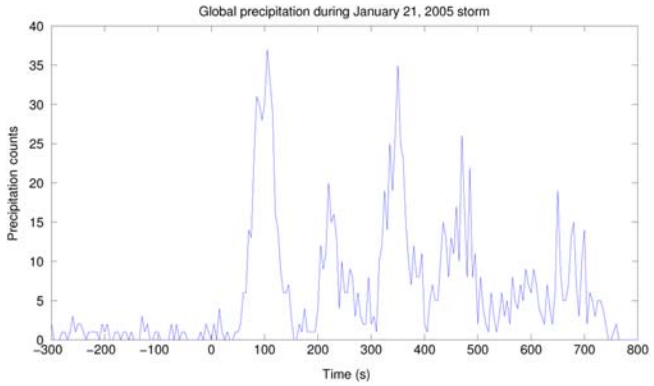

Figure 2.4 Global electron precipitation with 5-s averaged integrated counts versus time in the test-particle simulation. $t = 0$ marks the arrival of the shock at the magnetopause.

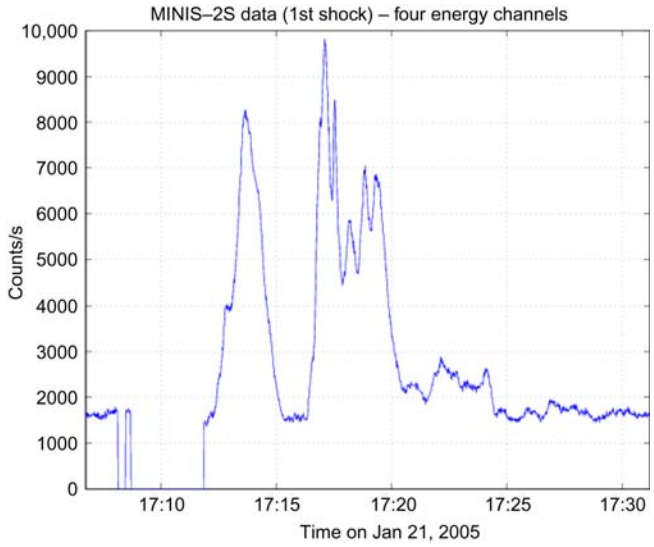

Figure 2.5 Precipitation counts integrated over all four energy channels from 20 keV to 1.5 MeV during a shock event on January 21, 2005, observed by the 2S balloon during the MINIS campaign. The balloon location was at approximately $L = 3.6$ and 1400 MLT mapped to the equatorial plane using the TS04 model.

precipitation frequency observed by the MINIS balloons in Fig. 2.5 shows that they are comparable. Even though it is not possible to make a quantitative comparison of counts between simulation and observation, this same study shows that the predominant frequency in the simulated electron loss, ~8 mHz, is correlated with the peak in power in the dayside electric field simulated with MHD. The observation of precipitation in the simulations and at MINIS at the 8 mHz spectral peak of E_Φ, provides information on the energy range of the drift-resonance interacting electrons. Particles

that satisfy the resonance condition $\omega = m\omega_d$ will observe a constant azimuthal electric field (E_Φ) in their frame of reference as they drift eastward.

Since the International Geomagnetic Reference Field (IGRF) model is used for the inner magnetosphere in the simulation presented in this study, the South Atlantic Anomaly (SAA) contained in the model acts as a determinant of the longitude of the simulated precipitation. The disturbances in the simulated magnetosphere are not sufficient to bring the electrons into the loss cone unless they are also located near the Magnetic Local Time (MLT) region of the SAA. Horne et al. (2009), studying data from the low-altitude POES satellites for different phases of geomagnetic storms, found that for the outer radiation belt, precipitation of >1 MeV occurs mainly poleward of a broad maximum peaking from −90 to +45 degrees longitude about the SAA region.

The energy of precipitated electrons increases with time, which is as expected from the inward transport of drift-resonant electrons and has been seen in earlier test-particle simulations of CME-shock events (Elkington et al., 2002, 2004; Kress et al., 2007). E_Φ acts to transport the electrons radially inward gaining energy while conserving their first (and second) adiabatic invariant.

Brito et al. (2015) conducted a more detailed study about ULF-induced electron precipitation using the same simulation methodology. They analyzed the spatial and temporal evolution of the precipitation during the March 17, 2013, CME-shock event. The authors studied the evolution of precipitation flux mapped to the equatorial plane during this event. The propagation of the precipitation happens immediately after the arrival of the shock at the magnetopause. It starts on the dayside, as the shock compresses the magnetosphere, displaces the trapped electron population, and propagates eastward across several *L*-shells following the shock front and, in a few minutes, the precipitation "wave" reaches the nightside. Once it reaches the midnight sector, all the subsequent precipitation occurs in the MLT location of the SAA. The ULF oscillations have larger amplitudes immediately after the shock arrival at the magnetosphere during its initial propagation and therefore cause more changes in the trapped population. It is possible that only large-amplitude oscillations in the fields can cause energetic electron precipitation with this ULF signature outside the SAA region, but smaller amplitude waves may be responsible for it close to the SAA.

The disturbances in the fields cause both the perpendicular and the parallel momenta of the particles, measured at the equatorial plane, to change. Because of the inward motion following the initial compression and the conservation of the first adiabatic invariant, $p_\perp$ typically increases. For the parallel component, the behavior is slightly more complex. The parallel component of the momentum also varies following the inward motion in the *L*-shell. A more in-depth analysis of the simulation shows that the mirror force is the largest term that contributes to the changes in $p_{||}$. The inward motion causes an increase in $p_{||}$ owing to the mirror points coming close together; this energization is thus related to the Fermi acceleration process (Fermi, 1949) that occurs when the magnetic mirror points approach each other.

The predominant effect responsible for the precipitation, represented in the simulation, is the change in the loss cone angle at the position of the particle, denoted by its radial inward motion. Increases in the parallel component and/or decreases in the perpendicular component of the momentum also cause the electrons to move closer to the loss cone, and if they are already close enough to the loss cone boundary, they may be lost to the atmosphere. Variations in $p_{\perp}$ (and $p_{||}$) occur on timescales much smaller than the drift motion of the electrons, thus causing a violation of the third adiabatic invariant. Variations in $p_{||}$, caused by Fermi acceleration, are often comparatively smaller and occur on the same timescales as the $p_{\perp}$ variations, over several bounce periods ($\tau < 1$ second), therefore the second adiabatic invariant of the electrons is not broken.

In addition to the variations in $p_{\perp}$ and $p_{||}$ caused by the ULF waves as the electrons move inward and outward in the *L*-shell, the change in the *L*-shell of the particles in itself is responsible for a change in the loss cone angle seen by the electrons. As electrons move inward, the increase in the loss cone angle, which is proportional to $\sqrt{B_{eq}/B_m}$, plays a decisive role in this mechanism. A combination of betatron acceleration conserving μ, the Fermi acceleration conserving the second invariant, and the loss cone angle variation with the *L*-shell, all determined by the ULF oscillations, are responsible for the precipitation modulation.

2.3.1.3 Changing loss cone

Rae et al. (2018) considered the effect of ULF waves on the size of the loss cone. They considered ULF waves observed at GOES and near-conjugate to BARREL and riometer observations of inferred electron precipitation modulated with the same frequency. Following the derivations outlined in Wygant et al. (1994) and Halford et al. (2015), it can be shown that the equatorial pitch angle due to the ULF wave modulation α_{eq_w} as a function of the background magnetic field (B_b) and the observed magnetic field during the wave (B_w) can be written as

$$\sin \alpha_{eq_w} = \frac{-B_b^{1/2} \cos^2 \alpha_{eq_b}}{2B_w^{1/2} \sin \alpha_{eq_b}} + \frac{1}{2}\left(\frac{B_b \cos^4 \alpha_{eq_b}}{B_w \sin^2 \alpha_{eq_b}} + 4\right)^{1/2} \tag{2.1}$$

where the equatorial pitch angle for the particle in the background field is given as α_{eq_b}. The change in the size of the loss cone can easily be determined using

$$\Delta\alpha = \sin^{-1}\left(\frac{B_b}{B_l}\right) - \sin^{-1}\left(\frac{B_w}{B_l}\right) \tag{2.2}$$

where the magnetic field at the loss height in the ionosphere is given as B_l. The results for the case given in Rae et al. (2018) can be seen in Fig. 2.6.

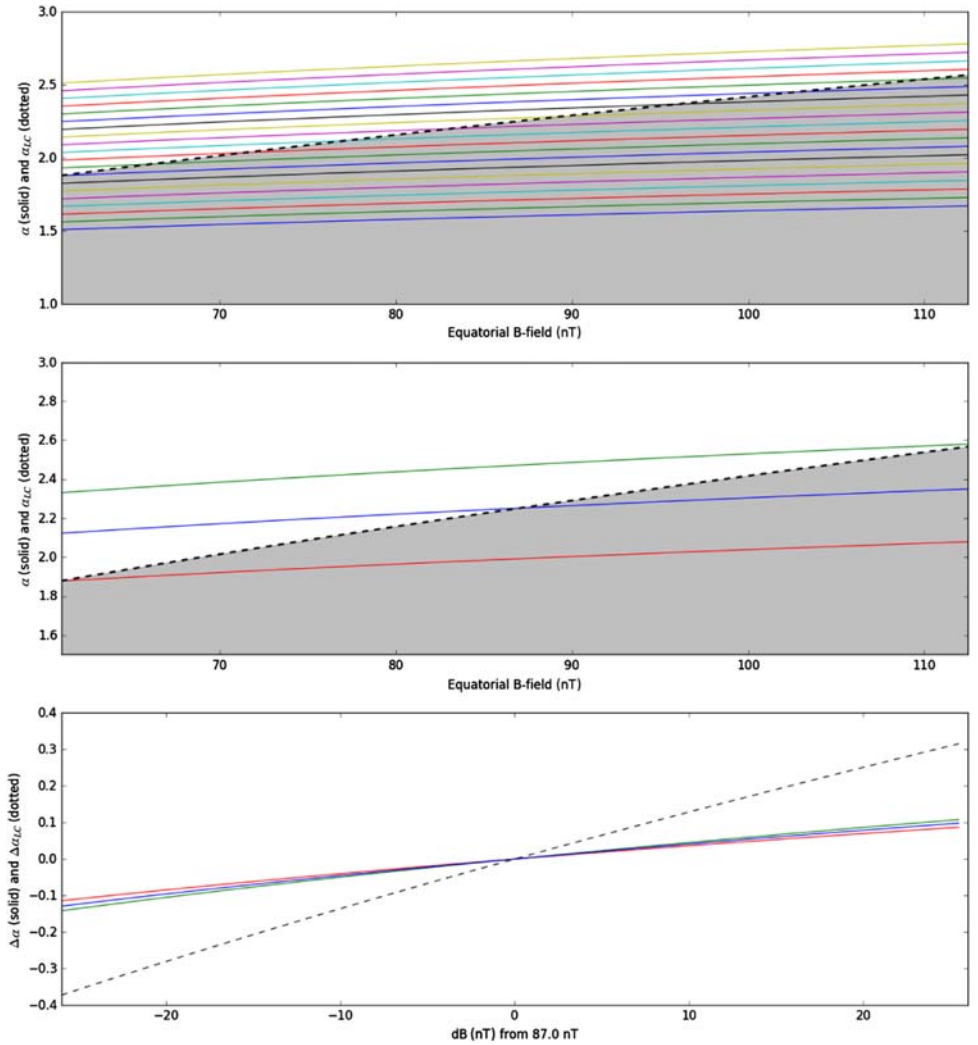

Figure 2.6 The expected change in the size of the loss cone due to the ULF wave observed at GOES on January 26, 2013 (Rae et al., 2018).

Although the process described above does not change the size of the loss cone significantly, it is found to be sufficient to appreciably modulate the flux of electrons lost to the atmosphere. It is, however, not sufficient to cause significant loss from the trapped population. Often the loss of radiation belt electrons with pulsations is attributed to the pulsations of higher frequency wave-particle interactions—for instance, chorus waves possibly being modulated by ULF waves, which will be discussed later in this chapter. However, the mechanism described in

Rae et al. (2018) provides an example of how ULF waves can cause the precipitation, or at least the modulation of the precipitation through modulation of the size of the loss cone.

2.3.2 Ultralow frequency-generated magnetopause shadowing

Radiation belt losses to the magnetopause can occur either by its inward motion (*magnetopause shadowing*) due to compression caused by the solar wind dynamic pressure, by the outward radial diffusion of the electron population, or by a combination of the two. In the second scenario, the ULF waves play a significant role, since they are the main mechanism for electron radial diffusion. The debate around whether magnetopause loss is more significant than loss to the atmosphere has not been settled. Some statistical studies have concluded that losses to the atmosphere are more relevant during the main phase and the recovery phase of geomagnetic storms (Borovsky and Denton, 2009; Horne et al., 2009). However, a study by Turner et al. (2012) has shown that the majority of nonadiabatic losses with energies above 300 keV during one particular storm driven by a corotating interaction region was caused by a combination of magnetopause shadowing and subsequent radial outward transport driven by ULF waves. These waves, as mentioned previously, are a regularly occurring phenomenon in the inner magnetosphere and can cause a violation of the third adiabatic invariant of the drifting electrons and therefore push them both inward and outward. As also discussed in previous sections, ULF power is correlated with geomagnetic activity, which makes the scenario described in this study very plausible.

It is safe to assume that the amount of loss caused by magnetopause shadowing is proportional to how far inward the magnetopause moves during a storm (Ohtani et al., 2009) and also to the rate of outward radial transport caused by ULF wave activity (Shprits et al., 2006). Previous studies (Claudepierre et al., 2009, 2010) have established that some MHD-based models capture well the ULF wave activity in the magnetosphere due both to the solar wind dynamic pressure variations and to the shear flow on the flanks of the magnetosphere causing Kelvin–Helmholtz instabilities, although it should be noted that it does not capture magnetospheric expansion due to full storm-time suppression of the fields in the inner magnetosphere. Therefore possibly using a simulation setup similar to the one used by Brito et al. (2012, 2015) to imitate magnetopause loss is a valid way to further explore this question, although it has not yet been pursued.

2.3.3 Ultralow frequency modulation of higher frequency waves

Although ULF waves are able to cause precipitation on their own, they are also able to enhance or dampen the ability of other waves to resonate and ultimately cause the loss of radiation belt electrons. It is thought that the ULF waves may affect these other

wave-particle interactions through two methods: (1) affecting the local plasma parameters leading to the growth of the waves and (2) affecting the local plasma parameters governing the resonance conditions of the waves with the particles.

EMIC waves have been observed at times to have a periodic nature. These sets of waves are identified as pearls, as they look like a string of pearls in spectrograms (Mursula et al., 2001; Demekhov, 2007; Loto'aniu et al., 2009). It had previously been thought that these structures may be due to the EMIC wave packet bouncing along the field line. Loto'aniu et al. (2009) showed, using data from the Combined Release and Radiation Effects Satellite (CRRES), that the Poynting flux of the EMIC waves were observed only to be moving away from the source region, and thus the bouncing wave packet model does not adequately account for the observations of EMIC wave power being modulated at ULF timescales. The observation of EMIC Poynting flux being observed only to move away from the source region has been extended with cluster results (Allen et al., 2015), which include the off-equator source regions on the dayside due to magnetopause compressions. Loto'aniu et al. (2009) then showed that for these pearl strings observed by CRRES, Pc5 waves were simultaneously observed, similar to those in the event shown in Fig. 2.7. They hypothesized that the ULF waves modulated the necessary plasma conditions for EMIC wave growth, thus giving the pearl structure.

Although Loto'aniu et al. (2009) did not extrapolate these results to the EMIC affect on radiation belt dynamics, EMIC temporal structures were found to agree with inferred observations of electrons during the BARREL campaign (Li et al., 2014) (see Fig. 2.8). This work does not distinguish between the possibility of the ULF wave modulating the EMIC wave growth or the resonance conditions, and it probably affects both, as many parameters such as the background magnetic field and cold plasma density are important to both the wave growth and the resonance.

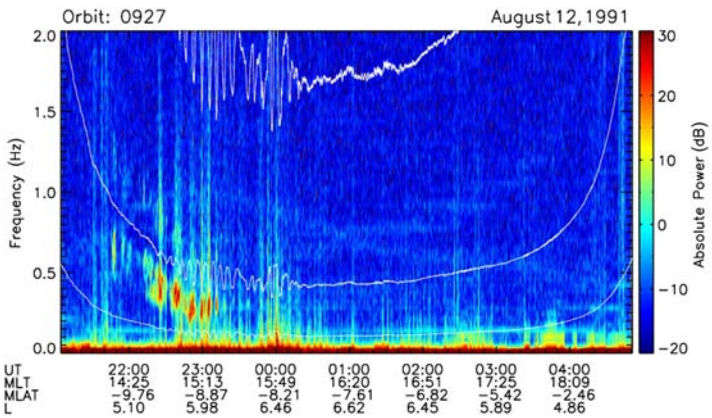

Figure 2.7 An example of EMIC waves on CRRES, which may be modulated by the ULF wave and can be observed in the oscillations of the cyclotron frequencies.

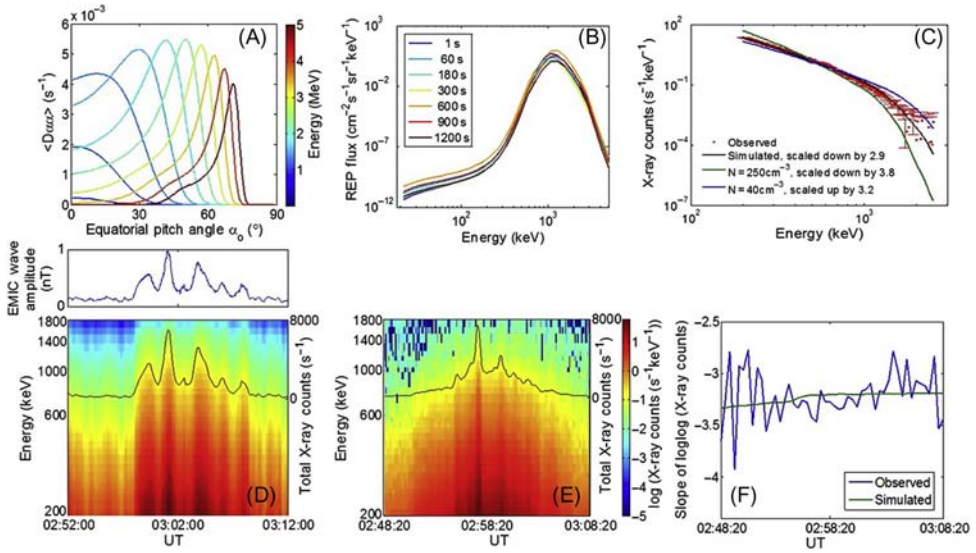

Figure 2.8 Modulation of both EMIC and inferred electron precipitation from bremsstrahlung X-rays on the timescales of ULF waves is shown in panels (D) and (E). Other panels show: (A) bounce- and drift-averaged pitch angle diffusion coefficients for EMIC waves interacting with electrons. (B) Time variation of the energy distribution of the simulated precipitating electrons. (C) Energy distribution of the bremsstrahlung X-ray count rate averaged over 02:57:30–02:59:30 UT from the medium spectrum of BARREL balloon 1G. (F) Time variation of the slope of the linear fit on [400, 800] keV of the log–log line plot of the simulated and observed (background subtracted) bremsstrahlung X-ray energy spectrum (Li et al., 2014).

Li et al. (2014) simulated the electron pitch angle diffusion using wave and particle parameters observed by GOES 13 and Van Allen Probes and compared results with BARREL balloon observations. They showed that the simulated precipitation reproduced the balloon observations to a large degree in count rate, energy distribution, and the temporal variation, indicating that EMIC wave scattering was a likely cause for the precipitation event. However, this study did not examine the effect of the ULF waves on either the generation or resonance conditions of the EMIC waves.

ULF timescales have often been observed in electron precipitation at a wide range of energies. Breneman et al. (2015) examined a set of events during the second Antarctic BARREL campaign, where there were inferred observations of soft (<1 MeV) electron precipitation with temporal structures on ULF timescales. One of the events they discuss is shown in Fig. 2.9. During these periods, the relevant BARREL payloads were in conjunction with the Van Allen Probes, which observed hiss waves with the same temporal modulations. They showed that the hiss waves were the likely cause of the precipitation, and that it was likely the modulation of the cold plasma density by the ULF waves which modulated the growth of the hiss wave.

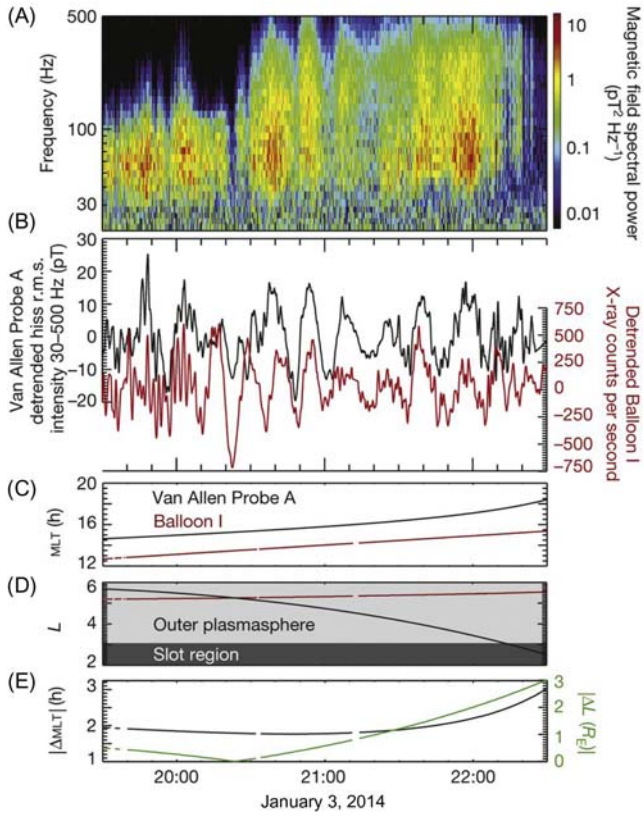

Figure 2.9 Modulation of both plasmaspheric hiss (A) and inferred electron precipitation (B) on the timescales of ULF waves. Other panels show the MLT (C), L (D), |dMLT| and |dL| (E) values for where the spacecraft (A) and balloon (B) measurements were made (Breneman et al., 2015).

Furthermore, they show that plasmaspheric hiss waves are not featureless broadband waves, but have more structure than previously thought.

In addition to the ULF modulation of hiss described in Breneman et al. (2015), there is also a possible secondary effect described by Rae et al. (2018), in which electron precipitation may be enhanced by a varying loss cone. The increased precipitation leads to an enhancement of the anisotropy that drives whistler-mode waves unstable, which may lead to either enhanced wave amplitudes or longer lifetimes and thus increased precipitation.

2.4 Conclusion

ULF waves are ubiquitous in the magnetospheric environment, including the inner magnetosphere, where the radiation belt population is present. Even though ULF

waves are regarded as an important part of the process by which radiation belt electrons are accelerated and transported, their role in the loss processes in general, and loss to the atmosphere in particular, is often neglected. The main reason for the skepticism is that ULF wave periods occur on longer timescales than those of the radiation belt electron bounce motion and therefore it is not immediately clear how this interaction could happen and cause the particles to violate their second adiabatic invariant. The intensity and dynamics of ULF waves are correlated with geomagnetic activity, but there is not yet a full understanding of their interactions with the energetic population, especially electrons, and with other higher frequency waves that coexist in the same region. However, some studies using both simulations and in situ observations have shone new light on this topic and have demonstrated that ULF waves can indeed be a factor in radiation belt precipitation. This is possible either through a direct method (i.e., Fermi acceleration in the inner magnetosphere) or as an indirect effect, by affecting growth rates of other waves. Nevertheless, there are clear observational connections between ULF oscillations and other phenomena and observations such as precipitation observed by riometers (Spanswick et al., 2005), aurora (Rae et al., 2018), and balloon-borne observations of X-ray emissions related to relativistic electron precipitation (Breneman et al., 2015; Halford et al., 2015).

MHD simulations of a geomagnetic storm performed by Brito et al. (2012, 2015) provide support for the idea that changes in both components of momentum, and thus changes in the equatorial pitch angle, of the simulated relativistic electron population can be driven by the ULF oscillations. The predominant effect responsible for the precipitation is the rapid inward radial motion of the electrons to regions of larger loss cone angle, effectively varying the loss cone of the particles. It is important to note that MHD simulations do not capture high-frequency waves approaching the ion cyclotron frequency. Thus by keeping EMIC waves from interacting with the electrons, which is believed to play an important role in duskside energetic electron precipitation, it is possible to perform a controlled experiment in which only the ULF oscillations can have an effect on the electrons. Using this scenario, the authors have reproduced the prompt, ULF-wave–modulated precipitation observed by balloon missions after the arrival of an interplanetary shock exclusively from the effects of the MHD fields on test particles. The simulated precipitation has the same period and same longitudinal location as the balloon precipitation measurements.

In a study by Rae et al. (2018), it was shown statistically that that large-amplitude ULF waves can modulate the loss cone by approximately 20%, which allows a significantly greater fraction of the electron Phase Space Density (PSD) to precipitate than previously thought, substantiating the simulation results. The authors show direct evidence of ULF-modulated precipitation spatially correlated with localized compressional large-amplitude ULF wave activity and therefore point out that these waves should be considered along with other electron precipitation mechanisms.

The complete understanding of how ULF waves affect radiation belt loss in general is still a long way off. Besides the questions surrounding direct ULF-driven precipitation, there is the effect of indirect ULF precipitation, as discussed in Breneman et al. (2015), who suggest that the coupling between ULF wave formation and propagation and the radiation belts is important to their dynamics and loss caused by ULF-modulated plasmaspheric hiss during active times. Also important is the question of which type of loss (atmospheric vs magnetopause) is most relevant, especially during the commonly observed electron dropout events. ULF waves play a significant role in this question, since their effect on electron outward transport is well known. It is therefore now recognized that ULF waves have an major role in several processes involving radiation belt loss, but the task remains to better characterize and quantify these processes to form a more accurate global picture of radiation belt dynamics.

Acknowledgment

The authors would like to acknowledge NASA grant NNX15AF59G.

References

Allen, R.C., Zhang, J.-C., Kistler, L.M., Spence, H.E., Lin, R.-L., Klecker, B., et al., 2015. A statistical study of emic waves observed by cluster: 1. Wave properties. J. Geophys. Res. Space Phys. 120 (7), 5574–5592. Available from: https://doi.org/10.1002/2015JA021333. 2015JA021333.

Anderson, K.A., Milton, D.W., 1964. Balloon observations of x rays in the auroral zone: 3. High time resolution studies. J. Geophys. Res. 69 (21), 4457–4479. Available from: https://doi.org/10.1029/JZ069i021p04457.

Baker, D.N., Pulkkinen, T.I., Li, X., Kanekal, S.G., Blake, J.B., Selesnick, R.S., et al., 1998. Coronal mass ejections, magnetic clouds, and relativistic magnetospheric electron events: ISTP. J. Geophys. Res. Atmos. 103 (A8), 17,279–17,291. Available from: https://doi.org/10.1029/97JA03329.

Borovsky, J.E., Denton, M.H., 2009. Relativisticelectron dropouts and recovery: A superposed epoch study of the magnetosphere and the solar wind. J. Geophys. Res. Space Phys. 114 (A2). Available from: https://doi.org/10.1029/2008JA013128.

Breneman, A.W., Halford, A.J., Millan, R., McCarthy, M., Fennell, J., Sample, J., et al., 2015. Global-scale coherence modulation of radiation-belt electron loss from plasmaspheric hiss. Nature 523, 193–195.

Brito, T., Woodger, L., Hudson, M., Millan, R., 2012. Energetic radiation belt electron precipitation showing ULF modulation. Geophys. Res. Lett. 39 (22). Available from: https://doi.org/10.1029/2012GL053790. L22,104.

Brito, T., Hudson, M.K., Kress, B., Paral, J., Halford, A., Millan, R., et al., 2015. Simulation of ULF wavemodulated radiation belt electron precipitation during the 17 March 2013 storm. J. Geophys. Res. Space Phys. 120 (5), 3444–3461. Available from: https://doi.org/10.1002/2014JA020838.

Brown, R.R., Barcus, J.R., Parsons, N.R., 1965. Balloon observations of auroral zone x rays in conjugate regions: 2. microbursts and pulsations. J. Geophys. Res. Space Phys. 70 (11), 2599–2612. Available from: https://doi.org/10.1029/JZ070i011p02599.

Chen, L., Hasegawa, A., 1991. Kinetic theory of geomagnetic pulsations 1: internal excitations by energetic particles. J. Geophys. Res. 96 (A2), 1503–1512.

Claudepierre, S.G., Wiltberger, M., Elkington, S.R., Lotko, W., Hudson, M.K., 2009. Magnetospheric cavity modes driven by solar wind dynamic pressure fluctuations. Geophys. Res. Lett. 36 (13). Available from: https://doi.org/10.1029/2009GL039045. L13,101.

Claudepierre, S.G., Hudson, M.K., Lotko, W., Lyon, J.G., Denton, R.E., 2010. Solar wind driving of magnetospheric ULF waves: field line resonances driven by dynamic pressure fluctuations. J. Geophys. Res. Space Phys. 115 (A11). Available from: https://doi.org/10.1029/2010JA015399.

Claudepierre, S.G., Mann, I.R., Takahashi, K., Fennell, J.F., Hudson, M.K., Blake, J.B., et al., 2013. Van Allen Probes observation of localized drift resonance between poloidal mode ultra-low frequency waves and 60 keV electrons. Geophys. Res. Lett. Available from: https://doi.org/10.1002/grl.50901.

Demekhov, A., 2007. Recent progress in understanding pc1 pearl formation. J. Atmos. Sol. Terr. Phys. 69 (14), 1609–1622. Available from: https://doi.org/10.1016/j.jastp.2007.01.014.

Elkington, S.R., 2013. A Review of ULF Interactions With Radiation Belt Electrons. American Geophysical Union (AGU), pp. 177–193. Available from: https://doi.org/10.1029/169GM12.

Elkington, S.R., Hudson, M.K., Wiltberger, M.J., Lyon, J.G., 2002. MHD/particle simulations of radiation belt dynamics. J. Atmos. Sol. Terr. Phys. 64 (56), 607–615. Available from: https://doi.org/10.1016/S1364-6826(02)00018-4.

Elkington, S.R., Hudson, M.K., Chan, A.A., 2003. Resonant acceleration and diffusion of outer zone electrons in an asymmetric geomagnetic field. J. Geophys. Res. Space Phys. 108 (A3), 1116. Available from: https://doi.org/10.1029/2001JA009202.

Elkington, S.R., Wiltberger, M., Chan, A.A., Baker, D.N., 2004. Physical models of the geospace radiation environment. J. Atmos. Sol. Terres. Phys. 66 (1516), 1371–1387. Available from: https://doi.org/10.1016/j.jastp.2004.03.023.

Elkington, S.R., Chan, A.A., Wiltberger, M., 2013. Global Structure of ULF Waves During the 2426 September 1998 Geomagnetic Storm. American Geophysical Union (AGU), pp. 127–138. Available from: https://doi.org/10.1029/2012GM001348.

Fermi, E., 1949. On the origin of the cosmic radiation. Phys. Rev. 75, 1169–1174. Available from: https://doi.org/10.1103/PhysRev.75.1169.

Goldstein, J., Hudson, M.K., Lotko, W., 1999. Possible evidence of damped cavity mode oscillations stimulated by the January, 1997 magnetic cloud event. Geophys. Res. Lett. 26 (24), 3589–3592. Available from: https://doi.org/10.1029/1999GL003636.

Halford, A.J., McGregor, S.L., Murphy, K.R., Millan, R.M., Hudson, M.K., Woodger, L.A., et al., 2015. Barrel observations of an icme-shock impact with the magnetosphere and the resultant radiation belt electron loss. J. Geophys. Res. Space Phys. 120 (4), 2557–2570. Available from: https://doi.org/10.1002/2014JA020873. 2014JA020873.

Hasegawa, A., 1969. Drift mirror instability in the magnetosphere. Phys. Fluids 12 (12), 2642.

Horne, R.B., Lam, M.M., Green, J.C., 2009. Energetic electron precipitation from the outer radiation belt during geomagnetic storms. Geophys. Res. Lett. 36 (19).

Hughes, W.J., 1994. Magnetospheric ULF Waves: A Tutorial with a Historical Perspective. American Geophysical Union, Washington, DC, pp. 1–11. Available from: https://doi.org/10.1029/GM081p0001.

Jacobs, J.A., Kato, Y., Matsushita, S., Troitskaya, V.A., 1964. Classification of geomagnetic micropulsations. J. Geophys. Res. Space Phys. 69 (1), 180–181. Available from: https://doi.org/10.1029/JZ069i001p00180.

Kokorowski, M., Bering, E., Ruohoniemi, M., Sample, J., Holzworth, R., Bale, S., et al., 2008. Magnetospheric electric field variations caused by storm-time shock fronts. Adv. Space Res. 42 (1), 181–191. Available from: https://doi.org/10.1016/j.asr.2008.03.006.

Kress, B.T., Hudson, M.K., Looper, M.D., Albert, J., Lyon, J.G., Goodrich, C.C., 2007. Global MHD test particle simulations of $>$ 10 MeV radiation belt electrons during storm sudden commencement. J. Geophys. Res. Space Phys. 112, A09215. Available from: https://doi.org/10.1029/2006JA012218.

Li, Z., Millan, R.M., Hudson, M.K., Woodger, L.A., Smith, D.M., Chen, Y., et al., 2014. Investigation of emic wave scattering as the cause for the barrel 17 January 2013 relativistic electron precipitation event: a quantitative comparison of simulation with observations. Geophys. Res. Lett. 41 (24), 8722–8729. Available from: https://doi.org/10.1002/2014GL062273,2014GL062273.

Loto'aniu, T.M., Fraser, B.J., Waters, C.L., 2009. The modulation of electromagnetic ion cyclotron waves by pc 5 ULF waves. Ann. Geophys. 27 (1), 121–130. Available from: https://doi.org/10.5194/angeo-27-121-2009.

Mathie, R.A., Mann, I.R., 2000. A correlation between extended intervals of ULF wave power and storm-time geosynchronous relativistic electron flux enhancements. Geophys. Res. Lett. 27 (20), 3261–3264. Available from: https://doi.org/10.1029/2000GL003822.

Menk, F.W., 2011. Magnetospheric ULF waves: a review. The Dynamic Magnetosphere. Springer, New York, pp. 223–256.

Millan, R.M., Lin, R.P., Smith, D.M., McCarthy, M.P., 2007. Observation of relativistic electron precipitation during a rapid decrease of trapped relativistic electron flux. Geophys. Res. Lett. 34 (10). Available from: https://doi.org/10.1029/2006GL028653.

Millan, R.M., McCarthy, M.P., Sample, J.G., Smith, D.M., Thompson, L.D., McGaw, D.G., et al., 2013. The balloon array for rbsp relativistic electron losses (barrel). Space Sci. Rev. 179 (1), 503–530. Available from: https://doi.org/10.1007/s11214-013-9971-z.

Mursula, K., Brysy, T., Niskala, K., Russell, C.T., 2001. Pc1 pearls revisited: Structured electromagnetic ion cyclotron waves on polar satellite and on ground. J. Geophys. Res. Space Phys. 106 (A12), 29,543–29,553. Available from: https://doi.org/10.1029/2000JA003044.

O'Brien, T.P., Lorentzen, K.R., Mann, I.R., Meredith, N.P., Blake, J.B., Fennell, J.F., et al., 2003. Energization of relativistic electrons in the presence of ULF power and MeV microbursts: evidence for dual ULF and VLF acceleration. J. Geophys. Res. Space Phys. 108 (A8). Available from: https://doi.org/10.1029/2002JA009784.

Ohtani, S., Miyoshi, Y., Singer, H.J., Weygand, J.M., 2009. On the loss of relativistic electrons at geosynchronous altitude: its dependence on magnetic configurations and external conditions. J. Geophys. Res. Space Phys. 114 (A1). Available from: https://doi.org/10.1029/2008JA013391.

Rae, J.I., Murphy, K.R., Watt, C.E.J., Halford, A.J., Mann, I.R., Ozeke, L.G., et al., 2018. The role of localised compressional ultra-low frequency waves in energetic electron precipitation. J. Geophys. Res. Space Phys. Available from: https://doi.org/10.1002/2017JA024674,2017JA024674.

Rostoker, G., Skone, S., Baker, D.N., 1998. On the origin of relativistic electrons in the magnetosphere associated with some geomagnetic storms. Geophys. Res. Lett. 25 (19), 3701–3704. Available from: https://doi.org/10.1029/98GL02801.

Samson, J.C., Rostoker, G., 1972. Latitude-dependent characteristics of high-latitude Pc 4 and Pc 5 micropulsations. J. Geophys. Res. Space Phys. 77 (31), 6133–6144. Available from: https://doi.org/10.1029/JA077i031p06133.

Schulz, M., Lanzerotti, L.J., 1974. *Particle Diffusion in the Radiation Belts*, Physics and Chemistry in Space, vol. 7. Springer-Verlag, New York.

Shprits, Y.Y., Thorne, R.M., Friedel, R., Reeves, G.D., Fennell, J., Baker, D.N., et al., 2006. Outward radial diffusion driven by losses at magnetopause. J. Geophys. Res. Space Phys. 111 (A11). Available from: https://doi.org/10.1029/2006JA011657.

Shprits, Y.Y., Elkington, S.R., Meredith, N.P., Subbotin, D.A., 2008. Review of modeling of losses and sources of relativistic electrons in the outer radiation belt i: radial transport. J. Atmos. Sol. Terr. Phys. 70 (14), 1679–1693.

Southwood, D.J., Kivelson, M.G., 1981. Charged particle behavior in low-frequency geomagnetic pulsations 1. Transverse waves. J. Geophys. Res. Space Phys. 86 (A7), 5643–5655. Available from: https://doi.org/10.1029/JA086iA07p05643.

Southwood, D.J., Dungey, J.W., Etherington, R.J., 1969. Bounce resonant interaction between pulsations and trapped particles. Planet Space Sci. 17, 349.

Spanswick, E., Donovan, E., Baker, G., 2005. Pc5 modulation of high energy electron precipitation: particle interaction regions and scattering efficiency. Ann. Geophys. 23 (5), 1533–1542.

Summers, D., Ma, C., Mukai, T., 2004. Competition between acceleration and loss mechanisms of relativistic electrons during geomagnetic storms. J. Geophys. Res. Space Phys. 109 (A4). Available from: https://doi.org/10.1029/2004JA010437.

Summers, D., Ni, B., Meredith, N.P., 2007. Timescales for radiation belt electron acceleration and loss due to resonant wave-particle interactions: 2. Evaluation for VLF chorus, ELF hiss, and electromagnetic ion cyclotron waves. J. Geophys. Res. Space Phys. 112 (A4). Available from: https://doi.org/10.1029/2006JA011993.

Turner, D.L., Shprits, Y., Hartinger, M., Angelopoulos, V., 2012. Explaining sudden losses of outer radiation belt electrons during geomagnetic storms. Nat. Phys. 8 (3), 208–212. Available from: https://doi.org/10.1038/nphys2185.

Woodger, L.A., Halford, A.J., Millan, R.M., McCarthy, M.P., Smith, D.M., Bowers, G.S., et al., 2015. A summary of the barrel campaigns: technique for studying electron precipitation. J. Geophys. Res. Space Phys. 120 (6), 4922–4935. Available from: https://doi.org/10.1002/2014JA020874.

Wygant, J., Mozer, F., Temerin, M., Blake, J., Maynard, N., Singer, H., et al., 1994. Large amplitude electric and magnetic field signatures in the inner magnetosphere during injection of 15 mev electron drift echoes. Geophys. Res. Lett. 21 (16), 1739–1742. Available from: https://doi.org/10.1029/94GL00375.

Zong, Q.-G., Zhou, X.-Z., Wang, Y.F., Li, X., Song, P., Baker, D.N., et al., 2009. Energetic electron response to ULF waves induced by interplanetary shocks in the outer radiation belt. J. Geophys. Res. Space Phys. 114 (A10), . Available from: https://doi.org/10.1029/2009JA014393. A10,204.

CHAPTER 3

Observations of radiation belt losses due to cyclotron wave-particle interactions

Lauren W. Blum[1] **and Aaron W. Breneman**[2]
[1]NASA Goddard Space Flight Center, Greenbelt, MD, United States
[2]School of Physics and Astronomy, University of Minnesota, Twin Cities, Minneapolis, MN, United States

Contents

3.1 Introduction

The Van Allen radiation belts are tori of semi-trapped, high-energy electrons and ions surrounding the Earth (e.g., Van Allen, 1959). Typical belt structure consists of an inner zone of stably trapped energetic ions and electrons and a dynamic outer zone of energetic electrons. These are often separated by a slot region devoid of energetic particles. Storm-time dynamics of the radiation belts arise from competition between a number of time-varying processes that enhance or deplete energetic electron populations. These include energization or deenergization from radial transport (Li et al., 1997; Shprits et al., 2006), outer boundary loss (Turner et al., 2012; Hudson et al., 2014; Ukhorskiy et al., 2015), dramatic local acceleration events

The Dynamic Loss of Earth's Radiation Belts
DOI: https://doi.org/10.1016/B978-0-12-813371-2.00003-2

(Horne et al., 2005; Thorne et al., 2013a,b; Matsui et al., 2017), and steady or bursty precipitation loss to the atmosphere (Thorne et al., 2010; Millan and The BARREL Team, 2011). The complex interplay of these processes, driven by a dynamic solar wind (Hudson et al., 2008; Reeves et al., 2011; Li et al., 2015c; Boynton et al., 2017) and influenced by prestorm magnetospheric conditions (Kilpua et al., 2015), ultimately leaves the radiation belts enhanced, depleted, or relatively unchanged over prestorm levels (Friedel et al., 2002; Reeves et al., 2003; Turner et al., 2015; Moya et al., 2017).

Understanding the relative importance, time variability, and interrelationships of these drivers is required for predicting short- and long-term space weather. Enhanced predictive capability (National Research Council, 2013; Meredith et al., 2017) provides the foundation for mitigation strategies protecting satellites against accumulated radiation dose or single-event damage (Wrenn and Smith, 1996; Horne et al., 2013), enhancements in global positioning system (GPS) accuracy, and understanding the effects of space weather on climate via modification of upper atmosphere chemistry (Mironova et al., 2015) including ozone depletion (Andersson et al., 2014).

This review focuses on one aspect of this complex system; loss of energetic ($>\sim$100 keV), relativistic ($>$500 keV) and ultrarelativistic ($>$2 MeV) electrons to the atmosphere through Doppler-shifted cyclotron resonance with waves. In particular, the focus is on observational signatures of electron precipitation and comparison with measured properties of the plasma waves that drive a substantial part of this loss. Section 3.2 reviews the basics of Doppler-shifted cyclotron resonance scattering of electrons by plasma waves, along with quasi-linear theory, which is the dominant paradigm for describing the collective effects of scattering. We provide a brief overview of the various types of energetic electron precipitation observed, followed by a review of the three waves most often responsible for causing radiation belt precipitation loss: plasmaspheric hiss, chorus, and electromagnetic ion cyclotron (EMIC) waves. Section 3.3 then discusses the structure and dynamics of the radiation belts, and in particular the role of cyclotron resonance scattering via these three waves in dictating belt morphology. Section 3.4 presents single-satellite observations of wave properties and simultaneous, multipayload comparative observations of waves and precipitation. These observations provide further insight into resonant scattering and allow the close comparison of waves and precipitation loss that are necessary for testing models. We conclude this review by discussing important issues currently being explored, new approaches to radiation belt understanding (modeling), and the use of new techniques that promise to enhance our understanding of precipitation loss via Doppler-shifted cyclotron resonant scattering.

3.2 Background

3.2.1 Doppler-shifted cyclotron resonance and quasi-linear theory

Magnetospheric electrons have helical trajectories that are a combination of cyclotron motion about the magnetic field and translation along the field line. The vector sum of these motions describes a cone of velocity vectors with a *pitch angle* relative to the magnetic field. In the magnetosphere, these electrons exist in a magnetic bottle configuration. As electrons propagate to higher magnetic latitudes, magnetic field line convergence produces an effective *mirror* force that opposes the electron motion. For electrons with pitch angles outside the *loss cone*, this force is sufficient to reverse the guiding center motion, sending the electrons back toward the opposite hemisphere and effectively trapping them inside the magnetic bottle. Electrons with pitch angles inside the loss cone, however, have sufficient velocity parallel to the background field to overcome this mirror force and will precipitate into the atmosphere. Owing to the azimuthally asymmetric nature of the Earth's magnetic field, the size of the loss cone varies with geographic longitude and hemisphere. Particles scattered into the *bounce loss cone* (BLC) will precipitate within a single bounce period, while particles scattered into the larger *drift loss cone* (DLC) will precipitate within one drift period once they reach a region of weaker magnetic field called the "South Atlantic Anomaly."

Electrons trapped in the magnetic bottle geometry can be scattered into the loss cone by interaction with circularly/elliptically polarized waves in a process called "Doppler-shifted cyclotron resonance" (e.g., Tsurutani and Lakhina, 1997). *Normal* resonance occurs between a counterstreaming electron with field-aligned velocity $v_{||}$ and a right-hand polarized wave, with field-aligned wave number $k_{||}$ and angular frequency $\omega < \omega_{ce}$, where ω_{ce} is the cyclotron frequency. Resonant electrons observe the wave Doppler-shifted to an integral multiple n ($n = 0, \pm 1, \pm 2, \ldots$) of their cyclotron frequency, satisfying the resonance condition:

$$\omega - k_{||} v_{||} = n\Omega_{ce}/\gamma, \tag{3.1}$$

where is the relativistic Lorentz factor. *Anomalous* resonance (Ginzburg, 1960) can occur between a copropagating electron and left-hand polarized wave if the electron velocity exceeds the wave phase velocity. In the frame of the electron, this shifts the sense of wave rotation from left to right, allowing resonance to occur. Anomalous resonance allows left-hand polarized waves, such as EMIC waves, to interact with highly energetic (typically of several MeV) electrons. Electrons in resonance (either normal or anomalous) see a constant wave phase and are able to efficiently exchange energy and momentum with the wave (Brice, 1964).

To determine the importance of Doppler-shifted cyclotron resonance interactions in magnetospheric dynamics we're seldom interested in the details of any single wave/electron interaction. In the quasi-linear paradigm, the combined effect of a number of weak scattering interactions involving small amplitude, broadband waves and a phase-randomized distribution of electrons results in diffusion of electrons in pitch angle and energy (Kennel and Petschek, 1966; Kennel and Engelmann, 1966). For decades, quasi-linear theory, owing to its relative simplicity and utility, has been an important foundation for modeling and understanding radiation belt dynamics (see review by Horne et al., 2016). Modern quasi-linear simulations, using the most up-to-date wave statistical parameterizations and plasma models constructed from decades of satellite observations, have found success describing long-duration (days to weeks) evolution of radiation belt populations (e.g., Subbotin et al., 2011; Kim and Shprits, 2013; Tu et al., 2013; Shprits et al., 2009).

A simple metric calculated from quasi-linear theory for describing the integrated effect of multiple source and loss processes is the *electron lifetime*, defined as the e-folding loss timescale for electrons (e.g., Shprits et al., 2007; Albert and Shprits, 2009b). In the Earth's radiation belts, electron lifetimes are driven largely by Doppler-shifted cyclotron resonance scattering with three prominent plasma waves: plasmaspheric hiss, chorus, and EMIC. These are discussed in detail in Section 3.2.3. Loss by these waves plays an important role in creating the classic two-belt structure of the Earth's radiation belts.

3.2.2 Overview of precipitation observations

A long history of observations has established that precipitation into the atmosphere is an important source of radiation belt electron loss. Precipitation is observed to come in a variety of forms, ranging from slow drizzle to impulsive, subsecond events. Tying the various forms of precipitation to potential causative waves, typically observed near the equator, is critical for understanding this connection. This comparison turns out to be exceedingly difficult in practice. Equatorial satellites are ideally suited for measuring in situ wave populations generated near the magnetic equator, but they are often unable to distinguish between trapped and precipitating electrons. High inclination, low earth orbit (LEO) satellites can directly observe precipitating electrons but are usually far from the wave source. More continuous, albeit indirect, precipitation observations come from balloons, which infer precipitating spectra from measurements of X-rays produced by bremsstrahlung interaction with atmospheric neutrals (Woodger et al., 2015; Millan et al., 2013; Foat et al., 1998), as well as from ground-based platforms like riometers and very low frequency (VLF) receivers, which indirectly measure precipitation through its effect on atmospheric ionization (e.g., Rodger et al., 2012; Clilverd et al., 2009). Owing to their accessibility and

relatively low cost, balloons and ground-based platforms provided the majority of precipitation observations in the early decades of radiation belt research (e.g., Rosenberg et al., 1971).

LEO spacecraft, owing to their fast traversal of the radiation belts, provide a snapshot of electron precipitating populations at a given time interval. Fig. 3.1, adapted from Nakamura et al. (2000), shows two example passes through the outer radiation belt of >1-MeV electron flux measured by the LEO satellite SAMPEX (Solar, Anomalous, and Magnetospheric Particle Explorer; Baker et al. 1993). Fig. 3.1A shows a well-populated outer belt from $L \sim 3-7$ superimposed with a relativistic electron precipitation (REP) band of strongly enhanced flux at $L \sim 6$. These bands are often seen on consecutive orbits and/or in conjugate hemispheres. The observed repeatability and duration is thought to reflect a persistent (lasting minutes to hours), latitudinally narrow precipitation region (Nakamura et al., 1995; Blake et al., 1996). Balloon and satellite observations show that REP events occur predominantly in the afternoon and night sectors, with increased frequency during

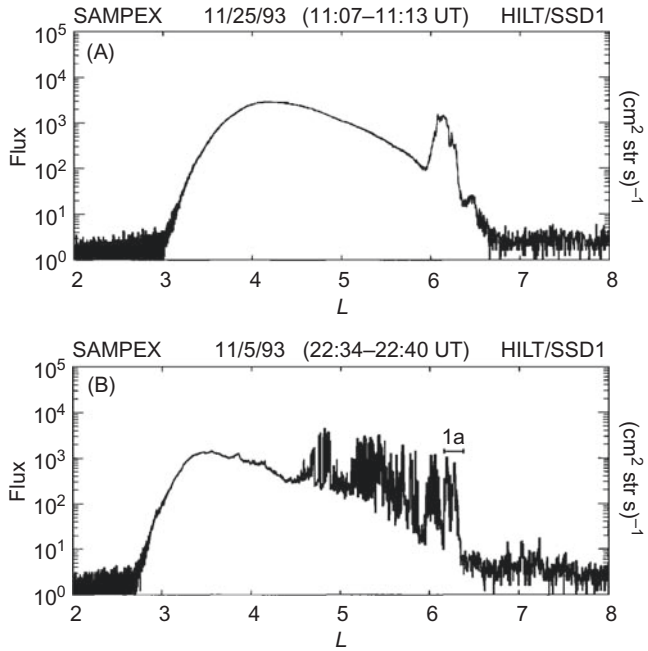

Figure 3.1 SAMPEX observations of >1-MeV electron flux from two passes through the outer radiation belts, with (A) showing smoothly varying flux with a well-defined precipitation band, and (B) showing strong flux contributions from relativistic microbursts. *Adapted from Nakamura, R., Isowa, M., Kamide, Y., Baker, D.N., Blake, J.B., Looper, M., 2000. SAMPEX observations of precipitation bursts in the outer radiation belt. J. Geophys. Res. Atmos. 105 (A7), 15875–15885. Available from: https://doi.org/10.1029/2000JA900018.*

geomagnetic activity (Millan et al., 2002; Imhof et al., 1986; Nakamura et al., 2000; Comess et al., 2013; Blum et al., 2015a). Numerous studies attempting to identify the causes of these precipitation events have categorized them into different groups based on shape, duration, and whether simultaneous lower energy electron or ion precipitation is observed (e.g., Yahnin et al., 2016; Vampola et al., 1971; Imhof et al., 1986). Some of these precipitation events have been attributed to a breakdown of adiabaticity in the warped nightside magnetic field geometry, while others have been attributed to scattering by various wave modes (Vampola et al., 1971; Koons and McPherson, 1972; Brown and Stone 1972). They have been estimated to be an important source of >MeV electron loss, particularly during geomagnetically active periods (Bortnik et al., 2006; Millan et al., 2002; Blum et al., 2013).

Fig. 3.1B shows an example of a well-populated outer zone superimposed with short-duration spikes of high precipitation flux. These spikes, occurring on subsecond timescales, are termed "microbursts." Microbursts were initially observed at ~keV energies (Winckler et al., 1962; Anderson and Milton 1964; Tsurutani et al., 2013; Lampton, 1967), and more recently at relativistic (MeV) energies (Imhof et al., 1992; Blake et al., 1996; Crew et al., 2016). Microbursts are most common during storm main and early recovery phases (O'Brien et al., 2004), are typically found in the morning sector and outside of the plasmasphere (Lorentzen et al., 2001a,b; Johnston and Anderson, 2010; Douma et al., 2017), and often occur in long trains (e.g., Fig. 3.1B). These observations have led to suggestions that they are caused by impulsive, nonlinear scattering (e.g., Blake et al., 1996; Hikishima et al., 2010; Osmane et al., 2016). Comparisons of estimates of precipitating microburst flux to trapped population are subject to large uncertainties, but they indicate that long-lasting and extended sources of relativistic microbursts (Anderson et al., 2017) can be a major source of electron loss during storm times (Lorentzen et al., 2001b; O'Brien et al., 2004; Breneman et al., 2017).

Despite decades of observations, large gaps remain in our understanding of energetic, relativistic, and ultrarelativistic electron precipitation. It is still unclear what fraction of precipitation loss results from wave resonance scattering as opposed to other mechanisms, such as breakdown of adiabaticity in the tail region. Also unclear is how the theoretical energy dependence of scattering by various wave modes matches up with observations. Finally, there is an incomplete understanding of the relative importance of precipitation loss compared to other loss mechanisms, such as outer boundary loss. To complicate matters, the relative importance of wave-induced loss, as well as the details of this loss, can be highly variable within the evolution of a single storm and from storm to storm. The remainder of this review aims to address the role that different wave modes play in causing electron precipitation and the overall contribution of this precipitation to the dynamics of the Earth's radiation belts.

3.2.3 Key wave modes involved in radiation belt electron loss

We now provide a brief overview of plasmaspheric hiss, chorus, and EMIC waves. These wave types are thought to dominate resonant scattering loss of radiation belt electrons. Other wave types, such as VLF transmitters, lightning whistlers, magnetosonic waves, and kinetic Alfvén waves, play small or supporting roles in scattering loss (Abel and Thorne, 1998) and are not discussed extensively here.

3.2.3.1 Plasmaspheric hiss

Plasmaspheric hiss (Thorne et al., 1973) is a typically structureless, broadband electromagnetic whistler-mode emission (Fig. 3.2A) found within the high-density plasmasphere and plasmaspheric plumes. The range of wave amplitudes is usually 10−100 pT, and they peak at ∼300−400 Hz (Meredith et al., 2004; Golden et al., 2012; Yu et al., 2017a,b; Li et al., 2015b). Various other types of hiss have been observed, such as midlatitude hiss (see review by Hayakawa and Sazhin, 1992), dayside hiss following shock compressions (Tsurutani et al., 2015), low-altitude or ionospheric hiss (Chen et al., 2017; Zhima et al., 2017), and plasma trough exohiss (Zhu et al., 2015), but the focus in this review is on the more dynamically important plasmaspheric hiss.

Despite being one of the most ubiquitous plasma waves, the processes leading to hiss growth have been difficult to pin down. Early theories (e.g., Thorne et al., 1973) suggested local growth near the magnetic equator via temperature anisotropy instability, but this idea was later rejected as offering insufficient growth (Huang et al., 1983; Church and Thorne, 1983). Recent Poynting flux observations from the Van Allen Probes, however, indicate in situ generation near the magnetic equator for at least some fraction of plamaspheric hiss (Kletzing et al., 2014, AGU abstract). Local generation can also occur within radial extensions of the plasmasphere called "plumes" (Laakso et al., 2015). Hiss that does not grow locally appears to originate with a whistler-mode chorus that has propagated into the plasmasphere after reflection at low altitudes (Parrot et al., 2004; Chum et al., 2005; Bortnik et al., 2008a, 2009; Santolík et al., 2006, 2009; Yue et al., 2017; Hartley et al., 2018). Once inside, damping rates are significantly reduced (Li et al., 2010), allowing these waves to propagate long distances and to mix to form a hiss-like spectrum. This direct connection between chorus and hiss has been verified observationally (Li et al., 2015a; Bortnik et al., 2011; Chen et al., 2012; Delport et al., 2012; Meredith et al., 2013; Zhou et al., 2016) and with ray tracing invoking modest in situ growth (Bortnik et al., 2011; Chen et al., 2012; Thorne et al., 1979; Tsurutani et al., 2012).

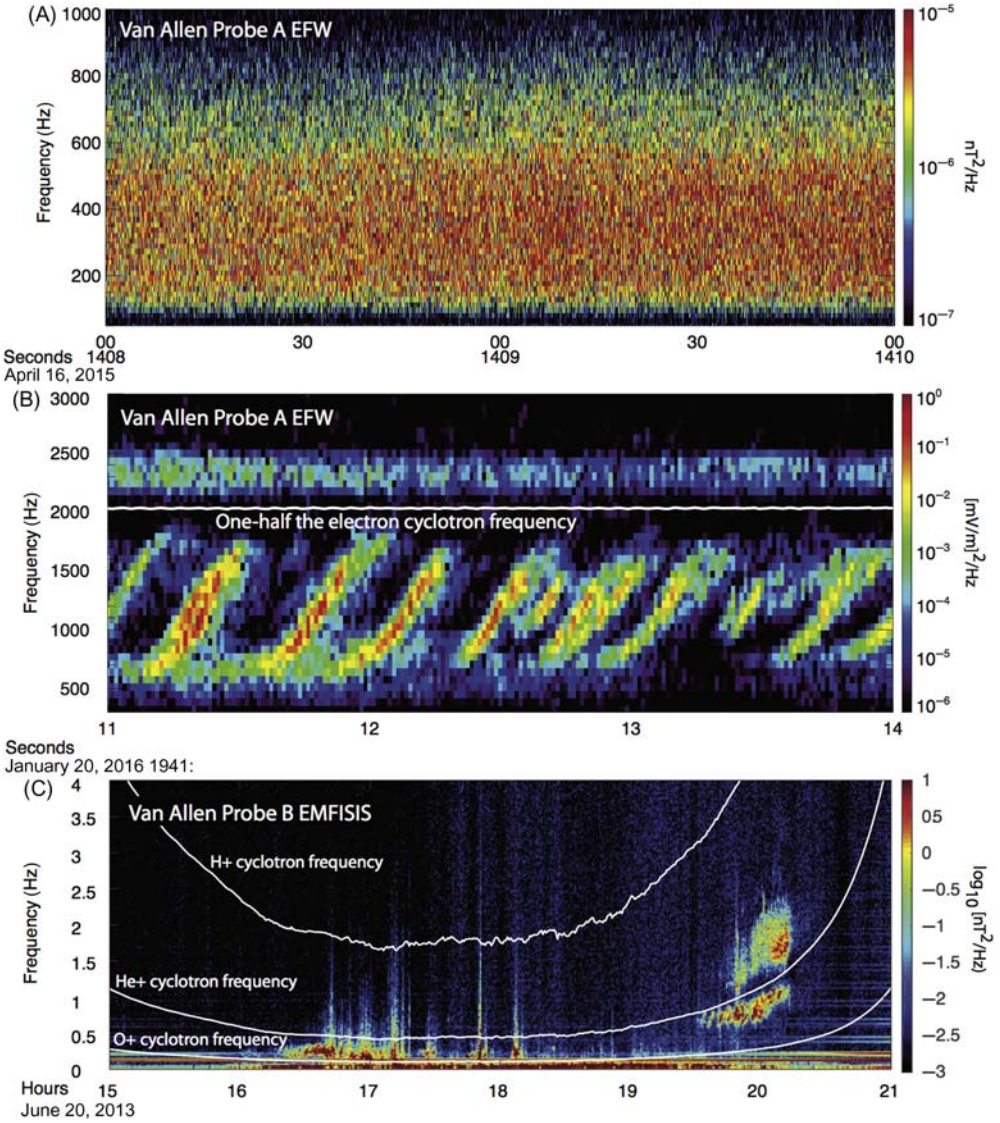

Figure 3.2 Magnetic field power spectral density during periods of (A) unstructured plasmaspheric hiss, (B) lower and upper-band chorus, and (C) EMIC-wave activity.

Hiss waves can interact via cyclotron resonance with a wide range of electron energies, from a few keV to MeV, and scattering by hiss waves within the plasmasphere is recognized to play a dominant role in creating the quiet-time structure of the slot region and radiation belts (Lyons et al., 1972; He et al., 2016).

3.2.3.2 Chorus

Whistler-mode chorus is a prominent VLF wave that exists in the low-density magnetosphere outside the plasmasphere (Burtis and Helliwell, 1969; Tsurutani and Smith, 1974; Sazhin and Hayakawa, 1992). Chorus waves (Fig. 3.2B) are often observed as distinctive rising or (less frequently) falling tones of several kHz/s (Santolík et al., 2004b; Macúšová et al., 2010). Wave power is separated into a lower band ($\sim 0.1-0.5\ f_{ce0}$, where f_{ce0} is the minimum electron cyclotron frequency along a particular field line) and an upper band ($0.5-0.8\ f_{ce0}$), often with a gap at $0.5\ f_{ce0}$ (Tsurutani and Smith, 1977; Santolík et al., 2005). Lower-band chorus is typically much stronger and more common than upper-band chorus (Li et al., 2012), and it interacts with higher-energy electrons.

Chorus grows near the magnetic equator (Nagano et al., 1996; LeDocq et al., 1998; Parrot et al., 2003; Santolík et al., 2005) around midnight in association with injections of a few keV to tens of keV plasma sheet electrons during substorm onset (Tsurutani and Smith, 1974; Xiao et al., 1998; Meredith et al., 2001; Li et al., 2009; Summers et al., 2009; Jordanova et al., 2012; Yue et al., 2017), on the dawn side in association with enhanced convection that can occur presubstorm or during the substorm growth phase (Hwang et al., 2007), and in higher latitude minimum magnetic field pockets formed during times of enhanced dayside compression (Spasojevic and Inan, 2010; Tsurutani and Smith, 1977; Meredith et al., 2001). In all these cases, initial wave growth arises from the temperature anisotropy instability (Kennel and Petschek, 1966; Omura and Summers, 2004; Summers et al., 2009; Fu et al., 2014; Yue et al., 2016) and results in electron scattering to lower pitch angles (Brice, 1964), leading to precipitation in the form of a few keV diffuse aurora (Thorne et al., 2010), tens of keV pulsating aurora (Nishimura et al., 2010), and microbursts (Oliven and Gurnett, 1968; Rosenberg et al., 1981). Once amplitudes grow beyond a critical threshold, nonlinear phase bunching and trapping occur (Nunn 1974; Omura and Summers, 2006; Katoh and Omura, 2007; Shklyar and Matsumoto, 2009; Omura et al., 2012; Matsui et al., 2016); facilitated by magnetic field inhomogeneity, this can lead to the classic chirping, narrowband tones (Katoh and Omura, 2013; Teng et al., 2017) and allows energy and momentum exchange with resonant electrons.

For hundreds of keV electrons, chorus waves are both theorized (Summers et al., 1998, Horne and Thorne, 1998; Roth et al., 1999; Horne et al., 2003, 2005; Horne and Thorne, 2003a) and observed (Meredith et al., 2002, 2003a; Chen et al., 2007; Xiao et al., 2014; Su et al., 2014; Jaynes et al., 2015; Rodger et al., 2016; Foster et al., 2017) to play a dual role (Bortnik and Thorne, 2007; Millan and Baker, 2012) of driving both dramatic, localized storm-time enhancements of electrons to MeV energies and to cause significant electron precipitation loss up to MeV energies, including microbursts (Agapitov et al., 2013; Lorentzen et al., 2001a).

3.2.3.3 Electromagnetic ion cyclotron

EMIC waves are electromagnetic fluctuations that occur at frequencies below and approaching the local ion (H^+, He^+, O^+) cyclotron frequencies, around 0.1–5 Hz in the heart of the outer radiation belt (see Fig. 3.2C). Occurrence rates peak across the dayside and afternoon sectors (e.g., Saikin et al., 2015; Wang et al., 2015), with He^+ band waves often more prevalent and of larger amplitude in the dusk sector, while H^+ band waves are more often located in the day and morning sectors (e.g., Min et al., 2012; Keika et al., 2013). Yu et al. (2015) studied O^+ band waves, which are less often surveyed than H^+ and He^+ band waves, and found them to be prevalent in the morning and noon sectors as well.

EMIC waves are thought to be generated from keV ion populations with an unstable temperature anisotropy ($T_\perp > T_\parallel$) (Cornwall, 1965; Horne and Thorne, 1994). The presence of cold plasma lowers the instability threshold, enabling enhanced wave growth (e.g., Gary 1993). In the inner magnetosphere, EMIC waves often occur in the afternoon sector, where keV ring current ions overlap cool, dense plasmaspheric plumes (e.g., Spasojevic et al., 2005; Clausen et al., 2011; Halford et al., 2010). EMIC waves can also be generated across the dayside during times of enhanced solar wind dynamic pressure, which acts as a source of temperature anisotropy as well (McCollough et al., 2010; Usanova et al., 2012). Ray-tracing models have suggested that density gradients, found at the plasmapause and in the fine structure of plasmaspheric plumes, can support enhanced EMIC-wave growth (Chen et al., 2009; de Soria-Santacruz et al., 2013). However, observationally, dependence of EMIC waves on cold plasma structures is less clear, with some studies finding a relationship between EMIC occurrence and enhanced cold plasma density and/or density gradients (e.g., Halford et al., 2015a) and others finding little statistical correspondence (e.g., Usanova et al., 2013; Posch et al., 2010; Fraser and Nguyen, 2001).

EMIC waves have long been theorized to precipitate radiation belt electrons through anomalous cyclotron resonance (Thorne and Kennel, 1971). The energy of electrons resonant with EMIC waves, based on observed plasma and wave parameters, typically falls in the multiple MeV range (Meredith et al., 2003b; Loto'aniu et al., 2006; Ni et al., 2015), but can be lowered with increased cold plasma density (Li et al., 2013d) or as the wave frequency approaches a heavy ion cyclotron frequency (Ukhorskiy et al., 2010). EMIC waves can also resonate with and scatter keV ions, acting as a loss process for the ring current (Cornwall et al., 1970; Jordanova et al., 2007). For this reason, simultaneous keV ion and MeV electron precipitation is often interpreted as a signature of EMIC-wave scattering (e.g., Sandanger et al., 2007; Miyoshi et al., 2008; Carson et al., 2013). Theoretical estimates have shown that EMIC waves can produce scattering near the strong diffusion limit and thus may contribute to rapid losses of outer belt electrons

(e.g., Summers and Thorne, 2003). However, warm plasma, nonlinear, and nonresonant effects can all complicate these interactions, potentially leading to increased minimum resonant energies, reduction in scattering rates, or scattering into the loss cone at nonresonant energies (e.g., Chen et al., 2011, 2016; Silin et al., 2011; Albert and Bortnik, 2009a). This will be discussed in more detail in Section 3.3.

3.3 Radiation belt structure and morphology

The classic quiet-time structure of the radiation belts consists of two tori of energetic particles surrounding the Earth—a relatively static inner zone of energetic ions and electrons and a more dynamic outer zone of energetic electrons. These are separated by a slot region largely devoid of energetic electrons. What is often not depicted in this classic picture is the strong energy, *L*-shell, and geomagnetic activity dependence of these fluxes and zone boundaries, as illustrated in the Van Allen Probes observations shown in Fig. 3.3 (Reeves et al., 2016). Radiation belt structure during quiet times (Fig. 3.3A) and following active-time enhancements (Fig. 3.3B) is distinctly different. This structure is formed as a balance of different acceleration and loss processes that vary in relative importance with storm phase. The efficiency of each process depends on electron energy, wave frequency, and location, with important differences occurring inside and outside the plasmapause.

Quiet-time morphology shows a distinct separation between inner and outer zones. This zonal separation diminishes during active times, when enhanced radial transport (Brautigam and Albert, 2000; Zhao and Li, 2013) and local energization processes (e.g., Baker et al., 2014a; Ma et al., 2017a) enhance flux levels, partially or

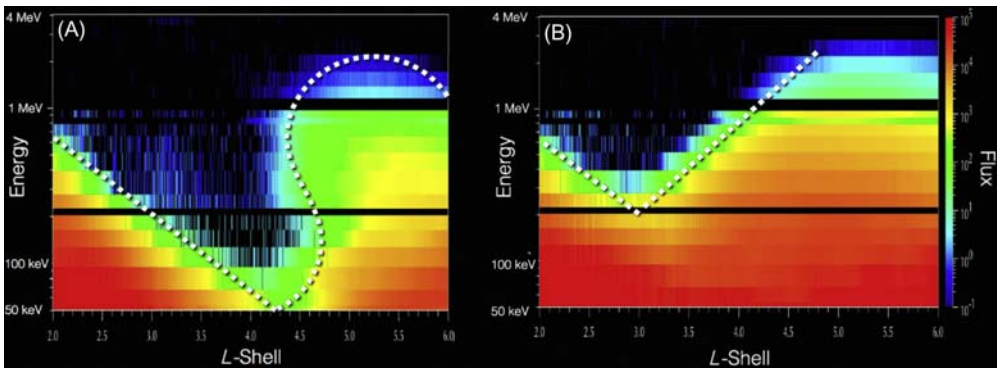

Figure 3.3 Electron flux levels as a function of *L*-shell and energy from Van Allen Probes measurements showing (A) the nominal quiet-time structure with clear separation between inner zone, slot, and outer belt regions across a wide range of energies, and (B) belt structure following active-time enhancements showing a much less distinct separation between the three zones. *From Reeves, G.D., Friedel, R.H.W., Larsen, B.A., Skoug, R.M., Funsten, H.O., Claudepierre, S.G., et al., 2016. Energy-dependent dynamics of keV to MeV electrons in the inner zone, outer zone, and slot regions. J. Geo. Res. Space Phy 121, 397412. Available from: https://doi.org/10.1002/2015JA021569.*

fully filling the slot region. These enhancements temporarily overwhelm loss processes, which include outward radial diffusion, outer boundary loss at the magnetopause, and precipitation loss. As the driving geomagnetic activity subsides, transport and energization processes begin to lose out to wave-induced precipitation loss and the radiation belts gradually return to the quiet-time configuration shown in Fig. 3.3A.

We will now discuss the details of how this balance leads to both the quiescent and dynamic structure of the radiation belts, focusing on the important role of cyclotron resonant scattering loss caused by plasmaspheric hiss, chorus, and EMIC waves.

3.3.1 Inner zone and slot

The inner zone is a region of stably trapped ions and energetic electrons, for which lifetimes can vary from months to years (e.g., Hess 1963; Walt 1994). Lifetimes drop sharply to days to weeks in the adjacent slot region. This sharp transition forms from the combined *L*-dependence of wave-induced precipitation rates and efficiency of radial transport (Lyons et al., 1972; Lyons and Thorne, 1973; Kim et al., 2011; He et al., 2016). Precipitation rates are dependent on resonance access, meaning that local particles must exceed the minimum cyclotron resonance energy, plotted in Fig. 3.4 versus *L* for a range of frequencies. Resonance energy increases with decreasing *L*, owing to the increase in background magnetic field strength, and decreases with wave frequency. Electrons with energies below (or well above) this minimum cyclotron energy are unable to effectively resonate with the waves. Near the boundary of the

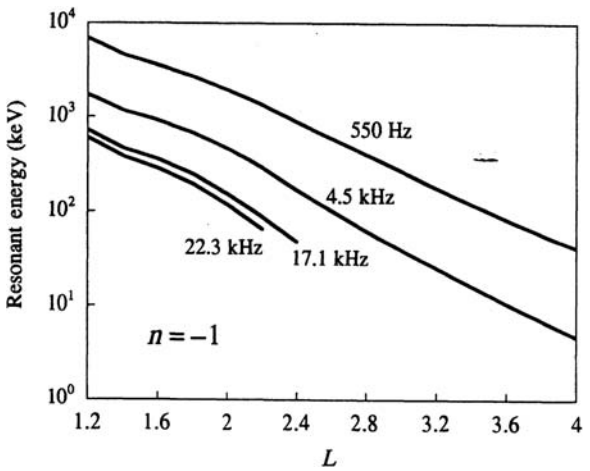

Figure 3.4 Typical minimum resonant cyclotron energies versus *L*-shell for a range of wave frequencies corresponding to plasmaspheric hiss (~550 Hz), lightning-generated whistlers (4.5 kHz), and VLF transmitters (17.1 and 22.3 kHz). *From Abel, B., Thorne, R.M., 1998. Electron scattering loss in Earth's inner magnetosphere: 1. dominant physical processes. J. Geophys. Res. 103 (A2), 23852396. Available from: https://doi.org/10.1029/97JA02919.*

inner zone and slot, this minimum resonance energy begins to exceed available electron populations and lifetimes drastically increase.

Electrons are supplied into the slot and inner zone by injections or inward radial transport by ultralow frequency (ULF) waves. Transport rates strongly decrease with increasing energy and decreasing L-shell. Low-energy (<100 keV) electron injections, which can occur multiple times per day (Zhao and Li, 2013; Turner et al., 2017), are able to penetrate further than higher-energy electrons because they have relatively high-radial transport rates and their energies are below the minimum cyclotron resonant energy for plasmaspheric hiss. At a given L, as energy increases, injections become less frequent, and electron energies can exceed the minimum cyclotron resonance energy for plasmaspheric hiss, tipping the balance between inward transport and loss gradually toward loss. This results in a widening of the slot region with energy.

At ultrarelativistic (a few MeV) energies, radial transport rates are so low (e.g., Ma et al., 2017a, Fig. 4; O'Brien et al., 2016; Zhao and Li, 2013) that wave scattering rates, despite being low, dominate radial transport, creating a sharp inner boundary near $L = 2.8$ termed the *impenetrable barrier* (Baker et al., 2014b; Foster et al., 2016a,b). This barrier is not absolute, and relativistic electron incursions into the inner belt do occasionally happen during rare and very powerful storms (Blake et al., 1996; Li et al., 1993), though no >1.5 MeV electrons have been observed in the inner zone as of yet during the Van Allen Probes era (2012–17) due to historically low recorded solar activity (Claudepierre et al., 2017; Fennell et al., 2015; Li et al., 2015).

This simple picture of a balance of radial transport and plasmaspheric hiss scattering fairly accurately describes the global structure and long-term (days) evolution of the inner belt and slot region during storm recovery. Not included, but also important, are contributions to scattering loss due to higher frequency (1–2 kHz) lightning-generated *whistlers* (Storey, 1953; Helliwell, 1965; Sonwalkar and Inan, 1989; Abel et al., 1998; Meredith et al., 2006a, 2009; Agapitov et al., 2014; Rodger et al., 2003; Kim et al., 2011) and 10–40 kHz whistler-mode VLF transmitters (Inan et al., 2007; Ma et al., 2017b). Though generally containing far less spectral power than plasmaspheric hiss, the higher frequencies of these waves allow them to scatter electrons with energies below the range in resonance with plasmaspheric hiss.

3.3.2 Outer zone

Beyond the previously discussed inner zone and slot region lies the far more dynamic outer zone (Paulikas and Blake, 1979). Precipitation loss via cyclotron resonance with plasmaspheric hiss, chorus, and EMIC waves plays a large role in this zone's structure and variability. Both steady, longer term decay of the outer radiation belt

(e.g., due to scattering by plasmaspheric hiss) as well as more dynamic changes in the population from faster timescale scattering processes, including precipitation loss from EMIC and chorus waves, are observed.

The location of the plasmapause, and waves contained inside this higher density region versus those in the low-density region beyond, plays an important role in the structure and evolution of the outer radiation belt. Inside the plasmasphere, plasmaspheric hiss is largely responsible for gradual depletion of electron flux during the storm recovery and quiet times, as is the case with inner-belt electron decay. Electron lifetimes, derived from observations of precipitation (e.g., Selesnick et al., 2003; Jaynes et al., 2014), as well as from the decay of trapped outer radiation belt electrons (Meredith et al., 2006b; O'Brien et al., 2014), show good agreement with expected scattering rates driven by hiss waves. On timescales of days to months, the inner edge of the outer radiation belt tracks the plasmapause location very closely, further supporting the relationship between plasmaspheric hiss and electron loss (Li et al., 2006; Goldstein et al., 2005).

Outside the plasmasphere, loss can be more dynamic and highly energy dependent. Rapid (minutes to hours) electron flux dropouts are commonly observed during storm main phase, often wiping out the entire outer radiation belt. Loss to the magnetopause, facilitated by outward radial transport, has been shown to account for a large portion of these depletions, but additional loss is often needed, particularly at lower *L*-shells (e.g., Turner et al., 2014; Hudson et al., 2014). Enhanced precipitation to the atmosphere, associated with EMIC and chorus wave scattering, has been observed during some storm main phases and may contribute to these depletions (Green et al., 2004; Xiang et al., 2017; Yu et al., 2015; Blum et al., 2015a; O'Brien et al., 2004). Radial profiles of phase space density (PSD) have been used to infer the primary mechanisms active in radiation belt enhancements and depletions. Decaying peaks in PSD can indicate rapid losses to the magnetopause from a combination of magnetopause shadowing and outward radial diffusion (Turner et al., 2012). In contrast, local minima in PSD profiles at ultrarelativistic energies, observed by Shprits et al. (2017), suggest a rapid energy-selective loss process in the heart of the outer belt, potentially due to scattering by EMIC waves.

However, owing to the multitude of possible time-varying acceleration and loss processes acting in the outer zone, it is often difficult to separate out any single process. To accurately estimate enhancement events, one must also account for simultaneous losses. A further layer of complexity comes in the form of warping (or asymmetric configuration) of the plasmasphere, which manifests as plumes, shoulders, etc. (Sandel et al., 2003). This can allow energetic electrons access to both high- and low-density plasma environments during the course of a drift orbit. Summers et al. (2008) showed that loss due to plasmaspheric hiss scattering in a warped plasmasphere or plume can limit electron energization owing to interaction

with chorus. In this scenario, an electron may experience cyclotron resonant interactions with both whistler mode and EMIC waves over the course of its drift orbit, and thus the combined scattering effects of multiple wave modes must be taken into account (Ma et al., 2015; Mourenas et al., 2016; Zhang et al., 2017).

An example of this complexity is the formation and subsequent slow depletion of a temporary third *storage* ring at multiple MeV energies following a September 2012 geomagnetic storm (Baker et al., 2013). On September 3, 2012, an interplanetary shock triggered a geomagnetic storm and resulted in the rapid depletion of electron flux at $L > 3.5$. Within this distance, though, a narrow belt of ultrarelativistic electrons remained. As local energization processes then reconstituted the outer belt beyond $L = 4$, this storage ring persisted undisturbed for multiple weeks, showing gradual decay consistent with energy-dependent scattering by plasmaspheric hiss (Thorne et al., 2013a,b). Some studies have suggested that scattering from EMIC waves may be important for the formation of this three-belt structure (Shprits et al., 2013), while others emphasize the role of ULF-driven radial transport (Mann et al., 2016). The plasmapause boundary and its relationship to these more complex, energy-dependent radiation belt structures is less straightforward than the longer term averaged picture described previously (Darrouzet et al., 2013; Goldstein et al., 2016). Eventually, the storage belt was abruptly destroyed after the passage of another interplanetary shock. Storage rings have since been identified in previous periods (e.g., Yuan and Zong, 2013; Kellerman et al., 2014), and a better understanding of the role of cyclotron resonance in their formation, stability, and ultimate decay is still needed.

The processes contributing to radiation belt precipitation losses have long been studied, but recent observations have revealed new features of the inner belt, slot region, and outer belt morphology and require renewed investigation into the role of various waves and processes in dictating the structure and dynamics of the radiation belts.

3.4 Modern single- and multiple-point observations, and updating the classic picture

Observations of detailed wave properties, brought about by an increasingly large data set of sophisticated spacecraft observations spanning the inner to outer zone, have provided a new look at waves that have long been measured in Earth's magnetosphere. In the first half of Section 3.4, we discussed some of these recently observed wave properties and the effects they may have on our understanding of wave-particle resonant scattering. In the second half, we discuss results from simultaneous multipayload observations, which allow the separation of temporal and spatial effects, and can provide global context during times of rapidly changing radiation belt dynamics.

3.4.1 New (Single-satellite) observations of wave characteristics

An increasing number of sophisticated satellite observations are revealing new properties of waves that have been studied for decades. These include measurements suggesting extended ranges of frequency and wave normal angle, large amplitudes, and wave−plasma and wave-wave coupling. These properties influence how waves interact with electrons, the energies with which they resonate, and the efficiency of loss cone scattering.

3.4.1.1 Wave populations at extended frequency ranges

Wave frequency helps to determine the energy of cyclotron resonance. For fixed wave normal angle, plasma parameters, and harmonic number, Eq. 3.1 shows that cyclotron resonant energy increases (decreases) as frequency decreases (increases). Proper measurement of wave spectra is necessary for determining the effective range of resonant energies.

A low-frequency ($\sim$20−100 Hz) population of plasmaspheric hiss has been identified (Li et al., 2013a) in association with injections of >100-keV plasma sheet electrons that drift (gradient/curvature) into an asymmetric plasmasphere (Shi et al., 2017). This is an entirely separate population from the more common >100-Hz hiss discussed in Section 2.3.1 (Malaspina et al., 2017). Ray-tracing studies suggest that these low-frequency hiss waves repeatedly traverse the equatorial amplification region via cyclical ray paths made possible by the low frequencies and refraction near the plasmapause, leading to path-integrated amplification to observed values (Chen et al., 2014). Electron lifetime models derived from hiss scattering show that a few hundred keV electron lifetimes can be shortened by a few orders of magnitude owing to this low-frequency component (Ni et al., 2014a; Orlova et al., 2016).

Chorus waves are also occasionally observed to extend below their typical frequency range. Meredith et al. (2014) observed a low-frequency extension of chorus power at higher latitudes, where the increasing magnetic field strength results in a relative drop in frequency to $f/f_{ce} < 0.1$. This frequency range is often not accounted for in the chorus spectra included in radiation belt models, but it may provide important energization and scattering of 100s keV electrons. Chorus is also occasionally observed at $f/f_{ce} < 0.1$ near the equator. Cattell et al. (2015) observed drops in chorus frequency to $f < 0.1\, f_{ce}$ in association with storm-time injections of $\sim$100-keV electrons, rather than the 10s keV electrons thought to typically lead to chorus growth. Wave amplitudes are often large, and the low frequencies provide much stronger pitch-angle diffusion for >500 keV than typical chorus (Gao et al., 2016; Xiao et al., 2017).

Some Van Allen Probes observations have identified oxygen cyclotron harmonic waves, as a common occurrence in the inner magnetosphere during geomagnetic storms (Usanova et al., 2016). While EMIC harmonic waves have been observed

previously in the inner magnetosphere and plasma sheet boundary layer (e.g., Perraut et al., 1982; Denton et al., 2010), these observations have been of predominantly compressional, proton harmonic waves. The ion cyclotron harmonic waves investigated by Usanova et al. (2016) (distinct from O^+ band EMIC waves) were instead most often at O^+ harmonic frequencies propagating close to the background magnetic field, with small wave normal angles. These waves, likely previously assumed to be the same as EMIC waves, have wave power concentrated at the O^+ cyclotron frequency and its harmonics, rather than having a stop-band at ion cyclotron frequencies, as is typical for EMIC waves (e.g., Kozyra et al., 1984). Ukhorskiy et al. (2010) showed that as the wave frequency approaches the ion cyclotron frequency, EMIC waves can more efficiently scatter electrons of lower energies. The effects of these ion cyclotron harmonic waves are still to be explored.

3.4.1.2 Wave populations with a wide range of wave normal angles

In addition to frequency, wave normal angles can determine resonant energy for cyclotron interaction as well as pitch-angle diffusion rates. Wave polarization changes with increasing wave normal angle, including the development of an electrostatic component along the wave vector (Stix, 1992). This can significantly modify wave-particle resonance, modify the wave dispersion relation, increase the importance of higher order harmonic ($|n| > 1$) contributions to scattering, and introduce significant *Landau* ($n = 0$) interaction (e.g., Artemyev et al., 2012b; Agapitov et al., 2015; Hsieh and Omura, 2017). Owing to these complexities, a lack of comprehensive statistics, and difficulty of proper inclusion into models, the overall effect of wave obliquity on precipitation rates is not well understood. However, it is possible that oblique waves may contribute significantly to precipitation loss. For example, inclusion of a range of wave normal angles of plasmaspheric hiss is thought to be required (e.g., Tsurutani et al., 2012) to explain the wide energy extent of the slot region (Lyons et al., 1972; Meredith et al., 2007; Ni et al., 2013; Albert, 1994; Glauert et al., 2014; Gao et al., 2015; He et al., 2016; Ripoll et al., 2017). Oblique chorus waves prevalent above about 25 latitude (e.g., Haque et al., 2010) may be responsible for creating relativistic microbursts (Horne and Thorne, 2003; Breneman et al., 2017).

Near the magnetic equator, a subpopulation of highly oblique, quasi-electrostatic chorus with wave normal angles near the resonance cone is often observed (Taubenschuss et al., 2014; Li et al., 2016). Despite carrying only a small fraction of the total wave magnetic energy, these may lead to a significant reduction of electron lifetimes (1−2 orders of magnitude) over a wide range of activity levels (Artemyev et al., 2012a, 2015; Mourenas et al., 2012, 2014; Li et al., 2014a). Near the loss cone, wave properties are highly sensitive to small variations in wave normal angle, and accurately measuring the maximum index of refraction is critical in determining whether diffusion rates are ultimately higher or lower than field-aligned waves

(Albert, 2017; Ma et al., 2017c). Significant observational and theoretical/modeling work (e.g., Artemyev et al., 2016; Agapitov et al., 2018a) remains to properly quantify the role oblique chorus plays in energetic outer belt electron loss.

3.4.1.3 Wave-element structure/coherence

Structure and/or coherence in waves can have an important effect on electron scattering. Coherent scattering interactions may result in significantly enhanced rates of pitch-angle scattering relative to broadband, unstructured waves (e.g., Lakhina et al., 2010; Bellan, 2013). The stereotypical example of this is chorus waves, which are often observed to consist of a succession of narrowband, chirping tones (e.g., Gao et al., 2014; Crabtree et al., 2017; Santolík et al., 2014a,b). Nonlinear test-particle simulations show that discrete chorus packets can lead to discrete microbursts over a wide range of energies, from 10–100 keV (Rosenberg et al., 1990; Hikishima et al., 2010) to MeV (Saito et al., 2012).

Plasmaspheric hiss, as its name implies, is traditionally characterized as a structureless, broadband emission. This is supported by decades of observations from low-resolution satellite spectra (e.g., Fig. 3.2A). However, Summers et al. (2014) presented the result that hiss spectra produced from high time-resolution "burst" waveform data from the Van Allen Probes occasionally show highly polarized, coherent (over a few wave periods) rising and falling tones. Structured hiss emissions are strongly associated with intervals of high solar wind pressure, and at larger *L shells*, they can be highly oblique and have large amplitudes (Tsurutani et al., 2015).

EMIC waves, also traditionally characterized as structureless, are occasionally observed to contain coherent, triggered emissions (Pickett et al., 2010; Grison et al., 2013; Nakamura et al., 2014). Fig. 3.5 shows examples of these highly structured EMIC waves, as observed by Grison et al. (2013) on Cluster spacecraft, with rising tones reminiscent of whistler-mode chorus wave elements. Roughly 30% of EMIC-wave observations from the THEMIS spacecraft (Time History of Events and Macroscale Interactions during Substorms; Angelopoulos, 2008) beyond 6 Earth radii included rising or falling tones, primarily during larger amplitude events and more disturbed times (Nakamura et al., 2016). Simulations by Omura and Zhao (2013) have suggested that these EMIC-triggered emissions can produce nonlinear trapping and rapid scattering of MeV electrons in the form of relativistic microburst precipitation. During an intense EMIC-wave event observed by the Van Allen Probes, Engebretson et al. (2015) found signatures of relativistic electron depletions in the outer belt qualitatively consistent with the nonlinear trapping theory by Omura and Zhao (2012, 2013). Remya et al. (2015) show that large-amplitude (nT), coherent EMIC waves can result in relativistic electron loss rates orders of magnitude higher than those produced by incoherent waves, suggesting that estimates of EMIC scattering should take into account wave coherence and structure.

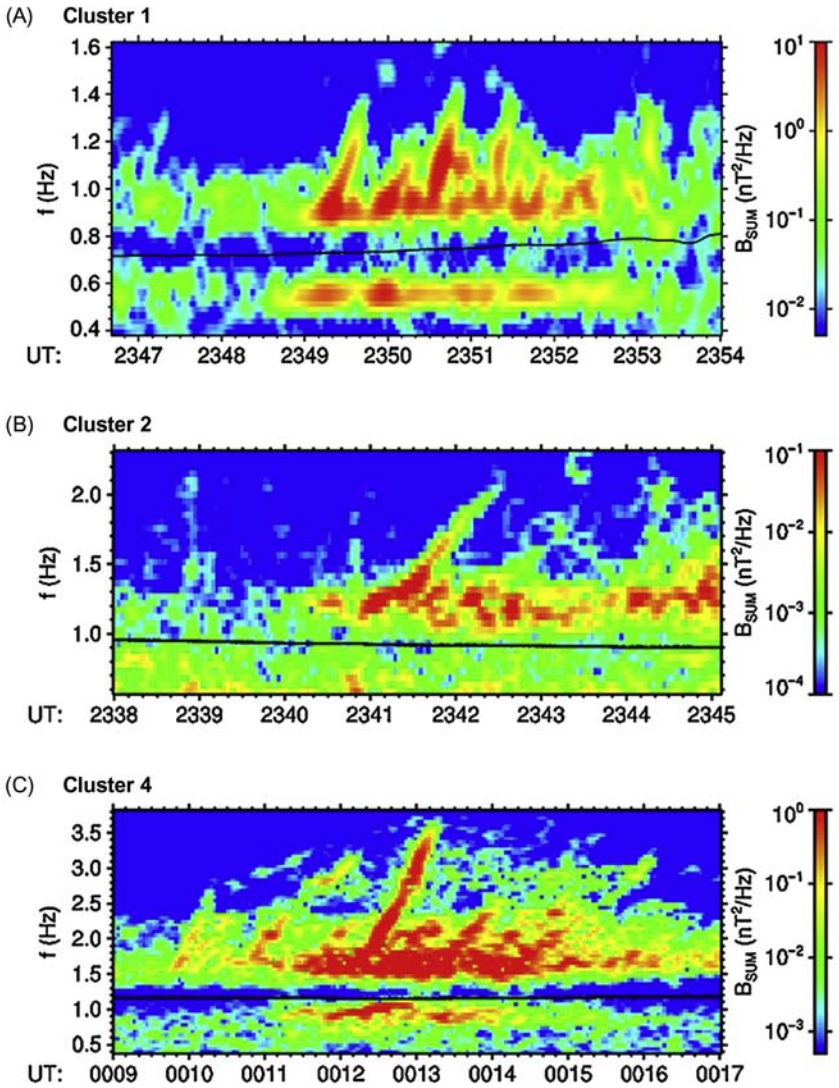

Figure 3.5 Structured EMIC waves observed simultaneously on three Cluster satellites. *From Grison, B., Santolk, O., Cornilleau-Wehrlin, N., Masson, A., Engebretson, M.J., Pickett, J.S., et al., 2013. EMIC triggered chorus emissions in cluster data. J. Geophys. Res.: Space Phys. 118, 1159–1169. Available from: https://doi.org/10.1002/jgra.50178.*

3.4.1.4 Large-amplitude waves

Wave power, though not affecting the conditions of cyclotron resonance, can have a large effect on scattering rates. Under the quasi-linear paradigm, diffusive scattering is proportional to wave magnetic field power. However, interaction between

large-amplitude waves and electrons is fundamentally nonlinear, and under these conditions electron transport toward the loss cone may be advective, rather than stochastic.

Unfortunately, the occurrences and properties of large-amplitude waves are poorly understood. Time- and frequency-averaged spectral data, traditionally used to study wave properties, overwhelmingly show populations of small amplitude (e.g., $B_w << B_o$), broadband waves, consistent with assumptions inherent in quasi-linear theory. Modern measurements using high-cadence resolution "burst" spectra or waveforms, which have much greater time and frequency resolution, often show a much larger range of wave amplitudes on short timescales. Perhaps the most dramatic example of this was the discovery by Cattell et al. (2008) of extremely large-amplitude (hundreds of mV/m) chorus waves using STEREO (Solar TErrestrial RElations Observatory) (Kaiser, 2005) burst waveform captures. These waves can carry orders of magnitude more Poynting flux (Santolík et al., 2010) than their smaller amplitude counterparts, and they can have an unusually large, nonlinearly steepened parallel (to the magnetic field) electric field component (Agapitov et al., 2018b). Owing to chorus element interspacings, time-averaged amplitudes can under represent true peak amplitudes by an order of magnitude or more (Cully et al., 2008; Tsurutani et al., 2009).

This discovery has prompted a closer look at past burst waveform data sets for large-amplitude chorus (Wilson et al., 2011; Kellogg et al., 2011; Cattell et al., 2012), as well as for other types of waves. Some observations show that plasmaspheric hiss waves can be large-amplitude, coherent, and oblique on the dayside during times of enhanced magnetospheric compression caused by high solar wind ram pressure (Tsurutani et al., 2015; Su et al., 2018). EMIC waves, which can occur with amplitudes up to a few 10 s nT (e.g., Engebretson et al., 2015), can also exhibit nonlinear formation and interaction with particles (Shoji and Omura, 2013; Tsintsadze et al., 2010), potentially actually reducing their effectiveness as a loss mechanism (Albert and Bortnik, 2009b; Liu et al., 2012).

Large-amplitude waves, though far less common than small-amplitude waves, may play an important role in radiation belt electron energization and loss. They can cause phase bunching and phase trapping (Albert, 2002; Bortnik et al., 2008b; Kellogg et al., 2011) and dramatic acceleration of electrons (Mozer et al., 2014). Further studies over a full solar cycle are needed to quantify wave properties such as amplitudes, periodicities, subpacket structure, and the conditions under which they grow to large amplitudes. This will help in the full understanding of the role large-amplitude waves play in radiation belt dynamics.

3.4.2 New (multipayload) observations of wave/precipitation characteristics

Connecting wave-induced loss cone scattering of electrons to observed precipitation is difficult to do with single-satellite instrumentation. Near the magnetic equator, where hiss, chorus, and EMIC amplitudes are typically maximized, the size of the loss cone

(~a few degrees at $L = 5$) is often smaller than the angular resolution of particle detectors, thus making it difficult or impossible to distinguish between magnetically trapped and loss cone electrons. Owing to this limitation, relating electron loss rates to observed wave populations is then often done by comparing equatorial wave and trapped electron decay rates. Unfortunately, this technique is often unable to distinguish between actual precipitation loss and apparent loss due to energization/deenergization or transport.

Direct comparisons of precipitating electrons to waves requires combining low-altitude and high-altitude measurements. Low-altitude balloons, ground observatories, and LEO satellites directly measure precipitating (BLC) electrons or their atmospheric signatures. These observations can then be compared to comprehensive wave observations, making use of the ever-increasing numbers of satellites and constellation missions in the Earth's magnetosphere (e.g., four Cluster, five THEMIS, two Van Allen Probes, and four Magnetospheric Multiscale (MMS) satellites) to provide more event-specific loss and scattering comparisons. Multipoint observations allow the resolution of radiation belt evolution on timescales of minutes to hours, less than the orbital period of any single equatorial satellite. In addition, multipoint observations made simultaneously by magnetically conjugate platforms can be used to disentangle spatial from temporal variability of waves and precipitation. These combined measurements allow a more detailed comparison between observations and theory. We now discuss comparative low- and high-altitude observations in the context of precipitation associated with plasmaspheric hiss, chorus, and EMIC waves.

3.4.2.1 Linking precipitation and plasmaspheric hiss observations

It has been observed for decades that, statistically, the slow (days to weeks) decay of trapped radiation belt electron populations during storm recovery phase is consistent with predicted diffusive scattering loss by plasmaspheric hiss. A more direct comparison of hiss to precipitation loss was provided by Rodger et al. (2007), who showed that >150-keV precipitating electron fluxes estimated from subionospheric radio signal propagation at $L = 3.2$, and plasmaspheric hiss amplitudes observed on DEMETER (Detection of Electro-Magnetic Emissions Transmitted from Earthquake Regions) had similar orders of magnitude day−night asymmetries for a 6-day storm recovery, suggesting that hiss waves were primarily responsible for this storm recovery.

Jaynes et al. (2015) compared precipitating electrons measured on the CSSWE CubeSat (Colorado Student Space Weather Experiment; Li et al., 2013c) to trapped populations observed on the Van Allen Probes during a period of low geomagnetic activity, during which loss contributions from hiss, estimated from Van Allen Probes measurements, could be isolated. Electron lifetimes near $L = 4.5$ were observed to be less than 3 days, consistent with loss estimates from the observed hiss, but shorter than values typically used in models at the time.

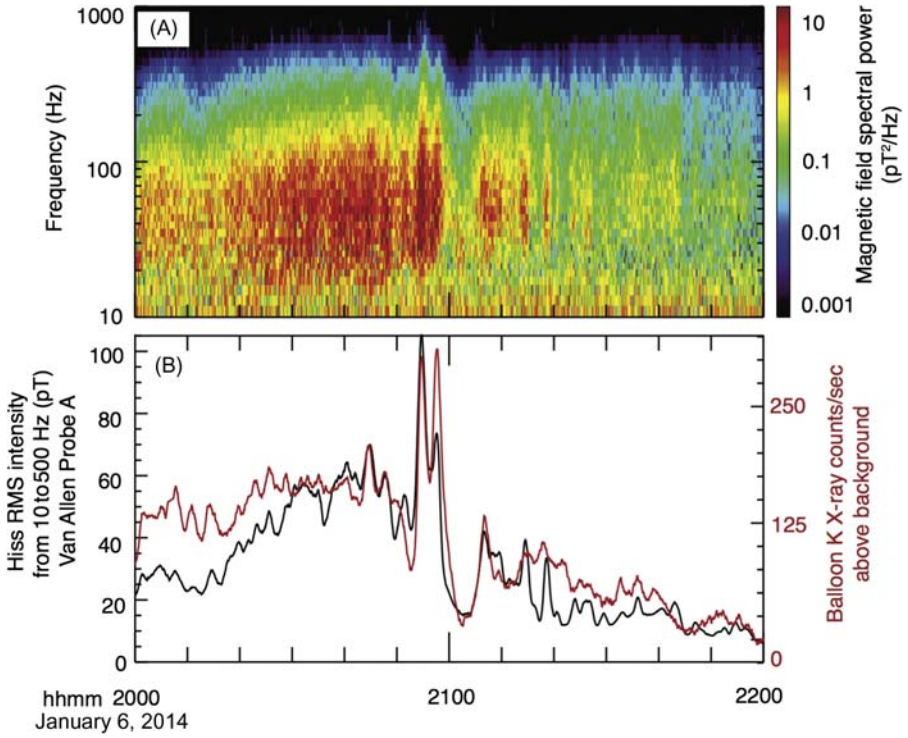

Figure 3.6 Global-scale coherence observed in plasmaspheric hiss and <180-keV precipitation observed during a close magnetic conjunction between Van Allen Probe A and a BARREL balloon. (A) Magnetic field spectral power of hiss showing distinctive modulations from ~20 to 400 Hz. (B) Comparison of hiss intensity and X-ray counts showing strong similarities for 2 hours. *From Breneman A. et al., 2017. Observations directly linking relativistic electron microbursts to whistler mode chorus: Van Allen Probes and FIREBIRD II. Geophys. Res. Lett. 44. Available from: https://doi.org/10.1002/2017GL075001.*

The most direct comparison of plasmaspheric hiss to electron loss was made by Breneman et al. (2015), who compared BARREL (balloon array for radiation belt relativistic electron losses) (Millan et al., 2013) and Van Allen Probe observations during two intervals of close magnetic conjunction. Distinctive double-peaked modulations (Fig. 3.6), observed in both hiss intensity and electron precipitation up to 180 keV (inferred from the balloon X-ray spectrum) during one of these conjunctions, showed a direct connection between hiss and precipitation, with observed loss rates consistent with estimates from quasi-linear theory. These modulations, also observed in plasma density and magnetic field (see also, Li et al., 2017b), were near global in scale, as observed from multiple balloons, satellites, and ground magnetometers. These results show that intricate cross–scale wave-wave coupling can significantly modulate both wave intensities and precipitation loss. Similar comparisons of hiss and precipitation at energies >180 keV are necessary for exploring the full energy extent of the influence of plasmaspheric hiss on scattering loss.

3.4.2.2 Linking precipitation and chorus observations

Direct comparisons of chorus to precipitation is, in general, more difficult than for hiss, owing to its stronger spatial and temporal variability. At subrelativistic energies, multipoint observations have firmly established the role chorus plays in precipitation loss of 10 s keV pulsating aurora (Nishimura et al., 2010; Kasahara et al., 2018), microbursts (Rosenberg et al., 1971, 1981), and regional precipitation (Lam et al., 2010; Halford et al., 2015b). Measurements of >30-keV precipitating electron flux on the POES LEO constellation are now routinely used to infer equatorial amplitudes (Li et al., 2013b; Ni et al., 2014b).

Observations are sparser at relativistic energies, largely due to lower flux levels and lack of energy coverage/resolution on low-altitude particle detectors. Chorus is perhaps the leading wave candidate for the creation of relativistic microbursts from ~100 keV to up to ~MeV. Large-scale regions producing chorus and precipitation can last for hours and extend across multiple L shells and magnetic local times (MLTs). (Anderson et al., 2017). These regions are constrained beyond the plasmapause, typically across the morningside, and have occurrences that increase with geomagnetic activity (Johnston and Anderson 2010). Within these extended generation regions, smaller chorus and microburst substructures are observed (Kersten et al., 2011; Aryan et al., 2016; Anderson et al., 2017), though their relation has not been established.

On smaller scales, individual chorus subpackets and microbursts share similar durations and cadences. Spatial scales perpendicular to the background magnetic field, as determined from simultaneous multipoint measurements, range from many tens (Santolík and Gurnett, 2003; Santolík et al., 2004a) to more than a thousand km (Agapitov et al. 2011, 2017). When mapped to the topside ionosphere, these scales are roughly consistent with the few to 10 s km scale size of individual relativistic microbursts, inferred from single spacecraft (e.g., Blake et al., 1996) and multipoint CubeSats (Crew et al., 2016) measurements.

Direct comparison of chorus to microbursts is difficult, however, owing to their small transverse scale sizes. Breneman et al. (2017) provided the first direct evidence that lower-band, rising tone chorus waves create relativistic microbursts by analyzing a near-perfect magnetic conjunction between Van Allen Probe A and one of two FIREBIRD II (Focused Investigations of Relativistic Electron Bursts: Intensity, Range, and Dynamics) CubeSats (Klumpar et al., 2015). The combined data sets showed that the chorus created microbursts over a wide energy range (200−850 keV) along a single magnetic field line. The likely mechanism was $n = -1$ cyclotron resonance scattering away from the chorus source at 20−30° mlat, consistent with the theoretical suggestion of Thorne et al. (2005), and with quasi-linear (Shprits et al., 2009) and nonlinear test-particle simulations (Hikishima et al., 2010; Saito et al., 2012). Comparisons of the microburst flux to the trapped electron population at $L = 5.6$

showed that a long-lasting chorus source region extended over a few hours MLT, consistent with the observations of Anderson et al. (2017), would provide a major source of radiation belt electron loss (200−850 keV). Using SAMPEX measurements of >1-MeV electrons, Douma et al. (2018) found microburst events in close conjunction with VLF signatures suggestive of chorus observed on the ground, but also found some with ground observations of EMIC waves, suggesting that, on occasion, some MeV microbursts may be caused by EMIC rather than chorus waves.

At lower energies, Mozer et al. (2018) compared Van Allen Probe B and AC6-B CubeSat (Blake and O'Brien, 2016) observations mapping to the same patchy region of larger precipitation showing strongly correlated one second averages of chorus and >35-keV microbursts. These scattering interactions must be fundamentally nonlinear owing to the large (1 nT) chorus amplitudes, but observed fluxes were shown to be consistent with quasi-linear scattering rates, suggesting that the overall effect of many nonlinear scattering interactions can resemble quasi-linear diffusion (also see Tao et al., 2012).

The aforementioned multipoint studies provide strong evidence that chorus creates microbursts from subrelativistic (10 s keV) to relativistic (∼MeV) energies. However, owing to the small number of comparative studies, many details of this connection remain unresolved. Examples include small-scale spatial structures, termed *curtains* (Blake and O'Brien, 2016), thought to come about from DLC microburst populations, microburst energy and storm phase dependence, and the overall importance of relativistic microbursts to outer belt electron loss.

3.4.2.3 Linking precipitation and EMIC observations

Direct links between EMIC waves and REP have increasingly been observed with recent multiobservatory measurements. Early observations of REP events preferentially occurring on the duskside and close to the plasmapause, provided the first suggestion of their connection to EMIC waves (e.g., Imhof et al., 1986; Millan et al., 2002). The narrow radial extent of REP events observed by LEO spacecraft is consistent with the often radially narrow EMIC-wave spatial extents suggested by combined ground and in situ wave observations (e.g., Mann et al., 2014; Paulson et al., 2014). Multipoint in situ observations have now begun to quantify these spatial and temporal extents of EMIC waves (e.g., Lee et al., 2013; Clausen et al., 2011; Engebretson et al., 2008, 2015; Sigsbee et al., 2016; Blum et al., 2017; Yu et al., 2017a,b), for better comparison to precipitation region properties. Multipoint observations of REP regions (e.g., from the BARREL balloon and POES satellite constellations) suggest that precipitation events are often very localized (Shekhar et al., 2017; Millan, 2016, AGU abstract).

Coordinated observations of EMIC-wave activity have been seen at locations magnetically conjugate to simultaneously observed REP events, further strengthening

their association. EMIC waves were observed by ground-based magnetometers in conjunction with keV ion and MeV electron precipitation (Miyoshi et al., 2008; Hendry et al., 2016) as well as with ground-based electron precipitation signatures (Rodger et al., 2008). However, because of ducting of EMIC waves as they propagate to lower altitudes, it can be difficult to identify the localized region in space of wave generation from ground observations (Greifinger and Greifinger, 1968; Fujita and Tamao, 1988). More recently, studies have observed precipitation in close magnetic conjunction with in situ EMIC waves near the equator, often with similar modulation between precipitation and waves (Li et al., 2014b; Blum et al., 2015b; Rodger et al., 2015). Applying quasi-linear theory to observed EMIC-wave properties measured near the equator, Li et al. (2014b) were able to reproduce the precipitation signature observed at one of the BARREL balloons during an event in January 2013. These event studies have confirmed that at least some REP events are produced by EMIC-wave scattering in the magnetosphere. Quantification of precipitation due to these events (e.g., Blum et al., 2013) suggests that they can provide significant loss to the localized *L*-shells over which they occur, in agreement with the minima in PSD profiles observed by Shprits et al. (2017).

Through these conjugate studies, additional questions have arisen with regard to the nature of the relationship between EMIC waves and REP. While individual events confirm that EMIC waves can produce REP events seen by balloons, LEO spacecraft, and ground-based platforms, the global distributions of EMIC waves and REP events show significant differences—with EMIC-wave occurrences peaking in the noon and afternoon sectors, while REP events show a premidnight peak (e.g., Smith et al., 2016). It is necessary to determine what fraction of EMIC waves produce relativistic electron precipitation and what fraction of these precipitation events are due to EMIC-wave scattering. While field line curvature scattering was initially proposed as a process producing MeV electron precipitation on the nightside (Imhof et al., 1991), Smith et al. (2016) suggested that this might also produce some of the coincident MeV electron and keV proton precipitation features often interpreted as being due to EMIC-wave scattering.

The energy spectrum and structure of EMIC-wave–driven precipitation is also an open topic of investigation. A number of REP events show precipitating energy spectra peaked at $\sim$1–2 MeV (Li et al., 2014b; Woodger et al., 2015; Clilverd et al., 2017), in agreement with theoretical estimates than EMIC waves primarily scatter electrons above an $\sim$MeV minimum resonant energy (Thorne and Kennel, 1971). However, a handful of studies have found evidence of sub-MeV electron precipitation, down to energies at low as $\sim$300 keV, in association with EMIC waves (Clilverd et al., 2015; Hendry et al., 2017). EMIC-wave anomalous cyclotron resonant scattering of these low energies can occur only under extreme, likely unrealistic, plasma and field conditions; however, nonresonant or bounce resonance interactions

might allow EMIC waves to scatter electrons at these lower energies (Chen et al., 2016; Cao et al., 2017). This motivates investigation into the detailed nature of the wave-particle interaction and precipitating electron energy spectrum driven by EMIC waves

Together, recent conjugate wave and precipitation studies have helped solidify the causal relationship between various types of waves and precipitation events. However, new questions have arisen from these observations, and continued study of such events will enable more detailed understanding of the energy spectrum, spatial structure, and global distributions of different types of precipitation and their drivers.

3.5 Discussion and conclusions

3.5.1 Incorporating cyclotron resonant scattering into radiation belt models

Comprehensive data sets provided by the single- and multiple-point observations discussed in Section 3.4 are necessary for constraining radiation belt models, which facilitate our understanding of radiation belt dynamics. Models are only as good as the accuracy of the empirical data that drives them, and incomplete knowledge of diffusion coefficients, for example, can lead to significant (even orders of magnitude) uncertainties in electron lifetimes (e.g., Tu et al., 2013; Pham et al., 2017; Agapitov et al., 2018a). Input with the aforementioned up-to-date wave distributions, parameterized with respect to spatial location and activity level (e.g., Shprits et al., 2007; Spasojevic and Shprits, 2013), modern simulations show relatively good agreement with comprehensive observations of radiation belt electron decay on multiple-day timescales. They also provide further support for the general importance of resonant scattering by hiss, chorus, and EMIC waves.

Further improvements to parameterization are being explored. Hiss and chorus wave populations, for example, are bounded inside and outside the plasmasphere, respectively, and sorting their properties relative to plasma boundaries, rather than strict L, which varies only statistically with L, is a more natural system, as shown in Fig. 3.7 (Malaspina et al., 2016). Parameterizations of waves relative to the plasmapause location have not yet been integrated into quasi-linear diffusion models, but may significantly enhance their accuracy during highly dynamic times.

Despite all these improvements, using statistical models to describe radiation belt evolution has severe limitations. Some waves, because of their sporadic nature—like EMIC waves (Drozdov et al., 2017) or <100 Hz hiss (Malaspina et al., 2017)—are difficult to properly parameterize. In addition, storm-time radiation belts often show significant variation on timescales of minutes and hours (e.g., Yu et al., 2015), which cannot be accurately captured using empirical models based on highly averaged data. Instead, event-specific waves, particles, and plasma boundaries with good spatial, energy, and time resolution are needed (Thorne et al., 2013a,b; Tu et al., 2014;

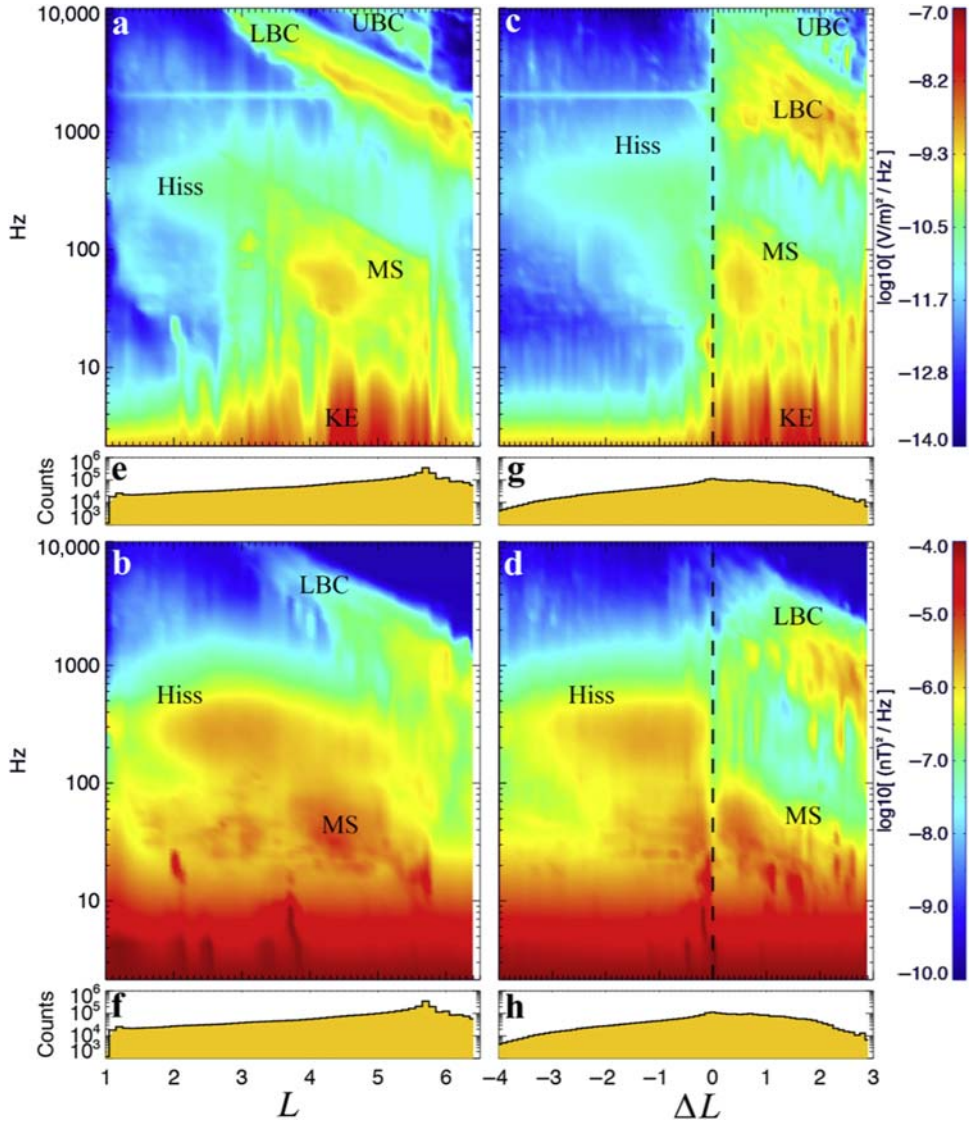

Figure 3.7 Comparative sorting of plasmaspheric hiss and chorus wave power by *L*-shell and distance relative to the plasmapause (ΔL). (A and B) Wave power sorted traditionally by *L*-shell, and (C and D) wave power sorted relative to distance from the plasmapause, which provides a clear delineation of wave power. *From Malaspina, D.M., Jaynes, A.N., Boulé, C., Bortnik, J., Thaller, S.A., Ergun, R.E., et al., 2016. The distribution of plasmaspheric hiss wave power with respect to plasmapause location. Geophys. Res. Lett. 43, 7878–7886. Available from: https://doi.org/10.1002/2016GL069982.*

Xiao et al., 2014; Schiller et al., 2017). This allows models to differentiate between different important physical processes. For example, certain dramatic outer belt electron flux dropouts (not caused by outer boundary loss) during storms (e.g., Morley et al., 2010) require either consideration of nonlinear scattering loss or more accurate

input to quasi-linear models with high spatiotemporal, and energy-resolution input. This necessitates a better quantification of REP (e.g., Shekhar et al., 2017).

3.5.2 Summary

In this review, we discussed the role of wave-particle interactions in driving loss of radiation belt electrons, with an emphasis on observational signatures of this process. These include direct measurements of precipitation, wave properties, and variations in the trapped electron population as a result of cyclotron resonance.

Precipitation loss from cyclotron resonance with plasma waves—primarily hiss, chorus, and EMIC—is one of the primary drivers of radiation belt morphology. The energy-dependent structure of the slot region and inner belt is formed primarily by the balance of inward radial transport and scattering loss from plasmaspheric hiss. In the outer belt, and outside the plasmasphere, chorus waves can cause significant scattering loss over a wide range of energies. EMIC waves, not limited by the plasmapause boundary, likely control the loss of ultrarelativistic electrons. While the role of these three waves in forming the large-scale structure of the belts is well established, their contributions to the more complex dynamics and fine-scale features recently observed are still under investigation.

Sophisticated wave instrumentation on recent satellite missions has provided new details of wave properties, including observations of large-amplitude, highly oblique waves, power at extended frequency ranges, and previously undiscovered wave coherence and structure. These observations motivate the revisitation of theories of wave-particle interactions and the contribution of these waves to radiation belt electron loss and overall dynamics.

Lastly, a new paradigm of simultaneous multiplatform observations, including equatorial and LEO satellites, balloons, and ground-based observations, has led to new insights into wave-induced precipitation. These observations show temporal and large-scale spatial structures of waves and precipitation. Simultaneous, magnetically conjugate measurements allow close comparisons of scattering by various wave types and electron precipitation loss, vital for understanding the relative roles played by various wave types. Investigation continues into the energy dependence of precipitation events, as well as when, where, and how often various wave modes cause different types of precipitation.

Ultimately, the importance of precipitation loss, including comparisons among different precipitation loss processes, cannot be ascertained without careful consideration of other time-dependent loss processes, such as outward radial diffusion and magnetopause shadowing (e.g., Tu et al., 2013; Murphy et al., 2016; Watt et al., 2017; Mann et al., 2016). Also, care must be taken when generalizing modern results owing to the historically quiet solar cycle 23 (Russell et al., 2010) and relatively quiet cycle 24 (Li et al., 2017a; Riley and Love, 2017).

References

Abel, B., Thorne, R.M., 1998. Electron scattering loss in Earth's inner magnetosphere: 1. dominant physical processes. J. Geophys. Res. 103 (A2), 2385–2396. Available from: https://doi.org/10.1029/97JA02919.

Agapitov, O., Krasnoselskikh, V., Dudok de Wit, T., Khotyaintsev, Y., Pickett, J.S., Santolík, O., et al., 2011. Multispacecraft observations of chorus emissions as a tool for the plasma density fluctuations' remote sensing. J. Geophys. Res. 116, A09222. Available from: https://doi.org/10.1029/2011JA016540.

Agapitov, O., Artemyev, A., Krasnoselskikh, V., Khotyaintsev, Y.V., Mourenas, D., Breuillard, H., et al., 2013. Statistics of whistler-mode waves in the outer radiation belt: cluster STAFF-SA measurements. J. Geophys. Res. Space Phys. 118, 3407–3420. Available from: https://doi.org/10.1002/jgra.50312.

Agapitov, O.V., Artemyev, A.V., Mourenas, D., Kasahara, Y., Krasnoselskikh, V., 2014. Inner belt and slot region electron lifetimes and energization rates based on AKEBONO statistics of whistler waves. J. Geophys. Res. Space Phys. 119, 2876–2893. Available from: https://doi.org/10.1002/2014JA019886.

Agapitov, O.V., Artemyev, A.V., Mourenas, D., Mozer, F.S., Krasnoselskikh, V., 2015. Nonlinear local parallel acceleration of electrons through Landau trapping by oblique whistler mode waves in the outer radiation belt. Geophys. Res. Lett. 42, 10,140–10,149. Available from: https://doi.org/10.1002/2015GL066887.

Agapitov, O., Blum, L.W., Mozer, F.S., Bonnell, J.W., Wygant, J., 2017. Chorus whistler wave source scales as determined from multipoint Van Allen Probe measurements. Geophys. Res. Lett. 44, 2634–2642. Available from: https://doi.org/10.1002/2017GL072701.

Agapitov, O.V., Mourenas, D., Artemyev, A.V., Mozer, F.S., Hospodarsky, G., Bonnell, J., et al., 2018a. Synthetic empirical chorus wave model from combined Van Allen Probes and Cluster statistics. J. Geophys. Res. Space Phys. 123. Available from: https://doi.org/10.1002/2017JA024843.

Agapitov, O., Drake, J.F., Vasko, I., Mozer, F.S., Artemyev, A., Krasnoselskikh, V., et al., 2018b. Nonlinear electrostatic steepening of whistler waves: the guiding factors and dynamics in inhomogeneous systems. Geophys. Res. Lett. 45, 2168–2176. Available from: https://doi.org/10.1002/2017GL076957.

Albert, J.M., 1994. Quasi-linear pitch angle diffusion coefficients: retaining high harmonics. J. Geophys. Res. 99 (A12), 23741–23745. Available from: https://doi.org/10.1029/94JA02345.

Albert, J.M., 2002. Nonlinear interaction of outer zone electrons with VLF waves. Geophys. Res. Lett. 29 (8), 1275. Available from: https://doi.org/10.1029/2001GL013941.

Albert, J.M., 2017. Quasi-linear diffusion coefficients for highly oblique whistler mode waves. J. Geophys. Res. Space Phys. 122. Available from: https://doi.org/10.1002/2017JA024124.

Albert, J.M., Bortnik, J., 2009a. Nonlinear interaction of radiation belt electrons with electromagnetic ion cyclotron waves. Geophys. Res. Lett. 36, L12110. Available from: https://doi.org/10.1029/2009GL038904.

Albert, J.M., Shprits, Y.Y., 2009b. Estimates of lifetimes against pitch angle diffusion. J. Atmos. Sol.-Terr. Phys. 71 (2009), 1647–1652.

Anderson, K.A., Milton, D.W., 1964. Balloon observations of X rays in the auroral zone: 3. High time resolution studies. J. Geophys. Res. 69 (21), 4457–4479. Available from: https://doi.org/10.1029/JZ069i021p04457.

Anderson, B.R., Shekhar, S., Millan, R.M., Crew, A.B., Spence, H.E., Klumpar, D.M., et al., 2017. Spatial scale and duration of one microburst region on 13 August 2015. J. Geophys. Res. Space Phys. 122. Available from: https://doi.org/10.1002/2016JA023752.

Andersson, M.E., Verronen, P.T., Rodger, C.J., Clilverd, M.A., Seppälä, A., 2014. Missing driver in the Sun–Earth connection from energetic electron precipitation impacts mesospheric ozone. Nature Communications 5, 5197.

Angelopoulos, V., 2008. The THEMIS mission. Space Sci. Rev. 141 (1-4), 5–34. Available from: https://doi.org/10.1007/s11214-008-9336-1.

Artemyev, A., Agapitov, O., Breuillard, H., Krasnoselskikh, V., Rolland, G., 2012a. Electron pitch-angle diffusion in radiation belts: the effects of whistler wave oblique propagation. Geophys. Res. Lett. 39, L08105. Available from: https://doi.org/10.1029/2012GL051393.

Artemyev, A.V., Krasnoselskikh, V.V., Agapitov, O.V., Mourenas, D., Rolland, G., 2012b. Non-diffusive resonant acceleration of electrons in the radiation belts. Phys. Plasmas 19, 122901.

Artemyev, A.V., Agapitov, O.V., Mourenas, D., Krasnoselskikh, V.V., Mozer, F.S., 2015. Wave energy budget analysis in the Earth's radiation belts uncovers a missing energy. Nat. Commun 6, 8143. Available from: https://doi.org/10.1038/ncomms8143.

Artemyev, A., Agapitov, O., Mourenas, D., Krasnoselskikh, V., Shastun, V., Mozer, F., 2016. Oblique whistler-mode waves in the Earth's inner magnetosphere: energy distribution, origins, and role in radiation belt dynamics. Space Sci. Rev. 200, 261–355. Available from: https://doi.org/10.1007/s11214-016-0252-5.

Aryan, H., Sibeck, D., Balikhin, M., Agapitov, O., Kletzing, C., 2016. Observation of chorus waves by the Van Allen Probes: dependence on solar wind parameters and scale size. J. Geophys. Res. Space Phys. 121, 7608–7621. Available from: https://doi.org/10.1002/2016JA022775.

Baker, D.N., et al., 1993. An overview of the Solar Anomalous and Magnetospheric Particle Explorer (SAMPEX) mission. IEEE Trans. Geosci. Remote Sen. 31, 531.

Baker, D.N., et al., 2013. A long-lived relativistic electron storage ring embedded in earth's outer Van Allen Belt. Science 340, 186–190. Available from: https://doi.org/10.1126/science.1233518.

Baker, D.N., et al., 2014a. Gradual diffusion and punctuated phase space density enhancements of highly relativistic electrons: Van Allen Probes observations. Geophys. Res. Lett. 41, 1351–1358. Available from: https://doi.org/10.1002/2013GL058942.

Baker, D.N., et al., 2014b. An impenetrable barrier to ultra-relativistic electrons in the Van Allen radiation belts. Nature 515, 531–534. Available from: https://doi.org/10.1038/nature13956.

Bellan, P.M., 2013. Pitch angle scattering of an energetic magnetized particle by a circularly polarized electromagnetic wave. Phys. Plasmas 20, 042117. Available from: https://doi.org/10.1063/1.4801055.

Blake, J.B., Looper, M.D., Baker, D.N., Nakamura, R., Klecker, B., Hovestadt, D., 1996. New high temporal and spatial resolution measurements by SAMPEX of the precipitation of relativistic electrons. Adv. Space Res. 18 (8), 171–186. Available from: https://doi.org/10.1016/0273-1177(95)00969-8.

Blake, J.B., O'Brien, T.P., 2016. Observations of small-scale latitudinal structure in energetic electron precipitation. J. Geophys. Res. Space Phys. 121, 3031–3035. Available from: https://doi.org/10.1002/2015JA021815.

Blum, L.W., Schiller, Q., Li, X., Millan, R., Halford, A., Woodger, L., 2013. New conjunctive CubeSat and balloon measurements to quantify rapid energetic electron precipitation. Geophys. Res. Lett. 40, 5833–5837. Available from: https://doi.org/10.1002/2013GL058546.

Blum, L.W., Li, X., Denton, M., 2015a. Rapid MeV electron precipitation as observed by SAMPEX/HILT during high-speed stream-driven storms. J. Geophys. Res. Space Phys. 120. Available from: https://doi.org/10.1002/2014JA020633.

Blum, L.W., et al., 2015b. Observations of coincident EMIC wave activity and duskside energetic electron precipitation on 18–19 January 2013. Geophys. Res. Lett. 42, 5727–5735. Available from: https://doi.org/10.1002/2015GL065245.

Blum, L.W., Bonnell, J.W., Agapitov, O., Paulson, K., Kletzing, C., 2017. EMIC wave scale size in the inner magnetosphere: observations from the dual Van Allen Probes. Geophys. Res. Lett. 44. Available from: https://doi.org/10.1002/2016GL072316.

Bortnik, J., Thorne, R.M., 2007. The dual role of ELF/VLF chorus waves in the acceleration and precipitation of radiation belt electrons. J. Atmos. Sol.-Terr. Phys. 69, 378–386.

Bortnik, J., Thorne, R.M., O'Brien, T.P., Green, J.C., Strangeway, R.J., Shprits, Y.Y., et al., 2006. Observation of two distinct, rapid loss mechanisms during the 20 November 2003 radiation belt dropout event. J. Geophys. Res. 111, A12216. Available from: https://doi.org/10.1029/2006JA011802.

Bortnik, J., Thorne, R.M., Meredith, N.P., 2008a. The unexpected origin of plasmaspheric hiss from discrete chorus emissions. Nature 452, 62–66. Available from: https://doi.org/10.1038/nature06741.

Bortnik, J., Thorne, R.M., Inan, U.S., 2008b. Nonlinear interaction of energetic electrons with large amplitude chorus. Geophys. Res. Lett. 35, L21102. Available from: https://doi.org/10.1029/2008GL035500.

Bortnik, J., et al., 2009. First observation linking the origin of plasmaspheric hiss to discrete chorus emissions. Science 324, 775–778. Available from: https://doi.org/10.1126/science.1171273.

Bortnik, J., Chen, L., Li, W., Thorne, R.M., Horne, R.B., 2011. Modeling the evolution of chorus waves into plasmaspheric hiss. J. Geophys. Res. 116, A08221. Available from: https://doi.org/10.1029/2011JA016499.

Boynton, R.J., Mourenas, D., Balikhin, M.A., 2017. Electron flux dropouts at $L \sim 4.2$ from global positioning system satellites: occurrences, magnitudes, and main driving factors. J. Geophys. Res. Space Phys. 122. Available from: https://doi.org/10.1002/2017JA024523.

Brautigam, D.H., Albert, J.M., 2000. Radial diffusion analysis of outer radiation belt electrons during the October 9, 1990, magnetic storm. J. Geophys. Res. 105 (A1), 291–309. Available from: https://doi.org/10.1029/1999JA900344.

Breneman, A.W., Halford, A., Millan, R., McCarthy, M., Fennell, J., Sample, J., et al., 2015. Global-scale coherence modulation of radiation-belt electron loss from plasmaspheric hiss. Nature 523, 193–195. Available from: https://doi.org/10.1038/nature14515.

Breneman, A., et al., 2017. Observations directly linking relativistic electron microbursts to whistler mode chorus: Van Allen Probes and FIREBIRD II. Geophys. Res. Lett. 44. Available from: https://doi.org/10.1002/2017GL075001.

Brice, N., 1964. Fundamentals of very low frequency emission generation mechanisms. J. Geophys. Res. 69 (21), 4515–4522. Available from: https://doi.org/10.1029/JZ069i021p04515.

Brown, J.W., Stone, E.C., 1972. High-energy electron spikes at high latitudes. J. Geophys. Res. 77, 3384–3396. Available from: https://doi.org/10.1029/JA077i019p03384.

Burtis, W.J., Helliwell, R.A., 1969. Banded chorus—a new type of VLF radiation observed in the magnetosphere by OGO 1 and OGO 3. J. Geophys. Res. 74 (11), 3002–3010.

Cao, X., et al., 2017. Bounce resonance scattering of radiation belt electrons by H^+ band EMIC waves. J. Geophys. Res. Space Phys. 122. Available from: https://doi.org/10.1002/2016JA023607.

Carson, B.R., Rodger, C.J., Clilverd, M.A., 2013. POES satellite observations of EMIC-wave driven relativistic electron precipitation during 1998–2010. J. Geophys. Res. Space Phys. 118, 232–243. Available from: https://doi.org/10.1029/2012JA017998.

Cattell, C., et al., 2008. Discovery of very large amplitude whistler-mode waves in Earth's radiation belts. Geophys. Res. Lett. 35, L01105. Available from: https://doi.org/10.1029/2007GL032009.

Cattell, C.A., Breneman, A., Goetz, K., Kellogg, P.J., Kersten, K., Wygant, J.R., et al., 2012. Large-amplitude whistler waves and electron acceleration in the earth's radiation belts: a review of stereo and wind observations. In: Summers, D., Mann, I.R., Baker, D.N., Schulz, M. (Eds.), Dynamics of the Earth's Radiation Belts and Inner Magnetosphere. American Geophysical Union, Washington, D.C. Available from: https://doi.org/10.1029/2012GM001322.

Cattell, C.A., Breneman, A.W., Thaller, S.A., Wygant, J.R., Kletzing, C.A., Kurth, W.S., 2015. Van Allen Probes observations of unusually low frequency whistler mode waves observed in association with moderate magnetic storms: statistical study. Geophys. Res. Lett. 42, 7273–7281. Available from: https://doi.org/10.1002/2015GL065565.

Chen, Y., Reeves, G.D., Friedel, R.H.W., 2007. The energization of relativistic electrons in the outer Van Allen radiation belt. Nat. Phys. 3, 614–617. Available from: https://doi.org/10.1038/nphys655.

Chen, L., Thorne, R.M., Horne, R.B., 2009. Simulation of EMIC wave excitation in a model magnetosphere including structured high-density plumes. J. Geophys. Res. 114, A07221. Available from: https://doi.org/10.1029/2009JA014204.

Chen, L., Thorne, R.M., Bortnik, J., 2011. The controlling effect of ion temperature on EMIC wave excitation and scattering. Geophys. Res. Lett. 38, L16109. Available from: https://doi.org/10.1029/2011GL048653.

Chen, L., Bortnik, J., Li, W., Thorne, R.M., Horne, R.B., 2012. Modeling the properties of plasmaspheric hiss: 1. Dependence on chorus wave emission. J. Geophys. Res. 117, A05201. Available from: https://doi.org/10.1029/2011JA017201.

Chen, L., et al., 2014. Generation of unusually low frequency plasmaspheric hiss. Geophys. Res. Lett. 41, 5702–5709. Available from: https://doi.org/10.1002/2014GL060628.

Chen, L., Thorne, R.M., Bortnik, J., Zhang, X.-J., 2016. Nonresonant interactions of electromagnetic ion cyclotron waves with relativistic electrons. J. Geophys. Res. Space Phys. 121, 9913–9925. Available from: https://doi.org/10.1002/2016JA022813.

Chen, L., Santolík, O., Hajoš, M., Zheng, L., Zhima, Z., Heelis, R., et al., 2017. Source of the low-altitude hiss in the ionosphere. Geophys. Res. Lett. 44, 2060–2069. Available from: https://doi.org/10.1002/2016GL072181.

Chum, J., Santolík, O., 2005. Propagation of whistler-mode chorus to low altitudes: divergent ray trajectories and ground accessibility. Ann. Geophys. 23, 3727–3738. Available from: https://doi.org/10.5194/angeo-23-3727-2005.

Church, S.R., Thorne, R.M., 1983. On the origin of plasmaspheric hiss: Ray path integrated amplification. J. Geophys. Res. 88 (A10), 7941–7957. Available from: https://doi.org/10.1029/JA088iA10p07941.

Claudepierre, S.G., et al., 2017. The hidden dynamics of relativistic electrons (0.7-1.5 MeV) in the inner zone and slot region. J. Geophys. Res. Space Physics 122. Available from: https://doi.org/10.1002/2016JA023719.

Clausen, L.B.N., Baker, J.B.H., Ruohoniemi, J.M., Singer, H.J., 2011. EMIC waves observed at geosynchronous orbit during solar minimum: statistics and excitation. J. Geophys. Res. 116, A10205. Available from: https://doi.org/10.1029/2011JA016823.

Clilverd, M.A., et al., 2009. Remote sensing space weather events: the AARDDVARK network. Space Weather 7, S04001. Available from: https://doi.org/10.1029/2008SW000412.

Clilverd, M.A., Duthie, R., Hardman, R., Hendry, A.T., Rodger, C.J., Raita, T., et al., 2015. Electron precipitation from EMIC waves: a case study from 31 May 2013. J. Geophys. Res. Space Phys. 120. Available from: https://doi.org/10.1002/2015JA021090.

Clilverd, M.A., Rodger, C.J., McCarthy, M., Millan, R., Blum, L.W., Cobbett, N., et al., 2017. Investigating energetic electron precipitation through combining ground-based and balloon observations. J. Geophys. Res. Space Phys. 122. Available from: https://doi.org/10.1002/2016JA022812.

Comess, M.D., Smith, D.M., Selesnick, R.S., Millan, R.M., Sample, J.G., 2013. Duskside relativistic electron precipitation as measured by SAMPEX: a statistical survey. J. Geophys. Res. Space Phys. 118, 5050–5058. Available from: https://doi.org/10.1002/jgra.50481.

Cornwall, J.M., 1965. Cyclotron instabilities and electromagnetic emission in the ultra low frequency and very low frequency ranges. J. Geophys. Res. 70 (1), 61–69. Available from: https://doi.org/10.1029/JZ070i001p00061.

Cornwall, J.M., Coroniti, F.V., Thorne, R.M., 1970. Turbulent loss of ring current protons. J. Geophys. Res. 75, 4699.

Crabtree, C., Tejero, E., Ganguli, G., Hospodarsky, G.B., Kletzing, C.A., 2017. Bayesian spectral analysis of chorus subelements from the Van Allen Probes. J. Geophys. Res. Space Phys. 122. Available from: https://doi.org/10.1002/2016JA023547.

Crew, A.B., et al., 2016. First multipoint in situ observations of electron microbursts: initial results from the NSF FIREBIRD II mission. J. Geophys. Res. Space Phys. 121. Available from: https://doi.org/10.1002/2016JA022485.

Cully, C.M., Bonnell, J.W., Ergun, R.E., 2008. THEMIS observations of long-lived regions of large-amplitude whistler waves in the inner magnetosphere. Geophys. Res. Lett. 35, L17S16. Available from: https://doi.org/10.1029/2008GL033643.

Darrouzet, F., Pierrard, V., Benck, S., Lointier, G., Cabrera, J., Borremans, K., et al., 2013. Links between the plasmapause and the radiation belt boundaries as observed by the instruments CIS, RAPID and WHISPER onboard Cluster. J. Geophys. Res. Space Phys. 118, 4176–4188. Available from: https://doi.org/10.1002/jgra.50239.

Delport, B., Collier, A.B., Lichtenberger, J., Rodger, C.J., Parrot, M., Clilverd, M.A., Friedel, R.H.W., 2012. Simultaneous observation of chorus and hiss near the plasmapause. J. Geophys. Res. 117, A12218. Available from: https://doi.org/10.1029/2012JA017609.

Denton, R.E., Engebretson, M.J., Keiling, A., Walsh, A.P., Gary, S.P., Décréau, P.M.E., et al., 2010. Multiple harmonic ULF waves in the plasma sheet boundary layer: instability analysis. J. Geophys. Res. 115, A12224. Available from: https://doi.org/10.1029/2010JA015928.

de Soria-Santacruz, M., Spasojevic, M., Chen, L., 2013. EMIC waves growth and guiding in the presence of cold plasma density irregularities. Geophys. Res. Lett. 40. Available from: https://doi.org/10.1002/grl.50484.

Douma, E., Rodger, C.J., Blum, L.W., Clilverd, M.A., 2017. Occurrence characteristics of relativistic electron microbursts from SAMPEX observations. J. Geophys. Res. Space Phys. 122, 8096–8107. Available from: https://doi.org/10.1002/2017JA024067.

Douma, E., Rodger, C.J., Clilverd, M.A., Hendry, A.T., Engebretson, M.J., Lessard, M.R., 2018. Comparison of relativistic microburst activity seen by SAMPEX with ground-based wave

measurements at Halley. Antarctica. J. Geophy. Res. Space Phy. 123, 1279–1294. Available from: https://doi.org/10.1002/2017JA024754.
Drozdov, A.Y., Shprits, Y.Y., Usanova, M.E., Aseev, N.A., Kellerman, A.C., Zhu, H., 2017. EMIC wave parameterization in the long-term VERB code simulation. J. Geophys. Res. Space Phys. 122, 8488–8501. Available from: https://doi.org/10.1002/2017JA024389.
Engebretson, M.J., Posch, J.L., Westerman, A.M., Otto, N.J., Slavin, J.A., Le, G., et al., 2008. Temporal and spatial characteristics of Pc1 waves observed by ST5. J. Geophys. Res. 113, A07206. Available from: https://doi.org/10.1029/2008JA013145.
Engebretson, M.J., et al., 2015. Van Allen probes, NOAA, GOES, and ground observations of an intense EMIC wave event extending over 12 h in magnetic local time. J. Geophys. Res. Space Phys. 120, 5465–5488. Available from: https://doi.org/10.1002/2015JA021227.
Fennell, J.F., Claudepierre, S.G., Blake, J.B., O'Brien, T.P., Clemmons, J.H., Baker, D.N., et al., 2015. Van Allen Probes show that the inner radiation zone contains no MeV electrons: ECT/MagEIS data. Geophys. Res. Lett. 42, 1283–1289. Available from: https://doi.org/10.1002/2014GL062874.
Foat, J.E., et al., 1998. First detection of a terrestrial MeV X-ray burst. Geophys. Res. Lett. Available from: https://doi.org/10.1029/1998GL900134.
Foster, J.C., Erickson, P.J., Baker, D.N., Jaynes, A.N., Mishin, E.V., Fennel, J.F., et al., 2016a. Observations of the impenetrable barrier, the plasmapause, and the VLF bubble during the 17 March 2015 storm. J. Geophys. Res. Space Phys. 121, 5537–5548. Available from: https://doi.org/10.1002/2016JA022509.
Foster, J.C., Erickson, P.J., Omura, Y., Baker, D.N., Kletzing, C.A., Claudepierre, S.G., 2016b. Van Allen Probes observations of prompt MeV radiation belt electron acceleration in nonlinear interactions with VLF chorus. J. Geophys. Res. Space Phys. 122. Available from: https://doi.org/10.1002/2016JA023429.
Foster, J.C., Erickson, P.J., Omura, Y., Baker, D.N., Kletzing, C.A., Claudepierre, S.G., 2017. Van Allen Probes observations of prompt MeV radiation belt electron acceleration in nonlinear interactions with VLF chorus. J. Geophys. Res. Space Phy. 122, 324–339. Available from: https://doi.org/10.1002/2016JA023429.
Fraser, B.J., Nguyen, T.S., 2001. Is the plasmapause a preferred source region of electromagnetic cyclotron waves in the magnetosphere. J. Atmos. Sol-Terr. Phys. 63, 1225–1247.
Friedel, R.H.W., Reeves, G.D., Obara, T., 2002. Relativistic electron dynamics in the inner magnetosphere—a review. J. Atmos. Sol.-Terr. Phys. Available from: https://doi.org/10.1016/S1364-6826(01)00088-8.
Fu, X., et al., 2014. Whistler anisotropy instabilities as the source of banded chorus: Van Allen Probes observations and particle-in-cell simulations. J. Geophys. Res. Space Phys. 119, 8288–8298. Available from: https://doi.org/10.1002/2014JA020364.
Fujita, S., Tamao, T., 1988. Duct propagation of hydromagnetic waves in the upper ionosphere: 1. Electromagnetic field distributions in high latitudes associated with localized incidence of a shear Alfvén wave. J. Geophys. Res. 93, 14,665–14,673. Available from: https://doi.org/10.1029/JA093iA12p14665.
Gao, X., Li, W., Thorne, R.M., Bortnik, J., Angelopoulos, V., Lu, Q., et al., 2014. Statistical results describing the bandwidth and coherence coefficient of whistler mode waves using THEMIS waveform data. J. Geophys. Res. Space Phys. 119, 8992–9003. Available from: https://doi.org/10.1002/2014JA020158.
Gao, Y., Xiao, F., Yan, Q., Yang, C., Liu, S., He, Y., et al., 2015. Influence of wave normal angles on hiss-electron interaction in Earth's slot region. J. Geophys. Res. Space Phys. 120, 9385–9400. Available from: https://doi.org/10.1002/2015JA021786.
Gao, Z., Su, Z., Zhu, H., Xiao, F., Zheng, H., Wang, Y., et al., 2016. Intense low-frequency chorus waves observed by Van Allen Probes: fine structures and potential effect on radiation belt electrons. Geophys. Res. Lett. 43, 967–977. Available from: https://doi.org/10.1002/2016GL067687.
Gary, S.P., 1993. Theory of Space Plasma Microinstabilities. Cambridge University Press, New York.
Ginzburg, 1960. Certain theoretical aspects of radiation due to superluminal motion in a medium. Sov. Phys. Usp 2, 874. Available from: https://doi.org/10.1070/PU1960v002n06ABEH003185.
Glauert, S.A., Horne, R.B., Meredith, N.P., 2014. Three-dimensional electron radiation belt simulations using the BAS Radiation Belt Model with new diffusion models for chorus, plasmaspheric hiss, and

lightning-generated whistlers. J. Geophys. Res. Space Phys. 119, 268–289. Available from: https://doi.org/10.1002/2013JA019281.
Golden, D.I., Spasojevic, M., Li, W., Nishimura, Y., 2012. Statistical modeling of plasmaspheric hiss amplitude using solar wind measurements and geomagnetic indices. Geophys. Res. Lett. 39, L06103. Available from: https://doi.org/10.1029/2012GL051185.
Goldstein, J., Kanekal, S., Baker, D.N., Sandel, B.R., 2005. Dynamic relationship between the outer radiation belt and the plasmapause during March–May 2001. Geophys. Res. Lett. 32, L15104. Available from: https://doi.org/10.1029/2005GL023431.
Goldstein, J., et al., 2016. The relationship between the plasmapause and outer belt electrons. J. Geophys. Res. Space Phys. 121. Available from: https://doi.org/10.1002/2016JA023046.
Green, J.C., Onsager, T.G., O'Brien, T.P., Baker, D.N., 2004. Testing loss mechanisms capable of rapidly depleting relativistic electron flux in the Earth's outer radiation belt. J. Geophys. Res. 109, A12211. Available from: https://doi.org/10.1029/2004JA010579.
Greifinger, C., Greifinger, P.S., 1968. Theory of hydromagnetic propagation in the ionosphere waveguide. J. Geophys. Res. 73, 7473–7490. Available from: https://doi.org/10.1029/JA073i023p07473.
Grison, B., Santolk, O., Cornilleau-Wehrlin, N., Masson, A., Engebretson, M.J., Pickett, J.S., et al., 2013. EMIC triggered chorus emissions in cluster data. J. Geophys. Res. Space Phys. 118, 1159–1169. Available from: https://doi.org/10.1002/jgra.50178.
Halford, A.J., Fraser, B.J., Morley, S.K., 2010. EMIC wave activity during geomagnetic storm and nonstorm periods: CRRES results. J. Geophys. Res. 115, A12248. Available from: https://doi.org/10.1029/2010JA015716.
Halford, A.J., Fraser, B.J., Morley, S.K., 2015a. EMIC waves and plasmaspheric and plume density: CRRES results. J. Geophys. Res. Space Phys. 120. Available from: https://doi.org/10.1002/2014JA020338.
Halford, A.J., et al., 2015b. BARREL observations of an ICME-shock impact with the magnetosphere and the resultant radiation belt electron loss. J. Geophys. Res. Space Phys. 120, 2557–2570. Available from: https://doi.org/10.1002/2014JA020873.
Haque, N., Spasojevic, M., Santolík, O., Inan, U.S., 2010. Wave normal angles of magnetospheric chorus emissions observed on the Polar spacecraft. J. Geophys. Res. 115, A00F07. Available from: https://doi.org/10.1029/2009JA014717.
Hartley, D.P., Kletzing, C.A., Santolík, O., Chen, L., Horne, R.B., 2018. Statistical properties of plasmaspheric hiss from Van Allen Probes observations. J. Geophys. Res. Space Phys. 123. Available from: https://doi.org/10.1002/2017JA024593.
Hayakawa, Masashi, Sazhin, Sergei, 1992. Mid-latitude and plasmaspheric HISS—A review. Planetary Space Sci. 40, 1325–1338. Available from: https://doi.org/10.1016/0032-0633(92)90089-7.
He, Z., Yan, Q., Chu, Y., Cao, Y., 2016. Wave-driven gradual loss of energetic electrons in the slot region. J. Geophys. Res. Space Phys. 121, 8614–8623. Available from: https://doi.org/10.1002/2016JA023087.
Helliwell, R.A., 1965. Whistlers and related ionospheric phenomena. Stanford University Press, Stanford Calif.
Hendry, A.T., Rodger, C.J., Clilverd, M.A., Engebretson, M.J., Mann, I.R., Lessard, M.R., et al., 2016. Confirmation of EMIC wave-driven relativistic electron precipitation. J. Geophys. Res. Space Phy. 121, 5366–5383. Available from: https://doi.org/10.1002/2015JA022224.
Hendry, A.T., Rodger, C.J., Clilverd, M.A., 2017. Evidence of sub-MeV EMIC-driven electron precipitation. Geophys. Res. Lett. 44, 1210–1218. Available from: https://doi.org/10.1002/2016GL071807.
Hess, W.N., 1963. The artificial radiation belt made on July 9, 1962. J. Geophys. Res. 68 (3), 667–683. Available from: https://doi.org/10.1029/JZ068i003p00667.
Hikishima, M., Omura, Y., Summers, D., 2010. Microburst precipitation of energetic electrons associated with chorus wave generation. Geophys. Res. Lett. 37, L07103. Available from: https://doi.org/10.1029/2010GL042678.
Horne, R.B., Thorne, R., 1994. Convective instabilities of electromagnetic ion cyclotron waves in the outer magnetosphere. J. Geophys. Res. 99, 17,259–17,273.

Horne, R.B., Thorne, R.M., 1998. Potential waves for relativistic electron scattering and stochastic acceleration during magnetic storms. Geophys. Res. Lett. 25, 3011–3014.

Horne, R.B., Glauert, S.A., Thorne, R.M., 2003a. Resonant diffusion of radiation belt electrons by whistler-mode chorus. Geophys. Res. Lett. 30 (9), 1493. Available from: https://doi.org/10.1029/2003GL016963.

Horne, R.B., Thorne, R.M., 2003. Relativistic electron acceleration and precipitation during resonant interactions with whistler-mode chorus. Geophys. Res. Lett. 30 (10), 1527. Available from: https://doi.org/10.1029/2003GL016973.

Horne, R.B., Thorne, R.M., Shprits, Y.Y., Meredith, N.P., Glauert, S.A., 2005. Wave acceleration of electrons in the Van Allen radiation belts. Nature 437, 227–230. Available from: https://doi.org/10.1038/nature03939.

Horne, R.B., Glauert, S.A., Meredith, N.P., Boscher, D., Maget, V., Heynderickx, D., et al., 2013. Space weather impacts on satellites and forecasting the Earth's electron radiation belts with SPACECAST. Space Weather 11, 169–186. Available from: https://doi.org/10.1002/swe.20023.

Horne, R.B., Meredith, N.P., Glauert, S.A., Kersten, T., 2016. Wave-driven diffusion in radiation belt dynamics. https://doi.org/10.1093/acprof:oso/9780198705246.003.0010.

Hsieh, Y.-K., Omura, Y., 2017. Study of wave-particle interactions for whistler mode waves at oblique angles by utilizing the gyroaveraging method. Radio Sci. 52. Available from: https://doi.org/10.1002/2017RS006245.

Huang, C.Y., Goertz, C.K., Anderson, R.R., 1983. A theoretical study of plasmaspheric hiss generation. J. Geophys. Res. 88 (A10), 7927–7940. Available from: https://doi.org/10.1029/JA088iA10p07927.

Hudson, M.K., Kress, B.T., Mueller, H.-R., Zastrow, J.A., Blake, J.B., 2008. Relationship of the Van Allen radiation belts to solar wind drivers. J. Atmos. Sol-Terr. Phys. 70 (5). Available from: https://doi.org/10.1016/j.jastp.2007.11.003.

Hudson, M.K., Baker, D.N., Goldstein, J., Kress, B.T., Paral, J., Toffoletto, F.R., et al., 2014. Simulated magnetopause losses and Van Allen Probe flux dropouts. Geophys. Res. Lett. 41, 1113–1118. Available from: https://doi.org/10.1002/2014GL059222.

Hwang, J.A., Lee, D.-Y., Lyons, L.R., Smith, A.J., Zou, S., Min, K.W., et al., 2007. Statistical significance of association between whistler-mode chorus enhancements and enhanced convection periods during high- speed streams. J. Geophys. Res. 112, A09213. Available from: https://doi.org/10.1029/2007JA012388.

Imhof, W.L., Voss, H.D., Reagan, J.B., Datlowe, D.W., Gaines, E.E., Mobilia, J., et al., 1986. Relativistic electron and energetic ion precipitation spikes near the plasmapause. J. Geophys. Res. 91 (A3), 3077–3088. Available from: https://doi.org/10.1029/JA091iA03p03077.

Imhof, W.L., Voss, H.D., Mobilia, J., Datlowe, D.W., Gaines, E.E., 1991. The precipitation of relativistic electrons near the trapping boundary. J. Geophys. Res. 96 (A4), 5619–5629. Available from: https://doi.org/10.1029/90JA02343.

Imhof, W.L., Voss, H.D., Mobilia, J., Datlowe, D.W., Gaines, E.E., McGlennon, J.P., et al., 1992. Relativistic electron microbursts. J. Geophys. Res. 97 (A9), 13829–13837. Available from: https://doi.org/10.1029/92JA01138.

Inan, U.S., Golkowski, M., Casey, M.K., Moore, R.C., Peter, W., Kulkarni, P., et al., 2007. Subionospheric VLF observations of transmitter-induced precipitation of inner radiation belt electrons. Geophys. Res. Lett. 34, L02106. Available from: https://doi.org/10.1029/2006GL028494.

Jaynes, A.N., et al., 2014. Evolution of relativistic outer belt electrons during an extended quiescent period. J. Geophys. Res. Space Phys. 119, 9558–9566. Available from: https://doi.org/10.1002/2014JA020125.

Jaynes, A.N., et al., 2015. Source and seed populations for relativistic electrons: their roles in radiation belt changes. J. Geophys. Res. Space Phys. 120, 7240–7254. Available from: https://doi.org/10.1002/2015JA021234.

Johnston, W.R., Anderson, P.C., 2010. Storm time occurrence of relativistic electron microbursts in relation to the plasmapause. J. Geophys. Res. 115, A02205. Available from: https://doi.org/10.1029/2009JA014328.

Jordanova, V.K., Spasojevic, M., Thomsen, M.F., 2007. Modeling the electromagnetic ion cyclotron wave-induced formation of detached subauroral proton arcs. J. Geophys. Res. 112, A08209. Available from: https://doi.org/10.1029/2006JA012215.

Jordanova, V.K., Welling, D.T., Zaharia, S.G., Chen, L., Thorne, R.M., 2012. Modeling ring current ion and electron dynamics and plasma instabilities during a high-speed stream driven storm. J. Geophys. Res. 117, A00L08. Available from: https://doi.org/10.1029/2011JA017433.

Kaiser, M.L., 2005. The STEREO mission. Adv. Space Res. 36 (8), 1483.

Kasahara, S., et al., 2018. Pulsating aurora from electron scattering by chorus waves. Nature 554, 337. Available from: https://doi.org/10.1038/nature25505.

Katoh, Y., Omura, Y., 2007. Computer simulation of chorus wave generation in the Earth's inner magnetosphere. Geophys. Res. Lett. 34, L03102. Available from: https://doi.org/10.1029/2006GL028594.

Katoh, Y., Omura, Y., 2013. Effect of the background magnetic field inhomogeneity on generation processes of whistler-mode chorus and broadband hiss-like emissions. J. Geophys. Res. Space Phys. 118, 4189–4198. Available from: https://doi.org/10.1002/jgra.50395.

Keika, K., Takahashi, K., Ukhorskiy, A.Y., Miyoshi, Y., 2013. Global characteristics of electromagnetic ion cyclotron waves: occurrence rate and its storm dependence. J. Geophys. Res. Space Phys. 118. Available from: https://doi.org/10.1002/jgra.50385.

Kellerman, A.C., Shprits, Y.Y., Kondrashov, D., Subbotin, D., Makarevich, R.A., Donovan, E., et al., 2014. Three-dimensional data assimilation and reanalysis of radiation belt electrons: observations of a four-zone structure using five spacecraft and the VERB code. J. Geophys. Res. Space Phys. 119, 8764–8783. Available from: https://doi.org/10.1002/2014JA020171.

Kellogg, P.J., Cattell, C.A., Goetz, K., Monson, S.J., Wilson III, L.B., 2011. Large amplitude whistlers in the magnetosphere observed with Wind Waves. J. Geophys. Res. 116, A09224. Available from: https://doi.org/10.1029/2010JA015919.

Kennel, C.F., Engelmann, F., 1966. Velocity space diffusion from weak plasma turbulence in a magnetic field. Phys. Fluids 9, 2377.

Kennel, C.F., Petschek, H.E., 1966. Limit on stably trapped particle fluxes. J. Geophys. Res. 71 (1), 1–28. Available from: https://doi.org/10.1029/JZ071i001p00001.

Kersten, K., Cattell, C.A., Breneman, A., Goetz, K., Kellogg, P.J., Wygant, J.R., et al., 2011. Observation of relativistic electron microbursts in conjunction with intense radiation belt whistler mode waves. Geophys. Res. Lett. 38, L08107. Available from: https://doi.org/10.1029/2011GL046810.

Kilpua, E.K.J., Hietala, H., Turner, D.L., Koskinen, H.E.J., Pulkkinen, T.I., Rodriguez, J.V., et al., 2015. Unraveling the drivers of the storm time radiation belt response. Geophys. Res. Lett. 42, 3076–3084. Available from: https://doi.org/10.1002/2015GL063542.

Kim, K.C., Shprits, Y., 2013. Long-term relativistic radiation belt electron responses to GEM magnetic storms. J. Atmos. Sol.-Terr. Phys. 100–101, 59–67.

Kim, K.C., Shprits, Y., Subbotin, D., Ni, B., 2011. Understanding the dynamic evolution of the relativistic electron slot region including radial and pitch angle diffusion. J. Geophys. Res. 116, A10214. Available from: https://doi.org/10.1029/2011JA016684.

Kletzing, C.A., et al., 2014. Evidence for Significant Local Generation of Plasmaspheric Hiss, American Geophysical Union, Fall Meeting 2014, abstract id. SM14A-09, 2014AGUFMSM14A.09K.

Klumpar, D., et al., 2015. Flight system technologies enabling the twin-CubeSat FIREBIRD-II scientific mission. In: Proceedings of the 29th Annual AIAA/USU Conference on Small Satellites.

Koons, C.H., McPherson, A.D., 1972. Observation of very-low-frequency whistler-mode waves in the region of the radiation-belt slot. J. Geophys. Res. 77, 3475–3482. Available from: https://doi.org/10.1029/JA077i019p03475.

Kozyra, J.U., Cravens, T.E., Nagy, A.F., Fontheim, E.G., Ong, R.S.B., 1984. Effects of energetic heavy ions on electromagnetic ion cyclotron wave generation in the plasmapause region. J. Geophys. Res. 89 (A4), 2217–2233. Available from: https://doi.org/10.1029/JA089iA04p02217.

Laakso, H., Santolik, O., Horne, R., Kolmasová, I., Escoubet, P., Masson, A., et al., 2015. Identifying the source region of plasmaspheric hiss. Geophys. Res. Lett. 42, 3141–3149. Available from: https://doi.org/10.1002/2015GL063755.

Lakhina, G.S., Tsurutani, B.T., Verkhoglyadova, O.P., Pickett, J.S., 2010. Pitch angle transport of electrons due to cyclotron interactions with the coherent chorus subelements. J. Geophys. Res. 115, A00F15. Available from: https://doi.org/10.1029/2009JA014885.

Lam, M.M., Horne, R.B., Meredith, N.P., Glauert, S.A., Moffat-Griffin, T., Green, J.C., 2010. Origin of energetic electron precipitation >30 keV into the atmosphere. J. Geophys. Res. 115, A00F08. Available from: https://doi.org/10.1029/2009JA014619.

Lampton, M., 1967. Daytime observations of energetic auroral-zone electrons. J. Geophys. Res. 72 (23), 5817–5823. Available from: https://doi.org/10.1029/JZ072i023p05817.

LeDocq, M.J., Gurnett, D.A., Hospodarsky, G.B., 1998. Chorus source locations from VLF Poynting flux measurements with the Polar spacecraft. Geophys. Res. Lett. Available from: https://doi.org/10.1029/1998GL900071.

Lee, J., Min, K., Kim, K.-S., 2013. Characteristic dimension of electromagnetic ion cyclotron wave activity in the magnetosphere. J. Geophys. Res. Space Phys. 118, 1651–1658. Available from: https://doi.org/10.1002/jgra.50242.

Li, X., et al., 1993. Simulation of the prompt energization and transport of radiation belt particles during the March 24, 1991 SSC. Geophys. Res. Lett. Available from: https://doi.org/10.1029/93GL02701.

Li, X., Baker, D.N., Temerin, M., Cayton, T.E., Reeves, E.G.D., Christensen, R.A., et al., 1997. Multisatellite observations of the outer zone electron variation during the November 3–4, 1993, magnetic storm. J. Geophys. Res. 102, 14,123–114,140.

Li, X., Baker, D.N., O'Brien, T.P., Xie, L., Zong, Q.G., 2006. Correlation between the inner edge of outer radiation belt electrons and the innermost plasmapause location. Geophys. Res. Lett. 33, L14107. Available from: https://doi.org/10.1029/2006GL026294.

Li, X., Barker, A.B., Baker, D.N., Tu, W.C., Sarris, T.E., Selesnick, R.S., et al., 2009. Modeling the deep penetration of outer belt electrons during the "Halloween" magnetic storm in 2003. Space Weather 7, S02004. Available from: https://doi.org/10.1029/2008SW000418.

Li, W., Thorne, R.M., Bortnik, J., Nishimura, Y., Angelopoulos, V., Chen, L., et al., 2010. Global distributions of suprathermal electrons observed on THEMIS and potential mechanisms for access into the plasmasphere. J. Geophys. Res. 115, A00J10. Available from: https://doi.org/10.1029/2010JA015687.

Li, W., Thorne, R.M., Bortnik, J., Tao, X., Angelopoulos, V., 2012. Characteristics of hiss-like and discrete whistler-mode emissions. Geophys. Res. Lett. 39, L18106. Available from: https://doi.org/10.1029/2012GL053206.

Li, W., et al., 2013a. An unusual enhancement of low-frequency plasmaspheric hiss in the outer plasmasphere associated with substorm-injected electrons. Geophys. Res. Lett. 40, 3798–3803. Available from: https://doi.org/10.1002/grl.50787.

Li, W., Ni, B., Thorne, R.M., Bortnik, J., Green, J.C., Kletzing, C.A., et al., 2013b. Constructing the global distribution of chorus wave intensity using measurements of electrons by the POES satellites and waves by the Van Allen Probes. Geophys. Res. Lett. 40. Available from: https://doi.org/10.1002/grl.50920.

Li, X., et al., 2013c. First results from CSSWE CubeSat: characteristics of relativistic electrons in the near-earth environment during the October 2012 magnetic storms. J. Geophys. Res. Space Phys. 118. Available from: https://doi.org/10.1002/2013JA019342.

Li, Z., Millan, R.M., Hudson, M.K., 2013d. Simulation of the energy distribution of relativistic electron precipitation caused by quasi-linear interactions with EMIC waves. J. Geophys. Res. Space Phys. 118. Available from: https://doi.org/10.1002/2013JA019163.

Li, W., et al., 2014a. Evidence of stronger pitch angle scattering loss caused by oblique whistler-mode waves as compared with quasi-parallel waves. Geophys. Res. Lett. 41, 6063–6070. Available from: https://doi.org/10.1002/2014GL061260.

Li, Z., et al., 2014b. Investigation of EMIC wave scattering as the cause for the BARREL 17 January 2013 relativistic electron precipitation event: a quantitative comparison of simulation with observations. Geophys. Res. Lett. 41, 8722–8729. Available from: https://doi.org/10.1002/2014GL062273.

Li, X., Selesnick, R.S., Baker, D.N., Jaynes, A.N., Kanekal, S.G., Schiller, Q., et al., 2015. Upper limit on the inner radiation belt MeV electron intensity. J. Geophys. Res. Space Phys. 120, 1215–1228. Available from: https://doi.org/10.1002/2014JA020777.

Li, W., Chen, L., Bortnik, J., Thorne, R.M., Angelopoulos, V., Kletzing, C.A., et al., 2015a. First evidence for chorus at a large geocentric distance as a source of plasmaspheric hiss: coordinated

THEMIS and Van Allen Probes observation. Geophys. Res. Lett. 42, 241–248. Available from: https://doi.org/10.1002/2014GL062832.

Li, W., Ma, Q., Thorne, R.M., Bortnik, J., Kletzing, C.A., Kurth, W.S., et al., 2015b. Statistical properties of plasmaspheric hiss derived from Van Allen Probes data and their effects on radiation belt electron dynamics. J. Geophys. Res. Space Phys. 120, 3393–3405. Available from: https://doi.org/10.1002/2015JA021048.

Li, W., Thorne, R.M., Bortnik, J., Baker, D.N., Reeves, G.D., Kanekal, S.G., et al., 2015c. Solar wind conditions leading to efficient radiation belt electron acceleration: a superposed epoch analysis. Geophys. Res. Lett. 42, 6906–6915. Available from: https://doi.org/10.1002/2015GL065342.

Li, W., Santolik, O., Bortnik, J., Thorne, R.M., Kletzing, C.A., Kurth, W.S., et al., 2016. New chorus wave properties near the equator from Van Allen Probes wave observations. Geophys. Res. Lett. 43, 4725–4735. Available from: https://doi.org/10.1002/2016GL068780.

Li, X., Baker, D.N., Zhao, H., Zhang, K., Jaynes, A.N., Schiller, Q., et al., 2017a. Radiation belt electron dynamics at low L (<4): Van Allen Probes era versus previous two solar cycles. J. Geophys. Res. Space Phys. 122. Available from: https://doi.org/10.1002/2017JA023924.

Li, J., et al., 2017b. Coherently modulated whistler mode waves simultaneously observed over unexpectedly large spatial scales. J. Geophys. Res. Space Phys. 122, 1871–1882. Available from: https://doi.org/10.1002/2016JA023706.

Liu, K., Winske, D., Gary, S.P., Reeves, G.D., 2012. Relativistic electron scattering by large amplitude electromagnetic ion cyclotron waves: the role of phase bunching and trapping. J. Geophys. Res. 117, A06218. Available from: https://doi.org/10.1029/2011JA017476.

Lorentzen, K.R., Blake, J.B., Inan, U.S., Bortnik, J., 2001a. Observations of relativistic electron microbursts in association with VLF chorus. J. Geophys. Res. 106 (A4), 6017–6027. Available from: https://doi.org/10.1029/2000JA003018.

Lorentzen, K.R., Blake, J.B., Inan, U.S., Bortnik, J., 2001b. Relativistic electron microbursts during the GEM storms. Geophys. Res. Lett. 28 (13), 2573–2576. Available from: https://doi.org/10.1029/2001GL012926.

Loto'aniu, T.M., Thorne, R.M., Fraser, B.J., Summers, D., 2006. Estimating relativistic electron pitch angle scattering rates using properties of the electromagnetic ion cyclotron wave spectrum. J. Geophys. Res. 111, A04220. Available from: https://doi.org/10.1029/2005JA011452.

Lyons, L.R., Thorne, R.M., 1973. Equilibrium structure of radiation belt electrons. J. Geophys. Res. 78 (13), 2142–2149. Available from: https://doi.org/10.1029/JA078i013p02142.

Lyons, L.R., Thorne, R.M., Kennel, C.F., 1972. Pitch-angle diffusion of radiation belt electrons within the plasmasphere. J. Geophys. Res. 77 (19), 3455–3474. Available from: https://doi.org/10.1029/JA077i019p03455.

Ma, Q., Li, W., Thorne, R.M., Ni, B., Kletzing, C.A., Kurth, W.S., et al., 2015. Modeling inward diffusion and slow decay of energetic electrons in the Earth's outer radiation belt. Geophys. Res. Lett. 42, 987–995. Available from: https://doi.org/10.1002/2014GL062977.

Ma, Q., Li, W., Thorne, R.M., Bortnik, J., Reeves, G.D., Spence, H.E., et al., 2017a. Diffusive transport of several hundred keV electrons in the Earth's slot region. J. Geophys. Res. Space Phys. 122, 10,235–10,246. Available from: https://doi.org/10.1002/2017JA024452.

Ma, Q., Mourenas, D., Li, W., Artemyev, A., Thorne, R.M., 2017b. VLF waves from ground-based transmitters observed by the Van Allen Probes: statistical model and effects on plasmaspheric electrons. Geophys. Res. Lett. 44. Available from: https://doi.org/10.1002/2017GL073885.

Ma, Q., Artemyev, A.V., Mourenas, D., Li, W., Thorne, R.M., Kletzing, C.A., et al., 2017c. Very oblique whistler mode propagation in the radiation belts: effects of hot plasma and Landau damping. Geophys. Res. Lett. 44. Available from: https://doi.org/10.1002/2017GL075892.

Macúšová, E., et al., 2010. Observations of the relationship between frequency sweep rates of chorus wave packets and plasma density. J. Geophys. Res. 115, A12257. Available from: https://doi.org/10.1029/2010JA015468.

Malaspina, D.M., Jaynes, A.N., Boule, C., Bortnik, J., Thaller, S.A., Ergun, R.E., et al., 2016. The distribution of plasmaspheric hiss wave power with respect to plasmapause location. Geophys. Res. Lett. 43, 7878–7886. Available from: https://doi.org/10.1002/2016GL069982.

Malaspina, D.M., Jaynes, A.N., Hospodarsky, G., Bortnik, J., Ergun, R.E., Wygant, J., 2017. Statistical properties of low-frequency plasmaspheric hiss. J. Geophys. Res. Space Phys. 122. Available from: https://doi.org/10.1002/2017JA024328.

Mann, I.R., Usanova, M.E., Murphy, K., Robertson, M.T., Milling, D.K., Kale, A., et al., 2014. Spatial localization and ducting of EMIC waves: Van Allen Probes and ground-based observations. Geophys. Res. Lett. 41, 785–792. Available from: https://doi.org/10.1002/2013GL058581.

Mann, I.R., et al., 2016. Explaining the dynamics of the ultra-relativistic third Van Allen radiation belt. Nat. Phys. Available from: https://doi.org/10.1038/NPHYS3799.

Matsui, H., Paulson, K.W., Torbert, R.B., Spence, H.E., Kletzing, C.A., Kurth, W.S., et al., 2016. Nonlinearity in chorus waves during a geomagnetic storm on 1 November 2012. J. Geophys. Res. Space Phys. 121, 358–373. Available from: https://doi.org/10.1002/2015JA021772.

Matsui, H., Torbert, R.B., Spence, H.E., Argall, M.R., Alm, L., Farrugia, C.J., et al., 2017. Relativistic electron increase during chorus wave activities on the 6–8 March 2016 geomagnetic storm. J. Geophys. Res. Space Phys. 122. Available from: https://doi.org/10.1002/2017JA024540.

Meredith, N.P., Horne, R.B., Sandberg, I., Papadimitriou, C., Evans, H.D.R., 2017. Extreme relativistic electron fluxes in the Earth's outer radiation belt: Analysis of INTEGRAL IREM data. Space Weather 15, 917–933. Available from: https://doi.org/10.1002/2017SW001651.

McCollough, J.P., Elkington, S.R., Usanova, M.E., Mann, I.R., Baker, D.N., Kale, Z.C., 2010. Physical mechanisms of compressional EMIC wave growth. J. Geophys. Res. 115, A10214. Available from: https://doi.org/10.1029/2010JA015393.

Meredith, N.P., Horne, R.B., Anderson, R.R., 2001. Substorm dependence of chorus amplitudes: implications for the acceleration of electrons to relativistic energies. J. Geophys. Res. 106 (A7), 13165–13178. Available from: https://doi.org/10.1029/2000JA900156.

Meredith, N.P., Horne, R.B., Iles, R.H.A., Thorne, R.M., Heynderickx, D., Anderson, R.R., 2002. Outer zone relativistic electron acceleration associated with substorm-enhanced whistler mode chorus. J. Geophys. Res. 107 (A7). Available from: https://doi.org/10.1029/2001JA900146.

Meredith, N.P., Horne, R.B., Thorne, R.M., Anderson, R.R., 2003a. Favored regions for chorus-driven electron acceleration to relativistic energies in the Earth's outer radiation belt. Geophys. Res. Lett. 30 (16), 1871. Available from: https://doi.org/10.1029/2003GL017698.

Meredith, N.P., Thorne, R.M., Horne, R.B., Summers, D., Fraser, B.J., Anderson, R.R., 2003b. Statistical analysis of relativistic electron energies for cyclotron resonance with EMIC waves observed on CRRES. J. Geophys. Res. 108 (A6), 1250. Available from: https://doi.org/10.1029/2002JA009700.

Meredith, N.P., Horne, R.B., Thorne, R.M., Summers, D., Anderson, R.R., 2004. Substorm dependence of plasmaspheric hiss. J. Geophys. Res. 109, A06209. Available from: https://doi.org/10.1029/2004JA010387.

Meredith, N.P., Horne, R.B., Clilverd, M.A., Horsfall, D., Thorne, R.M., Anderson, R.R., 2006a. Origins of plasmaspheric hiss. J. Geophys. Res. 111, A09217. Available from: https://doi.org/10.1029/2006JA011707.

Meredith, N.P., Horne, R.B., Glauert, S.A., Thorne, R.M., Summers, D., Albert, J.M., et al., 2006b. Energetic outer zone electron loss timescales during low geomagnetic activity. J. Geophys. Res. 111, A05212. Available from: https://doi.org/10.1029/2005JA011516.

Meredith, N.P., Horne, R.B., Glauert, S.A., Anderson, R.R., 2007. Slot region electron loss timescales due to plasmaspheric hiss and lightning-generated whistlers. J. Geophys. Res. 112, A08214. Available from: https://doi.org/10.1029/2007JA012413.

Meredith, N.P., Horne, R.B., Glauert, S.A., Baker, D.N., Kanekal, S.G., Albert, J.M., 2009. Relativistic electron loss timescales in the slot region. J. Geophys. Res. 114, A03222. Available from: https://doi.org/10.1029/2008JA013889.

Meredith, N.P., Horne, R.B., Bortnik, J., Thorne, R.M., Chen, L., Li, W., Sicard-Piet, A., 2013. Global statistical evidence for chorus as the embryonic source of plasmaspheric hiss. Geophys. Res. Lett 40, 2891–2896. Available from: https://doi.org/10.1002/grl.50593.

Meredith, N.P., Horne, R.B., Li, W., Thorne, R.M., Sicard-Piet, A., 2014. Global model of low-frequency chorus ($f_{LHR} < f < 0.1\ f_{ce}$) from multiple satellite observations. Geophys. Res. Lett. 41, 280–286. Available from: https://doi.org/10.1002/2013GL059050.

Millan, R.M., The BARREL Team, 2011. Understanding relativistic electron losses with BARREL. J. Atmos. Sol.-Terr. Phys. 73, 1425–1434.

Millan, R.M., 2016. Science Highlights From the Balloon Array for Radiation Belt Electron Losses (BARREL), American Geophysical Union, Fall Meeting 2016, abstract id. SM42A-01, 2016AGUFMSM42A.01M.

Millan, R.M., Baker, D.N., 2012. Acceleration of particles to high energies in Earth's radiation belts. Space Sci. Rev. 173, 103–131. Available from: https://doi.org/10.1007/s11214-012-9941-x.

Millan, R.M., Lin, R.P., Smith, D.M., Lorentzen, K.R., McCarthy, M.P., 2002. X-ray observations of MeV electron precipitation with a balloon-borne germanium spectrometer. Geophys. Res. Lett. 29 (24), 2194. Available from: https://doi.org/10.1029/2002GL015922.

Millan, R.M., McCarthy, M.P., Sample, J.G., et al., 2013. The Balloon Array for RBSP Relativistic Electron Losses (BARREL). Space Sci. Rev. 179, 503. Available from: https://doi.org/10.1007/s11214-013-9971-z.

Min, K., Lee, J., Keika, K., Li, W., 2012. Global distribution of EMIC waves derived from THEMIS observations. J. Geophys. Res. 117, A05219. Available from: https://doi.org/10.1029/2012JA017515.

Mironova, I.A., Aplin, K.L., Arnold, F., Bazilevskaya, G.A., Harrison, R.G., Krivolutsky, A.A., et al., 2015. Energetic particle influence on the earth's atmosphere. Space Sci. Rev. 194 (1–4), 1–96.

Miyoshi, Y., Sakaguchi, K., Shiokawa, K., Evans, D., Albert, J., Connors, M., et al., 2008. Precipitation of radiation belt electrons by EMIC waves, observed from ground and space. Geophys. Res. Lett. 35 (23). Available from: https://doi.org/10.1029/2008GL035727.

Morley, S.K., Friedel, R.H.W., Cayton, T.E., Noveroske, E., 2010. A rapid, global and prolonged electron radiation belt dropout observed with the Global Positioning System constellation. Geophys. Res. Lett. 37, L06102. Available from: https://doi.org/10.1029/2010GL042772.

Mourenas, D., Artemyev, A.V., Ripoll, J.-F., Agapitov, O.V., Krasnoselskikh, V.V., 2012. Timescales for electron quasi-linear diffusion by parallel and oblique lower-band chorus waves. J. Geophys. Res. 117, A06234. Available from: https://doi.org/10.1029/2012JA017717.

Mourenas, D., Artemyev, A.V., Agapitov, O.V., Krasnoselskikh, V., 2014. Consequences of geomagnetic activity on energization and loss of radiation belt electrons by oblique chorus waves. J. Geophys. Res. Space Phys. 119, 2775–2796. Available from: https://doi.org/10.1002/2013JA019674.

Mourenas, D., Artemyev, A.V., Ma, Q., Agapitov, O.V., Li, W., 2016. Fast dropouts of multi-MeV electrons due to combined effects of EMIC and whistler mode waves. Geophys. Res. Lett. 43, 4155–4163. Available from: https://doi.org/10.1002/2016GL068921.

Moya, P.S., Pinto, V.A., Sibeck, D.G., Kanekal, S.G., Baker, D.N., 2017. On the effect of geomagnetic storms on relativistic electrons in the outer radiation belt: Van Allen Probes observations. J. Geophys. Res. 122. Available from: https://doi.org/10.1002/2017JA024735.

Mozer, F.S., Agapitov, O., Krasnoselskikh, V., Lejosne, S., Reeves, G.D., Roth, I., 2014. Direct observation of radiation-belt electron acceleration from electron-volt energies to megavolts by nonlinear whistlers. Phys. Rev. Lett. 113 (3). Available from: https://doi.org/10.1103/PhysRevLett.113.035001.

Mozer, F.S., Agapitov, O.V., Blake, J.B., Vasko, I.Y., 2018. Simultaneous observations of lower band chorus emissions at the equator and microburst precipitating electrons in the ionosphere. Geophys. Res. Lett. 45. Available from: https://doi.org/10.1002/2017GL076120.

Murphy, K.R., Mann, I.R., Rae, I.J., Sibeck, D.G., Watt, C.E.J., 2016. Accurately characterizing the importance of wave-particle interactions in radiation belt dynamics: the pitfalls of statistical wave representations. J. Geophys. Res. Space Phys. 121, 7895–7899. Available from: https://doi.org/10.1002/2016JA022618.

Nagano, I., S., Yagitani, H., Kojima, and H. Matsumoto (1996), Analysis of wave normal and poynting vectors of the chorus emissions observed by GEOTAIL, *J. Geomagnet. Geoelec, 48*(3), 299-307, https://doi.org/10.5636/jgg.48.299.

Nakamura, R., Baker, D.N., Blake, J.B., Kanekal, S., Klecker, B., Hovestadt, D., 1995. Relativistic electron precipitation enhancements near the outer edge of the radiation belt. Geophys. Res. Lett. 22 (9), 1129–1132.

Nakamura, R., Isowa, M., Kamide, Y., Baker, D.N., Blake, J.B., Looper, M., 2000. SAMPEX observations of precipitation bursts in the outer radiation belt. J. Geophys. Res. 105 (A7), 15875–15885. Available from: https://doi.org/10.1029/2000JA900018.

Nakamura, S., Omura, Y., Machida, S., Shoji, M., Nosé, M., Angelopoulos, V., 2014. Electromagnetic ion cyclotron rising tone emissions observed by THEMIS probes outside the plasmapause.

J. Geophys. Res. Space Phys. 119, 1874–1886. Available from: https://doi.org/10.1002/2013JA019146.

Nakamura, S., Omura, Y., Angelopoulos, V., 2016. A statistical study of EMIC rising and falling tone emissions observed by THEMIS. J. Geophys. Res. Space Phys. 121. Available from: https://doi.org/10.1002/2016JA022353.

National Research Council, Division on Engineering and Physical Sciences, Space Studies Board, Aeronautics and Space Engineering Board, Committee on a Decadal Strategy for Solar and Space Physics (Heliophysics), Science for a Technological Society: The 2013–2022 Decadal Survey in Solar and Space Physics (National Academies Press, Washington, DC, 2013). http://dx.doi.org/10.17226/13060.

Ni, B., Bortnik, J., Thorne, R.M., Ma, Q., Chen, L., 2013. Resonant scattering and resultant pitch angle evolution of relativistic electrons by plasmaspheric hiss. J. Geophys. Res. Space Phys. 118, 7740–7751. Available from: https://doi.org/10.1002/2013JA019260.

Ni, B., et al., 2014a. Resonant scattering of energetic electrons by unusual low-frequency hiss. Geophys. Res. Lett. 41, 1854–1861. Available from: https://doi.org/10.1002/2014GL059389.

Ni, B., Li, W., Thorne, R.M., Bortnik, J., Green, J.C., Kletzing, C.A., et al., 2014b. A novel technique to construct the global distribution of whistler mode chorus wave intensity using low-altitude POES electron data. J. Geophys. Res. Space Phys. 119. Available from: https://doi.org/10.1002/2014JA019935.

Ni, B., et al., 2015. Resonant scattering of outer zone relativistic electrons by multiband EMIC waves and resultant electron loss time scales. J. Geophys. Res. Space Phys. 120, 7357–7373. Available from: https://doi.org/10.1002/2015JA021466.

Nishimura, Y., et al., 2010. Identifying the driver of pulsating aurora. Science 330, 81. Available from: https://doi.org/10.1126/science.1193186.

Nunn, D., 1974. A self-consistent theory of triggered VLF emissions. In: McCormac, B.M. (Ed.), *Magnetospheric Physics*, Astrophysics and Space Science Library (A Series of Books on the Recent Developments of Space Science and of General Geophysics and Astrophysics Published in Connection with the Journal Space Science Reviews), vol. 44. Springer, Dordrecht.

O'Brien, T.P., Looper, M.D., Blake, J.B., 2004. Quantification of relativistic electron microburst losses during the GEM storms. Geophys. Res. Lett. 31, L04802. Available from: https://doi.org/10.1029/2003GL018621.

O'Brien, T.P., Claudepierre, S.G., Blake, J.B., Fennell, J.F., Clemmons, J.H., Roeder, J.L., et al., 2014. An empirically observed pitch-angle diffusion eigenmode in the Earth's electron belt near $L^* = 5.0$. Geophys. Res. Lett. 41. Available from: https://doi.org/10.1002/2013GL058713.

O'Brien, T.P., Claudepierre, S.G., Guild, T.B., Fennell, J.F., Turner, D.L., Blake, J.B., et al., 2016. Inner zone and slot electron radial diffusion revisited. Geophys. Res. Lett. 43, 7301–7310. Available from: https://doi.org/10.1002/2016GL069749.

Oliven, M.N., Gurnett, D.A., 1968. Microburst phenomena: 3. An association between microbursts and VLF chorus. J. Geophys. Res. 73 (7), 2355–2362. Available from: https://doi.org/10.1029/JA073i007p02355.

Omura, Y.S., Summers, D., 2004. Computer simulations of relativistic whistler-mode wave–particle interactions. Phys. Plasmas 11, 3530. Available from: https://doi.org/10.1063/1.1757457.

Omura, Y., Summers, D., 2006. Dynamics of high-energy electrons interacting with whistler mode chorus emissions in the magnetosphere. J. Geophys. Res. 111, A09222. Available from: https://doi.org/10.1029/2006JA011600.

Omura, Y., Zhao, Q., 2012. Nonlinear pitch angle scattering of relativistic electrons by EMIC waves in the inner magnetosphere. J. Geophys. Res. 117, A08227. Available from: https://doi.org/10.1029/2012JA017943.

Omura, Y., Nunn, D., Summers, D., 2012. Generation processes of whistler mode chorus emissions: current status of nonlinear wave growth theory. In: Summers, D., Mann, I.R., Baker, D.N., Schulz, M. (Eds.), Dynamics of the Earth's Radiation Belts and Inner Magnetosphere. American Geophysical Union, Washington, D.C. Available from: https://doi.org/10.1029/2012GM001347.

Omura, Y., Zhao, Q., 2013. Relativistic electron microbursts due to nonlinear pitch angle scattering by EMIC triggered emissions. J. Geophys. Res. Space Phys. 118. Available from: https://doi.org/10.1002/jgra.50477.

Orlova, K., Shprits, Y., Spasojevic, M., 2016. New global loss model of energetic and relativistic electrons based on Van Allen Probes measurements. J. Geophys. Res. Space Phys. 121, 1308–1314. Available from: https://doi.org/10.1002/2015JA021878.

Osmane, A., Wilson III, L.B., Blum, L., Pulkkinen, T.I., 2016. On the connection between microbursts and nonlinear electronic structures in planetary radiation belts. The Astrophy. J. 816, 2.

Parrot, M., Santolik, O., Cornilleau-Wehrlin, N., Maksimovic, M., Harvey, C.C., 2003. Source location of chorus emissions observed by Cluster. Ann. Geophys. 21, 473–480.

Parrot, M., Santolík, O., Gurnett, D.A., Pickett, J.S., Cornilleau-Wehrlin, N., 2004. Characteristics of magnetospherically reflected chorus waves observed by CLUSTER. Ann. Geophys. 22, 2597–2606. Available from: https://doi.org/10.5194/angeo-22-2597-2004.

Paulikas, G.A., Blake, J.B., 1979. Effects of the solar wind on magnetospheric dynamics: energetic electrons at the synchronous orbit, Quantitative Modeling of Magnetospheric Processes, Geophysical Monograph Series, vol. 21. AGU, Washington, D.C, pp. 180–202.

Paulson, K.W., Smith, C.W., Lessard, M.R., Engebretson, M.J., Torbert, R.B., Kletzing, C.A., 2014. In situ observations of Pc1 pearl pulsations by the Van Allen Probes. Geophys. Res. Lett. 41, 1823–1829. Available from: https://doi.org/10.1002/2013GL059187.

Perraut, S., Roux, A., Robert, P., Gendrin, R., Sauvaud, J.-A., Bosqued, J.-M., et al., 1982. A systematic study of ULF waves above F_H^+ from GEOS 1 and 2 measurements and their relationships with proton ring distributions. J. Geophys. Res. 87, 6219–6236. Available from: https://doi.org/10.1029/JA087iA08p06219.

Pham, K.H., Tu, W., Xiang, Z., 2017. Quantifying the precipitation loss of radiation belt electrons during a rapid dropout event. J. Geophys. Res. Space Phys. 122. Available from: https://doi.org/10.1002/2017JA024519.

Pickett, J.S., et al., 2010. Cluster observations of EMIC triggered emissions in association with Pc1 waves near Earth's plasmapause. Geophys. Res. Lett. 37, L09104. Available from: https://doi.org/10.1029/2010GL042648.

Posch, J.L., Engebretson, M.J., Murphy, M.T., Denton, M.H., Lessard, M.R., Horne, R.B., 2010. Probing the relationship between electromagnetic ion cyclotron waves and plasmaspheric plumes near geosynchronous orbit. J. Geophys. Res. 115, A11205. Available from: https://doi.org/10.1029/2010JA015446.

Reeves, G.D., McAdams, K.L., Friedel, R.H.W., O'Brien, T.P., 2003. Acceleration and loss of relativistic electrons during geomagnetic storms. Geophys. Res. Lett. 30 (10), 1529. Available from: https://doi.org/10.1029/2002GL016513.

Reeves, G.D., Morley, S.K., Friedel, R.H.W., Henderson, M.G., Cayton, T.E., Cunningham, G., et al., 2011. On the relationship between relativistic electron flux and solar wind velocity: Paulikas and Blake revisited. J. Geophys. Res. 116, A02213. Available from: https://doi.org/10.1029/2010JA015735.

Reeves, G.D., Friedel, R.H.W., Larsen, B.A., Skoug, R.M., Funsten, H.O., Claudepierre, S.G., et al., 2016. Energy-dependent dynamics of keV to MeV electrons in the inner zone, outer zone, and slot regions. J. Geo. Res. Space Phy 121, 397–412. Available from: https://doi.org/10.1002/2015JA021569.

Remya, B., Tsurutani, B.T., Reddy, R.V., Lakhina, G.S., Hajra, R., 2015. Electromagnetic cyclotron waves in the dayside subsolar outer magnetosphere generated by enhanced solar wind pressure: EMIC wave coherency. J. Geophys. Res. Space Phys. 120, 7536–7551. Available from: https://doi.org/10.1002/2015JA021327.

Riley, P., Love, J.J., 2017. Extreme geomagnetic storms: probabilistic forecasts and their uncertainties. Space Weather 15, 53–64. Available from: https://doi.org/10.1002/2016SW001470.

Ripoll, J.-F., Santolík, O., Reeves, G.D., Kurth, W.S., Denton, M.H., Loridan, V., et al., 2017. Effects of whistler mode hiss waves in March 2013. J. Geophys. Res. Space Phys. 122. Available from: https://doi.org/10.1002/2017JA024139.

Rodger, C.J., Clilverd, M.A., McCormick, R.J., 2003. Significance of lightning-generated whistlers to inner radiation belt electron lifetimes. J. Geophys. Res. 108, 1462. Available from: https://doi.org/10.1029/2003JA009906. A12.

Rodger, C.J., Clilverd, M.A., Thomson, N.R., Gamble, R.J., Seppälä, A., Turunen, E., et al., 2007. Radiation belt electron precipitation into the atmosphere: recovery from a geomagnetic storm. J. Geophys. Res. 112, A11307. Available from: https://doi.org/10.1029/2007JA012383.

Rodger, C.J., Raita, T., Clilverd, M.A., Seppälä, A., Dietrich, S., Thomson, N.R., et al., 2008. Observations of relativistic electron precipitation from the radiation belts driven by EMIC waves. Geophys. Res. Lett. 35, L16106. Available from: https://doi.org/10.1029/2008GL034804.

Rodger, C.J., Clilverd, M.A., Kavanagh, A.J., Watt, C.E.J., Verronen, P.T., Raita, T., 2012. Contrasting the responses of three different ground-based instruments to energetic electron precipitation. Radio Sci. 47, RS2021. Available from: https://doi.org/10.1029/2011RS004971.

Rodger, C.J., Hendry, A.T., Clilverd, M.A., Kletzing, C.A., Brundell, J.B., Reeves, G.D., 2015. High-resolution in situ observations of electron precipitation- causing EMIC waves. Geophys. Res. Lett. 42, 9633–9641. Available from: https://doi.org/10.1002/2015GL066581.

Rodger, C.J., Cresswell-Moorcock, K., Clilverd, M.A., 2016. Nature's grand experiment: linkage between magnetospheric convection and the radiation belts. J. Geophys. Res. Space Phys. 121, 171–189. Available from: https://doi.org/10.1002/2015JA021537.

Rosenberg, T.J., Helliwell, R.A., Katsufrakis, J.P., 1971. Electron precipitation associated with discrete very-low-frequency emissions. J. Geophys. Res. 76 (34), 8445–8452. Available from: https://doi.org/10.1029/JA076i034p08445.

Rosenberg, T.J., Siren, J.C., Matthews, D.L., Marthinsen, K., Holtet, J.A., Egeland, A., et al., 1981. Conjugacy of electron microbursts and VLF chorus. J. Geophys. Res. 86 (A7), 5819–5832. Available from: https://doi.org/10.1029/JA086iA07p05819.

Rosenberg, T.J., Wei, R., Detrick, D.L., Inan, U.S., 1990. Observations and modeling of wave-induced microburst electron precipitation. J. Geophys. Res. 95 (A5), 6467–6475. Available from: https://doi.org/10.1029/JA095iA05p06467.

Roth, I., Temerin, M., Hudson, M.K., 1999. Resonant enhancement of relativistic electron fluxes during geomagnetically active periods. Ann. Geophys. Eur. Geosci. Union 17 (5), 631–638.

Russell, C.T., Luhmann, J.G., Jian, L.K., 2010. How unprecedented a solar minimum? Rev. Geophys. 48, RG2004. Available from: https://doi.org/10.1029/2009RG000316.

Saikin, A.A., Zhang, J.-C., Allen, R.C., Smith, C.W., Kistler, L.M., Spence, H.E., et al., 2015. The occurrence and wave properties of H^+-, He^+-, and O^+-band EMIC waves observed by the Van Allen Probes. J. Geophys. Res. Space Phys. 120. Available from: https://doi.org/10.1002/2015JA021358.

Saito, S., Miyoshi, Y., Seki, K., 2012. Relativistic electron microbursts associated with whistler chorus rising tone elements: GEMSIS-RBW simulations. J. Geophys. Res. 117, A10206. Available from: https://doi.org/10.1029/2012JA018020.

Sandanger, M., Søraas, F., Aarsnes, K., Oksavik, K., Evans, D.S., 2007. Loss of relativistic electrons: evidence for pitch angle scattering by electromagnetic ion cyclotron waves excited by unstable ring current protons. J. Geophys. Res. 112 (A12). Available from: https://doi.org/10.1029/2006JA012138.

Sandel, B.R., Goldstein, J., Gallagher, D.L., Spasojevic, M., 2003. Extreme ultraviolet imager observations of the structure and dynamics of the plasmasphere. Space Sci. Rev. 109 (1–4), 25–46.

Santolík, O., Chum, J., 2009. The Origin of Plasmaspheric Hiss. Sci. 729–730.

Santolík, O., Chum, J., Parrot, M., Gurnett, D.A., Pickett, J.S., Cornilleau-Wehrlin, N., 2006. Propagation of whistler mode chorus to low altitudes: Spacecraft observations of structured ELF hiss. J. Geophys. Res. 111, A10208. Available from: https://doi.org/10.1029/2005JA011462.

Santolík, O., Gurnett, D., 2003. Transverse dimensions of chorus in the source region. Geophys. Res. Lett. 30 (2), 1031. Available from: https://doi.org/10.1029/2002GL016178.

Santolík, O., Gurnett, D.A., Pickett, J.S., 2004a. Multipoint investigation of the source region of storm-time chorus. Ann. Geophys. 22, 2555–2563.

Santolík, O., Gurnett, D.A., Pickett, J.S., Parrot, M., Cornilleau-Wehrlin, N., 2004b. A microscopic and nanoscopic view of storm-time chorus on 31 March 2001. Geophys. Res. Lett. 31, L02801. Available from: https://doi.org/10.1029/2003GL018757.

Santolík, O., Gurnett, D.A., Pickett, J.S., Parrot, M., Cornilleau-Wehrlin, N., 2005. Central position of the source region of storm-time chorus. Planetary Space Sci. 53 (1), 299–305. ISSN: 0032-0633.

Santolík, O., Pickett, J.S., Gurnett, D.A., Menietti, J.D., Tsurutani, B.T., Verkhoglyadova, O., 2010. Survey of Poynting flux of whistler mode chorus in the outer zone. J. Geophys. Res. 115, A00F13. Available from: https://doi.org/10.1029/2009JA014925.

Santolík, O., Kletzing, C.A., Kurth, W.S., Hospodarsky, G.B., Bounds, S.R., 2014a. Fine structure of large-amplitude chorus wave packets. Geophys. Res. Lett. 41. Available from: https://doi.org/10.1002/2013GL058889.

Santolík, O., Macúšová, E., Kolmašová, I., Cornilleau-Wehrlin, N., de Conchy, Y., 2014b. Propagation of lower-band whistler-mode waves in the outer Van Allen belt: systematic analysis of 11 years of multi-component data from the Cluster spacecraft. Geophys. Res. Lett. 41, 2729–2737. Available from: https://doi.org/10.1002/2014GL059815.

Sazhin, S.S., Hayakawa, M., 1992. Magnetospheric chorus emissions—a review. Planet. Space. Sci. 40, 681–697. Available from: https://doi.org/10.1016/0032-0633(92)90009-D.

Schiller, Q., Tu, W., Ali, A.F., Li, X., Godinez, H.C., Turner, D.L., et al., 2017. Simultaneous event-specific estimates of transport, loss, and source rates for relativistic outer radiation belt electrons. J. Geophys. Res. Space Phys. 122, 3354–3373. Available from: https://doi.org/10.1002/2016JA023093.

Selesnick, R.S., Blake, J.B., Mewaldt, R.A., 2003. Atmospheric losses of radiation belt electrons. J. Geophys. Res. 108, 1468. Available from: https://doi.org/10.1029/2003JA010160. A12.

Shekhar, S., Millan, R., Smith, D., 2017. A statistical study of the spatial extent of relativistic electron precipitation with polar orbiting environmental satellites. J. Geophys. Res. Space Phys. 122, 11,274–11,284. Available from: https://doi.org/10.1002/2017JA024716.

Shi, R., Li, W., Ma, Q., Reeves, G.D., Kletzing, C.A., Kurth, W.S., et al., 2017. Systematic evaluation of low-frequency hiss and energetic electron injections. J. Geophys. Res. Space Phys. 122. Available from: https://doi.org/10.1002/2017JA024571.

Shklyar, D., Matsumoto, H., 2009. Oblique whistler-mode waves in the inhomogenous magnetospheric plasma: resonant interactions with energetic charged particles. Surv. Geophys. 30, 55. Available from: https://doi.org/10.1007/s10712-009-9061-7.

Shoji, M., Omura, Y., 2013. Triggering process of electromagnetic ion cyclotron rising tone emissions in the inner magnetosphere. J. Geophys. Res. Space Phys. 118, 5553–5561. Available from: https://doi.org/10.1002/jgra.50523.

Shprits, Y.Y., Thorne, R.M., Friedel, R., Reeves, G.D., Fennell, J., Baker, D.N., et al., 2006. Outward radial diffusion driven by losses at magnetopause. J. Geophys. Res. 111, A11214. Available from: https://doi.org/10.1029/2006JA011657.

Shprits, Y.Y., Meredith, N.P., Thorne, R.M., 2007. Parameterization of radiation belt electron loss timescales due to interactions with chorus waves. Geophys. Res. Lett. 34, L11110. Available from: https://doi.org/10.1029/2006GL029050.

Shprits, Y.Y., Subbotin, D., Ni, B., 2009. Evolution of electron fluxes in the outer radiation belt computed with the VERB code. J. Geophys. Res. 114, A11209. Available from: https://doi.org/10.1029/2008JA013784.

Shprits, Y.Y., Subbotin, D., Drozdov, A., Usanova, M.E., Kellerman, A., Orlova, K., et al., 2013. Unusual stable trapping of the ultra-relativistic electrons in the Van Allen radiation belts. Nat. Phys. Available from: https://doi.org/10.1038/nphys2760.

Shprits, Y.Y., Kellerman, A., Aseev, N., Drozdov, A.Y., Michaelis, I., 2017. Multi-MeV electron loss in the heart of the radiation belts. Geophys. Res. Lett. 44, 1204–1209. Available from: https://doi.org/10.1002/2016GL072258.

Sigsbee, K., et al., 2016. Van Allen Probes, THEMIS, GOES, and Cluster observations of EMIC waves, ULF pulsations, and an electron flux dropout. J. Geophys. Res. Space Phys. 121, 1990–2008. Available from: https://doi.org/10.1002/2014JA020877.

Silin, I., Mann, I.R., Sydora, R.D., Summers, D., Mace, R.L., 2011. Warm plasma effects on electromagnetic ion cyclotron wave MeV electron interactions in the magnetosphere. J. Geophys. Res. 116, A05215. Available from: https://doi.org/10.1029/2010JA016398.

Smith, D.M., Casavant, E.P., Comess, M.D., Liang, X., Bowers, G.S., Selesnick, R.S., et al., 2016. The causes of the hardest electron precipitation events seen with SAMPEX. J. Geophys. Res. Space Phys. 121. Available from: https://doi.org/10.1002/2016JA022346.

Sonwalkar, V.S., Inan, U.S., 1989. Lightning as an embryonic source of VLF hiss. J. Geophys. Res. 94 (A6), 6986–6994. Available from: https://doi.org/10.1029/JA094iA06p06986.

Spasojevic, M., Shprits, Y.Y., 2013. Chorus functional dependencies derived from CRRES data. Geophys. Res. Lett. 40, 3793–3797. Available from: https://doi.org/10.1002/grl.50755.

Spasojevic, M., Thomsen, M.F., Chi, P.J., Sandel, B.R., 2005. Afternoon subauroral proton precipitation resulting from ring current—plasmasphere interaction. In: Burch, J., Schulz, M., Spence, H. (Eds.), Inner Magnetosphere Interactions: New Perspectives From Imaging, Geophysical Monogaph. Series, vol. 159. AGU, Washington, D.C, pp. 85–99.

Spasojevic, M., Inan, U.S., 2010. Drivers of chorus in the outer dayside magnetosphere. J. Geophys. Res. 115, A00F09. Available from: https://doi.org/10.1029/2009JA014452.

Stix, T.H., 1992. Waves in Plasmas. American Institute of Physics, New York.

Storey, L.R.O., 1953, An investigation of whistling atmospherics. Philos. Trans. R. Soc. A. Available from: doi.org/10.1098/rsta.1953.0011.

Su, Z., et al., 2014. Intense duskside lower band chorus waves observed by Van Allen Probes: generation and potential acceleration effect on radiation belt electrons. J. Geophys. Res. Space Phys. 119, 4266–4273. Available from: https://doi.org/10.1002/2014JA019919.

Su, Z., Liu, N., Zheng, H., Wang, Y., Wang, S., 2018. Large-amplitude extremely low frequency hiss waves in plasmaspheric plumes. Geophys. Res. Lett. 45. Available from: https://doi.org/10.1002/2017GL076754.

Subbotin, D.A., Shprits, Y.Y., Ni, B., 2011. Long-term radiation belt simulation with the VERB 3-D code: comparison with CRRES observations. J. Geophys. Res. 116, A12210. Available from: https://doi.org/10.1029/2011JA017019.

Summers, D., Thorne, R.M., 2003. Relativistic electron pitch-angle scattering by electromagnetic ion cyclotron waves during geomagnetic storms. J. Geophys. Res. 108 (A4), 1143. Available from: https://doi.org/10.1029/2002JA009489.

Summers, D., Thorne, R.M., Xiao, F., 1998. Relativistic theory of wave-particle resonant diffusion with application to electron acceleration in the magnetosphere. J. Geophys. Res. 103 (A9), 20487–20500. Available from: https://doi.org/10.1029/98JA01740.

Summers, D., Ni, B., Meredith, N.P., Horne, R.B., Thorne, R.M., Moldwin, M.B., et al., 2008. Electron scattering by whistler-mode ELF hiss in plasmaspheric plumes. J. Geophys. Res. 113, A04219. Available from: https://doi.org/10.1029/2007JA012678.

Summers, D., Tang, R., Thorne, R.M., 2009. Limit on stably trapped particle fluxes in planetary magnetospheres. J. Geophys. Res. 114, A10210. Available from: https://doi.org/10.1029/2009JA014428.

Summers, D., Omura, Y., Nakamura, S., Kletzing, C.A., 2014. Fine structure of plasmaspheric hiss. J. Geophys. Res. Space Phys. 119, 9134–9149. Available from: https://doi.org/10.1002/2014JA020437.

Tao, X., Bortnik, J., Albert, J.M., Thorne, R.M., 2012. Comparison of bounce-averaged quasi-linear diffusion coefficients for parallel propagating whistler mode waves with test particle simulations. J. Geophys. Res. 117, A10205. Available from: https://doi.org/10.1029/2012JA017931.

Taubenschuss, U., Khotyaintsev, Y.V., Santolík, O., Vaivads, A., Cully, C.M., Le Contel, O., et al., 2014. Wave normal angles of whistler mode chorus rising and falling tones. J. Geophys. Res. Space Phys. 119, 9567–9578. Available from: https://doi.org/10.1002/2014JA020575.

Teng, S., Tao, X., Xie, Y., Zonca, F., Chen, L., Fang, W.B., et al., 2017. Analysis of the duration of rising tone chorus elements. Geophys. Res. Lett. 44. Available from: https://doi.org/10.1002/2017GL075824.

Thorne, R.M., Kennel, C.F., 1971. Relativistic electron precipitation during magnetic storm main phase. J. Geophys. Res. 76, 4446.

Thorne, R.M., Smith, E.J., Burton, R.K., Holzer, R.E., 1973. Plasmaspheric hiss. J. Geophys. Res. 78 (10), 1581–1596. Available from: https://doi.org/10.1029/JA078i010p01581.

Thorne, R., Church, S., Gorney, D., 1979. On the origin of plasmaspheric hiss: the importance of wave propagation and the plasmapause. J. Geophys. Res. 84 (A9), 5241–5247. Available from: https://doi.org/10.1029/JA084iA09p05241.

Thorne, R.M., Horne, R.B., Glauert, S., Meredith, N.P., Shprits, Y.Y., Summers, D., et al., 2005. The Influence of wave-particle interactions on relativistic electron dynamics during storms. In: Burch, J.,

Schulz, M., Spence, H. (Eds.), Inner Magnetosphere Interactions: New Perspectives from Imaging. American Geophysical Union, Washington, D.C. Available from: https://doi.org/10.1029/159GM07.

Thorne, R.M., Ni, B., Tao, X., Horne, R.B., Meredith, N.P., 2010. Scattering by chorus waves as the dominant cause of diffuse auroral precipitation. Nature 467, 943–946. Available from: https://doi.org/10.1038/nature09467.

Thorne, R.M., et al., 2013a. Evolution and slow decay of an unusual narrow ring of relativistic electrons near L ~ 3.2 following the September 2012 magnetic storm. Geophys. Res. Lett. 40. Available from: https://doi.org/10.1002/grl.50627.

Thorne, R.M., et al., 2013b. Rapid local acceleration of relativistic radiation-belt electrons by magnetospheric chorus. Nature 504, 411–414. Available from: https://doi.org/10.1038/nature12889.

Tsintsadze, N.L., Kaladze, T.D., Van Dam, J.W., Horton, W., Fu, X.R., Garner, T.W., 2010. Nonlinear dynamics of the electromagnetic ion cyclotron structures in the inner magnetosphere. J. Geophys. Res. 115, A07204. Available from: https://doi.org/10.1029/2009JA014555.

Tsurutani, B.T., Smith, E.J., 1974. Postmidnight chorus: a substorm phenomenon. J. Geophys. Res. 79 (1), 118–127. Available from: https://doi.org/10.1029/JA079i001p00118.

Tsurutani, B.T., Smith, E.J., 1977. Two types of magnetospheric ELF chorus and their substorm dependences. J. Geophys. Res. 82 (32), 5112–5128. Available from: https://doi.org/10.1029/JA082i032p05112.

Tsurutani, B.T., Lakhina, G.S., 1997. Some basic concepts of wave-particle interactions in collisionless plasmas. Rev. Geophys. 35 (4), 491–501.

Tsurutani, B.T., Verkhoglyadova, O.P., Lakhina, G.S., Yagitani, S., 2009. Properties of dayside outer zone chorus during HILDCAA events: loss of energetic electrons. J. Geophys. Res. 114, A03207. Available from: https://doi.org/10.1029/2008JA013353.

Tsurutani, B.T., Falkowski, B.J., Verkhoglyadova, O.P., Pickett, J.S., Santolík, O., Lakhina, G.S., 2012. Dayside ELF electromagnetic wave survey: a polar statistical study of chorus and hiss. J. Geophys. Res. 117, A00L12. Available from: https://doi.org/10.1029/2011JA017180.

Tsurutani, B.T., Lakhina, G.S., Verkhoglyadova, O.P., 2013. Energetic electron (>10 keV) microburst precipitation, ~5–15 s X-ray pulsations, chorus, and wave-particle interactions: A review. J. Geophys. Res. Space Physics. 118, 2296–2312. Available from: https://doi.org/10.1002/jgra.50264.

Tsurutani, B.T., Falkowski, B.J., Pickett, J.S., Santolik, O., Lakhina, G.S., 2015. Plasmaspheric hiss properties: observations from Polar. J. Geophys. Res. Space Phys. 120. Available from: https://doi.org/10.1002/2014JA020518.

Tu, W., Cunningham, G.S., Chen, Y., Henderson, M.G., Camporeale, E., Reeves, G.D., 2013. Modeling radiation belt electron dynamics during GEM challenge intervals with the DREAM3D diffusion model. J. Geophys. Res. Space Phys. 118, 6197–6211. Available from: https://doi.org/10.1002/jgra.50560.

Tu, W., Cunningham, G.S., Chen, Y., Morley, S.K., Reeves, G.D., Blake, J.B., et al., 2014. Event-specific chorus wave and electron seed population models in DREAM3D using the Van Allen Probes. Geophys. Res. Lett. 41, 1359–1366. Available from: https://doi.org/10.1002/2013GL058819.

Turner, D.L., Shprits, Y.Y., Hartinger, M., Angelopoulos, V., 2012. Explaining sudden losses of outer radiation belt electrons during geomagnetic storms. Nat. Phys. 8, 208–212. Available from: https://doi.org/10.1038/nphys2185.

Turner, D.L., et al., 2014. On the cause and extent of outer radiation belt losses during the 30 September 2012 dropout event. J. Geophys. Res. Space Phys. 119. Available from: https://doi.org/10.1002/2013JA019446.

Turner, D.L., O'Brien, T.P., Fennell, J.F., Claudepierre, S.G., Blake, J.B., Kilpua, E.K.J., et al., 2015. The effects of geomagnetic storms on electrons in Earth's radiation belts. Geophys. Res. Lett. 42, 9176–9184. Available from: https://doi.org/10.1002/2015GL064747.

Turner, D.L., Lee, J.H., Claudepierre, S.G., Fennell, J.F., Blake, J.B., Jaynes, A.N., et al., 2017. Examining coherency scales, substructure, and propagation of whistler mode chorus elements with

magnetospheric multiscale (MMS). J. Geophys. Res. Space Phys. 122. Available from: https://doi.org/10.1002/2017JA024474.

Ukhorskiy, A.Y., Shprits, Y.Y., Anderson, B.J., Takahashi, K., Thorne, R.M., 2010. Rapid scattering of radiation belt electrons by storm-time EMIC waves. Geophys. Res. Lett. 37, L09101. Available from: https://doi.org/10.1029/2010GL042906.

Ukhorskiy, A.Y., Sitnov, M.I., Millan, R.M., Kress, B.T., Fennell, J.F., Claudepierre, S.G., et al., 2015. Global storm time depletion of the outer electron belt. J. Geophys. Res. Space Phys. 120, 2543–2556. Available from: https://doi.org/10.1002/2014JA020645.

Usanova, M.E., Mann, I.R., Bortnik, J., Shao, L., Angelopoulos, V., 2012. THEMIS observations of electromagnetic ion cyclotron wave occurrence: dependence on AE, SYMH, and solar wind dynamic pressure. J. Geophys. Res. 117, A10218. Available from: https://doi.org/10.1029/2012JA018049.

Usanova, M.E., Darrouzet, F., Mann, I.R., Bortnik, J., 2013. Statistical analysis of EMIC waves in plasmaspheric plumes from Cluster observations. J. Geophys. Res. Space Phys. 118 (8), 4946–4951. Available from: https://doi.org/10.1002/jgra.50464.

Usanova, M.E., Malaspina, D.M., Jaynes, A.N., Bruder, R.J., Mann, I.R., Wygant, J.R., et al., 2016. Van Allen Probes observations of oxygen cyclotron harmonic waves in the inner magnetosphere. Geophys. Res. Lett. 43, 8827–8834. Available from: https://doi.org/10.1002/2016GL070233.

Vampola, A.L., Koons, H.C., McPherson, D.A., 1971. Outer-zone electron precipitation. J. Geophys. Res. 76 (31), 7609–7617. Available from: https://doi.org/10.1029/JA076i031p07609.

Van Allen, J.A., 1959. The geomagnetically trapped corpuscular radiation. J. Geophys. Res. 64 (11), 1683–1689. Available from: https://doi.org/10.1029/JZ064i011p01683.

Walt, M., 1994. Introduction to Geomagnetically Trapped Radiation. Cambridge University Press, Cambridge, UK.

Wang, D., et al., 2015. Statistical characteristics of EMIC waves: Van Allen Probe observations. J. Geophys. Res. Space Phys. 120, 4400–4408. Available from: https://doi.org/10.1002/2015JA021089.

Watt, C.E.J., Rae, I.J., Murphy, K.R., Anekallu, C., Bentley, S.N., Forsyth, C., 2017. The parameterization of wave-particle interactions in the outer radiation belt. J. Geophys. Res. Space Phys. 122. Available from: https://doi.org/10.1002/2017JA024339.

Wilson III, L.B., Cattell, C.A., Kellogg, P.J., Wygant, J.R., Goetz, K., Breneman, A., et al., 2011. The properties of large amplitude whistler mode waves in the magnetosphere: propagation and relationship with geomagnetic activity. Geophys. Res. Lett. 38, L17107. Available from: https://doi.org/10.1029/2011GL048671.

Winckler, J.R., et al., 1962. A study of the precipitation of energetic electrons from the geomagnetic field during magnetic storms. J. Geophys. Res. 67 (10), 3717–3736. Available from: https://doi.org/10.1029/JZ067i010p03717.

Woodger, L.A., Halford, A.J., Millan, R.M., McCarthy, M.P., Smith, D.M., Bowers, G.S., et al., 2015. A summary of the BARREL campaigns: technique for studying electron precipitation. J. Geophys. Res. Space Phys. 120, 4922–4935. Available from: https://doi.org/10.1002/2014JA020874.

Wrenn, G.L., Smith, R.J.K., 1996. The ESD threat to GEO satellites: empirical models for observed effects due to both surface and internal charging. In: Burke, W., Guyenne, T.-D (Eds.), Environment Modelling for Space-Based Applications, Symposium Proceedings (ESA SP-392). ESTEC Noordwijk, 18-20 September 1996, p. 121, 1996ESASP.392.121W.

Xiang, Z., Tu, W., Li, X., Ni, B., Morley, S.K., Baker, D.N., 2017. Understanding the mechanisms of radiation belt dropouts observed by Van Allen Probes. J. Geophys. Res. Space Phys. 122, 9858–9879. Available from: https://doi.org/10.1002/2017JA024487.

Xiao, F., Thorne, R.M., Summers, D., 1998. Instability of electromagnetic R-mode waves in a relativistic plasma. Phys. Plasmas 5, 2489–2497.

Xiao, F., et al. 2013, Wave-driven butterfly distribution of Van Allen belt relativistic electrons, *Nat. Commun.*, doi:10.1038/ncomms9590.

Xiao, F., et al., 2014. Chorus acceleration of radiation belt relativistic electrons during March 2013 geomagnetic storm. J. Geophys. Res. Space Phys. 119, 3325–3332. Available from: https://doi.org/10.1002/2014JA019822.

Xiao, F., et al., 2017. Generation of extremely low frequency chorus in Van Allen radiation belts. J. Geophys. Res. Space Phys. 122, 3201–3211. Available from: https://doi.org/10.1002/2016JA023561.

Yahnin, A.G., Yahnina, T.A., Semenova, N.V., Gvozdevsky, B.B., Pashin, A.B., 2016. Relativistic electron precipitation as seen by NOAA POES. J. Geophys. Res. Space Phys. 121. Available from: https://doi.org/10.1002/2016JA022765.

Yu, J., Li, L.Y., Cao, J.B., Yuan, Z.G., Reeves, G.D., Baker, D.N., et al., 2015. Multiple loss processes of relativistic electrons outside the heart of outer radiation belt during a storm sudden commencement. J. Geophys. Res. Space Phys. 120, 10,275–10,288. Available from: https://doi.org/10.1002/2015JA021460.

Yu, J., Li, L.Y., Cao, J.B., Chen, L., Wang, J., Yang, J., 2017a. Propagation characteristics of plasmaspheric hiss: Van Allen Probe observations and global empirical models. J. Geophys. Res. Space Phys. 122, 4156–4167. Available from: https://doi.org/10.1002/2016JA023372.

Yu, X., Yuan, Z., Huang, S., Wang, D., Li, H., Qiao, Z., et al., 2017b. EMIC waves covering wide L shells: MMS and Van Allen Probes observations. J. Geophys. Res. Space Phys. 122, 7387–7395. Available from: https://doi.org/10.1002/2017JA023982.

Yuan, C., Zong, Q., 2013. The double-belt outer radiation belt during CME- and CIR-driven geomagnetic storms. J. Geophys. Res. Space Phys. 118, 6291–6301. Available from: https://doi.org/10.1002/jgra.50564.

Yue, C., An, X., Bortnik, J., Ma, Q., Li, W., Thorne, R.M., et al., 2016. The relationship between the macroscopic state of electrons and the properties of chorus waves observed by the Van Allen Probes. Geophys. Res. Lett. 43, 7804–7812. Available from: https://doi.org/10.1002/2016GL070084.

Yue, C., Chen, L., Bortnik, J., Ma, Q., Thorne, R.M., Angelopoulos, V., et al., 2017. The characteristic response of whistler mode waves to interplanetary shocks. J. Geophys. Res. Space Phys. 122, 10,047–10,057. Available from: https://doi.org/10.1002/2017JA024574.

Zhang, X.-J., Mourenas, D., Artemyev, A.V., Angelopoulos, V., Thorne, R.M., 2017. Contemporaneous EMIC and whistler mode waves: observations and consequences for MeV electron loss. Geophys. Res. Lett. 44, 8113–8121. Available from: https://doi.org/10.1002/2017GL073886.

Zhao, H., Li, X., 2013. Modeling energetic electron penetration into the slot region and inner radiation belt. J. Geophys. Res. Space Phys. 118, 6936–6945. Available from: https://doi.org/10.1002/2013JA019240.

Zhima, Z., Chen, L., Xiong, Y., Cao, J., Fu, H., 2017. On the origin of ionospheric hiss: a conjugate observation. J. Geophys. Res. Space Phys. 122. Available from: https://doi.org/10.1002/2017JA024803.

Zhou, Q., Xiao, F., Yang, C., Liu, S., He, Y., Wygant, J.R., et al., 2016. Evolution of chorus emissions into plasmaspheric hiss observed by Van Allen Probes. J. Geophys. Res. Space Phy. 121, 4518–4529. Available from: https://doi.org/10.1002/2016JA022366.

Zhu, H., et al., 2015. Plasmatrough exohiss waves observed by Van Allen Probes: evidence for leakage from plasmasphere and resonant scattering of radiation belt electrons. Geophys. Res. Lett. 42, 1012–1019. Available from: https://doi.org/10.1002/2014GL062964.

Further reading

Albert, J.M., 2003. Evaluation of quasi-linear diffusion coefficients for EMIC waves in a multispecies plasma. J. Geophys. Res. 108 (A6), 1249. Available from: https://doi.org/10.1029/2002JA009792.

Albert, J.M., 2010. Diffusion by one wave and by many waves. J. Geophys. Res. 115, A00F05. Available from: https://doi.org/10.1029/2009JA014732.

Albert, J.M., 2012. Dependence of quasi-linear diffusion coefficients on wave parameters. J. Geophys. Res. 117, A09224. Available from: https://doi.org/10.1029/2012JA017718.

Albert, J.M., Shprits, Y.Y., 2008. Estimates of lifetimes against pitch angle diffusion. J. Atmos. Sol. Terr. Phys. 71 (16), 1647–1652. Available from: https://doi.org/10.1016/j.jastp.2008.07.004.

Albert, J.M., Starks, M.J., Horne, R.B., Meredith, N.P., Glauert, S.A., 2016. Quasi-linear simulations of inner radiation belt electron pitch angle and energy distributions. Geophys. Res. Lett. 43, 2381–2388. Available from: https://doi.org/10.1002/2016GL067938.

Allen, R.C., Zhang, J.-C., Kistler, L.M., Spence, H.E., Lin, R.-L., Klecker, B., et al., 2015. A statistical study of EMIC waves observed by Cluster: 1. Wave properties. J. Geophys. Res. Space Phys. 120. Available from: https://doi.org/10.1002/2015JA021333.

Burton, R.K., Holzer, R.E., 1974. The origin and propagation of chorus in the outer magnetosphere. J. Geophys. Res. 79 (7), 1014–1023. Available from: https://doi.org/10.1029/JA079i007p01014.

Chaston, C.C., et al., 2014. Observations of kinetic scale field line resonances. Geophys. Res. Lett. 41, 209–215. Available from: https://doi.org/10.1002/2013GL058507.

Clilverd, M.A., Thomson, N.R., Smith, A.J., 1993. The influence of ionospheric absorption on midlatitude whistler-mode signal occurrence from VLF transmitters. J. Atmos. Sol. Terr. Phys. 55, 1469–1477. Available from: https://doi.org/10.1016/0021-9169(93)90112-C.

Clilverd, M.A., Rodger, C.J., Gamble, R., Meredith, N.P., Parrot, M., Berthelier, J.-J., et al., 2008. Ground-based transmitter signals observed from space: ducted or nonducted? J. Geophys. Res. Space Phys. 113, A04211. Available from: https://doi.org/10.1029/2007JA012602.

Engebretson, M., Zesta, E., 2017. The future of ground magnetometer arrays in support of space weather monitoring and research. Space Weather 15. Available from: https://doi.org/10.1002/2017SW001718.

Gamble, R.J., Rodger, C.J., Clilverd, M.A., Sauvaud, J.-A., Thomson, N.R., Stewart, S.L., et al., 2008. Radiation belt electron precipitation by man-made VLF transmissions. J. Geophys. Res. Space Phys. 113, A10211. Available from: https://doi.org/10.1029/2008JA013369.

Glauert, S.A., Horne, R.B., 2005. Calculation of pitch angle and energy diffusion coefficients with the PADIE code. J. Geophys. Res. Space Phys. 110, A04206. Available from: https://doi.org/10.1029/2004JA010851.

Hayakawa, M., Yamanaka, Y., Parrot, M., Lefeuvre, F., 1984. The wave normals of magnetospheric chorus emissions observed on board GEOS 2. J. Geophys. Res. Space Phys. 89 (A5), 2811–2821. Available from: https://doi.org/10.1029/JA089iA05p02811.

He, Y., Xiao, F., Zhou, Q., Yang, C., Liu, S., Baker, D.N., et al., 2015. Van Allen Probes observation and modeling of chorus excitation and propagation during weak geomagnetic activities. J. Geophys. Res. Space Phys. 120, 6371–6385. Available from: https://doi.org/10.1002/2015JA021376.

Inan, U.S., Chiu, Y.T., Davison, G.T., 1992. Whistler-mode chorus and morningside aurorae. Geophys. Res. Lett. 19 (7), 653–656.

Johnstone, A.D., Walton, D.M., Liu, R., Hardy, D.A., 1993. Pitch angle diffusion of low-energy electrons by whistler mode waves. J. Geophys. Res. Space Phys. 98 (A4), 5959–5967. Available from: https://doi.org/10.1029/92JA02376.

Malaspina, D.M., Wygant, J.R., Ergun, R.E., Reeves, G.D., Skoug, R.M., Larsen, B.A., 2015. Electric field structures and waves at plasma boundaries in the inner magnetosphere. J. Geophys. Res. Space Phys. 120, 4246–4263. Available from: https://doi.org/10.1002/2015JA021137.

Mann, I.R., Ozeke, L.G., 2016. How quickly, how deeply, and how strongly can dynamical outer boundary conditions impact Van Allen radiation belt morphology? J. Geophys. Res. Space Phys. 121, 5553–5558. Available from: https://doi.org/10.1002/2016JA022647.

Němec, F., Santolík, O., Parrot, M., Rodger, C.J., 2010. Relationship between median intensities of electromagnetic emissions in the VLF range and lightning activity. J. Geophys. Res. Space Phys. 115, A08315. Available from: https://doi.org/10.1029/2010JA015296.

Němec, F., Santolík, O., Pickett, J.S., Parrot, M., Cornilleau-Wehrlin, N., 2013. Quasiperiodic emissions observed by the Cluster spacecraft and their association with ULF magnetic pulsations. J. Geophys. Res. Space Phys. 118, 4210–4220. Available from: https://doi.org/10.1002/jgra.50406.

Omura, Y., Nakamura, S., Kletzing, C.A., Summers, D., Hikishima, M., 2015. Nonlinear wave growth theory of coherent hiss emissions in the plasmasphere. J. Geophys. Res. Space Phys. 120, 7642–7657. Available from: https://doi.org/10.1002/2015JA021520.

Orlova, K., Spasojevic, M., Shprits, Y., 2014. Activity-dependent global model of electron loss inside the plasmasphere. Geophys. Res. Lett. 41, 3744–3751. Available from: https://doi.org/10.1002/2014GL060100.

Rodger, C.J., et al., 2010. Contrasting the efficiency of radiation belt losses caused by ducted and non-ducted whistler-mode waves from ground-based transmitters. J. Geophys. Res. Space Phys. 115, A12208. Available from: https://doi.org/10.1029/2010JA015880.

Russell, C.T., McPherron, R.L., Coleman, P.J., 1972. Fluctuating magnetic fields in the magnetosphere. I: ELF and VLF fluctuations. Space Sci. Rev. 12, 810. Available from: https://doi.org/10.1007/BF00173072.

SenGupta, A., Kletzing, C.A., Howk, R., Kurth, W.S., Matheny, M., 2017. Automated identification and shape analysis of chorus elements in the Van Allen radiation belts. J. Geophys. Res. Space Phys. 122. Available from: https://doi.org/10.1002/2017JA023949.

Shprits, Y.Y., Ni, B., 2009. Dependence of the quasi-linear scattering rates on the wave normal distribution of chorus waves. J. Geophys. Res. Space Phys. 114, A11205. Available from: https://doi.org/10.1029/2009JA014223.

Sivadas, N., Semeter, J., Nishimura, Y., Kero, A., 2017. Simultaneous measurements of substorm-related electron energization in the ionosphere and the plasma sheet. J. Geophys. Res. Space Phys., Space Phys. 122. Available from: https://doi.org/10.1002/2017JA023995.

Thorne, R.M., 2010. Radiation belt dynamics: the importance of wave particle interactions. Geophys. Res. Lett. 37, L22107. Available from: https://doi.org/10.1029/2010GL044990.

Titova, E.E., Kozelov, B.V., Demekhov, A.G., Manninen, J., Santolik, O., Kletzing, C.A., et al., 2015. Identification of the source of quasiperiodic VLF emissions using ground-based and Van Allen Probes satellite observations. Geophys. Res. Lett. 42, 6137–6145. Available from: https://doi.org/10.1002/2015GL064911.

Villalón, E., Burke, W.J., 1995. Pitch angle scattering of diffuse auroral electrons by whistler mode waves. J. Geophys. Res. Space Phys. 100 (A10), 19361–19369. Available from: https://doi.org/10.1029/95JA01161.

CHAPTER 4

Wave-particle interactions with coherent magnetosonic waves

Lunjin Chen[1] **and Jacob Bortnik**[2]
[1]Department of Physics, University of Texas at Dallas, Richardson, TX, United States
[2]Department of Atmospheric and Oceanic Sciences, University of California at Los Angeles, Los Angeles, CA, United States

Contents

4.1 Introduction

Energetic electrons in the radiation belts undergo three quasi-periodic motions: gyration, bounce, and drift. The motions have distinct periods and each of them corresponds to an adiabatic invariant, referred to as the first, second, and third invariants, respectively (Schulz and Lanzerotti, 1974). The presence of plasma waves can violate one or more of the three invariants through wave-particle resonant interactions, leading to irreversible changes in electron phase space density (Thorne, 2010). The process of wave-particle interaction plays an important role in the variability of the radiation belt electrons. Much more attention has been paid to gyroresonance (see review by Albert et al., 2013, and references therein) and drift resonance interaction than bounce resonance, which can be responsible for the violation of the second invariant. Violation of the third invariant through drift interaction with ultralow frequency waves (e.g., Dai et al., 2013) can lead to radial diffusion, while violation of the first invariant through gyoresonance interaction can lead to pitch angle and energy scattering (e.g., Albert et al., 2013).

The investigation of bounce resonance started about five decades ago when Parker (1961) and Roberts and Schulz (1968) suggested that electrons can be subject to scattering by means of bounce resonance with hydrodynamic waves whose frequency is equal to multiples of electron bounce frequency. More recently, the idea of bounce

The Dynamic Loss of Earth's Radiation Belts
DOI: https://doi.org/10.1016/B978-0-12-813371-2.00004-4

resonance has gained increasing attention, in an attempt to explain the observed global coherent variability of the radiation belt electron fluxes (Kanekal et al., 2001; Shprits et al., 2007). Specifically, during geomagnetic storms, the radiation belt electron fluxes may vanish rapidly at all *L*-shells, indicating that electrons at all equatorial pitch angles are effectively scattered by waves. This is also true for equatorially mirroring electrons with equatorial pitch angles $\alpha_{eq} = 90$ degrees. However, those electrons are generally immune to the gyroresonance interaction, which requires a finite electron velocity component along the field line to satisfy the gyroresonance condition unless the relativistic mass correction is sufficient to reduce the electron gyrofrequency to match the wave frequency. However, when the relativistic correction factor is relatively small, it appears that the electrons with $\alpha_{eq} = 90$ degrees cannot be scattered by the waves with gyroresonance.

Among a variety of plasma waves in the magnetosphere, equatorial noise (Russell et al., 1969) is a potential candidate for bounce resonance with energetic electrons. Equatorial noise, also known as fast magnetosonic waves or ion Bernstein mode waves (Gary et al., 2010), consist of electromagnetic emissions confined within a few degrees of the equator (e.g., Santolík et al., 2004; Hrbáčková et al., 2015), occurring above the proton gyrofrequency f_{cp} and below the lower hybrid resonance frequency f_{LHR}. Magnetosonic wave frequencies typically range from a few Hz to $\sim$100 Hz, and the low-frequency portion of the wave band is close to the bounce frequency of energetic electrons above hundreds of keV Shprits (2009). The dominant component of the magnetosonic wave's magnetic field is along the background magnetic field, leading to considerable magnetic mirror force along the electrons' bounce motion. The wave has average amplitudes of $\sim$50 pT (Ma et al., 2013), but much more intense magnetosonic waves, with amplitudes up to $\sim$1 nT, have also been reported (Tsurutani et al., 2014). Ring velocity distributions of the ring current energetic protons can excite these waves with nearly perpendicular wave normal angles (and hence near-perpendicular propagation directions) at multiples of the ion gyrofrequency (e.g., Perraut et al., 1982; Meredith et al., 2008; Chen et al., 2010, 2011). Discrete and harmonic spectral structures of magnetosonic waves have been reported during various satellite missions (e.g., Balikhin et al., 2015; Min et al., 2018).

These waves have also been shown to be effective for causing Landau resonance interactions, which are responsible for electron acceleration (Horne et al., 2007) and for inducing additional transit-time scattering (Bortnik and Thorne, 2010; Li et al., 2014). Both bounce resonant and Landau resonant scattering by magnetosonic waves have been proposed as mechanisms for the formation of butterfly distributions which require a depletion in equatorial and near-equatorially mirroring electron fluxes and/or enhancements of lower pitch angle electrons (Xiao et al., 2015; Li et al., 2016; Ma et al., 2016). Albert et al. (2016) demonstrated that a minimum phase space density at 90 degrees pitch angle for the inner radiation belt electrons can be reproduced by

the inclusion of cross pitch angle and energy diffusion without the presence of magnetosonic waves. In addition to diffusive interactions with magnetosonic waves, Maldonado et al. (2016) demonstrated that bounce resonance with coherent magnetosonic waves can lead to the observed rapid formation of butterfly distributions within seconds. In this chapter, we will cover recent developments in bounce resonance theory. We start with a test-particle model for studying the wave-particle interaction process, and then review Landau resonance, nonresonance, and bounce resonance with magnetosonic waves. Special attention is paid to the dynamics of equatorially mirroring electrons and coherent interactions over timescales longer than the bounce period. Finally, quasi-linear diffusion theory is reviewed, which accounts for the bounce resonance interactions with broadband waves.

4.2 Mathematical model

The mathematical model of nonrelativistic electron motion due to wave-particle gyroresonant interaction with oblique whistler waves was developed by Bell (1984), based on averaging the Lorentz force equations over the fast varying gyrophases and assuming a small wave magnetic amplitude as compared with the background magnetic field. A relativistic model was later generalized by Tao and Bortnik (2010) and Albert et al. (2013). Many various forms of the gyro-averaged equations have been used to study wave-particle gyroresonant interactions and Landau resonance (Bortnik and Thorne, 2010; Li et al., 2015; Hsieh and Omura, 2017). Such equations are also applicable for studying bounce resonance interactions (Chen et al., 2015; Maldonado et al., 2016; Li et al., 2015). Here we summarize the set of general gyro-averaged equations for electrons or ions, near an arbitrary resonance n, in a convention convenient for an arbitrary wave polarization and arbitrarily charged particles (electrons or ions):

$$\frac{dp_z}{dt} = -\frac{p_\perp^2}{2\gamma m B_0}\frac{dB_0}{dz} + g \times \Sigma_j \left[\frac{q e^{i\phi_{j,n}}}{2}\left(\tilde{E}_{z,j} J_n + i v_\perp \tilde{B}_{-,j} J_{n+1} e^{i\psi_j} - i v_\perp \tilde{B}_{+,j} J_{n-1} e^{-i\psi_j}\right) + c.c.\right] \tag{4.1}$$

$$\frac{dp_\perp}{dt} = +\frac{p_z p_\perp}{2\gamma m B_0}\frac{dB_0}{dz} + g \times \Sigma_j \left[\frac{q e^{i\phi_{j,n}}}{2}\left((\tilde{E}_{-,j} - i v_z \tilde{B}_{-,j}) J_{n+1} e^{i\psi_j} + (\tilde{E}_{+,j} + i v_z \tilde{B}_{+,j}) J_{n-1} e^{-i\psi_j}\right) + c.c.\right] \tag{4.2}$$

$$\frac{d\phi_{j,n}}{dt} = n\Omega - \omega_j + k_{z,j}v_z + \mathrm{k}_{\perp,j}\cdot\mathrm{v}_d + g$$
$$\times n\sum_j \left[\frac{qe^{i\phi_{j,n}}}{2}\left(\frac{\tilde{E}_{-,j} - iv_z\tilde{B}_{-,j}}{-ip_\perp}J_{n+1}e^{i\psi_j} + \frac{\tilde{E}_{+,j} + iv_z\tilde{B}_{+,j}}{ip_\perp}J_{n-1}e^{-i\psi_j} - \frac{\tilde{B}_{z,j}}{\gamma m}J_n\right) + c.c.\right] \tag{4.3}$$

$$\frac{dz}{dt} = v_z \tag{4.4}$$

Here a field-aligned coordinate system is used, where z is oriented with the background magnetic field line B_0 and x and y are two perpendicular directions. Our background field B is assumed to be dipolar and z is the arc-distance along the field line measured from the geomagnetic equator; m is the charged particle's mass and q is the charge (with sign); γ is the Lorentz factor, and $p_z(v_z)$ and $p_\perp(v_\perp)$ are the particle's parallel and perpendicular momentum (velocity) components, respectively. v_d denotes particle drift velocity, that is, the velocity of the guiding center across the field line. The first terms on the right-hand side of Eqs. (4.1) and (4.2) represent the adiabatic variation due to background magnetic field, while the terms associated with summation denote the changes due to multiple wave effects. The subscript $_j$ denotes jth wave component with a corresponding frequency ω_j, parallel and perpendicular wave numbers, $k_{z,j}$ and $k_{\perp,j}$. $\tilde{E}$ and $\tilde{B}$ denote wave electric and magnetic complex amplitude, respectively. The wave components in a rotating coordinate system are denoted as $\tilde{B}_{\pm,j} = \left(\tilde{B}_{x,j} \pm i\tilde{B}_{y,j}\right)/2, \tilde{E}_{\pm,j} = \left(\tilde{E}_{x,j} \pm i\tilde{E}_{y,j}\right)/2$. The ratios among wave electric and magnetic complex amplitudes can be determined by the dispersion relation corresponding to a given wave mode with ω_j and k_j and local plasma parameters such as B_0 and plasma density. The local dispersion relation is solved for a plane wave of the form $\sim e^{ik_j\cdot r - i\omega_j t}$. The *c.c.* terms represent the complex conjugate of the wave force terms. The complex quantities are useful for implementing a general dispersion relation, not limited to the cold plasma dispersion relation often used previously. To be more general, the factor containing wave number azimuthal angle ψ_j is also retained. ψ_j is defined as the azimuthal angle of the wave vector $k_{\perp,j}$ with respect to the x axis.

The terms $J_n(\beta_j)$ are Bessel functions of the first kind with argument $\beta_j = \frac{k_{\perp j}p_\perp}{qB_0}$. The charged-particle gyrofrequency is $\Omega = qB_0/(\gamma m)$. These Bessel terms arise owing to the wave-phase variation along the gyromotion path, which is also known as the finite Larmor radius effect. It should be pointed out that $|J_0(\beta)| < 1$ and $|J_{+1}(\beta)| < \beta/2$, and therefore the Larmor radius effect produces a smaller driving force than the typical guiding-center approximation, which ignores the size of the Larmor radius. By letting β approach 0, Eqs. (4.1) and (4.2) can be

reduced to the guiding center approximation (e.g., Li et al., 2015) and the conservation of magnetic moment $\mu = p^2/(2mB_0)$. The term $\phi_{j,n}$ in Eq. (4.3) is the difference between the jth wave phase as seen by the center of the particle gyromotion and the nth multiple of the particle gyrophase. This difference takes into account the Doppler shift due to both parallel motion along the field line ($k_{z,j}v_z$) and the perpendicular drift motion ($\boldsymbol{K}_{\perp,\boldsymbol{j}} \cdot \boldsymbol{v_d}$),

The scale factor $g(\lambda,\ t) = g_\lambda(\lambda)g_t(t)$, where λ is the magnetic latitude, $g_\lambda(\lambda) = \exp\left(-\frac{\lambda^2}{\lambda_w^2}\right)$ and

$$g_t(t) \begin{cases} = \exp\left(-\dfrac{(t-t_1)^2}{\Delta t_1^2}\right) \text{for } t < t_1 \\ = 1 \text{ for } t_1 \le t \le t_2 \\ = \exp\left(-\dfrac{(t-t_2)^2}{\Delta t_2^2}\right) \text{for } t > t_2 \end{cases}$$

g_λ is introduced to represent latitudinal variation of the wave power with a latitudinal width of λ_w, which is relevant for equatorially confined magnetosonic waves. The term g_t is introduced to account for temporal amplitude variation when particles drift through the wave fields over the localized azimuthal extent, that is, when particles enter or leave the field lines of interest. The waves turns on at $t = t_1$ and turns off at $t = t_2$. Launching test particles inside the wave field would induce unphysical scattering, in addition to the scattering due to the waves. Since we consider the interaction only along a fixed field line, it is implicitly assumed that the timescale of the wave existence $\tau = t_2 - t_1$ is much less than drift period τ_d and is typically less than a few bounce periods τ_b.

Often one deals with a single primary resonance at a time, that is, only one possible solution for an integer n that is close to, if not equal to, the gyroresonance condition $n\Omega - \omega + k_z v_z = 0$. For magnetosonic waves, $|-\omega + k_z v_z| << |\Omega_e|$. Therefore, it is safe to consider $n = 0$ only and as a result, electron trajectories are independent of the particle gyrophases, but the Larmor radius effect is still kept. For the case of $n = 0$, the angle $\phi_{j,n=0}$ is simply the jth wave phase seen at the center of the gyration. The set of test particle Eqs. (4.1–4.4) with $n = 0$ can be also used to investigate the bounce resonance interaction between electrons and magnetosonic waves for τ on the order of a few electron bounce periods. Here, we do not consider the effect of drift velocity v_d and consider only $n = 0$, for which $\phi_{j,n=0}$; thus, Eqs. (4.1–4.4) are independent of gyration phases. Therefore, a wave number azimuthal angle of $\psi_j = 0$ is adopted (meaning k is on the plane containing x and z axes). It is worth noting that gyroresonant interactions (i.e., $n \neq 0$) depend on the gyrophases, and the value of ψ_j does affect the initial value of $\phi_{j,n\neq 0}$. As a consequence, particles' response to the wave field depends on ψ_j.

Before discussing bounce resonance due to waves, we cover adiabatic bounce motion of electrons in the dipole magnetic field. The bounce motion is similar to motion in a potential well associated with background magnetic mirror, given by $\mu B_0(z)/\gamma^2$. The periods of relativistic bounce motion can be approximated by (e.g., Walt, 1994, Eq. 4.28)

$$\tau_b[\text{in s}] = 0.117 \times \frac{L\nu}{c}\left(1 - 0.4635\sin^{0.75}\alpha_{eq}\right),$$

where ν is the electron velocity, L is L-shell value, and c is the speed of light. Fig. 4.1 shows the electron bounce frequency, $f_b = 2\pi/\tau_b$, over a wide range of kinetic energies E in the magnetosphere; f_b ranges from a fraction of a Hz to 10 Hz and becomes greater for lower L values, higher equatorial pitch angles α_{eq}, and higher electron energies E. For ring current and radiation belt electrons ($E >$ keV, $3 < L < 9$), f_b is on the order of several Hz. Note that there exists a bounce frequency for exactly equatorially mirroring electrons ($\alpha_{eq} = 90$ degrees), although their trajectories remain on the equatorial plane. As noted in Chen et al. (2015), the behavior of equatorially mirroring electrons is analogous to particles at the bottom of the potential. Infinitesimal electric and magnetic perturbation, if any, will result in simple harmonic

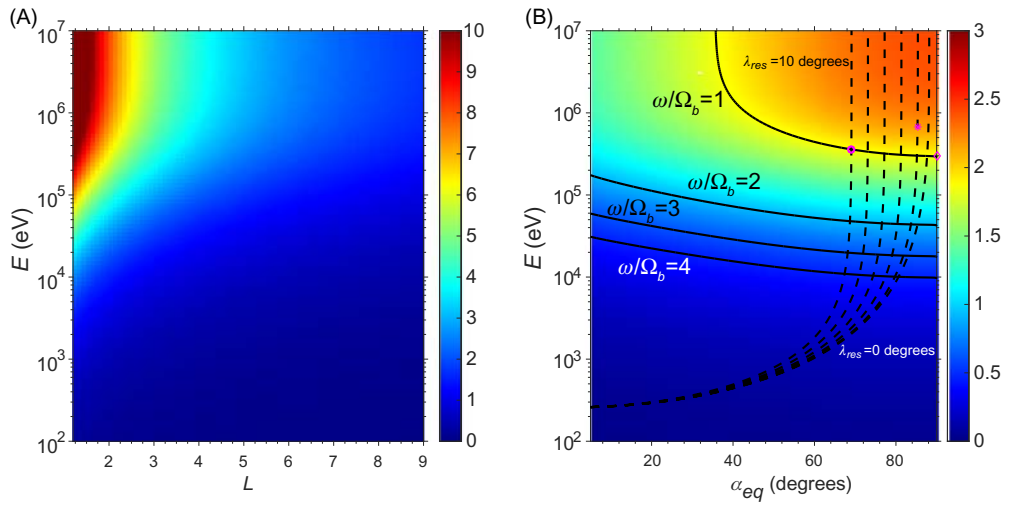

Figure 4.1 (A) Bounce frequency (in Hz) of equatorially mirroring electrons in the dipole magnetic field as a function of L-shell and kinetic energy. (B) Electron bounce frequency (in Hz) as a function of equatorial pitch angle α_{eq} and kinetic energy at $L = 6.6$. The solid lines denote the bounce resonant condition $\omega = m_b\Omega_b$, where Ω_b is the angular frequency of electron bounce motion and m is an integer, 1, 2, 3, and 4. ω is set to Ω_b of electron with $E = 300$ keV and $\alpha_{eq} = 90$ degrees. The dashed lines denote Landau resonance condition $\omega - k_z v_z = 0$ that takes place at magnetic latitude $\lambda_{res} = 0$, 2, 4, 6, 8, and 10 degrees.

oscillation for those equatorially mirroring electrons with angular bounce frequency Ω_b given by $\Omega_b^2 = \left(\mu/\gamma^2 m_e\right)\left(d^2B_0(z)/dz^2\right)|_{z=0}$. For a dipole field, bounce frequency for those electrons $\Omega_b^2 = \left(\mu/\gamma^2 m_e\right)\left(9B_0(z=0)/(LR_E)^2\right)$, where R_E is the Earth's radius.

4.3 Wave-particle interactions with magnetosonic waves—coherent

Here we deal with bounce resonant interactions between electrons and monochromatic magnetosonic wave fields. For a single wave, we simply remove the summation over j and suppress the subscript j in Eqs. (4.1–4.3). There are three possible nonadiabatic effects due to interaction with magnetosonic waves—Landau resonance, transit-time scattering, and bounce resonance. To illustrate these effects, we set $L = 6.6$, equatorial plasma density $50\ \mathrm{cm}^{-3}$, $t_1 = 0.4$ s, $\delta t_1 = 0.1$ s, $t_2 = \infty$ and wave frequency $\omega = 11$ rad/s with wave normal angle 89 degrees and latitudinal width $\lambda_w = 3$ degrees. In Fig. 4.1B, the dashed black lines denote the electrons that are in Landau resonance with the wave at various magnetic latitudes ($\omega - k_{\tilde{z}}v_{z0} = 0$), where v_{z0} is parallel velocity of the adiabatic motion, while solid black lines denotes the conditions when $\omega = m\Omega_b$, where m is an integer. Fig. 4.2A and C show trajectories of electrons with initial $E = 354.8$ keV and $\alpha_{eq} = 69.1$ degrees (marked by an asterisk in Fig. 4.1B) and random initial values of ϕ_0. They are in Landau resonance at $\lambda_{res} = 2$ degrees but out of bounce resonance. Those electrons experience nonadiabatic changes in α_{eq} and E when electrons go through the resonant latitude because of slow variation of ϕ during Landau resonance (Eq. 4.3). These changes depend on the value of ϕ_0, which is initially a random number. If the wave coherence does not hold longer than one bounce period ($\tau_c < \tau_b$), then the value of ϕ and thus the changes in momentum are randomized during the subsequent bounce. That is, the random change in momentum is independent of the random change during previous bounces, and therefore one should expect diffusive processes due to the Landau resonance.

Additional nonadiabatic changes occur because of equatorial confinement of magnetosonic wave power even when electrons are out of Landau resonance. This change is also known as transit-time scattering or nonresonance (Bortnik and Thorne, 2010). Fig. 4.2B and D shows the behavior of electrons with initial E and α_{eq} marked by the circle in Fig. 4.1B. There are net changes in α_{eq} and E whenever electrons pass through the equator. Such changes are induced when electrons rapidly pass through the edge of spatially confined wave power. Bortnik et al. (2015) analyzed the transit-time scattering in E and α_{eq} with the aid of two assumptions. First, the adiabatic variation of the particle velocity is ignored during equatorial crossing; that is, the zero-order parallel velocity v_{z0} remains a constant when electrons pass through the wave field (Bortnik et al., 2015, Eq. 21), Second, the mirror latitudes are larger than the

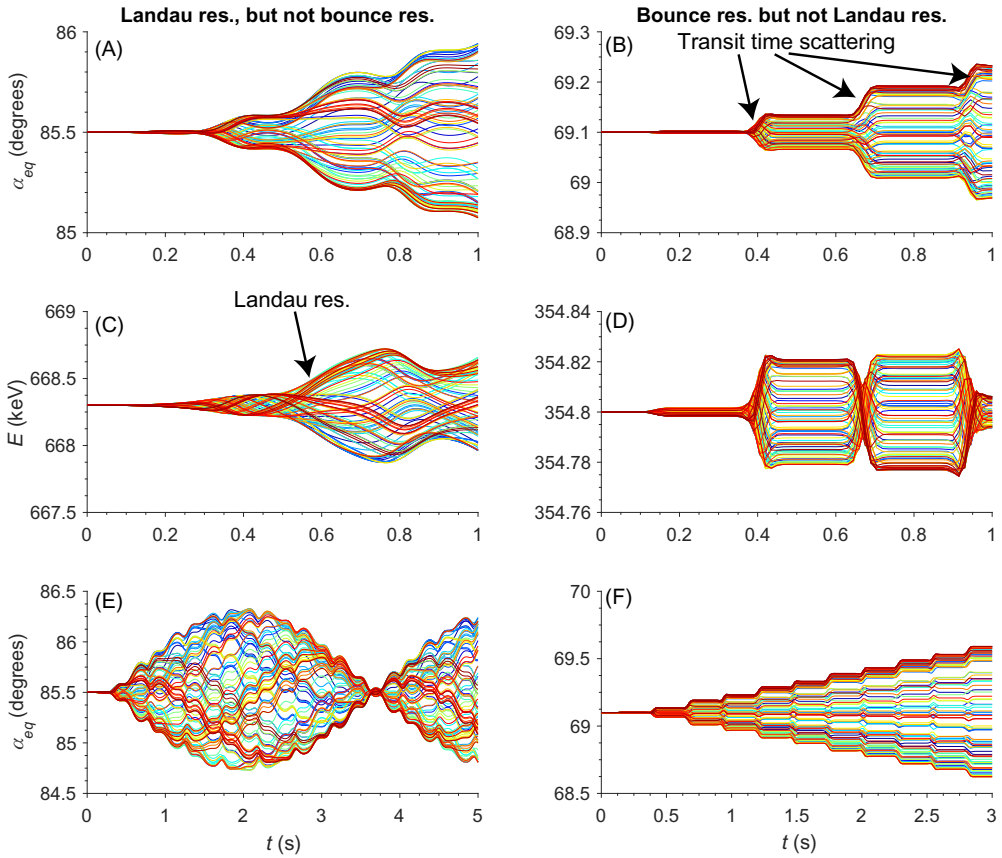

Figure 4.2 Simulated trajectories of electrons in a monochromatic magnetosonic wave field for electrons in Landau resonance with the magnetosonic wave but out of bounce resonance (*left column: A, C and E*) and for electrons out of Landau resonance but in bounce resonance (*left column: B, D and E*). Shown are electrons' equatorial pitch angle (*A, B*) and kinetic energy (*C, D*) as a function of time and pitch angle (*E, F*) for a longer time interval. The different colors represent different choices of random initial wave phases, ϕ_0.

extent of the wave. Linear changes of the electron equatorial pitch angle (or E) due to a monochromatic wave follows

$$\Delta\alpha_{eq} \text{ or } \Delta E \sim \tau_{tr} \sin\phi_{eq} \exp\left(- \frac{(\omega - k_z v_{z0})^2 \tau_{tr}^2}{4} \right), \tag{4.5}$$

where ϕ_{eq} is evaluated at the equator. The time to transit through the equatorial wave region, $\tau_{tr} = z_w / v_{z0}$, where z_w is the spatial width of wave power along the field line. The change is randomized for a random ϕ_{eq} and also depends on the change in wave phase during the passage $\Delta\phi \approx (-\omega + k_z v_{z0})\tau_{tr}$ through the exponential factor.

If $|\Delta\phi|$ is large, then the effect vanishes, and for small $|\Delta\phi|$ ($< \sim 2$), the net change occurs. The nonadiabatic effect favors the following two regimes: (1) for electrons near Landau resonance ($-\omega + k_z v_{z0} \approx 0$) and (2) for electrons transiting through the wave field rapidly (small τ_{tr}). For a large value of λ_w, only electrons near Landau resonance are scattered. For a sufficiently small λ_w, electrons, including those not in Landau resonance, can experience additional transit-time scattering. Such nonresonant scattering tends to broaden the regime of Landau resonant scattering. For $\tau_c < \tau_b$, one can expect transit time effects to induce diffusion in pitch angle and energy. The nonresonant effect has been also demonstrated in the interaction between subrelativistic/relativistic electrons and parallel electromagnetic ion cyclotron (EMIC) wave packets (Chen et al., 2016), where the narrow spatial edge of the wave packet reduces the effective electron minimum energy of pitch angle scattering owing to interaction with gyromotion. For nonresonant interactions with EMIC wave packets, the nonresonant scattering becomes effective for the small phase change $|(-\omega - k_z v_z - \Omega_e)\tau_{\rm tr}| < \sim 1$, where $\tau_{\rm tr}$ is the time for electrons to pass through the spatial edge of the EMIC wave packet. The nonresonance vanishes when the phase change is larger. Such nonresonant effects associated with spatially confined wave packets broaden the interaction condition for gyroresonance and Landau resonance.

In addition to Landau resonance and transit-time effects, electrons can be in bounce resonance with the magnetosonic waves. Fig. 4.2F illustrates what happens during the bounce resonance over a few bounce periods. The electrons experience net nonadiabatic changes in α_{eq} and E due to nonresonant interactions. The net change depends on ϕ_{eq}. When in bounce resonance with waves of coherence of a timescale τ_c longer than τ_b, ϕ_{eq} remains unchanged during subsequent equatorial passage, and as a result, the same amount of nonadiabatic change is gained. In other words, the change $\Delta\alpha_{eq}$ is proportional to τ_c when in bounce resonance (as seen in Fig. 4.2F). Over the timescale comparable to τ_c, although particles having different bounce phases have a different change in $\Delta\alpha_{eq}$, it is not a diffusive process. Fig. 4.3 shows the diffusive change and the advective change in α_{eq} and E as a function of time. During bounce resonance, the advective change remains small while the diffusive change increases linearly with time. If the wave phase is randomized after the coherent timescale τ_c, then the effect of bounce resonance is randomized. As a result it becomes a random walk motion with each step per τ_c with standard deviation proportional to τ_c^2. If the timescale of interest is $t \gg \tau_c$, then the process can be described as diffusive with averaged diffusion coefficients proportional to τ_c. That is, the longer the coherence timescale is for the bounce resonance, the stronger is the diffusion coefficient.

Now consider electrons that are in Landau resonance but not in bounce resonance (Fig. 4.2A, D, and E) for the case of $\tau_c \gg \tau_b$. Electrons experience a net change in momentum via Landau resonance during a bounce. Because the electrons are out of bounce resonance ($\omega \neq \Omega_b$), one would expect that they experience different

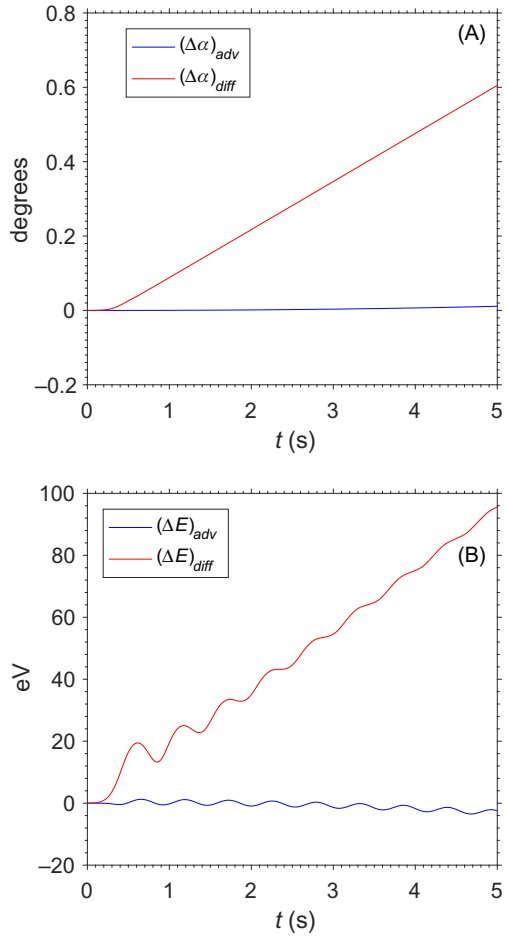

Figure 4.3 Advective (*blue*) and diffusive (*red*) transport in equatorial pitch angle (A) and kinetic (B) energy as a function of *t*, for electrons shown in the right column of Fig. 4.2.

momentum changes for each bounce, and then return to nearly initial values after a time period of $\sim\left[2\pi/(\Omega_b-\omega)\right]$ (as seen at $t\sim3.5$ seconds in Fig. 4.2E). Although the substantial oscillation in α_{eq} and E is induced by the Landau resonance, the change essentially vanishes at $t\sim3.5$ seconds after several bounce motions. Therefore, one would expect vanishing net effect for electrons not in bounce resonance when $\tau_c \gg \tau_b$.

4.4 Equatorially mirroring electrons

Equatorially and nearly equatorially mirroring electrons are generally immune to gyroresonance and Landau resonances that require a finite value of parallel velocity.

Those electrons also do not pass out of the wave-field region to experience transit-time scattering. Note that the mirror latitude of 3 degrees corresponds to $\alpha_{eq} = 83.6$ degrees. For these, $v_{z,0}$ is small and the adiabatic variation of $v_{z,0}$ cannot be ignored. As noted before, those electrons, much like staying on the bottom of the potential well, can exhibit bounce motion if perturbed by even infinitesimal electromagnetic fluctuations. One way to remove the electrons from the equatorial plane is through bounce resonance. Fig. 4.4 shows the responses of equatorially mirroring electrons (with initial conditions marked by the diamond in Fig. 4.1B) to the

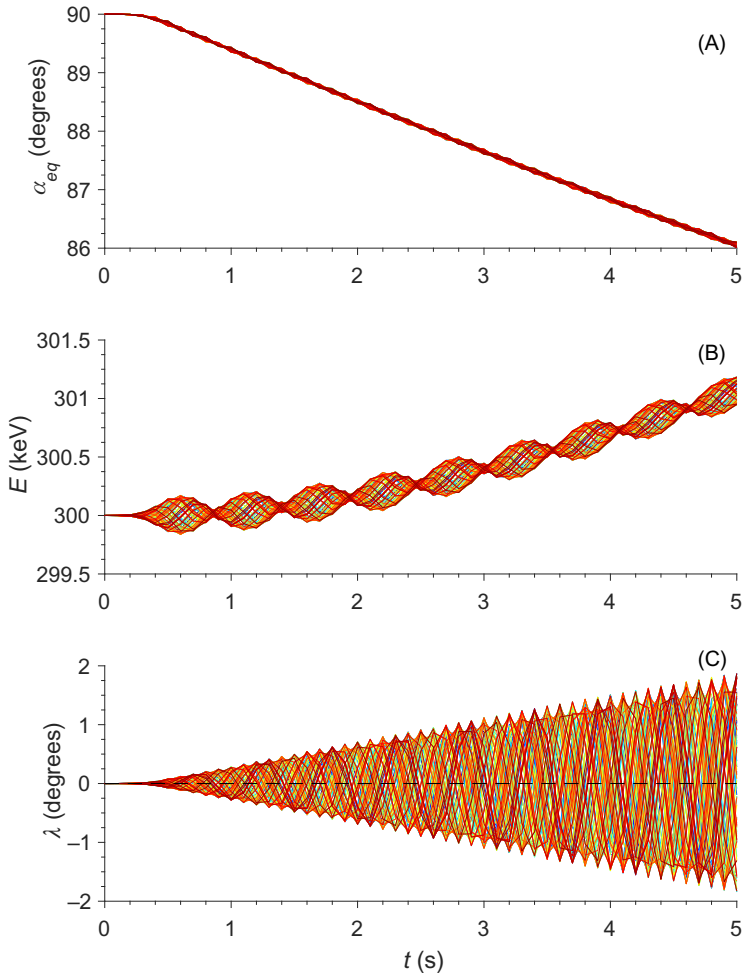

Figure 4.4 Illustration of equatorially mirroring electrons experiencing bounce resonance due to a monochromatic magnetosonic wave. Shown are electrons' equatorial pitch angles (A), kinetic energy (B), and magnetic latitudes as a function of time (C). Different colors represent different choices of random initial wave phases, ϕ_0.

monochromatic wave described above. The dependence of electron responses to the initial phases ϕ_0 vanishes and the advective changes in α_{eq} (or E) dominate the diffusive changes. Those initially equatorially mirroring electrons experience a negative drift in α_{eq} and a positive drift E during the bounce resonance. Correspondingly they are removed from the equatorial plane with increasing mirror latitude (Fig. 4.4C). As shown by Chen et al. (2015), the response is sensitive to the ratio of wave frequency to electron bounce frequency. Fig. 4.5 demonstrates the bounce resonance that occurs when $\omega \sim n\Omega_b$, where n is an integer. No significant bounce resonance for $n \geq 4$ takes place for the choice of wave setup. For such high harmonic bounce resonance to take place, higher critical values of wave amplitude and wave number are required.

Eqs. (4.1–4.4) in Section 4.2 contain various physical components: relativistic motion, adiabatic effect due to the background magnetic field, the finite Larmor radius effects, transient scattering associated with latitudinal distribution $g(\lambda)$, bounce resonance, and Landau resonance (the $\omega - k_z v_z$ term). To gain more physical insight, a simplified nonlinear oscillation model in z for initially equatorially mirroring electrons is proposed by Chen et al. (2015), where changes in μ and in γ are ignored. Doing so allows the governing equations for the interaction between equatorially mirroring electrons and a monochromatic magnetosonic wave to be expressed as a nonlinear oscillation model, written as a second-order differential equation in a nondimensional form as:

$$d^2\tilde{z}/d\tilde{t}^{\,2} + \tilde{z} + \tfrac{39}{18}\tilde{z}^3 = -\tilde{A}\sin\left(\tilde{\omega}\tilde{t} - \tilde{k}_z\tilde{z} + \phi_0\right)g(\lambda) \tag{4.6}$$

$$\tilde{z}|_{\tilde{t}=0} = d\tilde{z}/d\tilde{t}|_{\tilde{t}=0} = 0 \tag{4.7}$$

where nondimensional quantities $\tilde{z} = z/(LR_E)$, $\tilde{t} = \Omega_b t$, $\tilde{k}_z = k_z LR_E$, $\tilde{\omega} = \omega/\Omega_b$, and

$$\tilde{A} = \frac{\tilde{B}_z k_z LR_E}{9B_0}\frac{2J_1(\beta)}{\beta} + \frac{\tilde{E}_z J_0(\beta) e\gamma LR_E}{9\mu B_0}. \tag{4.8}$$

Ω_b is the bounce frequency for electrons at $\alpha_{eq} = 90$ degrees. The normalized wave amplitude $\tilde{A}$ contains the contribution from B_z^w and E_z^w. The $\tilde{A}$ is equivalent to Eq. (4.11) of Roberts and Schulz (1968) in the limit of $\beta = 0$ ($J_0(\beta) = 1$ and $2J_1(\beta)/\beta = 1$) when the finite Larmor radius effect disappears. The $\tilde{B}_z$ term, representing wave oscillatory magnetic mirror force, is generally much greater than the $\tilde{E}_z$ term corresponding to the wave parallel electric force. The linear term and the nonlinear cubic term on the left-hand side of Eq. 4.6 arise from adiabatic changes, the first two terms on the left-hand side are responsible for harmonic bounce oscillations, and the nonlinear sine term on the right-hand side is driven by the wave with initial wave phase at the equator ϕ_0 and normalized wave amplitude at the equator.

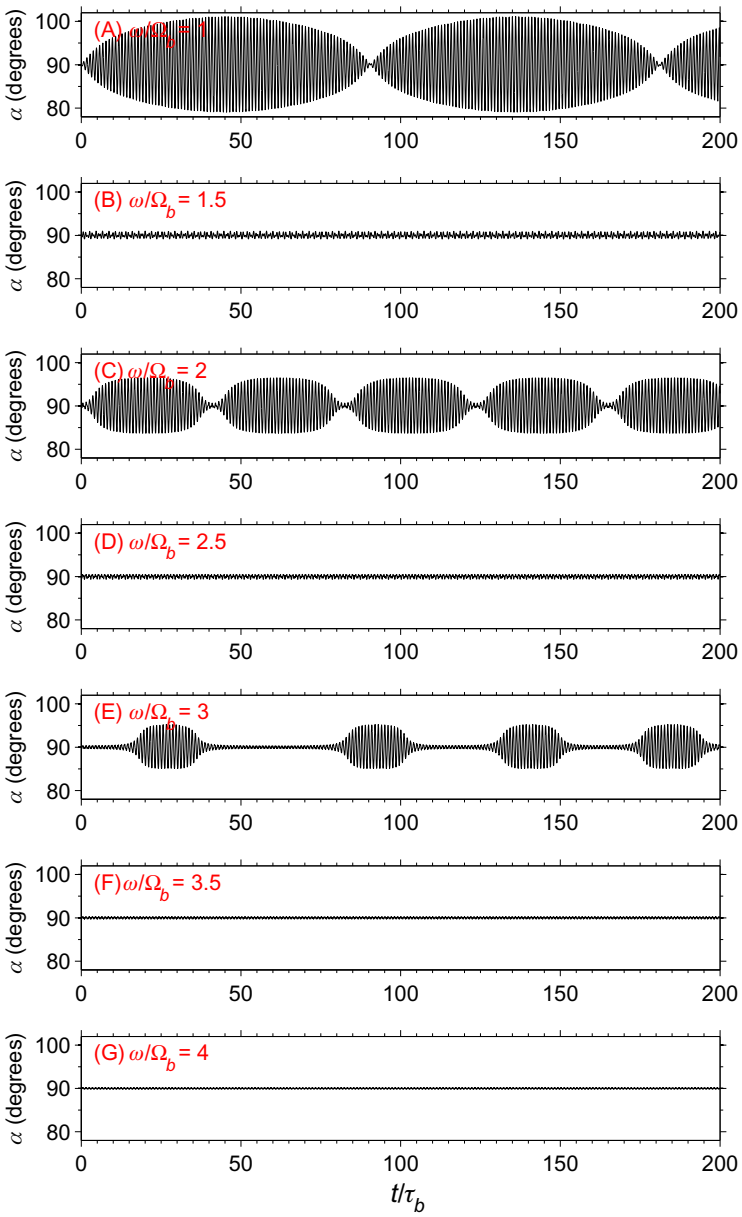

Figure 4.5 Local pitch angle as a function of time, normalized by bounce period τ_b, for electrons launched at the equator at $L = 6.6$ with an initial pitch angle of 90 degrees and energy of 300 keV, driven by a monotonic magnetosonic wave with varying wave frequency: (A) 1.0 f_b, (B) 1.5 f_b, (C) 2.0 f_b, (D) 2.5 f_b, (E) 3.0 f_b, (F) 3.5 f_b, and(G) 4.0 f_b. *Adapted from Fig. 4.2 of Chen, L., Maldonado, A., Bortnik, J., Thorne, R.M., Li, J., Dai, L., et al., 2015. Nonlinear bounce resonances between magnetosonic waves and equatorially mirroring electrons. J. Geophys. Res.*

For $\left|\tilde{k}_z\tilde{z}\right| << 1$, Eq. (4.6) can be linearized as

$$d^2\tilde{z}/d\tilde{t}^2 + \tilde{z}\left(1 - \tilde{A}\,\tilde{k}_z\cos\left(\tilde{\omega}\tilde{t} + \phi_0\right)\right) = -\tilde{A}\sin\left(\tilde{\omega}\tilde{t} + \phi_0\right). \tag{4.9}$$

This linear equation is a driven Mathieu equation, permitting unstable solutions (i.e., bounce resonance solution) when $\tilde{\omega}$ is $2/q$ (where q is an integer). When bounce resonance occurs, the $\tilde{z}$ amplitude increases and then nonlinear terms cannot be ignored and, therefore, this linear equation is not applicable.

For such coherent bounce interaction, equatorially mirroring electrons can experience a net drift toward smaller equatorial pitch angles, leading to a reduction of phase space density at $\alpha_{eq} = 90$ degrees. Maldonado et al. (2016) report a modulation of electron butterfly distribution (with a minimum of phase space density at $\alpha_{eq} = 90$ degrees) by varying the magnetosonic wave amplitude of a discrete spectrum. When the wave amplitude rises rapidly, an electron butterfly distribution forms. When the wave amplitude decays, the electron butterfly distribution vanishes. Such correlations demonstrate the response of electrons to the discrete magnetosonic spectrum. The direct test-particle simulation in the modeled single discrete frequency with a small frequency spread not only reproduces a rapid formation of butterfly distribution over the observed time scale of 10 seconds but also accounts for the energy range of the butterfly pitch angle distribution.

4.5 Bounce resonance diffusion theory

The response of electrons due to bounce resonance can be described through quasi-linear diffusion with the assumption of weak turbulence with a small amplitude, random phase, and broadband spectrum. One can model the electron responses due to the weak turbulence by first solving the system of ordinary differential equations (Eqs. 4.1–4.4) with multiple waves. Unlike the coherent interactions discussed in Section 4.3, which involves single monochromatic waves, interactions with weak turbulence are realized by implementing multiple waves with a set of randomly selected initial wave phases and for electrons that were initially distributed at different bounce phases and then performing an ensemble average of the electron responses over the wave phases and bounce phases. Li et al. (2015) demonstrated that for broadband magnetosonic waves, the electron response can be treated as a diffusive process. Fig. 4.6A shows examples of electron trajectories with the same initial energy and equatorial pitch angle for different sets of initial wave phases. The equatorial pitch angle experiences random changes whenever there is bounce resonance with a frequency component of the magnetosonic wave broadband spectrum. The deviation of electron equatorial pitch angles from simulated responses over an ensemble of initial wave phases increases linearly over time (Fig. 4.6B), corresponding to a diffusion

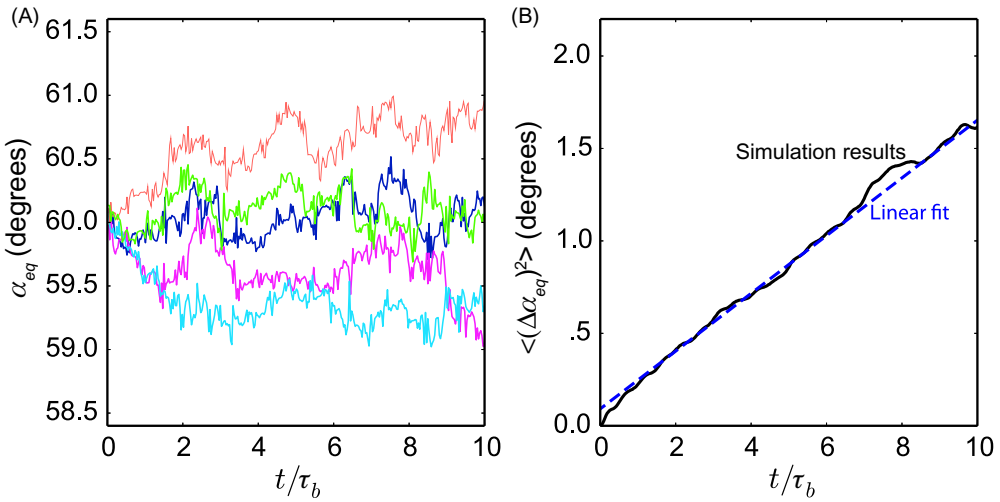

Figure 4.6 (A) Changes in α_{eq} of five randomly selected electrons with initial $\alpha_{eq} = 60$ degrees, represented by different colors. (B) The evolution of corresponding $<(\Delta\alpha_{eq})^2>$ with time. The blue line denotes the corresponding linear fitting. *Adapted from Fig. 4.1 of Li, X., Tao, X., Lu, Q., Dai, L., 2015. Bounce resonance diffusion coefficients for spatially confined waves. Geophys. Res. Lett. 42 (22), 9591–9599, doi:10.1002/2015GL066324.*

process in equatorial pitch angle for the electron population. The slope of the deviation with respect to time, representing diffusion coefficient, can be obtained from numerical test-particle simulation.

Theoretical diffusion coefficients have been derived under different assumptions. Roberts (1968) and Schulz and Lanzerotti (1974) assume a guiding-center approximation for electron motion (i.e., for small β and conservation of magnetic moment) and a flat latitudinal distribution of magnetohydrodynamic wave power distribution. The diffusion coefficient formula is applied to magnetosonic waves (Shprits, 2016) following the same method. Li et al. (2015) extended the formula to a wave power distribution that exists and is flat only over a specified magnetic latitude range, taking into account the equatorial confinement of magnetosonic wave power. Maldonado and Chen (2018) further extend the bounce resonance diffusion formula to a more realistic magnetosonic wave model, with the finite Larmor radius effect, a more realistic Gaussian latitudinal distribution instead of the square distribution used in Li et al. (2015), and potential violation of magnetic moment μ are included. The finite Larmor radius effect takes place when the wavelength of those magnetosonic waves is comparable to, and shorter than, the gyroradius of energetic electrons (i.e., the ratio of electron gyroradius to perpendicular wavelength, $\rho_g k_\perp > \sim 1$). This is especially true for the interaction between nearly perpendicularly propagating magnetosonic waves and energetic radiation belt electrons. For $\rho_g k_\perp > \sim 1$, the first adiabatic invariant can

be violated, because electrons experience significant spatial variation of wave fields over one gyration. One should use the set of Eqs. 4.1–4.4 for the electron responses, instead of a simplified guiding center approximation. Furthermore, the observed latitudinal wave power distribution shows a narrow peak near the equator instead of being flat (Němec et al., 2005). These factors are valuable for quantifying the effects of magnetosonic waves on electron scattering. Therefore, we review a general bounce resonant diffusion theory with the above three factors included; a detailed derivation can be found in Li et al. (2015) and Maldonado and Chen (2018).

Three assumptions are made to obtain the diffusion coefficients. (1) Assume unperturbed adiabatic motion, that is, $z = z_m \sin(\Omega_b t + \theta_0)$ and thus $v_z = z_m \Omega_b \cos(\Omega_b t + \theta_0)$, where θ_0 denotes the initial bounce phase of the electron motion. This assumption is different from the assumption made in Bortnik and Thorne (2010) for evaluating transit-time scattering, who assume no adiabatic variation when passing through the wave field. Since the waves are confined near the equator, we assume that $v_\perp$ and $p_\perp$ of the wave terms in Eqs. (4.1) and (4.2) remain unchanged as the equatorial values of the zero-order adiabatic motion. (2) Assume linear perturbation is much less than the zero-order motion, that is, wave field is so weak that no significant change in α_{eq} and E occurs after a bounce cycle. This assumption may not be valid for equatorially mirroring electrons, whose zero-order adiabatic motion is not well defined. (3) Consider multiple wave components with a Gaussian latitudinal distribution of wave power and adopt Eqs. (4.1) and (4.2) with finite Larmor radius effects included.

With those assumptions, one can integrate Eqs. (4.1) and (4.2) along the unperturbed bounce motion, to obtain α_{eq} and E due to multiple magnetosonic waves over time τ and obtain the change of α_{eq} and E as a function of time τ,

$$\Delta E = \tau \sum_{\text{integer}\ \ x_j > 0} \exp\left(i\phi'_{j0}\right) \tilde{B}_{z,j} X_E + c.c. \tag{4.10}$$

and

$$\Delta \alpha_{eq} = \tau \sum_{\text{integer}\ \ x_j > 0} \exp\left(i\phi'_{j0}\right) \tilde{B}_{z,j} X_\alpha + c.c. \tag{4.11}$$

where $\phi'_{j0} = \phi_{j,0} + x_j \theta_0$, $x_j = \omega_j / \Omega_b$, Ω_b is electron bounce frequency, and the two complex numbers are given by

$$X_E = \sum_{k_2} I_{k2} e^{-c_0} \left[\frac{1}{4} \sum_{l_1 = x_j \pm 2k_2} -iq \frac{\tilde{E}_{y,j}}{\tilde{B}_{z,j}} v_{\perp 0} J_1 J_{l_1} + \frac{1}{8} \sum_{l_1 = x_j \pm 2k_2 \pm 1} z_m \Omega_b q \frac{\tilde{E}_{z,j}}{\tilde{B}_{z,j}} J_0 J_{l_1} \right]$$

and

$$X_\alpha = \sum_{k_2} I_{k_2} e^{-c_0} \left[\frac{1}{4} \sum_{l_1 = x_j \pm 2k_2} iq \frac{\tilde{E}_{y,j}}{\tilde{B}_{z,j}} J_1 J_{l_1} \frac{-p_{z0}}{p_0^2} \right. \tag{4.12}$$

$$\left. + \frac{1}{8} \sum_{l_1 = x_j \pm 2k_2 \pm 1} - \frac{z_m \Omega_b q v_{\perp 0}}{v^2 p_{z0}} \frac{\tilde{E}_{z,j}}{\tilde{B}_{z,j}} J_0 J_{l_1} + \frac{z_m \Omega_b iq}{p_{z0}} \frac{\tilde{B}_{x,j}}{\tilde{B}_{z,j}} J_1 J_{l_1} \right] \tag{4.13}$$

The argument of J_0 and J_1, $k_\perp p_{\perp,0}/qB_0$, measures the ratio of gyromotion radius and perpendicular wavelength. Similarly, the argument for J_{l_1}, $k_{z,j} z_m$, measures the ratio of bounce amplitude and parallel wavelength. The argument for I_{k_2} is $c_0 = \lambda_m^2/2\lambda_w^2$, measuring the ratio of bounce amplitude and the field-aligned width of equatorially confined waves. λ_m is the electron mirror magnetic latitude.

A few points are noted from Eqs. (4.10) and (4.11). First, the wave amplitudes $\tilde{B}$ and $\tilde{E}$ represent their equatorial values and can be normalized by any component of the wave electromagnetic fields, $\tilde{B}_z$, in these two equations. The ratios among the wave field components are obtained by local dispersion relation at the equator. Second, ΔE and $\Delta\alpha_{eq}$ are proportional to τ when electrons are subject to bounce resonance, which requires integer values of x_j ($= \omega_j/\Omega_b$). In other words, only waves in bounce resonance lead to ΔE and $\Delta\alpha_{eq}$, while other waves produce no net change. (3) ΔE and $\Delta\alpha_{eq}$ are oscillatory because of the term $\exp(i\phi'_{j0})$, where ϕ'_{j0} is a linear combination of initial wave phase (ϕ_{j0}) and initial bounce phase (θ_0). The ensemble average of $<(\Delta\alpha_{eq})>$ over the two phases vanishes while the ensemble average of $<(\Delta\alpha_{eq})^2>$ is proportional to the wave power.

Diffusion coefficients due to bounce resonance with broadband magnetosonic waves can be obtained through

$$D_{\alpha\alpha} = \left\langle \frac{(\Delta\alpha_{eq})(\Delta\alpha_{eq})}{2\tau} \right\rangle = 2 \sum_{\text{integer } x_j > 0} P_{Bz}(f = x_j f_b) \Re\left(X_\alpha X_\alpha^*\right) \tag{4.14}$$

$$D_{\alpha E} = \left\langle \frac{(\Delta\alpha_{eq})(\Delta E)}{2\tau} \right\rangle = 2 \sum_{\text{integer } x_j > 0} P_{Bz}(f = x_j f_b) \Re\left(X_\alpha X_E^*\right) \tag{4.15}$$

$$D_{EE} = \left\langle \frac{(\Delta E)(\Delta E)}{2\tau} \right\rangle = 2 \sum_{\text{integer } x_j > 0} P_{Bz}(f = x_j f_b) \Re\left(X_E X_E^*\right) \tag{4.16}$$

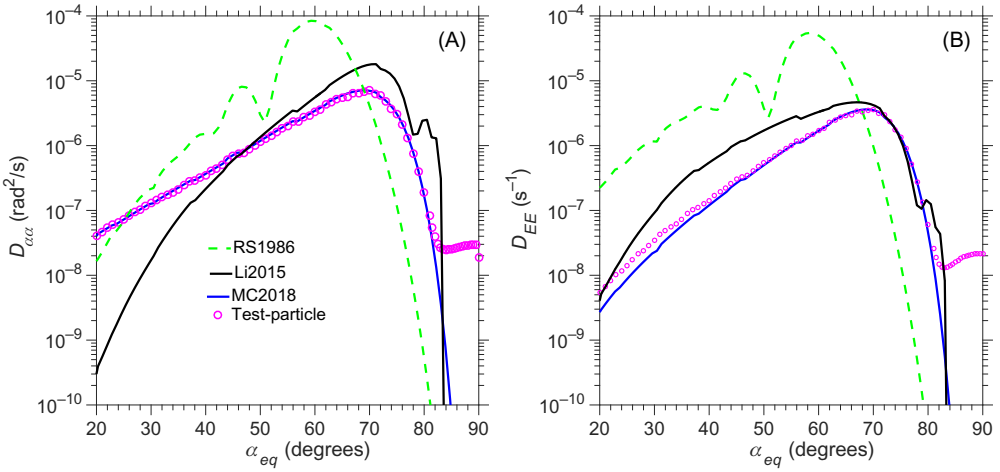

Figure 4.7 Comparison of (A) pitch angle and (B) energy diffusion coefficients among Roberts and Schulz (1968) (*green dashed line*), Li et al. (2015) (*black solid line*), and Maldonado and Chen (2018) (*blue solid line*). Also shown are the diffusion coefficients derived from the numerical test-particle simulation (*magenta circles*). *Adapted From Fig. 4.1 of Maldonado, A.A., Chen, L., 2018. On the diffusion rates of electron bounce resonant scattering by magnetosonic waves. Geophys. Res. Lett., 45, 3328–3337. doi:10.1002/2017GL076560.*

where the brackets represent the ensemble average, P_{Bz} represents the power spectrum density of the wave magnetic parallel component, in units of T^2/Hz, as a function of wave frequency f, the subscript * denotes complex conjugate, and $\mathfrak{R}$ represents real part.

Fig. 4.7 shows a comparison among the three formulas as a function of electron pitch angles developed by Roberts and Schulz (1968), Li et al. (2015), and Maldonado and Chen (2018) for electrons at $L = 4.5$ with kinetic energy $E = 1$ MeV. The three curves in Fig. 4.7 have the same plasma-frequency-to-electron-gyrofrequency ratio $f_{pe}/f_{ce} = 3$, and the same magnetosonic wave spectral parameters. The magnetosonic wave parameters are adopted from Horne et al. (2007). The waves assume a root-mean-squared amplitude 218 pT, a single wave normal angle of 89 degrees, and a Gaussian frequency spectrum of $B(\omega) \propto exp(-(\omega-\omega_m)^2/\delta\omega^2)$, where $\omega_m = 3.49\times10^{-3}\Omega_e$, and $\delta\omega = 8.86\times10^{-4}\Omega_e$. The frequency range of the spectral density distribution spans from the lower cutoff $\omega_{LC} = 2\times10^{-3}\Omega_e$ to the upper cutoff $\omega_{UC} = 5\times10^{-3}\Omega_e$. The RS1968 and Li2015 curves adopt guiding center approximation (with conservation of magnetic moment and zero Larmor radius) but assume different latitudinal distributions of wave power, being flat throughout the field line for the former while being flat over only a limited $\lambda \leq 3$ degrees for the latter. One can see that compared with RS1968, the Li2015 curve expects less scattering over low $\alpha_{eq} < 67$ degrees owing to the lack of wave power at high latitude ($\lambda > 3$ degrees) and higher scattering for 67 degrees $< \alpha_{eq} <$ 87 degrees because of additional scattering

when those electrons transit through the wave edge at $\lambda = 3$ degrees. The MC2018 formula adopts test-particle equations in Eqs. (4.1) and (4.2), which considers finite Larmor radius and does not assume magnetic moment conservation, and a more realistic Gaussian latitudinal distribution of wave power centered at the equator and latitudinal width of 3 degrees. When comparing MC2018 with Li2015, one can notice two discrepancies. First, MC2018 produces less scattering at 45 degrees $< \alpha_{eq} <$ 85 degrees due to the finite Larmor radius effect, which tends to be more significant for large α_{eq} and to weaken the wave force. Second, MC2018 enhances scattering at low $\alpha_{eq} <$ 45 degrees. The enhancement is attributed to the additional scattering caused by the change in magnetic moment μ when electrons experience rapid spatial variation of wave fields over gyration.

To verify the analytic diffusion coefficient, the test particle simulation using Eqs. (4.1) and (4.2) is performed. For a given initial energy and pitch angle, the simulation is performed for 100 randomly selected initial bounce phases and 101 sets of randomly assigned initial wave phases. Ensemble average of this 100×101 set of simulation results is performed to obtain the numerical diffusion coefficients (shown by magenta circles in Fig. 4.7). One can see that diffusion coefficients derived from numerical test-particle simulation are in close agreement with the theoretical MC2018 curve. One discrepancy between the numerical coefficients and the analytic ones occurs for α_{eq} near 90 degrees, which may be due to the breakdown of the second assumption and to the additional advective responses (see Section 4.4). Dependences of the diffusion coefficients on various plasma and waves parameters are explored systematically in Maldonado and Chen (2018).

Tao and Li (2016) further consider wave normal angle distribution to examine the bounce resonant scattering and find that the inclusion of wave normal angle distribution favors pitch angle scattering for equatorially and nearly equatorially mirroring electrons, which is later validated using guiding-center test-particle simulations (Li and Tao, 2017). Bounce resonance diffusion theory has also been applied to other types of plasma waves, for example, EMIC waves below ion gyrofrequency (Cao et al., 2017a) and the low-frequency portion of plasmaspheric hiss waves (Cao et al., 2017b).

4.6 Summary

Bounce resonance interaction with magnetosonic waves has been developed both in terms of coherent interaction and quasi-linear scattering. The bounce resonance diffusion or advection by magnetosonic waves could be an important mechanism to account for dynamics of equatorially and nearly equatorially mirroring electrons. Those newly developed coefficients are expected to be incorporated into existing Fokker–Planck framework for radiation belt modeling.

Acknowledgments

This work was supported by NSF grants 1405041 and 1702805 through the Geospace Environment Modeling program, an AFOSR grant FA9550-16-1-0344, and NASA grants NNX15AF55G and NNX17AI52G. JB gratefully acknowledges the joint Department of Energy and the National Science Foundation grant DE-SC0010578, which was awarded to UCLA through the NSF/DOE Plasma Partnership program and also NASA grant NNX16AG21G.

References

Albert, J.M., Tao, X., Bortnik, J., 2013. Aspects of nonlinear wave–particle interactions. In: Summers, D., Mann, I.R., Baker, D.N., Schulz, M. (Eds.), Dynamics of the Earth's Radiation Belts and Inner Magnetosphere, Geophysical Monograph Series. American Geophysical Union, pp. 255–264. Available from: https://doi.org/10.1029/2012GM001324.

Albert, J.M., Starks, M.J., Horne, R.B., Meredith, N.P., Glauert, S.A., 2016. Quasi-linear simulations of inner radiation belt electron pitch angle and energy distributions. Geophys. Res. Lett. 43 (6), 2381–2388. https://agupubs.onlinelibrary.wiley.com/doi/abs/ 10.1002/ 2016GL067938.

Balikhin, M.A., Shprits, Y.Y., Walker, S.N., Chen, L., Cornilleau-Wehrlin, N., Dandouras, I., et al., 2015. Observations of discrete harmonics emerging from equatorial noise. Nat. Commun. 6, 7703.

Bell, T.F., 1984. The nonlinear gyroresonance interaction between energetic electrons and coherent VLF waves propagating at an arbitrary angle with respect to the earth's magnetic field. J. Geophys. Res. 89, 905–918.

Bortnik, J., Thorne, R.M., 2010. Transit time scattering of energetic electrons due to equatorially confined magnetosonic waves. J. Geophys. Res. 115, 7213.

Bortnik, J., Thorne, R.M., Ni, B., Li, J., 2015. Analytical approximation of transit time scattering due to magnetosonic waves. Geophys. Res. Lett. 42 (5), 1318–1325. Available from: https://doi.org/10.1002/2014GL062710.

Cao, X., Ni, B., Summers, D., Bortnik, J., Tao, X., Shprits, Y.Y., et al., 2017a. Bounce resonance scattering of radiation belt electrons by H + band emic waves. J. Geophys. Res. Space Phys. 122 (2), 1702–1713. Available from: https://doi.org/10.1002/2016JA023607. 2016JA023607.

Cao, X., Ni, B., Summers, D., Zou, Z., Fu, S., Zhang, W., 2017b. Bounce resonance scattering of radiation belt electrons by low-frequency hiss: comparison with cyclotron and landau resonances. Geophys. Res. Lett. 44 (19), 9547–9554. Available from: https://doi.org/10.1002/2017GL075104.

Chen, L., Thorne, R.M., Jordanova, V.K., Horne, R.B., 2010. Global simulation of magnetosonic waves instability in the storm time magnetosphere. J. Geophys. Res. 115, A11222. Available from: https://doi.org/10.1029/2010JA015707.

Chen, L., Thorne, R.M., Jordanova, V.K., Thomsen, M.F., Horne, R.B., 2011. Magnetosonic wave instability analysis for proton ring distributions observed by the LANL magnetospheric plasma analyzer. J. Geophys. Res. 116, 3223.

Chen, L., Maldonado, A., Bortnik, J., Thorne, R.M., Li, J., Dai, L., et al., 2015. Nonlinear bounce resonances between magnetosonic waves and equatorially mirroring electrons. J. Geophys. Res 120, 6514–6527. Available from: https://doi.org/10.1002/2015JA021174.

Chen, L., Thorne, R.M., Bortnik, J., Zhang, X.-J., 2016. Nonresonant interactions of electromagnetic ion cyclotron waves with relativistic electrons. J. Geophys. Res. Space Phys. 121 (10), 9913–9925. Available from: https://doi.org/10.1002/2016JA022813. 2016JA022813.

Dai, L., Takahashi, K., Wygant, J.R., Chen, L., Bonnell, J., Cattell, C.A., et al., 2013. Excitation of poloidal standing Alfvén waves through drift resonance wave–particle interaction. Geophys. Res. Lett. 40, 4127–4132.

Gary, S.P., Liu, K., Winske, D., Denton, R.E., 2010. Ion Bernstein instability in the terrestrial magnetosphere: linear dispersion theory. J. Geophys. Res. 115, 12209.

Horne, R.B., Thorne, R.M., Glauert, S.A., Meredith, N.P., Pokhotelov, D., Santolík, O., 2007. Electron acceleration in the Van Allen radiation belts by fast magnetosonic waves. Geophys. Res. Lett. 34, L17107.

Hrbáčková, Z., Santolík, O., Němec, F., Macúšová, E., Cornilleau-Wehrlin, N., 2015. Systematic analysis of occurrence of equatorial noise emissions using 10 years of data from the Cluster mission. J. Geophys. Res. 120, 1007–1021.

Hsieh, Y.-K., Omura, Y., 2017. Nonlinear dynamics of electrons interacting with oblique whistler mode chorus in the magnetosphere. J. Geophys. Res. Space Phys. 122 (1), 675–694. Available from: https://doi.org/10.1002/2016JA023255. 2016JA023255.

Kanekal, S., Baker, D., Blake, J., 2001. Multisatellite measurements of relativistic electrons: global coherence. J. Geophys. Res. 106 (A12), 29721–29732.

Li, J., Ni, B., Xie, L., Pu, Z., Bortnik, J., Thorne, R.M., et al., 2014. Interactions between magnetosonic waves and radiation belt electrons: comparisons of quasi-linear calculations with test particle simulations. Geophys. Res. Lett. 41 (14), 4828–4834.

Li, J., Bortnik, J., Xie, L., Pu, Z., Chen, L., Ni, B., et al., 2015. Comparison of formulas for resonant interactions between energetic electrons and oblique whistler-mode waves. Phys. Plasmas 22 (5), 052902.

Li, J., Ni, B., Ma, Q., Xie, L., Pu, Z., Fu, S., et al., 2016. Formation of energetic electron butterfly distributions by magnetosonic waves via landau resonance. Geophys. Res. Lett. 43 (7), 3009–3016. Available from: https://doi.org/10.1002/2016GL067853. 2016GL067853.

Li, X., Tao, X., 2017. Validation and analysis of bounce resonance diffusion coefficients. J. Geophys. Res. Space Phys. 123, 104–113. Available from: https://doi.org/10.1002/2017JA024506.

Li, X., Tao, X., Lu, Q., Dai, L., 2015. Bounce resonance diffusion coefficients for spatially confined waves. Geophys. Res. Lett. 42 (22), 9591–9599. Available from: https://doi.org/10.1002/2015GL066324.

Ma, Q., Li, W., Thorne, R.M., Angelopoulos, V., 2013. Global distribution of equatorial magnetosonic waves observed by themis. Geophys. Res. Lett. 40 (10), 1895–1901. Available from: https://doi.org/10.1002/grl.50434.

Ma, Q., Li, W., Thorne, R.M., Bortnik, J., Kletzing, C.A., Kurth, W.S., et al., 2016. Electron scattering by magnetosonic waves in the inner magnetosphere. J. Geophys. Res. Space Phys. 121 (1), 274–285. Available from: https://doi.org/10.1002/2015JA021992.

Maldonado, A.A., Chen, L., 2018. On the diffusion rates of electron bounce resonant scattering by magnetosonic waves. Geophys. Res. Lett. 45, 3328–3337. Available from: https://doi.org/10.1002/2017GL076560.

Maldonado, A.A., Chen, L., Claudepierre, S.G., Bortnik, J., Thorne, R.M., Spence, H., 2016. Electron butterfly distribution modulation by magnetosonic waves. Geophys. Res. Lett. 43 (7), 3051–3059. Available from: https://doi.org/10.1002/2016GL068161. 2016GL068161.

Meredith, N.P., Horne, R.B., Anderson, R.R., 2008. Survey of magnetosonic waves and proton ring distributions in the Earth's inner magnetosphere. J. Geophys. Res. 113, 6213.

Min, K., Liu, K., Wang, X., Chen, L., Denton, R.E., 2018. Fast magnetosonic waves observed by Van Allen Probes: testing local wave excitation mechanism. J. Geophys. Res. Space Phys. Available from: https://doi.org/10.1002/2017JA0248672169–94022017JA024867.

Němec, F., Santolík, O., Gereová, K., Macúšová, E., de Conchy, Y., Cornilleau-Wehrlin, N., 2005. Initial results of a survey of equatorial noise emissions observed by the Cluster spacecraft. Planet. Space Sci., 53, 291–298.

Parker, E.N., 1961. Effect of hydromagnetic waves in a dipole field on the longitudinal invariant. J. Geophys. Res. 66 (3), 693–708. Available from: https://doi.org/10.1029/JZ066i003p00693.

Perraut, S., Roux, A., Robert, P., Gendrin, R., Sauvaud, J., Bosqued, J., et al., 1982. A systematic study of ULF waves above F/H plus/ from GEOS 1 and 2 measurements and their relationships with proton ring distributions. J. Geophys. Res. 87, 6219–6236.

Roberts, C.S., 1968. Cyclotron-resonance and bounce-resonance scattering of electrons trapped in the earth's magnetic field. In: Earth's Particles and Fields. J. Geophys. Res., 73 (23), 7361–7376, https://doi.org/10.1029/JA073i023p07361.

Roberts, C.S., Schulz, M., 1968. Bounce resonant scattering of particles trapped in the earth's magnetic field. J. Geophys. Res. 73 (23), 7361–7376.
Russell, C.T., Holzer, R.E., Smith, E.J., 1969. OGO 3 observations of ELF noise in the magnetosphere. 1. Spatial extent and frequency of occurrence. J. Geophys. Res. 74, 755–777.
Santolík, O., Nemec, F., Gereová, K., Macúšová, E., Conchy, Y., Cornilleau-Wehrlin, N., 2004. Systematic analysis of equatorial noise below the lower hybrid frequency. Ann. Geophys. 22, 2587–2595.
Schulz, M., Lanzerotti, L.J., 1974. *Particle Diffusion in the Radiation Belts*. Physics and Chemistry in Space, Vol. 7. Springer-Verlag, Berlin, Heidelberg, pp. 62–65, Ch. II.4.
Shprits, Y., Kondrashov, D., Chen, Y., Thorne, R., Ghil, M., Friedel, R., et al., 2007. Reanalysis of relativistic radiation belt electron fluxes using crres satellite data, a radial diffusion model, and a kalman filter. J. Geophys. Res. 112 (A12).
Shprits, Y.Y., 2009. Potential waves for pitch-angle scattering of near-equatorially mirroring energetic electrons due to the violation of the second adiabatic invariant. Geophys. Res. Lett. 36, 12106.
Shprits, Y.Y., 2016. Estimation of bounce resonant scattering by fast magnetosonic waves. Geophys. Res. Lett. 43 (3), 998–1006. Available from: https://doi.org/10.1002/2015GL066796. 2015GL066796.
Tao, X., Bortnik, J., 2010. Nonlinear interactions between relativistic radiation belt electrons and oblique whistler mode waves. Nonlinear Process. Geophys. 17 (5), 599–604. Available from: https://www.nonlin-processes-geophys.net/17/599/2010/.
Tao, X., Li, X., 2016. Theoretical bounce resonance diffusion coefficient for waves generated near the equatorial plane. Geophys. Res. Lett. 43, 7389–7397.
Thorne, R.M., 2010. Radiation belt dynamics: the importance of wave–particle interactions. Geophys. Res. Lett. 37 (22).
Tsurutani, B.T., Falkowski, B.J., Pickett, J.S., Verkhoglyadova, O.P., Santolik, O., Lakhina, G.S., 2014. Extremely intense ELF magnetosonic waves: a survey of polar observations. J. Geophys. Res. 119, 964–977.
Walt, M., 1994. Introduction to geomagnetically trapped radiation. Camb. Atmos. Space Sci. Ser. 10, 10.
Xiao, F., Yang, C., Su, Z., Zhou, Q., He, Z., He, Y., et al., 2015. Wave-driven butterfly distribution of Van Allen belt relativistic electrons. Nat. Commun. 6, 8590.

CHAPTER 5

Nanosat and balloon-based studies of radiation belt loss: low-cost access to space

John G. Sample[1], Robyn M. Millan[2] and Leslie A. Woodger[2]
[1]Department of Physics, Montana State University, Bozeman MT, United States
[2]Department of Physics and Astronomy, Dartmouth College, Hanover, New Hampshire, United States

Contents

5.1 Introduction

The earliest measurements of energetic electron precipitation to the atmosphere were made from a balloon platform. Balloon-borne, auroral X-rays were discovered over Minneapolis during a magnetic storm on July 1, 1957, six months before the launch of Explorer 1 (Winckler and Peterson, 1957). These X-rays were correctly identified as atmospheric bremsstrahlung X-rays produced by precipitated energetic electrons (estimated at the time as $\sim$65 keV) interacting with atmospheric constituents. Soon after, balloon-based observations were combined with Van Allen's measurements from the early explorers (Winckler et al., 1962), which were at low inclination, to try to understand the relationship between acceleration, precipitation, and the global balance of radiation belt fluxes. The combination of balloon and equatorial measurements continues today; almost 60 years after balloon data were compared with Explorer 3, data from the Balloon Array for Radiation belt Relativistic Electron Loss (BARREL) have been combined with measurements from NASA's twin Van Allen probes (Li et al., 2014; Breneman et al., 2015; Woodger et al., 2015). While much work has been done, many of the original questions regarding the balance of acceleration and loss as well as the various microphysics of electron precipitation are still under investigation.

The Dynamic Loss of Earth's Radiation Belts
DOI: https://doi.org/10.1016/B978-0-12-813371-2.00005-6

Recently, a new observational platform has emerged that allows high-quality measurements from small semistandard satellites called CubeSats (Twiggs, 2008) that allow rapid, low-cost, and student access to space. CubeSat missions measuring Energetic Electron Precipitation (EEP) have been a success as standalone missions (Li et al., 2013a; Crew et al., 2016; Shumko et al., 2018), and perhaps especially when made in conjunction with other missions (Blum et al., 2013; Jaynes et al., 2014; Anderson et al., 2017; Breneman et al., 2017). CubeSats have progressed from simple student-engineering and education missions, to proof-of-concept missions, through to National Science Foundation (NSF) funded science and space−weather focused missions. NASA recently added them to the Low-Cost Access to Space (part of the Heliophysics Technology Instrument Development for Science; HTIDS) portfolio, and now CubeSat-focused missions are proposed as missions of opportunity within heliophysics science. Selected missions of four or more CubeSats such as the SNIPE mission from South Korea (Hwang et al., 2018) and long-term proposals for extensive constellations of these satellites are all in progress. Although long confined to Low Earth Orbit (LEO), CubeSats have been proposed and are under development for GeoTransfer Orbit (GTO), Highly Eliptical Orbit (HEO), translunar, and even planetary missions. The CubeSat landscape is changing rapidly. The recent National Academies of Science, Engineering, and Medicine report "Achieving Science with CubeSats: Thinking Inside the Box" (National Academies of Science, Engineering, and Medicine, 2016) acknowledged that even with a diverse committee and several fact-finding forums they could only make recommendations for the very near future. This chapter will focus on a review of recent results in EEP that were supported by CubeSats, but by no means can it provide a complete picture of the ongoing work.

In addition to their potential for science return, balloon missions and CubeSats serve as valuable hardware-based training for young scientists, engineering teams, and project managers. The balloon-flight environment poses many of the same challenges as spaceflight, including a complex thermal environment, telemetry constraints, size, weight, and power concerns, and general remote operations required for long-duration missions. Thus balloons provide an ideal training ground for future space−hardware scientists in addition to being an excellent test platform for new space-based instrumentation. This training is necessary for future experimental scientists, but also provides a unique opportunity to train personnel in systems engineering and project management. Indeed, this similarity is recognized in the technology readiness level classification system, where balloon flights serve as a proving ground for future spaceflight. The National Academy's CubeSat report referenced above and several previous National Research Council (NRC) reports for the NASA suborbital program (which has long included balloons and rockets, but now encompasses CubeSats) recognize the importance of these lower-cost science missions as essential to developing long-term personnel capabilities for larger missions. A significant number of large NASA mission PIs cut their teeth on balloons and rockets and this Principal Investigator (PI) preparation is likely soon to include CubeSats.

5.2 The early days of energetic particle precipitation

An excellent review of the early balloon measurements of energetic particle precipitation is found in Parks et al. (1993). Although early measurements were often referred to as auroral precipitation, many of the observations took place at what we would now consider subauroral, radiation belt latitudes. Using the T89 (Tsyganenko, 1989) magnetic field model, Minneapolis, MN mapped to $L \sim 3.6$ at the disturbed times the first observations were made by Winckler. And while many of the early works also focus on auroral energy ranges (measurements usually stopped below 200 keV), there were hints at higher-energy precipitation. Further reviews that extend to nonballoon measurements can be found in Tsurutani et al. (2013) and Millan and Thorne (2007).

One useful quality of balloon-based precipitation observations still in use today is the ability to set up a network of coordinated measurements by utilizing multiple launch locations and the known flows of upper atmospheric winds. Winckler et al. (1962), launched X-ray observing balloon payloads from four sites along an approximate magnetic meridian from L-shells at $\sim 2.5-6$ and showed that simultaneous precipitation was often extended in latitude, although the location of the peak in precipitation was not always consistent, nor was it always colocated with the peak in fluxes measured by Explorer VII. This paper also showed the first recorded microbursts, impulsive, 100–200 ms increases in the locally precipitating flux.

The term microburst was coined somewhat later by Anderson and Milton (1964). As more sensitive detectors were flown, and microburst-time–resolution became more common, it was recognized that microbursts were a common and intense mode of precipitation across the dawnside (Parks, 1978). The connection to whistler mode chorus distributions was made before then. Microbursts were a frequent observational target of early balloon campaigns and this may have contributed to the low-energy focus of observations. Microbursts with energies greater than 1 MeV have not been observed from a balloon, but have been observed from spacecraft (e.g., Blake et al., 1996). From the first measurements (Winckler et al., 1962), bursts were often measured in quasi periodic trains and an initial explanation, related to the electron bounce time was proposed, although this explanation is still debated today (e.g., Saito et al., 2012).

Rosenberg et al. (1977) demonstrated the utility of balloon measurements as nearly stationary observing platforms on the time scales of precipitation events. They report on electron precipitation occurring as electron microbursts near Siple Station, Antarctica ($L \sim 4.2$), observed in a series of flights with local and conjugate very low frequency (VLF) wave measurements. Bursts were separated into those that were initially scattered toward the southern hemisphere and those that were observed after a mirrored bounce in the northern hemisphere. Time–energy dispersion was evident in the reflected bursts that showed longer duration and lower intensity. An early test particle simulation showed that direct and mirrored scattering was consistent with a near-equatorial source.

As with many early balloon observations, the precipitation spectra were soft, with e-folding energies of ~30 keV, and little variation in the spectral hardness between the bursts and the slowly varying continuum precipitation. Although Rosenburg's instrument was read out to 500 keV, no significant counts were shown above 100 keV. Many of these early balloon flights focused on electrons below ~100 keV and few read out their detectors above 200 keV. The Rosenberg detector being read out to 500 keV was relatively unique; however, the 1.7 cm-thick NaI matches the attenuation length of ~300 keV X-rays, and detector sensitivity above this energy would have been somewhat limited. Thicker detectors were harder to manufacture, more expensive, and had higher background rates.

Balloon measurements of precipitation above 200 keV X-ray energy were nearly nonexistent with numerous authors reporting no counts above background at higher energies. Occasionally events were identified as "relativistic" by the hardness of the spectrum at low energies (Parks et al., 1979). The analysis in West and Parks (1984) described an event with an early Monte Carlo forward–fit model to show that the precipitation was consistent with a 200 keV e-folding distribution between $L = 4.5$ and 5. The use of short flights focused on dawnside precipitation to study microbursts may have limited the observation of less frequent, but more energetic, precipitation that would later be discovered on the duskside (Foat et al., 1998; Millan et al., 2002) and observed more often due to the advent of long duration balloon (LDB) flight. Fig. 5.1 shows the cumulative distribution of microburst, local-time occurrence that resulted from several dozen short-duration balloon flights (Parks et al., 1968). None of these flights reported precipitation above 200 keV.

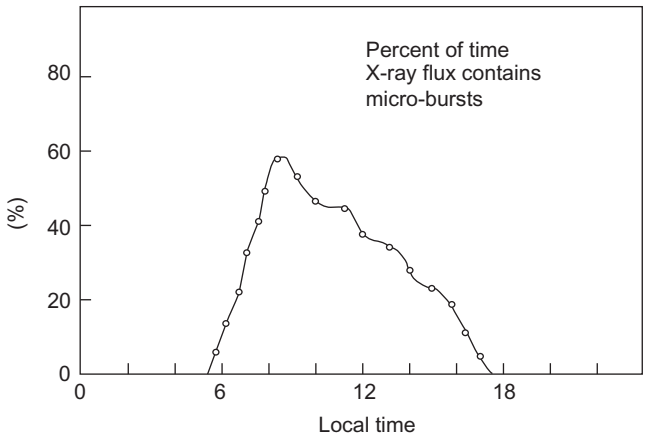

Figure 5.1 Cumulative local time distribution of microbursts from more than 1000 h of short-duration balloon flights.

Since balloon-based measurements rely on the bremsstrahlung process, the highest number flux in X-rays is almost always found below 200 keV. Even in this energy range the X-ray spectral hardness can be used to show something of the extended energy range. (Millan, 2002, Sample, 2013). Fig. 5.2 shows how the spectral hardness in detected 100–180 keV X-rays maps onto much higher energy e-folding (and monoenergetic), precipitating electron spectra. Accurate determination of the electron source requires significant X-ray counts at the highest energies of electron precipitation as was shown later by Foat et al. (1998). This is illustrated in Fig. 5.3 which shows the similarity in the X-ray spectrum expected from a monoenergetic precipitating electron distribution, a flat distribution, and an exponential distribution.

While multiple balloon campaigns studied the large scales of precipitation, a few experiments (Barcus et al., 1966; Trefall et al., 1966) attempted to look at smaller scales using closely separated flights of multiple balloons. Brown et al. (1965) made observations with two balloons separated by about 150 km in the east–west direction and found no correlation for about 33% of microbursts observed on the two platforms. These observations suggest a size-scale smaller than 150 km at balloon altitude for

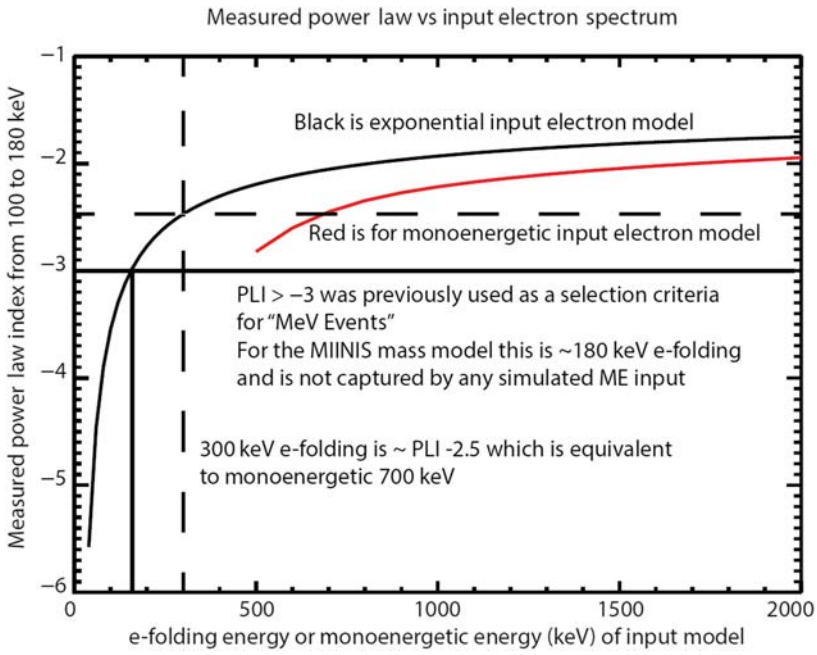

Figure 5.2 The results of a Monte Carlo simulation showing how the spectral hardness of a power law fit between 100 and 180 keV in the measured X-ray spectrum relates to the e-folding energy (*black curve*) or monoenergetic energy (*red curve*) of the precipitating electron distribution. Vertical and horizontal lines highlight specific points relating the two distribution types and the power law index at levels previously used to identify relativistic electron precipitation.

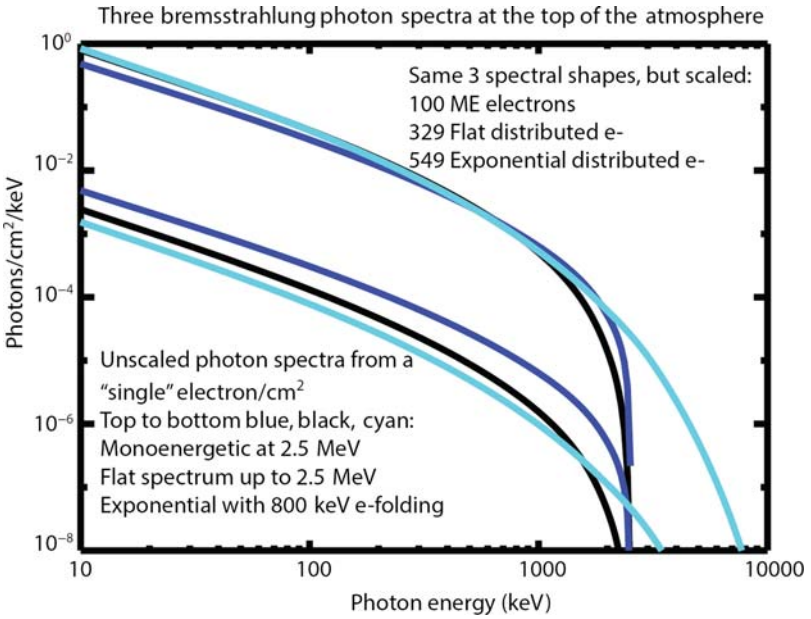

Figure 5.3 Ideal photon spectra from three different input electron distributions.

most bursts. Similar observations by Trefall et al. (1966) put the burst size scale at 200 km. An example of a pair of BARREL balloons flying at ~150 km separation from Kiruna, Sweden is shown in Fig. 5.4.

Balloon measurements also sought out spatial resolution within the field-of-view of a single balloon. Parks (1967) used a series of four collimated X-ray detectors to observe variation in the precipitation across the local sky. He found that microbursts were often smaller than the 18 km limit resolvable by the instrument. Interestingly, one observation showed a source that was drifting eastward, though the drift speed was not consistent with that of electrons in the 30–40 keV energy range, therefore suggesting motion due to something else, possibly the chorus wave generation region itself.

More spatial resolution was achieved by flying X-ray pinhole cameras (e.g., Mauk et al., 1981; Werden and Parks, 1987; Yamagami et al., 1990). For an X-ray image to accurately show the precipitation region it must be within a Compton scattering length of the precipitation altitude. For X-rays in the 20–120 keV range this is typically >38 km (Parks, 1967). This requirement, combined with the required high sensitivity to separate scarce bremsstrahlung counts into spatially resolved bins has generally limited imaging efforts to brighter, lower-energy features with timescales of a few seconds or longer. However, the Parks (1967) result shows the possible utility of imaging at microburst timescales even at the spatially coarse scales found at that time.

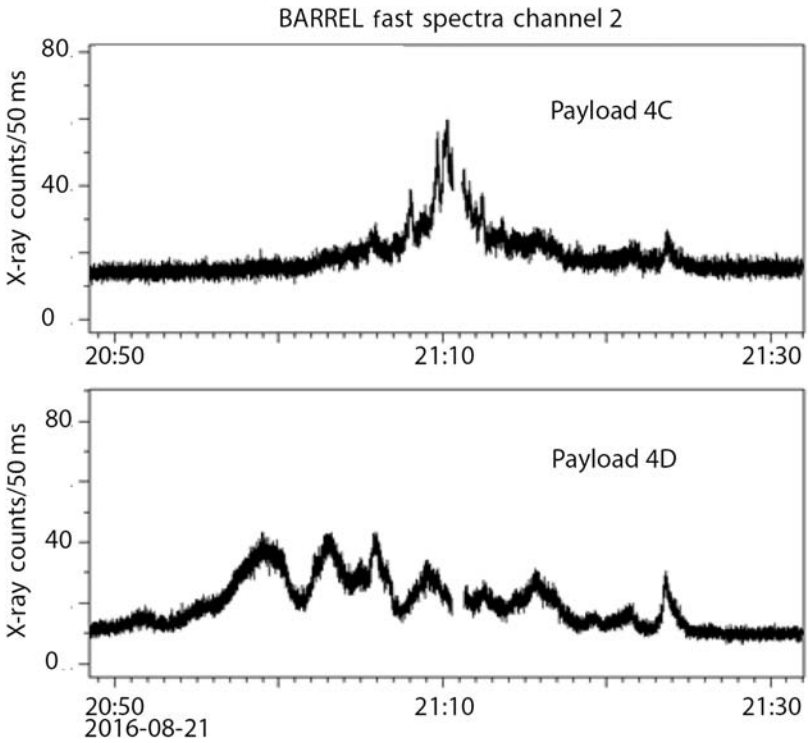

Figure 5.4 Although separated by less than a full field of view, the two BARREL balloons see very different precipitation time series.

Balloon observations cannot typically distinguish any information about the parent electron angular distributions and balloons cannot always uniquely identify the spectral shape of the precipitating electrons. Although rocket-based measurements are a frequent tool to study electron precipitation at lower energies, they have rarely been used at >30 keV, since higher-energy precipitation does not have a uniquely identified, visible-light indicator (or other real-time, ground-based indicators) to trigger the rocket launch. One unique mission concept used on several occasions (Anderson et al., 1966; Skoug, 1995) takes a real-time data link to an X-ray measuring balloon payload flying near the rocket range. When the balloon observations indicate microbursts/EEP, the rocket launch is triggered. This observation scheme can provide direct in situ measurements of the precipitating electrons. Datta et al. (1996) reported rocket measurements that showed very soft microburst electron spectra with <10 keV e-folding out to 150 keV at five different precipitating pitch angles. Interestingly they showed a distinct lack of microburst precipitation below ~ 20 keV, a measurement which would not be possible with a balloon alone.

5.3 Extending the precipitation spectra to higher energies

The study by Smith et al. (1995) was based on a balloon mission that was primarily focused on astrophysical sources, extended the energy range of precipitating electrons observed via bremsstrahlung out to 300 keV and was an early example of using a Monte Carlo model to invert the measured bremsstrahlung X-rays into a well-characterized precipitating electron spectrum. This paper showed a general approach to fitting electron precipitation spectra from observed X-rays. It also explored effects from the electron spatial distribution within the field of view on the observed X-ray spectrum.

A serendipitous measurement occurred with the INTERBOA mission from Kiruna, Sweden. Flown in 1996, the germanium spectrometer was read out to 1.4 MeV because it was a leftover from a previous solar observing mission (Lorentzen et al., 2000; Foat et al., 1998). INTERBOA flew the germanium spectrometer twice over the course of August 19–28, 1996, and on August 20, 1996, it observed the hardest spectrum of precipitation X-rays ever observed. Although the spectrometer was read out to 1.4 MeV, the spectrum appeared to continue beyond that. Since the highest energies of photons weren't observed, the spectrum was found to be consistent with a monoenergetic beam of 1.7 MeV electrons as the parent source. In future missions it would become apparent that clean, significant observations at the highest energies were necessary to further constrain the electron spectrum. The INTERBOA mission also flew a pinhole X-ray camera, sensitive up to 120 keV, and showed that precipitation filled the field-of-view of the balloon, showed no smaller scale structures, and showed the sky brightening uniformly with the high-energy countrate (Lorentzen et al., 2000). Because the Kiruna precipitation was observed near local dusk and its spectrum was extremely hard, indicating a substantial number of high energy electrons, perhaps even a monoenergetic or peaked spectrum, precipitation by electromagnetic ion cyclotron (EMIC) waves was considered as a possible scattering mechanism (Lorentzen et al., 2000).

The Kiruna event sparked renewed interest in searching for particle precipitation above a few hundred keV and the MAXIS mission soon followed. MAXIS flew a similar germanium spectrometer on a flight from Fairbanks, AK, but experienced power-systems failure after $\sim$1 day. MAXIS was originally set to refly from Fairbanks, Alaska, on another balloon, but eventually the mission was moved to an LDB launched from McMurdo, Antarctica. Over the course of its 18-day flight MAXIS observed significant precipitation above 500 keV. Millan et al. (2002) termed the nine periods with spectra similar to the Foat et al. (1998) event "MeV events" and all of them were located at dusk local times. One such event is shown in Fig. 5.5 where soft precipitation surrounds a brief (one of the shortest seen) period of much higher-energy precipitation. On average, over the eight days at radiation belt latitudes, the

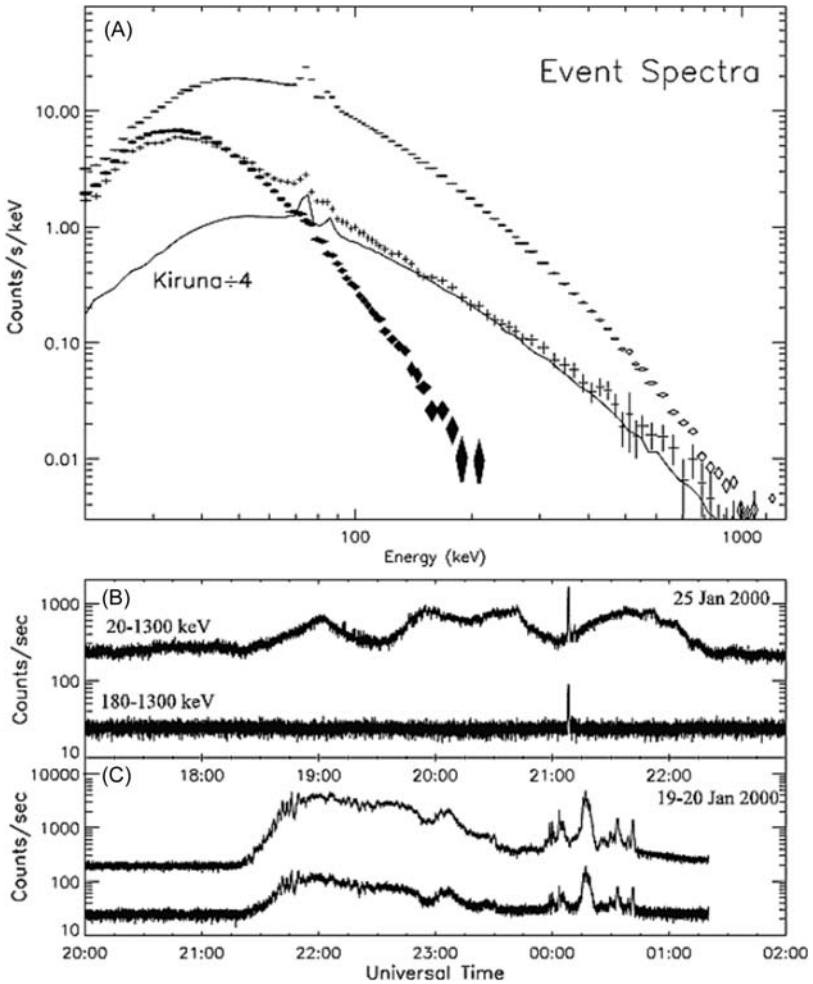

Figure 5.5 (A) The Kiruna spectrum (solid line), normal soft spectra in solid diamonds from the gradual envelope shown in the top curve in the panel (B) time series, and a hard spectrum (crosses) taken just around the time in the bottom time series spike. Top spectrum unfilled diamonds are from a separate MeV event that was the longest and brightest observed by MAXIS with time series shown in panel (C).

MeV events were a significant enough loss process (360 e-/cm^2/s) to drain the radiation belts of their $>$500 keV electrons in 3 days. Many hours of microburst precipitation were also observed, but microbursts were again confined to lower energies.

MAXIS found that the duskside precipitation had significantly harder spectra than the microbursts and unstructured precipitation observed at all local times. The minimum e-folding energy for any of the MeV events was $\sim$300 keV (shown for reference as a vertical dashed line in Fig. 5.2) and several events were consistent with

monoenergetic MeV electron precipitation or multi-MeV e-folding energies. One event, described in detail in Millan et al. (2007), lasted for several hours and accounted for roughly 80% of the electrons observed to be lost during the flight. Since the MeV events all occurred on the duskside (14:30−00:00) with significant high energy electron content (>500 keV for Millan et al., 2002), authors continued to draw a connection to EMIC waves resonating with very energetic electrons on the duskside in the plasmaspheric bulge or in plume structures.

McMurdo, the base for NASA's ballooning in Antarctica, is at a high initial magnetic latitude, and the circumpolar trajectories usually start by taking balloon payloads further into the polar cap before sometimes returning to radiation belt latitudes, as MAXIS did after day 8 in flight. Average L-shell observing profiles for payloads launched from McMurdo are shown in Fig. 5.6. In order to launch directly into the region corresponding to the radiation belts, the MINIS program chose to fly on smaller balloons which can be hand-launched and carry payloads up to ~40 kg and used the South African National Antarctic Expedition (SANAE) base at 72.6°S and 2.8°W, which is $L = \sim 3.6$ at quiet times. This allowed for flights to spend several days at appropriate L-shells without the need to drift from McMurdo.

MINIS flew during the large flares, SEPs, and −99 nT Dst geomagnetic storm of late January 2005. MINIS used a 7.62 diameter × 7.62 cm height NaI scintillator and read out its spectra to 10 MeV in a slow spectral product and a 20 Hz rate at four energy channels to time-resolve microbursts. The payload also included a three-axis AC electric field measurement and a single-axis (local vertical) search coil magnetometer, which were read out in three frequency bands of 1, 10, and 25 kHz, but saw no significant wave activity at their sensitivity (Kokorowski, 2008).

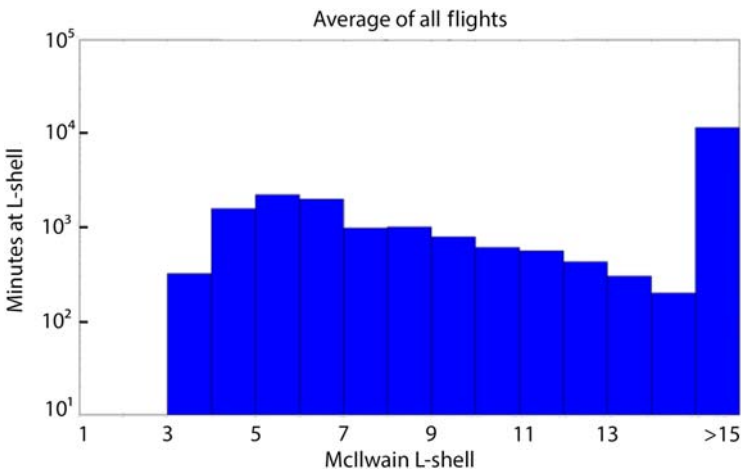

Figure 5.6 An average *L*-profile over 16 flights launched from McMurdo by NASA-CSBF. Average flight duration was ~15 days but 75% of that time is at $L > 7$ even in magnetically quiet times.

Although MINIS observed high-energy precipitation over a large scale, roughly an hour of magnetic local time (MLT) and half an L-shell, the overall loss calculation was not as significant as during MAXIS, either in a flight-averaged sense ($\sim$50 e-/cm^2/s $>$ 500 keV) or an instantaneous sense during the most intense parts of the precipitation (Sample, 2013). A map of the minimum precipitation region and the time series of high-energy X-rays is shown in Fig. 5.7.

The MINIS multipoint measurement of large-scale precipitation with 600 + keV e-folding energy served as a pathfinder for BARREL, which was a mission of opportunity to fly in conjunction with the Van Allen Probes (Millan et al., 2013). BARREL conducted several years of test flights, including a 54-day piggyback flight on an ultralong duration balloon (ULDB) in early-2009, and shorter standalone flights

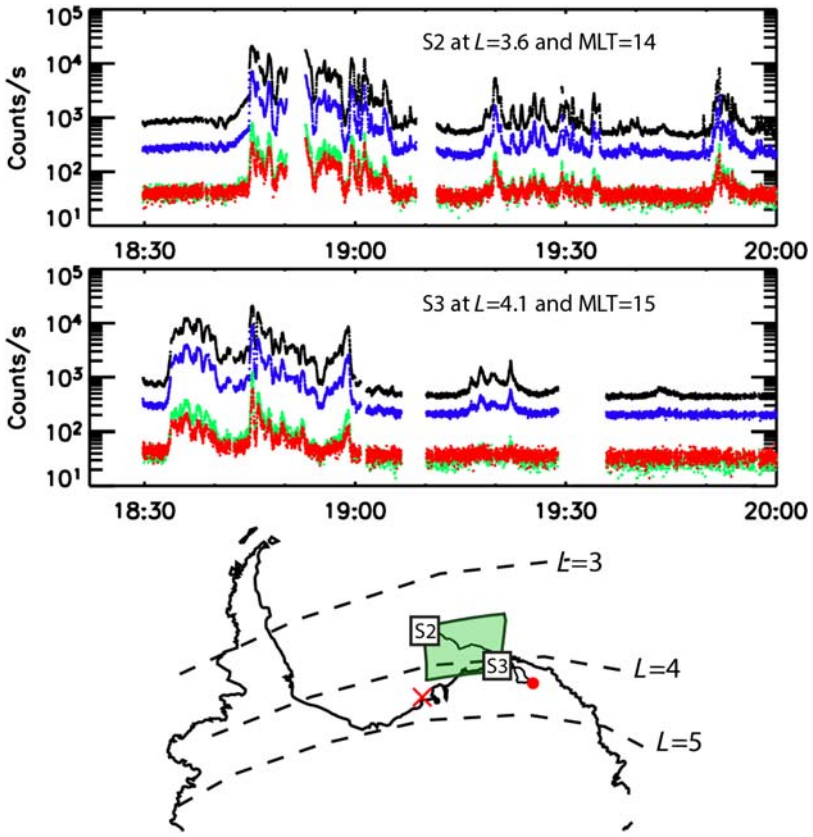

Figure 5.7 (Top panels) MINIS showed near simultaneous (within 3 s) increases in relativistic electron precipitation across almost an hour of local time and half an L shell (660 km separation at balloon altitudes). Colors indicate X-ray energies, from top (*black*) 20–175, 175–540, 540–825 keV, to bottom (*red*) 825 keV–1.5 MeV (bottom map) The red X indicates Halley Bay, the Red dot indicates SANAE. The green shaded area represents the minimum L-MLT bounds of observed REP.

the following two years. BARREL then conduced its two Antarctic science campaigns from a pair of launch sites over the course of 2012/2013 and 2013/2014 Antarctic summers, launching 40 balloons total, each carrying the same NaI spectrometer as found in MINIS. In addition to the previously used SANAE launch site, Halley Bay, Antarctica, was used to guarantee higher L coverage immediately on launch, prevent local surface weather at one site from preventing maintenance of the in-flight array, and rapidly establishing an array of observing points.

BARREL conducted two additional campaigns from Kiruna, Sweden in August 2015 and 2016 with 15 additional short flights (~1 day typical) during the "turnaround" season. Turnaround is a time of year when the prevailing atmospheric winds at 30–40 km shift from westward (local summer) to eastward (local winter) in both hemispheres. This allowed for the BARREL payloads to be recovered after each flight and reflown, either in the same campaign or in the next. Recovered payloads were also being repurposed for piggyback flights in 2018–19 on larger NASA balloon launches.

An overview of the BARREL Antarctic campaigns is provided in Woodger et al. (2015) and Fig. 5.8 is updated from that reference to include the turnaround campaigns of 2015 and 2016. The figure shows the L and MLT coverage of BARREL when the balloons were in conjunction with the Van Allen Probes. The Sweden campaigns were conducted, in part, to increase the number of conjunctions occurring at higher L in the late-morning and late-afternoon sectors. Launches were timed to

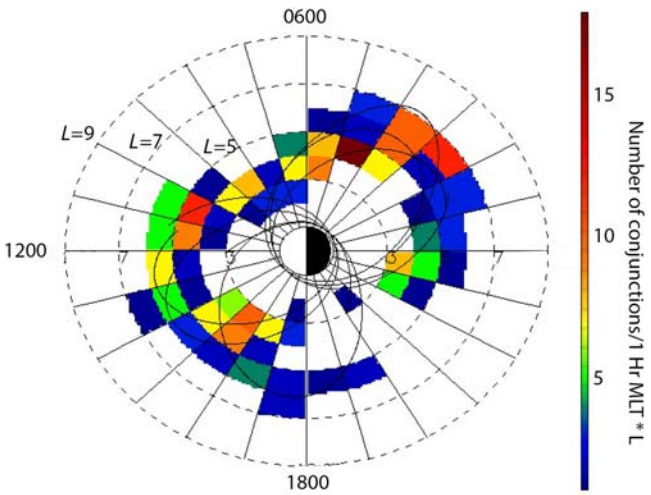

Figure 5.8 Shows the L-shell and local-time distribution of conjunctions between the BARREL balloons and the Van Allen probes. The solid black ellipses are characteristic orbits of the spacecraft during the primary BARREL campaigns. The Sweden campaigns added times when the probes' apogee was ~3.5 and 18 MLT.

achieve a substantial number of conjunctions despite the shorter turnaround flights. The precession of Van Allen Probe's orbit to apogees nearer dusk (2015) and dawn (2016) ensured more dusk and dawn MLTs had coordinated observations.

One of the principal goals of the BARREL mission was to map out the large-scale structure and extent of energetic electron precipitation. Interestingly, the BARREL payloads did not observe coincident duskside, hard-spectrum precipitation at the inter-payload separations BARREL achieved, perhaps showing that the MINIS large-scale observation was anomalous. However, the nearly global scale of precipitation was explicitly measured for plasmaspheric hiss waves that were coincidently measured on the Van Allen probes (Breneman et al., 2015). Plasmaspheric hiss and the energetic precipitation were coherent over 6 hours of MLT, and the combination of the balloon-measured precipitation spectrum and the Van Allen probes (RBSP) plasma and wave measurements allowed for multiple lines of evidence showing that hiss was directly responsible for the observed precipitation.

Clilverd et al. (2017) combined a single BARREL payload with ground-based riometer measurements and subionospheric VLF propagation data (timing context was also provided by the CSSWE CubeSat described later) to measure the scale, motion, and energy spectrum of large precipitation regions on January 18/19, 2013. They used BARREL to find hard-spectrum precipitation consistent with monoenergetic electrons in the 1−1.2 MeV range (with some time variation) and used the riometer data and VLF propagation data to establish the scale of the precipitation as well as identify that the region was westward moving, consistent with the drift speed and direction of 10−100 keV protons. It is interesting to note that this large extent of a high-energy precipitation was never directly observed by the BARREL balloons, but by combining them with other measurements a more complete picture can be established. Critically in Clilverd et al. (2017), BARREL is able to provide a stationary measurement of the energy spectrum which is then forward-fit to compare with the riometer and VLF measurements. The westward motion and hard-energy spectra allowed the authors to identify the precipitation as likely caused by EMIC waves.

In additional to the spatial structure of EEP, BARREL also sought to look at the microphysics of wave-particle scattering of energetic electrons out of the radiation belts. This goal was explored for hiss waves in Breneman et al. (2015), and was explored for EMIC waves in Zhang et al. (2016) and Li et al. (2014). The latter paper used observations of precipitation from BARREL and wave and plasma data from GOES and Van Allen probes to simulate the precipitation predicted by a diffusion model (Li et al., 2013b). The authors showed good agreement between the predicted and measured precipitation. Woodger et al. (2018) extended the Li model to several more precipitation observations and importantly found times when no precipitation was found despite EMIC wave presence. The model also correctly reproduced this nonobservation due to predicted resonant energies being higher than the energy

where significant flux was present in the belts. Zhang et al. (2016) used the closest conjunction between a Van Allen–measured EMIC wave event and a BARREL-observed REP event to compare and connect the predicted electron scattering with the measured precipitation. Woodger et al. (2018) went on to use precipitation observations from BARREL, MINIS, and MAXIS to demonstrate the importance of the equatorial B-field magnitude on the scattering. The direct, quantitative connection of hard-spectrum duskside precipitation with in situ measurements of plasma and waves is an essential step to understanding the microphysics of this scattering mechanism.

5.4 CubeSats

CubeSats have become a valuable new addition to observations of energetic electron precipitation. Early missions such as the Colorado Student Space Weather Experiment (CSSWE) and the Focused Investigation of Relativistic Electron Bursts: Intensity, Range, and Dynamics (FIREBIRD) CubeSats have already contributed significantly to measurements of EEP. Both programs were part of the first few rounds of the NSF space weather CubeSat program and began in late 2009. FIREBIRD was, as conceived, largely focused on the microburst precipitation described in the balloon section, but extending from 200 keV to >1 MeV, while CSSWE observed to even higher energies, but at lower time resolution.

CSSWE was launched on September 13, 2012 (Li et al., 2013a), carrying REPTile, a miniaturized version of the REPT (Baker et al., 2012) instrument found on the Van Allen probes. REPTile gave electron precipitation measurements at 6 seconds resolution and in three energy channels: 0.58–1.63, 1.63–3.8, and >3.8 MeV with 0.58 cm^2 sr of geometric factor. Proton channels were also available and downlinked. The CSSWE data were telemetered by a 9.6 kbps link and data are available from the launch through to March 7, 2013, then again from June 27, 2013, intermittently through to December 2014. CSSWE data has been used in more than 10 refereed science publications, demonstrating the potential for remarkable science return from a CubeSat.

CSSWE data was combined with low-latitude, high-altitude measurements of source particles and wave measurements by Schiller et al. (2017) using a data assimilation technique and a 1-dimensional model to compare conjunctions between CSSWE and the Van Allen probes as well as with several THEMIS (Time History of Events and Macroscale Interactions during Substorms) spacecraft. Direct conjunctions were not necessary to provide a complete, event-specific set of terms for transport, loss, and source processes. CSSWE data were also combined with Van Allen and THEMIS data by Jaynes et al. (2014) and were used to quantify losses during quiet time. They showed significantly higher loss rates than previously measured. Both studies

demonstrate the value in having both LEO and equatorial measurements in understanding radiation belt processes. As originally conceived, the Van Allen probes mission included a LEO measurement platform that was eventually dropped (e.g., NRC, 2003). BARREL was proposed as a mission of opportunity in part to fill in that measurement gap, but CubeSats have significantly augmented this capability. It is a testament to how rapidly CubeSats have developed significant science capabilities given that they were virtually unknown at the time that the Van Allen probes were conceived.

FIREBIRD-I launched on December 6, 2013 and the two satellites were barely in contact with the ground station. Flight Unit 2 (FU2) operated for 6 weeks and FU1 operated from March to July. They reported no microburst observations and never reported coincident data. True to the promise of CubeSats as vehicles with rapid development cycles, the FIREBIRD-II CubeSats were launched 13 months later, on January 31, 2015. Both satellites were immediately operational and observed coincident microbursts over a separation of 11 km (Crew et al., 2016) and 20 km (Shumko et al., 2018). The latter paper used the first multipoint observation of a bouncing packet of electrons to establish a scale of at least 51 km longitudinal and 29 km in latitudinal scale. The FIREBIRD CubeSats have now been operational for more than 4 years.

Data throughput for many CubeSats has been limited by downlink capacity; however, developing technologies are working to reduce this limit on more and more CubeSats (National Academies of Science, Engineering, and Medicine, 2016). While CSSWE transmitted a continuous low-resolution time and energy product, the FIREBIRD chose to operate in a campaign mode, transmitting a similar 6 seconds and two electron energy data product for limited periods, but with the addition of a higher resolution product at select times. Having completed 17 campaigns, the FIREBIRD-II data is marked by long periods of time when data are downloaded from the previous campaign, but no new data are taken, as seen in Fig. 5.9 which summarizes the mission. Within the campaigns the finer resolution data product, referred to as HiRes, consists of six energy channels at a time resolution between 12.5 and 50 ms depending on the campaign. A time resolution of 18.75 ms was common through the first year and a half and 50 ms resolution has been the default for the most recent campaigns.

Approximately 1% of the HiRes data collected in a given campaign is downloaded. Data selection is made on the ground by the FIREBIRD team based on the 6 seconds data and times when in conjunction with other missions including BARREL, Van Allen Probes, and others. Recent improvements in the FIREBIRD ground station process have improved data throughput by more than a factor of 3, but FIREBIRD's sparse data coverage remains, and the data downlink selection process can easily introduce an observer bias into the data archive that should be considered when using FIREBIRD data beyond case studies. But even just considering case studies,

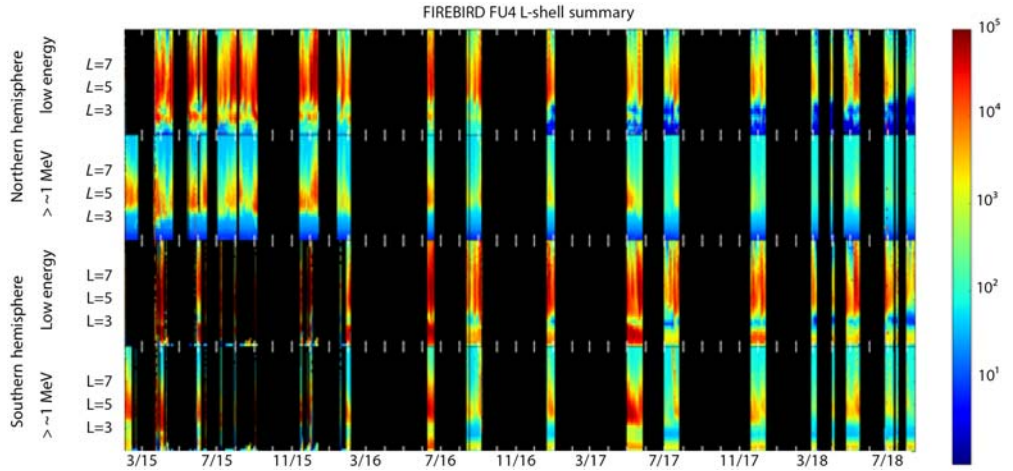

Figure 5.9 The FIREBIRD-II Cubesat campaigns showing L-sorted electron flux in two energy channels for one of the spacecraft with northern hemisphere observations in the top two panels and southern hemisphere observations in the bottom two panels. Panels 1 and 3 represent ~300 keV flux while panels 2 and 4 represent the >1 MeV channel.

FIREBIRD established the first direct in situ scale-size for microbursts (Crew et al., 2016), observed coincident microbursts in conjunction with Van Allen Probes wave measurements (Breneman et al., 2017), and used a bounce echoing microburst to extend some microburst scale-size measurements out to ~50 km (Shumko et al., 2018). Ongoing observations are specifically targeting conjunctions with Arase, Van Allen probes, POES, and other CubeSats so that a more complete picture of the complex and dynamic structure of energetic particle precipitation can be developed.

The AeroCube-6 (AC6) mission, launched on June 19, 2014, also consists of a pair of CubeSats in a remarkable 0.5 U ($5 \times 10 \times 10$ cm) form factor for each satellite. Each satellite carries a set of dosimeters that are read out at rates as fast as 10 Hz. The AC6 CubeSats utilized differential drag to control the in-track spacecraft separation by varying their attitude. This process allowed them to examine the spatial and temporal variation in precipitation at controlled, time-varying, separations. The AC6 CubeSats demonstration of precisely controlled in-track separation, without the resources required by propulsion, is a valuable first step toward larger CubeSat formations.

AC6 primarily has targeted lower energies than the FIREBIRD spacecraft, but the ability to control the spacecraft separation without fuel has been exceptional. A plot of the FIREBIRD-II separation with time and the AC6 separation with time is included in Fig. 5.10. Both missions targeted small precipitation structures, but FIREBIRD observations of these were limited to its first campaign, while AC6 was able to extend the observations throughout their lifetime. The FIREBIRD analysis of larger structures and longer-time variation in precipitation is ongoing, see Fig. 5.11. Meanwhile,

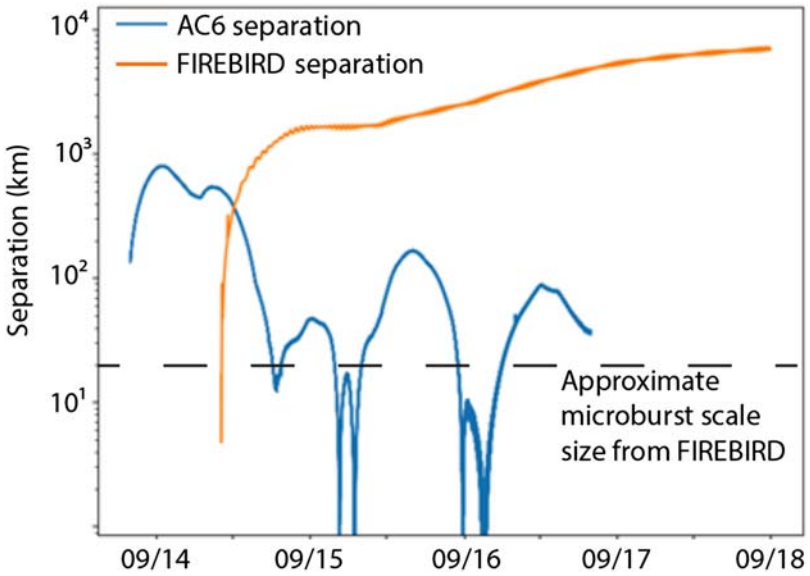

Figure 5.10 The inter-spacecraft (along track) separation of the pair of AC6 CubeSats (*blue*) and FIREBIRD-II (*orange*).

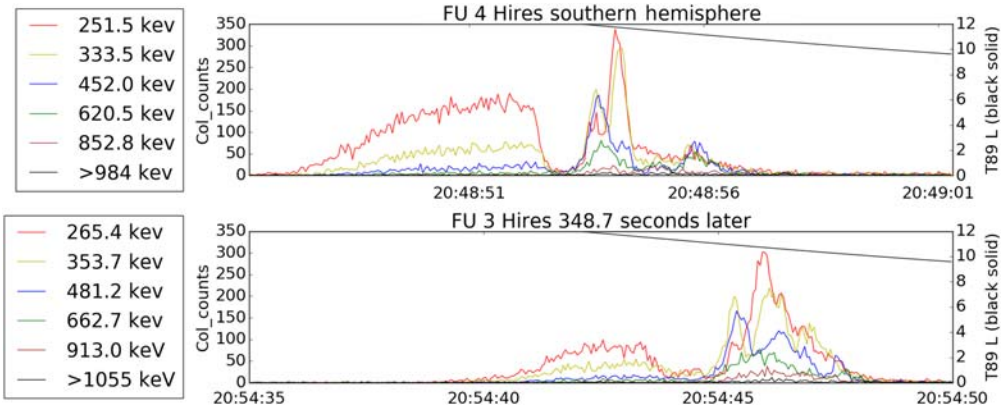

Figure 5.11 Shows the FIREBIRD-II HiRes with the FU3 data time shifted to match the location of Fu4. This data is from August 21, 2016 when the inter-spacecraft separation was 348 s. The FU3 measurement shows how the precipitation structure has evolved on a ~6 min time scale.

FIREBIRD and AC6 have recently (March 2018) precessed through the other's orbital plane allowing "lapping events"—joint observations at small separations—with the surviving spacecraft (AC6-B is no longer operational).

The most significant AC6 measurements, to date, have been made with the integral >35 keV electron dose channel. These include the observation of precipitation "curtains" that were made possible by having a pair of spacecraft making extended

observations at a small separation (Blake and O'Brien, 2016). Precipitation curtains manifest themselves as spatially confined persistent low-altitude flux that appears almost identically when the in-track time shift is applied to one of the spacecraft. Separations of up to 65 seconds have been shown. An example of AC6 time shifts is presented in Fig. 5.12 showing the remarkable agreement between short time structures when the second spacecraft data is time-shifted by the in-track lag of 6.4 seconds (bottom panel). Blake and O'Brien (2016) propose that the curtains are the drift remnants of small latitudinal precipitation. The result is an important reminder that not all LEO electrons are immediately lost, and that a single-point measurement can easily confuse a small, but persistent, spatial structure, like a curtain, with an impulsive event, such as a microburst.

Mozer et al. (2018) used AC6 >35 keV observations in conjunction with the Van Allen probes to show that microbursts were directly associated with whistler mode chorus, and further, that the envelope of precipitation, but not the microbursts themselves, were well-modeled by quasilinear diffusion calculations using the measured waves. This result may explain the smoothly varying envelope that many of the balloon measurements see in addition to microbursts.

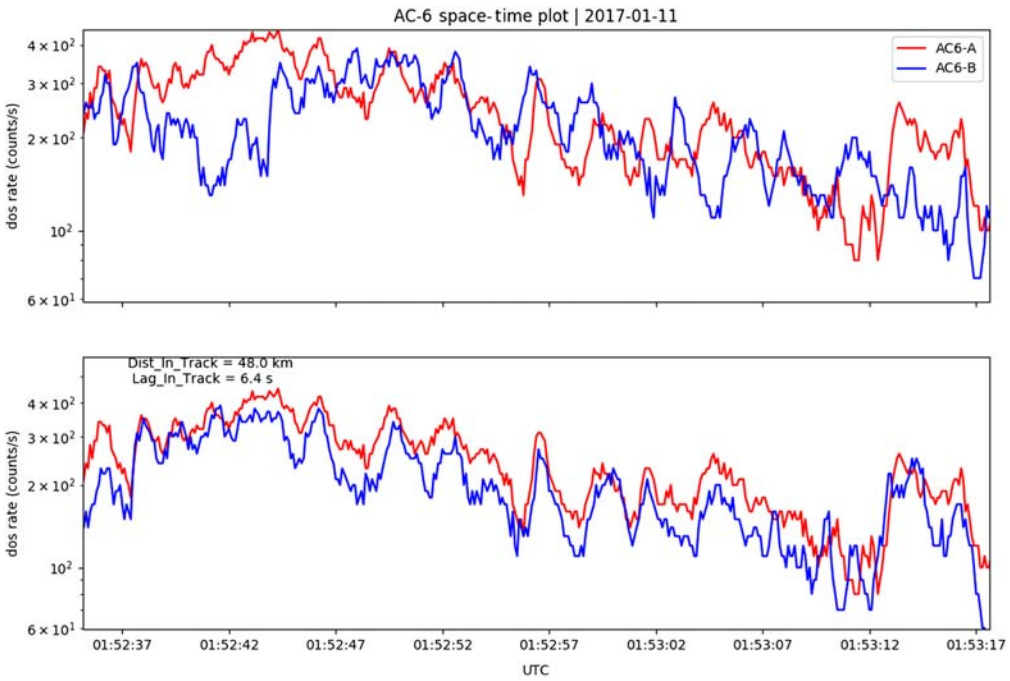

Figure 5.12 AC6 data plotted lined up in time (top) and lined up in spatial position (bottom). The bottom plot has shifted AC6-B to the left by 6.4 s which matches the time for AC6-B to reach the same position as AC-6-A at this time.

A study by Anderson et al. (2017) showed some of the possible utility of combining balloon and CubeSat observations to look at the largest scales of precipitating regions. Using AC6, BARREL, and FIREBIRD they were able to map out the microburst precipitation region across several hours of time, many hours of MLT, and several L-shells. The persistent observation perspective of the balloon platform combined with the revisit times of multiple satellites provided a more complete picture than any single satellite or balloon could. As more CubeSat missions come online, the case for central clearing houses of data to make such large-scale coordinated observations possible becomes more obvious.

Publicly available data analysis tools and open-source software tools to process and view disparate data sets are also of great utility. The Space Physics Environment Data Analysis System (SPEDAS) (Angelopoulos et al., 2019) is one data analysis system that allows a user to pull data from numerous missions, including BARREL. Autoplot (Faden et al., 2010) and SpacePy (Morley et al., 2010) are two additional, commonly used, open-source tools. Various implementations of magnetic field models can be accessed by the open source IRBEM library (Boscher et al., 2010) allowing magnetic conjunctions between missions to be more easily computed as well. Since SPEDAS and these others are community driven, additional missions including CubeSats can be added as they are developed. There is also substantial use in multimission orbit plotters/predictors such as the Van Allen probes multimission plotter, available on their web gateway, and the SSCWeb system which is part of the Goddard Space Physics Data Facility (SPDF) which can be used to find conjunctions between numerous spacecraft. This system has recently guided FIREBIRD-II's data taking when in conjunction with POES and Arase.

Another demonstration of the combination of balloon, CubeSat, and high-altitude measurements can be found in Blum et al. (2013) who used joint observations from CSSWE and BARREL to look at the scale of precipitation bands, high-energy regions that LEO satellites have observed for many decades. LEO satellites traverse these regions rather quickly, while a balloon remains stationary underneath them. Combining these perspectives allows for a thorough investigation of their spatial structure, time evolution, energy spectrum, and importance for the radiation belts. Blum found a direct connection between LEO satellite-observed bands and balloon-observed REP, connecting two disparate measurement regimes for the first time. Further, they explored the spatial regions of precipitation and found that a significant percent (5%) of radiation belt relativistic electrons were lost in one individual event, in line with estimates from the average loss-rate measured by MAXIS balloons alone (Millan et al., 2002). Zhang et al. (2016) used the same combination of CSSWE and BARREL to further refine the loss-rate from precipitation and used CSSWE to show abundant >600 keV electrons in the slot region during disturbed geomagnetic conditions.

5.5 Looking forward

Although balloon measurements of EEP have been made from the earliest days of the space age, many outstanding questions remain, and balloons can still contribute to answering these questions. Balloons represent a unique observing perspective and combining balloon-based measurements with satellite observations of EEP provides a more complete picture of the spatial evolution and time evolution of EEP. CubeSats are rapidly improving the frequency and variety of EEP measurement. SAMPEX with its long life, high-geometric−factor and microburst-time−resolution from HILT (e.g., Blake et al., 1996) and some energy resolution from PET (e.g., Comess et al., 2013) has been an essential tool for understanding EEP. However, it has had limitations; it was a single-point measurement, with limited energy resolution, indirect pitch-angle measurements, and little overlap with comprehensive high-altitude wave, energetic particle, and plasma measurements. The POES satellites have proven valuable in understanding EEP (e.g., Yahnin et al., 2016; Shekhar et al., 2017; Rodger et al., 2010). POES measures electrons in several energy channels and two pitch angle bins. There are many POES satellites and the ongoing POES measurements have long-term historical data, but POES measurements have limited time and energy resolution and high-energy response only from contamination (Yando et al., 2011).

CubeSats are flying and in-development to augment these LEO measurements of EEP. CSSWE demonstrated important, energy-resolved measurements of precipitation, and FIREBIRD and AC6 have shown the significant power of multipoint, close-separation measurements. Indeed, AC6 measurements at close range show that there are still time and spatial regimes to be examined, and that a smooth-spatial, slow-evolution picture of the precipitation environment is false. This complicated precipitation picture should come as no surprise given the structured and dynamic aurora at lower energies. Future CubeSat missions allow us to explore this complicated picture with increased capabilities. The recently launched ELFIN mission will provide energy and pitch angle-resolved measurements from a pair of spinning CubeSats. The recently-selected REAL CubeSat will provide a wide energy-range of instantaneous precipitating pitch-angle distributions fast enough to resolve the pitch-angle distribution of individual microbursts. SNIPE is planned to fly up to four CubeSats in formation to further characterize the evolution and spatial distribution of EEP. Many of these are flying or will fly in the Van Allen probes era, or with Arase, improved GOES measurements, or even during active radiation-belt remediation experiments from soon-to-be-launched DSX or proposed field-line mapping experiments. CubeSats, including the in-development GTOSat scheduled for the early 2020s, are starting to move beyond LEO and may provide additional equatorial reference points even after the Van Allen Probe mission ends.

Individual CubeSats (or pairs) are an exciting expansion of our measurement capabilities, but perhaps the most interesting results will come from future combinations of CubeSat and balloon measurements or from constellations of CubeSats that allow us to separate spatial and temporal variations in precipitation. For imaging small scales, balloons provide an advantage because of their nearly stationary nature which allows for the separation of temporal and spatial variations at a range of scales. The recently-selected BOOMS mission will image the spatial distribution of energetic electron precipitation that, when combined by an ever-solidifying understanding of the theory of wave-particle interactions, will allow remote imaging of wave regions, understanding of the spatial scale of loss processes, and quantifying, understanding the physics of, and predicting the significance of EEP's contribution to the dynamic radiation belt balance. All these goals depend on continuing contributions from funding agencies, support for heliophysics balloons, carefully calibrated instruments, coordinated observations, the creativity of the community in overcoming CubeSat data pipeline limitations, other CubeSat limitations, and finally public availability of wide-ranging data sources. While more work is always to be done, it has been, and continues to be, an exciting time for understanding EEP.

References

Anderson, K.A., Milton, D.W., 1964. Balloon observations of X rays in the auroral zone: 3. High time resolution studies. J. Geophys. Res. 69 (21), 4457–4479.

Anderson, K.A., Chase, L.M., Hudson, H.S., Lampton, M., Milton, D.W., Parks, G.K., 1966. Balloon and rocket observations of auroral-zone microbursts. J. Geophys. Res. 71 (19), 4617–4629.

Anderson, B.R., Shekhar, S., Millan, R.M., Crew, A.B., Spence, H.E., Klumpar, D.M., et al., 2017. Spatial scale and duration of one microburst region on 13 August 2015. J. Geophys. Res. Space Phys. 122 (6), 5949–5964.

Angelopoulos, V., Cruce, P., Drozdov, A., Grimes, E.W., Hatzigeorgiu, N., King, D.A., et al., 2019. The space physics environment data analysis system (SPEDAS). Space Sci. Rev. 215 (1), 9.

Baker, D.N., Kanekal, S.G., Hoxie, V.C., Batiste, S., Bolton, M., Li, X., et al., 2012. The relativistic electron-proton telescope (REPT) instrument on board the radiation belt storm probes (RBSP) spacecraft: characterization of Earth's radiation belt high-energy particle populations. The Van Allen Probes Mission. Springer, Boston, MA, pp. 337–381.

Barcus, J.R., Brown, R.R., Rosenberg, T.J., 1966. Spatial and temporal character of fast variations in auroral-zone X rays. J. Geophys. Res. 71 (1), 125–141.

Blake, J.B., O'Brien, T.P., 2016. Observations of small-scale latitudinal structure in energetic electron precipitation. J. Geophys. Res. Space Phys. 121 (4), 3031–3035.

Blake, J.B., Looper, M.D., Baker, D.N., Nakamura, R., Klecker, B., Hovestadt, D., 1996. New high temporal and spatial resolution measurements by SAMPEX of the precipitation of relativistic electrons. Adv. Space Res. 18 (8), 171–186.

Blum, L.W., Schiller, Q., Li, X., Millan, R., Halford, A., Woodger, L., 2013. New conjunctive CubeSat and balloon measurements to quantify rapid energetic electron precipitation. Geophys. Res. Lett. 40 (22), 5833–5837.

Boscher, D., Bourdarie, S., O'Brien, P., Guild, T., 2010. IRBEM Library V4. 3, 2004–2008. ONERA-DESP, Toulouse France, Aerospace Corporation, Washington, DC.

Breneman, A.W., Halford, A., Millan, R., McCarthy, M., Fennell, J., Sample, J., et al., 2015. Global-scale coherence modulation of radiation-belt electron loss from plasmaspheric hiss. Nature 523 (7559), 193.

Breneman, A.W., Crew, A., Sample, J., Klumpar, D., Johnson, A., Agapitov, O., et al., 2017. Observations directly linking relativistic electron microbursts to whistler mode chorus: Van Allen Probes and FIREBIRD II. Geophys. Res. Lett. 44, 22.

Brown, R.R., Barcus, J.R., Parsons, N.R., 1965. Balloon observations of auroral zone X rays in conjugate regions: 2. Microbursts and pulsations. J. Geophys. Res. 70 (11), 2599–2612.

Clilverd, M.A., Rodger, C.J., McCarthy, M., Millan, R., Blum, L.W., Cobbett, N., et al., 2017. Investigating energetic electron precipitation through combining ground-based and balloon observations. J. Geophys. Res. Space Phys. 122 (1), 534–546.

Comess, M.D., Smith, D.M., Selesnick, R.S., Millan, R.M., Sample, J.G., 2013. Duskside relativistic electron precipitation as measured by SAMPEX: a statistical survey. J. Geophys. Res. Space Phys. 118 (8), 5050–5058.

Crew, A.B., Spence, H.E., Blake, J.B., Klumpar, D.M., Larsen, B.A., O'Brien, T.P., et al., 2016. First multipoint in situ observations of electron microbursts: initial results from the NSF FIREBIRD II mission. J. Geophys. Res. Space Phys. 121 (6), 5272–5283.

Datta, S., Skoug, R.M., McCarthy, M.P., Parks, G.K., 1996. Analysis and modeling of microburst precipitation. Geophys. Res. Lett. 23 (14), 1729–1732.

Faden, J.B., Weigel, R.S., Merka, J., Friedel, R.H., 2010. Autoplot: a browser for scientific data on the web. Earth Sci. Inf. 3 (1–2), 41–49.

Foat, J.E., Lin, R.P., Smith, D.M., Fenrich, F., Millan, R., Roth, I., et al., 1998. First detection of a terrestrial MeV X-ray burst. Geophys. Res. Lett. 25 (22), 4109–4112.

Hwang, J., Kim, H., Park, J., Lee, J., 2018. Limitations of electromagnetic ion cyclotron wave observations in low earth orbit. J. Astron. Space Sci. 35 (1), 31–37.

Jaynes, A.N., Li, X., Schiller, Q.G., Blum, L.W., Tu, W., Turner, D.L., et al., 2014. Evolution of relativistic outer belt electrons during an extended quiescent period. J. Geophys. Res. Space Phys. 119 (12), 9558–9566.

Kokorowski, M., 2008. Energetic particle precipitation effects on the electrodynamics of the coupled magnetosphere-ionosphere-atmosphere. Doctoral dissertation, University of Washington.

Li, X., Schiller, Q., Blum, L., Califf, S., Zhao, H., Tu, W., et al., 2013a. First results from CSSWE CubeSat: characteristics of relativistic electrons in the near-Earth environment during the October 2012 magnetic storms. J. Geophys. Res. Space Phys. 118 (10), 6489–6499.

Li, Z., Millan, R.M., Hudson, M.K., 2013b. Simulation of the energy distribution of relativistic electron precipitation caused by quasi-linear interactions with EMIC waves. J. Geophys. Res. Space Phys. 118 (12), 7576–7583.

Li, Z., Millan, R.M., Hudson, M.K., Woodger, L.A., Smith, D.M., Chen, Y., et al., 2014. Investigation of EMIC wave scattering as the cause for the BARREL 17 January 2013 relativistic electron precipitation event: a quantitative comparison of simulation with observations. Geophys. Res. Lett. 41 (24), 8722–8729.

Lorentzen, K.R., McCarthy, M.P., Parks, G.K., Foat, J.E., Millan, R.M., Smith, D.M., et al., 2000. Precipitation of relativistic electrons by interaction with electromagnetic ion cyclotron waves. J. Geophys. Res. Space Phys. 105 (A3), 5381–5389.

Mauk, B.H., Chin, J., Parks, G., 1981. Auroral X ray images. J. Geophys. Res. Space Phys. 86 (A8), 6827–6835.

Millan, R.M., 2002. X-ray observations of MeV electron precipitation with a balloon-borne germanium spectrometer. Doctoral dissertation, UC Berkeley.

Millan, R.M., Thorne, R.M., 2007. Review of radiation belt relativistic electron losses. J. Atmos. Sol. Terres. Phys. 69 (3), 362–377.

Millan, R.M., Lin, R.P., Smith, D.M., Lorentzen, K.R., McCarthy, M.P., 2002. X-ray observations of MeV electron precipitation with a balloon-borne germanium spectrometer. Geophys. Res. Lett. 29 (24), 47-1.

Millan, R.M., Lin, R.P., Smith, D.M., McCarthy, M.P., 2007. Observation of relativistic electron precipitation during a rapid decrease of trapped relativistic electron flux. Geophys. Res. Lett. 34 (10).

Millan, R.M., McCarthy, M.P., Sample, J.G., Smith, D.M., Thompson, L.D., McGaw, D.G., et al., 2013. The balloon array for RBSP relativistic electron losses (BARREL). The Van Allen Probes Mission. Springer, Boston, MA, pp. 503–530.

Morley, S.K., Welling, D.T., Koller, J., Larsen, B.A., Henderson, M.G., 2010. Spacepy—A Python-Based Library of Tools for the Space Sciences (No. LA-UR-10-04308; LA-UR-10-4308). Los Alamos National Lab. (LANL), Los Alamos, NM.

Mozer, F.S., Agapitov, O.V., Blake, J.B., Vasko, I.Y., 2018. Simultaneous observations of lower band chorus emissions at the equator and microburst precipitating electrons in the ionosphere. Geophys. Res. Lett. 45 (2), 511–516.

National Academies of Sciences, Engineering, and Medicine, 2016. Achieving Science With CubeSats: Thinking Inside the Box. National Academies Press.

National Research Council, 2003. The Sun to the Earth—and Beyond: A Decadal Research Strategy in Solar and Space Physics. The National Academies Press, Washington, DC. Available from: https://doi.org/10.17226/10477.

Parks, G.K., 1967. Spatial characteristics of auroral-zone X-ray microbursts. J. Geophys. Res. 72 (1), 215–226. Available from: http://doi.org/10.1029/JZ072i001p00215.

Parks, G.K., Coroniti, F.V., McPherron, R.L., Anderson, K.A., 1968. Studies of the magnetospheric substorm: 1. Characteristics of modulated energetic electron precipitation occurring during auroral substorms. J. Geophys. Res. 73 (5), 1685–1696.

Parks, G.K., Gurgiolo, C., West, R., 1979. Relativistic electron precipitation. Geophys. Res. Lett. 6 (5), 393–396.

Parks, G.K., 1978. Microburst precipitation phenomena. Journal of geomagnetism and geoelectricity 30 (4), 327–341.

Parks, G.K., Freeman, T.J., Mccarthy, M.P., Werden, S.H., 1993. The discovery of auroral X-rays by balloon-borne detectors and their contributions to magnetospheric research, Auroral Plasma Dynamics, vol. 80. American Geophysical Union Geophysical Monograph Series, Washington, DC, pp. 17–23.

Rodger, C.J., Clilverd, M.A., Green, J.C., Lam, M.M., 2010. Use of POES SEM-2 observations to examine radiation belt dynamics and energetic electron precipitation into the atmosphere. J. Geophys. Res. Space Phys. 115 (A4).

Rosenberg, T.J., Foster, J.C., Matthews, D.L., Sheldon, W.R., Benbrook, J.R., 1977. Microburst electron precipitation at $L \approx 4$. J. Geophys. Res. 82 (1), 177–180.

Saito, S., Miyoshi, Y., Seki, K., 2012. Relativistic electron microbursts associated with whistler chorus rising tone elements: GEMSIS-RBW simulations. J. Geophys. Res. Space Phys. 117 (A10).

Sample, J.G., 2013. The MINIS balloon campaign: duskside relativistic electron precipitation. Doctoral dissertation, UC Berkeley.

Schiller, Q., Tu, W., Ali, A.F., Li, X., Godinez, H.C., Turner, D.L., et al., 2017. Simultaneous event-specific estimates of transport, loss, and source rates for relativistic outer radiation belt electrons. J. Geophys. Res. Space Phys. 122 (3), 3354–3373.

Shekhar, S., Millan, R., Smith, D., 2017. A statistical study of the spatial extent of relativistic electron precipitation with polar orbiting environmental satellites. J. Geophys. Res. Space Phys. 122 (11).

Shumko, M., Sample, J., Johnson, A., Blake, B., Crew, A., Spence, H., et al., 2018. Microburst scale size derived from multiple bounces of a microburst simultaneously observed with the FIREBIRD-II CubeSats. Geophys. Res. Lett. 45 (17), 8811–8818.

Skoug, R.M., 1995. The origin of narrow band cyclotron wave emissions called chorus. Ph.D. thesis. University of Washington, Seattle.

Smith, D.M., Lin, R.P., Anderson, K.A., Hurley, K., Johns, C.M., 1995. High-resolution spectra of 20–300 keV hard X-rays from electron precipitation over Antarctica. J. Geophys. Res. Space Phys. 100 (A10), 19675–19685.

Trefall, H., Bjordal, J., Ullaland, S.L., Stadsnes, J., 1966. On the extension of auroral-zone X-ray microbursts. J. Atmos. Terres. Phys. 28 (2), 225–233.

Tsyganenko, N.A., 1989. A magnetospheric magnetic field model with a warped tail current sheet. Planet. Space Sci. 37 (1), 5–20.

Tsurutani, B.T., Lakhina, G.S., Verkhoglyadova, O.P., 2013. Energetic electron (>10 keV) microburst precipitation, ~5–15 s X-ray pulsations, chorus, and wave-particle interactions: A review. J. Geophys. Res. Space Phys. 118 (5), 2296–2312.

Twiggs, R., 2008. Origin of CubeSat. In: Helvajian, H., Janson, S.W. (Eds.), Small Satellites: Past, Present, and Future. The Aerospace Press, El Segundo, CA.
Werden, S.H., Parks, G.K., 1987. Auroral X-ray images during a pulsation event. In: European Rocket & Balloon Programmes and Related Research. vol. 270.
West, R.H., Parks, G.K., 1984. ELF emissions and relativistic electron precipitation. J. Geophys. Res. Space Phys. 89 (A1), 159–167.
Winckler, J.R., Peterson, L., 1957. Large auroral effect on cosmic-ray detectors observed at 8 g/cm 2 atmospheric depth. Phys. Rev. 108 (3), 903.
Winckler, J.R., Bhavsar, P.D., Anderson, K.A., 1962. A study of the precipitation of energetic electrons from the geomagnetic field during magnetic storms. J. Geophys. Res. 67 (10), 3717–3736.
Woodger, L.A., Halford, A.J., Millan, R.M., McCarthy, M.P., Smith, D.M., Bowers, G.S., et al., 2015. A summary of the BARREL campaigns: technique for studying electron precipitation. J. Geophys. Res. Space Phys. 120 (6), 4922–4935.
Woodger, L.A., Millan, R.M., Li, Z., Sample, J.G., 2018. Impact of background magnetic field for EMIC wave-driven electron precipitation. J. Geophys. Res. Space Phys. 123 (10), 8518–8532.
Yahnin, A.G., Yahnina, T.A., Semenova, N.V., Gvozdevsky, B.B., Pashin, A.B., 2016. Relativistic electron precipitation as seen by NOAA POES. J. Geophys. Res. Space Phys. 121 (9), 8286–8299.
Yamagami, T., Miyaoka, H., Nakamoto, A., Hirasima, Y., Ohta, S., Namiki, M., et al., 1990. Two-dimensional auroral X-ray image observation at a balloon altitude in the northern auroral zone. J. Geomagn. Geoelectr. 42 (10), 1175–1191.
Yando, K., Millan, R.M., Green, J.C., Evans, D.S., 2011. A Monte Carlo simulation of the NOAA POES medium energy proton and electron detector instrument. J. Geophys. Res. Space Phys. 116 (A10).
Zhang, J., Halford, A.J., Saikin, A.A., Huang, C.L., Spence, H.E., Larsen, B.A., et al., 2016. EMIC waves and associated relativistic electron precipitation on 25–26 January 2013. J. Geophys. Res. Space Phys. 121 (11), 11–086.

Further reading

Rosenberg, T.J., Wei, R., Detrick, D.L., Inan, U.S., 1990. Observations and modeling of wave-induced microburst electron precipitation. J. Geophys. Res. Space Phys. 95 (A5), 6467–6475.

CHAPTER 6

Incoherent scatter radar observations of 10–100 keV precipitation: review and outlook

Stephen R. Kaeppler[1], Ennio Sanchez[2], Roger H. Varney[2], Robert J. Irvin[2,3], Robert A. Marshall[4], Jacob Bortnik[5], Ashton S. Reimer[2] and Pablo M. Reyes[2]

[1]Department of Physics and Astronomy, Clemson University, Clemson, SC, United States
[2]SRI International, Menlo Park, CA, United States
[3]Department of Electrical and Computer Engineering, University of Illinois at Urbana-Champaign, Urbana, IL, United States
[4]Ann and H. J. Smead Department of Aerospace Engineering Sciences, University of Colorado, Boulder, CO, United States
[5]Department of Atmospheric and Oceanic Sciences, University of California, Los Angeles, CA, United States

Contents

6.1 Introduction

Magnetospheric precipitation of electrons with energies from tens to hundreds of keV can cause ionization in the E- and D-regions of the ionosphere. The optical manifestation of energetic electron precipitation is known as the aurora (e.g., McIlwain, 1960), which is broadly characterized as being either discrete or diffuse. Multiple mechanisms

The Dynamic Loss of Earth's Radiation Belts
DOI: https://doi.org/10.1016/B978-0-12-813371-2.00006-8

can cause ions and electrons to be accelerated to 10–100 keV energies that are subsequently precipitated into the atmosphere. The picture that has emerged for discrete auroral arcs involves parallel electric fields generated along a magnetic flux tube, which accelerate particles toward the ionosphere; these particles generate visible auroral emissions and cause enhanced ionization at E-region altitudes (e.g., Evans, 1974; Carlson et al., 1998; Kaeppler, 2013, and references therein). For the case of diffuse auroral precipitation and pulsating aurorae, the dominant mechanism thought to cause precipitation is wave-particle interactions near the geomagnetic equator (e.g., Kennel and Petschek, 1966; Johnstone, 1978; Thorne et al., 2010; Ni et al., 2011a,b; Nishimura et al., 2010, 2011, 2013; Lessard, 2013; Miyoshi et al., 2015; Kasahara et al., 2018). In the classic picture of diffuse aurorae, wave-particle interactions cause pitch-angle scattering, in which particles effectively execute a random walk in pitch angle phase space until they enter the loss cone (e.g., Kennel and Petschek, 1966).

Wave-particle interactions in the inner magnetosphere are thought to be the dominant mechanism that causes loss of very high energy (>100 keV) radiation belt particles into the atmosphere–thermosphere–ionosphere (see reviews by Millan and Thorne, 2007; Thorne, 2010). These highly energetic particles can have an optical and ionization response in the lower altitude D-region even for modest number fluxes (e.g., Marshall et al., 2014). One of the most important outstanding questions is how to understand and quantify the loss processes associated with high-energy particle precipitation—specifically, to understand which plasma waves in the inner magnetosphere are responsible for enhanced pitch-angle scattering, which subsequently causes the losses that are observed in the D-region. A variety of plasma waves are thought to contribute to particle precipitation, including whistler-mode lower-band chorus, whistler-mode plasmaspheric hiss, electromagnetic ion-cyclotron waves, and electron cyclotron harmonic (ECH) waves (e.g., Millan and Thorne, 2007; Nishimura et al., 2010; Thorne, 2010; Thorne et al., 2010). However, despite the observed correlation between certain types of precipitation and contemporaneous waves in the magnetosphere, whether any of these wave modes are responsible for the different types of observed precipitation is exceptionally difficult to verify directly.

To make definitive observations that correlate plasma waves to particle precipitation into the atmosphere requires simultaneous observations along the magnetic flux tube, ideally near the geomagnetic equator, and at the ionospheric footpoint. From a purely in situ perspective, this is a requirement is a challenge to achieve, although Kasahara et al. (2018) have made direct conjugate observations of driving chorus waves and pulsating aurorae. However, in some cases, the waves that drive precipitation in space are coherent across relatively large spatial scales, so an ideal (point-to-point) conjunction is not a strict requirement for observing coincident wave modulation in space and precipitation on the ground. The Balloon Array for Radiation Belt Relativistic Electron Losses (BARREL) mission was developed to investigate energetic

precipitation using X-ray detectors aboard balloons launched from Antarctica (e.g., Millan, 2011; Millan et al., 2013; Woodger et al., 2015). The BARREL mission was composed of two campaigns, with many individual scientific investigations resulting from these observations (e.g., Blum et al., 2013; Li et al., 2013, 2014; Woodger et al., 2015; Halford et al., 2015, 2016; Breneman et al., 2015). One notable result was by Breneman et al. (2015), who performed a detailed examination of the coherence properties of electromagnetic plasmaspheric hiss waves and multiballoon precipitation. They found that the observed precipitation signature exhibited coherence scales over spatial regions as wide as $\sim$3.5–4 hours in magnetic local time (MLT). One of the limitations of this method is that the experiment is temporally constrained to intervals when the balloons are airborne.

Ground-based optical and radar observatories provide a potential solution to this temporal constraint (e.g., Marshall et al., 2014) by effectively fixing the ionospheric footpoint, although these methods can be spatially constrained. However, there are two requirements for a ground-based observatory to be used. First, the satellite must magnetically map to within an acceptable distance from the field of the view of the observatory. Second, the physics describing the observable (e.g., enhanced electron density, visual light emission, etc.) must be understood well enough that the observable can be appropriately modeled. Routine observations of the D-region have been conducted since 2007 with the Poker Flat Incoherent Scatter Radar (PFISR). Since 2015, an incoherent scatter radar (ISR) mode that has sensitivity appropriate for the resolution of enhanced E- and D-region electron density enhancements has been run during near-conjunctions with both the Van Allen Probes (hereafter referred to as "RBSP") and Arase satellites.

This chapter presents a review and outlook of ground-based ISR techniques and observations of energetic precipitation, with energies predominantly in the 10–100 keV range that impact the E- and D-regions of the ionosphere. The ISR observations are most sensitive to the impact of 10–100 keV precipitation, and we further focus this review primarily on electron precipitation. We restrict our attention to ISR-based observations rather than presenting results from all ground-based techniques, and we focus primarily on observations from PFISR, which is located near Poker Flat, Alaska, USA. Section 6.2 reviews the methodology used to generate the forward model that describes how precipitation generates enhanced electron density that can be observed by the ISR. This includes a review of precipitation physics described by transport and chemistry models, and also a discussion of ISR techniques for "inverting" electron number density to estimate the precipitating differential number flux. Section 6.3 reviews phenomena that produce energetic particle precipitation, including a brief review of substorms and pulsating aurora. Section 6.4 provides an overview of the radar mode that is run at PFISR specifically to make observations of enhanced E- and D-region electron density. Section 6.5 presents a summary of

observations that have been collected, and there we show an example event from January 13, 2015, of D-region ionization, including preliminary analysis of this event. Finally, we conclude with a summary and outlook with an emphasis on open questions that can be addressed using ISR observations.

6.2 Review of methodology

ISRs measure backscattered power that is proportional to electron density in the ionosphere (e.g., Dougherty and Farley, 1961; Evans, 1969). To quantify electron density enhancements, a forward model that characterizes the physics of particle precipitation must be developed. Transport models describe the physics of how particle precipitation generates ionization enhancements, while chemistry models describe how ionization modifies the background electron density. In this section, we briefly review particle transport processes and chemistry and provide a brief review of techniques used to estimate particle differential number flux from enhanced electron density measurements.

6.2.1 Particle transport and ionization

6.2.1.1 Empirical models

Three methods have been developed to model transport and ionization physics caused by particle precipitation from the magnetosphere to the ionosphere: empirically derived methods from laboratory experiments, numerical solutions to transport equations, and Monte Carlo methods. We first describe the laboratory-based empirical methods. McIlwain (1960) discovered that visual discrete aurorae were caused by precipitating electrons and further inferred that these particles were likely accelerated up to keV energies by parallel electric fields. To quantify the impact of ionization on the ionosphere–thermosphere system, Rees (1963) derived a relation between the differential number flux incident to the ionosphere (Φ_{top}) and the altitude distribution of ionization, $q(z)$,

$$q(z) = \frac{\lambda[z/R(E)]\rho(z)E\Phi_{top}(E)}{R(E)\Delta E} \tag{6.1}$$

where E is energy, $\rho(z)$ is the atmospheric mass density (e.g., Picone et al., 2002) as a function of altitude, $R(E)$ the experimentally derived range energy function, λ $[z/R(E)]$ the fraction of energy lost per fraction of mass distance traveled (Semeter and Kamalabadi, 2005), and z the altitude along the magnetic flux tube. An average value for ΔE of 35 eV is commonly used (e.g., Rees, 1963; Semeter and Kamalabadi, 2005). Also, Semeter and Kamalabadi (2005) provide a table of values for λ $[z/R(E)]$.

The critical aspect that enables this calculation is the definition of an experimentally derived range-energy function, $R(E)$. The range-energy function (related to the

stopping power) specifies the amount of mass that an incident flux with a particular energy, E, will penetrate, and has units of kg/m^2. This function can be used to calculate the stopping altitude, which is the altitude at which a precipitating particle has experienced enough collisions and has lost enough energy to become indistinguishable from the background population (Kivelson and Russell, 1995). The stopping altitude occurs at

$$R(E) = \int_{z_{stop}}^{\infty} p(z')dz' \tag{6.2}$$

where z_{stop} is the stopping altitude (Kivelson and Russell, 1995). Grün (1957) was one of the first to quantify the range-energy function using a laboratory experiment that fired a beam of monoenergetic electrons between 5 and 54 keV into a nitrogen-filled chamber and measured optical emission from N_2^+ (see Rees, 1989, for an experimental diagram). The results of Grün (1957) were used directly in Rees (1963). These laboratory experiments were expanded and updated by Barrett and Hays (1976) for a continuous range of energies of 0.3–54 keV. Sergienko and Ivanov (1993) instead used a Monte Carlo simulation, along with laboratory results of excitation energy thresholds, to calculate the ionization as a function of altitude for auroral precipitation. Kirkwood and Osepian (1995) summarized range-energy relations for protons and electrons, which are shown in Table 6.1. Fig. 6.1 shows the stopping altitude for both protons and electrons using equations found in Table 6.1. It is clear from Fig. 6.1 that protons require higher energies than electrons to penetrate to the same altitude. Fig. 6.1 also gives reference depths in the thermosphere and mesosphere that ionization is likely to penetrate given a specific energy. The advantage of the empirically derived range-energy functions is that they are computationally efficient to calculate compared to other methods.

Table 6.1 Range-energy functions for electrons and ions.

Electrons	**Valid energy (keV)**
$R(E)^{a} = 4.57 \times 10^{-5} E^{1.75}$	5–54
$R(E)^{b} = 4.30 \times 10^{-6} + 5.36 \times 10^{-5} E^{1.67} - 0.38 \times 10^{-7} E^{-0.7}$	0.3–5
$R(E)^{b} = 5.50 \times 10^{-5} E^{1.66}$	5–54
$R(E)^{c} = 1.804 \times 10^{-5} E^{1.67} (1 + 9.48 \times 10^{-2} E^{-1.57})$	
Protons	**Valid energy (keV)**
$R(E)^{d} = 2.059 \times 10^{-5} E^{1.13}$	< 10
$R(E)^{d} = 5.415 \times 10^{-5} E^{0.71}$	10–300
$R(E)^{d} = 5.415 \times 10^{-5} \times 300^{0.71} + 2.5 \times 10^{-8} (E - 300)^2$	> 300

[a]Grün (1957),
[b]Barrett and Hays (1976),
[c]Sergienko and Ivanov (1993),
[d]Kirkwood and Osepian, (1995), and references therein. The units in this table are kg/m^2.

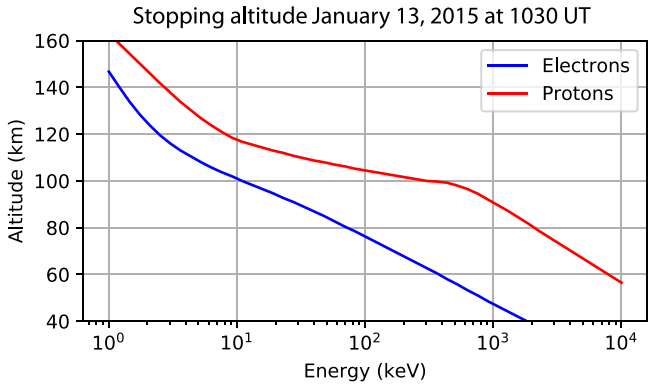

Figure 6.1 The stopping altitude of protons and electrons using a NRLMSISE-00 (Picone et al., 2002) thermosphere on January 13, 2015. The equations used can be found in Table 6.1 for protons (*red*) and electrons (*blue*).

6.2.1.2 Transport models

The second method to quantify transport is to use first-principle physics and solve the Boltzmann equation directly. The Boltzmann equation describes the time evolution of the phase space distribution for ions and electrons (e.g., Baumjohann and Treumann, 2012; Schunk and Nagy, 2004). The differential number flux, $\Phi(E)$ can be related back to the phase space distribution function, $f(\mathbf{x}, \mathbf{v})$ using the following relation,

$$\Phi(E) = \frac{2E}{m_e^2} f(\mathbf{x}, \mathbf{v}) \tag{6.3}$$

where the energy E has units of eV, $f(\mathbf{x}, \mathbf{v})$ has units of s^3/m^6, the electron mass m_e has units of eV/c^2, and $\Phi(E)$ has units of $m^{-2}\ s^{-1}\ eV^{-1}$ (Baumjohann and Treumann, 2012).

In the early 1970s, Nagy and Banks (1970) and Banks and Nagy (1970) developed a two-stream approach to quantify the transport of photoelectrons similar to the radiative transport equations for two streams. The radiative transport equations solve for an upward and downward flux in a thin slab of the atmosphere (Chandrasekhar, 1960; Coakley and Chylek, 1975). The two-stream approximation similarly divides the particle flux into two directions by integrating in pitch angle from 0 to 90 degrees (upward, +) and over 90 to 180 degrees (downward, −), as represented by the follow equations (Schunk and Nagy, 2004):

$$\Phi^+(r) = \int_0^{2\pi} d\phi \int_0^1 d\mu \Phi(\phi, \mu, r) \tag{6.4a}$$

$$\Phi^{-}(r) = \int_{0}^{2\pi} d\phi \int_{-1}^{0} d\mu \Phi(\phi, \mu, r) \tag{6.4b}$$

ϕ is the azimuthal dimension, μ is the pitch-angle cosine, and r corresponds approximately to altitude. This approximation reduces a three-dimensional (3-D) transport problem to one-dimension (1-D) along the local geomagnetic field if we consider only altitude variations. Following Schunk and Nagy (2004),

$$\langle \cos \alpha \rangle \frac{\partial \Phi^{+}}{\partial r} = -n_s \sigma_s^t \Phi^{+} + \frac{n_s \sigma_s^e}{2} \left(\Phi^{+} + \Phi^{-} \right) + \frac{Q_0}{2} \tag{6.5a}$$

$$-\langle \cos \alpha \rangle \frac{\partial \Phi^{-}}{\partial r} = -n_s \sigma_s^t \Phi^{-} + \frac{n_s \sigma_s^e}{2} \left(\Phi^{+} + \Phi^{-} \right) + \frac{Q_0}{2} \tag{6.5b}$$

$$Q_0(r) = \int_{0}^{2\pi} d\phi \int_{-1}^{1} d\mu P_e(\phi, \mu, r) \tag{6.5c}$$

where σ_s^t and σ_s^e correspond to the total and elastic cross sections for species s, n_s is the background number density, P_e is the electron production rate, and $\langle \cos \alpha \rangle$ is the average cosine of the pitch angle. Banks et al. (1974) extended this transport model to auroral particle precipitation and also included the generation of secondary electrons from the primary auroral electrons. Evans (1974) compared model results from Banks et al. (1974) with observations of precipitating auroral electrons from the Injun 5 satellite; Evans (1974, Fig. 7) showed good agreement between the secondary electrons observed by the satellite and model results. More recently, Solomon et al. (1988) applied the two-stream approximation to describe the transport of electrons in the GLobal airglOW model (GLOW), which quantifies airglow brightness at a variety of wavelengths driven by solar extreme ultraviolet (EUV) light and particle precipitation. Solomon (2017) has updated the GLOW model in support of the NASA Global-scale Observations of the Limb and Disk (GOLD) mission. Solomon (2001) compared the two-stream approximation with Monte Carlo simulations of auroral particle precipitation and found good agreement between the two methods. Many studies have used or applied the two-stream approximation for describing the transport of photo- and auroral-electrons (e.g., Stamnes, 1980, 1981; Link et al., 1988; Link, 1992; Richards and Torr, 1985, 1990; Richards et al., 2000) One of the advantages of the two-stream approximation, besides its relative simplicity, is that the GLOW model is open source and can be found at https://github.com/NCAR/GLOW. This version is consistent with the updates in Solomon (2017).

Strickland et al. (1976) developed an alternative formulation that directly solved the 1-D transport equations parallel to the geomagnetic field. In this formulation, the 1-D Boltzmann equation was solved as a function of pitch angle, energy, and altitude along a geomagnetic flux tube, which the authors termed the "equation of transfer." In addition, Strickland et al. (1976) also derived the Fokker–Planck equation as an approximate solution to the equation of transfer. The Fokker–Planck equation was solved using an eigenvalue technique and was found to be in generally good agreement with the equation of transfer. Note that Strickland et al. (1976) examined only electron precipitation; Strickland et al. (1989) expanded on that model to specifically quantify optical emission brightness as a function of the characteristic energy of electron precipitation and the response of these emission lines with respect to changes in neutral composition. Specifically, Strickland et al. (1989) modeled the response of 427.8-, 630.0-, 777.4-, and 844.6-nm emissions. Strickland et al. (1993) and Basu et al. (1993) extended the auroral electron model by Strickland et al. (1976) to directly solve the Boltzmann transport equations for electrons, protons, and hydrogen as a function of pitch angle, energy, and altitude. This three-species model is sometimes referred to as the "BC3" model and represents one of the most complete models to date describing the transport of particles into the auroral zone (J. Hecht, private communication, 2015). However, note that the source code for this model is not publicly available.

A similar, but independent, multispecies model was developed by Lummerzheim and Lilensten (1994). The approach developed was similar to that of Strickland et al. (1976); it solved the 1-D Boltzmann equation along a geomagnetic flux tube. The solution for the differential number flux in this model was a function of energy, pitch angle, and scattering depth into the ionosphere for different streams. The motivation for developing this model was to resolve whether the ratio of emission between the N_2^+ 1 N (first negative) to $N_2 2P$ (second positive) was dependent on altitude; thus, this ratio could be used as a means to evaluate the average energy of precipitating electrons. It was found that this ratio did not have an altitude dependence; however, the model that was developed was rigorously self-tested, and results from the model were compared against the aforementioned range–energy relations. This transport model was later used as an integral part of a flux-tube transport model (e.g., Blelly et al., 1996, 2005; Zettergren et al., 2008; Zettergren and Semeter, 2012; Semeter and Zettergren, 2014)

Fang et al. (2008, 2010) derived a parameterization of the Lummerzheim and Lilensten (1994) model. Roble and Ridley (1987) developed an accurate, computationally efficient method for determining ionization that was used in large-scale atmospheric models. Fang et al. (2008) derived an updated relation for ionization, similar to Roble and Ridley (1987), assuming that the precipitating differential number flux was characterized by a Maxwellian distribution. Fang et al. (2010) expanded on

Fang et al. (2008) by relaxing the Maxwellian assumption and instead used monoenergetic beams, thus enabling the use of other data sets (i.e., satellite data) on an energy grid. Effectively, Fang et al. (2008) and Fang et al. (2010) solved the following equations,

$$q(z) = \frac{Q_0}{2\Delta\varepsilon}\frac{f(\gamma, E_0)}{H(z)} \tag{6.6a}$$

$$f(\gamma, E_0) = C_1\gamma^{C_2}\exp\left(-C_3\gamma^{C_4}\right) + C_5\gamma^{C_6}\exp\left(-C_7\gamma^{C_8}\right) \tag{6.6b}$$

$$\gamma = \frac{1}{E_0}\left(\frac{p(z)H(z)}{\alpha_0}\right)^{\beta_0} \tag{6.6c}$$

$$C_i = \exp\left(\sum_j P_{ij}\ln\left(E_0\right)^j\right) \tag{6.6d}$$

where $\Delta\varepsilon$ is the ion-pair production energy (i.e., 35 eV), Q_0 is the energy flux, $H(z) = k_B T_n(z)/m(z)g(z)$ is the atmospheric scale height given by NRLMSISE-00 parameters (Picone et al., 2002), $\rho(z)$ is the atmospheric mass density given by NRLMSISE-00, and α_0 is a constant. P_{ij} and β_0 are fit parameters that depend on whether the incident differential number flux is Maxwellian (Fang et al., 2008) or monoenergetic (Fang et al., 2010) and are not repeated here. Fig. 6.2 shows examples of the Fang et al. (2010)

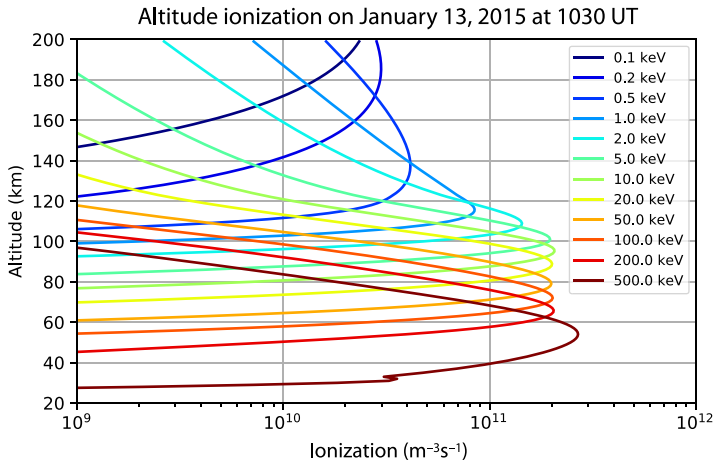

Figure 6.2 Altitude ionization as a function of altitude using the Fang et al. (2010) model with a Maxwellian input beam with a constant energy flux of 1 mW/m^2. The characteristic energy of the precipitating energy flux increases with deeper penetration of the particles.

model for a Maxwellian distribution with an energy flux of 1 mW/m^2 but with different characteristic energies for January 13, 2015. This demonstrates the clear altitude dependence and peak ionization altitudes given increasing characteristic energies.

6.2.1.3 Monte Carlo techniques

The third major method to model transport and ionization of precipitating particles treats the transport as a stochastic process. One dominant method is to use Monte Carlo techniques to describe the transport of electrons (e.g., Berger et al., 1970; Cicerone and Bowhill, 1970; Solomon, 2001, and references therein) and protons (e.g., Porter and Green, 1975; Solomon, 2001, and references therein). Monte Carlo techniques are sometimes referred to as "brute-force" methods, since they can be computationally expensive, but if the physics is accurately represented, very few simplifying assumptions are required (Solomon, 2001). The technique was revisited by Solomon (1993) to quantify whether emissions caused by low-energy secondary electron varied owing to changes in the characteristic energy of the primary electrons.

Solomon (2001) extended the Monte Carlo simulation for electrons and protons to include processes such as collisional energy transfer, scattering, and secondary electron generation and transport over all ranges of altitudes and energies. To date, this is one of the most complete Monte Carlo models developed. We briefly describe the Monte Carlo technique presented in Solomon (1993, 2001). An ion or electron enters the upper boundary with a random, but specified energy and pitch angle along a magnetic flux tube. This particle encounters random collisions, where the collision type has been weighted by the product of the cross sections and densities along the flux tube. At each location, using a definition similar to Beer's law, the optical depth τ along the flux tube is defined as

$$\tau_e = \sum_i n_i \sigma_i \tag{6.7}$$

where n_i is the atmospheric number density at a given altitude, and σ_i corresponds to the total cross section for all processes. Solomon (2001) states that $\Delta\tau_e = 1$ corresponds to the mean free path of the particle. The randomized distance an electron will move is determined by Beer's law as described in Solomon (2001); a pseudo-random number, r, between 0 and 1 is chosen as the value of $\Delta\tau = -\ln(r)$. At each altitude, the collisions are evaluated, along with the new pitch angle and the energy transfer from the primary electron to the generation of secondary elections. The authors further describe the analytic expressions that are used to quantify the secondary electron flux and approximations that are made on the precipitating primary electrons. Solomon (2001) stated that in principle the Monte Carlo technique can be extended up to 1-GeV energies, although that comes at the expense of more collisions and the requirement of at least 10^4 particles to obtain suitable statistics.

One of the key results from Solomon (1993) and Solomon (2001) are the comparison of the Monte Carlo simulations with the aforementioned two-stream approximation. In Solomon (1993), good agreement is found between the two-stream transport used in GLOW with Monte Carlo methods up to 2-keV energies, but there is less agreement for energies >10 keV. Solomon (2001) concluded that this discrepancy was due to insufficient altitude grid resolution. A comparison is made between the Strickland et al. (1989) model and the Monte Carlo method which shows very good agreement in the production rate of N_2^+.

Lehtinen (2000) implemented an alternative Monte Carlo method for describing the transport of relativistic particles. The transport is described as a stochastic process using the relativistic Langevin equation,

$$\frac{d\mathbf{p}}{dt} = q_e\mathbf{E} + \frac{q_e}{m_\gamma}\mathbf{p}\times\mathbf{B} + \mathbf{\Gamma(t)} \tag{6.8}$$

where $\mathbf{\Gamma(t)}$ is the stochastic force that accounts for collisions at each time step in the simulation. This stochastic collision term is decomposed into two parts. The first part corresponds to the energy loss by dynamical friction, and the second part to pitch-angle diffusion of the test particle as it moves along the flux tube (Marshall et al., 2014). Lehtinen (2000) used or derived analytic expressions that dictate the stochastic term, valid for electrons with energies >2 keV; however, Xu et al. (2018) extended the lower energy limit to ~ 1 eV. Lehtinen et al. (1999) went on to apply this model to understand red sprites and terrestrial gamma ray bursts. Marshall et al. (2014) have applied this method to quantify the ionospheric response that can be generated by a relativistic particle accelerator flown on a sounding rocket or satellite. Specifically, they used this code to examine the ionization and optical signatures produced by the accelerator that generates an electron beam with energies of 0.5–10 MeV. Marshall and Bortnik (2018) used this model to simulate backscatter and quantify the bounce loss cone as a function of energy.

6.2.2 Chemistry models

The D- and E-regions are the primary locations that are affected by 10–100 keV precipitating particles. The sources and losses of ionization are described in the continuity equation,

$$\frac{\partial n_e}{\partial t} + \nabla\cdot(\mathbf{u}n_e) = P - L \tag{6.9}$$

where $\mathbf{u}$ corresponds to the local plasma velocity, P includes all production terms, and L includes the loss terms. In the D- and E-regions, the divergence of the flux, $\nabla(\mathbf{u}n_e)$, can be ignored (Kirkwood and Osepian, 1995). The $\partial n_e/\partial t$ term can be ignored provided that the timescales over which the precipitation is varying are slow; under

these conditions, the continuity equation simply reduces to $P = L$. Semeter and Kamalabadi (2005, Fig. 3) show values of $\tau = 1/\alpha n_e$, the characteristic time, as a function of electron density and altitude. In the case of an electron density of 10^{12} m^{-3} at approximately 110 km altitude, the time constant is approximately 2 seconds, meaning that if the ionization source is stable for longer than 2 seconds, it is possible to neglect the time derivative of the electron density in Eq. (6.9).

6.2.2.1 E-region chemistry

Above 80 km altitude, the dominant ions are molecular NO^+ and O_2^+ (e.g., Schunk and Nagy, 2004). The dominant loss process is dissociative recombination, in which an excited molecular species will recombine with an electron to form a neutral species

$$AB^+ + e^- \rightarrow A + B \tag{6.10}$$

In the E-region, due to quasi-neutrality, this loss term in the continuity equation is typically written as $L = \alpha n_e^2$, where α is the dissociative recombination rate. Sheehan and St.-Maurice (2004) present the following recombination rates, for $T_e < 1200$ K:

$$\begin{aligned} \alpha_{O_2^+} &= 1.95 \times 10^{-13} \left(300/T_e\right)^{0.70} \\ \alpha_{NO^+} &= 3.50 \times 10^{-13} \left(300/T_e\right)^{0.69} \end{aligned} \tag{6.11}$$

and for $T_e > 1200$ K:

$$\begin{aligned} \alpha_{O_2^+} &= 1.95 \times 10^{-13} \left(300/T_e\right)^{0.56} \\ \alpha_{NO^+} &= 3.02 \times 10^{-13} \left(300/T_e\right)^{0.56} \end{aligned} \tag{6.12}$$

with units of m^3/s; T_e has units of K. Given a measured or empirical electron temperature (e.g., Bilitza and Reinisch, 2008), it is possible to calculate the recombination rates. These two recombination rates can be weighted using the relative concentrations of NO^+ and O_2^+:

$$\alpha(z) = \sum_i C_i(z)\alpha_i(z) \tag{6.13}$$

where C_i corresponds to the concentration that can be taken from the International Reference Ionosphere (IRI; Bilitza and Reinisch, 2008) or other appropriate chemistry models (e.g., Richards et al., 2010b).

An alternative form for the recombination rate was developed by Baron (1974) that was dependent only upon altitude. The method was described in Baron (1974) using 5 seconds integrated Chatanika ISR data. The method involved calculating $\alpha(t, z)$ according to:

$$\alpha(t,z) = \frac{1}{\Delta t}\left(\frac{1}{n_e(t+\Delta t, z)} - \frac{1}{n_e(t,z)}\right) \tag{6.14}$$

where $\alpha(t, z)$ amounts to a finite difference between successive $(t + \Delta t)$ high-cadence electron density measurements as a function of altitude z, assuming that a negative value corresponds to no production. This calculation was performed as a function of time and altitude, where the 90th percentile probability of occurrence was used at a particular altitude. Examination of the event on February 24, 1972, yielded results that were found to be bounded between laboratory-derived recombination rates for O_2^+ and NO^+, respectively (Biondi, 1969). Wickwar et al. (1975) optimized this height-dependent recombination rate to be in agreement between ISR observations and calibrated photometer measurements. Vickrey et al. (1982) published the following relation:

$$\alpha(z) = 2.5 \times 10^{-12} \exp\left(-z/h_0\right) \tag{6.15}$$

where the scale height $h_0 = 52.6$ km. Vickrey et al. (1982, Fig. 1) compared this relation with ISR, laboratory, and sounding rocket observations. The altitude-dependent relation put forth by Vickrey et al. (1982) has been used in other studies (e.g., Semeter and Kamalabadi, 2005). Gledhill (1986) expanded on this previous work using 18 different data sources to derive the following relation:

$$\alpha = 4.30 \times 10^{-12} \exp(-z/43) + 8.16 \times 10^{6} \exp(-0.542z) \tag{6.16}$$

where the second term in Eq. (6.16) takes into account the D-region below 95 km.

Fig. 6.3 summarizes the aforementioned methods for determining the E-region recombination rate. The figure shows an electron temperature profile from the IRI on

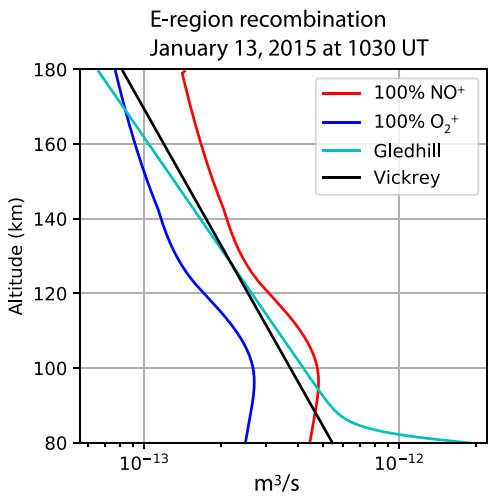

Figure 6.3 The recombination rate from Sheehan and St.-Maurice (2004), Vickrey et al. (1982), and Gledhill (1986), respectively. The blue and red curves correspond to laboratory-derived expressions, given an electron temperature from the International References Ionosphere. The black and cyan curves correspond to the Vickrey et al. (1982) and Gledhill (1986) altitude-only expressions, respectively.

January 13, 2015, at 1030 UT. The red and blue lines correspond to Eqs. (6.11) and (6.12) for a pure NO^+ and O_2^+ E-region, respectively. For comparison, we also include the expression by Vickrey et al. (1982) as the black curve and the Gledhill (1986) expression as the cyan curve. We note that below 90 km, the Gledhill (1986) expression diverges relative to the that of Vickrey et al. (1982). The altitude-dependent expressions have values that are bounded by the expressions for pure molecular ions and thus form a reasonable estimate of the molecular recombination. However, note that the empirically derived altitude relations are based on a relatively small set of ISR data.

6.2.2.2 D-region chemistry

Dissociative recombination describes the dominant loss process in the E-region; however, below 80 km in the D-region, other chemical processes become significant. Sounding rocket observations from the 1960s (e.g., Kelley, 2009, and sources therein) showed the presence of both positively and negatively charged ions and the presence of cluster ions, n_x. Taking into account all of these reactions amounts to simultaneously solving three (e.g., Rishbeth and Garriott, 1969; Kelley, 2009), four (e.g., Glukhov et al., 1992), or five (Lehtinen and Inan, 2007) ordinary differential equations. One numerical solution of these differential equations was undertaken by Glukhov et al. (1992) to model phase and amplitude changes on very low frequency (VLF) propagation that resulted from lightning-induced electron precipitation and lightning-induced electron heating. Previous observations of these phenomena showed that lightning is capable of producing short-duration bursts of precipitating particles with nearly relativistic energies (Glukhov et al., 1992, and sources therein). Lehtinen and Inan (2007) updated the equations by separating the negative ions into two categories—light and heavy negative ions. The equations from Lehtinen and Inan (2007) are

$$\frac{dn_e}{dt} = q + \gamma n^- + \gamma_x n_x^- - \beta n_e - \alpha_d n_e n^+ - \alpha_d^c n_e n_x^+ \tag{6.17a}$$

$$\frac{dn^-}{dt} = \beta n_e - \gamma n^- - \alpha_i n^- \left(n^+ + n_x^+\right) - A n^- \tag{6.17b}$$

$$\frac{dn_x^-}{dt} = -\gamma_x n_x^- - \alpha_i n_x^- \left(n^+ + n_x^+\right) - A n^- \tag{6.17c}$$

$$\frac{dn^+}{dt} = q - B n^+ - \alpha_d n_e n^+ - \alpha_i n^- n^+ - \alpha_i n_x^- n^+ \tag{6.17d}$$

$$\frac{dn_x^+}{dt} = -\alpha_d^c n_e n_x^+ + B n^+ - \alpha_i n^- n_x^+ - \alpha_i n_x^- n_x^+ \tag{6.17e}$$

Table 6.2 Variables that are used in Eqs. (6.17a)–(6.17e).

Symbol	Definition
n_e	Electron density
n^+	Positive ions
n^-	Light negative ions
n_x^-	Cluster negative ions
n_x^+	Positive cluster ions
Γ	Effective electron detachment rate
γ_x	Effective electron detachment rate for heavy ions
α_d	Effective coefficient of dissociative recombination
α_d^c	Effective recombination of electrons with positive cluster ions
α_i	Ion–ion recombination rate
B	Effective position ions into positive cluster ions
A	Conversion rate from light to heavy ions
β	Effective electron attachment rate
Q	Ionization rate

where Table 6.2 summarizes the terms found in Eqs. (6.17a)–(6.17e). The reaction rates found in Glukhov et al. (1992) and Lehtinen and Inan (2007) were typically found to be dependent on the neutral number density as a function of altitude. Fig. 6.4 shows an example of the D-region chemistry model by Lehtinen and Inan (2007), run for a model atmosphere on January 13, 2015, at 1030 UT. The left panel shows the different positive and negative ion and cluster molecule densities and the electron densities as a function of altitude produced by a background source that reproduces the IRI electron density profile for this time. The middle panel shows the positive and negative ions, positive and negative cluster molecules, and electrons, driven instead by a Maxwellian electron differential number flux with an energy flux of 1 mW/m^2 and a characteristic energy of 100 keV. These results show that positive cluster ions become dominant below 60 km. The right panel in Fig. 6.4 shows the background versus enhanced electron density given the Maxwellian electron differential number flux for comparison. One of the consequences of this model is the detectable ISR signal below the peak of the electron density as a result of the D-region chemistry.

To date, the Sodankylä Ion Chemistry (SIC) model is the most comprehensive model of D-region chemistry (e.g., Verronen et al., 2005; Turunen et al., 2009, 2016). SIC is a 1-D vertical transport code that is valid between 20 and 150 km, with 1-km resolution, and takes into account hundreds of chemical reactions that are driven by solar ultraviolet (UV), X-ray, or energetic particle precipitation. SIC solves for the concentrations of at least 65 ions, of which 36 are positive ions, 29 are negative ions, and 15 are minor neutral species (Turunen et al., 2009, and references therein).

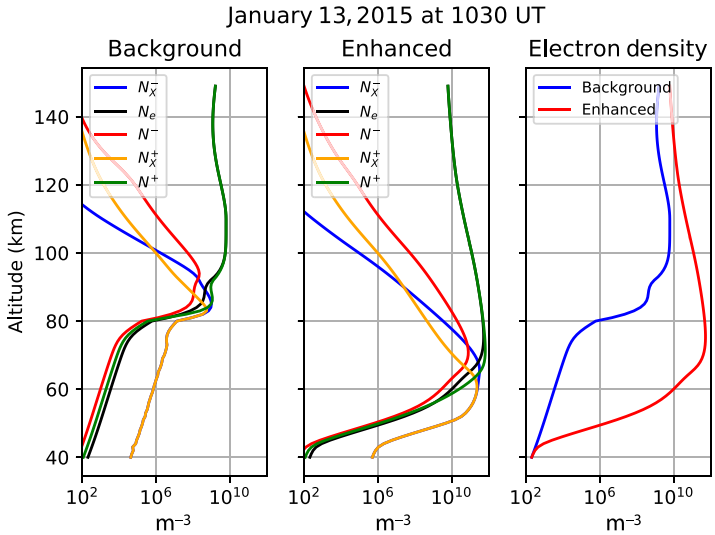

Figure 6.4 Example of D-region chemistry model by Glukhov et al. (1992) and Lehtinen (2000). The left panel shows the altitude profiles for a background source that is consistent with the IRI electron density profile for January 13, 2015. The middle panel shows the enhanced profiles resulting from energetic precipitation from a Maxwellian differential number flux of electrons with 1 mW/m^2 energy flux and a characteristic energy of 100 keV. The right panel shows the difference in the electron number density between the background and the enhanced altitude profile of the left and middle panels, respectively.

Of particular interest is the production of odd nitrogen (NO_x) and odd hydrogen (HO_x) as a result of energetic particle precipitation, which impacts the loss of ozone in the upper atmosphere (Turunen et al., 2009, 2016). There have been efforts to incorporate the SIC model into global whole-atmosphere models (e.g. Verronen et al., 2016; Kovács et al., 2016).

Instead of solving the full vertical transport and chemical equilibrium, an alternative method developed by Kirkwood and Osepian (1995) was to quantify an effective recombination rate, $\alpha_{eff} n_e^2$, similar to the E-region. This method relies on a simplified ion-chemistry model that primarily considers reactions with O_2^+, NO_2^+, O_2^-, and cluster ions (e.g., Torkar and Friedrich, 1983; Velinov et al., 1984; Smirnova et al., 1988). The authors found that during intervals of high electron density, molecular ions tend to dominate and this approximation is valid. If there is low electron density, cluster and negative ions become important, and in particular, negative ions are dominant at night below 85 km altitude. This method enables using E-region inversion techniques, provided that the ionization is of the form $q(z) = \alpha(z) n_e(z)^2$. This technique has been used to investigate various aspects of D-region response as a result of various driving mechanisms (e.g., Osepian et al., 2008, 2009a,b).

6.2.3 Quantifying precipitating differential number flux using incoherent scatter radar

We have discussed transport and chemistry models that are used to describe the ionization process in the ionosphere–thermosphere. In this section, we describe how these models are used in combination with ground-based observations from ISR to estimate the precipitating differential number flux into the D- and E-regions. Given appropriate models for transport and chemistry, the differential number flux can be inferred by inverting measurements of enhanced electron number density, which is directly related to backscattered power received by the ISR (e.g., Dougherty and Farley, 1961; Evans, 1969; Vickrey et al., 1982). The essence of this forward model can be represented by the following matrix equation (Brekke et al., 1989):

$$q(z) = \sum_{E} \mathbf{A}(E, z)\Phi(E)\Delta E \tag{6.18}$$

where $q(z)$ is the altitude ionization rate. The altitude ionization rate can be converted into electron number density using a chemistry model. The kernel, $\mathbf{A}(E, z)$, is calculated using a forward height ionization model as a function of altitude and energy. The differential number flux, $\Phi(E)$, is estimated by inverting $\mathbf{A}(E, z)$. This method corresponds to a high-dimensional linear inverse problem. An alternative approach to estimate the differential number flux is to solve a lower-dimensional nonlinear parameter estimation problem:

$$n_e(z) = \mathrm{T}(\Phi(E), z; p) \tag{6.19}$$

where T $(\Phi(E), z; p)$ corresponds to a transport model as a function of altitude, z, driven by parameters p. Typically in this form, some assumption needs to be made regarding the spectral shape of the differential number flux, $\Phi(E)$ (i.e., Maxwellian, kappa, etc.), and the parameters may include information that specifies the differential number flux.

Inverting the kernel, $\mathbf{A}(E, z)$, or estimating the electron density given a transport model are nontrivial problems. Many techniques have been used to solve Eq. (6.18). A review of the general methodology and techniques can be found in Semeter and Zettergren (2014). An early inversion technique named UNTANGLE was developed by Vondrak and Baron (1977). In this iterative method, ionization at the highest energy bin is calculated first, and each subsequent energy bin relies on the estimate from the previous energy bin. Since it is possible for uncertainty to propagate, this method is prone to errors (Brekke et al., 1989; Semeter and Kamalabadi, 2005). Brekke et al. (1989) obtained a solution to $\Phi(E)$ by minimizing the difference between the observed height ionization profile obtained by the European Incoherent Scatter Scientific Association (EISCAT) radar system and

forward model results using a least squares approach. The routine developed by Brekke et al. (1989) is called CARD.

A program called SPECTRUM (Kirkwood, 1988) was also developed to invert EISCAT ISR data. In the SPECTRUM approach, temporal variations in the electron density were also considered in contrast with UNTANGLE and CARD. SPECTRUM attempted to match the dimensions of the energy grid to the dimensions of the altitude observations to make a square matrix and apply standard matrix inversion methods. If they were unable to formulate a square matrix, the solution was obtained with a least squares method and a pseudoinverse (Kirkwood, 1988). Gattinger et al. (1991) showed that the model by Strickland et al. (1989) and UNTANGLE produced similar estimates of the energy flux and somewhat similar estimates of the characteristic energy for an auroral event observed on February 28, 1987, as part of a coordinated observation effort at the Sondrestrom ISR in Greenland. Strickland et al. (1994) expanded on the study by Gattinger et al. (1991) and presented results of the energy flux and characteristic energy for four additional auroral events observed on February 28, 1987. Strickland et al. (1994) directly fit the BC3 model (Strickland et al., 1993; Basu et al., 1993) to the ISR electron number density observations. They found that a diffuse aurora was best fit by a Maxwellian electron distribution and a discrete aurora was best fit to a Gaussian electron distribution. Doe et al. (1997) solved Eq. (6.18) using the method of singular value decomposition (Press et al., 2007), but this approach may at times produce negative electron differential number fluxes (R. Doe, personal communication, 2014).

Semeter and Kamalabadi (2005) revisited the method of determining the differential number flux using an iterative maximum entropy method (MEM). The benefit of using MEM is that the resulting electron differential number flux is a positive definite quantity. A second benefit is that no implicit assumption is required regarding the spectrum of the precipitating differential number flux. Simon Wedlund et al. (2013) also applied maximum entropy inversion techniques in application with ground-based imager data and ISR observations. Simon Wedlund et al. (2013) points out that the Semeter and Kamalabadi (2005) method maximizes the Berg entropy, $H_B = -\Sigma_i \log \varphi_i$, while the more traditional multiplicative algebraic reconstruction technique (MART) maximizes the Shannon entropy, $H_S = -\Sigma_i \varphi_i \log \varphi_i$ (Simon Wedlund et al., 2013). Simon Wedlund et al. (2013) compared these methods for a single instance and found that the MEM tended to produce smoother results than the MART technique. The MEM has been applied in many studies (e.g., Jones et al., 2009; Sivadas et al., 2017).

Kaeppler et al. (2015) revisited least squares fitting the electron density using the Rees (1963) and GLOW models for E-region ionization enhancements. The study focused on three auroral events that showed both discrete and diffuse aurorae.

The least squares fitting routine used was a standard Levenberg–Marquardt fitting algorithm (Markwardt, 2009) seeded with reasonable initial guesses. They found that in almost all cases it was possible to fit the electron density enhancements using a Maxwellian differential number flux distribution to describe the precipitating electrons. These results were further used to produce a modified conductance relation similar to the original relation shown by Robinson et al. (1987). The benefit of this method is that it is possible to incorporate it into other chemistry models fairly rapidly and produce a more direct fit with the ISR data.

Turunen et al. (2016) published a method for inverting D-region electron density measurements using a Metropolis-Hastings Markov Chain Monte Carlo (MCMC) technique and the full SIC chemistry model. The method is composed of two steps. In the first step, the altitude ionization profile is iteratively determined using the SIC model for a given observed electron density profile. The precipitating differential number flux described in Eq. (6.18) is quantified by using the MCMC algorithm to optimize a cost function including a Gaussian regularization term. This method was used because it also produced positive definite quantities and is capable of fitting over a large dynamic range of energies. Comparisons were made between this new method and the previous CARD technique and showed fairly good agreement between 50 and 120 keV energies.

6.2.4 Limitations of the incoherent scatter radar measurements

While ISR provides measurements near the ionospheric footpoint of energetic particle precipitation, there are a few important limitations associated with ISR observations. ISRs provide good altitude resolution locally; however, with $\sim$10 active ISR facilities in the world, the global coverage of ISRs is poor. PFISR was the one of the first ISRs to provide 24/7 coverage, which has enabled sampling across all MLT sectors at a fixed latitude. However, even within the full ISR field-of-view, at $<$100 km altitude, the spatial coverage is relatively limited. For example, in the International Polar Year (IPY) mode shown in Fig. 6.12, at 100 km altitude the maximum north–south separation and east–west separation of the beams is $\sim$157 and $\sim$122 km, respectively. An individual PFISR beam with an $\sim$1.1 degrees field-of-view at 100 km altitude has an actual size of 1.9 km in the sky. In cases of both beam to beam and looking at an individual beam on the sky, the actual size of the sky these probe is very small.

Another potential limitation of ISR is the detection threshold for observing energetic particle precipitation. There are two factors that must be considered. First, a minimum number of electrons in the illuminated volume must be present to generate an appreciable power return over an integration interval. In the case of energetic particle precipitation, production of electrons must occur at faster timescales than the chemical

recombination. The second factor is the ability to resolve structure, which depends on the statistical variance of the estimate of the received signal, which is also dependent on the signal-to-noise ratio (SNR). Farley (1969) derived the following relation for the statistical variance of the received signal (after subtracting the noise) for uncorrelated pulses:

$$\frac{\langle \hat{S} \rangle}{\hat{S}} = \frac{1}{\sqrt{N}} \left(1 + \frac{1}{\mathrm{SNR}} \right) \tag{6.20}$$

where N is the number of samples integrated. Note that for an interpulse period (IPP) of 2 ms, the pulses may not be completely uncorrelated, and thus Eq. (6.20) is a lower bound on the relative error of the signal estimate. To specify a 20% variance on the received signal with a SNR = −10 dB would require an integration of 3025 pulses for a 2-ms IPP that corresponds to an integration time of 6.05 seconds. This is easily achievable, as will be discussed in Section 6.4.

To quantify the sensitivity of the D-region mode, we calculate the SNR given an electron density profile generated using the model by Lehtinen and Inan (2007). The ISR SNR is given by the following formula:

$$\mathrm{SNR} = \frac{\tau P_T K_{sys}}{r^2 k_B T_{sys} \mathrm{BW}} \frac{n_e}{\left(1 + k^2 \lambda_D^2\right)\left(1 + k^2 \lambda_D^2 + T_r\right)} \tag{6.21}$$

where P_T is the transmitted power, τ is the pulse width, k_B is Boltzmann's constant, T_{sys} is the system temperature, BW is the bandwidth, k is the wave number corresponding to the Bragg condition for backscatter, λ_D is the Debye length, and T_r is the temperature ratio. Debye length effects can be significant for higher-frequency ISRs, for example, the Sondrestrom and EISCAT ultrahigh frequency (UHF) ISRs. The system constant, $K_{sys} = c\sigma_e A_{BS}/8\pi$, where σ_e is the Thomson cross section, and $\mathrm{A_{BS}}$ is the backscattered area that is illuminated by the radar beam. In practice, the system constant is estimated from comparisons between F-region ion line returns and absolute electron densities determined from plasma line measurements. Using values from PFISR (Experiment 20180315.003 MSWinds26.v03) a formula for SNR is

$$\mathrm{SNR} = 3.5 \times 10^{-12} \left(\frac{100}{r\,(\mathrm{km})} \right)^2 \frac{n_e\,(\mathrm{m}^{-3})}{\left(1 + k^2 \lambda_D^2\right)\left(1 + k^2 \lambda_D^2 + T_r\right)} \tag{6.22}$$

Fig. 6.5 shows the SNR for monoenergetic beams of increasing energy flux using Eq. (6.22) with the assumptions that $T_r = 1$ and $k^2 \lambda_D^2 = 0$. The figure is plotted at a 30, 70, 100, and 300 keV. We use −10 dB as the threshold. The green line corresponds to the −10 dB SNR threshold, while the red region is SNR > −10 dB and

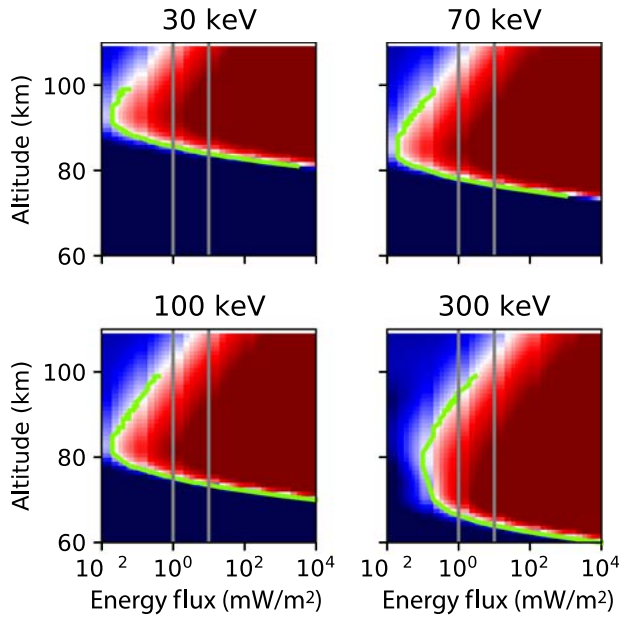

Figure 6.5 SNR calculated using Eq. (6.22) to show the detection altitude as a function of energy flux. Each panel corresponds to a different monoenergetic beam: 30, 70, 100, and 300 keV.

the blue region is SNR < -10 dB. For reference, the vertical gray lines correspond to the region of $1-10\ \mathrm{mW/m^2}$, which is a typical energy flux associated with discrete aurora. For the sake of completeness, we extended the energy flux range to unrealistically high values of $10^4\ \mathrm{mW/m^2}$ to illustrate the asymptotic characteristic of the threshold SNR; a very energetic discrete aurora may occasionally exceed $100\ \mathrm{mW/m^2}$. It is clear that as the characteristic energy and energy flux increase, the SNR threshold occurs at lower altitudes, even though the electron density peak is typically higher than the peak ionization altitude. At the lower energy fluxes and higher average energy, the ionization generated at much lower altitudes recombines so quickly that there is no detectable signal, thus causing a modest electron density peak at higher altitudes. For example, this case explains the electron density profile for the 300-keV electron precipitation at low-energy flux. However, at the unrealistically high-energy fluxes, the electron production is dominant over the recombination chemistry, thus causing an asymptotic characteristic in the detection threshold toward the ionization peak altitude and unrealistically high electron densities in the D-region. Again, this was done to illustrate the asymptotic behavior. A second feature is that the altitude range of the detectable SNR increases because the -10-dB SNR contour remains fixed, but the ionization increases since it is proportional to the energy flux. This causes a larger altitude range in the SNR.

6.3 Review of incoherent scatter radar observations of 10–100 keV phenomena

We present a review of two phenomena associated with energetic particle precipitation—pulsating aurora and auroral substorms. We also present an anomalous event of enhanced D-region electron density that is correlated with elevated geomagnetic conditions, but is not part of a larger geomagnetic storm. Although discrete aurorae are commonly observed at PFISR, typical energies are usually <10 keV, with enhanced electron density predominantly in the E-region (e.g., Kirkwood and Eliasson, 1990; Kirkwood and Osepian, 1995; Kaeppler et al., 2015). Diffuse aurorae are also common and are generated by high-energy precipitation; however, Kaeppler et al. (2015) showed in three events that the precipitation was constrained primarily to the E-region. We focus on phenomena that are associated with harder precipitation.

6.3.1 Auroral substorm

Auroral substorms have rapid changes in magnetic field topology, which can result in acceleration, energization, and movement of particles toward inner regions of the magnetosphere (e.g., Gabrielse et al., 2014; Beharrell et al., 2015, and references therein). Riometer observations during auroral substorms indicate precipitation of energetic particles with energies of 10s of keV (e.g., Spanswick et al., 2013; Beharrell et al., 2015). Moreover, VLF observations during substorms further confirm the association of energetic precipitation, with energies of the order of 10–100 keV (e.g., Cummer et al., 1997; Clilverd et al., 2012). Understanding auroral substorms remains one of the most unresolved topics in space physics; for the purposes of this chapter we reduce our focus to ISR observations of energetic precipitation associated with substorms. While ISR has played a critical role in understanding substorm dynamics (e.g., Cowley and Lockwood, 1997; Lyons et al., 2010, and references therein), relatively few papers show ISR results of the precipitating energy spectrum associated with substorms. ISRs provide altitude-resolved measurements of the electron density that can quantify the energy spectrum of the differential number flux.

Foster et al. (1980) conducted one of the first incoherent scatter radar studies of energetic particle precipitation; they used the Chatanika ISR (now the Sondrestrom ISR), AE-C satellite data, and nearly colocated riometers. The multipoint observations were taken on January 28, 1977, beginning at 1900 UT and ending at 0400 UT the next morning, with a substorm commencing at approximately 2100 UT (local noon was 2200 UT). The substorm commenced in response to strong southward IMF Bz. Ionization during the peak of the substorm occurred at 2045 UT and corresponded to a peak in the electron density at ~ 80 km, but with detectable electron density enhancements occurring at altitudes as low as 60 km. An inversion procedure was used (Vondrak and Baron, 1977) to infer the differential number flux and was

compared with Atmospheric Explorer (AE-C) observations, where the footpoint of the AE-C satellite was ~500 km to the east of the ISR. Despite this significant difference in location, the combined ISR and AE-C data provided a good fit to a Maxwellian differential number flux distribution with a characteristic energy of 80 keV, as shown in Fig. 5 of that paper (not shown here), and an energy flux of 50–100 erg/cm^2/s. These observations showed an enhancement of both characteristic energy and energy flux associated with a substorm.

A series of papers from 1988–1996 that were published or coauthored by Kirkwood and Osepian present many EISCAT observations of D-region ionization in association with auroral substorms. Kirkwood et al. (1989) presented an observational comparison between the differential number flux inferred by the EISCAT radars and measurements of the differential number flux observed by the Viking satellite during three phases of a substorm: the auroral bulge, westward-traveling surge, and post-breakup. While the Viking satellite was not conjugate with the radar during these observations, the purpose was to quantify similar characteristics so that the phases of substorms could be studied more routinely with ISR.

Kirkwood and Eliasson (1990) significantly expanded on this early work by presenting one of the most comprehensive ISR-based studies of the substorm growth phase. The authors examined six auroral substorms using data from the EISCAT ISR. For three of the events the antenna was in a fixed position mode, and for the remaining three events the antenna was in a latitudinal scan mode. One of the most significant features observed was two distinct peaks in the observed electron density during the substorm growth phase: one electron density peak above 100 km altitude, and a low-altitude peak near 90 km altitude. Fig. 6.6 illustrates one of the main results from Kirkwood and Eliasson (1990), showing the distinct second peak near 90 km altitude corresponding to the energetic precipitation. This lower altitude electron density peak was consistent with 20–60 keV electron precipitation. A single peak in the electron density, at altitudes >100 km, was typically observed poleward and equatorward of the double-peaked region. The double-peaked region was also narrow in latitude, with a characteristic size of 0.5–1 degrees; this led the authors to conclude that this region might represent a boundary between two regions in the plasmasheet. They also observed that the peak of this low-altitude ionization was ~90 km over all the events observed, although the magnitude of the lower-altitude electron density peak changed by as much as a factor of 2 over all events. In the poleward region, observations of structure in the higher-altitude electron density were correlated with optical and UV auroral imagery. Kirkwood and Eliasson (1990) concluded that the high-energy electrons might result from a localized region of enhanced electron precipitation associated with the so-called trapping boundary (which is defined as the latitude at which the pitch-angle distribution changes from isotropic to trapped). Osepian et al. (1993) examined auroral absorption (at 30 MHz) during phases of a substorm using the

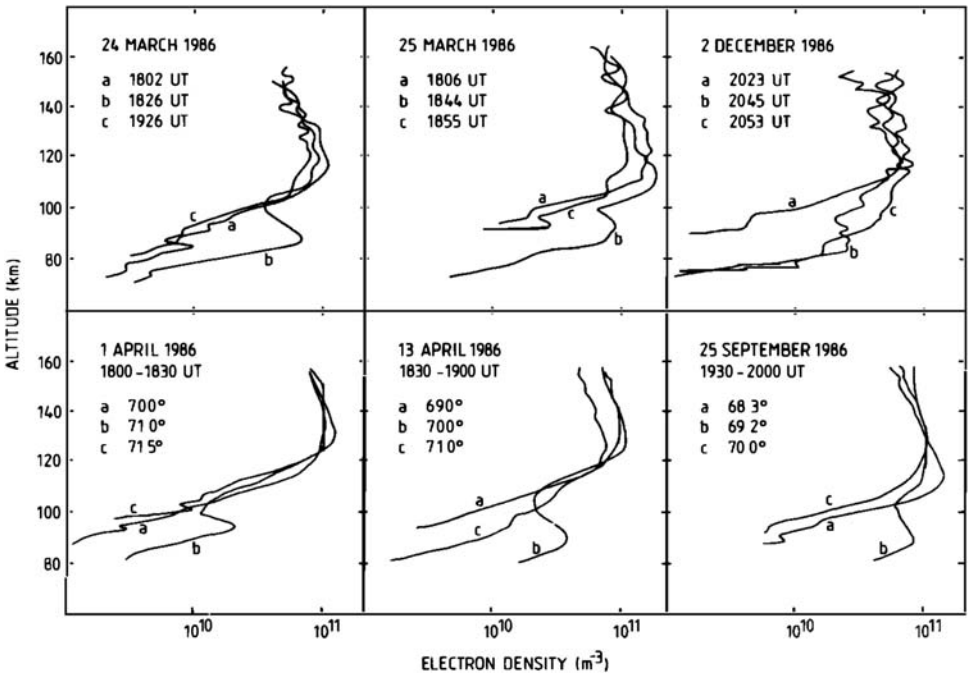

Figure 6.6 The electron density profiles labeled as "b" show a clear peak below 100 km consistent with particle precipitation >10 keV. *Reproduced from Fig. 3 in Kirkwood, S., Eliasson, L., 1990. Energetic particle precipitation in the substorm growth phase measured by eiscat and Viking. J. Geophys. Res. Space Phys. 95 (A5), 6025–6037. doi: 10.1029/JA095iA05p06025. Copyright 1990 American Geophysical Union.*

EISCAT radar for an event on November 17–18, 1983. During the growth phase of the substorm, the authors attributed the primary contribution to the D-region absorption to 7–10 keV electrons. However, the authors found that during substorm onset and the expansion phase, the characteristic energy of the precipitation hardened to 16–20 keV, which was the primary contribution to the D-region absorption.

Sivadas et al. (2017) performed a conjugate study between Time History of Events and Macroscale Interactions during Substorms (THEMIS) satellites and PFISR to examine potential source regions of energetic particle precipitation and acceleration mechanisms. The study focused on an event from March 28, 2008 from 0930–1200 UT in which the THEMIS-D and -E spacecraft had a near conjunction with PFISR. At the time of substorm onset, THEMIS-D was the closest satellite; it was separated in latitude by a few degrees, but separated by almost 1.5 hours in MLT. Despite the large longitudinal separation, THEMIS-D made in situ observations in the plasmasheet and magnetospheric lobe region while PFISR made ground-based observations. The ISR electron density observations were inverted using the MEM used by

Semeter and Kamalabadi (2005). During the substorm growth phase and the main phase, energetic particle precipitation was observed by PFISR, with precipitation extended as low as ~70 km altitude. Interestingly, there was a slight depletion in the electron differential number flux simultaneously observed by THEMIS-D and PFISR immediately preceding the substorm at 1144 UT. The authors attributed the in situ observations to THEMIS-D passing into the magnetospheric lobe region. One of the key findings is how much energy is captured by the energetic particle precipitation during the substorm. Sivadas et al. (2017) found that the energy flux carried by the 10–100 keV electrons increased to about 75% of the total energy flux after the substorm onset versus less than 15% of the total energy flux before the substorm's onset; this suggested that almost all of the energy is carried by these energetic particles during a substorm. In particular, PFISR observed a secondary peak in 70 keV ionization after the onset of the substorm. Also, note that the enhanced energetic ionization preceding the substorm was in agreement with previous findings by Kirkwood and Eliasson (1990).

6.3.2 Pulsating aurorae

One of the most common signatures of 10–100 keV precipitation is pulsating aurorae. Pulsating aurorae are characterized by quasi-periodic modulations with periods of a few to tens of seconds and with spatial extent from tens to hundreds of km in the sky (e.g., Johnstone, 1978; Lessard, 2013; Jones et al., 2013; Jaynes et al., 2013). Royrvik and Davis (1977) found that pulsating aurorae had a typical period of 8 seconds. In some cases, pulsating auroras can span multiple hours in MLT (e.g., Jones et al., 2013). Pulsating aurorae are typically weak in optical magnitude, Royrvik and Davis (1977) found that 427.8-nm emission did not exceed 10 kR. In addition, pulsating aurorae are commonly observed within a diffuse background (e.g., Royrvik and Davis, 1977; Jones et al., 2009), although there is some contention as to whether the diffuse background may in fact be the result of pulsating auroral processes (e.g., Evans et al., 1987; Jones et al., 2009). Pulsating aurora is observed after substorm breakup (e.g., Akasofu, 1964) and is more commonly observed in the morningside MLT sector (e.g., Hosokawa and Ogawa, 2015). Another defining feature of pulsating aurorae is distinct on–off modulation of luminosity. The characterization of these on–off periods have been investigated by Humberset et al. (2016) and Dahlgren et al. (2017). There are a few reviews on pulsating aurorae (e.g., Johnstone, 1978; Lessard, 2013) and it is important to note that pulsating aurorae are an optically based characterization.

There is general consensus that one of the dominant mechanisms responsible for the generation of pulsating aurorae is energetic particle precipitation caused by enhanced pitch-angle scattering due to wave-particle interactions near the geomagnetic equator (e.g., Nishimura et al., 2010; Jones et al., 2009; Miyoshi et al., 2010, 2015; Lessard, 2013; Jaynes et al., 2013; Li et al., 2013; Kasahara et al., 2018). Two of

the dominant candidate waves are whistler-mode chorus and ECH waves (Nishimura et al., 2010). Chorus is divided into two branches in which the upper-band chorus has $f > 0.5\ f_{ce}$, where f_{ce} is the electron cyclotron frequency, and the lower-band chorus has frequencies $f < 0.5\ f_{ce}$ (Nishimura et al., 2010). Upper- and lower-band chorus waves are resonant, with less than a few keV and > 10 keV, respectively (Ni et al., 2008). ECH waves occur at frequencies $> 1\ f_{ce}$ and are resonant with electrons less than a few keV (Horne et al., 2003). Nishimura et al. (2010) combined observations of chorus from the THEMIS satellites with ground-based imager observations of pulsating aurora. By cross-correlating the optical emission of each pixel in the imager data with the integrated lower-band chorus wave intensity, they found the most probable (highest cross-correlation) location of the optical emission given the chorus data. In an event from February 15, 2009, they found that the footpoint of the optical emission remained effectively fixed, even though the optical emission evolved over time. Not only does this provide a method for magnetic field mapping, but this was also one of the first direct observational confirmations that lower-band chorus can drive pulsating aurora.

Many rocket, satellite, and ground-based studies of pulsating aurorae have established the typical average energy of precipitation, with values ranging from 1-100 keV. Early rocket observations by Whalen et al. (1971) found that one-fifth of optical emissions were contributed by electrons with energies > 25 keV and that most of the optical emission could be accounted for by electrons with energies > 12 keV (Sandahl et al., 1980). Rocket observations by Bryant et al. (1971) showed that during pulsation maxima, the electron differential number flux could be characterized by a Maxwellian distribution with a characteristic energy of 8 keV; during pulsating minima, this characteristic energy was 6 keV. Sandahl et al. (1980) made observations similar to those of Whalen et al. (1971) and found that 75% of the energy was carried by electrons with energies > 27 keV in the pulsating maxima. In contrast to these observations, McEwen et al. (1981) made two rocket observations of pulsating aurorae in the same event that were characterized by a Maxwellian differential number flux with average characteristic energies of 1.8 and 2.0 keV during pulsation maxima for each event.

More recently, satellite observations have provided additional data of the energy spectrum of pulsating aurorae. Jaynes et al. (2013) used a technique similar to that of Nishimura et al. (2010), in which the cross-correlation was calculated pixel by pixel between all-sky imager data and data from the Geostationary Operational Environmental Satellite (GOES) 13 Magnetospheric Electron Detector (MAGED). For the event on March 15, 2008, Jaynes et al. (2013) found short-term modulations in the magnetospheric electron flux, with energies ranging from $30-100$ keV, that had high correlation with ground-based observations of pulsating aurorae. Samara et al. (2010) combined ground-based observations and REIMI satellite overpasses to find the typical energy of pulsating aurorae to be between 8 and 12 keV in four events. Samara et al. (2015) expanded on their previous study and examined six pulsating auroral events using data from the Defense Meteorological Satellite Program

(DMSP) and REIMI satellites to test whether precipitation characteristics were different during varying optical morphology. Two events occurred just after 0000 MLT and were found to have peak energies on the order of 8–12 keV. Three events were in the dawn MLT sector, between 0500 and 0600 MLT, and showed a harder precipitation, with peak electron energies in the range 8–20 keV. The final event was clearly in the morning MLT sector, near 0828 MLT, and had the largest range of energies, 4–30 keV. Samara et al. (2015) concluded that the typical range of energies was 3–20 keV. They also concluded that during pulsating intervals with increased temporal variations, there can be a reduction of secondary electrons. This reduction could be supported by a low energy (~1 keV or similar) parallel electric field, which blocks low-energy electrons. To date, the study by Samara et al. (2015) forms one of the most complete space-based statistical studies of the energy spectrum of precipitation associated with pulsating aurora.

ISR-based observations of pulsating aurorae relative to satellite and rocket observations have been a more recent development. A set of observations in the late 1980s using the EISCAT radars were some of the first radar observations of enhanced electron density associated with pulsating aurorae (e.g., Bösinger et al., 1996; Jones et al., 2009; Kaila and Rasinkangas, 1989; Kaila et al., 1989; Wahlund et al., 1989 , and references therein). Kaila and Rasinkangas (1989) observed two peaks in the electron density during a pulsating auroral event on February 1, 1987. The higher-altitude peak corresponded to a characteristic energy of 1.3 keV, while the lower-altitude peak corresponded to a characteristic energy near 7 keV. They found that the higher-altitude electron density decreased when energetic precipitation was present; the authors suggested that the pulsating aurora somehow quenched the background population. Wahlund et al. (1989) examined an event from December 3, 1986, of thin layers associated with pulsating aurorae, which were first reported by Stenbaek-Nielsen and Hallinan (1979). They observed both single- and double-peaked electron density profiles in EISCAT data, with the double-peaked profiles showing peaks at both 108 and 125 km. Wahlund et al. (1989) concluded that the thin layers were likely not sporadic-E; rather, they suggested, it could be a wave interaction affecting the precipitating electrons. Bösinger et al. (1996) further examined the EISCAT observations reported by Kaila and Rasinkangas (1989) for January 31–February 1, 1987. They found that there were two distinct periods of modulation in the pulsating aurorae, one period at 10 seconds and another at 60 seconds. The 60-second oscillations were also observed in a magnetometer chain extending 250 × 1000 km in latitude and longitude, respectively. Again, the observations they examined contained the two distinct peaks in the electron density at two distinct altitude. Hosokawa and Ogawa (2015) noted that these early studies did not have sufficient time resolution to be able to quantify the differences between on–off modulations of the pulsating aurorae.

Jones et al. (2009) examined PFISR data in tandem with observations from the Rocket Observations of Pulsating Aurora (ROPA) sounding rocket and the REMEI

satellite. The motivation for this study was to test whether pulsating aurorae correspond to very thin altitude layers (e.g., Stenbaek-Nielsen and Hallinan, 1979; Wahlund et al., 1989). Jones et al. (2009, Fig. 7), shows four nights of observations in which the pulsating aurora generated altitude profiles in the electron density consistent with particle precipitation. The enhanced ionization driven by the pulsating aurorae spanned an altitude range of ~15–25 km in the four observed events. There is clearly ionization at altitudes <100 km (>10-keV energies), except for the night of the rocket launch (February 12, 2007), when toward the end of the interval the bottom edge of the ionization goes above 100 km, indicating a softening of particle precipitation to 6–8 keV (Jones et al., 2009). Hosokawa and Ogawa (2015) noted that the observations made by Jones et al. (2009) were still integrated over a longer interval of time than individual on–off modulations in the pulsating aurora (Fig. 6.7)

One of the most complete ground-based studies to date of pulsating aurora was performed by Hosokawa and Ogawa (2015). The authors found 21 examples of simultaneous all-sky imagery combined with suitable observations from the EISCAT radars spanning five winter seasons from 2007 to 2012. As part of the analysis, for some of the events, data were analyzed at 5-second resolution, enabling the on and the off periods to be analyzed separately. They found consistently higher energies during the on periods of the pulsating phase and suggested that previous observations may result in an underestimation of the energy of electrons if the on and off phases are not separately considered. Fig. 6.8 shows one of notable observations in this study, in some cases the ionization associated with pulsating aurorae is above 100 km altitude (0000–0200 UT), while at other times it may be well below 100 km altitude (0400–0500 UT). This suggests that pulsating aurorae are sometimes associated with more and less energetic precipitation, which could be due to different wave-particle interactions. Dahlgren et al. (2017) examined on–off modulations using EISCAT observations compared with Auroral Structure and Kinematics (ASK) imager data for October 22, 2006 and January 19, 2007. In the two events, five intervals of EISCAT data were combined during each of the on and off intervals. It was found that a Maxwellian distribution fit the on and off periods well. The energy flux was reduced between the on and off periods, while the characteristic energy reduced in magnitude but not as significantly as the energy flux. However, the ASK imager data saw significant differences in energy flux and estimated characteristic energy, with ~60% reduction in both quantities between on and off periods. These differences could be partially due to the radar integrating over a longer interval than the imager.

Hosokawa and Ogawa (2015) presented statistical results that characterize the altitude (h_mE) and number density (N_mE) of the E-region peak. This analysis did not attempt to separate the on from the off phase; rather, these results are integrated with respect to time. The results from the statistical analysis using data from the EISCAT UHF radar, as presented in Fig. 6 of their paper, show that the majority of the

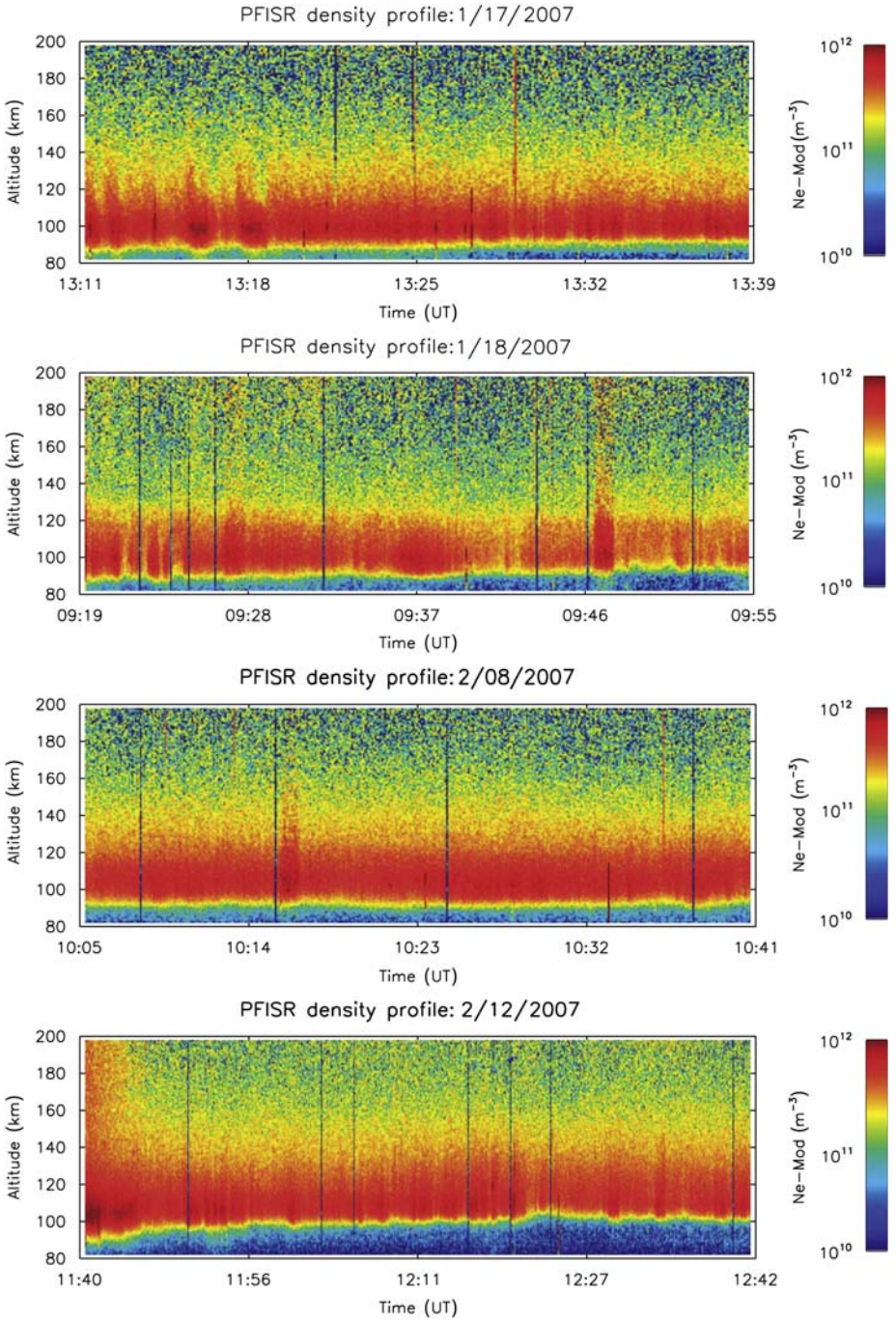

Figure 6.7 The altitude-resolved electron density profiles from PFISR are shown for four nights of pulsating aurora. In all four events, the enhanced E-region has a width of approximately 15−25 km, which is consistent with being driven by precipitation. *Reproduced from Fig. 2 in Jones, S., Lessard, M., Fernandes, P., Lummerzheim, D., Semeter, J., Heinselman, C., et al., 2009. PFISR and ROPA observations of pulsating aurora. J. Atmos. Sol. Terr. Phys. 71 (6), 708−716. doi: https://doi.org/10.1016/j.jastp.2008.10.004, advances in high latitude upper atmospheric science with the Poker Flat Incoherent Scatter Radar(PFISR), Copyright 2009 Elsevier.*

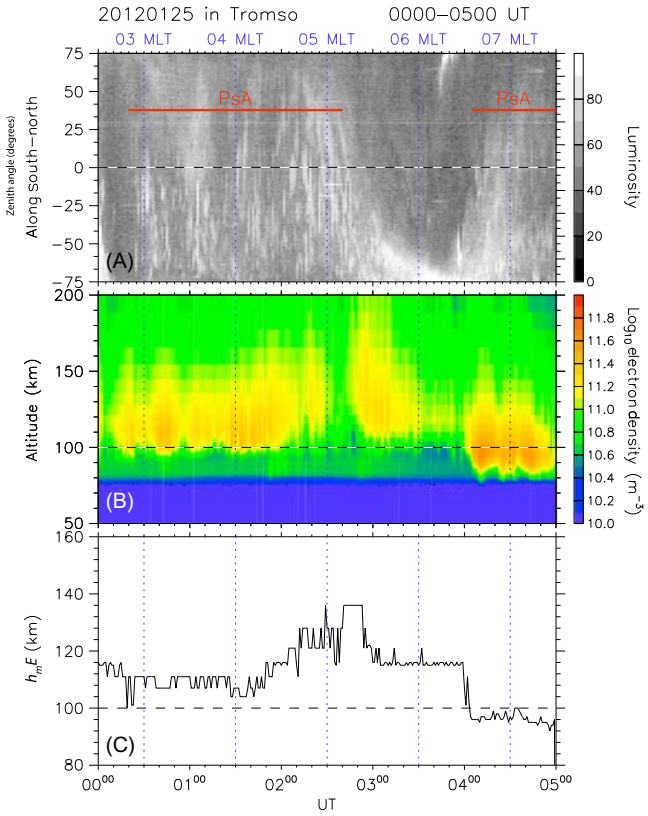

Figure 6.8 During 0000–0200 UT, there are electron density enhancements >100 km altitude (<10 keV precipitation), and between 0400 and 0500, there are electron density enhancements <100 km altitude (>10 keV precipitation). Both of these events were during pulsating aurorae. Panel A corresponds to a keogram of optical emission. Panel B are the EISCAT electron density observations with respect to altitude in the E-region. Panel C correspond to an estimate of the altitude of the peak electron density in the E-region, hmE. *Reproduced from Fig. 2 in Hosokawa, K., Ogawa, Y., 2015. Ionospheric variation during pulsating aurora. J. Geophys. Res. Space Phys. 120 (7), 5943–5957. doi:10.1002/2015JA021401. Copyright 2015 American Geophysical Union.*

observations have *hmE* above 100 km altitude, suggesting a characteristic energy of precipitation of <10 keV. A second result shows that there is a general hardening of precipitation to lower altitudes as the MLT goes toward the morningside (>0600 MLT) sector. This general hardening of precipitation is consistent with previous observations and understanding of morningside pulsating aurorae.

Miyoshi et al. (2015) presented a study that combined satellite and ISR measurements of energetic particle precipitation associated with pulsating aurora. Ground-based ISR observations from the EISCAT radar, combined with ground-based VLF observations, and observations from the Van Allen Probes were used to examine a

pulsating auroral event from November 17, 2012, from 0400–0600 UT. The EISCAT observations saw clear electron density enhancements between 70 and 90 km, with the lowest altitude found to be approximately 68 km, which corresponds to 200 keV electrons. VLF observations suggested precipitation with energies of at least 50 keV in regions near the ISR. At the same time, RBSP-A observed discrete lower-band chorus waves. These wave signatures were used to drive a Monte Carlo simulation (e.g., Miyoshi et al., 2010; Saito et al., 2012) describing how chorus waves interact with electrons. The results of this simulation produced an electron differential number flux that was compared directly with observations from RBSP and ISR data (after an inversion was performed on the electron density). The simulation results showed very good agreement at 10–50 keV; the authors concluded that it was possible for lower-band chorus waves to cause simultaneous precipitation from 10–100 keV, with the latitudinal distribution in the geomagnetic field of the lower-band chorus controlling the resonant energy. The results from this paper further support the previous results by Nishimura et al. (2010) and show direct evidence of chorus waves causing energetic precipitation.

6.3.3 Other ISR observations of energetic precipitation

In some cases, there can be fortuitous observations of D-region ionization that last for long intervals. Nicolls et al. (2010) published an example, which occurred during observations of upward propagating inertial gravity waves. The observations were obtained from PFISR on April 23, 2008, from 0000–2400 UT. The top panel of Fig. 6.10 is a reproduction from Nicolls et al. (2010, Fig. 3), which shows the electron density as a function of time and altitude. The gray region in the top panel of Fig. 6.10 corresponds to an electron density $< 10^9\ \mathrm{m}^{-3}$, which is below the detection threshold of PFISR. During this interval, three distinct periods of ionization were observed: 0200–0400 UT, 0800–1200 UT, and 1300–2300 UT. During the interval 0800–1200 UT, all-sky imager data were available from the THEMIS all-sky imager network at Gakona, Alaska, USA, located approximately 300 km to the southeast of PFISR. Fig. 6.9 is a keogram derived from those all-sky imager data for the interval 0800–1100 UT. Between 0800–0830 UT there were active auroral conditions, followed by diffuse and pulsating aurora between 0830–1045 UT. Auroral activity after this time diminishes; these observations are consistent with the results from Fig. 6.10. It was possible to derive spectra between $\sim$60 and 90 km during the first and last intervals, while the 0800–1200 UT did not have appreciable electron density below $\sim$75 km. The lower bound of 60 km corresponds to an energy of $\sim$300 keV. Using these regions of enhanced ionization, it was possible to infer the neutral wind from the D-region spectra.

The geomagnetic conditions for the day were moderately disturbed, although this ionization was not associated with a geomagnetic storm. Fig. 6.10B shows the AE

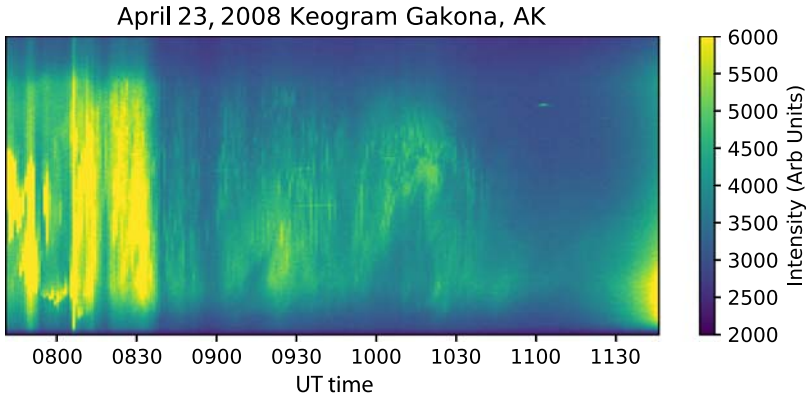

Figure 6.9 A keogram from a THEMIS ASI imager located at Gakona, AK, USA, approximately 300 km southeast of PFISR. Between 0800 and 0830 UT, there were active auroral conditions, followed by diffuse and pulsating aurorae between 0830 and 1045 UT. Auroral activity after this time diminishes; these observations are consistent with the results in Fig. 6.10.

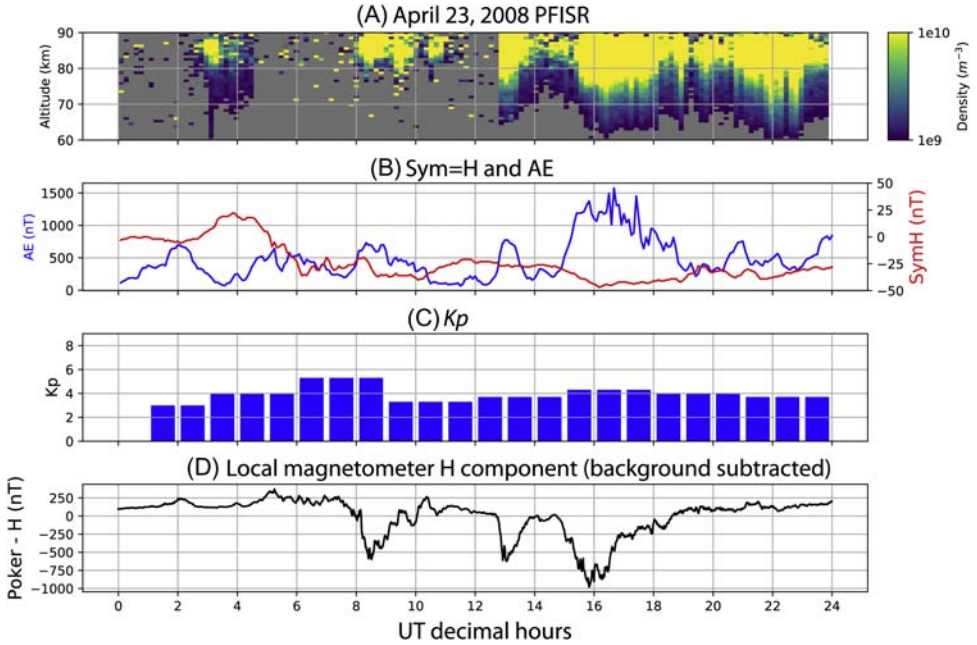

Figure 6.10 PFISR observations from April 23, 2008. (A) The electron density as a function of altitude and time. (B) Line plots of the SYM-H and AE indices. (C) The *Kp* index over the interval. (D) H-component of a colocated magnetometer at Poker Flat after a background subtraction has been performed. *Reproduced from Nicolls, M.J., Varney, R.H., Vadas, S.L., Stamus, P.A., Heinselman, C.J., Cosgrove, R.B., et al., 2010. Influence of an inertia-gravity wave on mesospheric dynamics: a case study with the poker flat incoherent scatter radar. J. Geophys. Res. Atmos. 115 (D3). doi:10.1029/2010JD014042, d00N02, n/a–n/a.*

index in blue and the SYM-H index in red. The SYM-H index for that 24-hour period had a minimum value of approximately 50 nT. The AE index was elevated with a maximum value >1500 nT at $\sim$1630–1640 UT. Fig. 6.10C shows that the *Kp* was relatively elevated, with values between 3 and 5, indicating moderate activity. However, the H-component of the local electrojet measured at PFISR showed three distinct minima at $\sim$0830 UT, $\sim$1300 UT, and 1530–1630 UT. These indicate that the local westward electrojet had developed and these signatures could have been associated with aurora with current signatures. It is clear that at 1300 and 1600 UT there is significant ionization occurring at low altitudes. However, it remains curious that the energetic precipitation remains beyond 1800 UT and also previously between 0200 and 0400 UT, when the perturbed H-component of the magnetic field returns to nearly zero. It remains an open question whether or not the precipitation that was observed was directly related to auroral activity. The data seem to indicate the absence of auroral activity, at least for some of the interval.

This event is an intriguing example in which ionization of the order of 100 keV can occur during nonstorm time intervals. Observations like this event were completely fortuitous and would not have been possible without regular sampling of the D-region. These observations highlight the importance of regular D-region observations, particularly to quantify nonstorm energetic particle precipitation.

6.4 D-region incoherent scatter radar mode

PFISR is a remotely operated, phased-array radar capable of beam steering on a pulse-to-pulse basis (Kelly and Heinselman, 2009). PFISR has run nearly continuously since 2007 and produces a low-duty cycle data product of alternating code and long-pulse data called the IPY mode. While this mode is useful for long-term studies of the auroral ionosphere and thermosphere, it is not an optimal mode for studies of D-region ionization. Dougherty (1963) and Dougherty and Farley (1963) derived the theory for the incoherent scatter radar spectrum in the presence of ion-neutral collisions, which are the conditions found in the D-region ionosphere. When collisions are dominant, the backscattered power spectrum is described as a Lorentzian distribution,

$$\sigma(\omega_0+\omega) \propto \frac{(\nu_{in}/k)}{1+(\nu_{in}/k)^2(\omega/k)^2} \tag{6.23}$$

where $k=\lambda/4\pi$ is the radar wave number corresponding to the Bragg condition for backscatter, ω_0 is the angular radar frequency, ω is the angular Doppler shift frequency, and ν_{in} is the ion-neutral collision frequency. The spectral half-width at half maximum of the Lorentzian distribution can be written as (e.g., Dougherty and Farley, 1963; Nicolls et al., 2010),

$$\Delta\omega \approx \frac{16\pi k_B T}{\lambda^2 m_i \nu_{in}} \tag{6.24}$$

where T is the temperature, assuming thermal equilibrium between ions, electrons, and neutrals, which is generally true in the D-region (e.g., Kelley, 2009; Schunk and Nagy, 2004), and m_i is the ion mass. Given typical D-region parameters, the effective spectral width is on the order of tens to hundreds of Hz, which is in contrast with typical E- and F-region spectral bandwidths, which are on the order of kHz. By the Wiener–Khintchine theorem, this narrow-bandwidth signal in the D-region corresponds to a long decorrelation lag in the time domain. This long decorrelation time, combined with the reduced range of the relatively nearby target (50–100 km), means that that pulse-to-pulse range Doppler radar processing techniques (e.g., Richards et al., 2010a) can be applied to the D-region. Fig. 6.11 shows an example of the median spectral power from April 23, 2008 at 1705–1721 UT from the vertical directed beam. The exponential decrease in the spectral width can be seen below 85 km altitude, consistent with the expected change in the ion-neutral collision frequency (e.g., Nicolls et al., 2010).

Two modes were designed to specifically probe the D-region electron density and also to derive winds. These modes use four beam-steering directions similar to the IPY mode—vertical, field-aligned, northwest-directed, and northeast-directed, labeled as beams 1, 2, 3, and 4, respectively. Fig. 6.12 shows a layout of the beam placement. The difference between the two modes is the coding scheme: one mode uses a 13-baud Barker code with 10 μs baud length and the other scheme uses a 47-baud pseudo-random coded pulse with a 4 μs baud length. The difference in the baud length corresponds to a 1.5 km and 600 m range resolution, respectively. The IPP of

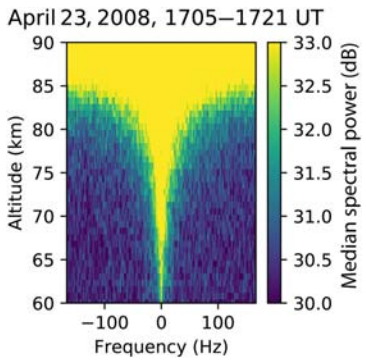

Figure 6.11 An example of the median of the PFISR spectral power from April 23, 2008, at 1705–1721 UT, from the vertical directed beam. The exponential decrease in the spectral width can be seen below 85 km altitude, consistent with the theory by Dougherty (1963) and Dougherty and Farley (1963).

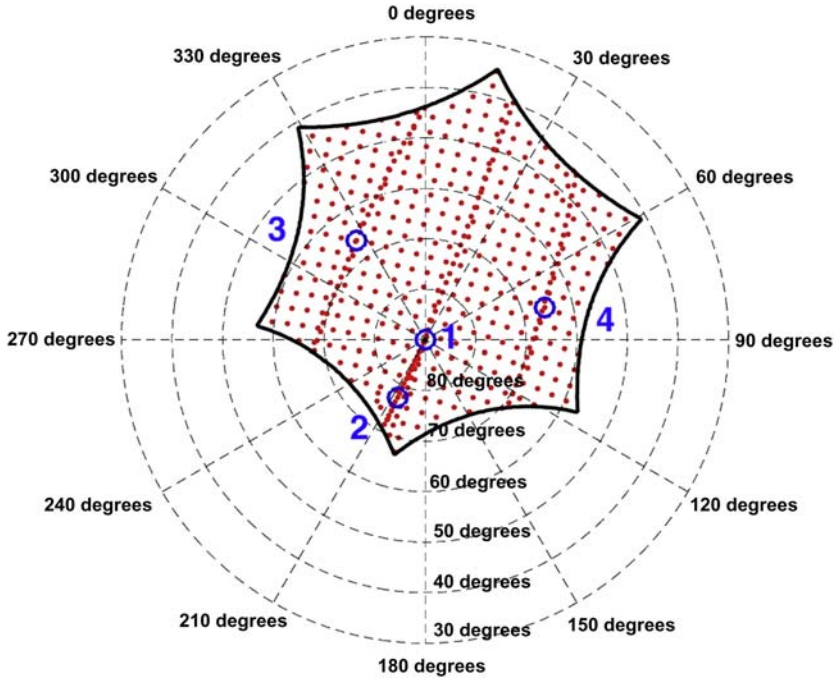

Figure 6.12 Placement of PFISR beams. Beam 2 is aligned with the local geomagnetic field, beam 1 is looking at the zenith, beam 3 is directed toward the northwest, and beam 4 is directed toward the northeast. The black outline denotes the phased-array grating lobes that form the limit of region the ISR can probe. Any beam can be formed within the grating lobes.

Table 6.3 Summary of the modes run at PFISR to quantify E- and D-region ionization.

Pulse pattern	Range resolution	Spectral resolution (Hz)	Nyquist frequency (Hz)	Dates
13 baud, 10 μs/baud Barker code	1.5 km	3.9	250	$< 02/2015 >$ 11/2016
47 baud, 4 μs/baud Pseudo-random code	600 m	3.9	250	$02/2015 < t <$ 11/2016

2 ms determines the maximum unambiguous range of 300 km and the maximum frequency of 250 Hz, respectively. For this mode, 256 pulses are integrated to produce a single spectral estimate every 0.512 seconds, having a corresponding spectral resolution of 3.9 Hz. Table 6.3 summarizes the modes that were run at PFISR from 2015 to the present.

6.5 PFISR observations

6.5.1 Events summary

Since the commissioning of PFISR in 2007, regular observations of D-region ionization have been conducted. These intervals use a radar mode similar to the one described in Section 6.4. These experiments had a typical duration of 24 hours and were run once a month, although not necessarily on the same day each month.

Since 2015, coordinated observations have been made with the Van Allen Probes, and since 2016 with the Arase satellite. Conjunctions between these satellites and PFISR were determined by mapping the satellite location along the geomagnetic field line to a footpoint at 100 km altitude. Footpoints within a 500-km radius (in geomagnetic coordinates) of PFISR were chosen, and a typical conjunction duration of 3–4 hours. For RBSP, the satellite footpoints are almost always >100 km to the south of the PFISR field-of-view, while for Arase, the nearest conjunction was <30 km from the PFISR field-of-view.

Fig. 6.13 shows all scheduled D-region experiments from 2015 to 2018 as vertical blue lines. We note that these are scheduled experiments, so the actual number of intervals run was less, but by not more than 10%. Fig. 6.13 also shows the SYM-H index in red, which is used as a proxy for geomagnetic activity. An algorithm has been developed that flags the collected D-region data for potentially bad intervals. Specifically, events flagged for noise and interference were determined by cross-referencing the zeroth moment—that is, the power of the spectral profile, with time-dependent noise estimates (taken at 50–55 km). Events with significant interference contain rapid and exaggerated temporal changes in the noise estimation, while noisy events have a flat power response that is nearly constant with respect to time and altitude. A future publication is forthcoming that will describe this algorithm in greater

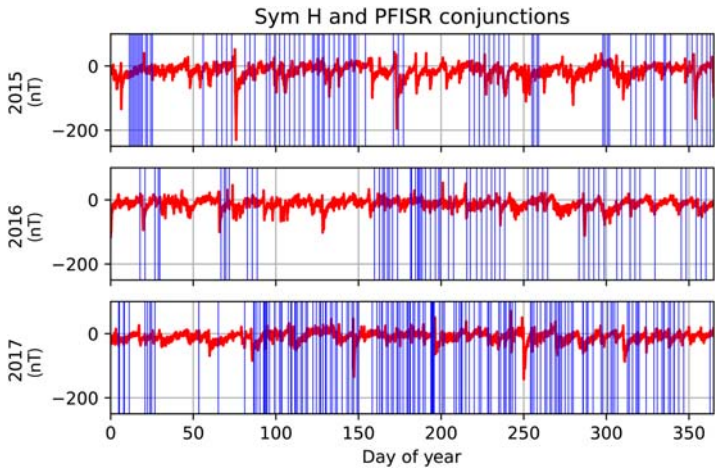

Figure 6.13 Coverage of PFISR conjunctions (*blue*) relative to the SYM-H (*red*).

depth, along with further statistical results. Some of the gaps in the data are due to preference for other experiments, maintenance of the radar, and due to these experiments not being requested. Note that overall there is good sampling during quiet intervals and there are a few instances of sampling during a storm or recovery phase. There is a significant uptick in the number of observations in 2017, which is due to conjunctions during Arase campaigns.

6.5.2 Example event: January 13, 2015

We present an example of the data we have collected showing a conjugation between Van Allen Probes B (hereafter referred to as "RBSP-B") and PFISR on January 13, 2015, during the interval from 1000 to 1200 UT. The interval for this event was relatively geomagnetically quiet, although there was activity starting at 1115 UT. The Dst index was −9 nT, *Kp* was 1 +, the AP index was 5, and the global AE index range was 29–180 nT. During the previous week, on January 7, 2015, a minor storm occurred with a minimum Dst of −100 nT. During the recovery, which occurred from January 8–13, 2015, daily average Dst increased from −38 to −16 nT.

Fig. 6.14 shows the footpoint locations of RBSP-B relative to PFISR for this case study. The black dots correspond to the four beam directions at 100 km altitude in

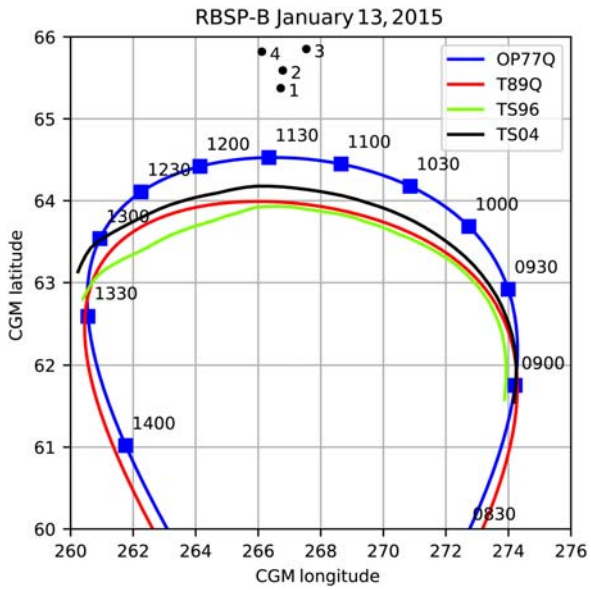

Figure 6.14 RBSP-B footpoints relative to 1P4F30ISR (at 100 km altitude) for the January 13, 2015, case study in Corrected GeoMagnetic coordinates (CGM) after mapping from the RBSP position to 100 km altitude using four magnetic field models. The times are listed in UT decimal hours. The blue, red, green, and black curves correspond to the Olsen-Pfitzer-77 (OP77), Tsyganenko-89 (T89) 0800, Tsyganenko-96 (TS96), and Tsyganenko-04 (TS04) magnetic field models, respectively.

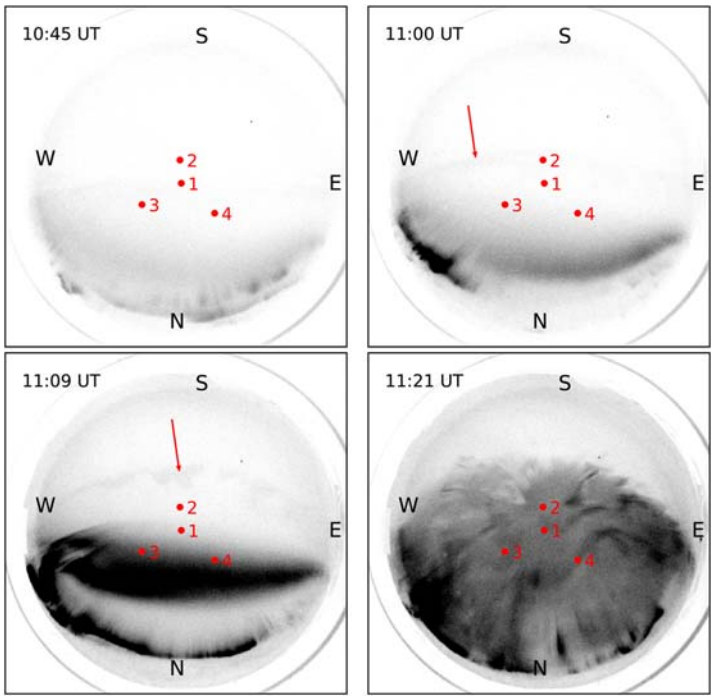

Figure 6.15 Montage of all-sky imager data detailing the event on January 13, 2015 at 1045, 1100, 1109, and 1121 UT.

Corrected GeoMagnetic coordinates (CGM) (Gustafsson et al., 1992). Four magnetic field models were used for comparison: the Olsen-Pfitzer-77 (OP77) model, the Tsyganenko-89 (T89) ($Kp = 2$) model (Tsyganenko, 1989), the Tsyganenko-96 model (TS96) (Tsyganenko and Stern, 1996), and the Tsyganenko-04 model (TS04) (Tsyganenko and Sitnov, 2005). RBSP-B footpoints were mapped to 100 km altitude in geographic coordinates and then converted into CGM magnetic coordinates to be consistent with PFISR. The Tsyganenko models produce consistent results, with nearly overlapping footpoints. The closest approach of the RBSP-B to PFISR is within 200 km.

Fig. 6.15 shows an all-sky imager montage of 557.7 nm green-line emissions, which occurs within 1 second of oxygen atoms being excited (e.g., Kelley, 2009). Each image contains the time, magnetic cardinal directions, and PFISR beam "pierce points" in the sky for all four of the beams, as shown in red. We show four representative intervals. At 1045 UT, there is a discrete aurora that appears to the north of all of the beams; however, there is a very weak diffuse aurora that intersects with the vertical beam (beam 2) and down-range beams (beams 3 and 4). Note that the magnitude of the 557.7-nm emission is almost below the detection threshold of the all-sky

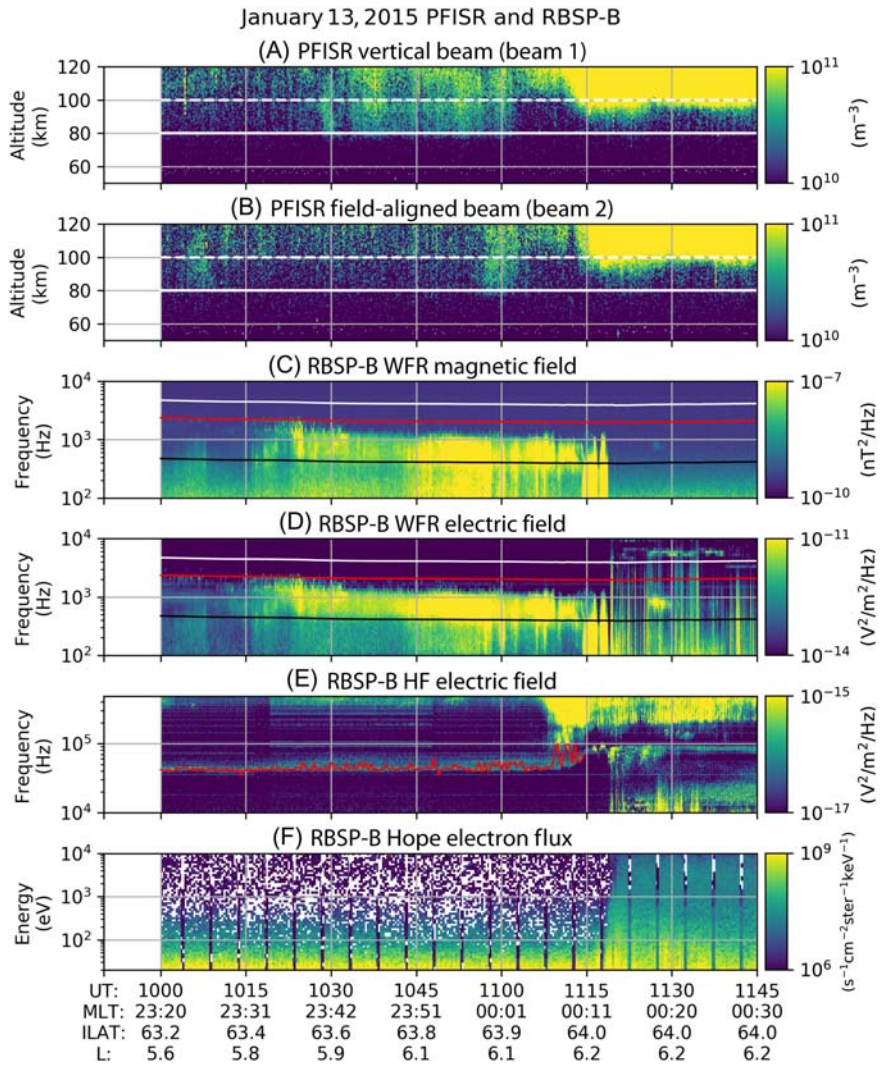

Figure 6.16 Summary of RBSP-B and PFISR data from January 13, 2015. *WFR*, waveform receiver. See text for detailed explanation.

imager. Fig. 6.16A shows that during this time there are clear ionization signatures observed by PFISR. At 1100 UT, there is a nearly subvisual auroral arc that has moved equatorward past the vertical (beam 1) and field-aligned (beam 2) radar beams. We indicate the westward edge of this arc with a red arrow; however, the arc does extend to the east over the vertical beam (beam 1). During this interval, an ionization signature occurs in Fig. 6.16B at 1100 UT, which likely is due to the passage of this faint arc across the vertical beam (beam 1). At 1109 UT, the poleward discrete aurora

has brightened into a single arc and has moved equatorward. In addition, the faint auroral arc that moved equatorward of the field-aligned beam (beam 2) has slightly brightened, with some wave-like structuring. At 1121 UT, the equatorward-moving auroral arc has broken up into pulsating aurorae that have filled the sky. Fig. 6.16A and B show clear ionization signatures at altitudes >100 km associated with this pulsating aurora. The overall morphology of this event appears to be consistent with a localized auroral substorm.

Fig. 6.16 presents a summary of the PFISR and RBSP-B observations. Fig. 6.16A and B are the electron density profiles observed by the vertical (beam 1) and field-aligned (beam 2) PFISR beams. These data are integrated for 10 seconds, and the dashed and solid white lines correspond to 100 km ($\sim$10 keV electron ionization) and 80 km ($\sim$100 keV electron ionization), respectively. Fig. 6.16C and D are waveform receiver (WFR) magnetic field and electric field spectrograms in the range 0.1−10 KHz (Kletzing et al., 2013). The horizontal white, red, and black lines are fractions of the electron cyclotron frequency (f_{ce}): f_{ce}, 0.5 f_{ce}, and 0.1 f_{ce}, respectively. Fig. 6.16E shows the wave power from the high-frequency components in the range 10−400 kHz. From this high-frequency range, it is possible to derive the in situ electron density by identifying the upper-hybrid resonance frequency, $\omega_{UHR}^2 = \omega_{pe}^2 + \Omega_{ce}^2$, where ω_{pe} and Ω_{ce} are the angular plasma frequency and electron cyclotron frequency, respectively. We have overplotted this red line, which corresponds to our estimate of the upper-hybrid frequency given by simply taking the maximum power within a frequency range. After 1115 UT, the estimation of the electron density from the upper-hybrid frequency becomes dubious. We then use that to calculate the electron density during this interval, which was on the order of 20 cm^{-3}. Fig. 6.16F corresponds to the plasma measurements from the ECT-HOPE instrument on the Van Allen Probes of the electron differential number flux from the 18 degrees pitch-angle bin (Spence et al., 2013). We note that the data from the 4.5 degrees pitch angle bin were not observed during this interval.

The interval we are interested in for this event is between 1025 and 1105 UT. PFISR observed relatively uniform ionization enhancements extending to lower altitudes ($\sim$80 km) in the vertical beam (beam 1) and somewhat more discrete segments in the field-aligned beam (beam 2). As mentioned previously, during this interval, auroral activity remained poleward of the PFISR field-of-view. Fig. 6.16A shows the PFISR vertical beam with uniform enhancements in the electron density between 80 and 120 km altitude. The more patchy nature in the field-aligned beam could be due in part to reduced sensitivity in the ISR antenna array in the field-aligned direction. Temporally coincident with the ISR electron density enhancements in Fig. 6.16A, there are also broad electromagnetic waves that are observed on RSBP-B, as shown in Figs. 6.16C and D, ranging in frequency from 100 to 1000 Hz. We note that within this structure there are intervals of more discrete electromagnetic wave activity.

Fig. 6.16B shows an electron density enhancement in the field-aligned radar beam at approximately 1100 UT, which correlates well with an intense enhancement of power in the RBSP magnetic and electric field components and the passage of the weak poleward-moving auroral arc. The electron density observed at RBSP-B, shown as a red line in Fig. 6.16E, during this interval was steady, with a value of approximately 20 cm^{-3}. Wave normal analysis of these data (not shown) indicate that broadband emission is within 20 degrees of being field aligned, and the waves are right-hand circularly polarized. Both of these findings are consistent with whistler-mode propagation, which includes plasmaspheric hiss and lower-band chorus (e.g., Millan and Thorne, 2007; Kletzing et al., 2013; Breneman et al., 2015). We interpret the broad electromagnetic emissions as likely being plasmaspheric hiss, although it is possible that some of the enhanced elements within this hiss are lower-band chorus waves. Finally, we note that the HOPE instrument did not observe electron flux enhancements associated directly with these wave signatures. This interval shows energetic particle precipitation associated with satellite observations of hiss or chorus signatures, but these signatures are not associated with a strong optical response.

After approximately 1110 UT, strong E-region ionization is observed at altitudes >100 km, as shown in Fig. 6.16A and B. These E-region electron density enhancements and pulsating aurorae are observed simultaneously; this is consistent with previous observations by Kaeppler et al. (2015). Nearly temporally coincident with the equatorward-moving aurora, at approximately 1115 UT, RBSP-B observes a distinct boundary crossing into a different magnetospheric region. We interpret the electromagnetic wave, plasma, and electron density observations before 1115 UT as being associated within the plasma trough. Before approximately 0930 UT (not shown), RBSP-B was in the plasmasphere, as indicated by the HFR data, in which the densities were on the order of 100–1000 cm^{-3}. However, after about 0930 UT, RBSP-B entered into the plasma trough with relatively stable densities near 20 cm^{-3}, and the plasma observations indicate warm electrons. After 1115 UT, the HOPE observations indicate a significantly hotter population of electrons. Fig. 6.16C and D show that there are different electric and magnetic wave signatures before and after 1115 UT; for example, there is a lack of magnetic wave activity after 1115 UT. We interpret these signatures as clear indications that RBSP-B passed through the plasmapause and into the hot plasmasheet at 1115 UT.

There are a few possible interpretations for the changes seen at $\sim$1110 UT in the combined RBSP-B and PFISR data. It is likely that before 1110 UT, PFISR was probing magnetic footpoints that correspond to the plasma trough or plasmasheet, while the RBSP-B observations were likely in the plasma trough. With the advancing equatorward aurora, after 1110 UT both RBSP-B and the magnetic footpoints at PFISR are in the equatorward side of the plasmasheet. Again, this is supported by the RBSP-B observations of distinctly different features. If we assume that the

measurements are conjugate, one interpretation is that the electromagnetic wave signatures could be chorus waves in the plasma trough and PFISR is observing the precipitation signatures associated with the chorus. However, the plasma trough has a high enough density that it may be possible that the wave signatures are plasmaspheric hiss. That could explain hiss (or hiss-like signature) observations by RBSP in a region similar to that for PFISR. However, this hypothesis suggests that the measurements are in fact conjugate; if we do not assume that the measurements are conjugate, perhaps the most plausible explanation is that the observations are purely a coincidence. In this case, RBSP may have been in the plasma trough, while the PFISR footpoints mapped outside the plasmapause into the plasmasheet. The full interpretation of this event requires further analysis and interpretation, which is outside of the scope of this chapter, but will be forthcoming in a future publication of the event.

Regardless, one of the most compelling aspects of this event from January 13, 2015, is the fact that energetic precipitation occurs between 1000 and 1110 UT, during an interval of relative quiet before a substorm. Moreover, the visual magnitude of this event is very weak and nearly subvisual. These observations were taken with coincident wave signatures, which may suggest that chorus or hiss waves were responsible for the observed precipitation signatures at the ionospheric footpoint. This event appears to be consistent with previous observations by Kirkwood and Eliasson (1990) and Sivadas et al. (2017). It suggests the importance of quantifying the D-region electron density even during intervals of relative quiet.

While the analysis for this event is ongoing, we present this event as an example of events we have collected as part of our ongoing satellite-ISR observation campaign. One of the important aspects of this event is the occurrence of the enhanced D-region electron density during a relatively quiet interval and immediately preceding a substorm. One of the challenges moving forward toward eventual scientific closure is to understand the impact of magnetic mapping on these observations. However, in the case, in which plasma waves may be correlated over large spatial regions at the geomagnetic equator, this constraint becomes less restrictive. A second aspect that will be addressed is performing inversions of the ISR data to estimate the precipitating electron differential number flux and comparing that against the theory of wave-particle interactions. This, too, is outside the scope of this chapter.

6.6 Outlook

There are many open and compelling questions that can be addressed with ISR observations of energetic particle precipitation. The most important outstanding issue is quantifying particle precipitation that is caused by wave-particle interactions with various plasma waves in the magnetosphere. Observations from ISR can be examined on a statistical or a case-by-case basis to constrain theoretical estimates for the magnitude

of fluxes that are scattered into the loss cone. These results can address which plasma waves are most responsible for loss into the atmosphere, and which plasma waves are important for generating diffuse aurora, pulsating aurorae, and radiation belt loss. A secondary consequence is the impact of this energetic precipitation on the atmosphere. Quantifying the differential number flux entering the atmosphere puts constraints on the wave-particle interaction theory and also on the inputs into models of the upper atmosphere.

A major outstanding unknown is the magnitude of the quiet-time energetic particle precipitation, and the impact of this "drizzle" of energetic precipitation. Is it always present or does energetic particle precipitation occur only during geomagnetically disturbed intervals? For example, Sivadas et al. (2017) found that the majority of the energy was carried by energetic electrons during the main phase of a substorm. Quantifying the loss during quiet intervals is therefore important for understanding the relative magnitude of loss processes in quiet or disturbed intervals. It is also important for quantifying the constant driving of the atmosphere by energetic particle precipitation.

With respect to pulsating aurorae, one of the interesting results by Hosokawa and Ogawa (2015) showed that two populations of precipitation could be observed in some pulsating aurorae, but not necessarily coincidentally. This may suggest that two types of plasma waves are responsible for the precipitation at different times, but this hypothesis requires further investigation. Such a study could suggest trends for which plasma waves are responsible for pulsating auroral precipitation at a given magnetic local time. High time cadence measurements from ISR can also contribute to understanding on–off modulation in pulsating aurorae. One of the most important outstanding questions regarding pulsating aurora is what causes the on–off modulation to occur? In addition, what are the magnitudes of changes in the characteristic energy and energy flux in the on and off phases of modulations? Some evidence suggests that they are significant, but only through more event studies can this question be resolved. Furthermore, what does this imply about potential plasma waves causing these modulations?

While this topic was largely unaddressed in this review, the response of the feedback from the ionosphere during pulsating auroral intervals remains unresolved. While the dominant thought may be toward primarily magnetospheric control, Stenbaek-Nielsen and Hallinan (1979) and Stenbaek-Nielsen (1980) suggest the importance of the ionospheric portion on pulsating aurorae. This aspect is optimally studied using ISR. In addition, the origin and observation of thin layers associated with pulsating aurorae also remains unresolved.

From the perspective of understanding substorms, an outstanding question is how the energy of particle precipitation changes as a function of phase in the substorm cycle. The observations presented in Section 6.3.1 seem to suggest the significance of

energetic particle precipitation in all phases of the substorm cycle; however, the observations that show energetic particle precipitation in each phase are from one or two case studies. Are these single events representative of the typical trend? More importantly, is understanding the connection between the ionospheric observations relative to processes that are occurring in the magnetosphere (i.e., injections, dipolarization, etc.)? A clear picture that connects energetic particle precipitation with magnetospheric processes and accounts for time delays remains to be discovered.

From the measurement perspective, the most important outstanding issue is the validation of D-region chemistry models. These models are important for understanding the generation of electron density in response to energetic particle precipitation. At this time, validation of these models through observations by suitable platforms remains an important task for bringing closure to our understanding of D-region chemistry.

Moving forward, there are two proactive steps that can be taken. The first is to continue routine monitoring of the D-region using ISR observation from the US and EISCAT communities. Only through regular and routine observations from ISRs will enough data be collected, of the correct type and quality, to bring closure to the above open scientific questions. The second is for an effort to be undertaken to mine the existing ISR data to try to resolve the aforementioned outstanding topics.

6.7 Summary

We have presented a review of incoherent scatter radar-based techniques for quantifying particle precipitation with energies of 10−100 keV. We presented a review of the technique for determining precipitating differential number fluxes given electron density measurements by ISR. Specifically, we presented a brief review of particle transport models and techniques, relevant E- and D-region chemistry models, and a review of techniques for combining these methods to model electron density enhancements that occur owing to energetic precipitation. We reviewed literature surrounding two of the most common sources of 10−100 keV particles: substorms and pulsating aurorae. We also presented results from an isolated event during a geomagnetically disturbance on April 23, 2008, which showed energetic precipitation with energies on the order of 200−300 keV. This event would likely not have been captured had it not been for regular observations of the D-region ionosphere.

Since 2015, PFISR has been run during intervals of near-conjunction with the Van Allen Probes and the Arase satellite. The special D-region PFISR mode was described, specifically how it is tuned for observations of the D-region. We showed the conjunction intervals from 2015−2017 relative to the SYM-H index to show the coverage of observations during geomagnetically quiet and active intervals. An example case event from January 13, 2015, was presented during a near-conjunction with

RBSP-B, in which enhanced electron densities were observed down to 80 km at the same time that observations of lower-band chorus or hiss waves were present. Our preliminary analysis suggests that these ionization signatures may have been driven by the observed electromagnetic waves on RBSP-B. This is one example out of many candidate events that can be studied individually or statistically to determine the properties of energetic precipitation into the ionosphere–thermosphere–mesosphere region.

Acknowledgments

This work was supported by National Science Foundation grant AGS-1732365 and cooperative agreement AGS-1133009 to SRI International. SRK wishes to thank C. Gabrielse-Lin for useful discussions regarding auroral substorms. We acknowledge NASA contract NAS5-02099 and V. Angelopoulos for use of data from the THEMIS Mission, specifically, S. Mende and E. Donovan for use of the ASI data, the CSA for logistical support in fielding and data retrieval from the GBO stations, and NSF for support of GIMNAST through grant AGS-1004736.

References

Akasofu, S.-I., 1964. The development of the auroral substorm. Planet. Space. Sci. 12 (4), 273–282. Available from: https://doi.org/10.1016/0032-0633(64)90151-5.

Banks, P.M., Nagy, A.F., 1970. Concerning the influence of elastic scattering upon photoelectron transport and escape. J. Geophys. Res. 75, 1902–1910. Available from: https://doi.org/10.1029/JA075i010p01902.

Banks, P.M., Chappell, C.R., Nagy, A.F., 1974. A new model for the interaction of auroral electrons with the atmosphere: spectral degradation, backscatter, optical emission, and ionization. J. Geophys. Res. 79, 1459. Available from: https://doi.org/10.1029/JA079i010p01459.

Baron, M.J., 1974. Electron densities within aurorae and other auroral e-region characteristics. Radio Sci. 9 (2), 341–348. Available from: https://doi.org/10.1029/RS009i002p00341.

Barrett, J.L., Hays, P.B., 1976. Spatial distribution of energy deposited in nitrogen by electrons. J. Chem. Phys. 64, 743–750. Available from: https://doi.org/10.1063/1.432221.

Basu, B., Jasperse, J.R., Strickland, D.J., Daniell Jr., R.E., 1993. Transport-theoretic model for the electron-proton-hydrogen atom aurora. 1: theory. J. Geophys. Res. 98, 21,517. Available from: https://doi.org/10.1029/93JA01646.

Baumjohann, W., Treumann, R., 2012. Basic Space Plasma Physics. Imperial College Press, London.

Beharrell, M.J., Honary, F., Rodger, C.J., Clilverd, M.A., 2015. Substorm-induced energetic electron precipitation: morphology and prediction. J. Geophys. Res. Space Phys. 120 (4), 2993–3008. Available from: https://doi.org/10.1002/2014JA020632. 2014JA020632.

Berger, M.J., Seltzer, S.M., Maeda, K., 1970. Energy deposition by auroral electrons in the atmosphere. J Atmos. Terr. Phys. 32 (6), 1015–1045. Available from: https://doi.org/10.1016/0021-9169(70)90115-7.

Bilitza, D., Reinisch, B.W., 2008. International reference ionosphere 2007: improvements and new parameters. Adv. Space. Res. 42, 599–609. Available from: https://doi.org/10.1016/j.asr.2007.07.048.

Biondi, M.A., 1969. Atmospheric electron-ion and ion-ion recombination processes. Can. J. Chem. 47 (10), 1711–1719. Available from: https://doi.org/10.1139/v69-282.

Blelly, P.L., Robineau, A., Lummerzheim, D., Lilensten, J., 1996. 8-moment fluid models of the terrestrial high latitude ionosphere between 100 and 3000 km. In: Schunk, R.W. (Ed.), Solar-Terrestrial Energy Program: Handbook of Ionospheric Models. Center for Atmospheric and Space Sciences, Logan, UT, p. 53.

Blelly, P.-L., Lathuillère, C., Emery, B., Lilensten, J., Fontanari, J., Alcaydé, D., 2005. An extended transcar model including ionospheric convection: simulation of eiscat observations using inputs from amie. Ann. Geophys. 23 (2), 419–431. Available from: https://doi.org/10.5194/angeo-23-419-2005.

Blum, L.W., Schiller, Q., Li, X., Millan, R., Halford, A., Woodger, L., 2013. New conjunctive cubesat and balloon measurements to quantify rapid energetic electron precipitation. Geophys. Res. Lett. 40 (22), 5833–5837. Available from: https://doi.org/10.1002/2013GL058546. 2013GL058546.

Brekke, A., Hall, C., Hansen, T.L., 1989. Auroral ionospheric conductances during disturbed conditions. Ann. Geophys. 7, 269–280.

Breneman, A.W., Halford, A., Millan, R., McCarthy, M., Fennell, J., Sample, J., et al., 2015. Global-scale coherence modulation of radiation-belt electron loss from plasmaspheric hiss. Nature 523, 193–195. Available from: https://doi.org/10.1038/nature14515.

Bryant, D., Courtier, G., Bennett, G., 1971. Equatorial modulation of electrons in a pulsating aurora. J. Atmos. Sol. Terr. Phys. 33 (6), 859–867. Available from: https://doi.org/10.1016/0021-9169(71)90086-9.

Bösinger, T., Kaila, K., Rasinkangas, R., Pollari, P., Kangas, J., Trakhtengerts, V., et al., 1996. An eiscat study of a pulsating auroral arc: simultaneous ionospheric electron density, auroral luminosity and magnetic field pulsations. J. Atmos. Sol. Terr. Phys. 58 (1), 23–35. Available from: https://doi.org/10.1016/0021-9169(95)00017-8. selected papers from the sixth international Eiscat Workshop.

Carlson, C.W., Pfaff, R.F., Watzin, J.G., 1998. The fast auroral snapshot (fast) mission. Geophys. Res. Lett. 25 (12), 2013–2016. Available from: https://doi.org/10.1029/98GL01592.

Chandrasekhar, S., 1960. Radiative transfer. Dover Books on Intermediate and Advanced Mathematics. Dover Publications.

Cicerone, R.J., Bowhill, S.A., 1970. Photoelectron escape fluxes obtained by a monte carlo technique. Radio Sci. 5 (1), 49–53. Available from: https://doi.org/10.1029/RS005i001p00049.

Clilverd, M.A., Rodger, C.J., Rae, I.J., Brundell, J.B., Thomson, N.R., Cobbett, N., et al., 2012. Combined themis and ground-based observations of a pair of substorm-associated electron precipitation events. J. Geophys. Res. Space Phys. 117 (A2), . Available from: https://doi.org/10.1029/2011JA016933a02313, n/a–n/a.

Coakley, J.A., Chylek, P., 1975. The two-stream approximation in radiative transfer: including the angle of the incident radiation. J. Atmos. Sci. 32 (2), 409–418. Available from: https://doi.org/10.1175/1520-0469(1975)032<0409:TTSAIR>2.0.CO;2.

Cowley, S., Lockwood, M., 1997. Incoherent scatter radar observations related to magnetospheric dynamics. Adv. Space. Res. 20 (4), 873–882. Available from: https://doi.org/10.1016/S0273-1177(97)00495-X.

Cummer, S.A., Bell, T.F., Inan, U.S., Chenette, D.L., 1997. VLF remote sensing of high-energy auroral particle precipitation. J. Geophys. Res. Space Phys. 102 (A4), 7477–7484. Available from: https://doi.org/10.1029/96JA03721.

Dahlgren, H., Lanchester, B.S., Ivchenko, N., Whiter, D.K., 2017. Variations in energy, flux, and brightness of pulsating aurora measured at high time resolution. Ann. Geophys. 35 (3), 493–503. Available from: https://doi.org/10.5194/angeo-35-493-2017.

Doe, R.A., Kelly, J.D., Lummerzheim, D., Parks, G.K., Brittnacher, M.J., Germany, G.A., et al., 1997. Initial comparison of POLAR UVI and Sondrestrom IS radar estimates for auroral electron energy flux. Geophys. Res. Lett. 24, 999–1002. Available from: https://doi.org/10.1029/97GL00376.

Dougherty, J.P., 1963. The conductivity of a partially ionized gas in alternating electric fields. J. Fluid. Mech. 16 (1), 126–137. Available from: https://doi.org/10.1017/S002211206300063X.

Dougherty, J.P., Farley, D.T., 1961. A theory of incoherent scattering of radio waves by a plasma. Proc. R. Soc. Lond. A Math. Phys. Eng. Sci. 259 (1296), 79–99. Available from: https://doi.org/10.1098/rspa.1960.0212.

Dougherty, J.P., Farley, D.T., 1963. A theory of incoherent scattering of radio waves by a plasma: 3. scattering in a partly ionized gas. J. Geophys. Res. 68 (19), 5473–5486. Available from: https://doi.org/10.1029/JZ068i019p05473.

Evans, J.V., 1969. Theory and practice of ionosphere study by thomson scatter radar. Proc. IEEE 57 (4), 496–530. Available from: https://doi.org/10.1109/PROC.1969.7005.

Evans, D.S., 1974. Precipitating electron fluxes formed by a magnetic field aligned potential difference. J. Geophys. Res. 79, 2853. Available from: https://doi.org/10.1029/JA079i019p02853.

Evans, D.S., Davidson, G.T., Voss, H.D., Imhof, W.L., Mobilia, J., Chiu, Y.T., 1987. Interpretation of electron spectra in morningside pulsating aurorae. J. Geophys. Res. Space Physics 92 (A11), 12,295–12,306. Available from: https://doi.org/10.1029/JA092iA11p12295.

Fang, X., Randall, C.E., Lummerzheim, D., Solomon, S.C., Mills, M.J., Marsh, D.R., et al., 2008. Electron impact ionization: a new parameterization for 100 ev to 1 mev electrons. J. Geophys. Res. Space Phys. 113 (A9). Available from: https://doi.org/10.1029/2008JA013384.

Fang, X., Randall, C.E., Lummerzheim, D., Wang, W., Lu, G., Solomon, S.C., et al., 2010. Parameterization of monoenergetic electron impact ionization. Geophys. Res. Lett. 37 (22). Available from: https://doi.org/10.1029/2010GL045406.

Farley, D.T., 1969. Incoherent scatter correlation function measurements. Radio Sci. 4 (10), 935953. Available from: https://doi.org/10.1029/RS004i010p00935.

Foster, J.C., Doupnik, J.R., Stiles, G.S., 1980. Ionospheric density enhancement during relativistic electron precipitation. Geophys. Res. Lett. 7 (11), 929–932. Available from: https://doi.org/10.1029/GL007i011p00929.

Gabrielse, C., Angelopoulos, V., Runov, A., Turner, D.L., 2014. Statistical characteristics of particle injections throughout the equatorial magnetotail. J. Geophys. Res. Space Phys. 119 (4), 2512–2535. Available from: https://doi.org/10.1002/2013JA019638.

Gattinger, R.L., Jones, A.V., Hecht, J.H., Strickland, D.J., Kelley, J., 1991. Comparison of ground-based optical observations of N2 second positive to N2(+) first negative emission ratios with electron precipitation energies inferred from the Sondre Stromfjord radar. J. Geophys. Res. 96, 11,341. Available from: https://doi.org/10.1029/91JA01015.

Gledhill, J.A., 1986. The effective recombination coefficient of electrons in the ionosphere between 50 and 150 km. Radio Sci. 2 (3), 399–408. Available from: https://doi.org/10.1029/RS021i003p00399.

Glukhov, V.S., Pasko, V.P., Inan, U.S., 1992. Relaxation of transient lower ionospheric disturbances caused by lightning-whistler-induced electron precipitation bursts. J. Geophys. Res. Space Phys. 97 (A11), 16,971–16,979. Available from: https://doi.org/10.1029/92JA01596.

Grün, A.E., 1957. Lumineszenz-photometrische Messunen der Energieabsorption im Strahlungsfeld von Electronenquellen. Eindimensionaler Fall in Luft, Z. Naturforsch. Teil A 12, 89–95. Available from: https://doi.org/10.1515/zna-1957-0201.

Gustafsson, G., Papitashvili, N.E., Papitashvili, V.O., 1992. A revised corrected geomagnetic coordinate system for Epochs 1985 and 1990. J. Atmos. Sol. Terr. Phys. 54, 1609–1631.

Halford, A.J., McGregor, S.L., Murphy, K.R., Millan, R.M., Hudson, M.K., Woodger, L.A., et al., 2015. Barrel observations of an icme-shock impact with the magnetosphere and the resultant radiation belt electron loss. J. Geophys. Res. Space Phys. 120 (4), 2557–2570. Available from: https://doi.org/10.1002/2014JA020873.

Halford, A.J., McGregor, S.L., Hudson, M.K., Millan, R.M., Kress, B.T., 2016. Barrel observations of a solar energetic electron and solar energetic proton event. J. Geophys. Res. Space Phys. 121 (5), 4205–4216. Available from: https://doi.org/10.1002/2016JA022462.

Horne, R.B., Glauert, S.A., Thorne, R.M., 2003. Resonant diffusion of radiation belt electrons by whistler-mode chorus. Geophys. Res. Lett. 30 (9). Available from: https://doi.org/10.1029/2003GL016963.

Hosokawa, K., Ogawa, Y., 2015. Ionospheric variation during pulsating aurora. J. Geophys. Res. Space Phys. 120 (7), 5943–5957. Available from: https://doi.org/10.1002/2015JA021401.

Humberset, B.K., Gjerloev, J.W., Samara, M., Michell, R.G., Mann, I.R., 2016. Temporal characteristics and energy deposition of pulsating auroral patches. J. Geophys. Res. Space Phys. 121 (7), 7087–7107. Available from: https://doi.org/10.1002/2016JA022921. 2016JA022921.

Jaynes, A.N., Lessard, M.R., Rodriguez, J.V., Donovan, E., Loto'aniu, T.M., Rychert, K., 2013. Pulsating auroral electron flux modulations in the equatorial magnetosphere. J. Geophys. Res. Space Phys. 118 (8), 4884–4894. Available from: https://doi.org/10.1002/jgra.50434.

Johnstone, A.D., 1978. Pulsating aurora. Nature 274, 119.

Jones, S., Lessard, M., Fernandes, P., Lummerzheim, D., Semeter, J., Heinselman, C., et al., 2009. PFISR and ROPA observations of pulsating aurora. J. Atmos. Sol. Terr. Phys. 71 (6), 708–716. Available from: https://doi.org/10.1016/j.jastp.2008.10.004. advances in high latitude upper atmospheric science with the Poker Flat Incoherent Scatter Radar (PFISR).

Jones, S.L., Lessard, M.R., Rychert, K., Spanswick, E., Donovan, E., Jaynes, A.N., 2013. Persistent, widespread pulsating aurora: a case study. J. Geophys. Res. Space Phys. 118 (6), 2998–3006. Available from: https://doi.org/10.1002/jgra.50301.

Kaeppler, S.R., 2013. A Rocket-Borne Investigation of Auroral Electrodynamics Within the Auroral-Ionosphere. University of Iowa, Iowa City, Ph.D. thesis.

Kaeppler, S.R., Hampton, D.L., Nicolls, M.J., Strömme, A., Solomon, S.C., Hecht, J.H., et al., 2015. An investigation comparing ground-based techniques that quantify auroral electron flux and conductance. J. Geophys. Res. Space Phys. 120 (10), 9038–9056. Available from: https://doi.org/10.1002/2015JA021396.

Kaila, K., Rasinkangas, R., 1989. Coordinated photometer and incoherent scatter radar measurement of pulsating arcs with high time resolution. Planet. Space. Sci. 37 (5), 545–553. Available from: https://doi.org/10.1016/0032-0633(89)90095-0.

Kaila, K., Rasinkangas, R., Pollari, P., Kuula, R., Kangas, J., Turunen, T., et al., 1989. High resolution measurements of pulsating aurora by eiscat, optical instruments and pulsation magnetometers. Adv. Space. Res. 9 (5), 53–56. Available from: https://doi.org/10.1016/0273-1177(89)90340-2.

Kasahara, S., Miyoshi, Y., Yokota, S., Mitani, T., Kasahara, Y., Matsuda, S., et al., 2018. Pulsating aurora from electron scattering by chorus waves. Nature 554, 337.

Kelley, M., 2009. The Earth's Ionosphere: Plasma Physics and Electrodynamics. International Geophysics, Academic Press, New York.

Kelly, J.D., Heinselman, C.J., 2009. Initial results from poker flat incoherent scatter radar (pfisr). J. Atmos. Sol. Terr. Phys. 71 (6), 635. Available from: https://doi.org/10.1016/j.jastp.2009.01.009.

Kennel, C.F., Petschek, H.E., 1966. Limit on stably trapped particle fluxes. J. Geophys. Res. 71, 1.

Kirkwood, S., 1988. SPECTRUM: a computer algorithm to derive the flux-energy spectrum of precipitating particles from EISCAT electron density profiles, IRF technical report, Swedish Institute of Space Physics, Kiruna.

Kirkwood, S., Eliasson, L., 1990. Energetic particle precipitation in the substorm growth phase measured by eiscat and viking. J. Geophys. Res. Space Phys. 95 (A5), 6025–6037. Available from: https://doi.org/10.1029/JA095iA05p06025.

Kirkwood, S., Osepian, A., 1995. Quantitative studies of energetic particle precipitation using incoherent scatter radar. J. Geomagnet. Geoelec. 47 (8), 783–799. Available from: https://doi.org/10.5636/jgg.47.783.

Kirkwood, S., Eliasson, L., Opgenoorth, H., Pellinen-Wannberg, A., 1989. A study of auroral electron acceleration using the eiscat radar and the viking satellite. Adv. Space. Res. 9 (5), 49–52. Available from: https://doi.org/10.1016/0273-1177(89)90339-6.

Kivelson, M.G., Russell, C.T., 1995. Introduction to Space Physics. Cambridge University Press, Cambridge, UK.

Kletzing, C.A., Kurth, W.S., Acuna, M., MacDowall, R.J., Torbert, R.B., Averkamp, T., et al., 2013. The electric and magnetic field instrument suite and integrated science (EMFISIS) on RBSP. Space Sci. Rev. 179, 127–181. Available from: https://doi.org/10.1007/s11214-013-9993-6.

Kovács, T., Plane, J.M.C., Feng, W., Nagy, T., Chipperfield, M.P., Verronen, P.T., et al., 2016. *d*-Region ion–neutral coupled chemistry (sodankylä ion chemistry, sic) within the whole atmosphere community climate model (waccm 4)–waccm-sic and waccm-rsic. Geosci. Model Dev. 9 (9), 3123–3136. Available from: https://doi.org/10.5194/gmd-9-3123-2016.

Lehtinen, N.G., 2000. Relativistic Runaway Electrons Above Thunderstorms. Ph.D. thesis, Stanford University, Stanford, CA.

Lehtinen, N.G., Inan, U.S., 2007. Possible persistent ionization caused by giant blue jets. Geophys. Res. Lett. 34 (8). Available from: https://doi.org/10.1029/2006GL029051.

Lehtinen, N.G., Bell, T.F., Inan, U.S., 1999. Monte Carlo simulation of runaway MeV electron breakdown with application to red sprites and terrestrial gamma ray flashes. J. Geophys. Res. 104, 24,699–24,712. Available from: https://doi.org/10.1029/1999JA900335.

Lessard, M.R., 2013. A Review of Pulsating Aurora. American Geophysical Union, pp. 55–68. Available from: https://doi.org/10.1029/2011GM001187.

Li, Z., Millan, R.M., Hudson, M.K., 2013. Simulation of the energy distribution of relativistic electron precipitation caused by quasi-linear interactions with EMIC waves. J. Geophys. Res. Space Phys. 118, 7576–7583. Available from: https://doi.org/10.1002/2013JA019163.

Li, Z., Millan, R.M., Hudson, M.K., Woodger, L.A., Smith, D.M., Chen, Y., et al., 2014. Investigation of EMIC wave scattering as the cause for the BARREL 17 January 2013 relativistic electron precipitation event: a quantitative comparison of simulation with observations. Geophys. Res. Lett. 41, 8722–8729. Available from: https://doi.org/10.1002/2014GL062273.

Link, R., 1992. Feautrier solution of the electron transport equation. J. Geophys. Res. Space Phys. 97 (A1), 159–169. Available from: https://doi.org/10.1029/91JA02214.

Link, R., Chakrabarti, S., Gladstone, G.R., McConnell, J.C., 1988. An analysis of satellite observations of the O I EUV dayglow. J. Geophys. Res. Space Phys. 93 (A4), 2693–2714. Available from: https://doi.org/10.1029/JA093iA04p02693.

Lummerzheim, D., Lilensten, J., 1994. Electron transport and energy degradation in the ionosphere: evaluation of the numerical solution, comparison with laboratory experiments and auroral observations. Ann. Geophys. 12, 1039–1051. Available from: https://doi.org/10.1007/s00585-994-1039-7.

Lyons, L.R., Nishimura, Y., Shi, Y., Zou, S., Kim, H.-J., Angelopoulos, V., et al., 2010. Substorm triggering by new plasma intrusion: incoherent-scatter radar observations. J. Geophys. Res. Space Phys. 115 (A7). Available from: https://doi.org/10.1029/2009JA015168.

Markwardt, C.B., 2009. Non-linear least-squares fitting in IDL with MP-FIT. In: Bohlender, D.A., Durand, D., Dowler, P. (Eds.), Astronomical Data Analysis Software and Systems XVIII, Astronomical Society of the Pacific Conference Series, vol. 411. Astronomical Society of the Pacific, San Francisco, p. 251.

Marshall, R.A., Bortnik, J., 2018. Pitch angle dependence of energetic electron precipitation: energy deposition, backscatter, and the bounce loss cone. J. Geophys. Res. 123. Available from: https://doi.org/10.1002/2017JA024873.

Marshall, R.A., Nicolls, M., Sanchez, E., Lehtinen, N.G., Neilson, J., 2014. Diagnostics of an artificial relativistic electron beam interacting with the atmosphere. J. Geophys. Res. Space Phys. 119 (10), 8560–8577. Available from: https://doi.org/10.1002/2014JA020427.

McEwen, D.J., Yee, E., Whalen, B.A., Yau, A.W., 1981. Electron energy measurements in pulsating auroras. Can. J. Phys. 59 (8), 1106–1115. Available from: https://doi.org/10.1139/p81-146.

McIlwain, C.E., 1960. Direct measurement of particles producing visible auroras. J. Geophys. Res. 65, 2727.

Millan, R., 2011. Understanding relativistic electron losses with barrel. J. Atmos. Sol. Terr. Phys. 73 (11), 1425–1434. Available from: https://doi.org/10.1016/j.jastp.2011.01.006.

Millan, R.M., Thorne, R.M., 2007. Review of radiation belt relativistic electron losses. J. Atmos. Sol. Terr. Phys. 69, 362–377. Available from: https://doi.org/10.1016/j.jastp.2006.06.019.

Millan, R.M., McCarthy, M.P., Sample, J.G., Smith, D.M., Thompson, L.D., McGaw, D.G., et al., 2013. The balloon array for RBSP relativistic electron losses (BARREL). Space Sci. Rev. 179, 503–530. Available from: https://doi.org/10.1007/s11214-013-9971-z.

Miyoshi, Y., Katoh, Y., Nishiyama, T., Sakanoi, T., Asamura, K., Hirahara, M., 2010. Time of flight analysis of pulsating aurora electrons, considering wave–particle interactions with propagating whistler mode waves. J. Geophys. Res. Space Phys. 115 (A10). Available from: https://doi.org/10.1029/2009JA015127.

Miyoshi, Y., Oyama, S., Saito, S., Kurita, S., Fujiwara, H., Kataoka, R., et al., 2015. Energetic electron precipitation associated with pulsating aurora: Eiscat and van allen probe observations. J. Geophys. Res. Space Phys. 120 (4), 2754–2766. Available from: https://doi.org/10.1002/2014JA020690.

Nagy, A.F., Banks, P.M., 1970. Photoelectron fluxes in the ionosphere. J. Geophys. Res. 75, 6260–6270. Available from: https://doi.org/10.1029/JA075i031p06260.

Ni, B., Thorne, R.M., Shprits, Y.Y., Bortnik, J., 2008. Resonant scattering of plasma sheet electrons by whistler-mode chorus: contribution to diffuse auroral precipitation. Geophys. Res. Lett. 35 (11). Available from: https://doi.org/10.1029/2008GL034032.

Ni, B., Thorne, R.M., Horne, R.B., Meredith, N.P., Shprits, Y.Y., Chen, L., et al., 2011a. Resonant scattering of plasma sheet electrons leading to diffuse auroral precipitation: 1. Evaluation for electrostatic electron cyclotron harmonic waves. J. Geophys. Res. Space Phys. 116, A04218. Available from: https://doi.org/10.1029/2010JA016232.

Ni, B., Thorne, R.M., Meredith, N.P., Horne, R.B., Shprits, Y.Y., 2011b. Resonant scattering of plasma sheet electrons leading to diffuse auroral precipitation: 2. Evaluation for whistler mode chorus waves. J. Geophys. Res. Space Phys. 116, A04219. Available from: https://doi.org/10.1029/2010JA016233.

Nicolls, M.J., Varney, R.H., Vadas, S.L., Stamus, P.A., Heinselman, C.J., Cosgrove, R.B., et al., 2010. Influence of an inertia-gravity wave on mesospheric dynamics: a case study with the poker flat incoherent scatter radar. J. Geophys. Res. Atmos. 115 (D3), . Available from: https://doi.org/10.1029/2010JD014042d00N02, n/a–n/a.

Nishimura, Y., Bortnik, J., Li, W., Thorne, R.M., Lyons, L.R., Angelopoulos, V., et al., 2010. Identifying the driver of pulsating aurora. Science 330 (6000), 81–84. Available from: https://doi.org/10.1126/science.1193186.

Nishimura, Y., Bortnik, J., Li, W., Thorne, R.M., Chen, L., Lyons, L.R., et al., 2011. Multievent study of the correlation between pulsating aurora and whistler mode chorus emissions. J. Geophys. Res. Space Phys. 116 (A11). Available from: https://doi.org/10.1029/2011JA016876.

Nishimura, Y., Bortnik, J., Li, W., Thorne, R.M., Ni, B., Lyons, L.R., et al., 2013. Structures of dayside whistler-mode waves deduced from conjugate diffuse aurora. J. Geophys. Res. Space Phys. 118 (2), 664–673. Available from: https://doi.org/10.1029/2012JA018242.

Osepian, A., Vlaskov, V., Ranta, H., Ranta, A., Turunen, E., 1993. High-latitude plasma densities in the middle atmosphere and characteristics of precipitating electrons during an auroral absorption substorm. Adv. Space. Res. 13 (4), 99–104. Available from: https://doi.org/10.1016/0273-1177(93)90319-7.

Osepian, A., Tereschenko, V., Dalin, P., Kirkwood, S., 2008. The role of atomic oxygen concentration in the ionization balance of the lower ionosphere during solar proton events. Ann. Geophys. 26 (1), 131–143. Available from: https://doi.org/10.5194/angeo-26-131-2008.

Osepian, A., Kirkwood, S., Dalin, P., 2009a. The influence of ozone concentration on the lower ionosphere: modelling and measurements during the 29 and 30 october 2003 solar proton event. Ann. Geophys. 27 (2), 577–589. Available from: https://doi.org/10.5194/angeo-27-577-2009.

Osepian, A., Kirkwood, S., Dalin, P., Tereschenko, V., 2009b. D-region electron density and effective recombination coefficients during twilight: experimental data and modelling during solar proton events. Ann. Geophys. 27 (10), 3713–3724. Available from: https://doi.org/10.5194/angeo-27-3713-2009.

Picone, J.M., Hedin, A.E., Drob, D.P., Aikin, A.C., 2002. NRLMSISE-00 empirical model of the atmosphere: statistical comparisons and scientific issues. J. Geophys. Res. Space Phys. 107, 1468. Available from: https://doi.org/10.1029/2002JA009430.

Porter, H.S., Green, A.E.S., 1975. Comparison of monte carlo and continuous slowing-down approximation treatments of 1-kev proton energy deposition in N2. J. Appl. Phys. 46 (11), 5030–5038. Available from: https://doi.org/10.1063/1.321493.

Press, W., Teukolsky, S., Vetterling, W., Flannery, B., 2007. Numerical Recipes: The Art of Scientific Computing, third ed. Cambridge University Press, Cambridge, UK.

Rees, M.H., 1963. Auroral ionization and excitation by incident energetic electrons. Planet. Space. Sci. 11, 1209. Available from: https://doi.org/10.1016/0032-0633(63)90252-6.

Rees, M.H., 1989. Physics and Chemistry of the Upper Atmosphere, Cambridge Atmospheric and Space Science Series. Cambridge University Press, Cambridge, UK.

Richards, P.G., Torr, D.G., 1985. The altitude variation of the ionospheric photoelectron flux: a comparison of theory and measurement. J. Geophys. Res. Space Phys. 90 (A3), 2877–2884. Available from: https://doi.org/10.1029/JA090iA03p02877.

Richards, P.G., Torr, D.G., 1990. Auroral modeling of the 3371 a emission rate: dependence on characteristic electron energy. J. Geophys. Res. Space Phys. 95 (A7), 10,337–10,344. Available from: https://doi.org/10.1029/JA095iA07p10337.

Richards, M., Holm, W., Scheer, J., 2010a. Principles of Modern Radar: Basic Principles, Electromagnetics and Radar. Institution of Engineering and Technology, SciTech Publishing, Raleigh, NC.

Richards, P.G., Bilitza, D., Voglozin, D., 2010b. Ion density calculator (IDC): a new efficient model of ionospheric ion densities. Radio Sci. 45 (5). Available from: https://doi.org/10.1029/2009RS004332.

Richards, P.G., Buonsanto, M.J., Reinisch, B.W., Holt, J., Fennelly, J.A., Scali, J.L., et al., 2000. On the relative importance of convection and temperature to the behavior of the ionosphere in North America during January 6–12, 1997. J. Geophys. Res. Space Phys. 105 (A6), 12,763–12,776. Available from: https://doi.org/10.1029/1999JA000253.

Rishbeth, H., Garriott, O.K., 1969. Introduction to Ionospheric Physics. Academic Press, New York.

Robinson, R.M., Vondrak, R.R., Miller, K., Dabbs, T., Hardy, D., 1987. On calculating ionospheric conductances from the flux and energy of precipitating electrons. J. Geophys. Res. 92, 2565–2569. Available from: https://doi.org/10.1029/JA092iA03p02565.

Roble, R.G., Ridley, E.C., 1987. An auroral model for the NCAR thermospheric general circulation model (TGCM). Ann. Geophys. 5, 369–382.

Royrvik, O., Davis, T.N., 1977. Pulsating aurora: local and global morphology. J. Geophys. Res. 82 (29), 4720–4740. Available from: https://doi.org/10.1029/JA082i029p04720.

Saito, S., Miyoshi, Y., Seki, K., 2012. Relativistic electron microbursts associated with whistler chorus rising tone elements: Gemsis-rbw simulations. J. Geophys. Res. Space Phys. 117 (A10). Available from: https://doi.org/10.1029/2012JA018020.

Samara, M., Michell, R.G., Asamura, K., Hirahara, M., Hampton, D.L., Stenbaek-Nielsen, H.C., 2010. Ground-based observations of diffuse auroral structures in conjunction with reimei measurements. Ann. Geophys. 28 (3), 873–881. Available from: https://doi.org/10.5194/angeo-28-873-2010.

Samara, M., Michell, R.G., Redmon, R.J., 2015. Low-altitude satellite measurements of pulsating auroral electrons. J. Geophys. Res. Space Phys. 120 (9), 8111–8124. Available from: https://doi.org/10.1002/2015JA021292.

Sandahl, I., Eliasson, L., Lundin, R., 1980. Rocket observations of precipitating electrons over a pulsating aurora. Geophys. Res. Lett. 7 (5), 309–312. Available from: https://doi.org/10.1029/GL007i005p00309.

Schunk, R.W., Nagy, A.F., 2004. Ionospheres. Cambridge University Press, Cambridge, UK.

Semeter, J., Kamalabadi, F., 2005. Determination of primary electron spectra from incoherent scatter radar measurements of the auroral E region. Radio Sci. 40, RS2006. Available from: https://doi.org/10.1029/2004RS003042.

Semeter, J., Zettergren, M., Lummerzheim, D., Lilensten, J., 2014. Model-based inversion of auroral processes. In: Huba, J., Schunk, R., Khazanov, G. (Eds.), Modeling the Ionosphere–Thermosphere System. Available from: https://doi.org/10.1002/9781118704417.ch25.

Sergienko, T.I., Ivanov, V.E., 1993. A new approach to calculate the excitation of atmospheric gases by auroral electron impact. Ann. Geophys. 11, 717–727.

Sheehan, C.H., St.-Maurice, J.-P., 2004. Dissociative recombination of N_2^+, O_2^+, and NO^+: rate coefficients for ground state and vibrationally excited ions. J. Geophys. Res. Space Phys. 109 (A3). Available from: https://doi.org/10.1029/2003JA010132.

Simon Wedlund, C., Lamy, H., Gustavsson, B., Sergienko, T., Brändström, U., 2013. Estimating energy spectra of electron precipitation above auroral arcs from ground-based observations with radar and optics. J. Geophys. Res. Space Phys. 118, 3672–3691. Available from: https://doi.org/10.1002/jgra.50347.

Sivadas, N., Semeter, J., Nishimura, Y., Kero, A., 2017. Simultaneous measurements of substorm-related electron energization in the ionosphere and the plasma sheet. J. Geophys. Res. Space Phys. 122 (10), 10,528–10,547. Available from: https://doi.org/10.1002/2017JA023995. 2017JA023995.

Smirnova, N.V., Ogloblina, O.F., Vlaskov, V.A., 1988. Modelling of the lower ionosphere. Pure Appl. Geophys. 127 (2), 353–379. Available from: https://doi.org/10.1007/BF00879817.

Solomon, S.C., 1993. Auroral electron transport using the monte carlo method. Geophys. Res. Lett. 20 (3), 185–188. Available from: https://doi.org/10.1029/93GL00081.

Solomon, S.C., 2001. Auroral particle transport using Monte Carlo and hybrid methods. J. Geophys. Res. 106, 107–116. Available from: https://doi.org/10.1029/2000JA002011.

Solomon, S.C., 2017. Global modeling of thermospheric airglow in the far ultraviolet. J. Geophys. Res. Space Phys. 122 (7), 7834–7848. Available from: https://doi.org/10.1002/2017JA024314. 2017JA024314.

Solomon, S.C., Hays, P.B., Abreu, V.J., 1988. The auroral 6300 A emission—observations and modeling. J. Geophys. Res. 93, 9867–9882. Available from: https://doi.org/10.1029/JA093iA09p09867.

Spanswick, E., Donovan, E., Liu, W., Wallis, D., Aasnes, A., Hiebert, T., et al., 2013. Substorm Associated Spikes in High Energy Particle Precipitation. American Geophysical Union, pp. 227–236. Available from: https://doi.org/10.1029/155GM24.

Spence, H.E., Reeves, G.D., Baker, D.N., Blake, J.B., Bolton, M., Bourdarie, S., et al., 2013. Science goals and overview of the radiation belt storm probes (RBSP) energetic particle, composition, and thermal plasma (ECT) suite on NASA's Van Allen Probes mission. Space Sci. Rev. 179, 311–336. Available from: https://doi.org/10.1007/s11214-013-0007-5.

Stamnes, K., 1980. Analytic approach to auroral electron transport and energy degradation. Planet. Space. Sci. 28 (4), 427–441. Available from: https://doi.org/10.1016/0032-0633(80)90046-X.

Stamnes, K., 1981. On the two-stream approach to electron transport and thermalization. J. Geophys. Res. Space Phys. 86 (A4), 2405–2410. Available from: https://doi.org/10.1029/JA086iA04p02405.

Stenbaek-Nielsen, H.C., 1980. Pulsating aurora: the importance of the ionosphere. Geophys. Res. Lett. 7 (5), 353–356. Available from: https://doi.org/10.1029/GL007i005p00353.

Stenbaek-Nielsen, H., Hallinan, T., 1979. Pulsating auroras: evidence for noncollisional thermalization of precipitating electrons. J. Geophys. Res. Space Phys. 84 (A7), 3257–3271. Available from: https://doi.org/10.1029/JA084iA07p03257.

Strickland, D.J., Book, D.L., Coffey, T.P., Fedder, J.A., 1976. Transport equation techniques for the deposition of auroral electrons. J. Geophys. Res. 81 (16), 2755–2764. Available from: https://doi.org/10.1029/JA081i016p02755.

Strickland, D.J., Meier, R.R., Hecht, J.H., Christensen, A.B., 1989. Deducing composition and incident electron spectra from ground-based auroral optical measurements. I—Theory and model results. II—A study of auroral red line processes. III—Variations in oxygen density. J. Geophys. Res. 94, 13,527–13,539. Available from: https://doi.org/10.1029/JA094iA10p13527.

Strickland, D.J., Daniell Jr., R.E., Jasperse, J.R., Basu, B., 1993. Transport-theoretic model for the electron-proton-hydrogen atom aurora. 2: model results. J. Geophys. Res. 98, 21,533. Available from: https://doi.org/10.1029/93JA01645.

Strickland, D.J., Hecht, J.H., Christensen, A.B., Kelly, J., 1994. Relationship between energy flux Q and mean energy (mean value of E) of auroral electron spectra based on radar data from the 1987 CEDAR Campaign at Sondre Stromfjord, Greenland. J. Geophys. Res. 99, 19,467. Available from: https://doi.org/10.1029/94JA01901.

Thorne, R.M., 2010. Radiation belt dynamics: the importance of wave–particle interactions. Geophys. Res. Lett. 37, L22107. Available from: https://doi.org/10.1029/2010GL044990.

Thorne, R.M., Ni, B., Tao, X., Horne, R.B., Meredith, N.P., 2010. Scattering by chorus waves as the dominant cause of diffuse auroral precipitation. Nature 467, 943–946. Available from: https://doi.org/10.1038/nature09467.

Torkar, K., Friedrich, M., 1983. Tests of an ion-chemical model of the D- and lower E-region. J. Atmos. Sol. Terr. Phys. 45 (6), 369–385. Available from: https://doi.org/10.1016/S0021-9169(83)81097-6.

Tsyganenko, N.A., 1989. A magnetospheric magnetic field model with a warped tail current sheet. Planet. Space Sci. 37, 5–20. Available from: https://doi.org/10.1016/0032-0633(89)90066-4.

Tsyganenko, N.A., Sitnov, M.I., 2005. Modeling the dynamics of the inner magnetosphere during strong geomagnetic storms. J. Geophys. Res. Space Phys. 110, A03208. Available from: https://doi.org/10.1029/2004JA010798.

Tsyganenko, N.A., Stern, D.P., 1996. Modeling the global magnetic field of the large-scale Birkeland current systems. J. Geophys. Res. 101, 27,187–27,198. Available from: https://doi.org/10.1029/96JA02735.

Turunen, E., Verronen, P.T., Seppälä, A., Rodger, C.J., Clilverd, M.A., Tamminen, J., et al., 2009. Impact of different energies of precipitating particles on nox generation in the middle and upper atmosphere during geomagnetic storms. J. Atmos. Sol. Terr. Phys. 71 (10), 1176–1189. Available from: https://doi.org/10.1016/j.jastp.2008.07.005. high Speed Solar Wind Streams and Geospace Interactions.

Turunen, E., Kero, A., Verronen, P.T., Miyoshi, Y., Oyama, S.-I., Saito, S., 2016. Mesospheric ozone destruction by high-energy electron precipitation associated with pulsating aurora. J. Geophys. Res. Atmos. 121 (19), 11,852–11,861. Available from: https://doi.org/10.1002/2016JD025015.

Velinov, P., Smirnova, N., Vlascov, V., 1984. Hybrid quadri-ionic model of the lower ionosphere. Adv. Space. Res. 4 (1), 123–130. Available from: https://doi.org/10.1016/0273-1177(84)90484-8.

Verronen, P.T., Seppälä, A., Clilverd, M.A., Rodger, C.J., KyröLä, E., Enell, C.-F., et al., 2005. Diurnal variation of ozone depletion during the October-November 2003 solar proton events. J. Geophys. Res. Space Phys. 110, A09S32. Available from: https://doi.org/10.1029/2004JA010932.

Verronen, P.T., Andersson, M.E., Marsh, D.R., Kovács, T., Plane, J.M.C., 2016. WACCM-D—Whole Atmosphere Community Climate Model with D-region ion chemistry. J. Adv. Model. Earth Syst. 8 (2), 954–975. Available from: https://doi.org/10.1002/2015MS000592.

Vickrey, J.F., Vondrak, R.R., Matthews, S.J., 1982. Energy deposition by precipitating particles and Joule dissipation in the auroral ionosphere. J. Geophys. Res. 87, 5184–5196. Available from: https://doi.org/10.1029/JA087iA07p05184.

Vondrak, R.R., Baron, M.J., 1977. A method of obtaining the energy distribution of auroral electrons from incoherent scatter radar measurements. In: Brekke, A. (Ed.), Radar Probing of the Auroral Plasma. International Atomic Energy Agency, Norway, pp. 315–330.

Wahlund, J.-E., Opgenoorth, H.J., Rothwell, P., 1989. Observations of thin auroral ionization layers by eiscat in connection with pulsating aurora. J. Geophys. Res. Space Phys. 94 (A12), 17,223–17,233. Available from: https://doi.org/10.1029/JA094iA12p17223.

Whalen, B.A., Miller, J.R., McDiarmid, I.B., 1971. Energetic particle measurements in a pulsating aurora. J. Geophys. Res. 76 (4), 978–986. Available from: https://doi.org/10.1029/JA076i004p00978.

Wickwar, V.B., Baron, M.J., Sears, R.D., 1975. Auroral energy input from energetic electrons and joule heating at Chatanika. J. Geophys. Res. 80 (31), 4364–4367. Available from: https://doi.org/10.1029/JA080i031p04364.

Woodger, L.A., Halford, A.J., Millan, R.M., McCarthy, M.P., Smith, D.M., Bowers, G.S., et al., 2015. A summary of the barrel campaigns: technique for studying electron precipitation. J. Geophys. Res. Space Phys. 120 (6), 4922–4935. Available from: https://doi.org/10.1002/2014JA020874.

Xu, W., Marshall, R.A., Fang, X., Turunen, E., Kero, A., 2018. On the effects of bremsstrahlung radiation during energetic electron precipitation. Geophys. Res. Lett. 45 (2), 1167–1176.

Zettergren, M., Semeter, J., 2012. Ionospheric plasma transport and loss in auroral downward current regions. J. Geophys. Res. Space Phys. 117 (A6). Available from: https://doi.org/10.1029/2012JA017637.

Zettergren, M., Semeter, J., Blelly, P.-L., Sivjee, G., Azeem, I., Mende, S., et al., 2008. Optical estimation of auroral ion upflow: 2. A case study. J. Geophys. Res. Space Phys. 113 (A7). Available from: https://doi.org/10.1029/2008JA013135.

This page intentionally left blank

CHAPTER 7

Atmospheric effects and signatures of high-energy electron precipitation

Robert A. Marshall[1] **and Chris M. Cully**[2]
[1]Ann and H. J. Smead Department of Aerospace Engineering Sciences, University of Colorado, Boulder, CO, United States
[2]Department of Physics and Astronomy, University of Calgary, Calgary, AB, Canada

Contents

7.1 Introduction

Electrons and protons traversing the Earth's magnetic field toward the Earth begin to encounter the neutral atmosphere at altitudes as high as 1000 km, but for higher energy particles (electrons of tens of keV and higher), the focus of this chapter, pronounced effects are seen below 100 km. As the particles encounter an increasingly dense neutral

The Dynamic Loss of Earth's Radiation Belts
DOI: https://doi.org/10.1016/B978-0-12-813371-2.00007-X

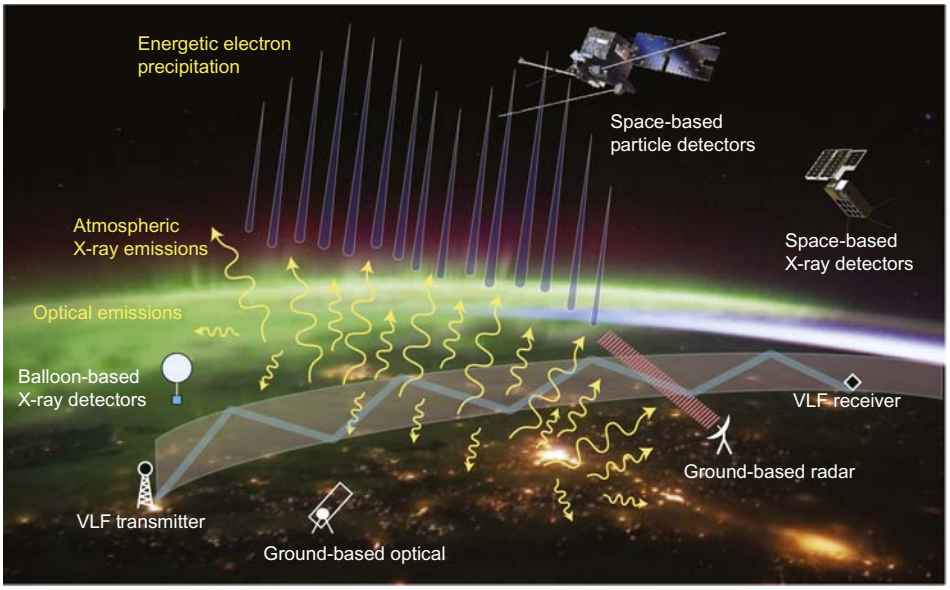

Figure 7.1 Overview of precipitation effects, signatures, and diagnostic techniques.

atmosphere, collisions begin to take place, and these increase exponentially in frequency as altitude decreases. Collisions may be elastic, altering the incident particle's pitch angle, or inelastic, including collisions involving excitation or ionization of the neutral molecules. In addition, bremsstrahlung may occur for electrons of reasonably high energy, producing energetic X-rays and gamma rays. Those X-rays and gamma rays can in turn transport precipitation energy to even lower altitudes, as we will describe in Section 7.2.2. A schematic overview of these atmospheric effects, and the diagnostic techniques used to detect them, is depicted in Fig. 7.1. The interaction between these energetic particles and the atmospheric neutrals causes them to be lost to the upper atmosphere in a process referred to as energetic particle precipitation (EPP).

EPP is one of the key loss mechanisms for radiation belt particles, in particular after the enhancements of these particles driven by geomagnetic storms and substorms (e.g., Tu et al., 2010; Thorne, 2010). Radiation belt fluxes can be enhanced by orders of magnitude during these events (e.g., Baker et al., 2012); these high-energy particles, above a few hundred keV, can be damaging to spacecraft (Baker et al., 2004). Understanding and predicting the loss rates of radiation belt fluxes thus has direct implications for the overall understanding of radiation belt dynamics and its impact on space-borne technology.

Uncertainties in the theoretical precipitation loss rates lead to a large discrepancy in electron lifetimes used in radiation belt models; this uncertainty is attributed to a number of factors. These include a lack of adequate observation of the waves (e.g., Engebretson et al., 2008), the validity of the linear approach for modeling

wave-particle coupling (e.g., Bortnik et al., 2008), and uncertainty in the pitch angle distribution of electrons near the loss cone (e.g., Friedel et al., 2002; Millan et al., 2007; Tu et al., 2009). The electron loss rates and lifetimes can vary by an order of magnitude between different studies. For example, Shprits et al. (2005) used a constant lifetime inside the plasmapause of $\tau = 10$ days, and outside the plasmapause they applied an empirical function of Kp (specifically, $\tau = 3/\text{Kp}$). Meanwhile, Barker et al. (2005) applied an L-dependent lifetime varying from 3 days at $L = 6$ to 29 days at $L = 4$. Thorne et al. (2005) determined that the effective lifetime is about 1 day in the outer radiation belt, based on microburst observations. Clearly, the radiation belt electron lifetimes and their dependence on magnetospheric conditions need to be better quantified.

Progress has been made by measuring and modeling wave distributions in the plasmasphere and using these to model diffusion coefficients. Meredith et al. (2012) used multiple satellite observations to build a model of chorus waves based on satellite observations; Glauert et al. (2014) used diffusion coefficients for whistlers, chorus, and hiss to build a global model of radiation belt dynamics. Lifetimes based on wave distributions have been estimated by Agapitov et al. (2014) based on Akebono wave data for the inner belt and slot region, by Orlova and Shprits (2014) based on chorus waves, and by Orlova et al. (2016) based on a model of hiss distribution derived by Spasojevic et al. (2015). These studies determined lifetimes in the range of $\sim 0.1-1000$ days, varying with L-shell, energy, and Kp. All of these studies considered only quasi-linear (weak) diffusion and incoherent scattering, neglecting the coherent interactions between intense waves and electrons that can have dramatic effects on pitch angles within a single bounce period (e.g., Meredith et al., 2012).

Direct observation of precipitation presents an opportunity to improve on models of radiation belt lifetimes by directly observing the loss of particles from the radiation belts. However, observations of precipitation have not yet been extensively utilized for this purpose. In this chapter, we provide an overview of the effects of EPP in the upper atmosphere. These effects include energy deposition and ionization, X-ray emissions, optical emissions, and chemical changes. We then describe techniques used to model these physical effects. Next, we discuss existing diagnostic techniques used to measure and quantify precipitation of energetic particles. Finally, we provide a brief discussion of future missions and experimental concepts recommended to improve our understanding of EPP effects and the quantification of radiation belt losses.

7.2 Effects of energetic precipitation in the atmosphere

7.2.1 Energy deposition and ionization

Consider a distribution of energetic electrons, propagating down magnetic field lines toward the Earth, and reaching the top of the atmosphere at 300 km altitude.

(Although some collisions occur above 300 km, in this chapter we will use this as the nominal "starting point" for our discussion of atmospheric effects.) Depending on their energies and pitch angles, a fraction of these electrons will precipitate—that is, deposit their energy in the atmosphere and be lost—and a fraction will return to space, either by magnetic mirroring or by backscatter from the atmosphere.

From the point of view of the radiation belt scientist, the important question is simply what part of the distribution is precipitated, and what is returned to space. On the other hand, the atmospheric scientist wishes to know the altitude distribution of energy deposition in order to understand their consequences on atmospheric chemistry and circulation. Fig. 7.2 provides insight into the energy deposition for different incident electron energies. Profiles of energy deposition in the atmosphere are calculated using Monte Carlo modeling methods, as described in Section 7.3. Each profile considers a monoenergetic beam of electrons with an initial pitch angle of 75 degrees at 300 km. Each distribution has the same total energy flux ($eV/cm^2/s$), resulting in very similar peaks in the energy deposition profile. As expected, higher energy electrons deposit deeper in the atmosphere.

A number of key qualitative observations can be gathered from Fig. 7.2. First, the profiles in Fig. 7.2A are plotted on a logarithmic x-axis scale; in absolute terms, the energy deposition for each monoenergetic beam is very narrow in altitude, with a full width at half maximum (FWHM) of 10–20 km, depending on energy. Second, the altitude of peak deposition (Fig. 7.2B) is nearly linear with log-scaled energy; this is no surprise, since the atmospheric density increases exponentially in the direction approaching the ground. Third, Fig. 7.2C shows that the altitude of energy deposition also depends on pitch angle. For particle energies above 3 MeV, the altitude of deposition can vary by up to 10 km based on the pitch angle. This implies that knowledge of the precipitating pitch angle distribution is critical to properly characterize the atmospheric deposition profile and resulting chemical and ionization effects. This dependence on pitch angle has been investigated by Marshall and Bortnik (2018), who further showed that the bounce loss cone (BLC)—defined as the range of pitch angles that will precipitate in the atmosphere—is energy dependent, thanks to significant backscatter in the atmosphere.

It is also notable from Fig. 7.2 that radiation belt electrons deposit their energy primarily in the altitude range 40–100 km, corresponding to the mesosphere and D-region ionosphere. Typical ionospheric electron density profiles for daytime and nighttime are shown in Fig. 7.3. The D-region is marked by very low electron densities as compared with higher altitudes; this is due to rapid recombination in this region of the atmosphere, where neutral densities are relatively high, leading to an increase in inelastic collisions, including recombination. As such, radiation belt precipitation can produce dramatic, but short-lived, enhancements to the D-region electron density. However, as we shall see, measuring even these dramatic electron density

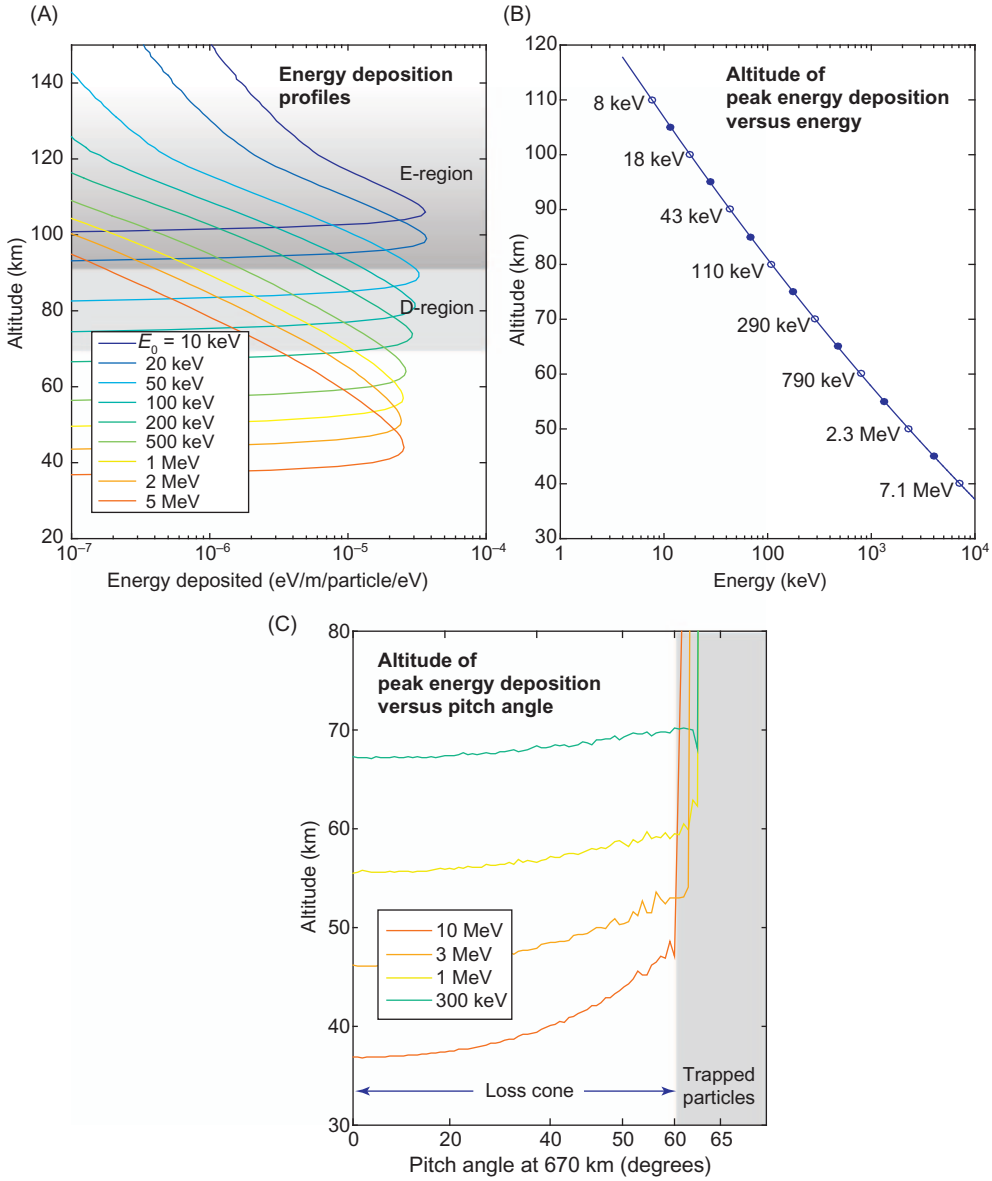

Figure 7.2 (A) Normalized energy deposition profiles for different monoenergetic inputs. Values shown on the *x*-axis are eV deposited per m altitude, per particle injected, normalized by particle energy (in eV). (B) Altitude of the peak of each deposition profile versus energy. (C) Variation in the peak deposition altitude with input pitch angle for four different energies. Calculated using the Electron Precipitation Monte Carlo (EPMC) model, described in Section 7.3.3.

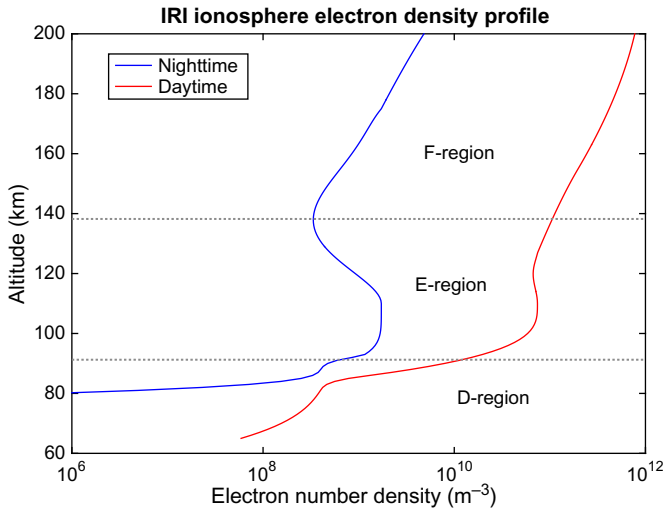

Figure 7.3 Typical ionosphere electron density profiles for nighttime and daytime. These were calculated using the 2012 International Reference Ionosphere (IRI) model (Bilitza et al., 2014), for local midnight and noon on January 1, 2017, over Poker Flat, Alaska.

enhancements in the D-region is very difficult. The region is too high for balloons or aircraft and too low for satellites, so remote sensing techniques are required. But because the electron density is very low, these remote sensing techniques require very high sensitivity. We discuss these measurement techniques in Section 7.4.

In addition to the monoenergetic distributions in Fig. 7.2, it is illustrative to consider the deposition profiles from realistic distributions. Using data from the Detection of Electromagnetic Emissions Transmitted From Earthquake Regions (DEMETER) spacecraft, Whittaker et al. (2013) showed that most precipitating electron distributions in the 100 keV−2.2 MeV range (the energy range of DEMETER) could be well fit to exponential or power-law energy distributions:

$$f(E) = C_e e^{-E/\beta_e} \quad \text{or} \quad f(E) = C_p E^{-\beta_p} \tag{7.1}$$

where β_e and β_p characterize the shape of the distribution. Whittaker et al. (2013) found that β_e ranges between 100 and 300 keV, and β_p ranges between 2 and 4, depending on L-shell and Kp index. Fig. 7.4 shows the energy deposition profiles for the range of exponential distributions; the input distributions have been normalized to the same total number flux of 10^5 electrons/cm^2/s, characteristic of long-term averages from DEMETER in the radiation belts; note, however, that the profiles have different total energy flux.

We observe that the higher values of β_e deposit energy deeper in the atmosphere and have somewhat stronger peaks; the peak for $\beta_e = 300$ keV is about 2.8 times

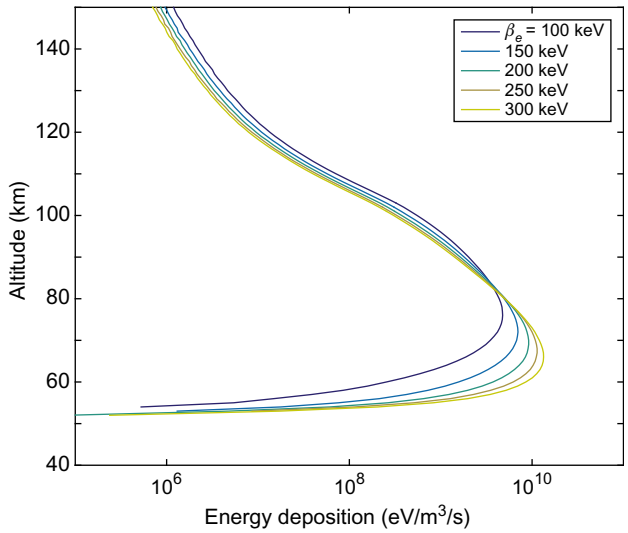

Figure 7.4 Deposition profiles for different exponential energy distributions of precipitating electrons.

higher than the peak for $\beta_e = 100$ keV. This is expected, as the higher value of β_e implies more higher energy electrons, which can penetrate deeper and carry a higher energy flux. The altitudes of peak energy deposition are 76 km for $\beta_e = 100$ keV, and 66 km for $\beta_e = 300$ keV. Clearly, the energy distribution makes a significant difference in the energy deposition profiles, and ultimately on the other atmospheric effects described later in this chapter.

7.2.2 Bremsstrahlung

Energetic electron collisions with atmospheric constituents may result in bremsstrahlung radiation of energetic photons (X-rays and gamma rays; for the purpose of this discussion, we will simply refer to these as X-rays). The efficiency of X-ray production by bremsstrahlung depends on the incident particle energy; the fraction of electron energy converted to X-rays by bremsstrahlung was calculated by Krause (1998). As a rule of thumb, for 1 MeV electrons precipitating in the atmosphere, about 0.3% of the total energy is converted to X-rays; for 10 MeV electrons, that fraction rises to 5%. At lower energies (hundreds of keV), only a small fraction of the precipitating energy is converted to photons, but as we shall see, enough photons are produced to be detected by balloons and spacecraft.

Fig. 7.5A shows the bremsstrahlung cross sections, in m^2, for incident electron energies from 1 keV to 3 MeV. The decrease in cross section with increasing photon energy implies that a given electron will produce many more lower energy photons than higher energy photons.

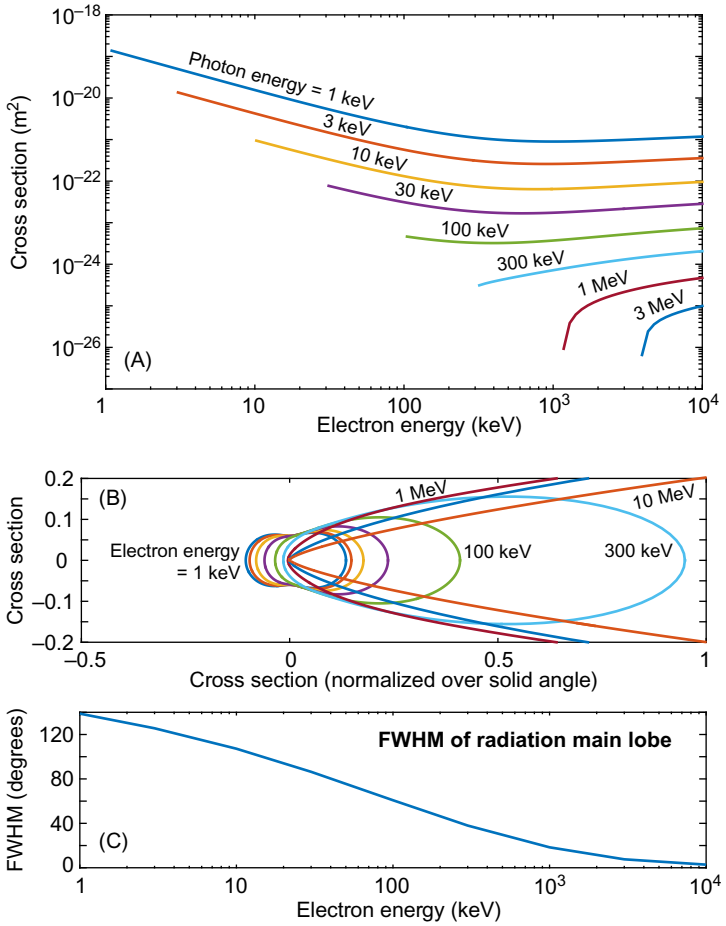

Figure 7.5 (A) Bremsstrahlung cross sections versus electron energy, for the production of different photon energies. (B) Angular cross section for different electron energies. (C) FWHM of the main lobe from panel (B), providing the beaming angle for photons.

The bremsstrahlung angular cross sections provide information about the distribution of initial photon directions immediately after they are produced. The angular distribution for a given electron energy is shown in Fig. 7.5B as a series of polar plots, for energies of 1 keV, 3 keV, 10 keV, and so forth up to 10 MeV. Generally speaking, higher energy electrons result in smaller scattering angles, and a more forward-directed photon distribution (i.e., close to the incident electron direction). Fig. 7.5C shows the beaming angle (as a FWHM) for the full range of electron energies of interest. While the bremsstrahlung radiation from 1 keV electrons is spread over 140 degrees, and even has a significant backward component, the photons produced by 10 MeV electrons are broadcast in a 2.8-degree FWHM beam.

For the purposes of electron precipitation in the atmosphere, these two energy dependencies imply that (1) higher energy electrons transfer more of their energy to photons through bremsstrahlung and (2) these photons can penetrate deeper into the atmosphere owing to their forward-beamed angular distribution.

Bremsstrahlung photons go on to either escape the atmosphere and propagate into space or to deposit their energy in the atmosphere through Compton scattering, photoelectron production, or electron–positron pair production. Photoelectron production is dominant for lower energy photons below about 30 keV; Compton scattering is dominant for photons up to 20 MeV; pair production is effective only for primary photons with energy greater than about 2 MeV, and becomes dominant above 20 MeV (Fig. 7.6).

Theoretically, bremsstrahlung photons can also reach the ground, but effectively, none do; the probability is extraordinarily low. Photons that do not escape thus deposit their energy in the atmosphere in the form of new ionization, just as the primary precipitating electrons deposit their energy. But because photons have a lower cross section in the atmosphere, they are able to propagate somewhat farther and deposit their energy (in the form of ionization) far from the location where they were created. Monte Carlo simulations have been conducted by Xu et al. (2018) to calculate the profile of new ionization by these photons, as shown in Fig. 7.7. The transport of energy by bremsstrahlung photons results in a secondary peak of ionization at altitudes below the main peak. For lower energy electrons (below 1 MeV), this peak extends far down in altitude, but the ionization peak is 3–4 orders of magnitude weaker than the primary peak. However, for higher energy electrons, the secondary peak can be just 1–2 orders of magnitude weaker than the primary peak and extend

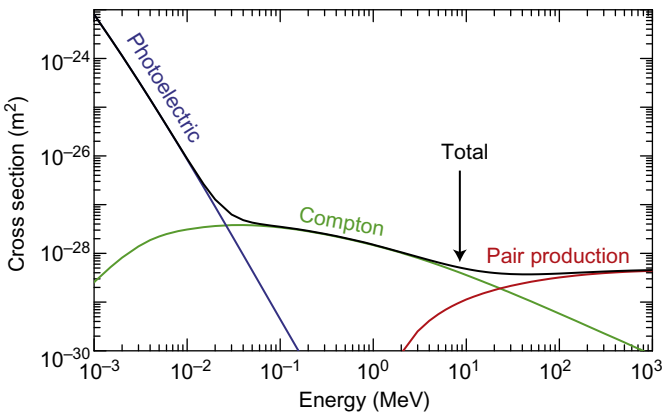

Figure 7.6 Cross sections of photon interactions, including photoelectron production, Compton scattering, and pair production. The total cross section is shown in black.

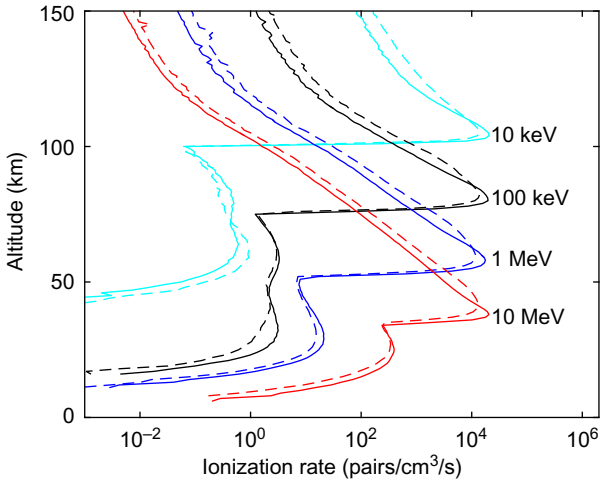

Figure 7.7 Energy deposition profiles for monoenergetic electron precipitation, at discrete pitch angles of 0 degree (*solid lines*) and 45 degrees (*dashed lines*), showing lower altitude photon-generated peaks. Electron precipitation inputs are normalized to a constant energy flux.

as low as 15 km altitude; as such these secondary, photon-generated electrons could be detected by balloon-borne instruments.

Observations of bremsstrahlung photons provide a valuable measurement of precipitation that is otherwise inaccessible. While the precipitating electrons do not reach below ~40 km altitude, the X-rays can propagate down to 15 km, where high-altitude balloons can measure these photons and/or the electrons produced by Compton scattering and photoelectron production. X-ray photons provide an unambiguous observation of high-energy electron precipitation, as electrons with low energies (below 30 keV or so) are very inefficient at producing photons. Because the cross sections for bremsstrahlung photon production are well known, and the atmospheric density profile is reasonably consistent, one can infer a reasonably accurate electron precipitation energy distribution from a measurement of the X-ray spectrum on a balloon (e.g., Clilverd et al., 2017). We describe the X-ray diagnostic method in more detail in Section 7.4.1.2.

7.2.3 Particle backscatter

The first-order understanding of particle precipitation suggests that radiation belt particles are "lost" to the atmosphere if they penetrate to 100 km altitude or below, whereas particles that do not reach 100 km are "trapped," mirroring within the magnetic bottle formed by the Earth's magnetic field. Particles that will reach 100 km or lower on the next bounce are said to be in the BLC. However, the atmosphere at 100 km is not an infinitely sharp boundary, but rather an exponentially increasing

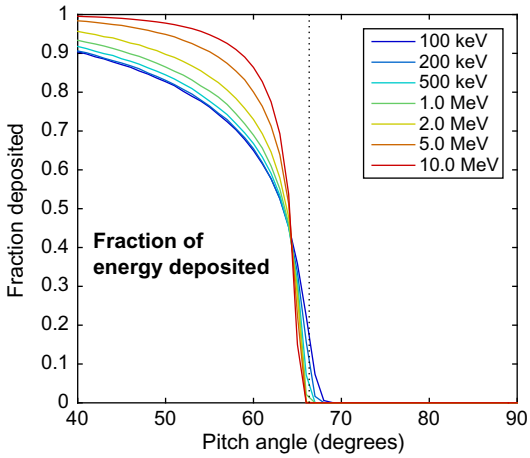

Figure 7.8 Fraction of incident energy deposited in the atmosphere as a function of pitch angle, for different incident electron energies. The nominal loss cone angle is 66.3 degrees.

density profile with descending altitude. As particles collide with atmospheric molecules above or below 100 km, they can be scattered either deeper into the loss cone or out of the loss cone and back into space. These particles are said to be backscattered.

Fig. 7.8 shows the results of Monte Carlo simulations of monoenergetic beams incident on the atmosphere at different energies and pitch angles. The incident pitch angle on the x-axis is defined at 500 km altitude, where the nominal BLC angle—the angle at which particles will mirror at 100 km altitude—is 66.3 degrees, shown by the vertical dashed line. We observe that even for low pitch angles of 40–60 degrees—deep within the loss cone—a sizable fraction of the incident energy is backscattered from the atmosphere. Even at 65 degrees, still a few degrees inside the loss cone, 50% of the incident energy is backscattered. The naive assumption that everything inside the loss cone is deposited would thus overestimate the energy deposition in a single bounce period by a factor of 2.

The backscattered electron populations may or may not precipitate in subsequent bounce periods, depending on the wave activity present in the magnetosphere, or they may precipitate in the drift loss cone. Nonetheless, observations of the backscattered population could provide valuable insight into the precipitating fluxes. To illustrate what these backscattered populations would look like, Fig. 7.9 shows calculated backscatter distributions for monoenergetic beams of 1 MeV electrons at discrete pitch angles. For electrons deep within the loss cone, at a pitch angle of 50 degrees (leftmost panels), the backscattered pitch angle distribution is relatively uniform, from 0 degrees (field aligned) up to the nominal BLC angle of 66.3 degrees. The energy distribution is similarly broad, with backscattered particles ranging from a few keV up

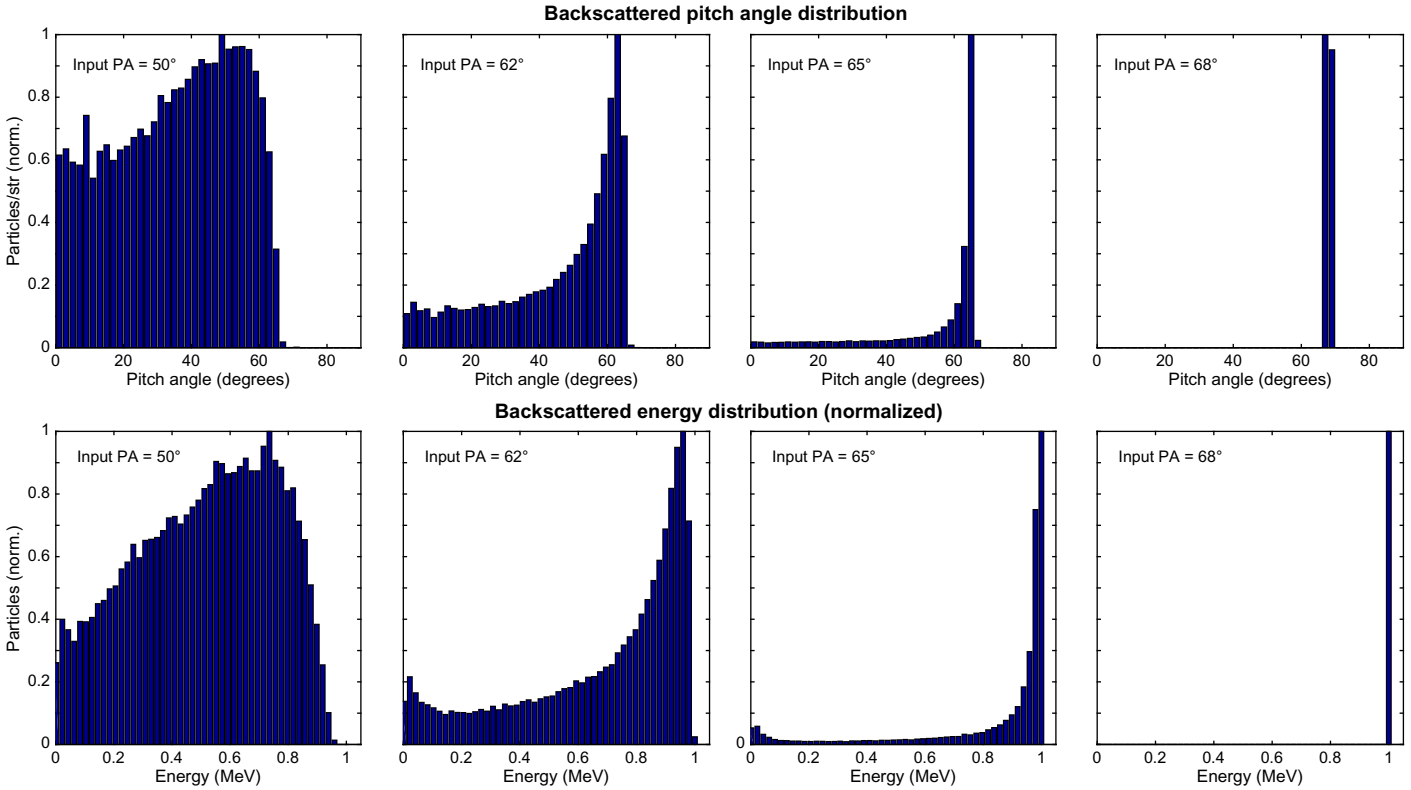

Figure 7.9 Backscattered electron distributions for 1 MeV incident electrons. (Top row) Backscattered pitch angle distributions, normalized to particles per steradian, for four different input pitch angles (PAs) as shown. (Bottom row) Energy distributions. The nominal loss cone angle is 66.3 degrees, but the loss cone angle for this energy is more accurately described as somewhere in the range 64−66 degrees.

to 1 MeV. As the pitch angle is increased to 62, 65, and 68 degrees, we observe that the backscattered distributions become closer to discrete distributions. However, even at 65 degrees, just inside the nominal BLC angle, a sizable number of particles are backscattered in the full range of pitch angles and energies.

Fig. 7.10 provides the backscattered distributions for our more realistic, DEMETER-like inputs, using an exponential energy distribution with $\beta_e = 200$ keV and a uniform or sine distribution in pitch angle. The backscattered distributions are on the same scale as the inputs. Observe that the backscattered energy distributions look very much like the input distributions, with the addition of lower energy particles that were not included in the input distribution (limited from 90 keV to 2 MeV). This suggests that observations of the backscattered energy distribution strongly emulate the input distribution, with flux levels reduced by about a factor of 2–3. The backscattered pitch angle distributions show a mirrored population (pitch angles

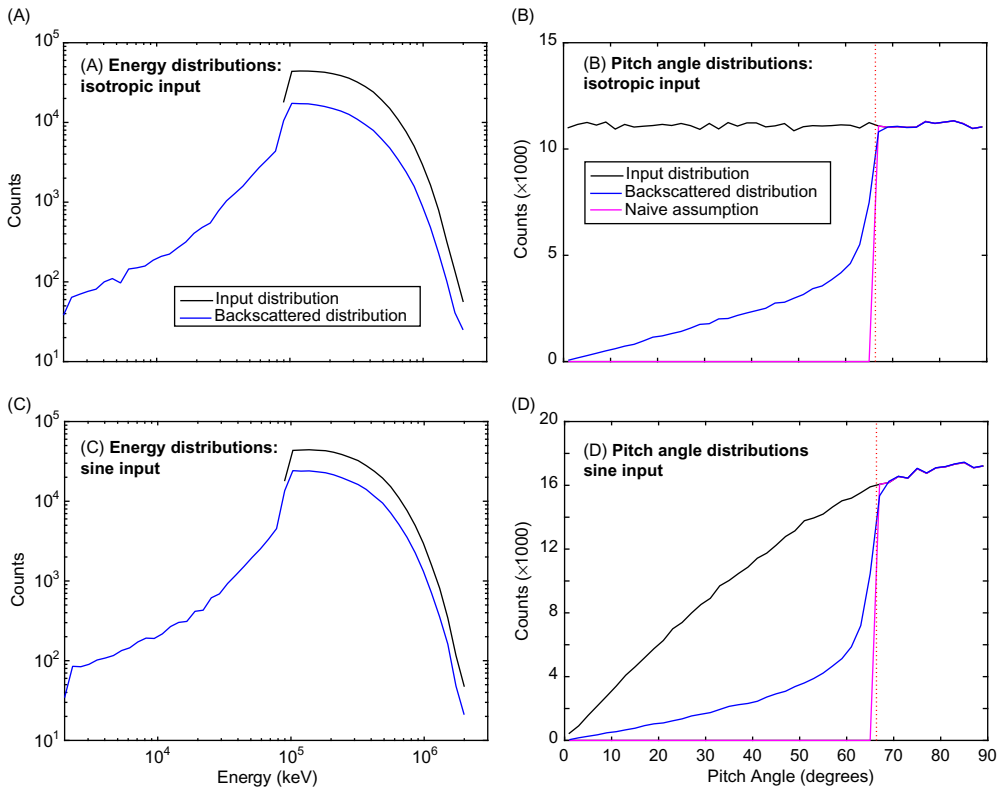

Figure 7.10 Response of the atmosphere to exponential energy distributions and sine or isotropic pitch angle distributions. (A) Input and backscattered energy distributions for an isotropic pitch angle distribution. (B) Input and backscattered pitch angle distributions. (C and D) Same for sine-shaped input pitch angle distribution.

>66.3 degrees) and a tail of pitch angles all the way down to 0 degrees. (Note that a pitch angle of 0 degree for the input distribution represents downgoing electrons, while 0 degree backscattered represents upgoing electrons.) We argue that observation of these electrons from within the loss cone would provide a definitive observation of precipitation, even in the absence of pitch angle resolution.

7.2.4 Optical emissions

While optical emissions are more commonly associated with the aurora, driven by precipitation of electrons with moderate energies below ~10 keV, the physical principles that lead to optical emissions are the same for higher energy electron precipitation. Precipitating electrons lose most of their energy to direct impact ionization of atmospheric constituents; that ionization results in secondary electrons, with energies in the tens of eV. Those secondary electrons go on to collide with other neutrals, where they can produce further ionization or excite neutrals into higher electronic states. When those excited states relax back to a lower electronic state, an optical photon is emitted. Additionally, the ions N_2^+ and O_2^+ produce optical emissions from their own excited states.

Optical emission rates are calculated from the ionization rate, which comes from the energy deposition profile, as a function of altitude, using the method described by Bell et al. (1995) and Lehtinen et al. (1999). This method uses a generic cross section given by Vallance Jones (1974, p. 92):

$$\sigma(E) = \frac{\sigma_{max} E_{max}^2 (E - I)}{E[E_{max}(E_{max} - 2I) + EI]} \tag{7.2}$$

where σ_{max} is the maximum cross section, E_{max} is the energy at which that maximum is attained, and I is the ionization potential. Here σ_{max} and E_{max} are taken from Vallance Jones (1974), and I is taken from Rees (1992). The production rate r_X of the excited state X is then calculated from the total ionization cross section using Eqs. (4.2.1f)−(4.2.1l) of Vallance Jones (1974, p. 105). Finally, the photon emission rates (γ) for different emission lines or band systems, in units of photons/m^3/s, are calculated according to the following relations, including quenching and cascading from higher states (Vallance Jones, 1974, p. 119):

$$\gamma_{N_2 2P} = a_{N_2 C}\left[\frac{r_{N_2 C}}{a_{N_2 C} + \alpha_{N_2 C,air}\left(N_{N_2} + N_{O_2}\right)}\right] \tag{7.3}$$

$$\gamma_{N_2 1P} = a_{N_2 B}\left[\frac{r_{N_2 B} + \gamma_{N_2 2P}}{a_{N_2 B} + \alpha_{N_2 B,air}\left(N_{N_2} + N_{O_2}\right)}\right] \tag{7.4}$$

$$\gamma_{N_2VK} = a_{N_2A}\left[\frac{r_{N_2A} + \gamma_{N_2 1P}}{a_{N_2A} + \alpha_{N_2A,O}N_O}\right] \tag{7.5}$$

$$\gamma_{N_2^+M} = a_{N_2^+A}\left[\frac{r_{N_2^+A}}{a_{N_2^+A} + \alpha_{N_2^+A,air}\left(N_{N_2} + N_{O_2}\right)}\right] \tag{7.6}$$

$$\gamma_{N_2^+1N} = a_{N_2^+B}\left[\frac{r_{N_2^+B}}{a_{N_2^+B} + \alpha_{N_2^+B,air}\left(N_{N_2} + N_{O_2}\right)}\right] \tag{7.7}$$

$$\gamma_{O_2^+1N} = a_{O_2^+b}\left[\frac{r_{O_2^+b}}{a_{O_2^+b} + \alpha_{O_2^+b,N_2}N_{N_2}}\right] \tag{7.8}$$

$$\gamma_{O^1S} = a_{O^1S}\left[\frac{r_{O^1S} + \alpha_{N_2A,O}N_{N_2A}N_O}{a_{O^1S} + \alpha_{O^1S,O_2}N_{O_2} + \alpha_{O^1S,O}N_O}\right] \tag{7.9}$$

$$\gamma_{O^1D} = a_{O^1D}\left[\frac{r_{O^1D} + \gamma_{O^1S}}{a_{O^1D} + \alpha_{O^1D,N_2}N_{N_2}}\right] \tag{7.10}$$

where a_X is the Einstein coefficient for state X (the inverse of the lifetime, τ) and $\alpha_{X,Y}$ are the quenching rate constants of X by collisions with Y, both taken from Vallance Jones (1974, p. 119). The N values are the neutral densities of each atmospheric constituent, taken from the MSISE-90 model (Hedin, 1991) or the NRLMSISE-00 model (Picone et al., 2002).

For primary electrons with energies above a few keV, the efficiencies of ionization and excited state production (rates r_X) are consistent no matter the precipitating energy. This is because the distribution of secondary electron energies is also consistent, thanks to the relationship in which every 35 eV of energy creates one electron–ion pair (e.g., Rees, 1963). Monte Carlo simulations confirm that this relationship holds true within the homosphere (i.e., below 100 km altitude), where the atmosphere is uniformly 78% N_2 and 21% O_2. In the mesosphere, the precipitating energy from 1 MeV incident electrons is partitioned into the excited states listed in Table 7.1.

With the exception of the forbidden atomic oxygen lines, these excited states are generally not quenched significantly in the mesosphere, although the lifetimes and quenching rates do modify the energy fractions above for different altitudes. Thus for every 100 J of precipitating energy, 0.6 J are emitted in the N_2^+ first negative-band system. In total, about 5% of the deposited electron energy is converted to optical emissions.

Table 7.1 Fraction of deposited energy converted to different emission bands.

Upper state	Emission	Energy fraction (%)
N_2 B^3 Σ	N_2 First positive (1 P)	2.2
N_2 C^3 Π	N_2 Second positive (2 P)	1.1
N_2 A^3 Σ_u^+	N_2 Vegard–Kaplan (VK)	1.0
N_2^+ B^2 Σ	N_2^+ First negative (1 N)	0.6
N_2^+ A^2 Π	N_2^+ Meinel (M)	0.1
O_2^+ b^4 Σ	O_2^+ 1 N	0.06
O ^{1}S	5577 Å green line	0.0007
O ^{1}D	6300 Å red line	0.0000003
	Total	~5.1

Calculated for 1 MeV precipitating electrons.

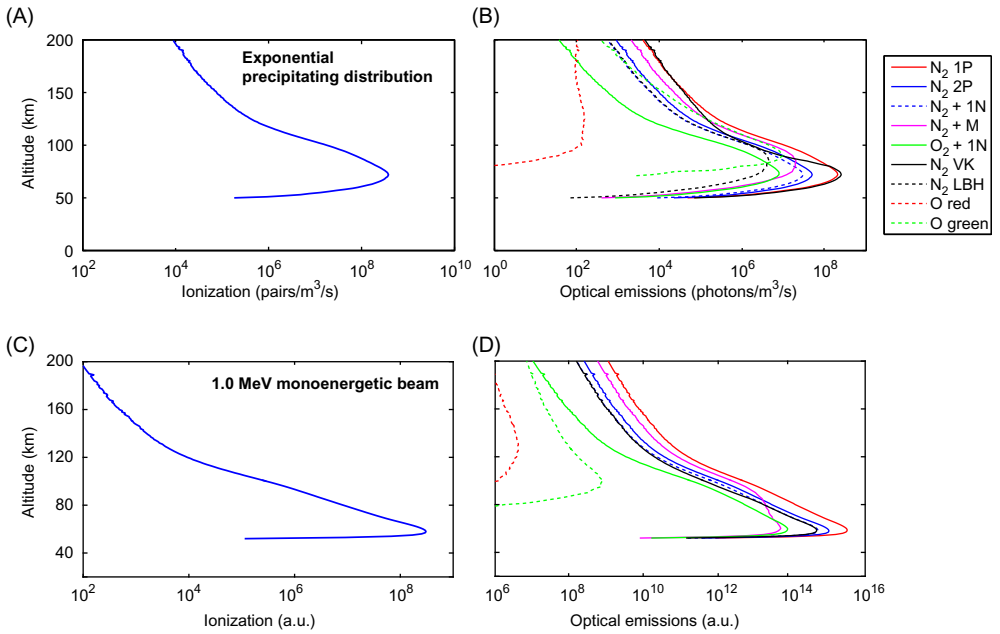

Figure 7.11 (A) Ionization profile and (B) optical emission production rates for different emissions band systems. Calculated for an exponential precipitating energy distribution with $\beta_e = 200$ keV, from 90 keV to 2.2 MeV, and total flux $F = 10^5$ electrons/cm^2/s. The same, calculated for a monoenergetic beam of 1 MeV electrons (C and D).

For a given precipitating electron distribution, then, we can predict the total optical emissions and the altitude distribution where they are produced directly from the energy deposition profile. Profiles for major emissions are shown in Fig. 7.11, including emission profiles for atomic oxygen red (O^1 D) and green (O^1 S) lines. These lines, at 6300 and 5577 Å, have lifetimes of 110 and 1 seconds, respectively (e.g., Chamberlain, 1995), and thus are highly quenched in the mesosphere.

In Section 7.4.2.4 we discuss the expected optical signatures measured on the ground and methods to make these measurements.

7.2.5 Chemical effects

The chemical effects of EPP are discussed in detail in Chapter 9. Here we provide a very brief discussion of the chemical effects as they pertain to some of the diagnostic signatures discussed in Section 7.4.

The D-region chemistry—involving the neutrals, ionized species, and electrons below about 90 km altitude—is complicated significantly by the many minor species in this altitude range. In particular, heavy cluster ions of the form $H^+(H_2O)_n$ modify the chemistry considerably, and thus are a key driver of electron densities and lifetimes (e.g., Fehsenfeld and Ferguson, 1969; Glukhov et al., 1992; Lehtinen and Inan, 2007). For many reasons, we wish to understand the relationship between the energy deposition from precipitation as a function of altitude and the resulting D-region electron density profile that is sustained by this precipitation. This relationship is key if we wish to invert the relationship and estimate the energy deposition (and thus the precipitating energy flux) from measurements of the D-region electron density.

The D-region electron density is driven primarily by the chemical reactions between the electrons, neutrals (N_2 and O_2), and positive and negative ions. Glukhov et al. (1992) and Lehtinen and Inan (2007) approximated the D-region chemistry to a four-species or five-species model, respectively, encompassing electrons, light positive ions, heavy positive ions, light negative ions, and heavy negative ions (the latter added by Lehtinen and Inan, 2007):

$$\frac{dN_e}{dt} = Q - \beta N_e + \gamma N^- + \gamma_x N_x^- - \left(\alpha_d N^+ + \alpha_d^c N_x^+\right) N_e \tag{7.11}$$

$$\frac{dN^-}{dt} = \beta N_e - \gamma N^- - \alpha_i \left(N^+ + N_x^+\right) N^- - A N^- \tag{7.12}$$

$$\frac{dN_x^-}{dt} = -\gamma_x N_x^- - \alpha_i \left(N^+ + N_x^+\right) N_x^- + A N^- \tag{7.13}$$

$$\frac{dN^+}{dt} = Q - \alpha_d N_e N^+ - \alpha_i \left(N^- + N_x^-\right) N^+ - B N^+ \tag{7.14}$$

$$\frac{dN_x^+}{dt} = -\alpha_d^c N_e N_x^+ - \alpha_i \left(N^- + N_x^-\right) N_x^+ + B N^+ \tag{7.15}$$

This model is referred to as the Glukhov, Pasko, and Inan (GPI) chemistry model. Here, N^+ and N^- represent light positive and negative ions, and N_x^+ and N_x^- represent heavy positive and negative ions, which include the H_2O cluster ions. Q is the ionization rate from precipitation or other sources, in pairs/m^3/s, producing electrons and positive ions (N^+); α_i is a neutralization coefficient; α_d and α_d^c are dissociative recombination coefficients for light and heavy positive ions; β is an attachment rate, including two-body and three-body attachment; γ is a detachment rate for light negative ions; γ_x is the detachment rate for heavy negative ions; and A and B are conversion rates from light to heavy negative ions and from light to heavy positive ions, respectively. Refer to Lehtinen and Inan (2007) for details on the sources of these rates and the background ion density profiles.

This simplified chemistry model is generally accurate in estimating the D-region electron density, which is the quantity of interest for probing methods described in Section 7.4. Comparison between this GPI model and the more extensive Sodankylä Ion Chemistry (SIC) model, described below, result in electron densities that agree to within about 40%.

Fig. 7.12 shows the resulting steady-state electron density profiles from different precipitating fluxes and distributions, during daytime and nighttime, calculated using the five-species GPI model. The background ionosphere here is calculated using the International Reference Ionosphere (IRI) 2012 model (Bilitza et al., 2014), run for local midnight and noon on January 1, 2017, over Poker Flat, Alaska; the IRI model does not provide electron densities below 60 km in the daytime or 80 km at night, so the values at these low altitudes are made artificially low. However, the low background electron density at low altitudes does not affect the results significantly.

The precipitating electron distributions used in Fig. 7.12 are again DEMETER-like exponential energy distributions and uniform pitch angle distributions. Observe that, as expected, higher fluxes lead to considerably higher electron densities; the electron density is markedly raised from the background profile between 80 and 100 km for fluxes above 10^5 electrons/cm^2/s. The nighttime profile is more significantly modified, as expected owing to the lower background. Precipitating distributions with higher β_e affect the ionosphere at lower altitudes, also as expected, due to the raised flux of higher energy electrons.

EPP creates secondary ionization, as described earlier, including free electrons and ionized atmospheric constituents N_2^+ and O_2^+. Additionally, EPP creates O^+, N^+, neutral atomic oxygen, and neutral atomic nitrogen in the ^4S and ^2D states (Verronen et al., 2016). These initial products of precipitation then go on to form a host of ionized and neutral species through a wide variety of chemical reactions. None of this more complex chemistry is captured in the simple five-species model described. A thorough illustration of the many key chemical constituents and reactions is presented

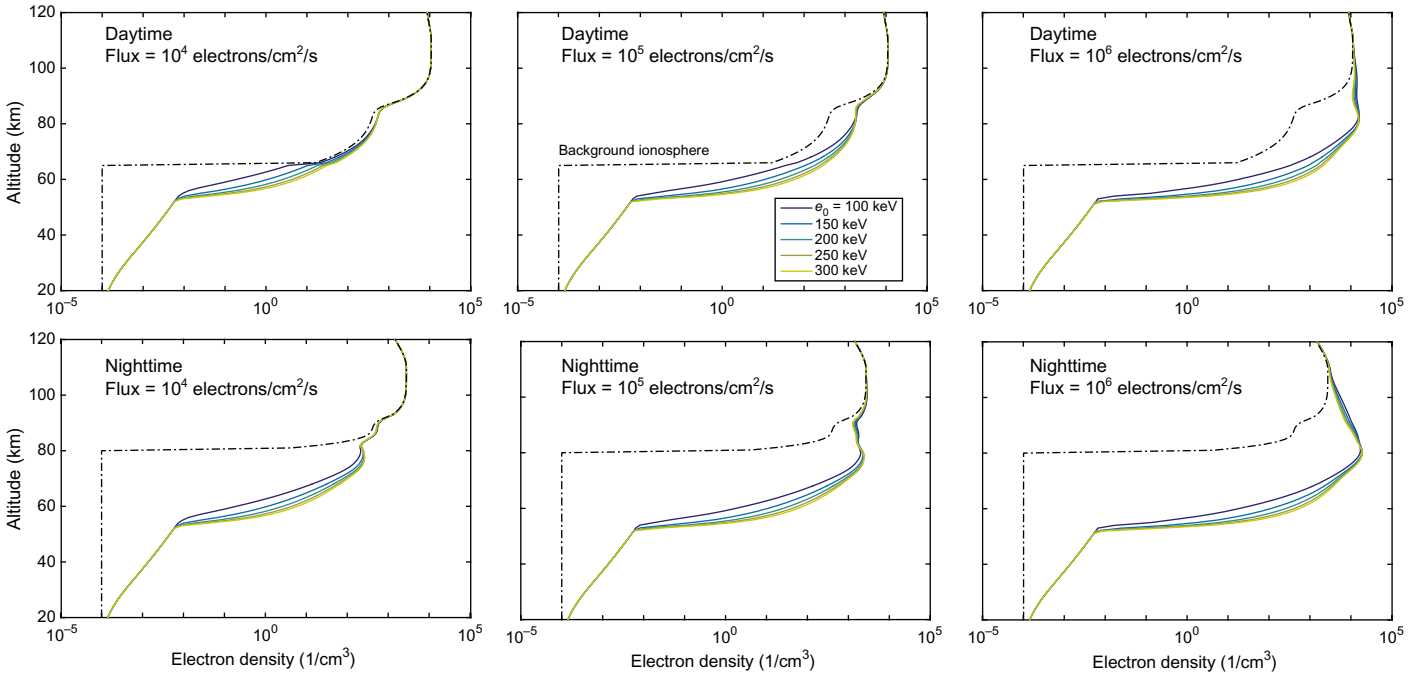

Figure 7.12 Steady-state electron density profiles following precipitation of the given electron fluxes, for exponential distributions with β_e given in the legend. The top row of plots is for daytime and the bottom row for nighttime.

in Verronen et al. (2016, Figs. 1 and 2). These figures show the range of species considered, and their interconnections through reactions, for the SIC model, the subset of reactions considered in the Whole Atmosphere Community Climate Model (WACCM; e.g., Richter et al., 2008), and similarly for WACCM-D, the D-region extension of WACCM (Verronen et al., 2016). Despite the reduced set of ions and reactions, Verronen et al. (2016) showed good agreement between SIC and WACCM-D for a variety of scenarios.

The SIC model also includes a large number of ion−electron and ion−ion recombination reactions, which form neutral constituents such as NO, NO_2, O, O_3, HO, HO_2, and others. These molecules are of most interest to atmospheric chemistry, and they are generally discussed together as odd nitrogen, or NO_x ($NO + NO_2 + NO_3$); odd hydrogen, or HO_x ($HO + HO_2$); and odd oxygen, or O_x ($O + O_3$).

HO_x produced in the mesosphere has a short lifetime, but can cause days-long ozone depletion of up to 90% (Andersson et al., 2014). NO_x produced by EPP (EPP-NO_x) directly in the stratosphere is immediately available to participate in catalytic ozone destruction. This requires particles on the higher end of the energy spectrum and occurs only sporadically, but the effects are immediate and dramatic (e.g., Callis et al., 1991; Jackman et al., 2011). More commonly, EPP-NO_x is produced in the mesosphere and lower thermosphere (MLT). During the polar winter the EPP-NO_x will descend in the polar vortex into the stratosphere, where it destroys ozone (e.g., Callis et al., 1998; Randall et al., 2007). This mechanism for coupling the upper and lower atmosphere was first examined more than two decades ago using a two-dimensional (2D) model (Solomon et al., 1982), and observational evidence for its occurrence has been prevalent (e.g., Bailey et al., 2014; Natarajan et al., 2004; Randall et al., 2006, 2009; Siskind, 2000).

Despite the overwhelming evidence that this is a common means by which EPP influences the atmosphere, models are incapable of simulating the effects satisfactorily. For example, in the Arctic winter of 2004, an enormous influx of EPP-NO_x was observed to descend from the MLT into the polar stratosphere (Natarajan et al., 2004). NO_x mixing ratios in the upper stratosphere increased by as much as a factor of 4, causing localized catalytic reductions in ozone of more than 60% (Randall et al., 2005). A number of authors have attempted to model the effects, including using the WACCM model (Marsh et al., 2007), but all underestimated the flux of EPP-NO_x into the stratosphere (see Randall et al., 2016).

It is not surprising that WACCM would underestimate NO_x production by EPP, since only electrons of auroral energies, and no higher energy electrons, were included in the model. But the reason for this omission is that there is no satisfactory data set of higher energy electron precipitation for input to the model. The primary satellite

measurements of precipitating electrons in the relevant energy range are from the Medium Energy Proton and Electron Detector (MEPED) (Evans and Greer, 2004). But these measurements suffer from proton contamination and poor spectral resolution, and they do not adequately sample the loss cone. Several authors have estimated precipitating particle flux spectra from the MEPED data, but all warn of significant caveats about their validity (Rodger et al., 2010; Peck et al., 2015; Nesse Tyssøy et al., 2016).

An accurate model of mesospheric chemistry is therefore important to our goal of inferring precipitation fluxes and spectra from ground-based measurements. In addition to the chemical response of the atmosphere, the high-power large-aperture (HPLA) radar technique and the subionospheric very-low-frequency (VLF) remote sensing technique are sensitive to the electron density in the mesosphere and D-region ionosphere, rather than the precipitation flux itself or the ionization rates. These diagnostics are described in detail in Section 7.4. The chemistry models provide the mapping from flux and ionization rates to electron density profiles.

Fig. 7.13 shows some example chemistry calculations using the SIC model. These are again driven by our DEMETER-like exponential energy distributions, with fluxes from 10^4 to 10^6 electrons/cm^3/s, for different β_e values. The left panels show the ionization rate profiles, in pairs/cm^3/s. The middle and right panels show the resulting O_x and NO_x maximum perturbations in the atmosphere, following a precipitation event lasting 30 minutes. The atmospheric O_x decreases only moderately for fluxes of 10^5 electrons/cm^3/s or lower, and up to a 30% reduction for a flux of 10^6 electrons/cm^3/s. The perturbations are mostly insensitive to the precipitating flux distribution. On the other hand, NO_x increases by only a few percent for low fluxes, up to tens of percent for a flux of 10^5 electrons/cm^3/s, and up to hundreds of percent for a flux of 10^6 electrons/cm^3/s. In addition, the peak response varies in altitude and magnitude with the precipitating electron distribution, trending toward lower altitudes and higher magnitudes for higher β_e, as expected owing to the increased flux of higher energy electrons.

7.3 Precipitation modeling

In this section, we provide an overview of precipitation modeling techniques to calculate ionization profiles in the atmosphere from precipitating electron fluxes, spectra, and pitch angle distributions. Here, we are focused on electron energies above $\sim$100 keV; precipitation of lower energy electrons is discussed in Chapter 6.

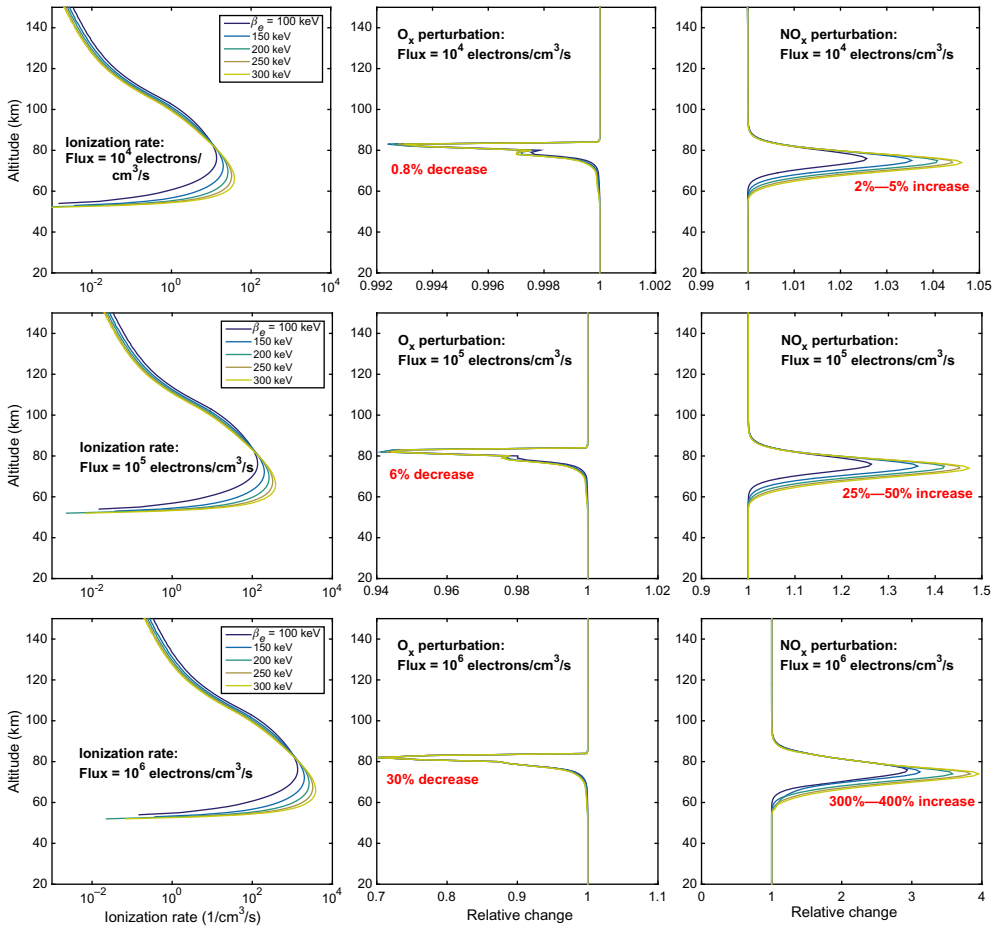

Figure 7.13 Chemistry calculations for the same set of precipitating distributions as in Fig. 7.12. Three rows are for different precipitating fluxes, and five different distributions are used in each. Chemistry calculations performed by A. Kero, Sodankylä Geophysical Observatory, University of Oulu.

7.3.1 Scaling methods

While the full range of interactions between precipitating particles and the atmosphere is complicated, many of the essential features can be understood through scaling arguments. As a first step, consider the problem of a unidirectional, monoenergetic beam of electrons normally incident on a one-dimensional (1D) (slab) atmosphere with no magnetic field. The electron loses energy primarily through long-range collisions with atoms. The energy deposition, therefore, depends on the number of target atoms encountered, and thus scales naturally with the target depth (or column depth):

$$d(z) = \int_{z}^{z_0} \rho(z')dz' \tag{7.16}$$

where z_0 is the top of the system at several hundred km. The target depth specifies the mass of material above the position z, and has units of g/cm^2. In a uniform gravitational field, d is equal to the equilibrium pressure divided by the gravitational acceleration g. Parameterizing by depth instead of altitude removes much of the sensitivity to variations in atmospheric composition.

Energetic particles create a shower of scattered and secondary particles. In the continuous slowing down approximation (CSDA; e.g., Berger, 1963), the primary particle continuously decelerates until it is completely stopped at a finite depth R, the range. R is a function of the target material and the energy and species of the source. Higher energy particles have a greater range than lower energy particles, and electrons have a greater range than ions. The range R can be measured directly or calculated; it is tabulated online for many materials at the National Institute of Standards and Technology ESTAR website (Berger et al., 2005) and is shown for air in Fig. 7.14. Nearly all of the incoming particle energy is deposited as the particle traverses an amount of material equal to R. Owing to scattering, the true path is not a straight line, so the peak in energy deposition occurs somewhat above the altitude at which the depth equals the range.

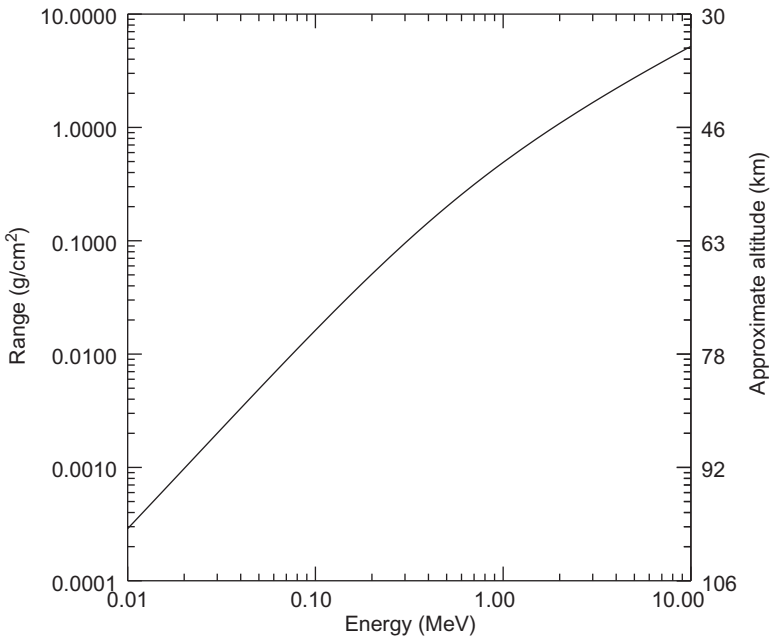

Figure 7.14 Electron range in air (Berger et al., 2005). The right-hand axis shows an approximate altitude corresponding to the range.

Following Rees (1963), we normalize the depth as d/R and define a dimensionless energy dissipation function λ:

$$\lambda = \lambda\left(\frac{d}{R}\right) = \frac{Q}{F}\frac{R}{\rho E_i} \tag{7.17}$$

where Q is the energy deposition rate per unit volume (MeV/cm^3/s), F is the incident flux of electrons (electrons/cm^2/s), ρ is the density and E_i is the incident energy. The normalization of λ ensures that the total energy E_i is deposited within the target:

$$\int_{-\infty}^{\infty} \lambda(z')dz' = 1 \tag{7.18}$$

The dimensionless function λ is nearly independent of the particle energy over a wide range of energies. This energy independence was exploited by Rees (1963, 1989) to derive an accurate semiempirical model of energy deposition based on laboratory measurements of a 32 keV electron beam in air (Grün, 1957). His energy-independent λ is shown as the dashed curve in Fig. 7.15 (left). The solid curves are normalized energy deposition curves computed for a range of energies using the modern general-purpose Monte Carlo N-Particle Transport Code (MCNP) (see below). From energies of order keV through many MeV, the dimensionless yield function λ is indeed relatively constant, even as the range R varies over many orders of magnitude.

The usefulness of the scaling models is further apparent when the normalized energy deposition is converted into physical units. Fig. 7.15 (right) shows the energy deposition of a 1 MeV beam incident on an MSISE-90 (Picone et al., 2002)

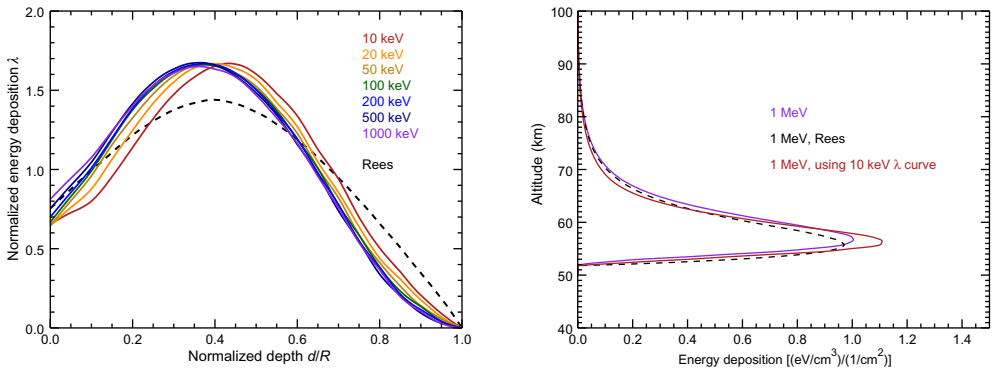

Figure 7.15 (Left) Normalized energy deposition λ for unidirectional and monoenergetic beams with varying energies, calculated using the MCNP Monte Carlo code. Also shown is the energy-independent curve used by Rees (1963). (Right) Energy deposition as a function of altitude for a 1 MeV beam impacting a realistic atmosphere, calculated using several normalized energy deposition curves (see text).

atmosphere, calculated using the normalized yield function curves (λ). The violet curve uses the MCNP-derived normalized curve appropriate for 1 MeV [i.e., the violet curve in Fig. 7.15 (left)], the dashed curve uses the Rees λ and the red curve uses the λ curve for 10 keV but the range scaling for 1 MeV. The relatively minor differences between these curves, even when plotted with a linear scale, demonstrate the robustness of the scaling solutions.

The treatment so far has neglected the magnetic field. A strictly vertical, uniform magnetic field is of little consequence to the energy deposition profiles, since the resulting Lorentz force has no vertical component. The magnetic field deflects charged particles in the horizontal plane, "wrapping up" the motion in that plane, but the deflection is irrelevant in a 1D model. However, if the magnetic field is not strictly vertical, then it does need to be considered. Similarly, if there is a gradient to the magnetic field, then a mirroring force causes the particle pitch angles to change during their descent. We have found through simulations that this mirroring force affects the energy deposition profiles, shifting them to higher altitudes, but the effect is relatively small (less than a few km).

The effect of an inclined magnetic field can be included straightforwardly, since the charged particles (primary, secondary, and knock-on) are all sufficiently magnetized so as to remain within a thin column. The problem can therefore be cast into a field-aligned coordinate system by replacing the atmospheric depth (Eq. 7.16) with the *slant depth*: the integral of the mass density along the field line. The effect is to move the energy deposition peaks to a higher altitude, since the incoming beam must pass through a larger number of atoms in order to reach a given altitude.

The solutions can be further generalized from monoenergetic distributions to more realistic energy spectra by summing over a linear combination of appropriately weighted monoenergetic energy deposition curves. Generalizing to an arbitrary angular distribution is somewhat more difficult. There is no straightforward way to scale the energy deposition profiles for varying pitch angles, since the primary particles are strongly scattered only after reaching a substantial depth. Instead, the angular distribution must be modeled explicitly. One approach is to calculate the function $\lambda(d/R)$ under several assumptions of the angular distribution (isotropic, unidirectional, etc.) (Rees, 1963, 1989). This yields several sets of energy deposition curves corresponding to the assumed angular distributions.

If an arbitrary angular distribution is required, an alternative approach is to calculate the energy deposition for monoenergetic beams at a range of pitch angles (Fig. 7.16, left). The resulting energy deposition for an arbitrary distribution can then be calculated by a double integral over energy and angle (Fig. 7.16, right). Particles at greater pitch angles deposit more energy at high altitudes, since the primary must travel a greater total distance along its helical trajectory in order to penetrate to a given altitude. However, strong angular scattering as the primary nears the energy deposition

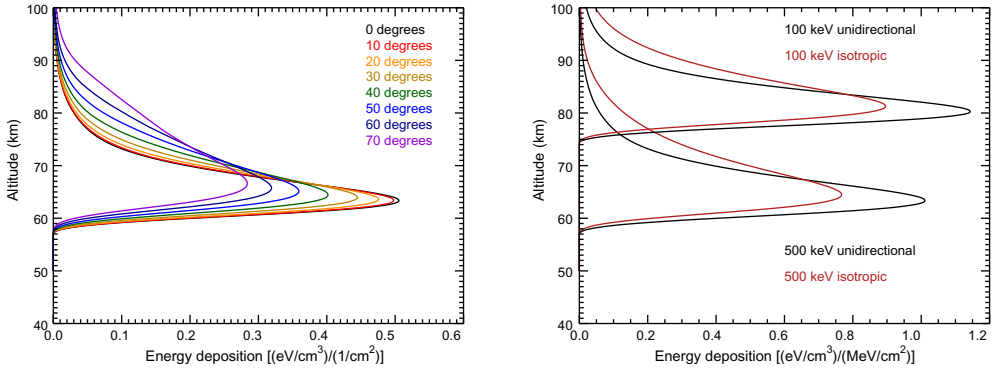

Figure 7.16 (Left) Energy deposition for a 500 keV beam of electrons incident at various pitch angles on a realistic atmosphere with 90-degree field inclination. Pitch angles are initialized at 300 km. (Right) Energy deposition for 500 keV and 1 MeV precipitating particles assuming different angular distributions. The two beams have been normalized to the same energy flux at the top surface so as to make the peak scales comparable.

peak rapidly diminishes the kinematic differences between different initial pitch angles. The resulting altitude profiles are therefore relatively similar; the altitude of peak energy deposition has only minor sensitivity to the pitch angle (see also Fig. 7.2), while the width is broadened for larger initial pitch angles. Since the integral of the energy deposition must equal the initial energy, the peak energy deposition rate decreases as the peak broadens. If the distribution is integrated over an assumed isotropic angular distribution (Fig. 7.16, right), the effect is similar: a minor broadening of the peak and consequent reduction in the peak energy deposition rate.

7.3.2 Monte Carlo techniques

For detailed *ab initio* modeling of precipitation effects, Monte Carlo techniques are an important and well-established tool (Berger, 1963; Berger and Seltzer, 1972; Berger et al., 1974; Solomon, 1993, 2001; Wissing and Kallenrode, 2009). The flexibility of the Monte Carlo framework allows a large number of physical processes to be included, and modern general-purpose Monte Carlo codes such as GEANT, MCNP, FLUKA, and EGSnrc (Agostinelli et al., 2003; Goorley et al., 2012; Böhlen et al., 2014; Kawrakow et al., 2017) have been extensively tested and validated over many years for use in high-reliability fields such as cancer treatment and nuclear reactor design. Detailed theory is treated in several texts, such as Rogers and Bielajew (1990), Jenkins et al. (1988), and Kalos and Whitlock (2008).

In its simplest form, a Monte Carlo model of particle precipitation starts with a single primary particle and then advances it in time by random sampling of the relevant interaction probabilities. Some of the interactions merely change the momentum vector of the incoming particle, while other interactions create new particles

(photons or charged knock-on particles) that are then advanced in the same manner. Every resulting particle is advanced until all of its available energy is either deposited into the medium or transported out to the boundaries. The process is then repeated, sampling many particle histories until sufficient statistics are accumulated to solve the problem to the desired degree of accuracy. This simplest direct form of simulation is sometimes known as an "analog" Monte Carlo scheme, since the simulated processes are exactly analogous to the real physical processes.

Since the charged-particle range decreases dramatically at lower energies, particle simulation histories can be stopped once the range becomes small compared to the spatial scales of interest. Otherwise, tracking lower energy particles in Monte Carlo becomes extremely computationally expensive. A low-energy threshold is defined, below which the particle energy is assumed to be locally absorbed into the medium. For particles precipitating into the terrestrial atmosphere, this energy may be on the order of 1 keV. Lower energy processes such as atomic excitation or recombination can then be accounted for analytically, leaving only the following higher energy processes for simulation: elastic and inelastic scattering of the charged particles, bremsstrahlung production, photoelectron production, Compton scattering, and pair production.

Although analog Monte Carlo simulation is appropriate for some aspects of the precipitation problem (specifically, the photon transport), it is infrequently used for charged-particle transport. Unlike photons, which tend to lose their energy through a relatively short sequence of catastrophic interactions, charged particles usually slow down through a large number (tens of thousands) of relatively minor interactions. Simulating each of these minor interactions individually is computationally expensive. A more efficient alternative is to group together many individual interactions and to use appropriate multiple scattering and energy loss theories to step through many interactions at once. Each step should be large enough to render the multiple scattering theory relevant but short enough to avoid boundaries, large-angle scattering, or large relative changes in the primary particle energy. The resulting "condensed history" Monte Carlo scheme retains the essential physics for elastic scattering and energy loss by charged particles at a greatly reduced computational cost.

Charged particles are typically assumed to lose energy according to the CSDA: the energy lost per unit length ("stopping power") is a function of the target material, the particle type, and the particle energy. The range R (Fig. 7.14) is the integral of the inverse of the stopping power. Stopping power has both a radiative component from bremsstrahlung production and a collisional (electronic) component from inelastic collisions with atomic electrons. Accurate reference values for the stopping power are maintained by the International Commission on Radiation Units and Measurements (ICRU, 2014) based on the theory of Bethe (Bethe, 1930; Bethe and Ashkin, 1953; Fano, 1963), with large-energy transfers governed by the Møller (1932) cross section for electrons. Many models also include statistical fluctuations in the

energy loss, an effect termed "straggling" and first described by Landau (1944). Because of straggling, a very small fraction of particles may reach depths greater than their CSDA range.

Elastic scattering of charged particles (Rutherford scattering) may be described by the multiple scattering theories of Goudsmit and Saunderson (1940), Moliere (1948), or others. The most fundamental quantity required is the probability $P(s,\theta)$ of scattering through an angle θ after a step length s. An additional quantity required for higher precision and longer steps is the path length correction. Since the particle multiply scatters along its step, it does not follow a straight-line trajectory, and the true distance traveled by the particle (the transport length) exceeds the simple straight-line distance between the start and stop points of the step. Since energy loss is dependent on the transport length, the path length should be corrected to account for this effect.

Photons are conceptually simpler to simulate. Since they lose energy in relatively few steps, direct (analog) simulation is entirely feasible. The relevant photon processes include photoelectron production, Compton scattering, pair production, and bremsstrahlung. For each process, the total energy-dependent cross section must be known as well as the angular distribution of outgoing particles. For the case of bremsstrahlung, these functions are shown in Fig. 7.5.

General-purpose Monte Carlo codes for electron–photon–matter interactions are large codes requiring careful validation. However, the interactions are well known, and the atmospheric geometry is simple. Results across different codes are often quite consistent. Fig. 7.17 shows a comparison between the modern general-purpose codes GEANT4 (Agostinelli et al., 2003) and MCNP6 (Goorley et al., 2012), for the case of a 1 MeV monoenergetic beam incident on an MSISE-90 atmosphere. Both codes have been extensively verified by large communities of users over decades of use; GEANT4 is particularly well used in the high-energy physics community, and MCNP is well used in medical physics and other areas. The energy deposition has been plotted in normalized units, which tends to highlight differences more readily than altitude profiles (e.g., Fig. 7.15). The two curves demonstrate excellent inter-model agreement.

7.3.3 Electron precipitation Monte Carlo modeling framework

Much of the work shown in Sections 7.2 and 7.4 was generated with the Electron Precipitation Monte Carlo (EPMC) framework, which has been assembled at the University of Colorado Boulder, building on the Monte Carlo model of Lehtinen et al. (1999). This set of models is used to simulate precipitation inputs (flux, energy, and pitch angle distributions) to calculate the full host of effects described in Section 7.2. The modeling flowchart is shown in Fig. 7.18. Input distributions are propagated in the Monte Carlo model; individual particles are tracked and energy is

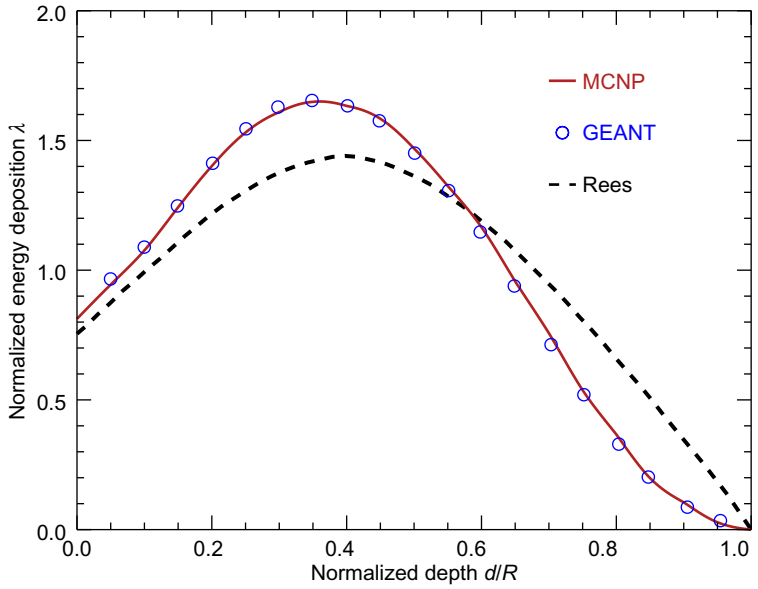

Figure 7.17 Comparison between the GEANT and MCNP6 Monte Carlo codes for a 1 MeV monoenergetic beam. The Rees (1963, 1989) results are also shown with a dashed line for comparison with Fig. 7.15.

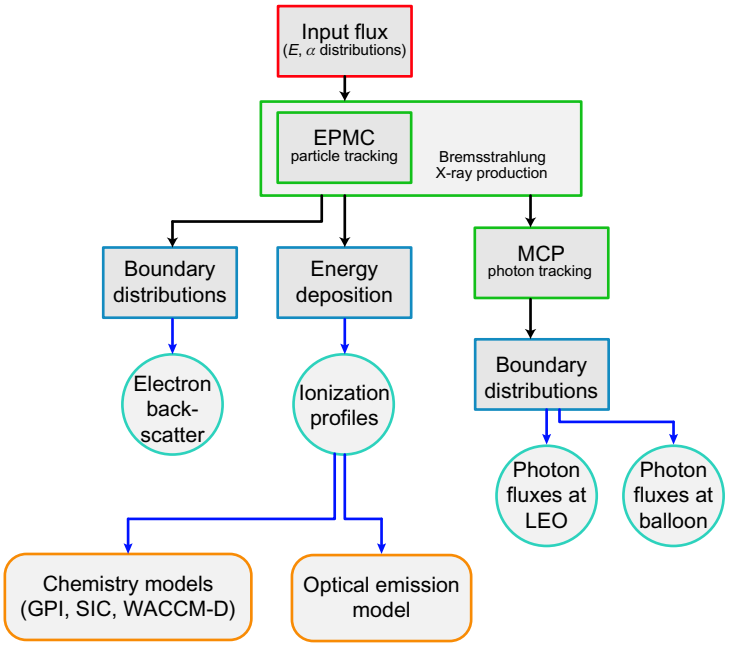

Figure 7.18 Monte Carlo framework used extensively in this chapter.

lost to neutral atmosphere by utilizing the dynamic friction or stopping power function (e.g., Moss et al., 2006), related to the CSDA already described. Small changes to the particle trajectory are calculated via angular diffusion. As energy is lost through dynamic friction, the location of energy deposition is tracked. In addition, secondary electrons are created via ionizing collisions, and those particles are added the Monte Carlo stack. When a particle has lost energy below some set threshold, typically 2 keV, it is considered fully absorbed into the atmosphere locally and is no longer tracked.

Particle distributions through a predefined lower or upper boundary can be used to determine fluxes at those locations. For example, by tracking particles propagating upward through a boundary at 300 km altitude, we track the backscattered particle distribution. Since the model tracks all six components for each particle (three positions and three velocities), the full energy and pitch angle distributions are available for these backscattered particles.

The EPMC model has been updated to self-consistently calculate the production of bremsstrahlung photons. Previously, electron distributions would be output to files at regular time intervals and photon distributions would be calculated from those electron distributions. Now, at each time step in an individual electron's propagation, the probability of creating a photon is calculated. A photon is then randomly generated based on this probability and using the bremsstrahlung cross section for the electron energy. When the probability is low ($<1\%$), photons are randomly generated 100–1000 times or more and the resulting photons are given a fractional weight; this ensures a distribution containing a large number of photons, representative of the true photon production rates.

Photons are propagated in the EPMC model simply by calculating the probability of a collision in each time step. When a collision does occur, it is either a Compton scattering, photoelectron production, or a pair production event, based on the relative cross sections (Fig. 7.6). In this way, the photon propagation can lead to new electrons, which are then propagated in the Monte Carlo framework as well, leading to further ionization production (Fig. 7.7). Similar to the electron distributions, photon distributions at upper and lower boundaries can be collected, providing the expected fluxes at balloon and spacecraft altitudes.

Ionization profiles follow directly from energy deposition profiles, using the assumption that every 35 eV of energy creates one electron–ion pair. Ionization profiles are then the input for models of optical emissions and chemical models, as described in Sections 7.2.4 and 7.2.5, respectively.

While the model is generally run in a 1D configuration, where a beam of N particles represents a flux in particles/cm^2/s (or differential flux in particles/cm^2/s/str/keV), the model is inherently 3D, as it tracks every particle's position in 3D space. This has been taken advantage of by Marshall et al. (2014), where an artificial beam of electrons

was injected into the upper atmosphere from above, simulating an active experiment utilizing a particle accelerator on a spacecraft. In these simulations, the collisional spreading of the beam in the upper atmosphere is directly simulated in the model, allowing us to estimate the energy deposition accurately for a finite-sized precipitation region. This spreading effect is critical for the optical, radar, and VLF diagnostic techniques, which rely on the ionization density per unit volume.

7.4 Diagnostic techniques

Quantifying EPP from the radiation belts requires accurate measurements of the precipitating flux, the energy distribution, and the spatial distribution as a function of time. In this section, we describe the different diagnostic techniques used to measure and quantify precipitation. We begin with a discussion of space-based techniques, and then we describe ground-based measurements. We end this section with a summary of the different diagnostic techniques, comparing their strengths and weaknesses.

7.4.1 Space-based measurements

We limit our discussion here to satellite measurements of precipitation from low-earth orbit (LEO), and balloon-based measurements. In LEO, the loss cone angle can be 45 degrees or larger, making it feasible to observe particles that are strictly in the loss cone and thus precipitating. Similarly, balloon-borne or space-borne X-ray measurements provide nearly direct observations of precipitation.

7.4.1.1 Direct particle measurements

The most obvious and direct observation of EPP is clearly the measurement of loss cone particles as they propagate toward the atmosphere. Observations of energetic particles from high altitude (i.e., at altitudes of $2R_e$ or greater) typically use the spin of the spacecraft to sample the pitch angle distribution. The instruments themselves have a field of view (FOV) typically on the order of $\sim$20 degrees. The slowly spinning spacecraft can ultimately provide a pitch angle distribution with $\sim$10-degree resolution (e.g., Baker et al., 2014). However, at $L = 3$, the equatorial loss cone angle α_{eq} is about 10 degrees, and smaller as altitude increases. Thus these instruments cannot resolve the loss cone at high altitude and differentiate between loss cone and trapped particles.

On the other hand, LEO spacecraft at, say, 500 km altitude experience a local loss cone angle α_{lc} of 45 degrees or larger. Thus an instrument can be designed to have its FOV completely within the loss cone, ensuring that all particles observed are precipitating. However, with a 20 degree FOV, an instrument still cannot resolve the edge of the loss cone, meaning that it cannot fully measure the precipitating distribution without also capturing some trapped particles. To properly resolve the loss cone

(i.e., to resolve the transition from trapped to loss cone flux), an instrument would require ~1 degree pitch angle resolution or better.

Nonetheless, LEO particle detectors have been used for many decades to observe and monitor EPP. The MEPED instrument on the Polar Operational Environmental Satellites (POES) series of spacecraft has yielded the most well-known among energetic particle measurements. Data from the MEPED instrument is commonly used by scientists in search of precipitating fluxes and spectra, primarily due to its longevity over the course of many POES and MetOp satellites, which are both in polar, sun-synchronous orbits at 850 km altitude. MEPED measures energy-integrated electron fluxes in different channels for energies >50, >100, and >300 keV, in two 30-degree FOV telescopes; one pointed toward the zenith and one at 90 degrees to the zenith. In this configuration, the zenith telescope exclusively observes precipitating electrons, while the 90-degree telescope observes primarily trapped electrons. These detectors also detect protons with five energy channels from 30 keV to 6.9 MeV and above; in fact, protons have been found to be a contaminant for the electron measurements, requiring great care to separate the two (Peck et al., 2015; Nesse Tyssøy et al., 2016).

Numerous other missions in LEO have made measurements of precipitating fluxes, including Solar Anomalous and Magnetospheric Particle Explorer (SAMPEX) (Baker et al., 1994) and DEMETER (Sauvaud, 2006). SAMPEX measured electrons from 0.4 to 30 MeV in three energy bands and observed the fluxes of radiation belt electrons (and protons) and their variation with time and *L*-shell. DEMETER's particle instrument for Particle Detection (IDP), was designed to measure electrons from 70 keV to 2.5 MeV in 130 energy bins, providing unprecedented energy resolution. This resolution was achieved through pulse analysis, providing the energy deposited in the silicon detector by each incident electron.

The missions that we have described provide excellent measurements of precipitating electron flux and the energy spectrum, which can be input into atmospheric models as described earlier. However, as single in situ instruments, they cannot provide measurements of the spatial-scale size of precipitating structures without other simultaneous measurements. To measure spatial scales, both FIREBIRD (Spence et al., 2012; Crew et al., 2016) and AeroCube-6 (Janson and Welle, 2014; Blake and O'Brien, 2016) flew pairs of CubeSats at known separation distances to resolve the spatial−temporal ambiguity inherent in single space-based measurements. Crew et al. (2016) used FIREBIRD data to resolve microburst spatial sizes of 120 km or greater when mapped to the equator, while Blake and O'Brien (2016) found structures on the order of 30−60 km spatial size.

The measurement of spatial scales of precipitation remains one of the key outstanding problems for radiation belt science. These spatial scales are needed in order to assess the total precipitation flux during precipitation events, and thus the total loss

from the radiation belts (e.g., Millan et al., 2007). Spatial scales will most certainly be a key scientific target of future missions.

7.4.1.2 X-ray observations

Chapter 5 of this book describes balloon- and CubeSat-based studies of radiation belt losses in detail; here, we provide a brief description of the X-ray observation method. The observation of X-ray emissions at energies of 50 keV or higher is an invaluable diagnostic tool for radiation belt precipitation. At these high energies, we can be certain that the source precipitation is of radiation belt origin, as lower energy electrons cannot produce these high-energy photons. Unfortunately, X-rays cannot be observed from the ground, as they are absorbed in the atmosphere above about 20 km altitude. However, both balloon and spacecraft observational platforms have the capability of providing excellent time and spatial resolution, either through imaging or through multiple instruments.

The most recent experiment to measure balloon-based X-ray signatures of electron precipitation was the Balloon Array for Radiation-belt Relativistic Electron Losses (BARREL) mission (Millan et al., 2013; Halford et al., 2015). BARREL was designed to make measurements with multiple balloons simultaneously, spread out in local time, to measure the spatial extent of precipitation regions. In addition, BARREL made conjunction measurements with the Van Allen Probes spacecraft, so the electron distributions measured with Van Allen Probes, along with the wave signatures, could be compared to the resulting precipitation fluxes and spectra.

Balloon measurements of X-rays rely on the downward propagation of photons from their source above 50 km to the balloon below. Some photons will be generated propagating laterally, as the electrons are in gyromotion around the local magnetic field. Through a number of scattering interactions, these photons can be turned around to propagate back toward space, where they can be detected from LEO. Fig. 7.19A shows the relative distributions of photons observed at 35 km altitude (balloon) and 500 km altitude (satellite) from the same precipitating source. In this case, the source of precipitating electrons is an exponential energy distribution with $\beta = 300$ keV and an isotropic pitch angle distribution. While the balloon and satellite locations receive a similar number of high-energy photons, the satellite receives a much larger number of lower energy photons, and a much larger number of photons overall.

No mission has yet flown to measure energetic (>50 keV) X-rays from LEO. The Atmospheric Effects of Precipitation through Energetic X-rays (AEPEX) mission concept is designed to make these space-based measurements of X-rays resulting from radiation belt precipitation. Such a mission would provide global coverage, imaging of X-ray sources and thus precipitation locations with $50-100$ km resolution, and a much longer mission duration compared to balloons. The AEPEX mission, as depicted in Fig. 7.19, would provide an invaluable tool for space weather monitoring from LEO.

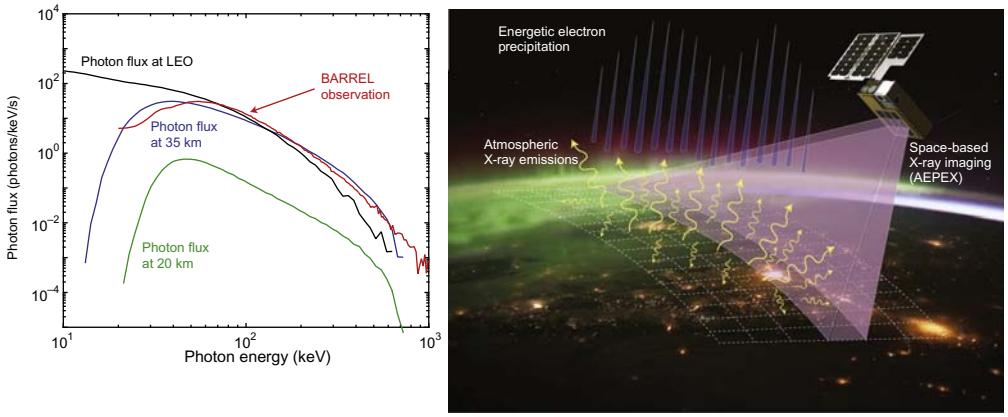

Figure 7.19 (Left) Photon fluxes predicted at LEO and balloon altitudes using Monte Carlo simulation, compared with an example BARREL-observed spectrum. (Right) AEPEX concept mission to measure image bremsstrahlung X-rays from LEO.

7.4.2 Ground-based measurements

Compared to space-based measurements, ground-based observations of precipitation have some advantages. Since the measurement location is fixed, ground-based observations can provide better temporal signatures of events in a fixed reference frame (neglecting the rotation of the Earth). Furthermore, it is easier to distribute a broad array of instruments on the ground as compared with in space, enabling the potential for measurements of spatial resolution.

However, all of the ground-based observations are indirect, measuring by-products of precipitation, and thus requiring some inversion modeling to infer the precipitating fluxes and spectra. Nonetheless, ground-based measurements provide a valuable tool for observing and measuring precipitation, especially in conjunction with space-based measurements.

7.4.2.1 Very-low-frequency subionospheric remote sensing

As shown in Fig. 7.2, radiation belt electrons primarily deposit their energy in the altitude range 50–100 km, constituting the MLT. This altitude range also corresponds with the D-region of the ionosphere, where background electron densities are low (10^2–10^4 electrons/cm^3; Fig. 7.3) and electron-neutral collisions are high. The D-region is a difficult region of the ionosphere to study because of its altitude and its very low electron densities; however, subionospheric VLF remote sensing has long proven be an effective tool for monitoring the D-region, and thus it provides a valuable measurement of radiation belt precipitation.

Subionospheric VLF is discussed in detail in Chapter 8. Here, we provide a brief overview of the means by which subionospheric VLF is sensitive to radiation belt precipitation, and a discussion of modeling techniques to infer the precipitating flux from VLF signatures.

The theory of VLF wave propagation in the Earth-ionosphere waveguide is covered in a number of classic texts (e.g., Ratcliffe, 1959; Budden, 1961; Davies, 1990). Ratcliffe (1959) shows that electromagnetic waves reflect from the cold, collisional lower ionosphere at the altitude where $X = Z$ (Fig. 7.20), where $X = \omega_p^2/\omega^2$ is the normalized plasma frequency, and $Z = \nu_{en}/\omega$ is the normalized electron-neutral collision frequency. Rearranging and using $\omega_p^2 = q^2 n_e/e_0 m_e$, this equation says that reflection occurs when the wave frequency $\omega \sim n_e/\nu_{en}$, where n_e is the electron number density and ν_{en} is the electron-neutral collision frequency.

Subionospheric VLF remote sensing of the D-region ionosphere can utilize a number of techniques, but the oldest and most common is the monitoring of powerful ground-based narrowband VLF transmitters. These transmitters operate in the 10–50 kHz range, most typically between 20 and 25 kHz, thus reflecting in the 70–90 km altitude range, and transmit tens of kW to as high as 2 MW of radiated power. Transmitters such as the NAA transmitter in Cutler, Maine—operated by the US Navy for long-distance submarine communication—are easily detectable from thousands of km away. Perturbations in amplitude and phase at a distant receiver are caused by variations in the D-region ionosphere somewhere (perhaps everywhere) along the path between the transmitter and the receiver. This poses a significant problem for inversion: inferring the ionosphere all along the path from the amplitude and phase at a single location is a highly underdetermined and nonlinear problem.

Because the VLF propagation is sensitive to the state of the D-region ionosphere at the reflection height, sudden increases in the electron density during precipitation events can have dramatic effects on the VLF signal, as shown in Fig. 7.21. This

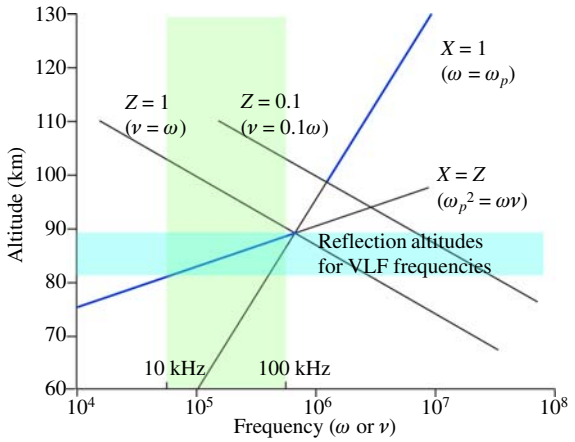

Figure 7.20 Approximate plasma and collision frequencies in the lower ionosphere at nighttime and associated reflection heights. During the daytime the electron density in the D-region is higher, so the reflection height is lowered to 70–75 km. *Adapted from Ratcliffe, J.A., 1959. The Magneto-Ionic Theory and Its Applications to the Ionosphere. Cambridge University Press, Cambridge, UK.*

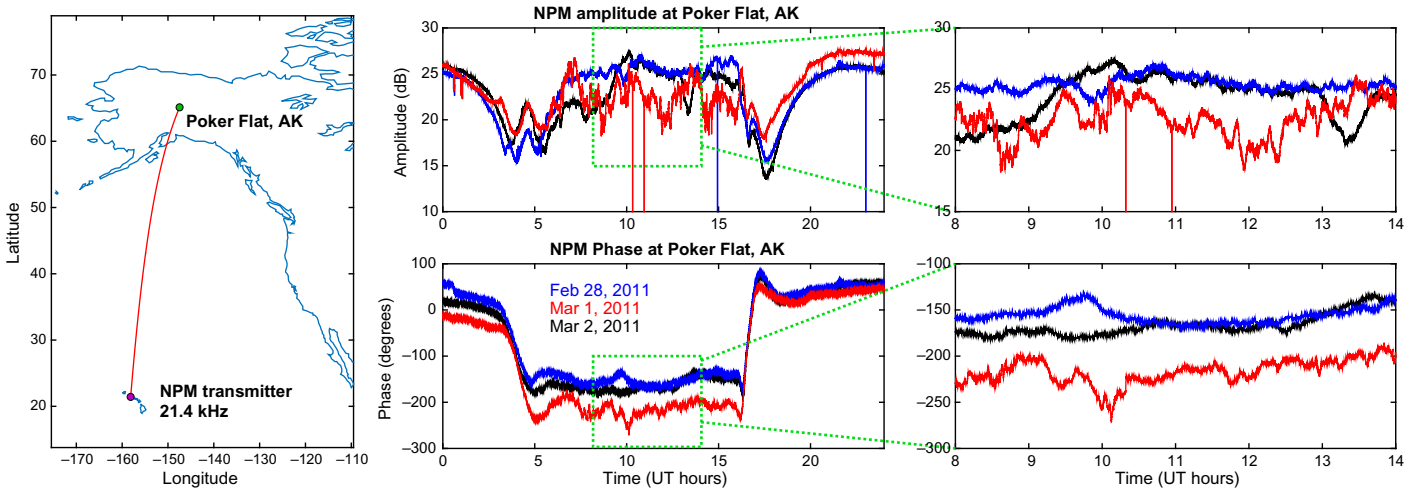

Figure 7.21 Precipitation observed by VLF at Poker Flat, AK, on March 1, 2011. (Left) Great circle path from NPM transmitter in Hawaii to VLF receiver at Poker Flat. (Middle) Amplitude (top) and phase (bottom) for 3 full days in 2011. (Right) Zoomed-in view showing 6 h of VLF amplitude and phase.

figure shows 3 days of data recorded at Poker Flat, Alaska, monitoring the 21.4 kHz NPM transmitter signal broadcast from Lualualei, Hawaii. The blue and black curves show the relatively "quiet" days of February 28 and March 2, 2011, whereas the red curve shows data from March 1, 2011, when a geomagnetic storm occurred around 10 universal time (UT). Amplitude changes of many dB, and phase changes of many tens of degrees, are regularly observed. However, because of the complex mode structure propagating in the Earth-ionosphere waveguide, the amplitude and phase changes do not provide a direct correlation with the precipitating flux. Thus detailed modeling is required to infer the precipitation signatures.

7.4.2.1.1 Very-low-frequency propagation modeling

The most ubiquitous modeling tool for subionospheric VLF is the Long-Wavelength Propagation Capability (LWPC), developed by the US Navy in using their network of VLF transmitters (e.g., Pappert and Snyder, 1972; Ferguson, 1980). LWPC is a mode solver that divides the Earth-ionosphere waveguide propagation channel into "segments" of a few hundred km and solves for the mode amplitudes in each segment. When one segment is solved, the amplitudes at the far end of that segment are used as the inputs to the next segment.

LWPC is a fast and efficient solver for Earth-ionosphere waveguide propagation and provides predicted amplitude and phase at any location on the globe, taking into account the conductivity of the Earth's surface, the magnetic field direction and amplitude, and arbitrary electron density profiles. Its largest drawbacks are that the model is limited to 2D, and the spatial resolution along the path is limited by the smallest slab that can be solved. In practice, LWPC will reliably converge for slabs of 100 km or larger, though some users have successfully run LWPC with segments of 20 km or even shorter (e.g., Thomson and McRae, 2009). However, LWPC will fail to converge when the gradient in the ionosphere is high in the along-path direction; under those circumstances, even smaller segment sizes are required.

An alternative to LWPC is the use of finite-difference time-domain (FDTD) or finite-difference frequency-domain (FDFD) techniques, which have been in use for this problem for about 20 years. FD techniques divide the space into a large number of small grid cells, typically no larger than one-tenth of a wavelength, and directly solve the discretized Maxwell's equations on the resulting grid. Since the wavelength at 20 kHz is 15 km, this implies grid cells on the order of 1 km. The Courant–Friedrich–Levy stability criterion for explicit FDTD methods further implies that the time step is limited by $v_p \Delta t/\Delta x \leq 1$ to ensure stability. For $\Delta x = 1$ km, this implies a maximum time step of 3.3 μs. Thus for a 2D simulation covering 100 km in altitude and 3000 km along the ground, we require 100×3000 grid cells, and we must simulate a minimum of 10 ms for the source to propagate 3000 km, or about 3000 time steps. In practice, the spatial step and time step must be

even smaller to account for shorter wavelengths in the D-region ionosphere plasma. All of this is to say that the FDTD method is computationally expensive, and it often requires many hours of simulation time for a single scenario, compared to just a few seconds for LWPC.

The major advantage of the FDTD method is that its spatial resolution is limited only by the grid size. If we use a 1 km grid cell, we can arbitrarily specify the electron density, collision frequency, and magnetic field with 1 km precision. This enables the simulation of small and highly structured precipitation signatures. A second advantage of FDTD is that by simulating an impulse and calculating real-time discrete Fourier transforms at frequencies of interest (e.g., Marshall et al., 2017), a large number of frequencies can be simulated in a single run.

Marshall et al. (2017) made comparisons between LWPC, the FDFD model of Chevalier and Inan (2006), and the FDTD model of Marshall (2012), modified for this long-distance propagation application. Fig. 7.22 shows a comparison between the LWPC and FDTD models for 10, 20, and 30 kHz, where both models used the same ground and ionosphere parameters. From left to right, the panels show the simulated amplitude along the ground, the phase along the ground, and a zoomed-in view of the phase. Agreement is very good for both amplitude and phase; the rightmost panels show that the error between the two models is no more than about 5 degrees, and most of the time is less than 1 degree.

To characterize the VLF response to precipitation, we have conducted simulations using a three-step modeling process. First, we use the EPMC model as described earlier to estimate the ionization rate profiles produced by precipitation. Next, we use the GPI chemistry model to estimate the electron density profiles resulting from this ionization source. Finally, those electron density profiles are input into the FDTD propagation model to simulate the VLF response.

Fig. 7.23 shows example results from these simulations. The topmost panel shows the ionospheric perturbation resulting from a precipitating flux of 10^5 electrons/cm^2/s, using an exponential distribution with $\beta_e = 200$ keV and a precipitation region that is Gaussian in shape, with $\sigma = 200$ km. The plots below show the resulting amplitude (left) and phase (right) response for a VLF transmitter at 20 kHz.

These results show that the amplitude and phase are perturbed, as expected, down-path from the disturbance. The perturbations in amplitude and phase clearly increase with the flux, but not by an order of magnitude. There is a clear trend in which the hardest precipitation (i.e., $\beta_e = 300$ keV) yields the largest perturbations, again due to the higher energy flux. However, as is true for many VLF observations, unfortunately, the particular measured perturbation depends on the receiver location along the path. While a receiver located at 1800 km would measure a large negative amplitude change, a receiver at 1500 km would measure almost no amplitude change.

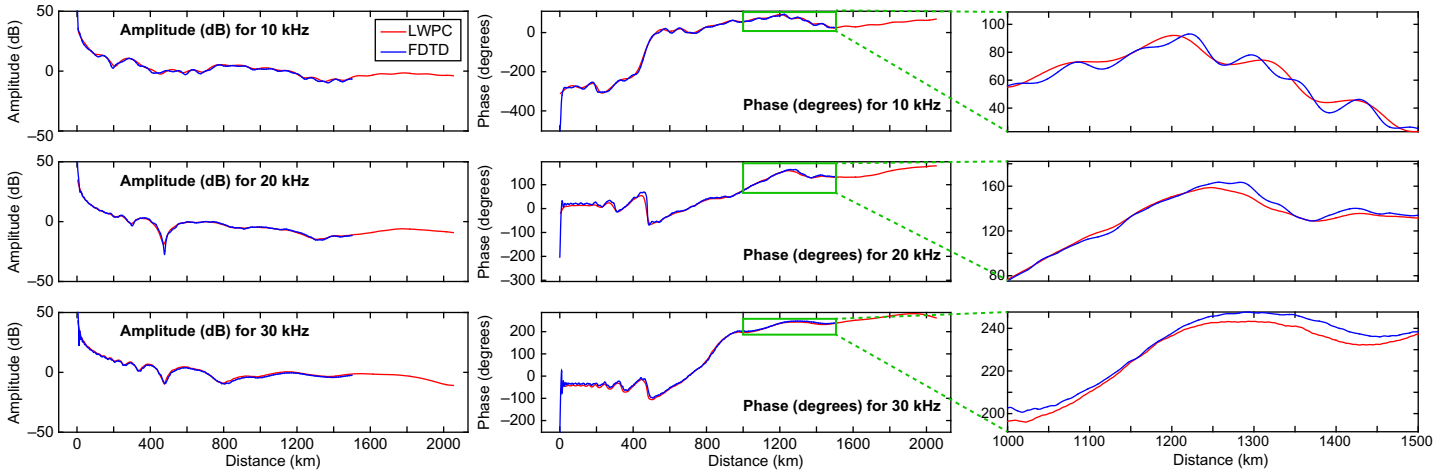

Figure 7.22 Comparison between LWPC and FDTD models of propagation in the Earth-ionosphere waveguide, showing amplitude and phase along the ground for three different transmitter frequencies.

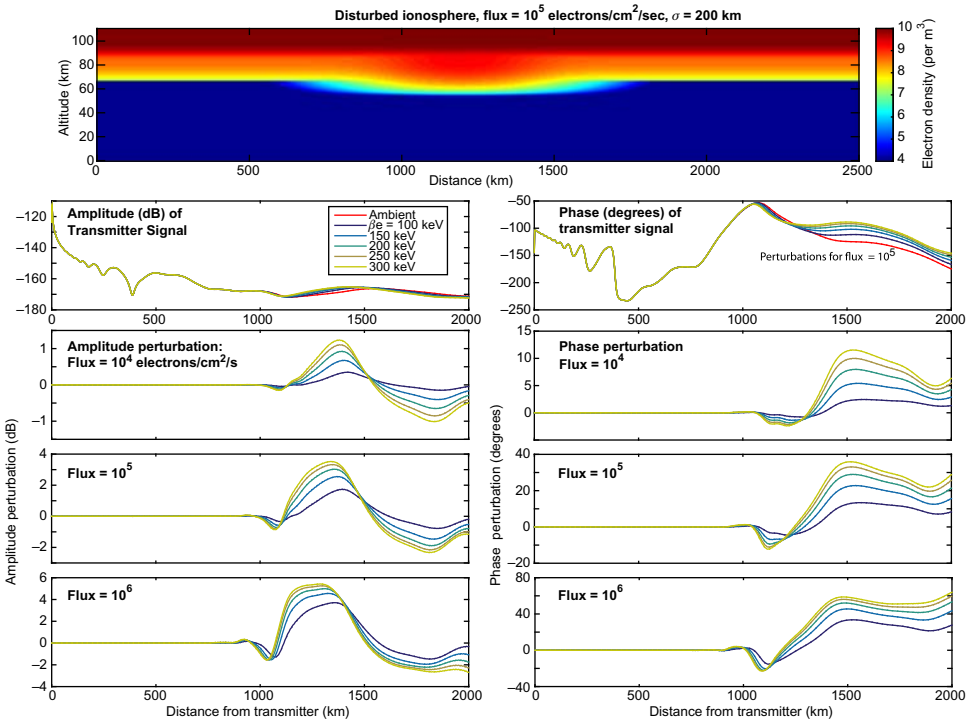

Figure 7.23 Results of FDTD modeling of the VLF response to precipitation. (Top) 2D ionosphere disturbance imposed. (Below) VLF response in amplitude (left) and phase (right) for different fluxes and distributions. For reference, VLF receivers can detect perturbations of about 0.1 dB and 1 degree in amplitude and phase, respectively.

As mentioned earlier, both LWPC and FDTD methods are limited in their ability to infer precipitation signatures from a single amplitude and phase at a receiver. The precipitation patch likely varies spatially over a large area, but none of the methods described thus far can image the precipitation region. The VLF method in particular is very sensitive to ionospheric variations, and the measured amplitude and phase are often not directly correlated with ionospheric changes, owing to the nature of the waveguide mode propagation. We address this problem with an eye toward future studies in Section 7.5.5.

7.4.2.2 Ground-based incoherent scatter radar

The incoherent scatter radar (ISR) technique to detect precipitation is discussed in detail in Chapter 6; here we provide a very brief overview. Radar observations of the ionosphere were pioneered by Gordon (1958), with the development of the ISR technique and the construction of the Arecibo facility, which opened in 1963. ISR relies on the transmission of high-power radio waves in the high-to-ultrahigh-frequency range; for example, the effective radiated power of the Arecibo UHF (430 MHz) radar is

2.5 TW. The radar wave scatters incoherently from the free electrons in the ionosphere, and the return power yields the electron density. In addition, the spectrum of the radar return can provide the electron and ion temperatures and the ion drift velocity.

The D-region, however, has electron densities that are 3–4 orders of magnitude lower than the F-region; therefore the radar returns are generally much weaker. Mathews (1984, 1986) provide overviews of D-region remote sensing using ISR. Mathews (1984) points out that Arecibo, until recently the most sensitive ISR in the world, can achieve a signal-to-noise ratio (SNR) of 3.0 for a single pulse. All other radars require pulse averaging to collect a useful signal from the D-region.

Over the past few decades, a number of studies have utilized ISR to measure the D-region electron density for a wide range of scientific purposes. Turunen et al. (1988) measured D-region enhancements during auroral precipitation and were able to fit the measured radar spectra to extract electron densities, ion-neutral collision frequencies, neutral temperatures, and ion mass and density. Other D-region observations using European Incoherent Scatter Scientific Association (EISCAT) data have included Polar Mesospheric Summer Echoes (e.g., Cho and Kelley, 1993; Röttger et al., 1988), polar cap absorption events (e.g., Hargreaves et al., 1987), and EPP (e.g., Kirkwood and Osepian, 1995; Miyoshi et al., 2015). Using a simplified ion chemistry model, Kirkwood and Osepian (1995) were able to reproduce the electron density profile measured by EISCAT and hence infer the precipitating electron spectrum. This analysis was applied to electrons of both moderate-energy 1–100 keV events as well as energetic >MeV precipitation events.

D-region remote sensing with ISR has been conducted at the Poker Flat ISR (PFISR) for the past few years; PFISR is an electronically steerable, phased-array radar that can steer its beam in the sky with every pulse. Janches et al. (2009) showed observations of D-region ionization enhancements and were able to use these to extract atmospheric winds and tides. In recent years, researchers have made observations of EPP from the radiation belts using PFISR (Kaeppler et al., 2015), though those observations have not yet been published. These results demonstrate that ISR holds great potential as a method for D-region remote sensing of EPP.

The benefits of ISR for D-region measurements are its accuracy, time resolution, spatial resolution (though limited to a few hundred km in range), and continuous observing ability. When the SNR is strong enough, the ISR returns provide a direct measurement of the altitude-resolved electron density. Since the ISR can transmit pulses every millisecond, it is possible to develop a high-time resolution measurement of the changing electron density profile. As for spatial resolution, with electronically steerable radar such as PFISR, the radar can "paint" a series of beams on the sky very rapidly, providing both spatial and temporal resolution (though the latter suffers as the former improves). Finally, as a ground-based instrument, the ISR can monitor a single location in the ionosphere for long periods of time.

7.4.2.3 Riometers

The relative ionospheric opacity meter, or riometer (Little and Leinbach, 1959), offers a routine ground-based method for monitoring moderately energetic precipitation. Riometers measure the amplitude of cosmic radio noise, typically in a narrowband somewhere between 20 and 70 MHz. At these frequencies, the undisturbed ionosphere is relatively transparent. During intervals of EPP, increased electron density causes absorption of the radio waves; the amount of precipitation can then be inferred based on the change in received amplitude.

Practically, the signal received at the instrument depends on the cosmic radio noise in the FOV (typically $\sim$60 degrees) as well as the opacity of the ionosphere. Apart from a few intense point sources such as Cassiopeia, the source can be considered as the diffuse Milky Way, and so the amplitude follows a relatively smooth diurnal curve that changes slowly throughout the year. Variations in the received amplitude from the expected quiet-day curve indicate ionization at $\sim$70–90 km, which may be caused by EPP. Other than EPP, ionization in the relevant altitude range can also be caused by solar X-rays and solar proton events, both of which should be routinely checked when using riometer data.

To understand how EPP causes riometer absorption, consider an electromagnetic wave propagating parallel to the Earth's magnetic field and incident on the topside ionosphere. For propagation parallel to the magnetic field, the Appleton–Hartree dispersion relation reduces to

$$\left(n - i\frac{c\gamma}{\omega}\right)^2 = 1 - \frac{\omega_p^2}{\omega^2 \pm \omega\Omega - i\nu\omega} \tag{7.19}$$

with n the real part of the refractive index, γ the damping coefficient, ω_p the plasma frequency, Ω the electron cyclotron frequency, and ν the electron-neutral collision frequency. The plus sign refers to the left-hand circularly polarized wave ("L mode," or "O mode" if the wave propagation is not strictly parallel), and the minus sign refers to the R mode (X mode). By examining the imaginary part of both sides and taking $n \approx 1$, the damping coefficient is

$$\gamma = -\frac{1}{2c}\frac{\omega_p^2 \nu}{\nu^2 + (\omega \pm \Omega)} \tag{7.20}$$

so that the differential attenuation dA expressed in dB/m over the path segment dl is (Hargreaves, 1969):

$$\begin{aligned} dA &= \frac{d}{dl}\left[20\log_{10}\left(e^{-\gamma l}\right)\right] = \frac{-20}{\ln 10}\gamma \\ &= 4.61 \times 10^{-5}\frac{n_e \nu}{\nu^2 + (\omega \pm \Omega)^2} \end{aligned} \tag{7.21}$$

and the total attenuation is obtained by integrating dA over all altitudes.

Since the electron density n_e increases rapidly with altitude while the collision frequency ν decreases rapidly, the attenuation takes place in a sharp peak. Fig. 7.24A shows the collision frequency along with electron density profiles assuming several different incident EPP distributions. The dashed line assumes 10^5 electrons/cm^2/s following an exponential distribution with $\beta_e = 100$ keV (as in Fig. 7.12, middle bottom). The solid colored lines assume monoenergetic beams at different energies but with the same total energy as the exponential distribution (0.016 mW/m^2). Ionization rates were calculated by scaling the MCNP results from Fig. 7.15 in an MSISE-90 atmosphere, and the resulting electron density was calculated with the nighttime GPI model (Section 7.2.5). As expected, the monoenergetic beams create sharp peaks in the electron density, while the exponential distribution creates a broad enhancement.

The Fig. 7.24B shows the resulting attenuation in dB/km for a 30-MHz O-mode wave from Eq. (7.21). For beam energies below about 30 keV, there is very little attenuation, since the energy is deposited at high altitudes, where the collision frequency is low. Above 30–50 keV, appreciable attenuation occurs, with integrated attenuation for the beams of several tenths of a dB, which is typically observable. Rodger et al. (2012) includes a thorough analysis of how riometers respond to monoenergetic beams, along with a comparison of how riometer measurements compare to VLF and total electron content measurements for inferring EPP.

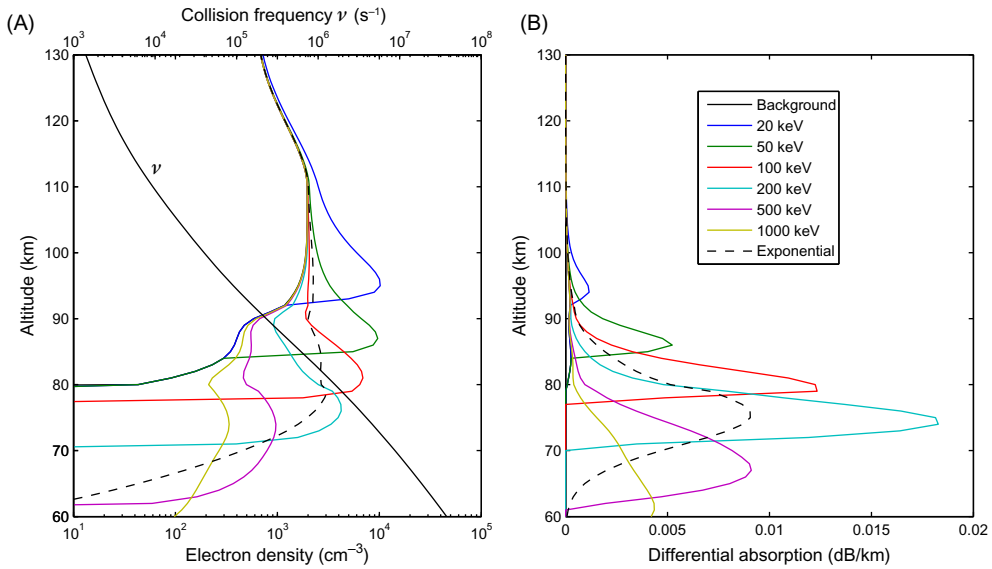

Figure 7.24 (A) Electron-neutral collision frequency and electron density resulting from various assumed EPP spectra. (B) Resulting absorption at 30 MHz.

Although riometers theoretically respond to higher energy (~MeV) precipitation, the required precipitation fluxes are seldom present. The beams in Fig. 7.24 all have equal assumed energy, and while 0.016 mW/m^2 is not unreasonable at several tens of keV, it would be an extreme flux at 1 MeV. There is a clear association between riometer absorption events and substorm injections (Spanswick et al., 2007; Kabin et al., 2011), while the association with MeV-energy radiation belt precipitation is decidedly less clear. Kellerman et al. (2015) found a close correlation between riometer signals and the equatorial 40–60 keV electron flux, with little correlation at 1 MeV.

There are several variations on the riometer design that can increase the information content of the observations. Imaging riometers (Detrick and Rosenberg, 1990; Rosenberg et al., 1991) use phased-array antennas to subdivide the ~60-degree FOV of a standard "wide-beam" instrument into many smaller FOVs. This affords a much finer spatial resolution. Multifrequency or "spectral" riometers have also been used (Kero et al., 2014); these give absorptions at many different frequencies. This in turn can yield an altitude profile of the electron density and hence a better indication of the energy spectrum of the precipitating particles.

7.4.2.4 Optical observations

The detection of optical signatures of EPP has the potential to provide valuable information about the precipitating distribution. With a network of all-sky cameras similar to the THEMIS array (e.g., Donovan et al., 2006), spatial scales of precipitation can be determined, as well as their variation with time. Spectral information—such as the ratio of emission line brightnesses—can be used to infer the precipitating energy distribution (e.g., Gustavsson et al., 2005). The first question to be addressed, however, is whether optical emissions could conceivably be detected from the ground.

Fig. 7.11 shows the emission profiles for a variety of atmospheric emissions. For the purposes of determining detectability, we focus on the N_2^+ 1 N band system. This system has reasonable brightness; falls in the bluish range of the visible spectrum, so that the background noise is lower; and has prominent band heads, so that a reasonably narrowband system can be used. In contrast, the N_2 1 P band system, while much brighter overall, is spread from 5000 to over 12,000 Å without particularly prominent lines.

Fig. 7.26 shows calculations of the resulting SNR for the N_2^+ 1 N band system for two different optical systems. For both systems, background airglow is estimated as a function of wavelength from Broadfoot and Kendall (1968), and SNR estimates include shot noise, read noise, background noise, and Johnson noise, where appropriate. The "photomultiplier tube (PMT)" system is based a real design that was built at Stanford in 2011 (Fig. 7.25). This system uses a Hamamatsu H10493 PMT, and a 6 in. diameter f/0.5 Fresnel lens. We use a filter with a passband from 3700 to 4300 Å to

Figure 7.25 Optical instruments: the Stanford large-aperture photometer (left) and an all-sky imager (right).

capture the prominent 3914 and 4278 Å band heads. (Calculations show that focusing on only the 3914 Å band head with a narrower filter results in very similar SNR.) The PMT system is designed with a 25 Hz bandwidth; a smaller bandwidth results in higher SNR.

The "camera" system is designed to emulate a typical all-sky camera system (Fig. 7.25) similar to what is used by the THEMIS all-sky imager array. Our modeled system uses an Andor iKon 912 CCD camera, with a 512×512 array of 24 μm pixels, binned 16×16 to achieve large pixels. We outfit it with an f/1.0 lens and the same filter as the PMT system. The camera system of course provides some spatial information to measurements, but at the expense of slower frame rates (10-second exposures) and smaller pixels compared to the PMT, the latter of which fully accounts for the lower SNR values. Note that increasing (decreasing) the frame rate decreases (increases) the SNR by a factor $\sqrt{T_{\mathrm{exp}}}$, where T_{exp} is the exposure time of one frame.

Overall, we find that for the DEMETER-measured total flux of 10^5 electrons/cm^2/s, and assuming a sine pitch angle distribution at the equator, optical emissions should be readily detectable using modern optical systems.

For a given pitch angle and energy distribution, the results shown here scale linearly by the total flux as measured by DEMETER. Note that Whittaker et al. (2013, Fig. 7.5) shows median fluxes ranging from 10^3 to over 10^5 electrons/cm^2/s, excluding the South Atlantic Anomaly, while mean fluxes are somewhat higher. If we take the median as the "background" precipitation, fluxes of 10^5 electrons/cm^2/s are a good estimate of the background precipitation from the outer radiation belt across all longitudes. As such, we would expect to measure $\sim 30-60$ R in the N_2^+ 1 N band system during times of moderate precipitation and then see significant enhancements during storm times.

The complicating factor in this observation is separating the optical signature of this high-energy electron precipitation from lower energy precipitation, such as the background aurora. The answer lies in the relative brightness of emission lines. Natural aurorae involve lower energy electrons, which deposit their energy at higher altitudes, thus primarily exciting the O^1 S emission (green line). During aurorae, the green line brightness is typically tens to hundreds of kR, compared to $\sim$10 R here. So, monitoring both the green line and the N_2^+ 1 N band system will provide a unique assessment of radiation belt precipitation during quiet times and during storm activity.

7.4.3 Summary of observational techniques

In this section, we compare the different observation techniques discussed above through their ability to measure important parameters of precipitation: the total flux; energy and pitch angle distributions; the resulting altitude profile of energy deposition; and time and spatial resolution of precipitation regions.

In situ particle detection from LEO provides a very good, but not perfect, measurement of the precipitating flux; it is imperfect because instruments cannot currently fully measure and resolve the loss cone. Energy distributions from particle measurements can be excellent when conducted with pulse-height analysis in silicon detectors, similar to DEMETER, which provided 128 energy bins. Measurement of the pitch angle distribution is best made here; although current instruments have limited capability, there remains the potential for future instruments with better angular resolution. Since the energy resolution is very well measured, this translates into a very good altitude distribution of energy deposition, which is only weakly dependent on pitch angle. Finally, the time resolution and spatial resolution are both reasonably good with in situ particle measurements, but they always suffer from the spatial–temporal ambiguity inherent in in situ spacecraft measurements. A constellation of spacecraft similar to FIREBIRD or AeroCube-6 begins to address this problem.

By comparison, space-based and balloon-based X-ray observations are not as good at determining the precipitating flux and energy distribution, simply because the observation is indirect and requires a physics-based model inversion. Pitch angle distributions are likely not achievable. However, X-ray observations can provide very good time resolution, and space-based observations in particular may provide very good spatial resolution due to imaging capability.

For ground-based observations, optical methods may provide very good measurements of the precipitating flux, since the optical brightness is directly related to the energy deposition. However, since the total energy deposition is dominated by

lower energy particles (less than a few keV), the methods may not be appropriate for estimating energetic particle flux. Time and spatial resolution have the potential to be excellent owing to imaging capability over a large area. Similarly, radar observations provide time and spatial resolution, although they are limited to the area of a few hundred km above the radar. Radar measurements provide the most direct observation of the altitude distribution of energy deposition, and this translates into good measurements of the precipitating flux and energy distribution; however, since HPLA radars are not as sensitive to the lowest altitudes and thus to the highest energy precipitation, determination of the high-energy part of the precipitating distribution is limited.

Subionospheric VLF measurement, by comparison, is the most sensitive technique for precipitation in the hundreds of keV, but inferring the flux, energy distribution, or pitch angle distribution is a very difficult problem owing to the complexity of the VLF propagation over long paths. On the other hand, VLF has the potential to provide spatial resolution over very large areas, potentially an entire hemisphere, with a network of many intersecting paths, such as the Antarctic-Arctic Radiation-belt (Dynamic) Deposition-VLF Atmospheric Research Konsortia (AARDDVARK) or the Array for Broadband Observations of VLF/ELF Emissions (ABOVE).

Wide-beam riometers can also provide spatial resolution over large areas through a network of instruments, and imaging riometers can provide resolution down to the km scale. Multifrequency riometers can additionally provide altitude profiling and energy distribution, although the number of results using multifrequency techniques is still small.

The question of spatial resolution deserves particular attention. A number of missions, including BARREL (Woodger et al., 2015; Halford et al., 2015), FIREBIRD (Spence et al., 2012; Crew et al., 2016), and AeroCube-6 (Blake and O'Brien, 2016), have attempted to address the key question of spatial-scale sizes of precipitation regions during radiation belt losses; we cannot determine total loss rates from the radiation belts without these spatial scales. Each of the methods listed here provides reasonably good to excellent spatial measurements, with certain caveats (e.g., they require multiple spacecraft for particle measurements); however, the spatial scales are widely different. Ground-based optical detection and radar have excellent spatial resolution, but over a regional scale size directly above the observatory location. A network of ground-based systems, such as the THEMIS array, can extend this spatial resolution to larger scales. On the other hand, the AEPEX X-ray imaging concept (Fig. 7.19) covers spatial scales of $\sim$1000 km on short timescales, but extends this to global spatial scales over the course of many orbits. Subionospheric VLF, meanwhile, can provide spatial coverage over an entire hemisphere through a network of receivers. Perhaps a combination of these measurements can truly target the full range of temporal and spatial scales.

7.5 Future experiments

7.5.1 Pitch angle–resolved particle measurements

Currently, most energetic electron instruments utilize a collimator and one or more silicon detectors, providing a conical FOV but no angular resolution within that FOV. Pitch angle distributions, when they are measured, are found through spinning the spacecraft in a plane through the background magnetic field.

To better quantify the precipitating flux from LEO, and to more accurately determine the altitude distribution of energy deposition in the atmosphere, pitch angle–resolved measurements are required. The results shown earlier in this chapter demonstrates that the altitude distribution of energy deposition in particular is strongly affected by the incoming pitch angle distribution (e.g., Figs. 7.2 and 7.16).

Technically, pitch angle–resolved measurements are a challenge. Most silicon detectors have only a single pixel, and so the pitch angle resolution is determined by the FOV; but shrinking the FOV reduces the sensitivity of the instrument. However, multipixel silicon detectors or position-sensitive detectors may have potential in this application. In particular, they may enable instruments with large apertures but pitch angle resolution as good as $\sim$1 degree (Banu et al., 2008).

7.5.2 X-ray imaging from low-earth orbit

As described in Section 7.4.3, space-based X-ray measurements provide the opportunity for spatially resolved measurements of precipitation patches, simultaneously with good time resolution, flux measurements, and energy distribution information. The AEPEX mission concept brings this capability into focus, as shown in Fig. 7.19. The AEPEX mission would provide spatial resolution of $\sim$50 km over a 1000 km swath, 5-second time resolution, and continuous global observations, providing a long-term view of precipitation trends. Similar to balloon-based missions such as BARREL, the precipitating energy distribution and total flux can be inferred from the Monte Carlo modeling described earlier.

7.5.3 X-ray imaging from balloons

At smaller scale sizes (km), the spatial structure of the precipitation can be imaged from below. The Energetic Precipitation Explorer (EPEx) balloons were launched in summer 2018 to perform such a measurement. The flights over Western Canada took advantage of existing ground-based optical, VLF, riometer and other infrastructure to situate the EPP measurements within the larger multiscale processes that shape geospace.

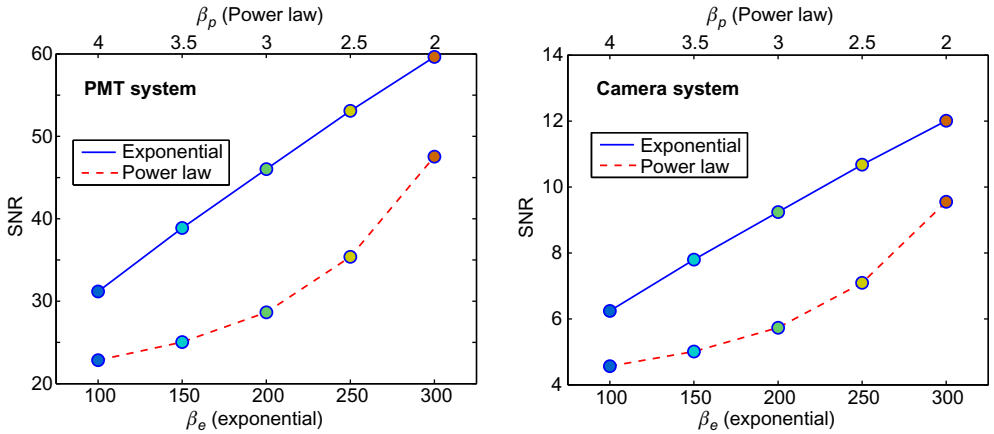

Figure 7.26 Optical SNR in the N_2^+ 1 N system calculated for a photometer system (left) and a camera system (right), with specifications described in the text. Different values of β_p and β_e are used for the precipitating electron energy power law and exponential distributions. Harder distributions (lower β_p or higher β_e) result in higher SNR simply because of higher precipitating energy flux.

7.5.4 Ground-based optical measurements

In 2011 one of us (RM) attempted to measure optical emissions from lightning-induced electron precipitation (LEP), based on predictions from Marshall et al. (2011), using the photometer shown in Fig. 7.25. No signatures of LEP were found, which was not necessarily surprising, as the predicted signatures were expected to be on the order of 1 Rayleigh.

However, optical emissions from EPP are predicted to be much stronger (Fig. 7.26) and to endure for a longer time, enabling time integration. Future experiments that include optical measurements of EPP could provide valuable insight into the precipitating flux and spectrum; the latter could be derived on the basis of the brightness ratios of different emission lines, similar to the method of Gustavsson et al. (2005) for heating experiments. However, it remains to be seen whether optical emissions due to EPP can be distinguished in the presence of auroral emissions.

7.5.5 D-region imaging by subionospheric very-low-frequency remote sensing

As described in Section 7.4.2.1, subionospheric VLF remote sensing is extremely sensitive to changes in the D-region ionization, but the spatial resolution is extremely poor, since the VLF signals "integrate" any ionospheric changes along the transmitter–receiver path. Furthermore, mode coupling causes the amplitude and phase changes to be poorly correlated with the ionospheric disturbance.

One potential solution to this problem is a network of VLF transmitters and receivers with overlapping paths in the region of interest. Such a concept was first utilized for lightning-induced disturbances to the D-region with the Holographic Array for Ionospheric Lightning (HAIL) at Stanford University (Johnson, 2000), which was used to discern the spatial-scale sizes of direct ionization due to lightning quasi-electrostatic fields (Johnson et al., 1999) and of LEP patches (Peter and Inan, 2007).

For EPP, a larger scale network at higher latitudes is required. The AARDDVARK network (Clilverd et al., 2009) is a global-scale system of narrowband VLF receivers, while the ABOVE network (Cully et al., 2015) focuses on Western Canada with a higher density of paths and wideband receivers. The AARDDVARK network has been used to estimate EPP fluxes (Clilverd et al., 2010; Neal et al., 2015), but the potential of the overlapping paths to discern spatial scales in either network has not been sufficiently explored. In addition, the process of inverting the observations on multiple paths to infer precipitating fluxes over wide spatial scales is a complex inverse problem due to the complex nature of the VLF propagation. Research into this inversion process is underway.

7.5.6 Multi-instrument campaigns

Finally, it is clear from Section 7.4.3 that each of the diagnostic methods has advantages and disadvantages, and none are fully capable of measuring all of the needed parameters to fully estimate the precipitation from the radiation belts during critical events. Ideally, we would like to have measurements of the flux, energy spectrum, pitch angle distribution, spatial distribution, and temporal variation. It is clear then that the only way to achieve this is through multi-instrument observations.

Such campaigns have been conducted with different pairs or combinations of methods, including combining subionospheric VLF with balloon X-ray measurements (e.g., Clilverd et al., 2017; Cully et al., 2016), combining balloon X-ray and space-based particle measurements from LEO (e.g., Blum et al., 2013), and combining ground-based radar with space-based particle measurements (e.g., Kaeppler et al., 2015). Future observations of precipitation should make further combinations of these measurements; for example, a ground campaign including colocated radar and optical, combined with multiple VLF signal paths similar to AARDDVARK or ABOVE, could be combined with LEO particle measurements and, ideally, X-ray measurements as well. Such a campaign could provide unprecedented characterization of the precipitation and help to constrain the uncertainties in each individual measurement.

7.5.6.1 Transition region explorer

The Transition Region Explorer (TREx) will heavily equip an area of Western Canada with ground-based instrumentation over the next few years. The targeted area spans subauroral to auroral latitudes with an East–West extent of $\sim$1500 km.

Instruments will include 10 imaging riometers; 6 blue-line (429 nm), 6 full-color (red/green/blue), and 6 near-infrared imagers; 2 spectrographs; and 13 Global Navigation Satellite System (GNSS) receiver stations. The TREx target region overlaps substantially with other instrument systems, including the ABOVE VLF network and the Canadian Array for Realtime Investigations of Magnetic Activity (CARISMA) magnetometer network. The TREx instruments will be tied together through a stream computing hub at the University of Calgary.

The TREx array will observe multiscale geophysical processes across a regional scale with good spatial resolution. With multiple types of instruments with overlapping coverage (riometers, optical, VLF), it will be possible to cross-validate methods and construct precipitation images at multiple energies. The extensive imaging component will allow EPP to be examined within the larger multiscale processes in geospace.

Acknowledgments

We wish to thank Antti Kero of the Sodankylä Geophysical Observatory for providing chemistry calculations using the SIC model, as well as Alexei Kouznetsov and Matthew Patrick for the MCNP and GEANT calculations, respectively. R. Marshall is supported by NSF MAG award 1732359. C. Cully acknowledges the support of the Canadian Space Agency Geospace Observatory program (GO-EPM) and the Natural Sciences and Engineering Research Council of Canada (NSERC), RGPIN/436201-2013.

References

Agapitov, O., Artemyev, A., Mourenas, D., Kasahara, Y., Krasnoselskikh, V., 2014. Inner belt and slot region electron lifetimes and energization rates based on Akebono statistics of whistler waves. J. Geophys. Res. Space Phys. 119 (4), 2876–2893.

Agostinelli, S., et al., 2003. Geant4a simulation toolkit. Nucl. Instrum. Methods Phys. Res. A 506 (3), 250–303. Available from: https://doi.org/10.1016/S0168-9002(03)01368-8.

Andersson, M., Verronen, P., Rodger, C., Clilverd, M., Seppälä, A., 2014. Missing driver in the sun–earth connection from energetic electron precipitation impacts mesospheric ozone. Nat. Commun. 5, 5197.

Bailey, S., Thurairajah, B., Randall, C., Holt, L., Siskind, D., Harvey, V., et al., 2014. A multi tracer analysis of thermosphere to stratosphere descent triggered by the 2013 stratospheric sudden warming. Geophys. Res. Lett. 41 (14), 5216–5222.

Baker, D., Blake, J., Callis, L., Cummings, J., Hovestadt, D., Kanekal, S., et al., 1994. Relativistic electron acceleration and decay time scales in the inner and outer radiation belts: Sampex. Geophys. Res. Lett. 21 (6), 409–412.

Baker, D., Daly, E., Daglis, I., Kappenman, J.G., Panasyuk, M., 2004. Effects of space weather on technology infrastructure. Space Weather 2 (2).

Baker, D.N., Kanekal, S.G., Hoxie, V.C., Batiste, S., Bolton, M., Li, X., et al., 2012. The Van Allen Probes mission, In: The Relativistic Electron-Proton Telescope (REPT) Instrument on Board the Radiation Belt Storm Proves (RBSP) Spacecraft: Characterization of Earth's Radiation Belt High-Energy Particle Populations. Springer, New York, pp. 337–381.

Baker, D.N., Jaynes, A.N., Hoxie, V.C., Thorne, R.M., Foster, J.C., Li, X., et al., 2014. An impenetrable barrier to ultrarelativistic electrons in the Van Allen radiation belts. Nature 515, 531–534.

Banu, A., Li, Y., McCleskey, M., Bullough, M., Walsh, S., Gagliardi, C.A., et al., 2008. Performance evaluation of position-sensitive silicon detector with four-corner readout. Nucl. Instrum. Methods Phys. Res. A 593 (3), 399–406.
Barker, A., Li, X., Selesnick, R., 2005. Modeling the radiation belt electrons with radial diffusion driven by the solar wind. Space Weather 3 (10).
Bell, T.F., Pasko, V.P., Inan, U.S., 1995. Runaway electrons as a source of red sprites in the mesosphere. Geophys. Res. Lett. 22 (16), 2127–2130.
Berger, M.J., 1963. Monte Carlo calculation of the penetration and diffusion of fast charged particles. Methods Comput. Phys. 1, 135–215.
Berger, M.J., Seltzer, S.M., 1972. Bremsstrahlung in the atmosphere. J. Atmos. Terr. Phys. 34 (1), 85–108.
Berger, M.J., Seltzer, S., Maeda, K., 1974. Some new results on electron transport in the atmosphere. J. Atmos. Terr. Phys. 36 (4), 591–617.
Berger, M.J., Coursey, J.S., Zucker, M.A., Chang, J., 2005. ESTAR, PSTAR, and ASTAR: Computer Programs for Calculating Stopping-Power and Range Tables for Electrons, Protons, and Helium Ions (Version 1.2.3). National Institute of Standards and Technology, Gaithersburg, MD. Available from: http://physics.nist.gov/Star.
Bethe, H., 1930. Zur theorie des durchgangs schneller korpuskularstrahlen durch materie. Ann. Physik 397 (3), 325–400. Available from: https://doi.org/10.1002/andp.19303970303.
Bethe, H.A., Ashkin, J., 1953. Experimental nuclear physics, in. Passage of Radiation Through Matter. Wiley, New York.
Bilitza, D., Altadill, D., Zhang, Y., Mertens, C., Truhlik, V., Richards, P., et al., 2014. The international reference ionosphere 2012—a model of international collaboration. J Space Weather Space Clim. 4, A07.
Blake, J., O'Brien, T., 2016. Observations of small-scale latitudinal structure in energetic electron precipitation. J. Geophys. Res. Space Phys. 121 (4), 3031–3035.
Blum, L., Schiller, Q., Li, X., Millan, R., Halford, A., Woodger, L., 2013. New conjunctive CubeSat and balloon measurements to quantify rapid energetic electron precipitation. Geophys. Res. Lett. 40 (22), 5833–5837.
Böhlen, T., Cerutti, F., Chin, M., Fass, A., Ferrari, A., Ortega, P., et al., 2014. The FLUKA code: developments and challenges for high energy and medical applications. Nucl. Data Sheets 120, 211–214. Available from: https://doi.org/10.1016/j.nds.2014.07.049.
Bortnik, J., Thorne, R.M., Meredith, N.P., 2008. The unexpected origin of plasmaspheric hiss from discrete chorus emissions. Nature 452, 62–66.
Broadfoot, A.L., Kendall, K.R., 1968. The airglow spectrum, 3100–10,000 A. J. Geophys Res. 73, 426–428.
Budden, K.G., 1961. The Wave-Guide Mode Theory of Wave Propagation. Prentice-Hall, Upper Saddle River, NJ.
Callis, L.B., Baker, D., Blake, J., Lambeth, J., Boughner, R., Natarajan, M., et al., 1991. Precipitating relativistic electrons: their long-term effect on stratospheric odd nitrogen levels. J. Geophys. Res. Atmos. 96 (D2), 2939–2976.
Callis, L.B., Natarajan, M., Evans, D.S., Lambeth, J.D., 1998. Solar atmospheric coupling by electrons (solace): 1. effects of the May 12, 1997 solar event on the middle atmosphere. J. Geophys. Res. Atmos. 103 (D21), 28. 405–29410.
Chamberlain, J.W., 1995. Physics of the Aurora and Airglow. American Geophysical Union, Washington, DC.
Chevalier, M.W., Inan, U.S., 2006. A technique for efficiently modeling long-path propagation for use in both FDFD and FDTD. IEEE Ant. Wireless Prop. Lett. 5, 525–528.
Cho, J.Y., Kelley, M.C., 1993. Polar mesosphere summer radar echoes: observations and current theories. Rev. Geophys. 31 (3), 243–265.
Clilverd, M.A., Rodger, C.J., Thomson, N.R., Brundell, J.B., Ulich, T., Lichtenberger, J., et al., 2009. Remote sensing space weather events: Antarctic-arctic radiation-belt (dynamic) deposition-VLF atmospheric research Konsortium network. Space Weather 7 (4).

Clilverd, M.A., Rodger, C.J., Gamble, R.J., Ulich, T., Raita, T., Seppälä, A., et al., 2010. Ground-based estimates of outer radiation belt energetic electron precipitation fluxes into the atmosphere. J. Geophys. Res. Space Phys. 115, A12304.

Clilverd, M.A., Rodger, C.J., McCarthy, M., Millan, R., Blum, L.W., Cobbett, N., et al., 2017. Investigating energetic electron precipitation through combining ground-based, and balloon observations. J. Geophys. Res. Space Phys. 122, 534–546.

Crew, A.B., Spence, H.E., Blake, J.B., Klumpar, D.M., Larsen, B.A., O'Brien, T.P., et al., 2016. First multipoint in situ observations of electron microbursts: Initial results from the NSF FIREBIRD II mission. J. Geophys. Res. Space Phys. 121 (6), 5272–5283.

Cully, C.M., Kouznetsov, A., Mazzino, L., Davis, E., Galts, D., 2015. Quantifying Energetic Particle Precipitation Using the Array for Broadband Observations of VLF/ELF Emissions (ABOVE, AGU Fall Meeting Abstracts). American Geophysical Union, Washington, DC.

Cully, C.M., Breneman, A.W., Cote, K., Danskin D.W., Duffin, C., Galts, D., et al., 2016. VLF Waves and Energetic Electron Precipitation Observed by the ABOVE^2 Stratospheric Balloon Mission, AGU Fall Meeting Abstracts. American Geophysical Union, Washington, DC.

Davies, K., 1990. Ionospheric Radio. Peter Peregrinus.

Detrick, D.L., Rosenberg, T.J., 1990. A phased-array radiowave imager for studies of cosmic noise absorption. Radio Sci. 25 (4), 325–338. Available from: https://doi.org/10.1029/RS025i004p00325.

Donovan, E., Mende, S., Jackel, B., Frey, H., Syrjäsuo, M., Voronkov, I., et al., 2006. The THEMIS all-sky imaging array: system design and initial results from the prototype imager. J. Atmos. Sol. Terr. Phys. 68 (13), 1472–1487.

Engebretson, M., Lessard, M., Bortnik, J., Green, J., Horne, R.B., Detrick, D., et al., 2008. Pc1–pc2 waves and energetic particle precipitation during and after magnetic storms: superposed epoch analysis and case studies. J. Geophys. Res. Space Phys. 113 (A1).

Evans, D.S., Greer, M.S., 2004. Polar orbiting environmental satellite space environment monitor–2 instrument descriptions and archive data documentation. Tech. Rep. NOAA Tech. Mem. 1.4. Space Environ. Lab., Boulder, CO.

Fano, U., 1963. Penetration of protons, alpha particles and mesons. Ann. Rev. Nucl. Sci. 13, 1–66. Available from: https://doi.org/10.1146/annurev.ns.13.120163.000245.

Fehsenfeld, F., Ferguson, E., 1969. Origin of water cluster ions in the d region. J. Geophys. Res. 74 (9), 2217–2222.

Ferguson, J.A., 1980. Ionospheric Profiles for Predicting Nighttime VLF/LF Propagation. Tech. Rep. 530, Naval Ocean Systems Center.

Friedel, R., Reeves, G., Obara, T., 2002. Relativistic electron dynamics in the inner magnetosphere review. J. Atmos. Sol.- Terr. Phys. 64 (2), 265–282.

Glauert, S.A., Horne, R.B., Meredith, N.P., 2014. Three-dimensional electron radiation belt simulations using the bas radiation belt model with new diffusion models for chorus, plasmaspheric hiss, and lightning-generated whistlers. J. Geophys. Res. Space Phys. 119 (1), 268–289.

Glukhov, V.S., Pasko, V.P., Inan, U.S., 1992. Relaxation of transient lower ionospheric disturbances caused by lightning-whister-induced electron precipitation bursts. J. Geophys. Res. 97 (A11), 16,971–16,979.

Goorley, T., James, M., Booth, T., Brown, F., Bull, J., Cox, L.J., et al., 2012. Initial MCNP6 release overview. Nucl. Technol. 180 (3), 298–315. Available from: https://doi.org/10.13182/NT11-135.

Gordon, W.E., 1958. Incoherent scattering of radio waves by free electrons with applications to space exploration by radar. Proc. IRE 46 (11), 1824–1829.

Goudsmit, S., Saunderson, J.L., 1940. Multiple scattering of electrons. Phys. Rev. 57, 24–29. Available from: https://doi.org/10.1103/PhysRev.57.24.

Grün, A., 1957. Lumineszenz, photometrische messungen der energie absorption in strahlungsfeld von electronquellen eindimensionaler fall in luft. Z. Naturf. 12a, 89–95.

Gustavsson, B., Sergienko, T., Kosch, M., Rietveld, M., Brändström, B., Leyser, T., et al., 2005. The electron energy distribution during HF pumping, a picture painted with all colors. Ann. Geophys. 23 (5), 1747–1754.

Halford, A., McGregor, S., Murphy, K., Millan, R., Hudson, M., Woodger, L., et al., 2015. Barrel observations of an ICME-shock impact with the magnetosphere and the resultant radiation belt electron loss. J. Geophys. Res. Space Phys. 120 (4), 2557–2570.

Hargreaves, J., Ranta, H., Ranta, A., Turunen, E., Turunen, T., 1987. Observations of the polar cap absorption event of February 1984 by the EISCAT incoherent scatter radar. Planet. Space Sci. 35 (7), 947–958.

Hargreaves, J.K., 1969. Auroral absorption of HF radio waves in the ionosphere: a review of results from the first decade of riometry. Proc. IEEE 57 (8), 1348–1373. Available from: https://doi.org/10.1109/PROC.1969.7275.

Hedin, A.E., 1991. Extension of the MSIS thermospheric model into the middle and lower atmosphere. J. Geophys Res. 96, 1159.

ICRU, 2014. Appendix. stopping power and range tables for charged particles. J. Int Comm. Radiat. Units Meas. 14 (1), 79–98. Available from: https://doi.org/10.1093/jicru/ndw030.

Jackman, C., Marsh, D., Vitt, F., Roble, R., Randall, C., Bernath, P., et al., 2011. Northern hemisphere atmospheric influence of the solar proton events and ground level enhancement in January 2005. Atmos. Chem. Phys. 11 (13), 6153–6166.

Janches, D., Dyrud, L., Broadley, S.L., Plane, J.M.C., 2009. First observation of micrometeoroid differential ablation in the atmosphere. Geophys. Res. Lett. 36 (6), L06. 101.

Janson, S.W., Welle, R.P., 2014. The NASA optical communication and sensor demonstration program: an update. In: 28th Annual AIAA/USU Conference on Small Satellites. American Geophysical Union, Washington, DC, pp. 4–7.

Jenkins, T.M., Nelson, W.R., Rindi, A. (Eds.), 1988. Monte Carlo Transport of Electrons and Photons. Springer, New York.

Johnson, M.P., 2000. VLF Imaging of Lightning-Induced Ionosphere Disturbances (Ph.D. thesis). Stanford University, Stanford CA.

Johnson, M.P., Inan, U.S., Lev-Tov, S.J., Bell, T.F., 1999. Scattering pattern of lightning-induced ionospheric disturbances associated with early/fast VLF events. Geophys. Res. Lett. 26 (15), 2363–2366.

Kabin, K., Spanswick, E., Rankin, R., Donovan, E., Samson, J.C., 2011. Modeling the relationship between substorm dipolarization and dispersionless injection. J. Geophys. Res. Space Phys. 116 (A4). Available from: https://doi.org/10.1029/2010JA015736.

Kaeppler, S., Jaynes, A., Sanchez, E., Nicolls, M., Varney, R., Marshall, R., 2015. Conjugate In-Situ and Incoherent Scatter Radar Observations of Radiation Belt Loss Mechanisms, AGU Fall Meeting Abstracts. American Geophysical Union, Washington, DC.

Kalos, M.H., Whitlock, P.A., 2008. Monte Carlo Methods. Wiley, New York.

Kawrakow, I., Mainegra-Hing, E., Rogers, D.W.O., Tessier, F., Walters, B.R.B., 2017. The EGSnrc Code System: Monte Carlo Simulation of Electron and Photon Transport. Tech. Rep. PIRS-701, National Research Council Canada, Ottawa.

Kellerman, A.C., Shprits, Y.Y., Makarevich, R.A., Spanswick, E., Donovan, E., Reeves, G., 2015. Characterization of the energy-dependent response of riometer absorption. J. Geophys. Res. Space Phys. 120 (1), 615–631. Available from: https://doi.org/10.1002/2014JA020027.

Kero, A., Vierinen, J., McKay-Bukowski, D., Enell, C.-F., Sinor, M., Roininen, L., et al., 2014. Ionospheric electron density profiles inverted from a spectral riometer measurement. Geophys. Res. Lett. 41 (15), 5370–5375. Available from: https://doi.org/10.1002/2014GL060986.

Kirkwood, S., Osepian, A., 1995. Quantitative studies of energetic particle precipitation using incoherent scatter radar. J. Geomagnet. Geoelec. 47 (8), 783–799.

Krause, L.H., 1998. The Interaction of Relativistic Electron Beams With the Near-Earth Space Environment (Ph.D. thesis). University of Michigan, Ann Arbor, MI.

Landau, L., 1944. On the energy loss of fast particles by ionization. J. Phys. (USSR) 8, 201–205.

Lehtinen, N.G., Inan, U.S., 2007. Possible persistent ionization caused by giant blue jets. Geophys. Res. Lett. 34, L08. Available from: https://doi.org/10.1029/2006GL029051.

Lehtinen, N.G., Bell, T.F., Inan, U.S., 1999. Monte Carlo simulation of runaway MeV electron breakdown with application to red sprites and terrestrial gamma ray flashes. J. Geophys. Res. 104 (A11), 24,699–24,712.

Little, C.G., Leinbach, H., 1959. The riometer—a device for the continuous measurement of ionospheric absorption. Proc. IRE 1, 315–320.
Marsh, D., Garcia, R., Kinnison, D., Boville, B., Sassi, F., Solomon, S., et al., 2007. Modeling the whole atmosphere response to solar cycle changes in radiative and geomagnetic forcing. J. Geophys. Res. Atmos. 112, D23306. Available from: https://doi.org/10.1029/2006JD008306.
Marshall, R., Bortnik, J., 2018. Pitch angle dependence of energetic electron precipitation: energy deposition, backscatter, and the bounce loss cone. J. Geophys. Res. Space Physics, 123 (3), 2412–2423.
Marshall, R.A., 2012. An improved model of the lightning electromagnetic field interaction with the D-region ionosphere. J. Geophys Res. 117, A03316.
Marshall, R.A., Bortnik, J., Lehtinen, N., Chakrabarti, S., 2011. Optical signatures of lightning-induced electron precipitation. J. Geophys. Res. Space Phys. 116, A8.
Marshall, R.A., Nicolls, M.J., Sanchez, E., Lehtinen, N.G., Neilson, J., 2014. Diagnostics of an artificial relativistic electron beam interacting with the atmosphere. J. Geophys. Res. 119, 8560–8577.
Marshall, R.A., Wallace, T., Turbe, M., 2017. Finite difference modeling of very-low-frequency propagation in the earth-ionosphere waveguide. IEEE Trans. Ant. Prop. 65 (12). Available from: https://doi.org/10.1109/TAP.2017.2758392.
Mathews, J., 1984. The incoherent scatter radar as a tool for studying the ionospheric d-region. J. Atmos. Terr. Phys. 46 (11), 975–986.
Mathews, J.D., 1986. Incoherent scatter radar probing of the 60-100-km atmosphere and ionosphere. IEEE Trans. Geosci. Remote Sens. 24 (5), 765–776. Available from: https://doi.org/10.1109/TGRS.1986.289625.
Meredith, N.P., Horne, R.B., Sicard-Piet, A., Boscher, D., Yearby, K.H., Li, W., et al., 2012. Global model of lower band and upper band chorus from multiple satellite observations. J. Geophys. Res. Space Phys. 117 (A10). Available from: https://doi.org/10.1029/2012JA017978.
Millan, R., Lin, R., Smith, D., McCarthy, M., 2007. Observation of relativistic electron precipitation during a rapid decrease of trapped relativistic electron flux. Geophys. Res. Lett. 34 (10). Available from: https://doi.org/10.1029/2006GL028653.
Millan, R., McCarthy, M., Sample, J., Smith, D., Thompson, L., McGaw, D., et al., 2013. The balloon array for RBSP relativistic electron losses (barrel). Space Sci. Rev. 179 (1–4), 503–530.
Miyoshi, Y., Oyama, S., Saito, S., Kurita, S., Fujiwara, H., Kataoka, R., et al., 2015. Energetic electron precipitation associated with pulsating aurora: EISCAT and Van Allen Probe observations. J. Geophys. Res. Space Phys. 120 (4), 2754–2766.
Moliere, G.Z., 1948. Theorie der streuung schneller geladener teilchen ii mehrfach-und vielfachstreuung. Z. Naturforsch. 3A, 78–97.
Møller, C., 1932. Zur theorie des durchgangs schneller elektronen durch materie. Ann. Phys. 406 (5), 531–585. Available from: https://doi.org/10.1002/andp.19324060506.
Moss, G.D., Pasko, V.P., Liu, N., Veronis, G., 2006. Monte Carlo model for analysis of thermal runaway electrons in streamer tips in transient luminous events and streamer zones of lightning leaders. J. Geophys. Res. 111 (A02307). Available from: https://doi.org/10.1029/2005JA011350.
Natarajan, M., Remsberg, E.E., Deaver, L.E., Russell, J.M., 2004. Anomalously high levels of NO_x in the polar upper stratosphere during April, 2004: photochemical consistency of HALOE observations. Geophys. Res. Lett. 31 (15). Available from: https://doi.org/10.1029/2004GL020566.
Neal, J.J., Rodger, C.J., Clilverd, M.A., Thomson, N.R., Raita, T., Ulich, T., 2015. Long-term determination of energetic electron precipitation into the atmosphere from AARDDVARK subionospheric VLF observations. J. Geophys. Res. Space Phys. 120 (3), 2194–2211.
Nesse Tyssøy, H., Sandanger, M., Ødegaard, L.-K., Stadsnes, J., Aasnes, A., Zawedde, A., 2016. Energetic electron precipitation into the middle atmosphere constructing the loss cone fluxes from MEPED POES. J. Geophys. Res. Space Phys. 121 (6), 5693–5707.
Orlova, K., Shprits, Y., 2014. Model of lifetimes of the outer radiation belt electrons in a realistic magnetic field using realistic chorus wave parameters. J. Geophys. Res. Space Phys. 119 (2), 770–780.

Orlova, K., Shprits, Y., Spasojevic, M., 2016. New global loss model of energetic and relativistic electrons based on Van Allen probes measurements. J. Geophys. Res. Space Phys. 121 (2), 1308–1314.

Pappert, R.A., Snyder, F.P., 1972. Some results of a mode-conversion program for VLF. Radio Sci. 7, 913.

Peck, E., Randall, C., Green, J., Rodriguez, J., Rodger, C., 2015. POES MEPED differential flux retrievals and electron channel contamination correction. J. Geophys. Res. Space Phys. 120 (6), 4596–4612.

Peter, W.B., Inan, U.S., 2007. A quantitative comparison of lightning-induced electron precipitation and VLF signal perturbations. J. Geophys. Res. 112 (A12), 212. Available from: https://doi.org/10.1029/2006JA012165.

Picone, J., Hedin, A., Drob, D.P., Aikin, A., 2002. NRLMSISE-00 empirical model of the atmosphere: statistical comparisons and scientific issues. J. Geophys. Res. Space Phys. 107 (A12), 1468.

Randall, C., Harvey, V., Manney, G., Orsolini, Y., Codrescu, M., Sioris, C., et al., 2005. Stratospheric effects of energetic particle precipitation in 2003–2004. Geophys. Res. Lett. 32 (5). Available from: https://doi.org/10.1029/2004GL022003.

Randall, C., Harvey, V., Singleton, C., Bernath, P., Boone, C., Kozyra, J., 2006. Enhanced NO_x in 2006 linked to strong upper stratospheric arctic vortex. Geophys. Res. Lett. 33 (18). Available from: https://doi.org/10.1029/2006GL027160.

Randall, C., Harvey, V., Singleton, C., Bailey, S., Bernath, P., Codrescu, M., et al., 2007. Energetic particle precipitation effects on the southern hemisphere stratosphere in 1992–2005. J. Geophys. Res. Atmos. 112 (D8). Available from: https://doi.org/10.1029/2006JD007696.

Randall, C., Harvey, V.L., Siskind, D., France, J., Bernath, P., Boone, C., et al., 2009. NO_x descent in the Arctic middle atmosphere in early 2009. Geophys. Res. Lett. 36 (18). Available from: https://doi.org/10.1029/2009GL039706.

Randall, C.E., Harvey, V.L., Holt, L.A., Marsh, D.R., Kinnison, D., Funke, B., et al., 2016. Simulation of energetic particle precipitation effects during the 2003–2004 Arctic winter. J. Geophys. Res. 120 (6), 5035–5048.

Ratcliffe, J.A., 1959. The Magnetio-Ionic Theory and Its Applications to the Ionosphere. Cambridge University Press, Cambridge, UK.

Rees, M.H., 1963. Auroral ionization and excitation by incident energetic electrons. Planet. Space Sci. 11 (10), 1209–1218.

Rees, M.H., 1989. Physics and Chemistry of the Upper Atmosphere. Cambridge University Press, Cambridge, UK.

Rees, M.H., 1992. Auroral energy deposition rate. Planet. Space Sci. 40 (2/3), 299–313.

Richter, J.H., Sassi, F., Garcia, R.R., Matthes, K., Fischer, C.A., 2008. Dynamics of the middle atmosphere as simulated by the Whole Atmosphere Community Climate Model, version 3 (WACCM3. J. Geophys. Res. Atmos. 113 (D8).

Rodger, C.J., Clilverd, M.A., Green, J.C., Lam, M.M., 2010. Use of POES SEM-2 observations to examine radiation belt dynamics and energetic electron precipitation into the atmosphere. J. Geophys. Res. Space Phys. 115 (A4).

Rodger, C.J., Clilverd, M.A., Kavanagh, A.J., Watt, C.E.J., Verronen, P.T., Raita, T., 2012. Contrasting the responses of three different ground-based instruments to energetic electron precipitation. Radio Sci. 47 (2). Available from: https://doi.org/10.1029/2011RS004971.

Rogers, D., Bielajew, A., 1990. Monte Carlo techniques of electron and photon transport for radiation dosimetry. In: Kase, K., Bjarngard, B.E., Attix, F.H. (Eds.), The Dosimetry of Ionizing Radiation, vol. 3. Academic Press, Cambridge, MA, pp. 427–539. Available from: https://doi.org/10.1016/B978-0-12-400403-0.50009-9.

Rosenberg, T.J., Detrick, D.L., Venkatesan, D., van Bavel, G., 1991. A comparative study of imaging and broad-beam riometer measurements: the effect of spatial structure on the frequency dependence of auroral absorption. J. Geophys. Res. Space Phys. 96 (A10), 17,793–17,803. Available from: https://doi.org/10.1029/91JA01827.

Röttger, J., La Hoz, C., Kelley, M.C., Hoppe, U.-P., Hall, C., 1988. The structure and dynamics of polar mesosphere summer echoes observed with the EISCAT 224 mHz radar. Geophys. Res. Lett. 15 (12), 1353–1356.

Sauvaud, J. A., et al, 2006. High-energy electron detection onboard DEMETER: The IDP spectrometer, description and first results on the inner belt. Planet. Space Sci. 54, 502–511.
Shprits, Y., Thorne, R., Reeves, G., Friedel, R., 2005. Radial diffusion modeling with empirical lifetimes: comparison with CRRES observations. Ann. Geophys. 23 (4), 1467–1471.
Siskind, D.E. (2000), On the Coupling Between Middle and Upper Atmospheric Odd Nitrogen, Geophysical Monograph Series, American Geophysical Union, Washington, DC, 101–116.
Solomon, S., 1993. Auroral electron transport using the Monte Carlo method. Geophys. Res. Lett. 20 (3), 185–188.
Solomon, S., Reid, G.C., Roble, R.G., Crutzen, P.J., 1982. Photochemical coupling between the thermosphere and the lower atmosphere: 2D region ion chemistry and the winter anomaly. J. Geophys. Res. 87 (C9), 7221–7227.
Solomon, S.C., 2001. Auroral particle transport using Monte Carlo and hybrid methods. J. Geophys. Res. 106, 107–116.
Spanswick, E., Donovan, E., Friedel, R., Korth, A., 2007. Ground based identification of dispersionless electron injections. Geophys. Res. Lett. 34 (3). Available from: https://doi.org/10.1029/2006GL028329.
Spasojevic, M., Shprits, Y., Orlova, K., 2015. Global empirical models of plasmaspheric hiss using Van Allen probes. J. Geophys. Res. Space Phys. 120 (12), 10,370-10,383.
Spence, H.E., Blake, J., Crew, A., Driscoll, S., Klumpar, D., Larsen, B., et al., 2012. Focusing on size and energy dependence of electron microbursts from the Van Allen radiation belts. Space Weather 10 (11), 1–3.
Thomson, N.R., McRae, W.M., 2009. Nighttime ionospheric D region: equatorial and nonequatorial. J. Geophys. Res. Space Phys. 114 (A8). Available from: https://doi.org/10.1029/2008JA014001.
Thorne, R.M., 2010. Radiation belt dynamics: the importance of wave-particle interactions. Geophys. Res. Lett. 37 (22). Available from: https://doi.org/10.1029/2010GL044990.
Thorne, R.M., O'Brien, T.P., Shprits, Y.Y., Summers, D., Horne, R.B., 2005. Timescale for MeV electron microburst loss during geomagnetic storms. J. Geophys Res. 110, 9202.
Tu, W., Li, X., Chen, Y., Reeves, G., Temerin, M., 2009. Storm-dependent radiation belt electron dynamics. J. Geophys. Res. Space Phys. 114 (A2). Available from: https://doi.org/10.1029/2008JA013480.
Tu, W., Selesnick, R., Li, X., Looper, M., 2010. Quantification of the precipitation loss of radiation belt electrons observed by SAMPEX. J. Geophys. Res. Space Phys. 115 (A7). Available from: https://doi.org/10.1029/2009JA014949.
Turunen, E., Collis, P., Turunen, T., 1988. Incoherent scatter spectral measurements of the summertime high-latitude D-region with the EISCAT UHF radar. J. Atmos. Terr. Phys. 50 (4–5), 289–299.
Vallance Jones, A., 1974. Aurora. Reidel, Dordrecht.
Verronen, P.T., Andersson, M.E., Marsh, D.R., Kovacs, T., Plane, J.M.C., 2016. WACCM-D—whole atmosphere community climate model with D-region ion chemistry. J. Adv. Model. Earth Syst. 8 (2), 945–975.
Whittaker, I.C., Gamble, R.J., Rodger, C.J., Clilverd, M.A., Sauvaud, J.-A., 2013. Determining the spectra of radiation belt electron losses: fitting DEMETER electron flux observations for typical and storm times. J. Geophys. Res. 118, 7611–7623.
Wissing, J., Kallenrode, M.-B., 2009. Atmospheric Ionization Module OSnabrück (AIMOS): a 3-D model to determine atmospheric ionization by energetic charged particles from different populations. J. Geophys. Res. 114 (A06104). Available from: https://doi.org/10.1029/2008JA013884.
Woodger, L., Halford, A., Millan, R., McCarthy, M., Smith, D., Bowers, G., et al., 2015. A summary of the barrel campaigns: technique for studying electron precipitation. J. Geophys. Res. Space Phys. 120 (6), 4922–4935.
Xu, W., Marshall, R.A., Fang, X., Turunen, E., Kero, A., 2018. On the effects of bremsstrahlung radiation during energetic electron precipitation. Geophys. Res. Lett. 45 (2), 1167–1176. Available from: https://doi.org/10.1002/2017GL076510.

This page intentionally left blank

CHAPTER 8

Ground-based very-low-frequency radio wave observations of energetic particle precipitation

Aaron T. Hendry[1], Mark A. Clilverd[2], Craig J. Rodger[3] and Mark J. Engebretson[4]
[1]Department of Space Physics, Institute of Atmospheric Physics, Prague, Czechia
[2]British Antarctic Survey (NERC), Cambridge, United Kingdom
[3]Department of Physics, University of Otago, Dunedin, New Zealand
[4]Augsburg University, Minneapolis, MN, United States

Contents

8.1 Introduction

The traditional definition of the very-low-frequency (VLF) electromagnetic spectrum spans 3–30 kHz. At frequencies >15 kHz, man-made transmissions from communication and navigation transmitters tend to dominate over lightning-generated sferic noise in most of the world for most of the day. The majority of the energy radiated by man-made VLF transmitters propagates "subionospherically"—that is, trapped between the conducting ground (land, sea, or ice) and the lower part of the ionosphere, forming the Earth-ionosphere waveguide (e.g., Cummer, 2000). The upper boundary of the waveguide is thus the lower part of the ionized D-region at $\sim$70–85 km. Perturbations of the amplitude and phase of fixed frequency VLF transmissions have been associated with excess ionization caused by energetic particle precipitation resulting from processes occurring within the magnetosphere (Barr et al., 2000) and can therefore be used to sense precipitation remotely.

The high radiated power of man-made naval transmitters (typically ranging from 50 kW to 1 MW), and their nearly continuous operation, provide great opportunities for long-range remote sensing (Barr et al., 2000; Clilverd et al., 2009). Subionospheric

The Dynamic Loss of Earth's Radiation Belts
DOI: https://doi.org/10.1016/B978-0-12-813371-2.00008-1

VLF radio waves can be received many thousands of kilometers from their source (e.g., Crombie, 1964). Observations of the amplitude and/or phase of VLF transmissions have provided information on the variation of the D-region on many time scales, as a result of many different energetic particle precipitation processes (e.g., Helliwell et al., 1973; Rodger et al., 2002, 2007; Clilverd et al., 2002, 2005, 2012; Dietrich et al., 2010; Hendry et al., 2017).

A schematic of subionospheric propagation is shown in Fig. 8.1. Subionospheric radio waves can be seen to propagate between the ionospheric D-region and Earth's surface for long distances. Changes to the effective altitude of the D-region, caused by energetic particle precipitation, modifies the propagation conditions for the radio waves and result in amplitude and phase perturbations relative to the normal signal levels. Although the underlying observation and interpretation techniques are similar for many different perturbation mechanisms, in the rest of this chapter we concentrate on ground-based observations of energetic precipitation characteristics driven by electromagnetic ion cyclotron (EMIC) waves (Engebretson et al., 2008).

Electron precipitation driven by EMIC waves in the Pc12 range (0.1–5 Hz) has been difficult to characterize owing to a scarcity of observations of the electron precipitation (e.g., Rodger et al., 2008). Proton precipitation (30–80 keV) coincident with EMIC wave occurrence has been observed (Søraas et al., 2005; Sandanger et al., 2007) and is an important clue as to the possible occurrence of electron precipitation. This signature has been utilized by Carson et al. (2013). However, 30–80-keV proton precipitation does not affect subionospheric propagation, as it creates ionization at altitudes well above the D-region. This allows the unambiguous observation of EMIC-driven electron precipitation by VLF subionospheric propagation techniques.

Electron precipitation measurements made using the NOAA polar-orbiting operational environmental satellite (POES) satellites (Evans and Greer, 2000; Rodger et al., 2010) have been used to investigate precipitation signatures associated with

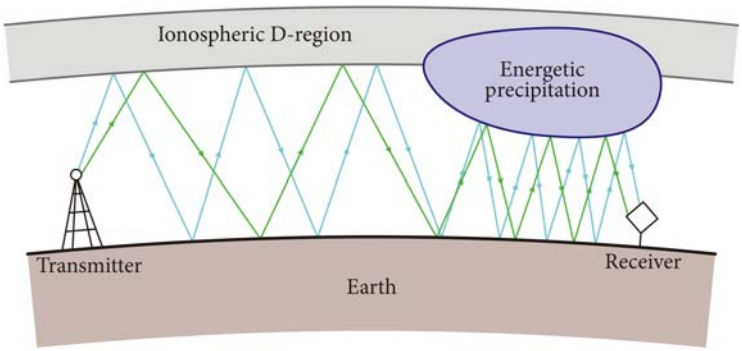

Figure 8.1 A schematic of subionospheric VLF propagation from a transmitter to a receiver, showing the influence of a patch of excess ionization produced by energetic particle precipitation on the waves in the Earth-ionosphere waveguide.

EMIC waves (Carson et al., 2013). A subset of EMIC waves defined as intervals of pulsations with diminishing periods (IPDP) have been preferentially associated with electron precipitation signatures detected by the NOAA POES satellites (Hendry et al., 2016). IPDP are typically observed in the magnetic local time (MLT) evening sector during periods of geomagnetic disturbance (Yahnina et al., 2003 and references therein). The typical duration of IPDP events observed on the ground is on the order of a few tens of minutes. Using subionospheric radio-wave propagation techniques Rodger et al. (2008) analyzed a small group of events to show that the electron precipitation events driven by EMIC−IPDP waves occurred close to the location of the duskside plasmapause ($L \sim 4.4$) and during moderate geomagnetic activity (Kp ∼ 4). The electron precipitation was assumed to have a monoenergetic spectrum of ∼2 MeV, primarily in order to explain the absence of any riometer absorption signatures.

Subionospherically propagating radio waves were also analyzed by Rodger et al. (2015) during a remarkably serendipitous close conjunction of the Van Allen Probes satellites with one of the POES satellites (NOAA 15) at the footprint of the same geomagnetic field line, with several subionospheric radio-wave signals propagating through the precipitation region, close to Iceland. Perturbations in the amplitude and phase of multiple narrowband transmitters were observed at the same time as EMIC waves were observed at the Van Allen Probes satellite. High time-resolution measurements were combined to determine the location, flux, and size of the precipitation region induced by the observed helium-band EMIC wave. The precipitation region was found to extend in longitude over several hours of MLT, but was narrow in latitudinal width ($\Delta L = 0.15$) and had a power-law energy distribution beginning at about 200 keV.

A detailed study of POES observations of electron precipitation events resulted in the development of a database covering about 17 years (1998−2014) and containing 3337 precipitation events (Hendry et al., 2016; 2017). The EMIC-induced precipitation event database was populated from the results of an algorithm originally developed by Carson et al. (2013). The algorithm searched POES particle measurements for one of the key characteristics expected of EMIC-driven electron precipitation, identified as the simultaneity between spikes in the P1 (52-keV differential proton flux channel) and P6 (>800-keV electron channel). As part of the validation of the algorithm, ground-based narrowband subionospheric radio waves recorded at Halley Station, Antarctica, on August 13, 2013, were analyzed (Hendry et al., 2016). Phase and amplitude perturbations occurred in the subionospheric measurements when an EMIC wave was observed by a search coil magnetometer at Halley and a POES EMIC precipitation event was detected. Further confirmation of electron precipitation came from a colocated riometer at Halley, which showed simultaneous absorption of cosmic radio noise at 30 MHz.

Additional analysis of EMIC-induced electron precipitation using narrowband subionospheric radio waves was undertaken by Clilverd et al. (2015). In a detailed case study of a westward-propagating electron precipitation region on May 31, 2013, the precipitation region was shown to be about 3 hours wide in MLT and narrow in latitude ($\Delta L \approx 1$). The westward drift of the EMIC-induced precipitation patch was observed for more than 2 hours, covering 140 degrees of longitude in that time. Coincident observation by POES during that time allowed the energy spectrum of the precipitation to be determined to have energies as low as 300 keV, using a technique of integral energy channel fitting as published by Hendry et al. (2017). Further analysis of the whole EMIC-induced precipitation event database has shown that a large percentage of electron precipitation events have peak energies of about 300 keV, while only a small fraction have peak energies in the range 1−4 MeV. This observation is at odds with some theories of EMIC-wave scattering (Thorne & Kennel, 1971; Albert and Bortnik, 2009; Kersten et al., 2014) but could be explained by others (Chen et al., 2016). To date it is unclear whether ground-based observations of energetic electron precipitation can help resolve this debate. What is clear is that ground-based observations of EMIC-induced electron precipitation have helped to confirm the role of EMIC waves in causing electron precipitation, which has long been predicted by theory but in practice proved difficult to verify. The ground-based observations have also aided in identifying some of the dimensional characteristics of the resultant precipitation patches.

8.2 Ground-based instruments, including the AARDDVARK network

Ground-based VLF observations of EMIC-induced energetic electron precipitation are facilitated by interpreting phase and amplitude perturbations of subionospheric narrowband VLF transmitter signals. This chapter primarily reports such observations made by the Antarctic-Arctic Radiation-belt (Dynamic) Deposition-VLF Atmospheric Research Konsortia (AARDDVARK). Typically, the narrowband minimum shift keying (MSK) transmitter signals are demodulated by specialist ultra-MSK software operated on a standard computer with a 96-kHz sound card. A more detailed description of the experimental setup of the AARDDVARK data loggers can be found in Clilverd et al. (2009). Along with riometers, the AARDDVARK radio-wave measurements have been observed to respond to changes in D-region ionization caused by EMIC waves. Ground-based instruments can complement in situ satellite measurements of EMIC waves and have the advantage of being cheaper to operate, longer running, and easier to maintain.

Another ground-based instrument that is complementary to ground-based VLF observations of EMIC-induced precipitation is the magnetometer, typically the search coil magnetometer (SCM) or the fluxgate magnetometer (FGM). These instruments

are described in detail throughout this book. Although SCM/FGM instruments do not themselves respond to EMIC-induced precipitation, they do provide observations of EMIC waves observed on the ground, and hence they can be very useful in providing context for the AARDDVARK and riometer measurements. In this section, we provide brief descriptions of the AARDDVARK network of VLF receivers plus brief descriptions of riometer cosmic noise absorption instruments and SCM/FGM instruments relevant to the ground-based VLF systems.

AARDDVARK is a global network of radio receivers capable of providing high time-resolution observations of the D-region ionosphere for mid- to high-latitude regions (Clilverd et al., 2009). The network of cheap, easy-to-install, easy-to-maintain sensors use preexisting man-made VLF radio waves to detect changes in ionization levels from altitudes of $\sim 30-90$ km. The network is ideally located to detect the effects of energetic electron precipitation driven by outer radiation belt processes such as VLF chorus waves, electromagnetic ion cyclotron waves, VLF plasmaspheric hiss, and magnetospheric substorms. A limitation of the AARDDVARK technique is its inability to determine whether all, or only part, of a transmitter–receiver subionospheric propagation path is affected by precipitating electrons. However, this difficulty can be overcome by using multiple, crossing paths and complementary data from other instruments (such as riometers).

The locations of the VLF narrowband transmitters monitored by AARDDVARK are shown in Fig. 8.2 (green circles). The locations of AARDDVARK receivers are indicated by red diamonds. The subionospheric propagation paths from transmitter to receiver are represented by the black connecting lines. AARDDVARK receivers have been preferentially placed to provide great-circle propagation (GCP) paths that are likely to be influenced by energetic particle precipitation occurring at middle to high latitudes. Each AARDDVARK receiver typically monitors about 10 transmitters for phase and amplitude, with a time resolution of 0.1–1 seconds. The criss-cross pattern of propagation paths provided by the 21 AARDDVARK sites allows information to be gathered about precipitation patch dimensions, particularly in the Europe to Canada region. In the Southern Hemisphere the more sparse GCP pattern still provides the potential to detect precipitation events, although dimensional information is harder to infer.

Fig. 8.3 shows the polar-view AARDDVARK propagation paths in relation to contours of geomagnetic L-shell, with $L = 3$, 4, and 6 calculated for 100-km altitude plotted for the Northern and Southern Hemispheres. Between $L = 3$ and 6 lies the region where outer radiation belt electrons are likely to be deposited into the D-region by electron acceleration and loss processes. At about $L = 4$ the inner magnetospheric plasmapause is likely to exist, providing a boundary between electron loss processes such as wave-particle interactions driven by VLF chorus (outside the plasmapause) and plasmaspheric hiss (inside the plasmapause). Additionally, EMIC-induced

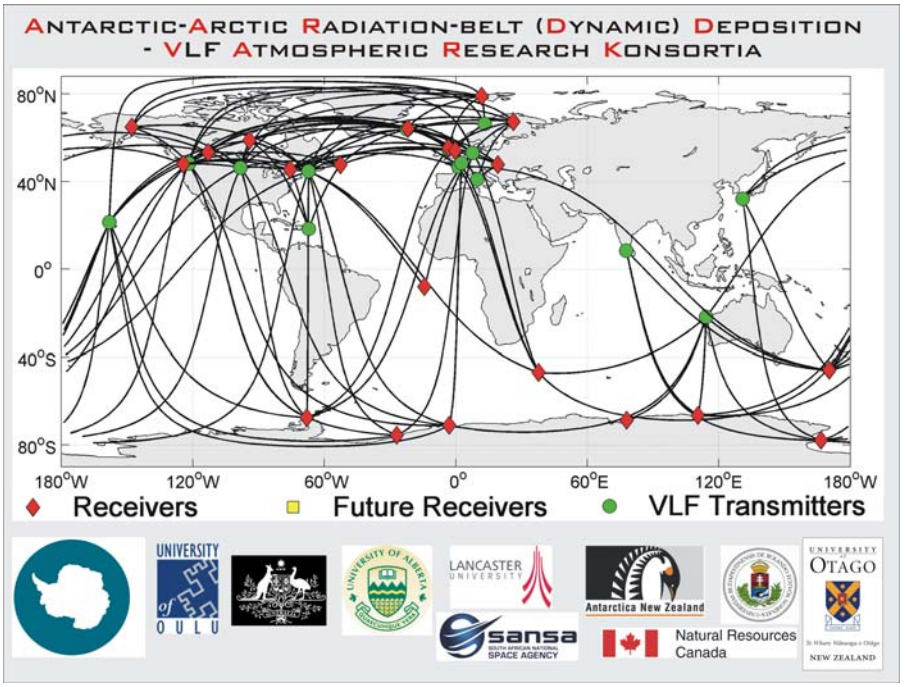

Figure 8.2 A map of the subionospheric propagations paths between VLF narrowband transmitters (*green circles*) and AARDDVARK receivers (*red diamonds*). Also shown are the logos of the collaborating institutes that operate the network of measurements.

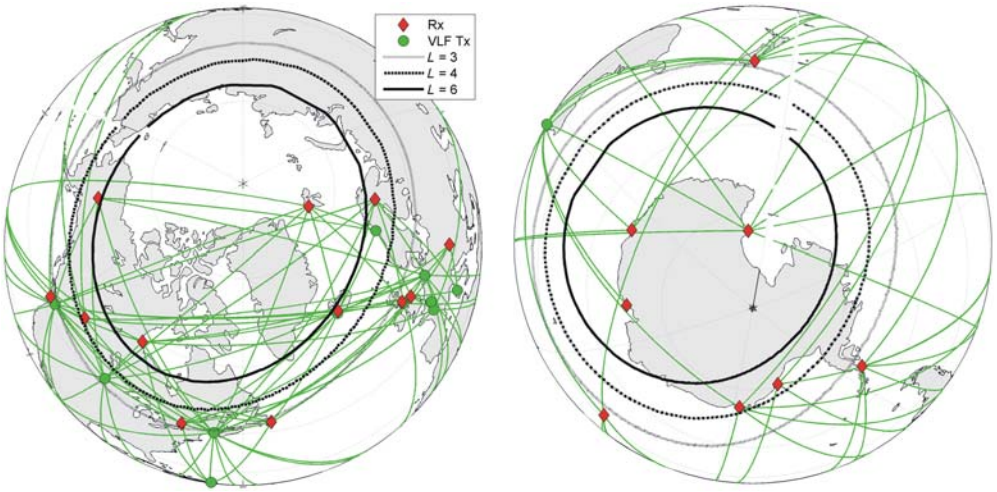

Figure 8.3 The Northern (*left*) and Southern (*right*) Hemisphere projections of the AARDDVARK propagation paths. *L*-shell contours for $L = 3$, 4, and 6 are shown. AARDDVARK receivers (Rx) are show as red diamonds and VLF transmitters (Tx) are shown as green circles.

Table 8.1 Details of the ground-based instruments discussed in this chapter.

VLF transmitter identifier	**Latitude (degrees)**	**Longitude (degrees)**	**Frequency (kHz)**	***L*-shell**
NRK, Iceland	63°51′N	22°28′W	37.5	5.5
NLK, Seattle, United States	48°12′N	121°55′W	24.8	2.9
NAA, Maine, United States	44°39′N	67°17′W	24.0	2.9
GBP (also called GVT), Penrith, United Kingdom	54°44′N	02°52′W	22.1	2.7
GQD Anthorn, United Kingdom	54°53′N	03°17′W	19.58	2.7
AARDDVARK receiver	**Latitude (degrees)**	**Longitude (degrees)**	**Map identifier**	***L*-shell**
St. John's, Newfoundland, Canada	47°36′N	52°41′W	STJ	2.7
Sodankylä, Finland	67°22′N	26°23′E	SOD	5.2
Halley, Antarctica	75°30′S	26°54′W	HAL	4.7
Churchill, Manitoba, Canada	58°45′N	94°54′W	CHUR	7.6
Riometer	**Frequency (MHz)**	**Beam**	**Map identifier**	**Operator**
Halley, Antarctica	30.0	Vertical	HAL	British Antarctic Survey (NERC)
Pinawa, Canada	30.0	Vertical	PINA	University of Calgary
Rovaniemi, Finland	32.4	Vertical	ROV	Sodankylä Geophysical Observatory

electron precipitation can occur close to the plasmapause (Sandanger et al., 2009); therefore, these events are likely to produce observable phase and amplitude perturbations on many of the AARDDVARK propagation paths shown. Table 8.1 provides information on the call sign identifiers used throughout this chapter, along with VLF transmitter locations, *L*-shells, and transmission frequencies. AARDDVARK receiver sites discussed in the chapter are also listed, as well as riometer sites of interest.

An example of the sort of data that the AARDDVARK receivers are able to provide is given in Fig. 8.4. The minute-averaged amplitude of the NRK transmitter located in Iceland ($L = 5.44$) received at St. John's, Newfoundland, Canada ($L = 2.9$) is shown, with the color scale representing intensity relative to an arbitrary level. The plot shows a complete month of data collected in March 2013. Daytime propagation

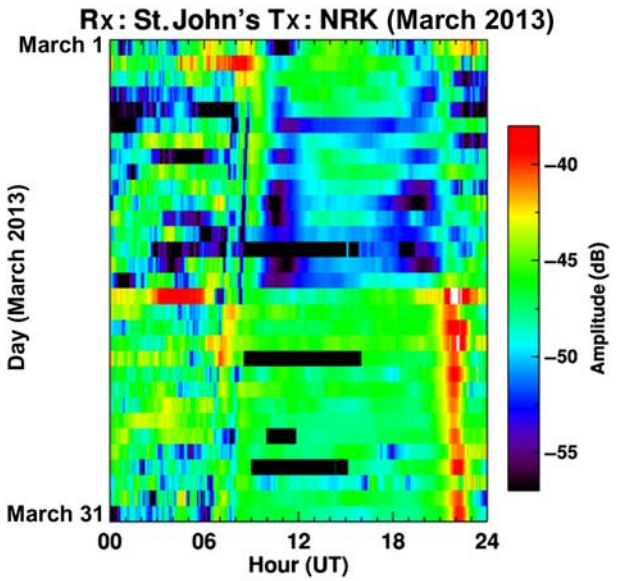

Figure 8.4 A summary example of the type of data collected by the AARDDVARK network. A month of 1-minute-average data is plotted for March 2013. Amplitude is represented by the color bar, with intensity relative to an arbitrary level.

conditions on this GCP occur from 10 to 20 UT (universal time) in this period, while nighttime conditions are typically seen from 00 to 06 UT. Periods of transmitter maintenance are apparent as black lines, typically occurring during the daytime and showing a 7-day repetition. A large geomagnetic storm occurred on March 17, 2013, when Dst reached −131 nT. The effect of the storm on the received amplitude can be seen in Fig. 8.4 as a change in the daytime amplitude values from their initial values of about −53 dB (blue) to values of −45 dB (green), at which they remain for most of the rest of the month. The March 17, 2013, geomagnetic storm effect on the sunset propagation conditions can be very clearly seen as a sudden increase in amplitude from −50 to −40 dB (red) at about 20–21 UT.

Ground-based magnetometers provide a useful platform for the detection of EMIC waves. FGMs measure the DC magnetic field, giving an absolute magnetic field strength B, while SCMs measure the AC field, giving the change in field strength dB/dt. SCMs are often more sensitive than FGMs, particularly in the frequency ranges at which EMICs occur (Kuwashima et al., 1981), and so are the preferred instrument for EMIC wave detection. In several locations, magnetometer measurements are undertaken and have been used to provide complementary observations of EMIC waves for ground-based VLF studies of EMIC-induced electron precipitation events:

- The Halley VI research station in Antarctica houses a high-quality search-coil magnetometer run by the British Antarctic Survey (BAS) for Augsburg University,

Minneapolis, and the University of New Hampshire. This magnetometer, located at $L = 4.7$, has been an excellent source of low-noise magnetic-field measurements sampled at 10 Hz, making it a prime instrument for studying EMIC waves.

- The Canadian Array for Realtime Investigations of Magnetic Activity (CARISMA) network is an array of magnetometers situated throughout Canada and the United States. With 27 sites in total, each of which houses an FGM and eight of which also feature an SCM, CARISMA provides an excellent source of magnetometer data for examining both the occurrence and the evolution of EMIC waves. The CARISMA FGMs sample at a rate of 8 Hz, while the SCMs sample at 20 Hz. Additionally, a search-coil magnetometer sampling at 64 Hz is also operated in Canada, located in Athabasca and run by the Institute for Space–Earth Environmental Research (ISEE).
- The Sodankylä Geophysical Observatory (SGO), a department of the University of Oulu, Finland, has an array of six high-quality search-coil magnetometers sampling at 40 Hz, located in a roughly north–south chain through Finland. With some of these stations having data reaching back to 1995, the SGO magnetometers provide a large, contiguous source of magnetometric data, ideal for investigating EMIC wave occurrence.

Riometers (from "relative ionospheric opacity meters") are instruments that measure cosmic radio noise to detect enhancements in ionization within the D-region ionosphere. At a given frequency, typically around 30 MHz, the cosmic radio noise seen from a fixed location on Earth is approximately constant, varying only as the galactic cosmic noise varies throughout the sidereal day. Any abrupt change in the received signal intensity is therefore due to changes in the absorption of the signal by changes in the D-region ionosphere at about 85 km. Locations where riometers have been used to provide complementary observations of EMIC waves for ground-based VLF studies of EMIC-induced electron precipitation events include a north–south chain in Finland operated by SGO; at Halley, Antarctica, operated by BAS; and over much of Canada as part of the NORSTAR array operated by the University of Calgary.

8.3 March 27, 2013, case example

The combination of ground-based observations of EMIC-induced electron precipitation is exemplified by Fig. 8.5. An event observed from 16:30 to 20:00 UT on March 27, 2013 is highlighted with panels from top to bottom showing the Halley SCM data, Halley riometer absorption data, and NRK-St. John's VLF phase and amplitude data. The riometer and VLF data have had the quiet-day variation removed and thus show perturbations relative to the baseline. The Halley SCM and riometers are essentially colocated, while the NRK-St. John's GCP passes close to the Halley geomagnetic conjugate point. A double pulse of enhanced EMIC wave power over the

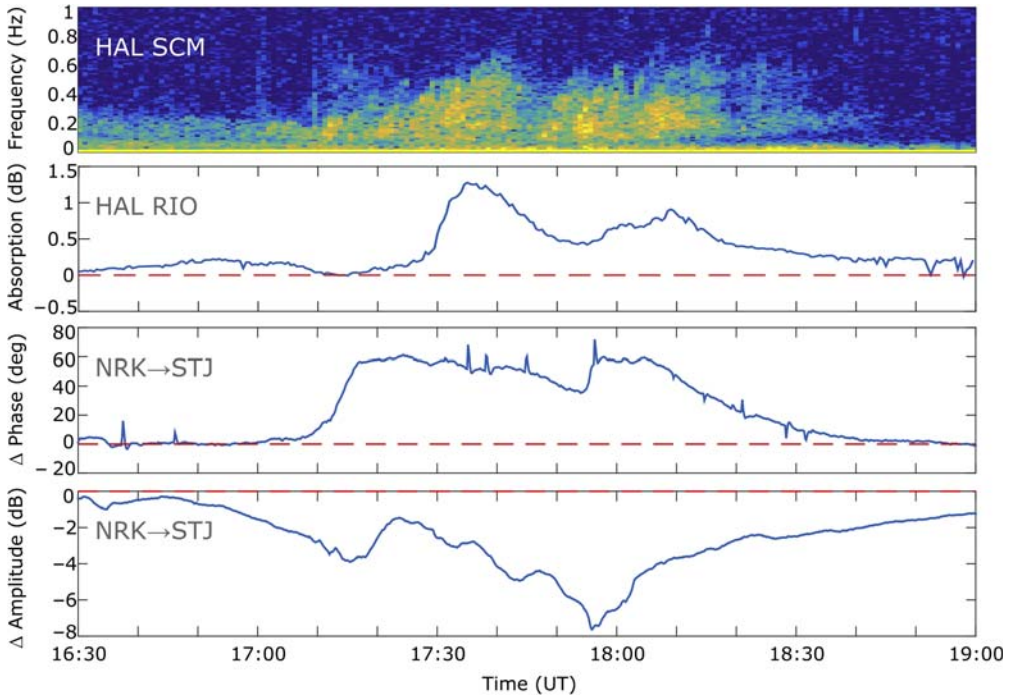

Figure 8.5 An example of the response of ground-based instrumentation to EMIC-induced electron precipitation on March 27, 2013. Search-coil magnetometer data from Halley (HAL), Antarctica, is compared with perturbations observed in Halley riometer absorption data (HAL RIO), and the AARDDVARK propagation path NRK (Iceland) to St. John's (STJ), Newfoundland, Canada which passes close to the Halley magnetic conjugate point. Nondisturbed baseline levels are shown by the red dashed lines.

range 0.1−0.5 Hz can be seen at the same time as increased riometer absorption, increased NRK phase, and decreased NRK amplitude. The observations shown in Fig. 8.5 are consistent with EMIC-induced energetic electron precipitation occurring at both $L = 4.7$ close to Halley, Antarctica, and also its conjugate region close to Newfoundland, Canada. The timing of the event (18 UT, 16 MLT) is typical of MLT evening sector EMIC waves associated with westward drifting 10−100 keV protons injected close to MLT midnight (Yahnina et al., 2003). The event depicted in Fig. 8.5 is also discernible in Fig. 8.4, as a sudden decrease in amplitude (blue) at 18 UT toward the bottom of the plot.

8.4 August 13, 2013, case example

An EMIC-induced energetic electron precipitation was detected by the METOP-02 satellite on August 13, 2013, at 18:01:12 UT, at $L = 5.0$ and 20:30 MLT (i.e., the

evening sector). The field-line location of the event, determined by tracing down the International Geomagnetic Reference Field (IGRF) magnetic field line from the satellite to an altitude of 110 km, was calculated to be 66.5°N 33.6°E; this is shown on the map in Fig. 8.6 (upper panel) as a yellow cross. An additional 11 precipitation spikes occurred between 17:00 and 03:00 UT, shown in Fig. 8.6 as red crosses. Each of these spikes was consistent with the signatures defined by Carson et al. (2013) for EMIC-driven electron precipitation. The 12 detected triggers spanned a geographical region of about 150 degrees in longitude from Scandinavia to central Canada and were confined to $4.5 < L < 5$ (see Table 8.2), with an average of $L = 4.8$. The MLT

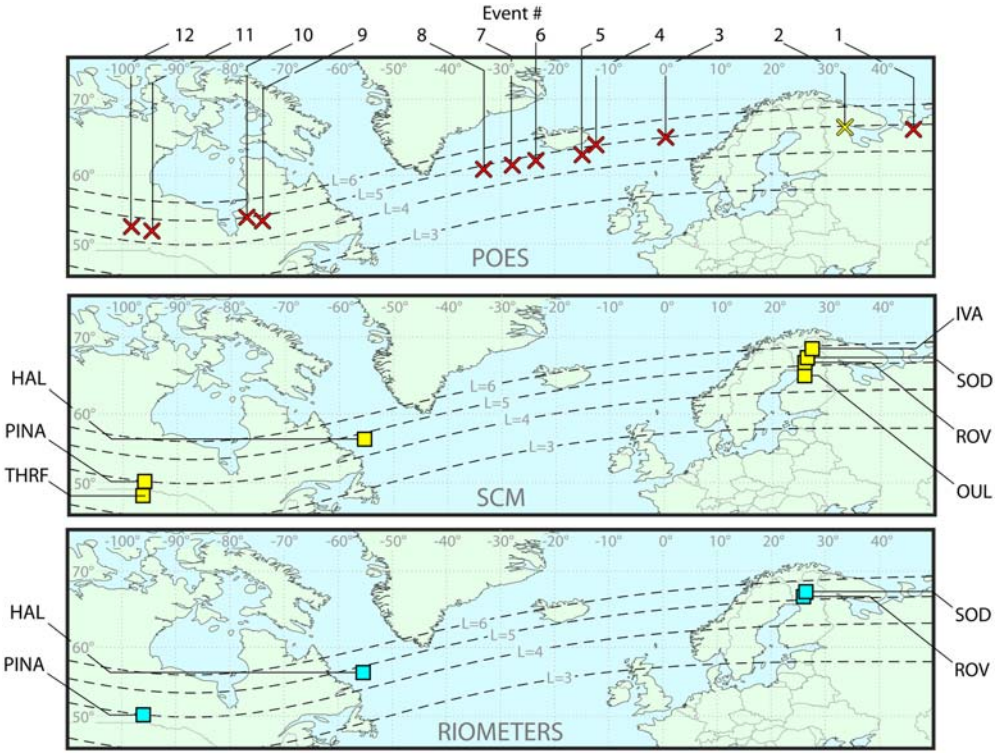

Figure 8.6 The upper panel shows POES detections for the August 13–14, 2013, case study. The Northern Hemisphere foot-of-the-field-line locations of the 12 POES electron precipitation flux burst detections identified this as an EMIC-induced event. For events that occurred in the Southern Hemisphere, the IGRF magnetic conjugate location is plotted. The yellow cross indicates the flux burst detected by the algorithm, while the red crosses indicate flux bursts identified through manual investigation. IGRF *L*-shells from 3 to 6 are shown as black dashed lines. The middle panel shows the locations of magnetometers (SCM) that detected EMIC waves during the event period, including the location of the conjugate point to the Halley, Antarctica, SCM (Hendry et al., 2016). In the lower panel, the locations of riometers that detected EMIC-induced electron precipitation during the event period included the Halley conjugate point (Hendry et al., 2016).

Table 8.2 Detailed POES observations for the August 13–14, 2013, EMIC event.

Event no.	Date and time (UT)	Satellite	Time (MLT)	Latitude (°N)	Longitude (°E)
1	2013/08/13 17:14:30	METOP-01	20.6	66.0	46.3
2	2013/08/13 18:01:12	METOP-02	20.5	66.5	33.6
3	2013/08/13 20:01:18	METOP-01	20.9	−62.4	42.8
4	2013/08/13 20:47:06	METOP-02	20.7	64.1	347.6
5	2013/08/13 21:22:44	METOP-02	20.9	62.8	345.0
6	2013/08/13 21:41:26	METOP-01	21.0	−67.1	20.54
7	2013/08/13 21:51:55	NOAA-16	20.5	61.4	332.1
8	2013/08/13 22:27:16	METOP-02	21.0	−69.9	10.6
9	2013/08/14 00:55:17	NOAA-15	19.7	51.0	283.1
10	2013/08/14 01:13:35	NOAA-16	20.5	53.5	286.0
11	2013/08/14 02:38:35	NOAA-15	19.8	52.0	265.5
12	2013/08/14 02:55:19	NOAA-16	20.4	52.6	261.8

for each trigger event indicates that the precipitation source was likely static in MLT—that is, drifting at 15°/hour, and occurring at 20.5 ± 0.4 MLT. A detailed discussion of this event is given in Hendry et al. (2016), but here we provide additional ground-based observations and infer new characteristics of the precipitation.

The area containing the 12 POES triggers was well monitored by numerous ground-based instruments, with multiple magnetometers, riometers, and AARDDVARK VLF stations throughout the event region. The locations of the magnetometers and riometers that detected EMIC waves (magnetometers) or energetic electron precipitation induced by the EMIC waves (riometers) are shown in Fig. 8.6, middle and lower panels, respectively.

The satellite locations were determined by tracing down the IGRF field line to an altitude of 110 km. Each event in the sequence is given an event number, and all are plotted on the map shown in Fig. 8.6.

The first observed perturbations caused by the EMIC-induced electron precipitation during the August 13, 2013, case study period came from instruments located in Scandinavia. The right-hand side of Fig. 8.7 shows a map that indicates the location of the Rovaniemi riometer in Finland (ROV) and the propagation paths of the UK transmitters GBP (also known as GVT) and GQD to an AARDDVARK receiver at Sodankylä, Finland (SOD). The transmitters are shown as yellow circles and the receiver as a green square. The left-hand panels show the data from these instruments, where time is expressed in local MLT. In the upper panel the Rovaniemi riometer instrument shows a peak in absorption at about 19:45 MLT, starting at 19:00 and finishing at just after 20:15 MLT. This is consistent with the timing of the events 1 and 2 given in Table 8.2 and shown in Fig. 8.6 (upper panel), which were detected

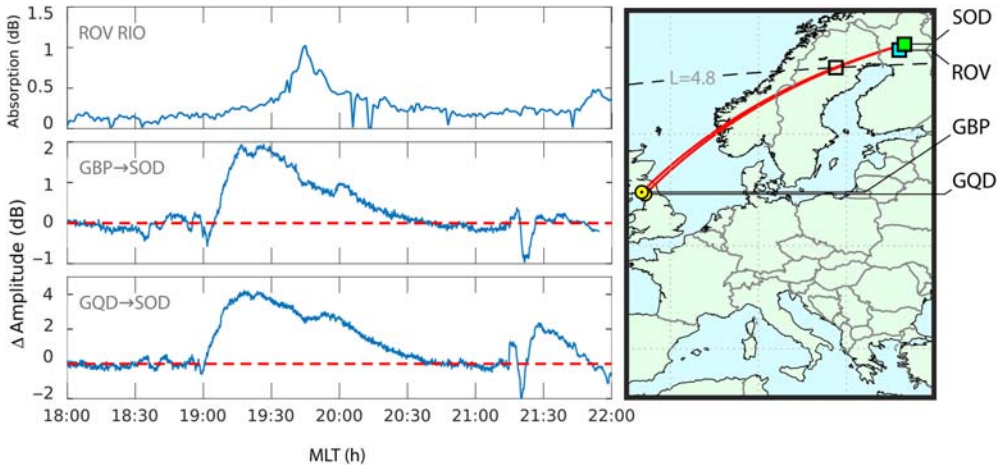

Figure 8.7 Observations made in the European sector on August 13, 2013. The locations of measurements are plotted on the left-hand side of the figure. Great-circle paths (*red lines*) are shown from VLF transmitters in the United Kingdom (*yellow circles* labeled GBP and GQD) to an AARDDVARK receiver in Sondankylä, Finland (*green square* labeled SOD). Riometer absorption measurements from Rovaniemi, Finland, are shown (*blue square* labeled ROV). Timings of the observations are plotted in MLT, where the timing for the AARDDVARK data is determined by the MLT at the path through the $L = 4.8$ *L*-shell contour, shown as a black square on the map.

as precipitation spikes in POES satellite data. In the middle and lower panels of Fig. 8.7, the amplitude perturbation (i.e., with the quiet-day-curve removed) shows an effect from 19:00 to 20:30 MLT (~17 to ~18:30 UT). The MLT for the UK-SOD GCPs is taken from the MLT calculated at the location of the black square on the map, which is where the GCPs cuts the $L = 4.8$ contour—that is, the average *L*-shell of the POES EMIC-induced precipitation events (Hendry et al., 2016).

At a later universal time (~23 UT) on August 13, 2013, but at approximately the same 20 MLT time, there is also ground-based evidence of the precipitation reported by POES. The right-hand side of Fig. 8.8 shows a map that indicates the propagation paths of the transmitters DHO in Germany, NAA on the east coast of the United States, and NLK on the west coast of the United States, each to the AARDDVARK receiver at Halley, Antarctica (75°S, 26°W, $L = 4.8$). Also located at Halley was a 30-MHz riometer and a search-coil magnetometer. The left-hand panels show the data from a representative sample of these instruments, where time is expressed in local MLT. Fig. 8.8 demonstrates a close coincidence of the EMIC wave seen with the SCM and the EMIC-induced perturbations in the riometer and the VLF data at 20 MLT. Notably, the perturbations last for only 15–20 minutes, which is in contrast to the initial period of ~90 minutes exhibited during the equivalent Scandinavian observations. The increase in amplitude at 19 MLT on the NLK to Halley GCP is caused by a C4.4 solar flare.

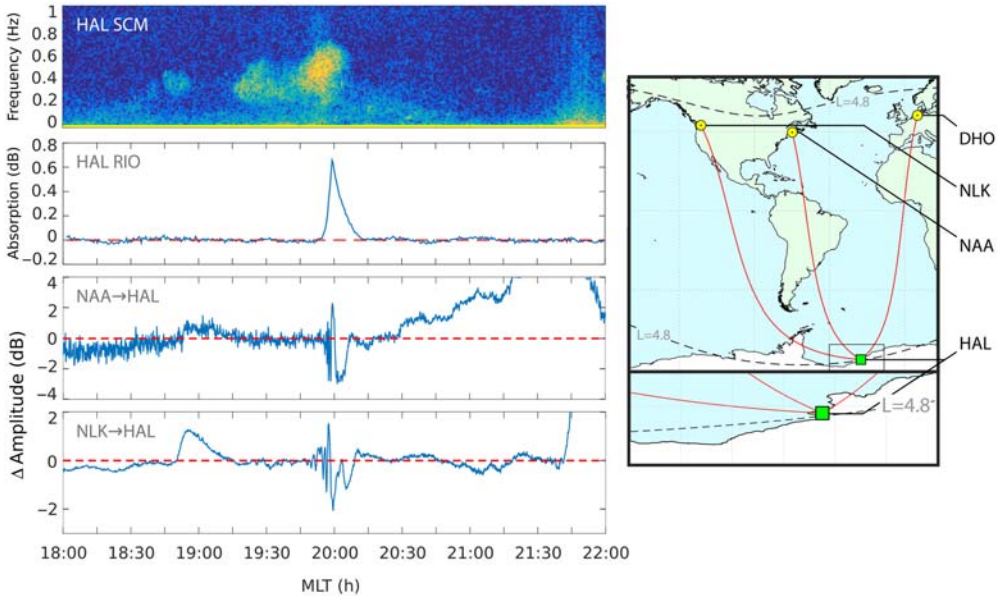

Figure 8.8 Observations made in the Atlantic sector on August 13, 2013. The left-hand side of the figure plots the configuration of measurements. The symbol format is the same as Fig. 8.6. Timings of the observations are plotted in MLT, where the timing for the AARDDVARK data is determined by the MLT at the path through the $L = 4.8$ L-shell contour—that is, at Halley. The plots of search-coil magnetometer data from Halley, Antarctica (labeled HAL), in the frequency range 0–1 Hz show an intense EMIC wave occurring at 20 MLT. Corresponding riometer absorption measurements from Halley are shown as HAL RIO.

At about 03 UT on August 14, 2013, which corresponds to 20 MLT on the previous day, evidence of EMIC-induced precipitation was observed in the eastern and central regions of Canada. The upper panel of Fig. 8.9 shows a map of the location of the Pinawa riometer (PINA), and two propagation paths to an AARDDVARK receiver located in Churchill, Manitoba, Canada. A dashed black line indicates the $L = 4.8$ contour, and black squares indicate the locations where each GCP intersects the contour—close to Iceland, and near Hudson Bay. The lower panels show VLF perturbations from the GBP-Churchill radio-wave signals, the NAA-Churchill signals, and absorption from the Pinawa riometer. MLT is determined from time of the $L = 4.8$ intersection location of the VLF paths, and from Pinawa. The perturbations lasting about 15 minutes can be seen, with a small progressive shift to later MLT in the timing of the ionospheric disturbance as it moves from Iceland to Pinawa.

This case study shows that EMIC-induced precipitation, detected on multiple POES satellite passes through the outer radiation belt at $4.5 < L < 5.0$, was also observable by ground-based instruments, including the AARDDVARK network of

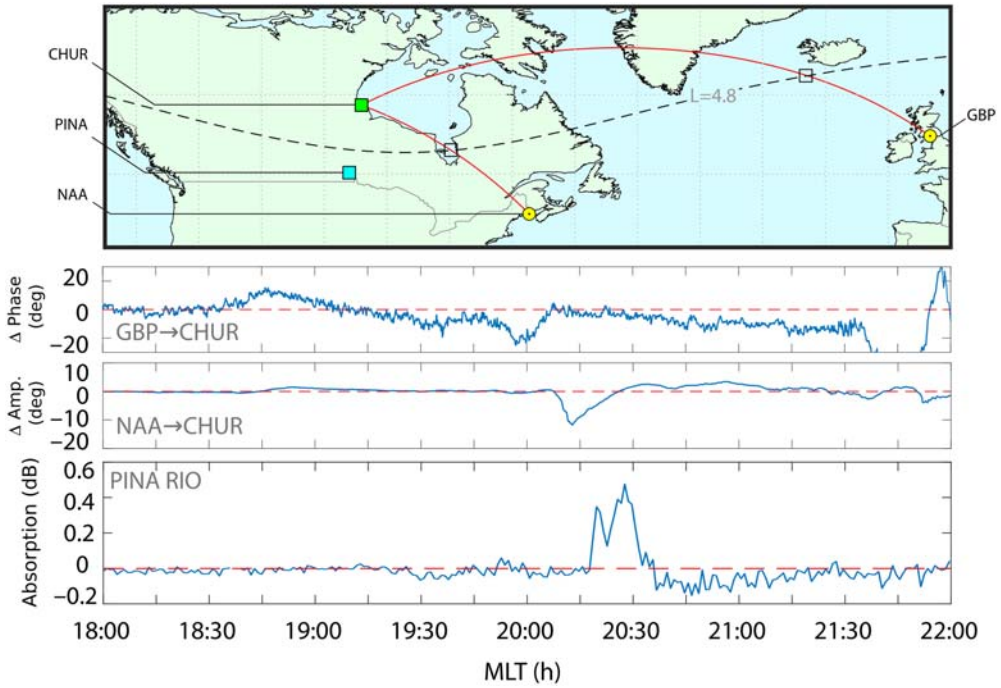

Figure 8.9 Observations made in the Canadian sector on August 13, 2013. The map shows the configurations of measurements plotted in the rest of the panels. The symbol format is the same as in Fig. 8.6. Timings of the observations are plotted in MLT, where the timing for the AARDDVARK data is determined by the MLT at the path through the $L = 4.8$ L-shell contour.

VLF receivers. The precipitation was observed over a range of universal time lasting nearly 8 hours, but exhibited only a very small shift in MLT of < 1 hour, remaining close to 20 MLT throughout. Initially, the duration of the precipitation burst was ~ 90 minutes, but it was predominantly observed as lasting only 15–20 minutes later as the precipitation region swept westward. Thus, although the EMIC-induced precipitation region was a long-lived event at near-constant MLT, the longitudinal extent of the region was limited to only a fraction of an MLT hour for much of the time, following the initial set of observations when it was on the order of 1–2 hours in MLT.

The ground-based VLF observations are suggestive of a relatively narrow latitudinal precipitation region, primarily through the observation of changes in sign of amplitude perturbations, as well as negative phase perturbations consistent with small-scale features (Clilverd et al., 2015). However, determining the latitudinal dimensions of electron precipitation from EMIC waves is not always possible, and it depends on the north–south or east–west geometry of the propagation paths perturbed at the time of the event.

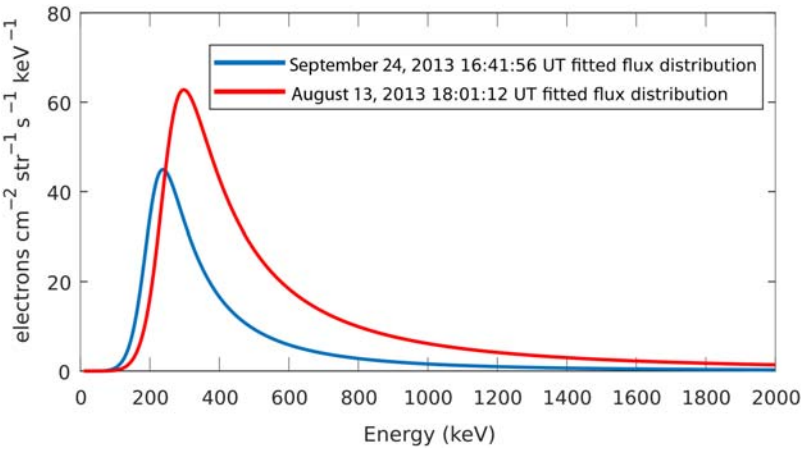

Figure 8.10 Fitted flux distributions determined from POES electron telescope measurements for the August 13, 2013, event and a comparison event on September 24, 2013, which was described in detail by Rodger et al. (2015).

Hendry et al. (2017) analyzed 662 EMIC-induced precipitation events detected in POES data in which the data quality was good enough to fit a peaked flux distribution. Slightly more than half of the events were found to have flux peaks in the energy range 200–500 keV, which is at odds with the conventional picture of EMIC-induced electron precipitation being dominated by >1-MeV fluxes (Thorne and Kennel, 1971). Fig. 8.10 shows the fitted flux distribution for the August 13, 2013 event. A peak in flux was determined at ~300 keV. The fitted flux distribution is similar to that found for the September 24, 2013 event (also shown) analyzed in detail during a Van Allen Probes–POES conjunction (Rodger et al., 2015). EMIC-induced electron precipitation events with flux distribution peaks in the 200–500 keV range have been shown, in the examples presented in this chapter, to provide substantial signatures in ground-based VLF and riometer data.

8.5 May 31, 2013, case example

Another case study presented data from AARDDVARK receivers located in and around Europe on May 31, 2013 (Clilverd et al., 2015). Rising-tone EMIC waves were observed from Scandinavia to central Canada, drifting 8 hours of MLT in about 3 hours of UT. The drift rate of the electron precipitation region was consistent with 30–60 keV protons injected close to midnight MLT (Spasojevic and Fuselier, 2009). The drift in MLT of the precipitation patch on May 31, 2013 was quite different from the case example given for August 13, 2013, because the May 31 event drifted over time toward earlier MLT rather than remaining stationary in MLT, as shown in

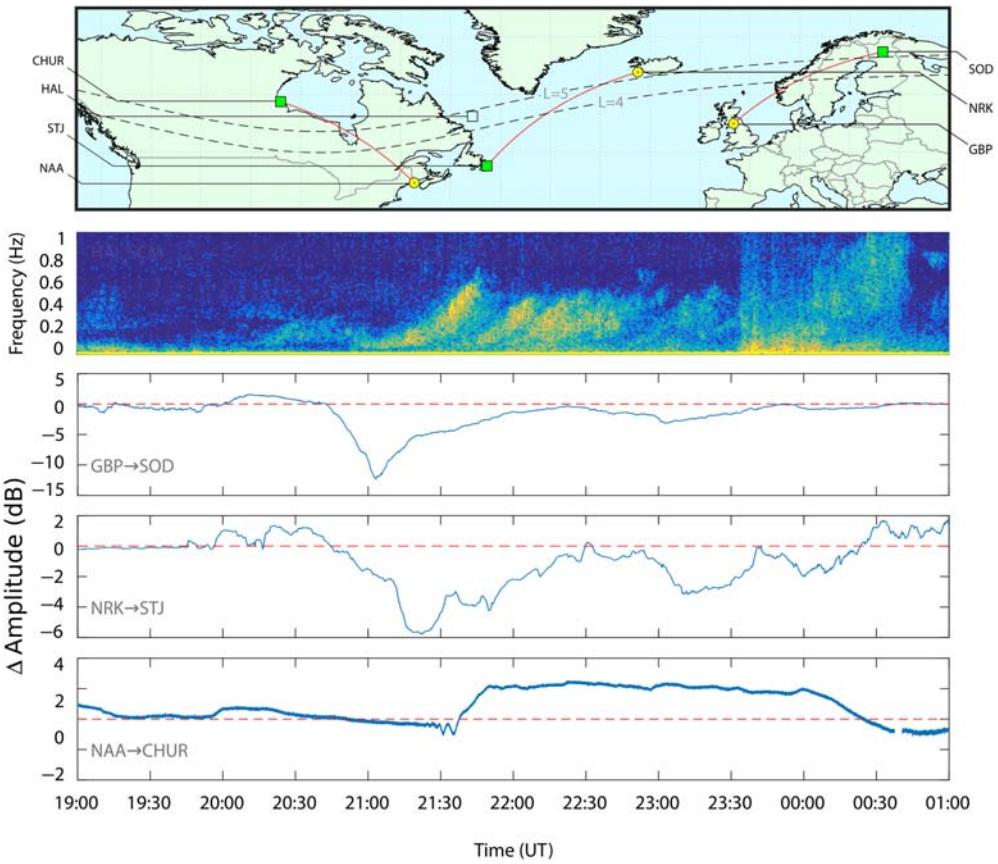

Figure 8.11 A plot of a May 24, 2013, event in a format similar to that of Fig. 8.6 shows SCM data from Halley and AARDDVARK data from European [GBP to Sodankylä (SOD)], Atlantic [NRK to St. John's (STJ)] and Canadian [NAA to Churchill (CHUR)] sectors. In this plot, time is shown in UT rather than MLT, which was the approach in all the similar plots.

the earlier case study. The EMIC-wave evolution is also different between the two case events in that the 0.1−0.5 Hz EMIC IPDP waves seen on May 31, 2013, became more dispersed over time, lasting initially for about 30 minutes (20:30−21:00 UT) in Finland, before eventually spanning several hours (21:30 to about 00 UT) in Canada (see Fig. 3 in Clilverd et al., 2015).

Fig. 8.11 summarizes the data for the May 31, 2013, case study. The upper panel shows a map of the AARDDVARK GCPs, including the Halley SCM conjugate point near the Canadian east coast. The regions where EMIC-induced precipitation perturbation effects occur in the AARDDVARK data can be identified as the locations where the GCPs pass between the *L*-shell contours. EMIC-wave occurrence in Halley SCM data from 19 UT to 01 UT (June 1, 2013) is shown on the panel

below the map. The panel shows rising-tone EMIC waves of the IPDP type starting at about 21:15 UT and lasting until 22:45 UT. The waves cover the 0.1−0.6 Hz range. In the lowest three panels AARDDVARK amplitude perturbations from a calculated quiet-day baseline are plotted for GBP (sometimes known as GVT) to Sodankylä in the upper of the three panels, NRK to St. John's in the middle panel, and NAA to Churchill in the bottom panel. The onset of an amplitude perturbation can be seen at about 20:45 UT at Sodankylä, progressively shifting to later UT for the more westerly paths, eventually beginning at 21:30 UT for the NAA observations that are equivalent to central Canada. The amplitude perturbations from the baseline given by the red dashed line also show that the EMIC-induced precipitation event lasted longer in the Canadian sector (2−3 hours) than it did during the initial perturbation seen in Scandinavia (1−1.5 hours), consistent with the evolution of the EMIC waves themselves.

8.6 Summary

In this chapter, we have looked at the use of ground-based VLF observations to detect and characterize energetic electron precipitation. The principal technique employed is analysis of perturbations to the phase and amplitude of man-made subionospheric narrowband VLF transmissions. The global AARDDVARK network of VLF receivers is an example of the type of measurements that can be made. The loss of radiation belt energetic electrons into the upper atmosphere can be detected by radio-wave techniques because of the production of excess ionization in the lower D-region as the precipitating electrons deposit their energy via scattering with the neutral atmosphere. Many radiation belt loss processes generate excess ionization and therefore can be detected by ground-based VLF observations.

In this chapter we have concentrated on the detection and characterization of EMIC-induced energetic electron precipitation using the ground-based AARDDVARK network. Complementary ground-based observations from riometers and magnetometers have also been used to provide context for the VLF observations. Measurements from in situ satellites are often used to provide key understanding of wave properties, and hence understanding of the characteristics of the resultant electron precipitation ultimately observed by ground-based instruments.

Several case studies were discussed in this chapter, piecing together a complex picture of electron precipitation over many hours and over a wide range of longitudes. However, some general observations can be made:

- Energetic electron precipitation events driven by EMIC waves are principally detected during the MLT evening sector by ground-based VLF instruments. Comprehensive monitoring is undertaken by the AARDDVARK network at all MLT. However, no EMIC-induced electron precipitation events have been unambiguously detected in the morning or noon MLT sectors.

- The electron precipitation patches have been observed to drift westward, remaining in the evening sector MLT, often lasting for many hours and drifting $>100^{\circ}$ of longitude while staying at an essentially constant MLT. However, EMIC-induced electron precipitation patches have also been observed to move in MLT, drifting westward from near midnight MLT toward the afternoon sector. In the latter case, the drift rates are consistent with the drift of source ≈ 50-keV protons that have been injected near midnight.
- The duration of EMIC-induced precipitation is also highly variable. From the perspective of a ground-based measurement point the electron precipitation patches have been seen to last for as long as several hours and as short as 15 minutes. The evolution of the precipitation patches has been seen to go from 1 hour long to 15 minutes (i.e., evolving to be shorter), as well as from 1 hour long to several hours in duration (i.e., evolving to be longer).
- Ground-based VLF observations of energetic electron precipitation from EMIC waves can, in principle, provide energy-resolved information. However, modeling the resultant phase and amplitude perturbations (following the approaches outlined in Rodger et al., 2012) can often produce a nonunique solution for the EMIC-induced electron precipitation flux and energy spectrum.
- In practice in situ measurements made by satellites, such as POES, SAMPEX, or DEMETER are more likely to provide definitive information about the EMIC-induced electron precipitation characteristics. Using the POES EMIC−event database developed by Carson et al. (2013) and improved by Hendry et al. (2017) we find that the EMIC events investigated in this chapter were generated by electron precipitation peaking in the energy range 200−500 keV. No clear EMIC-induced precipitation events with peak energy >1 MeV have been studied using ground-based VLF observations, although they may yet be shown to produce detectable perturbation signatures.

Acknowledgments

The authors would like to acknowledge the support of the people and institutions that host the AARDDVARK receivers, riometers, and magnetometers mentioned in this chapter—Sodankylä Geophysical Observatory, Natural Resources Canada, Natural Environmental Research council (BAS), University of Calgary, and Churchill Northern Studies Centre. U.S. support for the Halley search-coil magnetometer is provided by NSF grants PLR-1341493 to Augsburg University (Mark Engebretson) and PLR-1341677 to the University of New Hampshire (Marc Lessard). The research leading to some of these results has received funding from the European Union 407 Seventh Framework Programme (FP7/2007−2013) under grant agreement No. 263218. The authors wish to thank the many years worth of efforts from NOAA personnel, who developed, maintain and operate the NOAA/POES spacecraft. We would also like to thank Paul Muir, Physics Department, University of Otago, New Zealand for preparing Fig. 8.1.

References

Albert, J., Bortnik, J., 2009. Nonlinear interaction of radiation belt electrons with electromagnetic ion cyclotron waves. Geophys. Res. Lett. 36, L12110. Available from: https://doi.org/10.1029/2009GL038904.

Barr, R., Jones, D.L., Rodger, C.J., 2000. ELF and VLF radio waves. J. Atmos. Sol. Terr. Phys. 62, 1689–1718.

Carson, B.R., Rodger, C.J., Clilverd, M.A., 2013. POES satellite observations of EMIC-wave driven relativistic electron precipitation during 1998–2010. J. Geophys. Res. Space Phys. 118, 232–243. Available from: https://doi.org/10.1029/2012JA017998.

Chen, L., Thorne, R.M., Bortnik, J., Zhang, X.-J., 2016. Nonresonant interactions of electromagnetic ion cyclotron waves with relativistic electrons. J. Geophys. Res. Space Phys. 121, 9913–9925. Available from: https://doi.org/10.1002/2016JA022813.

Clilverd, M.A., Nunn, D., Lev-Tov, S.J., Inan, U.S., Dowden, R.L., Rodger, C.J., et al., 2002. Determining the size of lightning-induced electron precipitation patches. J. Geophys. Res. 107 (A8). Available from: https://doi.org/10.1029/2001JA000301.

Clilverd, M.A., Rodger, C.J., Ulich, T., Seppälä, A., Turunen, E., Botman, A., et al., 2005. Modeling a large solar proton event in the southern polar atmosphere. J. Geophys. Res. 110, A09307. Available from: https://doi.org/10.1029/2004JA010922.

Clilverd, M.A., Rodger, C.J., Thomson, N.R., Brundell, J.B., Ulich, Th, Lichtenberger, J., et al., 2009. Remote sensing space weather events: the AARDDVARK network. Space Weather 7, S04001. Available from: https://doi.org/10.1029/2008SW000412.

Clilverd, M.A., Rodger, C.J., Rae, I.J., Brundell, J.B., Thomson, N.R., Cobbett, N., et al., 2012. Combined THEMIS and ground-based observations of a pair of substorm-associated electron precipitation events. J. Geophys. Res. 117, A02313. Available from: https://doi.org/10.1029/2011JA016933.

Clilverd, M.A., Duthie, R., Hardman, R., Hendry, A.T., Rodger, C.J., Raita, T., et al., 2015. Electron precipitation from EMIC waves: a case study from 31 May 2013. J. Geophys. Res. Space Phys. 120, 3618–3631. Available from: https://doi.org/10.1002/2015JA021090.

Crombie, D.D., 1964. Periodic fading of VLF signals received over long paths during sunrise and sunset. J. Res. Natl. Bur. Stand., Sect. D 68, 27–34.

Cummer, S.A., 2000. Modeling electromagnetic propagation in the Earth-ionosphere waveguide. IEEE Trans. Antennas Propag. 48, 1420–1429.

Dietrich, S., Rodger, C.J., Clilverd, M.A., Bortnik, J., Raita, T., 2010. Relativistic microburst storm characteristics: combined satellite and ground-based observations. J. Geophys. Res. 115, A12240. Available from: https://doi.org/10.1029/2010JA015777.

Engebretson, M.J., Lessard, M.R., Bortnik, J., Green, J.C., Horne, R.B., Detrick, D.L., et al., 2008. Pc1–Pc2 waves and energetic particle precipitation during and after magnetic storms: superposed epoch analysis and case studies. J. Geophys. Res. 113, A01211. Available from: https://doi.org/10.1029/2007JA012362.

Evans, D.S., Greer, M.S., 2000. Polar Orbiting Environmental Satellite Space Environment Monitor-2: Instrument Description and Archive Data Documentation. US Department of Commerce, National Oceanic and Atmospheric Administration, Oceanic and Atmospheric Research Laboratory, Space Environment Center, Boulder, CO.

Helliwell, R.A., Katsufrakis, J.P., Trimpi, M.L., 1973. Whistler-induced amplitude perturbation in VLF propagation. J. Geophys. Res. 78 (22), 4679–4688. Available from: https://doi.org/10.1029/JA078i022p04679.

Hendry, A.T., Rodger, C.J., Clilverd, M.A., Engebretson, M.J., Mann, I.R., Lessard, M.R., et al., 2016. Confirmation of EMIC wave-driven relativistic electron precipitation. J. Geophys. Res. Space Phys. 121, 5366–5383. Available from: https://doi.org/10.1002/2015JA022224.

Hendry, A.T., Rodger, C.J., Clilverd, M.A., 2017. Evidence of sub-MeV EMIC-driven electron precipitation. Geophys. Res. Lett. 44, 1210–1218. Available from: https://doi.org/10.1002/2016GL071807.

Kersten, T., Horne, R.B., Glauert, S., Meredith, N.P., Fraser, B.J., Grew, R.S., 2014. Electron losses from the radiation belts caused by EMIC waves. J. Geophys. Res. Space Phys. 119, 8820–8837. Available from: https://doi.org/10.1002/2014JA020366.

Kuwashima, M., Toya, T., Kawamura, M., Hirasawa, T., Fukunishi, H., Ayukawa, M., 1981. Comparative Study of Magnetic Pc1 Pulsations Between Low Latitudes and High Latitudes: Statistical Study. Memoirs of National Institute of Polar Research, Special issue, no. 18, pp. 101–117.

Rodger, C.J., Clilverd, M.A., Dowden, R.L., 2002. D region reflection height modification by whistler-induced electron precipitation. J. Geophys. Res. 107 (A7). Available from: https://doi.org/10.1029/2001JA000311.

Rodger, C.J., Clilverd, M.A., Thomson, N.R., Gamble, R.J., Seppälä, A., Turunen, E., et al., 2007. Radiation belt electron precipitation into the atmosphere: recovery from a geomagnetic storm. J. Geophys. Res. 112, A11307. Available from: https://doi.org/10.1029/2007JA012383.

Rodger, C.J., Raita, T., Clilverd, M.A., Seppälä, A., Dietrich, S., Thomson, N.R., et al., 2008. Observations of relativistic electron precipitation from the radiation belts driven by EMIC waves. Geophys. Res. Lett. 35, L16106. Available from: https://doi.org/10.1029/2008GL034804.

Rodger, C.J., Clilverd, M.A., Green, J.C., Lam, M.M., 2010. Use of POES SEM-2 observations to examine radiation belt dynamics and energetic electron precipitation into the atmosphere. J. Geophys. Res. 115, A04202. Available from: https://doi.org/10.1029/2008JA014023.

Rodger, C.J., Clilverd, M.A., Kavanagh, A.J., Watt, C.E.J., Verronen, P.T., Raita, T., 2012. Contrasting the responses of three different ground-based instruments to energetic electron precipitation. Radio Sci. 47, RS2021. Available from: https://doi.org/10.1029/2011RS004971.

Rodger, C.J., Hendry, A.T., Clilverd, M.A., Kletzing, C.A., Brundell, J.B., Reeves, G.D., 2015. High-resolution in situ observations of electron precipitation-causing EMIC waves. Geophys. Res. Lett. 42, 9633–9641. Available from: https://doi.org/10.1002/2015GL066581.

Sandanger, M., Søraas, F., Aarsnes, K., Oksavik, K., Evans, D.S., 2007. Loss of relativistic electrons: evidence for pitch angle scattering by electromagnetic ion cyclotron waves excited by unstable ring current protons. J. Geophys. Res. 112, A12213. Available from: https://doi.org/10.1029/2006JA012138.

Sandanger, M., Søraas, F., Sørbø, M., Aarsnes, K., Oksavik, K., Evans, D., 2009. Relativistic electron losses related to EMIC waves during CIR and CME storms. J. Atmos. Sol. Terr. Phys. 71 (10–11), 1126–1144. Available from: https://doi.org/10.1016/j.jastp.2008.07.006.

Søraas, F., Aarsnes, K., Carlsen, D., Oksavik, K., Evans, D., 2005. Ring current behavior as revealed by energetic proton precipitation, The Inner Magnetosphere: Physics and Modeling, Geophysical Monograph Series, vol. 155. AGU, Washington, D.C, 237 pp.

Spasojevic, M., Fuselier, S.A., 2009. Temporal evolution of proton precipitation associated with the plasmaspheric plume. J. Geophys. Res. 114, A12201. Available from: https://doi.org/10.1029/2009JA014530.

Thorne, R.M., Kennel, C.F., 1971. Relativistic electron precipitation during magnetic storm main phase. J. Geophys. Res. 76 (19), 4446–4453.

Yahnina, T.A., Yahnin, A.G., Kangas, J., Manninen, J., Evans, D.S., Demekhov, A.G., et al., 2003. Energetic particle counterparts for geomagnetic pulsations of Pc1 and IPDP types. Ann. Geophys. 21, 2281–2292.

This page intentionally left blank

CHAPTER 9

Energetic electron precipitation into the atmosphere

Miriam Sinnhuber[1] **and Bernd Funke**[2]
[1]Institute of Meteorology and Climate Research, Karlsruhe Institute of Technology, Karlsruhe, Germany
[2]Institute of Astrophysics of Andalusia, CSIC, Granada, Spain

Contents

9.1 Introduction

Energetic particles precipitating into the Earth's atmosphere come from different sources: solar energetic protons, high-energy protons of energies up to a few hundreds of MeV from large eruptions on the surface of the sun, in solar flares and solar coronal mass ejections; galactic cosmic rays (GCRs) containing protons and heavier ions with energies from hundreds of MeV into the GeV, and in rare events even into the EeV range from outside the solar system (Anchordoqui et al., 2002; Thoudam et al., 2016); auroral electrons that are accelerated in the Earth's magnetotail to energies from a few keV to hundreds of keV during auroral substorms; and radiation belt electrons that are accelerated to energies of a few tens of keV to several MeV in the Van Allen belts during geomagnetic storms. The latter are also often referred to as *relativistic electrons*.

The Dynamic Loss of Earth's Radiation Belts
DOI: https://doi.org/10.1016/B978-0-12-813371-2.00009-3

All sources of energetic particles interact with the solar or interplanetary magnetic field and are therefore modulated by solar magnetic variability. As a consequence, all vary with the solar cycle on decadal to centennial timescales as well as with solar activity on much shorter periods of time, see Fig. 9.1. Solar proton events (SPEs) are related to

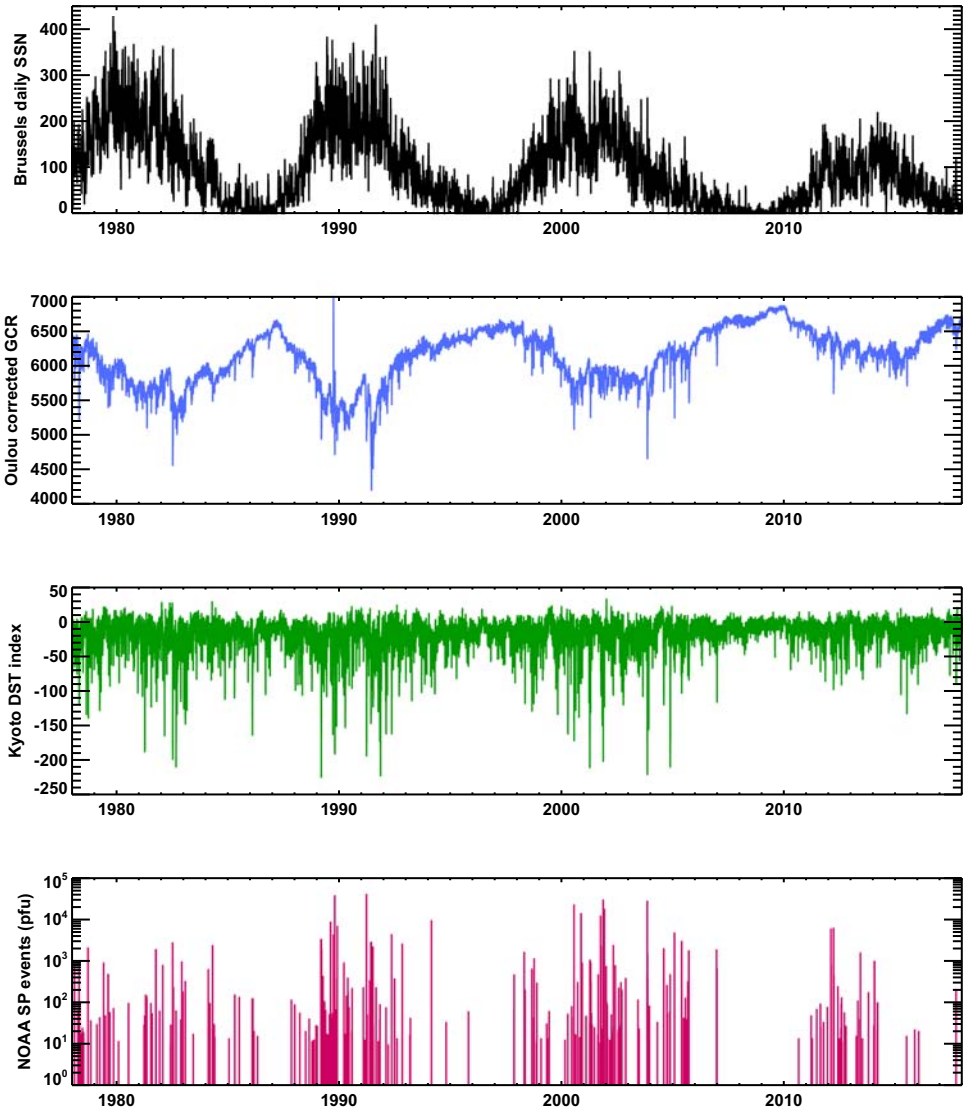

Figure 9.1 From top to bottom: daily sunspot number (SSN) (WDC-SILSO, Royal Observatory of Belgium, Brussels), the daily corrected galactic cosmic ray (GCR) flux from the Oulou neutron monitor in Finland (counts/min, from http://cosmicrays.oulu.fi), the daily DST index provided by the World Data Center for Geomagnetism in Kyoto, Japan (http://wdc.kugi.kyoto-u.ac.jp), and days with solar proton events (SPEs) as provided by the National Oceanic and Atmospheric Administration (NOAA) Space Weather Prediction Center. 1978–2018.

sunspot activity and occur mainly during the solar maximum; GCRs are deflected by the interplanetary magnetic field, which is weaker during solar minimum, so fluxes are generally higher; auroral substorms occur all through the solar cycle, but are more frequent and powerful during the maximum and declining phases of the solar cycle; relativistic electron precipitation (REP) is related to high-speed solar wind streams and corotating interaction regions and is most frequent during the transition from solar maximum to solar minimum.

How far particles precipitate into the atmosphere, on average, depends on their kinetic energy; the higher the energy, the further down into the atmosphere they will precipitate. Consequently, GCRs will mostly affect the lower stratosphere and troposphere, solar protons the midstratosphere to the mesosphere, auroral electrons the upper mesosphere and lower thermosphere, and relativistic electrons the midstratosphere to the upper mesosphere (see Fig. 9.2 for a comparison of ionization rates, Fig. 9.3 for an overview of the atmospheric layers and their connections by wave-driven large-scale circulation). All affect the atmospheric composition in a similar way—by collision reactions with the most abundant species followed by chemical reaction chains involving ions, excited species, and the neutral atmosphere. Both SPEs and energetic electron precipitation can have a long-lasting impact on the stratospheric composition, particularly, the stratospheric ozone during polar winter; as ozone is one of the key species in radiative heating and cooling of the stratosphere, changes in its

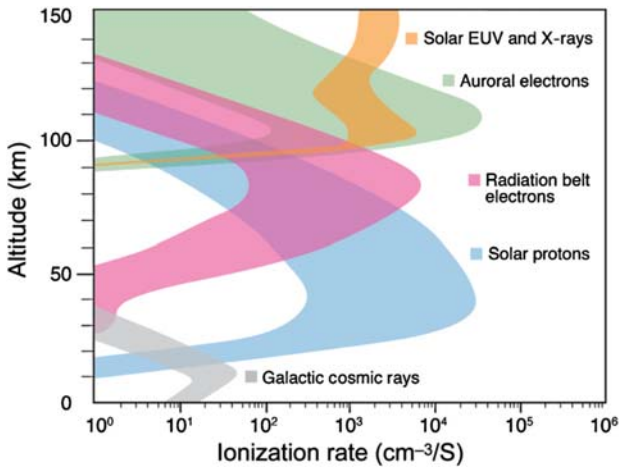

Figure 9.2 Atmospheric ionization as a function of altitude for different particle sources: galactic cosmic rays (*gray*), solar protons (*blue*), radiation belt electrons (*red*), and auroral electrons (*green*). Also shown is photoionization due to solar extreme ultraviolet (EUV) rays and X-rays (*orange*). *From Mironova, I.A., Aplin, K.L., Arnold, F., Bazilevskaya, G.A., Harrison, R.G., Krivolutsky, A.A., et al., 2015. Energetic particle influence on the earth's atmosphere. Space Sci. Rev. 194, 1–96, based on original figure by Baker, D.N., 2012. A small spacecraft mission with large accomplishments. EOS 93, 325–236 (Baker, 2012).*

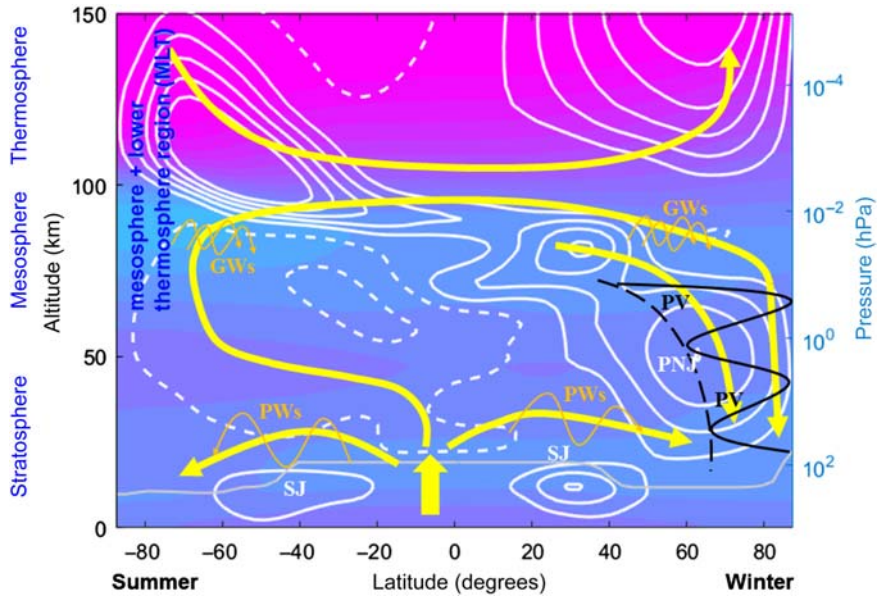

Figure 9.3 Schematic view of the atmosphere from the surface to the lower thermosphere. Approximate pressure levels are given on the right-hand axis. Colored contours in the background are monthly mean zonal temperatures for the Northern hemisphere winter, with the lowest temperatures of around 120K at the high-latitude summer mesopause (80−100 km, *light blue*) and the highest temperatures of more than 600K in the thermosphere above 130 km (*violet*). Atmospheric layers are conventionally defined by their vertical temperature gradient: troposphere (surface to 8−15 km, $dT/dz < 0$), stratosphere (up to 45 km, $dT/dz > 0$), mesosphere (up to 80−105 km, $dT/dz < 0$), thermosphere (above 80−105 km, $dT/dz > 0$). The thin gray line in the lower part of the figure marks the tropopause, the transition between the troposphere and the stratosphere. White lines mark the mean zonal winds (*dashed*: Easterlies; *solid*: Westerlies), indicating the subtropical jet (SJ) in the subtropical upper troposphere as well as the subpolar jet (PJ) at the edge of the polar vortex (PV, marked by *black lines*) in the stratosphere and lower mesosphere, and the change in wind direction around the mesopause. Yellow lines indicate the mean meridional (residual) circulation, an interhemispheric circulation system of the entire middle atmosphere (stratosphere−mesosphere) characterized by upwelling in the tropics, downward and poleward transport in the lower stratosphere in both hemispheres, upward motion throughout the summer hemisphere in the upper stratosphere and mesosphere, transport from the summer pole to the winter pole, and large-scale downwelling over the winter pole. The stratospheric branch of the circulation, the so-called *Brewer−Dobson circulation* is driven by dissipating planetary waves (PWs), which are more active in the Northern hemisphere in boreal winters. The mesospheric branch of the circulation, the *meridional overturning circulation* is driven by dissipating gravity waves (GWs), which are generated in the troposphere either by topography (orographic GWs) or fronts and convection (nonorographic GWs). Marked at the upper left of the figure is the mesosphere−lower thermosphere region (MLT region), typically used to encompass the upper mesosphere and lower thermosphere (70−150 km), a transitional region where signals from the space environment are transferred into the atmosphere and vice versa.

concentration induce dynamical changes in the middle atmosphere, which can couple down even into the troposphere and affect regional climate patterns. The impact of SPEs and aurorae on atmospheric composition is well constrained by observations and reasonably well reproduced by model studies. The impact of relativistic electrons from the radiation belts on the mesosphere above ≈ 70 km is now also well established from observations; however, a direct impact of relativistic electrons on stratospheric composition is still a matter of debate. More specific information on the different sources of particle precipitation and their variability as well as their treatment in state-of-the art climate models can be found in reviews by, for example, Sinnhuber et al. (2012), Mironova et al. (2015), and Matthes et al. (2017).

We will now give an overview of the impact of energetic electron precipitation from the aurorae and the radiation belts on the chemical composition and circulation of the atmosphere from the lower thermosphere to the surface. Primary processes related to the collision reactions are explained in Section 9.2, the indirect effect is discussed in Section 9.3, in Section 9.4, the state-of-the art concerning possible impacts on regional surface climate is summarized, and finally, open issues are discussed in Section 9.5.

9.2 The direct atmospheric impact of energetic particle precipitation

9.2.1 Primary processes

Energetic electrons precipitating into the atmosphere collide with the most abundant species—molecular nitrogen and molecular oxygen in the middle and lower atmosphere, atomic oxygen in the upper mesosphere and lower thermosphere, and atomic hydrogen even further up. The energy transfer during the collision reaction will either excite, ionize, or in the case of the molecular species, dissociate the collision partners, leading to a set of reactions such as:

$$M_2 + e^- \longrightarrow M_2^* + e^- \tag{9.1a}$$

$$M_2 + e^- \longrightarrow M_2^+ + e^- + e^- \tag{9.1b}$$

$$M_2 + e^- \longrightarrow M^+ + M + e^- \tag{9.1c}$$

$$M + e^- \longrightarrow M^+ + e^- + e^- \tag{9.1d}$$

$$M + e^- \longrightarrow M^* + e^- \tag{9.1e}$$

where the asterisk denotes electronically excited states and M is either nitrogen (N) or oxygen (O). The excited states of atomic oxygen [$O(^1D)$, $O(^1S)$] and ionized nitrogen [$N(^1D)^+$, $N(^1S)^+$] dominate the reds and greens of the aurora, with contributions from molecular nitrogen, ionized molecular nitrogen and nitric oxide (NO) in the violet and ultraviolet (UV) spectral range. However, note that some of these states are not excited by the primary collisions, but by quenching reactions of the most abundant species—N_2, O_2, NO—with the primary excited products (Gerard and Barth, 1976).

At the same time, the energy dissipation of the electron flux due to collisions with the neutral atmosphere leads to an effective Joule heating δQ of the atmosphere. This is related mainly to the Pedersen conductivity (the conductivity parallel to the accelerating electric field) and can be expressed as

$$\delta Q = \vec{j}\,(\vec{E} + \vec{v} \times \vec{B}) \approx \sigma_P E^2 \tag{9.2}$$

where $\vec{j}$ is the electron flux along the field lines, which can be denoted by $\sigma_P \vec{E}$ with the Pedersen conductivity σ_P. $\vec{v}$ is the neutral wind; the second term is usually considered small because of the comparatively low wind speeds and is thus omitted.

As the excited species and ions are much more reactive than the neutral ground-state atoms and molecules, their formation leads to a chain of very fast reactions, which considerably change the chemical composition of the atmosphere. This includes the formation of odd nitrogen species (N, NO, see Section 9.2.2) in the auroral regions of the lower thermosphere to the stratosphere, the formation of odd hydrogen species (H, OH, see Section 9.2.3) in the mesosphere, and formation of nitrous oxide (N_2O, Section 9.2.4) in the upper mesosphere and lower thermosphere, as well as catalytic ozone loss in the stratosphere and mesosphere. In the lower mesosphere and stratosphere, negative ion chemistry reactions also lead to the formation of HNO_3 (Verronen et al., 2011) and affect chlorine compounds (Winkler et al., 2009); however, these are restricted to altitudes below 70 km, where energetic electron precipitation presumably does not contribute significantly to ionization, and will not be discussed further here.

9.2.2 Formation of NO and $N(^4S)$

NO can be formed as a consequence of particle precipitation by three different mechanism, which act differently in different altitude regions.

Thermal formation in the thermosphere. NO is formed via the reaction of ground-state atomic nitrogen, $N(^4S)$, with molecular oxygen:

$$N(^4S) + O_2 \longrightarrow NO + O \tag{9.3}$$

The rate of this reaction is highly temperature-dependent, favoring high temperatures. It is balanced by the scavenging reaction with atomic nitrogen

$$N(^4S) + NO \longrightarrow N_2 + O \tag{9.4}$$

which is only weakly temperature dependent. The temperature dependency of the two opposing reactions leads to an efficient NO formation for temperatures higher than several hundreds of K, typically encountered in the thermosphere above ~150 km. Enhanced electron precipitation leads to enhanced Joule heating, maximizing in the auroral regions of the lower thermosphere above ~120 km; higher temperatures lead to higher values of NO owing to the stronger temperature dependence of formation reaction (Reaction 9.3) compared to the scavenging reaction (Reaction 9.4). The same set of reactions leads to the formation of NO in flash discharges in tropospheric thunderstorms, where temperatures of tens of thousands of K are reached (Zel'dovic and Raizer, 1967).

Ion chemistry: upper mesosphere and lower thermosphere. NO production is initiated by ion chemistry reaction chains forming NO^+, for example,

$$N_2^+ + O \longrightarrow NO^+ + N \tag{9.5a}$$

$$N^+ + O_2 \longrightarrow NO^+ + O \tag{9.5b}$$

$$O^+ + N_2 \longrightarrow NO^+ + N \tag{9.5c}$$

$$O_2^+ + N_2 \longrightarrow NO^+ + NO \tag{9.5d}$$

Recombination of NO^+ with electrons leads to the formation of atomic nitrogen:

$$NO^+ + e^- \longrightarrow N + O \tag{9.6}$$

NO is then formed by Reaction (9.3), which, however, is in competition with Reaction (9.4). Reactions (9.5a), (9.5c), and (9.6) dominantly form the excited state N (^{2}D) and not the ground state N(^{4}S), and Reaction (9.3) is orders of magnitude faster for the excited state than for the ground state. NO formation by ion chemistry and via the excited state of N dominates in the mesosphere and lower thermosphere. Below the midmesosphere, at altitudes below ~65 km, ion chemistry contributes about 13%–19% of the total NO formation (Rusch et al., 1981; Porter et al., 1976), but the efficiency of this reaction chain increases into the lower thermosphere because of the higher availability of the atomic oxygen needed for Reactions (9.5a) and (9.5c) (see Nieder et al., 2014).

Stratosphere and mesosphere: dissociation of N_2. NO is formed directly via Reaction (9.3) from the products of the N_2 dissociation—N(^{4}S), N(^{2}D), N(^{2}P)—and higher excited states. As the NO formation is much quicker for the excited states than for the

ground states, the transformation to NO is commonly assumed to occur "instantaneously." The effectiveness of the NO formation depends on the ratio of the formation of the excited to the ground state of N, as the ground state would predominantly lead to the scavenging loss of NO at temperatures below 500 K. However, the ratio of excited-state to ground-state N during the dissociation is not well known; it has been estimated from theoretical considerations to be nearly equal (45%) (Porter et al., 1976), but estimates based on observations yield a much lower ratio of the $N(^4S)$ production of 20% (Rusch et al., 1981) and 14%–27% (Baumgaertner et al., 2010).

9.2.3 Formation of H and OH

H and OH are formed by uptake of water vapor into large positive cluster ions. During the formation of the cluster ions, OH is released:

$$O_4^+ + H_2O \longrightarrow O_2^+(H_2O) + O_2 \tag{9.7a}$$

$$O_2^+(H_2O) + H_2O \longrightarrow H^+(H_2O) + OH + O_2 \tag{9.7b}$$

Protonized water cluster ions $H^+(H_2O)_n$ can grow by uptake of more water vapor, and recombination reactions with electrons release H:

$$H^+(H_2O)_n + e^- \longrightarrow H + nH_2O \tag{9.8}$$

Another possibility is the formation of H_3O^+-containing ions via

$$O_2^+(H_2O) + H_2O \longrightarrow H_3O^+(OH) + O_2 \tag{9.9}$$

which release both H and OH during recombination with electrons. In this chain, H and OH are formed in equal amounts, balancing the uptake of H_2O. Water cluster ions can also be formed by reaction of NO^+ with H_2O, forming $NO + (H_2O)$, and subsequent reaction with water vapor form the protonized water cluster:

$$NO^+(H_2O)_n + H_2O \longrightarrow H^+(H_2O) + HNO_2 \tag{9.10}$$

In this case, no OH is released during the formation of the water cluster ion, and model calculations with an ion chemistry model suggest that up to 10% less OH than H is formed owing to this reaction chain (Sinnhuber et al., 2012). Formation of HO_x depends on the availability of water vapor, which decreases significantly in the upper mesosphere above $\sim$80 km; HO_x formation is therefore restricted to the mid- to lower mesosphere and stratosphere.

It has been shown in a theoretical study that HO_x can also be produced by solely neutral gas-phase chemistry following enhanced particle precipitation as a consequence

of the increase in NO, which changes the partitioning between OH and HO_2, thus impacting the lifetime of HO_x (Verronen and Lehmenn, 2015)

9.2.4 Formation of N_2O in the upper mesosphere and lower thermosphere

There are two possible pathways for N_2O production as a consequence of atmospheric excitation and ionization. One is related to the production of an excited state of N_2, $N_2(A\Sigma_u^+)$, by collision reactions with precipitating electrons. The excited state reacts with molecular oxygen forming N_2O:

$$N_2(A\Sigma_u^+) + O_2 \longrightarrow N_2O + O \tag{9.11}$$

This was discussed, for example, by Zipf and Prasad (1980) and Prasad and Zipf (1981) and is supposed to form N_2O in the uppermost mesosphere and lower thermosphere ($\sim$80–120 km). Another pathway of N_2O formation is via the formation of atomic nitrogen in the ground state $N(^4S)$, and subsequent reaction with NO_2:

$$N(^4S) + NO_2 \longrightarrow N_2O + O \tag{9.12}$$

This pathway was discussed, for example, by Semeniuk et al. (2008) and Funke et al. (2008). NO_2 is formed from NO during nighttime in the stratosphere and mesosphere, but reforms NO quickly at altitudes above 80 km via reaction with atomic oxygen, so that this mechanism is most efficient during nighttime, and at altitudes below $\sim$80 km (Semeniuk et al., 2008).

9.2.5 Consequences of the NO_x and HO_x formation: ozone loss

Both HO_x and NO_x (the sum of N, NO, and NO_2) contribute to ozone loss in catalytic cycles of the form

$$X + O_3 \longrightarrow XO + O_2 \tag{9.13a}$$

$$XO + O \longrightarrow X + O_2 \tag{9.13b}$$

$$XO + h\nu \longrightarrow X + O \tag{9.13c}$$

As the reactant X is reformed in the second step, usually either by reaction with atomic oxygen or by photolysis, ozone destruction can be very efficient. In the mesosphere above $\sim$45 km, catalytic cycles with HO_x dominate, and X is either H or OH. In the upper stratosphere in the altitude range between 30 and 45 km, catalytic cycles with NO_x (i.e., X = NO in Reactions 9.13a–9.13c) are most important

(Lary, 1997). Energetic electron precipitation therefore leads to ozone loss in both the stratosphere and the mesosphere, though by different mechanisms; in the upper mesosphere and lower thermosphere, ozone loss is negligible because NO is not efficient for ozone loss there and HO_x production is low. At these altitudes, the oxygen chemistry will rather be dominated by the production of atomic oxygen due to dissociation of O_2.

9.2.6 Observations

The mechanism of NO_x and HO_x formation described above is the same for all types of energetic particle precipitation—SPEs, energetic electron precipitation related to auroral and geomagnetic activity, and GCRs—and there is ample observational evidence dating back to the 1970s that large SPEs have a strong immediate impact on the composition of the middle atmosphere down to at least 40 km (Weeks et al., 1972; Heath et al., 1977; McPeters and Jackman, 1985; Jackman et al., 2001, 2005a,b; Funke et al., 2011).

It was also already noted in the 1970s and 1980s that NO in the lower thermosphere is strongly increased in auroral arcs (Zipf et al., 1970) and is generally higher at high and midlatitudes than at low latitudes, presumably due to auroral production (Rusch and Barth, 1975; Cravens and Stewart, 1978; Iwagami and Ogawa, 1980; Cravens et al., 1985). In the high-latitude lower thermosphere, NO was shown to increase during geomagnetic storms (Gerard and Barth, 1977) and related to energetic electron precipitation (Sætre et al., 2004); it increases nearly linearly with geomagnetic activity there (Cravens and Stewart, 1978), providing further evidence that in the high-latitude lower thermosphere, NO is formed as a consequence of energetic electron precipitation during auroral substorms and not by photoionization as at low latitudes (Fesen et al., 1990; Siskind et al., 1998; Marsh et al., 2004; Bender et al., 2015; Hendrickx et al., 2017; Kiviranta et al., 2018). NO at mid- and high latitudes has its maximum density around 100–110 km (Cravens and Stewart, 1978) 105–110 km (Barth et al., 2003), respectively and clearly maps into the auroral oval (Barth et al., 2001). This auroral NO production is restricted mostly to altitudes above 90 km. Observations also indicate a layer of enhanced N_2O in the upper mesosphere and lower thermosphere at altitudes above 90 km during polar summer, suggesting formation from excited-state N_2 as a source (Sheese et al., 2016), though during polar winter, enhanced N_2O is observed down to the lower mesosphere above ≈ 50 km (Funke et al., 2008; Semeniuk et al., 2008).

Thorne (1977) speculated that during geomagnetic storms, relativistic electrons from the radiation belts and their bremsstrahlung ionization could lead to significant formation of NO down to about 30 km altitude and, consequently, could impact stratospheric NO_y and ozone at high latitudes. A number of model studies have suggested that this might be the case (Callis et al., 1991, 1998a,b, 2001), but there was

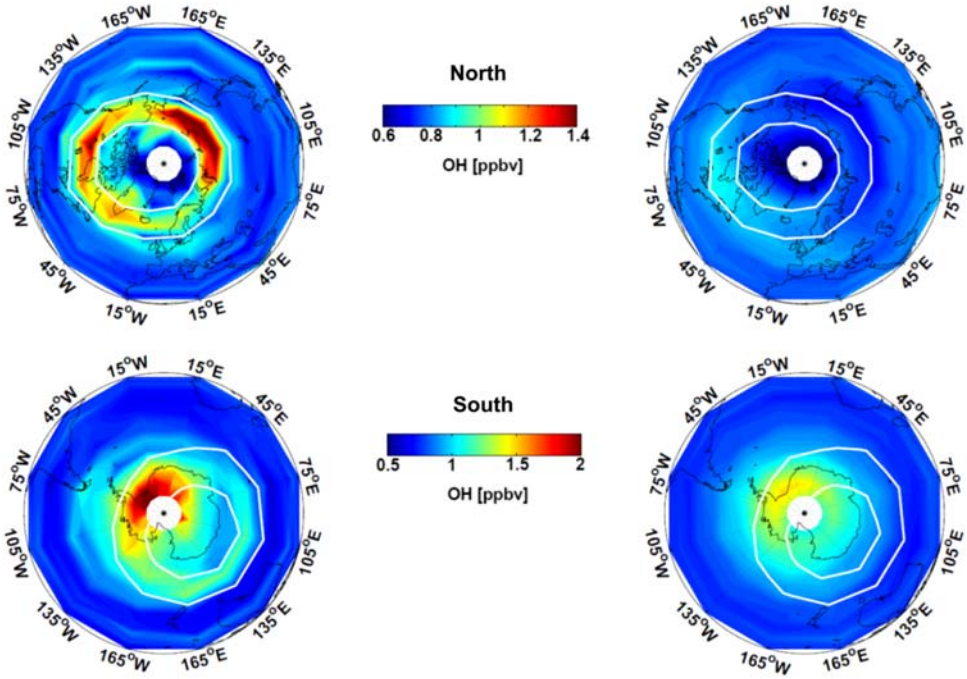

Figure 9.4 OH in the mesosphere (70–78 km) for high (*left*) and low (*right*) fluxes of medium-energy electrons in the Northern (*upper panel*) and Southern (*lower panel*) hemispheres, clearly mapping an auroral oval–like structure. MLS observations from 2005 to 09. The white lines mark 55 and 72 degrees magnetic latitude. *From Andersson, M.E., Verronen, P.T., Rodger, C.J., Clilverd, M.A., Wang, S., 2014b. Longitudinal hotspots in the mesospheric OH variations due to energetic electron precipitation. Atmos. Chem. Phys. 14 (2), 1095–1105. Provided under a creative commons licence (https://creativecommons.org/licenses/by/3.0)*

only scant observational evidence for it at the beginning. Callis et al. (1998a) reported observations of an enhancement of NO during one geomagnetic storm, though in this case, the increase was restricted to altitudes above 85 km. An increase in OH at geomagnetic latitudes mapping into the radiation belts has been detected related to fluxes of precipitating medium-energy electrons in the altitude range 70–78 km (Verronen et al., 2011), which is detectable down to ~55 km in some events (Andersson et al., 2012), and clearly maps an auroral oval–like structure in this altitude region (Andersson et al., 2014b) (see Fig. 9.4). High-latitude OH in the mesosphere shows a 27-day periodicity, suggesting a relation to high-speed solar wind streams (Fytterer et al., 2015b) (see upper panels of Fig. 9.5). Similarly, an increase in NO at high latitudes has been observed during energetic particle precipitation events (Newnham et al., 2011, 2013) or high-speed solar wind streams (Kirkwood et al., 2015) in the altitude region 70–90 km, though in the latter case, there was a temporal delay in the NO response, which suggests transport or mixing from higher altitudes rather than a

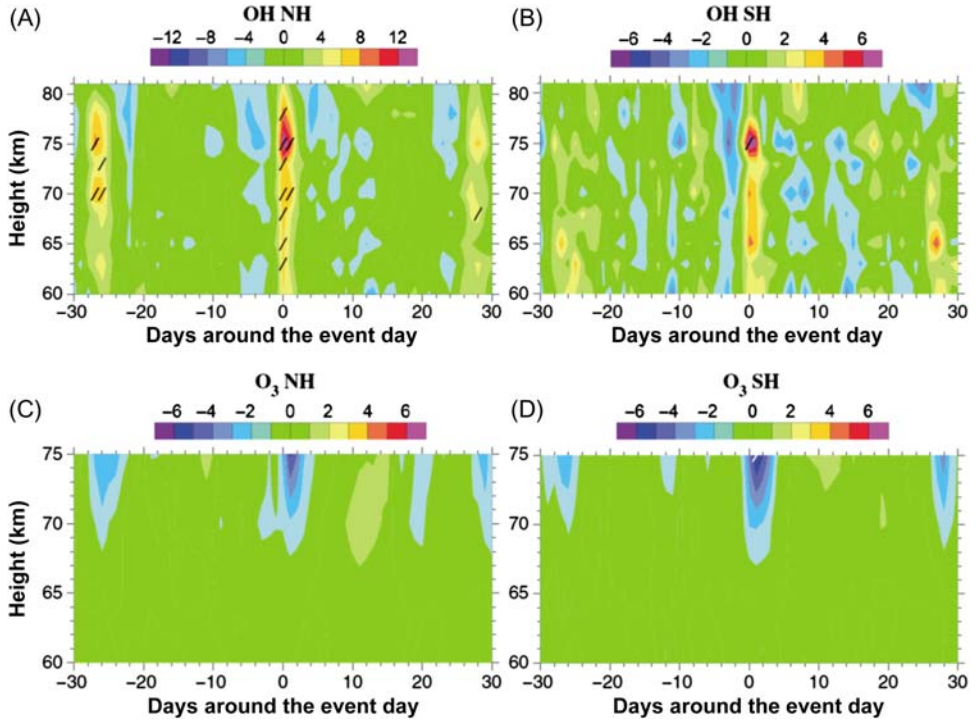

Figure 9.5 Results of a superposed epoch analysis for night-time polar winter OH (*upper panels*) and O_3 (*lower panels*) related to the geomagnetic Ap index in Northern (*left*) and Southern (*right*) magnetic latitudes 55−75 degrees, showing clear OH enhancements down to 60 km with corresponding ozone loss down to ≈68 km and a 27-day periodicity in both species. Based on MLS observations from 2004−09 (OH) and 2004−14 (O_3). *From Fytterer, T., Santee, M.L., Sinnhuber, M., Wang, S., 2015b. The 27-day solar rotational effect on mesospheric nighttime OH and O_3 observations induced by geomagnetic activity. J. Geophys. Res. 120, 7926−7936.*

direct production in the mesosphere. Mesospheric NO at radiation belt latitudes shows a clear linear relation to geomagnetic indices (Fig. 9.6) with a 27-day periodicity (Hendrickx et al., 2015; Sinnhuber et al., 2016) that extends down to at least 66 km (Fig. 9.7) and clearly maps an auroral oval−like structure (Sinnhuber et al., 2016). In one strong geomagnetic storm event, an immediate increase in NO was observed down to about 55 km (Smith-Johnsen et al., 2017). A careful investigation of the variability of nighttime NO_2 over several years revealed a correlation with geomagnetic activity and a clear 27-day cycle dependence even in the uppermost stratosphere (46−52 km), maximizing at magnetic latitudes of ∼60−70°N (Friederich et al., 2014). This suggests a response of middle atmosphere NO_x to radiation belt electron precipitation throughout the mesosphere down to the upper stratosphere. However, in the mid- and upper mesosphere, the observed enhancements of NO are the same

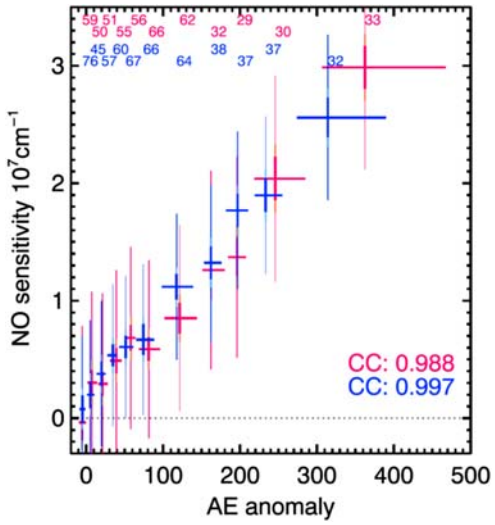

Figure 9.6 Relationship between changes in NO and in the geomagnetic Auroral Electrojet index (AE) in 70–74 km and at geomagnetic latitudes 55–70°N(*red*)/S(*blue*). Observations by the SCanning Imaging Absorption SpectroMeter for Atmospheric CHartographY (SCIAMACHY) from 2002 to 2012. *From Sinnhuber, M., Friederich, F., Bender, S., Burrows, J.P., 2016. The response of mesospheric NO to geomagnetic forcing in 2002–2012 as seen by SCIAMACHY. J. Geophys. Res. Space Phys. 121, 3603–3620.*

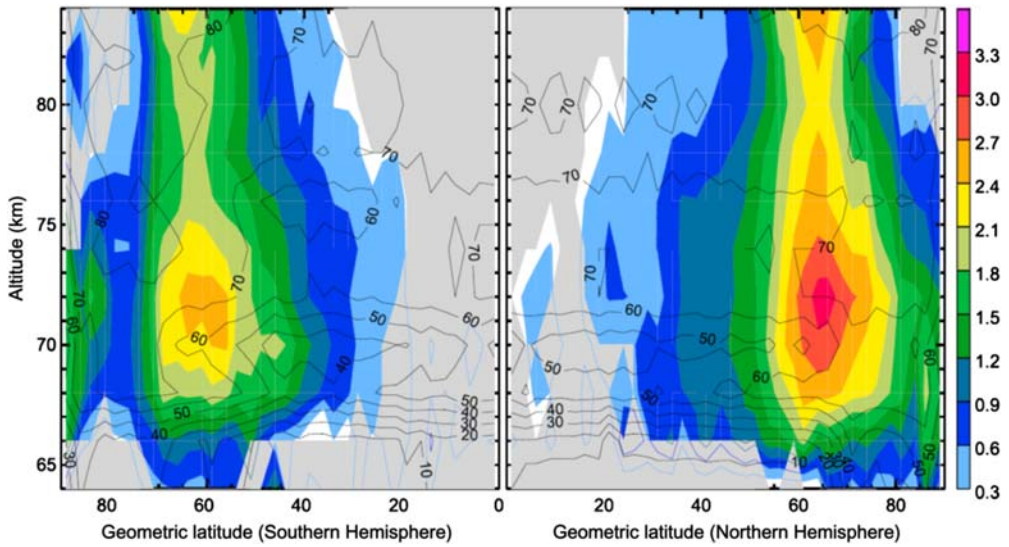

Figure 9.7 Polar summer NO density (in 10^7 cm^{-3}) for high geomagnetic activity as a function of latitude and altitude, clearly showing enhanced values at geomagnetic latitudes relating to the radiation belts in the mid- and upper mesosphere above 66 km. SCIAMACHY observations from 2002 to 2012. *From Sinnhuber, M., Friederich, F., Bender, S., Burrows, J.P., 2016. The response of mesospheric NO to geomagnetic forcing in 2002-2012 as seen by SCIAMACHY. J. Geophys. Res. Space Phys. 121, 3603–3620.*

order of magnitude as the background population, while in the upper stratosphere, the amplitude of the variation related to geomagnetic activity is in the range of a few percent of the background amount only; it seems unlikely that those small variations have a strong impact on the upper stratosphere ozone. A correlation of upper stratosphere polar ozone at ~30 km to the fluxes of relativistic electrons in the radiation belts has indeed been reported from ozonesonde data (Sinnhuber et al., 2006), but since there is no observational evidence for a similar response of the precursor species, NO_x and HO_x, at these altitudes, to date it is not clear whether there really is a physical relationship to electron precipitation. Large ozone losses related to increased fluxes of energetic electrons (Andersson et al., 2014a) and geomagnetic activity (Fytterer et al., 2015b) have, however, been observed in the high-latitude mesosphere above 68 km; mesospheric ozone losses also show a distinctive 27-day periodicity (Fytterer et al., 2015b) (lower panels of Fig. 9.5). In summary, there is clear observational evidence for NO and OH formation as well as ozone loss related to energetic electron precipitation at magnetic latitudes of ~55–75 degrees in the mesosphere down to about 68 km, mapping to an auroral oval–like structure, with a 27-day periodicity suggesting a relation to high-speed solar wind streams and hence a direct impact of medium-energy electrons accelerated in the radiation belts. In strong events, formation of NO_x species is detected even down to the upper stratosphere, indicating that relativistic electrons might play a role as well, as suggested by Thorne (1977); however, the amplitudes of these NO_x enhancements are very low (up to about 0.4 ppb in the uppermost stratosphere (Friederich et al., 2014) compared to ambient NO_y of a few ppb depending on time of year), and they are therefore unlikely to have a significant direct impact on stratospheric composition.

9.2.7 Model experiments

To model the impact of energetic particle precipitation on the stratosphere, mesosphere, and lower thermosphere, two ingredients are necessary: a description of the deposition of the particles' energy and a description of the impact on the chemical composition. The energy deposition is often described by the ion pair production rate (IPR). There is a range of possibilities for how to describe the impact of atmospheric ionization on the chemical composition. The most precise solution would be to include the full chemistry of ions and excited species in the chemical code of the model. This is more commonly done in the lower thermosphere, where the number of ions is limited, and five positive ions ($N_2^+, O_2^+, O^+, N^+, NO^+$), electrons, and excited states of O and N are assumed to be sufficient to describe the particle impacts on the neutral composition of the atmosphere. To do this, the formation of primary dissociation products—ions as well as excited and ground-state atoms—are provided as a function of the IPR. Following Jones and Rees (1973), the probability of formation

of excited or ionized species m* from collision of the incident electron with species [M] can be derived as

$$P(\mathrm{m}^*) = \frac{\sigma_{\mathrm{m}^*}[\mathrm{M}]}{\sigma_{\mathrm{O2}}[\mathrm{O_2}] + \sigma_{\mathrm{N2}}[\mathrm{N_2}] + \sigma_{\mathrm{O}}[\mathrm{O}]} \times \mathrm{IPR} \tag{9.14}$$

where σ_{m*} is the cross section of collisional formation of m* (where m is either N or O); [M] is the density of reactant M (either O_2, N_2, or O); σ_{O2}, σ_{N2}, and σ_O are the total reaction cross sections of O_2, N_2, or O; and IPR is the ion pair production rate.

In the mesosphere and stratosphere, the D-region of the terrestrial ionosphere, large positive and negative cluster ions dominate the ion composition, and the simple approach of using only five ions is no longer valid. Models incorporating full D-region ion chemistry exist, but are still computationally expensive. Therefore parameterizations of the particle impact on the formation of N, NO, H, and OH were already developed in the 1970s and 1980s, and they are still widely used in global chemistry–climate models of the middle and lower atmosphere. A number of parameterizations for the formation of NO_x species as a function of the IPR have been developed, with different complexity. The simplest parameterization, by Porter et al. (1976), is based on a detailed study of the energy levels of N_2 and O_2 in the homosphere (i.e., for a fixed N_2/O_2 ratio). This parameterization provides formation rates of $N(^4S)$, a sum of the excited states, and N^+ as well as a sum of all those as the total N-atom formation rate. The parameterization is widely in use mainly to study the impact of SPEs, which maximize in the upper stratosphere and mesosphere; in the most common form, the total N-atom formation rate of 1.27 N/IPR is used, and this number is distributed to $N(^4S)$ and $N(^2D)$ with the ratio given in Table V of Porter et al. (1976); $N(^2D)$ is supposed to form NO immediately. This is, strictly speaking, not correct, as the total N-atom formation also includes N^+, but this is a small amount (0.154 N^+/IPR). N and NO formation by ion chemistry is not considered in this parameterization; it is, therefore, not valid in the upper mesosphere and thermosphere, as it is formulated for the homosphere only and does not consider ion chemistry. The parameterization of Rusch et al. (1981) provides a more detailed description of the N production by ion chemistry: it considers formation of N atoms by three processes—namely, N_2 dissociation, one ion chemistry reaction forming NO^+ (Reaction 9.5c), and the primary formation of O^+ and N^+, which is considered to form $N(^4S)$. The resulting total N formation rate is 1.3–1.6 N/IPR, larger than the rate given by Porter et al. (1976), and increases into the lower thermosphere owing to the dependence on O^+. However, the N_2 and O_2 dissociation rates are still calculated for the homosphere, so the applicability in the lower thermosphere is limited. Also, this parameterization does not differentiate between the ground-state and the excited-state N, so the effective NO_x formation is probably too low. More recently, a parameterization based on the full D-region ion chemistry was developed; for this

parameterization, a lookup table was produced using a one-dimensional D-region ion chemistry of the stratosphere, mesosphere, and lower thermosphere for a wide range of atmospheric states, including temperature, pressure, the densities of H_2O, N, NO, and O, and the ionization rate (Nieder et al., 2014). Verronen and Lehmann (2013) also provided lookup tables for the production of NO_x as a function of altitude and atmospheric ionization based on results of a D-region ion chemistry model; in this case, positive and negative ion reactions are included, and the parameterization also provides rates for the redistribution of major NO_y species by ion chemistry as well as HO_x formation.

The formation of H and OH due to incorporation of water vapor into cluster ions (Reactions 9.7a, 9.7b, 9.8–9.10) has been parameterized by Solomon et al. (1981) depending on the densities of NO, O, and H_2O using a one-dimensional ion chemistry model. A simplified form of this parameterization has been derived by Jackman et al. (2005a) as a lookup table incorporating only the IPR and altitude; this parameterization is now widely used, and it has been shown to agree with results from full D-region ion chemistry reasonably well (Sinnhuber et al., 2012).

These parameterizations have been used extensively to study the impact of large SPEs on the middle atmosphere; however, they can be applied in the same way to investigate the impact of medium-energy and relativistic electrons. A first attempt was reported in 1991 (Callis et al., 1991) using daily averaged electron fluxes in the energy range 30 keV to 15 MeV observed by the SEE instruments on satellites in geostationary orbit. A fixed formation of 1.2 NO_x/IPR and 2 HO_x/IPR was used. Model results suggest large short-term and long-term impacts of energetic electron precipitation on NO_y and ozone around the stratopause during the model period (1979–90), varying over the solar cycle. The comparatively low altitude of the impact is consistent with the high energies considered, though the amplitudes of the observed modeled variabilities are higher than any direct response observed at these altitudes so far (see subsection 9.2.6). There are two possible reasons for this: (1) the electron fluxes used are from electrons trapped in the radiation belts, and determination of atmospheric loss from these is difficult and might lead to a significant overestimation; and (2) much of the modeled response might be due to the so-called energetic particle precipitation (EPP) indirect effect due to downwelling of NO_y in polar winter, which has a much larger impact on the mid- to upper stratosphere than the direct effect discussed here (see Section 9.3). Codrescu et al. (1997) used electron fluxes from a Sun-synchronous polar orbiting satellite (Television and Infrared Observation Satellite [TIROS]-NOAA) with slightly lower energies (30 keV to 2.5 MeV). NO_x formation was based on Rusch et al. (1981), HO_x formation was based on Solomon et al. (1981). Model results show an increase of HO_x, NO, and NO_2 as well as ozone loss in the mesosphere above $\approx$64 km, with a vertical and latitudinal variation in remarkably good agreement with the observations discussed in

Section 9.2.6, which, however, were not yet available for comparison at the time. Since then, a number of model studies incorporating ionization effects from medium-energy electrons have been carried out; however, they were mostly focused on the long-term impact on the stratosphere (Callis et al., 1998a,b, 2001; Semeniuk et al., 2011; Arsenovic et al., 2016; Sinnhuber et al., 2018; Andersson et al., 2017), that is, the indirect effect discussed in Section 9.3. All used ionization rates based on observed medium-energy electron fluxes from polar orbiting satellites (either TIROS or the Medium Energy Proton and Electron Detector [MEPED] instruments on the NOAA spacecrafts). Most used simple parameterizations of the NO_x and HO_x formation as described above, though Andersson et al. (2017) used a chemistry–climate model with a full D-region ion chemistry. Though it was not the focus of these publications, their model results show NO_y formation and ozone loss consistent with MEE precipitation in the high-latitude summer mesosphere above ~60 km (Semeniuk et al., 2011; Arsenovic et al., 2016; Andersson et al., 2017), an auroral oval–like structure in mesospheric summertime NO_x (Arsenovic et al., 2016) and wintertime HO_x (Arsenovic et al., 2016; Andersson et al., 2017), and NO_y formation in the summertime polar mesosphere related to geomagnetic storms with a distinctive solar cycle variation (Sinnhuber et al., 2018).

A focused study of the direct impact of medium-energy electron precipitation was carried out by Turunen et al. (2009), who used a one-dimensional model with a full D-region ion chemistry to compare the relative contributions of a large SPE, the aurora as well as a long-lasting REP event and a REP microburst. They found no detectable impact of the REP microburst but a significant impact of the long-lasting REP event on NO_y in the altitude region 60–80 km, in reasonable agreement with previous observations (see Section 9.2.6). A model study based on a reassessment of the fluxes and occurrence frequencies of REP microbursts shows a significant impact of microbursts on upper mesosphere NO_x, HO_x, and ozone lasting a few hours (Seppälä et al., 2018).

A dedicated model-observation comparison of the impact of medium-range electrons on mesospheric composition was carried out by Fytterer et al. (2016). They performed a model run with a global three-dimensional chemistry-transport model of the stratosphere, mesosphere, and lower thermosphere from 2002 to 2010, a period well covered by global observations of mesospheric OH and ozone [e.g., from the Aura Microwave Limb Sounder (MLS)] and NO (e.g., SCIAMACHY/Envisat). A superposed epoch analysis to geomagnetic activity was applied to the model results of OH, NO, and ozone, and results of this analysis were compared to observational analyses (Fytterer et al., 2015b; Sinnhuber et al., 2016). Qualitatively, a good agreement was found between increasing mesospheric OH and NO as function of geomagnetic activity and related ozone loss. However, the 27-day periodicity was not as pronounced in the model results

as in the observations, and the impact was restricted to altitudes above 70 km because ionization rates considered only electron energies up to 300 keV. Smith-Johnsen et al. (2018) did model experiments for one pronounced and well-isolated geomagnetic storm in April 2010 using different sets of ionization rates and different treatments of the ion chemistry impact: auroral electrons only and auroral and medium-energy electrons, as well as simple parameterizations and a full D-region ion chemistry. Model results were compared to NO observations from solar occultation for ice experiment (SOFIE)/AIM which show a clear increase of NO down to at least 55 km during the event (see also, Smith-Johnsen et al., 2017). The observed NO increase in the auroral region above 120 km is reproduced very well by the model, but the increase in the altitude range between 90 and 110 km, the altitude of the NO maximum, is underestimated in all model scenarios, suggesting an apparent lack of understanding of the ion and excited-state chemistry of the lowermost thermosphere (see Fig. 9.8). Below 80 km altitude, medium-energy electrons with energies larger than 30 keV have to be considered in addition to full D-region ion chemistry to reproduce the observed NO increase, emphasizing the importance of ion chemistry for the NO formation in this altitude range.

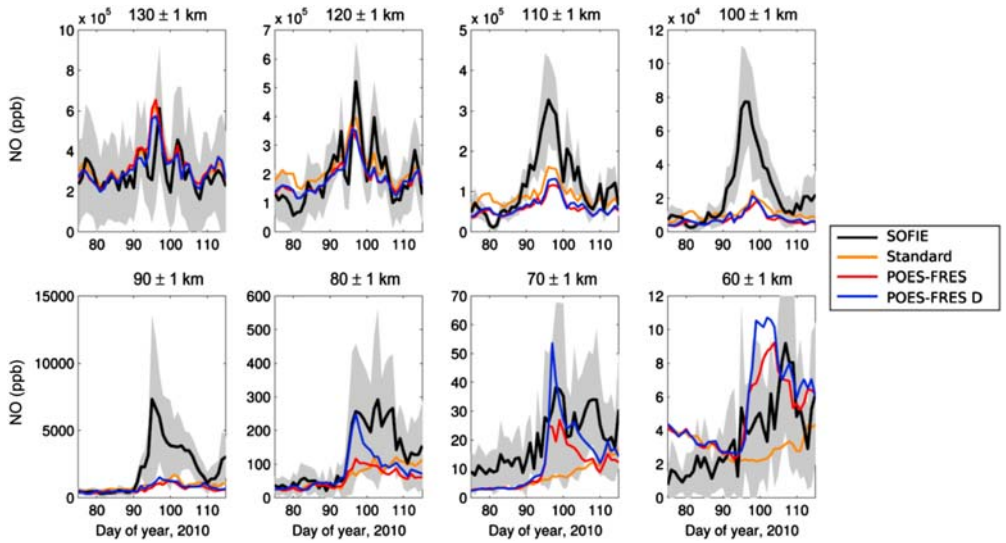

Figure 9.8 Daily averaged NO at high Southern latitudes in the mesosphere and lower thermosphere observed by solar occultation for ice experiment (SOFIE) (*black*) and modeled with different setting of the Whole Atmosphere Community Climate Model (WACCM): auroral forcing using only five-ion chemistry (Standard, *orange*); aurora + medium-energy electrons (MEE) forcing using constant NO_x formation (using a full range energy spectrum (POES-FRES), *red*) and aurora + MEE forcing using full D-region ion chemistry (POES-FRES D, *blue*). The shaded gray area is the spread of the observations (Smith-Johnsen et al., 2018).

9.3 The indirect effect of energetic particle precipitation

Atmospheric composition changes directly caused by precipitating particles, subject of the previous section, occur predominantly in the mesosphere and lower thermosphere, where ozone concentrations are relatively small. Particle-induced catalytic ozone destruction at these altitudes has only a weak impact on the radiative balance of the atmosphere and hence dynamics. However, it has already been proposed in the 1980s that dynamical coupling[1] could be responsible for transferring the chemical imprint of energetic particles down to the stratosphere, where most of the ozone resides (Solomon et al., 1982). This mechanism is well understood nowadays, and it is supported by a large number of observations and model studies.

The transport processes relevant to this coupling occur in the polar winter, during which the NO_x lifetime is long. NO created in the lower thermosphere, absent photodissociation and subsequent loss by Reaction (9.4), diffuses to the mesopause region on a timescale of hours to days. Large-scale transport then follows the residual circulation, a climatological circulation pattern characterized by ascent in the summer stratosphere and mesosphere, meridional transport near the mesopause directed toward the winter pole, and descent into the polar winter stratosphere (see Fig. 9.9). This circulation is driven mostly by gravity waves, propagating upward through the stratosphere and depositing momentum in the upper stratosphere and mesosphere. The wave energy drives the mesosphere far from radiative equilibrium, resulting in an equatorward circulation from the summer pole, and poleward in the winter hemisphere (see also, Fig. 9.3). Diabatic cooling at the winter pole leads, then, to strong downward transport of mesospheric air deep into the stratosphere with descent rates of 1−2 km/day in the lower mesosphere (Funke et al., 2014b). Transport to lower, sunlit latitudes by horizontal winds and eddies results in NO loss by photodissociation with a lifetime of hours to days. However, air that is not transported out of the polar region will eventually descend within the polar vortex, where downward transport is confined by the polar night jet, hence minimizing losses by photodissociation. Once in the stratosphere, the NO_x constituents rapidly convert to other NO_y constituents such as N_2O_5 and HNO_3 (Stiller et al., 2005). The photochemical lifetime of stratospheric NO_y is months to years, which thus defines the timescale over which it will participate in catalytic O_3 destruction.

EPP-generated NO_y of mesospheric and lower thermospheric origin contributes regularly to the polar winter NO_y column at 20−70 km by 10%−40% in the Southern Hemisphere (SH) and 1%−30% in the Northern hemisphere (NH) (Funke et al., 2014a). This so-called EPP indirect effect (IE) (Randall et al., 2007) causes significant variations of polar ozone, able to modify the thermal structure and winds in

[1] The term *dynamical coupling* is often used to describe coupling of atmospheric layers through wave forcing (Hamilton, 1999), but we use the term here in a broader sense, including also interactions between constituents and dynamical features like the large-scale descent during polar winter.

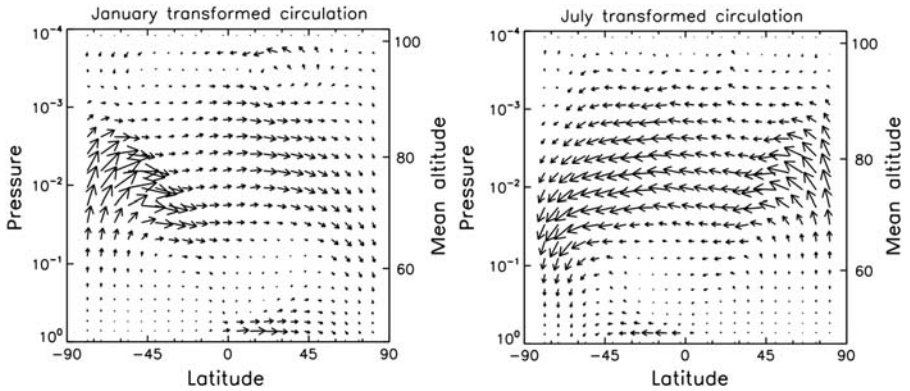

Figure 9.9 Arrows showing the direction of the transformed Eulerian mean winds, a measure of the residual circulation, from a multiyear climatology simulated by the climate model WACCM. The left panel shows the average for January and the right the average for July. *From Smith, A.K., 2012. Global dynamics of the MLT. Surv. Geophys. 33 (6), 1177–1230 (Smith, 2012). Provided under a creative commons license (https://creativecommons.org/licenses/by/2.0)*

the stratosphere, which in turn, modulate the strength of the Arctic polar vortex. The impact of energetic particle precipitation on upper stratospheric ozone also represents an important uncertainty in the evaluation of present and future ozone trends, particularly because of its long-term solar cycle dependence.

The solar cycle dependence is linked to the upper atmospheric EPP source, which is driven largely by geomagnetic activity. This has been clearly demonstrated by the tight correlation of observed EPP-generated NO_y amounts in the polar winter stratosphere with geomagnetic indices such as Kp or Ap (Seppälä et al., 2007; Randall et al., 2007; Sinnhuber et al., 2011; Funke et al., 2014b). These correlations are particularly strong in the Southern hemisphere (see Fig. 9.10, right panels). In the Northern hemisphere, dynamical variability is more pronounced, owing to stronger wave activity in midwinter; this results in a weaker net descent and hence smaller EPP-NO_y depositions into the stratosphere, as well as a less pronounced correlation with geomagnetic activity. However, surprisingly strong EPP indirect effects, much stronger than expected from the corresponding geomagnetic activity level, have been observed during several recent NH winters (see Fig. 9.10, left panels), particularly during January–March 2004, 2006, 2009, and 2013.

The extraordinarily strong mesospheric descent events during all these winters occurred in the recovery phase of sudden stratospheric warmings (SSWs). These are dramatic meteorological disturbances that affect the polar winter atmosphere in a wide altitude range. The key mechanism is the growth of upward-propagating planetary waves from the troposphere and their interaction with the mean zonal flow, which decelerates or reverses the eastward winter stratospheric jet causing downward

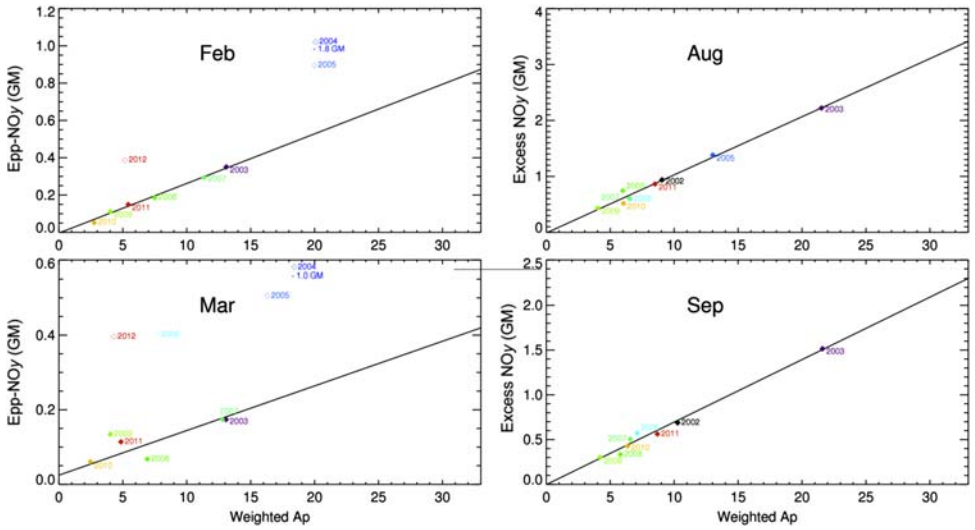

Figure 9.10 Correlations of EPP-NO_y amounts (in gigamoles, GM) descended below 70 km in the NH (*left*) and SH (*right*) winter hemispheres during February (NH), August (SH), March (NH), and September (SH) of the years 2002 to 2012 as function of the weighted Ap index, a composite of the Ap index of the preceding 3 months that has been adjusted by multilinear regression. *Adapted from Funke, B., Puertas, M.L., Holt, L., Randall, C.E., Stiller, G.P., von Clarmann, T., 2014b. Hemispheric distributions and interannual variability of NO_y produced by energetic particle precipitation in 2002–2012. J. Geophys. Res. 119 (23), 13565–13582.*

circulation in the stratosphere and adiabatic heating (Matsuno, 1971). The modified zonal mean flow changes the filtering conditions for gravity waves and induces a deceleration of the mesospheric descent and associated cooling above the stratopause. Thus in the core period of an SSW event, NO_x transport into the stratosphere is reduced. However, the changed dynamical conditions after the SSW favor the propagation of nonorographic gravity waves throughout the stratosphere and lower mesosphere. They eventually break in the upper mesosphere, providing enhanced westward momentum, which forces a poleward and downward residual circulation. These descent events, starting around 10 days after the SSW central date, are typically associated with an elevated stratopause (ES) at altitudes as high as 80 km (the climatological polar winter stratopause is located at around 50 km), as a consequence of adiabatic heating (e.g., Chandran et al., 2011). As a result, large amounts of NO_x are transported down to the stratosphere with a magnitude that is strongly affected by the timing of the event, resulting in higher amounts for midwinter SSW/ES events as compared with those occurring in late winter (see Holt et al., 2013, and Fig. 9.11). The reason for this behavior is twofold: on the one hand, the strength of the vertical winds following an event has a pronounced seasonal dependence, with a maximum in

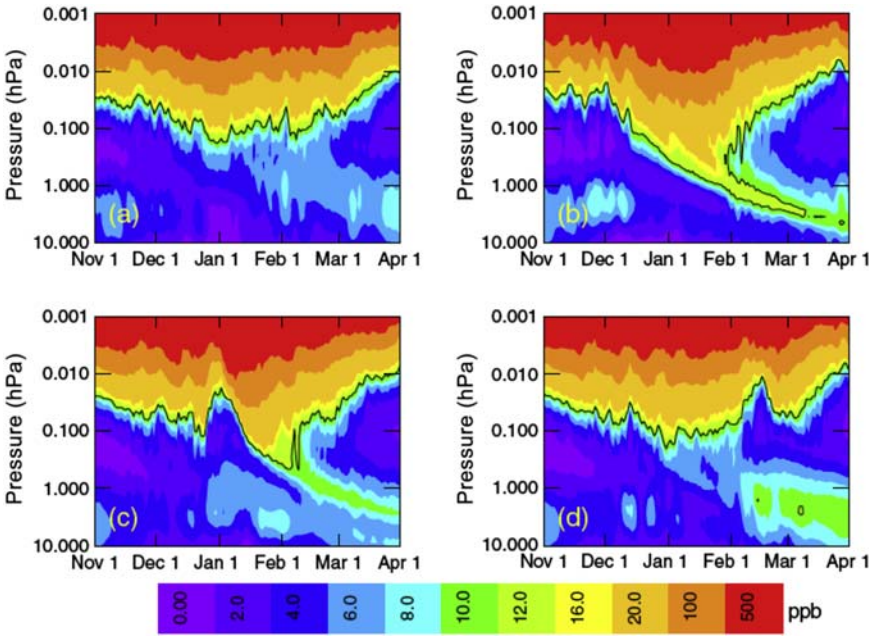

Figure 9.11 NO_x poleward of 70°N simulated with the climate model WACCM for winters with (a) no major SSW or ES event, (b) a December SSW/ES event, (c) a January SSW/ES event, and (d) a February SSW/ES event. *From Holt, L.A., Randall, C.E., Peck, E.D., Marsh, D.R., Smith, A.K., Lynn Harvey, V., 2013. The influence of major sudden stratospheric warming and elevated stratopause events on the effects of energetic particle precipitation in WACCM. J. Geophys. Res.*

midwinter, and on the other hand, the availability of NO is ruled by the illumination conditions in the EPP source region.

9.3.1 Observations

Satellite observations from the past three decades have provided a clear picture of the EPP IE occurring in every polar winter with a magnitude modulated by the solar cycle. The first experimental evidence for downward transport of thermospheric NO_x from satellite data was given by the Limb Infrared Monitor of the Stratosphere (LIMS), which measured enhanced upper stratospheric and mesospheric NO_2 levels of up to 175 ppbv at polar night conditions during the 1978–79 NH winter (Russell et al., 1984). NO_2 is a good proxy for NO_x at dark conditions below approximately 60 km, where NO is nearly entirely converted to NO_2. Similar enhancements of nighttime polar winter NO_2 in both hemispheres were observed by the Improved Stratospheric and Mesospheric Sounder (ISAMS) (Callis and Lambeth, 1998) and by the Atmospheric Trace Molecule Spectroscopy (ATMOS) experiment (Rinsland et al., 1999) during 1991–92. However, these early observations were restricted to single

polar winters and did not allow conclusions as to whether the observed NO_x enhancements were sporadic events or regular polar winter features.

Longer lasting NO_x observations in the polar winter stratosphere, providing evidence for a regular EPP IE, started in 1992 with the Halogen Occultation Experiment (HALOE) on the Upper Atmospheric Research Satellite (UARS, operational until 2005) (e.g., Siskind, 2000) and the Polar Ozone and Aerosol Measurement (POAM II and III) instruments, operating during 1993–96 and 1998–2005, respectively (e.g., Randall et al., 1998, 2001). Since 2004, observations of stratospheric EPP-NO_x enhancements are provided by the still operational Atmospheric Chemistry Experiment Fourier Transform Spectrometer (ACE-FTS) on the Canadian SciSat platform (e.g., Rinsland et al., 2005; Randall et al., 2007). However, all these instruments have been employing the solar occultation technique and are thus limited to observations of sunlit areas. Multiyear observations of EPP-NO_x, including the polar night regions, were first taken by the European Envisat instruments Global Ozone Monitoring by Occultation of Stars (GOMOS) (Seppälä et al., 2007) and the Michelson Interferometer for Passive Atmospheric Sounding (MIPAS) (Funke et al., 2005), both operational during 2002–12.

The main difficulty in quantifying the total amount of EPP-NO_x from NO_x observations resides in the discrimination of the upper atmospheric contribution that has descended into the polar stratosphere from the stratospheric background produced by oxidation of N_2O. Tracer correlations are commonly used to overcome this obstacle. For example, Siskind (2000) clearly demonstrated the existence of NO_x-rich upper atmospheric air in the Southern hemisphere polar winter stratosphere by correlating CH_4 and NO_x measured by HALOE. Funke et al. (2005) determined a net amount of NO_x of 2.4 gigamole (GM) being deposited into the stratosphere during the Antarctic winter of 2003 from global MIPAS observations. This accounts for about 9% of the NO_x generated locally in the stratosphere by oxidation of N_2O. Using HALOE occultation measurements, Randall et al. (2007) estimated the amount of EPP-NO_x descending into the Antarctic stratosphere to range from 0.1 to 2.6 GM per year during 1992–2005. CH_4–NO_x correlations have also been employed by Holt et al. (2012) to calculate the EPP-NO_x amounts crossing the stratopause in the 1979 and 2002–09 Northern hemisphere winters from LIMS, MIPAS, and ACE-FTS observations, resulting in generally smaller depositions (0.05–0.7 GM) than those in the Southern hemisphere, with the exception of the late 2003–04 winter (2.7 GM), which was characterized by a strong SSW/ES event in conjunction with a high level of geomagnetic activity.

In order to determine the long-term impact of the EPP IE on the entire stratosphere, however, global observations of all constituents of the NO_y family ($[NO_y] = [NO] + [NO_2] + [HNO_3] + 2[N_2O_5] + [ClONO_2]$) are required. Such observations have been provided by the MIPAS instrument. Funke et al. (2014a) used these

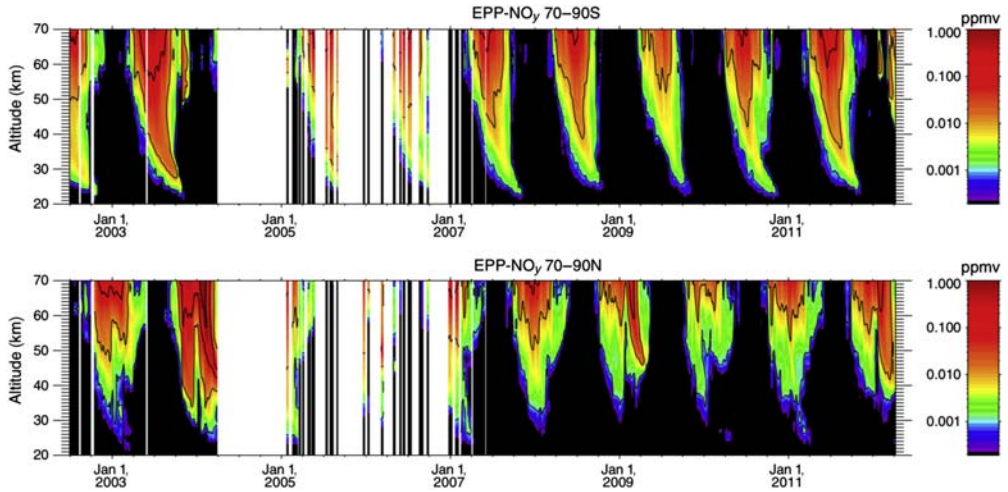

Figure 9.12 Temporal evolution of the EPP-NO_y volume mixing ratios observed by MIPAS at 70–90°S (*top*) and 70–90°N (*bottom*) during the Envisat mission lifetime (July 2002 to March 2012). *From Funke, B., López-Puertas, M., Stiller, G.P., von Clarmann, T., 2014a. Mesospheric and stratospheric NOy produced by energetic particle precipitation during 2002-2012. J. Geophys. Res. 119, 4429–4446.*

MIPAS NO_y measurements, together with colocated CH_4 and CO tracer measurements to calculate a 10-year record of EPP-NO_y in the 20–70 km vertical range with global coverage (see Fig. 9.12). This data set clearly demonstrates a regular EPP IE in the entire stratosphere with highest EPP-NO_y concentrations up to one part per million by volume (ppmv) in the winter solstice mesosphere, decreasing continuously with time and toward lower altitudes. Springtime peak concentrations of a few parts per billion by volume (ppbv) were observed at altitudes as low as 22–25 km. For comparison, peak concentrations of stratospheric NO_y produced by N_2O oxidation are on the order of 15 ppbv.

A question central to the understanding of possible climate impacts of the EPP IE is about the impact on stratospheric ozone. Although EPP-induced stratospheric ozone loss has been postulated by model experiments many times, the experimental determination of this effect is challenging because the pronounced background variability of polar stratospheric ozone makes an unequivocal attribution of ozone changes to EPP difficult. Observational evidence for ozone losses by the EPP IE has therefore been given only in the past few years by statistical analysis of multiyear ozone records in dependence of geomagnetic activity. For example, Fytterer et al. (2015a) applied a compositing technique to ozone data taken during 2002–11 by MIPAS, the Sounding of the Atmosphere using Broadband Emission Radiometry (SABER) instrument on board the Thermosphere Ionosphere Mesophere Energetics and Dynamics

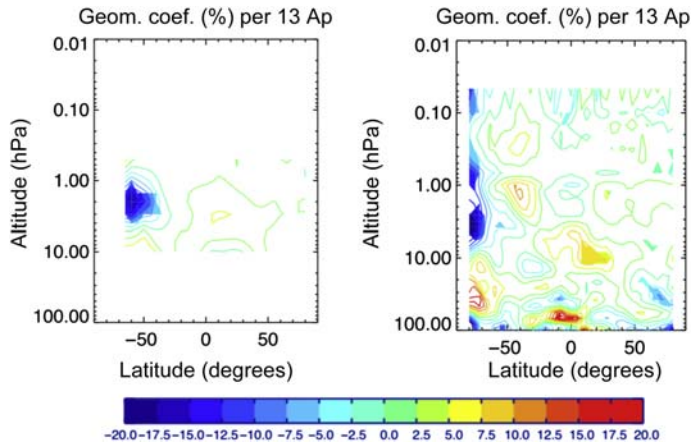

Figure 9.13 Percentage August ozone responses to geomagnetic variations expressed by changes of 13 Ap units (approximately the solar cycle amplitude) obtained by multilinear regression of observational ozone records based on SBUV data from 1979 to 2014 (*left*) and from MLS from 2005 to 2014 (*right*). *From Damiani, A., Funke, B., López-Puertas, M., Santee, M.L., Cordero, R.R., Laurenza, M., et al., 2016. Energetic particle precipitation: a major driver of the ozone budget in the Antarctic upper stratosphere. Geophys. Res. Lett. 2016GL068279.*

(TIMED), and the Sub-Millimetre Radiometer (SMR) on the Odin satellite. Damiani et al. (2016) used multilinear regression to analyze the NOAA Solar Backscatter Ultraviolet Instrument (SBUV) ozone merged cohesive climate data record and observations from the MLS on Aura spanning the periods 1979−2014 and 2005−14, respectively (see Fig. 9.13). In both studies, the analysis was restricted to SH winters, during which dynamical variability is less pronounced than in NH winters. The observed responses indicate that the EPP IE introduces solar cycle variations of Antarctic winter stratospheric ozone with a peak amplitude of about 15% at around 2 hPa (35−40 km) in late winter (i.e., August).

Evidence for changes in stratospheric zonal winds and temperatures related to high geomagnetic activity during high-latitude winter has been found in meteorological reanalysis data (Lu et al., 2008; Seppälä et al., 2013), with a warming in the late winter (March/September) upper stratosphere in both hemispheres. No analysis exists to date for the early winter and midwinter Southern hemisphere, but an analysis of Northern hemisphere winters suggests that this upper stratosphere warming already starts to form during midwinter (December), with an associated cooling area in the lower stratosphere that moves down throughout the winter and has vanished by March (Seppälä et al., 2013). These temperature changes are balanced by an increase of the zonal wind during midwinter, which, however, changes signs in spring (Seppälä et al., 2013), leading to a distinctive negative correlation between zonal wind speed and geomagnetic activity in the springtime (April) midstratosphere (Lu et al., 2008). However, as

meteorological reanalysis data for the stratosphere exist only since 1957, the sample size is small, and considering the high variability of the wintertime stratosphere, the attribution of the signals to energetic electron precipitation (EEP) appears difficult.

9.3.2 Model experiments

At present, many chemistry–climate models account for EPP-induced ionization and its chemical impact on the neutral atmosphere, which is required for the simulation of atmospheric EPP effects and ultimately for the investigation of potential EPP–climate links. However, only a few models such as the Whole Atmosphere Community Climate Model (WACCM), the Hamburg Model of the Neutral and Ionized Atmosphere (HAMMONIA), or the extended version of the ECHAM/MESSy Atmospheric Chemistry (EMAC) model system extend up into the lower thermosphere, where a large fraction of EPP-induced odd nitrogen production occurs. Other models have their upper lid in the upper mesosphere and require an odd nitrogen upper boundary condition (UBC), accounting for EPP production higher up, for simulating the introduced EPP IE in the model domain. In some model studies, the UBC was taken directly from NO_x observations (e.g., Reddmann et al., 2010; Salmi et al., 2011; Funke et al., 2017), which, however, implies a restriction to the relatively short time period spanned by the observations. In other cases, a simple parameterization in dependence of the seasonally averaged Ap index was employed (e.g., Baumgaertner et al., 2011; Rozanov et al., 2012), enabling extended simulations over multidecadal time periods. A semiempirical UBC model has been developed that has been trained with the EPP-NO_y record inferred from MIPAS observations (Funke et al., 2016). Interannual variations of the EPP indirect effect at a given time of the winter are related to variations of the EPP source strength, the latter being considered to depend linearly on the Ap index. A Green's function approach is employed to describe the impact of vertical transport on this modulation. Interannual variations of the EPP-NO_y seasonal dependence, driven by variations of chemical losses and transport patterns, are not considered in the standard mode of the UBC model. However, optionally, episodes of accelerated descent associated with ES events during Arctic winters can be considered by means of a dedicated parameterization, taking into account the dependence of the EPP-NOy amounts and fluxes on the event timing.

Sinnhuber et al. (2018) employed this UBC model in the EMAC model with simulations spanning the 2002–10 period and obtained both NO_x and ozone responses to the EPP IE in reasonable agreement with observational analysis (see Fig. 9.14). They also determined the radiative responses to the modeled ozone reduction due to EPP characterized by a cooling of up to 0.7 K/day in the sunlit late winter stratosphere due to reduced UV absorption and a heating of up to 0.5 K/day in the dark midwinter stratosphere due to reduced cooling to space in the infrared ozone bands. These polar radiative responses to EPP have a similar magnitude as those related to solar UV

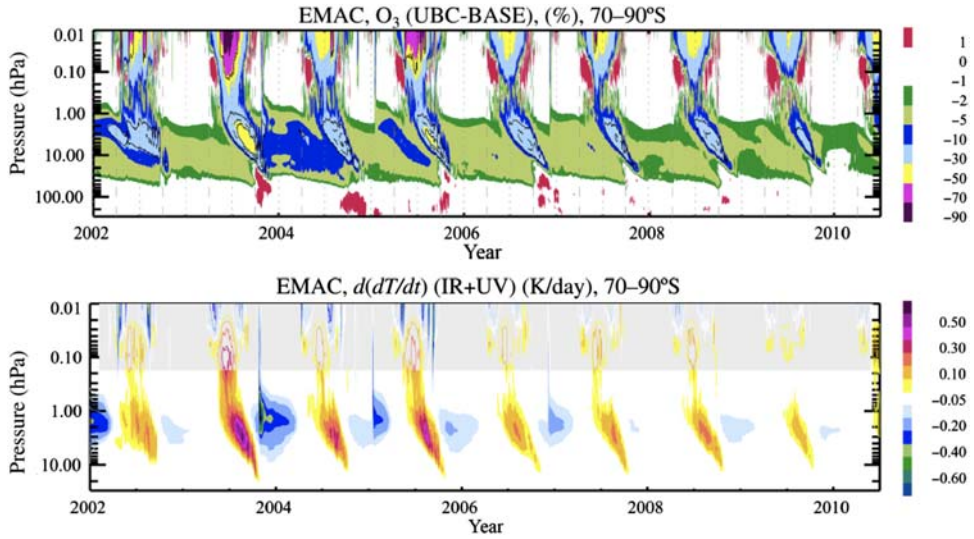

Figure 9.14 *Top*: Relative ozone anomalies due to energetic particle precipitation at high southern latitudes (70−90°S), calculated as the difference of the EMAC model runs with and without particle impact. *Bottom*: Changes in daily net radiative (shortwave and longwave) heating rates (K/day) due to particle-induced ozone changes derived from the model output (gray shaded heating rates above 0.2 hPa are likely affected by the neglect of non-LTE effects and should not be considered). *From Sinnhuber, M., Berger, U., Funke, B., Nieder, H., Reddmann, T., Stiller, G., et al., 2018. NO_y production, ozone loss and changes in net radiative heating due to energetic particle precipitation in 2002−2010. Atmos. Chem. Phys. 18, 1115−1147. Provided under a creative commons licence (https://creativecommons.org/licenses/by/3.0)*

variability in the tropics and are capable, through dynamical feedback mechanisms, to influence the lower atmosphere and the ocean (e.g., Gray et al., 2010).

A large number of model studies addressed the EPP IE and mesospheric descent during dynamically perturbed NH winters. For example, Salmi et al. (2011) and Päivärinta et al. (2016) used FinROSE with constrained NO_x at the upper boundary (80 km) for both early 2009 and 2012. The results show that FinROSE is able to qualitatively reproduce the downward descent of NO_x from the MLT region into the stratosphere, but the actual NO_x amounts can differ significantly from the observations. McLandress et al. (2013) used a version of the Canadian Middle Atmosphere Model (CMAM) that was constrained by meteorological reanalysis data up to 1 hPa to examine the impacts of parameterized orographic and nonorographic gravity wave drag (GWD) on the zonal mean circulation of the mesosphere during the perturbed NH winters of 2006 and 2009 in comparison with temperature and carbon monoxide (CO) observations from Aura/MLS. They found that nonorographic GWD is primarily responsible for driving the circulation that results in the descent of CO from the thermosphere following the warmings. Randall et al. (2015) investigated the NO_x descent during the Arctic winter/spring of 2004 with WACCM simulations that were constrained by Modern-Era

Retrospective Analysis for Research and Applications (MERRA) data below approximately 50 km. They found that their simulated NO_x, although qualitatively reproducing the enhanced descent after the ES event, was up to a factor of 5 too low as compared with satellite observations. This underestimation was attributed to missing NO production by high-energy electrons in the mesosphere in combination with an underestimation of mesospheric descent during the recovery phase after the SSW. Siskind et al. (2015) compared simulations of mesospheric tracer descent in the winter and spring of 2009 with two versions of WACCM, one constrained with data from MERRA, which extends up to 50 km, and the other constrained to the Navy Operational Global Atmospheric Prediction System–Advanced Level Physics High Altitude (NOGAPS-ALPHA), which extends up to 92 km. By comparison with SOFIE data they showed that constraining WACCM to NOGAPS-ALPHA yields a dramatic improvement in the simulated descent of enhanced NO_x and very low methane. Most of these studies suggest that the model representation of the perturbed dynamics during NH winters with SSW and ES events has a crucial impact on the simulated amount of NO_x transported into the stratosphere and that a proper parameterization of unresolved GWD is key to achieving agreement with observations.

The High Energy Particle Precipitation in the Atmosphere (HEPPA)-II study (Funke et al., 2017) compared simulations from eight atmospheric models with tracer and temperature observations from seven satellite instruments in order to evaluate the EPP IE during the perturbed NH winter of 2008–09. Most models provided a good representation of the mesospheric tracer descent in general, and the EPP IE in particular, during the unperturbed (pre-SSW) period of this winter. After the ES event, however, modeled mesospheric and stratospheric NO_x distributions deviated significantly from the observations. The too-fast and early downward propagation of the NO_x tongue, encountered in most simulations, coincides with a temperature high bias in the lower mesosphere (0.2–0.05 hPa), likely caused by an overestimation of descent velocities (see Fig. 9.15). In contrast, upper mesospheric temperatures (at 0.05–0.001 hPa) were generally underestimated by the high-top models[2] after the onset of the ES event, emphasizing the need for model improvements, particularly with respect to the representation of gravity waves, in order to allow for a better description of the EPP indirect effect under these particular conditions.

9.4 Possible surface climate impacts of energetic electron precipitation

Investigations of data such as temperatures, wind fields, and geopotential height provided by meteorological analyses suggest that anomalies in the leading mode of the

[2] High-top models with their upper lid above the mesopause, covering the lower thermosphere up to at least 120 km

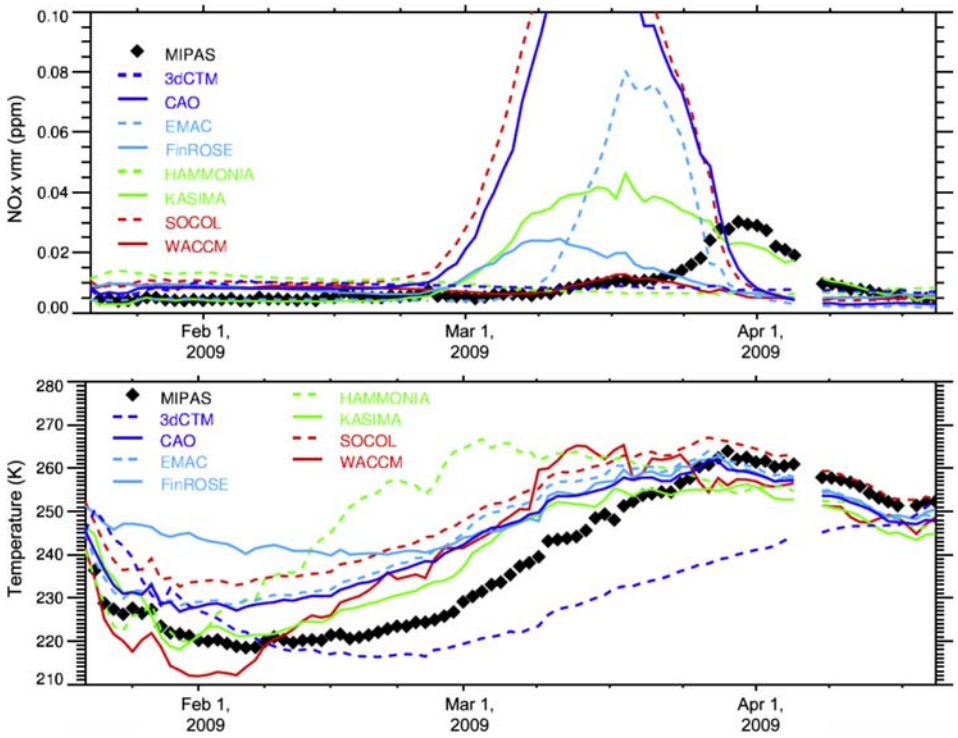

Figure 9.15 Observed (MIPAS) and modeled temporal evolutions of NO_x at 0.5 hPa (*top*) and of temperature at 0.2 hPa (*bottom*) at 70–90°N during the elevated stratopause event in 2009. Modeled NO_x peaks show a large spread in magnitude and occur systematically too early. Temperatures at 0.2 hPa are overestimated by most models during the event, hinting at too-strong lower mesospheric descent as a cause for the earlier NO_x peak occurrence in the models. 3dCTM, 3-dimensional Chemistry-Transport Model 3dCTM; SOCOL and CAO-SOCOL, the modelling tools for SOlar Climate Ozone Links studies; KASIMA, the Karlsruhe SImulation Model of the middle Atmosphere. *From Funke, B., Ball, W., Bender, S., Gardini, A., Harvey, V.L., Lambert, A., et al., 2017. HEPPA-II model–measurement intercomparison project: EPP indirect effects during the dynamically perturbed NH winter 2008–2009. Atmos. Chem. Phys. 17 (5), 3573–3604. Provided under a creative commons licence (https://creativecommons.org/licenses/by/3.0)*

midlatitude to high-latitude tropospheric circulation, the Arctic oscillation, sometimes extend over the entire atmosphere from the surface up to 10 hPa (around 30 km) particularly during Northern hemisphere winters, implying a dynamical coupling over a large vertical range, up to at least the midstratosphere (Baldwin and Dunkerton, 1999). In some winters, a clear downward motion of these anomalies is observed, suggesting a dynamical coupling of these signals from the stratospheric circulation down to the surface (Baldwin and Dunkerton, 1999, 2005). Though the Arctic oscillation is defined as the first principal component of the geopotential height, it is also linked to typical patterns of temperature and pressure anomalies acting on the prevailing wind systems,

in both the stratosphere and the troposphere. Results from climate model studies indicate that large changes to stratospheric temperatures can indeed have a significant impact on tropospheric regional weather systems, both in the Northern hemisphere (Scaife et al., 2005) and in the Southern hemisphere, where an impact of the Antarctic ozone hole on regional climate is well established (Thompson et al., 2011; World Meteorological Organization, 2014).

As energetic particle precipitation influences ozone in the midstratosphere to upper stratosphere during polar winter owing to the indirect effect (see Section 9.3), and ozone dominates both shortwave radiative heating and longwave radiative cooling in this altitude region, energetic particle precipitation is assumed to contribute to the so-called *top-down* solar forcing of the climate system (Matthes et al., 2017). The mechanism of the top-down solar forcing works as described in the following: The starting points for the top-down coupling are changes in the radiative balance. For energetic particle precipitation, these primarily affect the high latitude upper stratosphere, for changes in the solar UV flux, the tropical stratopause. These lead to changes in the large-scale temperature gradients, altering the thermally driven zonal winds in the stratosphere. The speed and direction of the zonal winds determine how waves excited in the lower atmosphere—mostly planetary-scale Rossby waves, but also much more localized gravity waves—propagate through the middle atmosphere. Though these are intrinsic changes to the middle atmosphere circulation, restricted to the altitude region where the initial disturbance took place (the upper stratosphere and stratopause) and above, there are two ways how this might also affect the altitude below. On the one hand, dissipation of planetary-scale waves drives the meridional circulation of the stratosphere, which is poleward and downward during winter. Changes to the altitude where waves dissipate thus can transport a signal both downward and poleward; this is the suggested pathway for the top-down coupling of a solar UV signal at the tropical stratopause (Kodera and Kuroda, 2005). Another possibility is that waves are not (only) dissipated, but they are also reflected downward, and this would have a more immediate impact on the atmosphere below, by increasing wave activity there (Reichler et al., 2005). Note that in both cases, the coupling from the stratosphere to the troposphere acts via waves excited in the troposphere, and the stratosphere modulates only a signal that comes from below; in this sense, any impact of the top-down coupling on tropospheric weather systems has to be statistical in nature.

Another coupling mechanism between particle precipitation and tropospheric weather that has been speculated is via the global electric circuit, where the downward current density is affected by precipitating particles from GCRs, relativistic electrons, and SPEs (Tinsley et al., 2007). Changes in the downward current density are then supposed to affect aerosol and cloud formation. This coupling would act very fast, without modulation by the middle atmosphere (Tinsley et al., 2007). Laboratory

measurements within the Cosmics Leaving OUtdoor Droplets (CLOUD) experiment at the Conseil Européen pour la Recherche Nucléaire (CERN) have indicated that ionization enhances the nucleation rate of small (<2.5 nm in diameter) aerosol particles for a large range of aerosol precursor substances—H_2SO_4, NH_3, monoterpenes, and nitrogen oxides (Wagner et al., 2017), particularly at low temperatures (Kirkby et al., 2011). However, field measurements so far do not confirm these results (Kirkby et al., 2011; Wagner et al., 2017), and cloud cover observations do not show a clear trend or solar cycle variation (e.g., Damon and Laut, 2004), indicating that other processes might be more important for aerosol or cloud formation.

Short-term variations of surface temperatures and geopotential height observed over Antarctica have been shown to vary with levels of geomagnetic activity (Francia et al., 2015) and the magnetic field component B_y (Lam et al., 2014); these are interpreted as indications of quick coupling via the global electric circuit, possibly involving the formation of aerosol or cloud condensation nuclei. The very short delay of only a few days between the observed geomagnetic disturbance and the response of the temperature (Francia et al., 2015), as well as the fact that anomalies progress upward throughout the troposphere (Lam et al., 2014) strongly suggest that these short-term variations are not driven by top-down coupling.

Analyses of surface air temperatures from 1958–2006, on the other hand, are interpreted as evidence of a top-down coupling via EEP and the EEP indirect effect; these show a pattern of temperature anomalies when contrasting years with high and low geomagnetic activity similar to a positive phase of the Northern Annular Mode, a circulation pattern closely related to the Arctic Oscillation (Seppälä et al., 2009), with cooler regions over Greenland and Northern North America, and warmer regions over Northern Europe and Northwest Asia during midwinter. A similar pattern related to the Southern Annular Mode is found during Southern hemisphere midwinter. However, while the results are statistically significant, and amplitudes can reach more than 4 K, the attribution to geomagnetic activity seems not unambiguous. Tropospheric temperatures are affected by a wide range of driving forces including volcanic eruptions and long-term trends, but also by major stratospheric warmings and possibly solar UV and total solar irradiance variation (Lean and Rind, 2008; Kidston et al., 2015). Seppälä et al. (2009) took this into account to some extent by excluding years with volcanic eruptions and major stratospheric warmings and considering only moderate and low solar activity. While this leads to a clear and strong signal, the number of years used for the composite analysis is then quite low, with six high-Ap and five low-Ap years. As data are not detrended, results could presumably be affected by an aliasing with increasing surface air temperatures due to global warming, a problem encountered in all observation or modeling studies if time series are rather short or have not been detrended. This would present a problem particularly at Northern high latitudes, as temperatures there in the past two

decades have increased much faster than globally or at midlatitudes and low latitudes (the so-called Arctic amplification, see, for example, Cohen et al., 2014; Pithan and Mauritsen, 2014). A much longer period of time from 1869 to 2009, spanning 13 solar cycles, was investigated by Maliniemi et al. (2014). In this case, surface air temperatures were used, which have been corrected for long-term trends first, and data are separated into four phases of the solar cycle: minimum, ascending, maximum, and descending. During Northern hemisphere winter, patterns of anomalies are observed throughout the solar cycle, which again resemble the Northern Annular Mode, with similar patterns in the ascending and maximum phase, but a change in sign and strongest amplitudes during the descending phase of the solar cycle, see Fig. 9.16. This is interpreted to be a confirmation of the results of Seppälä et al. (2009) and as further evidence of a response to electron precipitation, as radiation belt electron precipitation is strongly increased during the transition from maximum to minimum (Baker et al., 1993; Maliniemi et al., 2014). Analyses of solar signals in

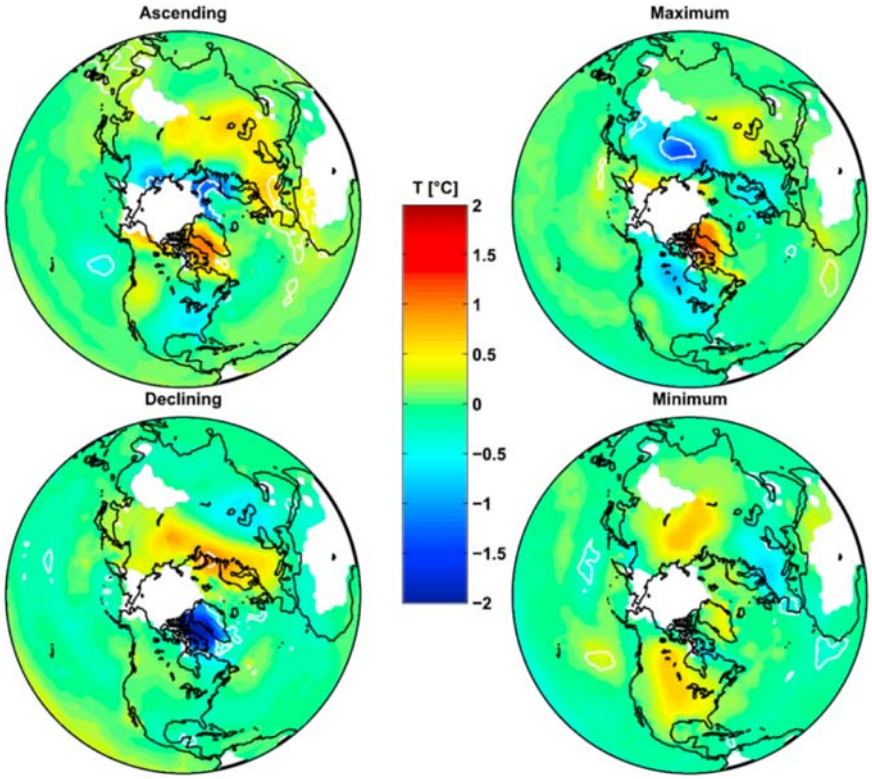

Figure 9.16 Northern hemisphere winter (DJF) anomalies of surface air temperature in the ascending, maximum, descending, and minimum phase of the solar cycle, based on 141 years of data. *From Maliniemi, V., Asikainen, T., Mursula, K., 2014. Spatial distribution of northern hemisphere winter temperatures during different phases of the solar cycle. J. Geophys. Res. 119 (16), 9752–9764.*

sea-level pressure show distinct patterns with a temporal lag of 2–5 years (Gray et al., 2013). Results in this case are interpreted as an indication for a positive-feedback mechanism involving the ocean mixing layer, which contains and transports heat. The idea is that the atmospheric top-down coupling caused by the UV impact on the tropical stratopause region projects onto the North Atlantic Oscillation which, in turn, amplifies the atmospheric response with a lag of 2–3 years due to the persistence and memory of the ocean (Scaife et al., 2013). The mechanism is explained solely as a response to the solar irradiance maximum, but as energetic electron fluxes and geomagnetic activity peak in the declining phase of the solar cycle 2–4 years after the peak of the solar maximum, the observations are consistent with the observed surface temperature responses discussed by Seppälä et al. (2009) and Maliniemi et al. (2014), and could presumably also be explained by a top-down coupling mechanism involving energetic electron precipitation.

Some evidence that the mechanism behind the observed solar signals in the troposphere is related to downward coupling from the stratosphere is given by analyses showing an apparent impact of the phase of the quasi-biennal oscillation (QBO) on the magnitude of the surface response (Maliniemi et al., 2013, 2016). The QBO is an oscillation in the direction of the equatorial zonal winds restricted to the middle atmosphere, which affects the propagation and reflectivity of stratospheric planetary-scale waves. Downward propagating patterns of the Northern Annular Mode lasting for at least 45 days and extending from the stratopause to the surface have also been observed in Northern hemisphere polar winter in relation to solar wind pressure (Lu et al., 2013), again emphasizing a top-down coupling related to energetic electron precipitation. However, it seems difficult to separate top-down coupling of an EEP response and a lagged response from the ocean unambiguously from observations alone owing to the congruence in timing throughout the solar cycle.

Model experiments have been carried out investigating the potential of both mechanisms and have shown that both the top-down coupling driven by the EEP indirect effect on stratospheric ozone (Rozanov et al., 2005, 2012; Baumgaertner et al., 2011; Semeniuk et al., 2011; Meraner and Schmidt, 2018) and of transport and delayed release of heat from ocean surface and near-surface water (Scaife et al., 2013) could explain the observation of a strong impact on the Northern Annular Mode a few years after the maximum of the solar cycle. In particular, the model results of Rozanov et al. (2005, 2012); Meraner and Schmidt (2018) all predict a pattern of warming and cooling areas resembling the Northern Annular Mode roughly consistent with observations, though amplitudes vary from less than 1 K (Rozanov et al., 2012; Meraner and Schmidt, 2018) to more than 2 K (Rozanov et al., 2005), less than observed in all other cases. This might indicate that both mechanisms play a role, and further chemistry–climate model studies incorporating both mechanisms separately and together will be necessary to resolve this issue (Matthes et al., 2017).

9.5 Open issues

Despite the recent advances in the investigation of atmospheric impacts of energetic electron precipitation on the middle atmosphere and their potential climate impacts, many open questions and issues remain. Most of them are related to the current limitations of available observations, laboratory measurements, and climate model capabilities. Others are caused by the lack of process understanding, particularly of processes related to the possible mechanisms that could lead to energetic electron impacts on regional surface climate. Summarized below are the major issues and obstacles for a better understanding and prediction of the atmospheric impacts of energetic electron precipitation.

- *Uncertainties in the magnitude and spatiotemporal distribution of atmospheric ionization by precipitating energetic electrons.* A good knowledge of the vertical shape of the atmospheric ionization profile is crucial for constraining direct and indirect atmospheric impacts of energetic electron precipitation. This is particularly relevant in the MLT region, where dynamical factors such as the interplay between diffusion and advection induce huge variations of the magnitude of particle-induced composition changes as a result of only small variations in the vertical distribution of ionization. The existing MEPED instrument on POES suffers from poor energy resolution, directly translating into poor vertical resolution of the derived atmospheric ionization. Further issues are contamination by medium-energy protons and uncertainties in terms of the fraction of precipitation observed. There is also poor coverage of relativistic electrons (>1 MeV), resulting in poor knowledge of direct EPP impacts in the upper stratosphere. Finally, there is a lack of pitch angle–resolved measurements over a wide angle range, which would allow a true measurement of all the electron fluxes precipitating into the atmosphere.
- *Implementation into chemistry–climate models.* The implementation of atmospheric ionization by EPP in chemistry–climate models is relevant in this context as well. High-top[2] chemistry–climate models used for multidecadal or centennial model experiments have to parameterize the impact of low-energy auroral electrons acting on the lower thermosphere. One approach used—for example, in the WACCM model—is scaling of a monoenergetic electron beam with the hemispheric auroral power; this may result in discrepancies with the "true" ionization rate profile and hence the vertical shape of the lower thermospheric NO density maximum (e.g., Hendrickx et al., 2017; Smith-Johnsen et al., 2018).
- *Uncertainties in the description of the direct chemical impact.* Another problem related to the implementation of the electron impact in chemistry–climate models is the choice of how detailed the described ion chemistry impact will be; the choice of parameterization for NO_x and HO_x production, as described in Section 9.2.7, will have an impact on the models' results. However, even if a full D-region ion

chemistry model is applied (e.g., as described in Verronen et al., 2016), large uncertainties remain. These are related, on the one hand, to the formation of primary species via Reactions (9.1a)–(9.1e), particularly because it is not clear how many of the excited states of N and O and their ions should be taken into account, as well as the partitioning between those. Also, the rates of the ion chemistry reactions carry large uncertainties; in some cases, no laboratory measurements exist and rates are assumed by assumptions of similarity with other reactions. This is most evident for the recombination reactions between positive and negative ion species, where commonly the same rate is used for all possible reactions (e.g., Sinnhuber et al., 2012; Verronen et al., 2016).

- *Lack and limitations of middle atmosphere observations*. Trace gas measurements in the middle atmosphere are difficult, particularly in its upper part, where most of the particle-induced composition changes occur. Except for isolated in situ measurements by instrumentation on rockets this region is accessible only by remote sensing techniques from space and ground. Limitations of these techniques with respect to spatial sampling, dependence on illumination, and vertical resolution often make it difficult to draw robust and/or quantitative conclusions about the magnitude and spatial variability of particle-induced chemical changes. This is particularly the case for NO in the MLT region because of its large vertical gradients and its pronounced variability. Nevertheless, the "Golden Age" of space observation of the past two decades has offered a unique opportunity to advance our knowledge of the energetic particle impact on the atmospheric composition. However, roughly two decades of observations are not sufficient for capturing possible long-term changes of both the direct chemical impacts (caused by changes of the ionization levels related to secular variations of the Sun) and the dynamical coupling of these impacts to the stratosphere (due to changing circulation patterns as consequence of greenhouse gas forcing). Perspectives for the future are not promising: several space missions targeting middle atmosphere observations have recently ended (e.g., Envisat) or are phasing out in the next few years (e.g., Aura, TIMED, Odin), with no replacements planned in the near future. As a consequence, an observational gap is expected that will seriously harm the continuity of long-term observational records of NO_x, temperature, and dynamical tracers such as CO and CH_4.
- *Deficiencies in the dynamical representation of the mesosphere and lower thermosphere in climate models*. The accurate representation of the dynamics in the MLT region in climate models is crucial not only for achieving quantitative agreement of the observed and simulated EPP IE, but also to properly consider dynamical modulations of the spatiotemporal distribution of NO in the EPP source region. The dynamics of the mesosphere and lower thermosphere is driven largely by small-scale waves, which are not explicitly considered in most climate models owing to limitations of horizontal resolution. Instead, parameterizations are often used to

emulate the impact of such waves. As mentioned in Section 9.3, deficiencies of these parameterizations are the likely cause of the mismatch between modeled and observed NO_x descent during dynamically perturbed NH winters. Currently, large efforts are being made to improve these parameterizations. Future progress will also benefit from the growing computing power, allowing the increase of horizontal model resolution, and hence, possibly allowing for explicit simulation of small-scale waves and their propagation through the atmosphere.

- *Lack of understanding of mechanism for particle-induced surface climate impacts*. As mentioned in the previous bullet point, unequivocal observational evidence for particle-induced surface climate signals has yet not been provided. This does not necessarily mean that such signals are negligible; rather, their identification with a high degree of confidence suffers from the dominance of the intrinsic background variability of the climate system and, possibly, from the nonlinearity of the responses caused by complex (dynamical) coupling mechanisms. The duration of observational records or meteorological reanalysis data sets are mostly too short to provide a meaningful statistical basis for the detection and attribution of particle-induced surface signals. Further, standard methods for statistical time-series analysis such as multilinear regression or compositing techniques do not account for possible nonlinearities. Regarding the latter aspect, progress has currently been achieved by the application of more advanced statistical methods, such as dynamical linear modeling (Laine et al., 2014). Of course, climate models are not limited by the temporal availability of observational records and would hence be allowed, in principle, to overcome the limitations of the observational analysis. However, it is not clear whether climate models include all relevant processes that might act (we simply do not know them for sure yet) and whether these are accurately represented. Although climate models roughly agree on the magnitude of EPP-induced ozone changes, at present, the same models often give different answers to the question of whether energetic electron precipitation is able to influence surface climate. However, the situation is not hopeless, and future progress will depend on advances in statistical analysis methods and model development.

9.6 Summary

Energetic electrons accelerated in the radiation belts and the magnetosheath precipitate into the high-latitude atmosphere during geomagnetic storms and auroral substorms. They affect the chemical composition, temperatures, and wind fields of the atmosphere from the lower thermosphere possibly down to the surface via a chain of processes starting with collision reactions and fast ion chemistry forming nitric oxide in the mesosphere and lower thermosphere and hydrogen oxide in the mesosphere, clearly mapping into an auroral oval–like structure. NO is very long-lived during

polar winter and can be transported down into the midstratosphere, where it then contributes to catalytic ozone loss. These processes are well constrained by observations and are reproduced morphologically in model experiments incorporating either ionization rates in the mesosphere and lower thermosphere or an UBC of EEP NO_x in the upper mesosphere. The coupling from the EEP direct impacts in the mesosphere and lower thermosphere to stratospheric ozone losses thus appears to be qualitatively well understood. However, some issues with respect to the quantitative description of the EEP impact in chemistry–climate models remain to be addressed. These are related to the description of the particle forcing in chemistry–climate models—for example, the spatial structure and strength of the ionization rates used, limitations of the parameterizations of EEP NO_x and HO_x production, as well as problems with the models' representation of diffusion and mixing in the MLT region and of large-scale transport during wintertime. Observations as well as model studies suggest an impact on stratospheric temperatures during mid- and late winter as well as a dynamical coupling to regional surface climate, though the mechanism and strength of this top-down coupling is yet not clear, and also other mechanisms—for example, a coupling with the ocean implying a time lag, have been proposed to explain those observations. Overall, the atmospheric impact of energetic electron precipitation has the potential to provide an important contribution to natural climate forcing on a regional scale and represents an active field of research.

Acknowledgments

This work was partially supported by the Spanish MICINN under grant ESP2017-87143-R and EC FEDER funds.

References

L. Anchordoqui, P. Thomas, S. Reucroft, J. Swain (2002), Ultrahigh energy cosmic rays: the state of the art before the Auger Observatory, arXiv.

Andersson, M.E., Verronen, P.T., Wang, S., Rodger, C.J., Clilverd, M.A., Bonar, R.C., 2012. Precipitating radiation belt electrons and enhancements of mesospheric hydroxyl during 2004-2009. J. Geophys. Res. 117, D09304.

Andersson, M.E., Verronen, P.T., Rodger, C.J., Clilverd, M.A., Seppälä, A., 2014a. Missing driver in the sun–earth connection from energetic electron precipitation impacts mesospheric ozone. Nat. Commun. 5, 5197.

Andersson, M.E., Verronen, P.T., Rodger, C.J., Clilverd, M.A., Wang, S., 2014b. Longitudinal hotspots in the mesospheric OH variations due to energetic electron precipitation. Atmos. Chem. Phys. 14 (2), 1095–1105.

Andersson, M.E., Verronen, P.T., Marsh, D.R., Seppälä, A., Päivärinta, S.-M., Rodger, C., et al., 2017. Polar ozone response to energetic particle precipitation over decadal time scales: the role of medium-energy electrons. J. Geophys. Res. 123, 607–672.

Arsenovic, P., Rozanov, E., Stenke, D., Funke, B., Wissing, J.M., Mursula, K., et al., 2016. The influence of middle range energy electrons on atmospheric chemistry and regional climate. J. Atmos. Sol. Terr. Phys. 149, 180–190.

Baker, D.N., 2012. A small spacecraft mission with large accomplishments. EOS 93, 325–336.
Baker, D.N., Goldberg, R.A., Herrero, F.A., Blake, J.B., Callis, L.B., 1993. Satellite and rocket studies of relativistic electrons and their influence on the middle atmosphere. J. Atmos. Terr. Phys 55, 1619–1628.
Baldwin, M.P., Dunkerton, T.J., 1999. Propagation of the Arctic oscillation from the stratosphere to the troposphere. J. Geophys. Res. 104, 30937–30946.
Baldwin, M.P., Dunkerton, T.J., 2005. The solar cycle and stratosphere-troposphere dynamical coupling. J. Atmos. Sol. Terr. Phys. 67, 71–82.
Barth, C.A., Baker, D.N., Mankoff, K.D., 2001. The northern auroral region as observed in nitric oxide. Geophys. Res. Lett. 28, 1463–1466.
Barth, C.A., Mankoff, K., Bailey, S.M., Solomon, S.C., 2003. Global observations of nitric oxide in the thermosphere. J. Geophys. Res. 108, 1027.
Baumgaertner, A.J.G., Jöckel, P., Riede, H., Stiller, G., Funke, B., 2010. Energetic particle precipitation in ECHAM5/MESSy—part 2: solar proton events. Atmos. Chem. Phys. 10, 7285–7302.
Baumgaertner, A.J.G., Seppälä, A., Jöckel, P., Clilverd, M.A., 2011. Geomagnetic activity related NO_x enhancements and polar surface air temperature variability in a chemistry climate model: modulation of the NAM index. Atmos. Chem. Phys. 11, 4521–4531.
Bender, S., Sinnhuber, M., von Clarmann, T., Stiller, G., Funke, B., Lopez-Puertas, M., et al., 2015. Comparison of nitric oxide measurements in the mesosphere and lower thermosphere from ACE-FTS, MIPAS, SCIAMACHY, and SMR. Atmos. Meas. Tech. 8, 4171–4195.
Callis, L.B., Lambeth, J.D., 1998. NOy formed by precipitating electron events in 1991 and 1992: descent into the stratosphere as observed by ISAMS. Geophys. Res. Lett. 25 (11), 1875–1878.
Callis, L.B., Baker, D.N., Blake, J.B., Lambeth, J.D., Boughner, R.E., Natarajan, M., et al., 1991. Precipitating relativistic electrons: their long-term effect on stratospheric odd nitrogen levels. J. Geophys. Res. 96, 2939–2976.
Callis, L.B., Natarajan, M., Evans, D.S., Lambeth, J.D., 1998a. Solar atmospheric coupling by electrons (SOLACE) 1. Effects of the May 12, 1997 solar event on the middle atmosphere. J. Geophys. Res. 103, 28405–28419.
Callis, L.B., Natarajan, M., Lambeth, J.D., Baker, D.N., 1998b. Solar atmospheric coupling by electrons (SOLACE) 2. Calculated stratospheric effects of precipitating electrons, 1979-1988. J. Geophys. Res. 103, 28421–28438.
Callis, L.B., Natarajan, M., Lambeth, J.D., 2001. Solar-atmospheric coupling by electrons (SOLACE) 3. Comparisons of simulations and observations, 1979-1997, issues and implications. J. Geophys. Res. 106 (D7), 7523–7539.
Chandran, A., Collins, R.L., Garcia, R.R., Marsh, D.R., 2011. A case study of an elevated stratopause generated in the Whole Atmosphere Community Climate Model. Geophys. Res. Lett. 38 (8), l08804.
Codrescu, M.V., Fuller-Rowell, T.J., Roble, R.G., Evans, D.S., 1997. Medium energy particle precipitation influences on the mesosphere and lower thermosphere. J. Geophys. Res. 102 (A9), 19977–19987.
Cohen, J., Screen, J.A., Furtado, J.C., Barlow, M., Whittleston, D., Coumou, D., et al., 2014. Recent Artic amplification and extreme mid-latitude weather. Nat. Geosci. 7, 627–637.
Cravens, T.E., Gerard, J.-C., LeCompte, M., Stewart, A.I., Rusch, D.W., 1985. The global distribution of nitric oxide in the thermosphere as determined by the atmosphere explorer D satellite. J. Geophys. Res. 90, 9862–9870.
Cravens, T.E., Stewart, A.I., 1978. Global morphology of nitric oxide in the lower E region. J. Geophys. Res. 83, 2446–2452.
Damiani, A., Funke, B., López-Puertas, M., Santee, M.L., Cordero, R.R., Laurenza, M., et al., 2016. Energetic particle precipitation: a major driver of the ozone budget in the Antarctic upper stratosphere. Geophys. Res. Lett. 2016GL068279.
Damon, P.E., Laut, P., 2004. Pattern of strange errors plagues solar activity and terrestrial climate data. Eos Trans. Am. Geophys. Union 85 (39), 370–374.
Fesen, C., Rusch, D., Gerard, J.-C., 1990. The latitudinal gradient of the NO peak density. J. Geophys. Res. 95, 19053–19059.
Francia, P., Regi, M., De Lauretis, M., 2015. Signatures of the ULF geomagnetic activity in the surface air temperature in Antarctica. J. Geophys. Res. 120, 2452–2459.

Friederich, F., Sinnhuber, M., Funke, B., von Clarmann, T., Orphal, J., 2014. Local impact of solar variation on NO_2 in the lower mesosphere and upper stratosphere from 2007 to 2011. Atmos. Chem. Phys. 14, 4055–4064.

Funke, B., Ball, W., Bender, S., Gardini, A., Harvey, V.L., Lambert, A., et al., 2017. HEPPA-II model–measurement intercomparison project: EPP indirect effects during the dynamically perturbed NH winter 2008–2009. Atmos. Chem. Phys. 17 (5), 3573–3604.

Funke, B., Baumgaertner, A., Calisto, M., Egorova, T., Jackman, C.H., Kieser, J., et al., 2011. Composition changes after the "Halloween" solar proton event: the high-energy particle precipitation in the atmosphere (HEPPA) model versus MIPAS data intercomparison study. Atmos. Chem. Phys. 11 (3), 9089–9139.

Funke, B., López-Puertas, M., García-Comas, M., Stiller, G.P., von Clarmann, T., Glatthor, N., 2008. Mesospheric N_2O enhancements as observed by MIPAS on Envisat during the polar winters in 2002-2004. Atmos. Chem. Phys. 8, 5787–5800.

Funke, B., López-Puertas, M., Gil-López, S., von Clarmann, T., Stiller, G.P., Fischer, H., et al., 2005. Downward transport of upper atmospheric NO_x into the polar stratosphere and lower mesosphere during the Antarctic 2003 and Arctic 2002/2003 winters. J. Geophys. Res. 110. Available from: https://doi.org/10.1029/2005JD006463.

Funke, B., López-Puertas, M., Stiller, G.P., Versick, S., von Clarmann, T., 2016. A semi-empirical model for mesospheric and stratospheric NO_y produced by energetic particle precipitation. Atmos. Chem. Phys. Discuss. 2016, 1–44.

Funke, B., López-Puertas, M., Stiller, G.P., von Clarmann, T., 2014a. Mesospheric and stratospheric NO_y produced by energetic particle precipitation during 2002–2012. J. Geophys. Res. 119, 4429–4446.

Funke, B., Puertas, M.L., Holt, L., Randall, C.E., Stiller, G.P., von Clarmann, T., 2014b. Hemispheric distributions and interannual variability of NO_y produced by energetic particle precipitation in 2002–2012. J. Geophys. Res. 119 (23), 13565–13582.

Fytterer, T., Mlynczak, M., Nieder, H., Perot, K., Sinnhuber, M., Stiller, G., et al., 2015a. Energetic particle induced intra-seasonal variability of ozone inside the Antarctic polar vortex observed in satellite data. Atmos. Chem. Phys. 15, 3327–3338.

Fytterer, T., Santee, M.L., Sinnhuber, M., Wang, S., 2015b. The 27-day solar rotational effect on mesospheric nighttime OH and O_3 observations induced by geomagnetic activity. J. Geophys. Res. 120, 7926–7936.

Fytterer, T., Bender, S., Berger, U., Nieder, H., Sinnhuber, M., Wissing, J., 2016. Model studies of short-term variations induced in trace gases by particle precipitation in the mesosphere and lower thermosphere. J. Geophys. Res. 121, 10431–10447.

Gerard, J.-C., Barth, C.A., 1976. OGO-4 observations of the ultraviolet auroral spectrum. Planet. Space. Sci. 24, 1059–1063.

Gerard, J.-C., Barth, C.A., 1977. High-latitude nitric oxide in the lower thermosphere. J. Geophys. Res. 82, 674–680.

Gray, L.J., Beer, J., Geller, M., Haigh, J.D., Lockwood, M., Matthes, K., et al., 2010. Solar influences on climate. Rev. Geophys. 48 (4), 1–53.

Gray, L.J., Scaife, A.A., Mitchell, D.M., Osprey, S., Ineson, S., Hardiman, S., et al., 2013. A lagged response to the 11 year solar cycle in observed winter Atlantic/European weather patterns. J. Geophys. Res. 118, 13405–13420.

Hamilton, K., 1999. Dynamical coupling of the lower and middle atmosphere: historical background to current research. J. Atmos. Sol. Terr. Phys. 61, 73–84.

Heath, D.F., Krueger, A.J., Crutzen, P.J., 1977. Solar proton event: influence on stratospheric ozone. Science 197, 886–889.

Hendrickx, K., Megner, L., Gumbel, J., Siskind, D.E., Orsolini, Y.J., Nesse Tyssøy, H., et al., 2015. Observation of 27-day solar cycles in the production and mesospheric descent of EPP-produced NO. J. Geophys. Res. 120 (10), 8978–8988.

Hendrickx, K., Megner, L., Marsh, D., Gumbel, J., Strandberg, R., Martinsson, F., 2017. Relative importance of nitric oxide physical drivers in the lower thermosphere. Geophys. Res. Lett. 44, 10081–10087.

Holt, L., Randall, C., Harvey, V., Remsberg, E., Stiller, G., Funke, B., et al., 2012. Atmospheric effects of energetic particle precipitation in the Arctic Winter 1978-1979 revisited. J. Geophys. Res. 117, D05315.

Holt, L.A., Randall, C.E., Peck, E.D., Marsh, D.R., Smith, A.K., Lynn Harvey, V., 2013. The influence of major sudden stratospheric warming and elevated stratopause events on the effects of energetic particle precipitation in WACCM. J. Geophys. Res 118, 11. 636–11,646.

Iwagami, N., Ogawa, T., 1980. An Antarctic NO density profile deduced from the gamma band airglow. Planet. Space Sci. 28, 867–873.

Jackman, C.H., McPeters, R.D., Labow, G.J., Fleming, E.L., Praderas, C.J., Russell, J.M., 2001. Northern hemisphere atmospheric effects due to the July 2000 solar proton event. Geophys. Res. Lett. 28 (15), 2883–2886.

Jackman, C.H., DeLand, M.T., Labow, G.J., Fleming, E.L., Weisenstein, D.K., Ko, M.K.W., et al., 2005a. The influence of the several very large solar proton events in years 2000-2003 on the neutral middle atmosphere. Adv. Space Res. 35 (3), 445–450.

Jackman, C.H., DeLand, M.T., Labow, G.J., Fleming, E.L., Weisenstein, D.K., Ko, M.K.W., et al., 2005b. Neutral atmospheric influences of the solar proton events in October–November 2003. J. Geophys. Res. 110, A09S27.

Jones, R.A., Rees, M.H., 1973. Time dependent studies of the aurora-I. ion density and composition. Planet. Space Sci. 21, 537–557.

Kidston, J., Scaife, A.A., Hardiman, S.C., Mitchell, D.M., Butchart, N., Baldwin, M.P., et al., 2015. Stratospheric influence on tropospheric jet streams, storm tracks and surface weather. Nature Geosci. 8, 433–440.

Kirkby, J., et al., 2011. Role of sulphuric acid, ammonia and galactic cosmic rays in atmospheric aerosol nucleation. Nature 476, 429–435.

Kirkwood, S., Osepian, A., Belova, E., Urban, J., Perot, K., Sinha, A., 2015. Ionization and NO production in the polar mesosphere during high-speed solar wind streams: model validation and comparison with NO enhancements observed by Odin-SMR. Ann. Geophys. 33, 561–572.

Kiviranta, J., Pérot, K., Eriksson, P., Murtagh, D., 2018. An empirical model of nitric oxide in the upper mesosphere and lower thermosphere based on 12 years of ODIN SMR measurements. Atmos. Chem. Phys. 18, 3393–13410.

Kodera, K., Kuroda, Y., 2005. A possible mechanism of solar modulation of the spatial structure of the north Atlantic oscillation. J. Geophys. Res. 110, D02111.

Laine, M., Latva-Pukkila, N., Kyrölä, E., 2014. Analysing time-varying trends in stratospheric ozone time series using the state space approach. Atmos. Chem. Phys. 14 (18), 9707–9725.

Lam, M.M., Chisham, G., Freeman, M.P., 2014. Solar wind-driven geopotential height anomalies originate in the Antarctic lower troposphere. Geophys. Res. Lett. 41, 6509–6514.

Lary, D.J., 1997. Catalytic destruction of stratospheric ozone. J. Geophys. Res. 102, 21515–21526.

Lean, J.L., Rind, D.H., 2008. How natural and anthropogenic influences alter global and regional surface temperatures: 1889 to 2006. Geophys. Res. Lett. 35 (18). Available from: https://doi.org/10.1029/2008GL034864.

Lu, H., Clilverd, M.A., Seppälä, A., Hood, L.L., 2008. Geomagnetic perturbations on stratospheric circulation in late winter and spring. J. Geophys. Res. 113, D16106.

Lu, H., Franzke, C., Martius, O., Jarvis, M.J., Phillips, T., 2013. Solar wind dynamic pressure effect on planetary wave propagation and synoptic-scale Rossby wave breaking. J. Geophys. Res. 118, 4476–4493.

Maliniemi, V., Asikainen, T., Mursula, K., Seppälä, A., 2013. QBO-dependent relation between electron precipitation and wintertime surface temperature. J. Geophys. Res. 118, 6302–6310.

Maliniemi, V., Asikainen, T., Mursula, K., 2014. Spatial distribution of northern hemisphere winter temperatures during different phases of the solar cycle. J. Geophys. Res. 119 (16), 9752–9764.

Maliniemi, V., Asikainen, T., Mursula, K., 2016. Effect of geomagnetic activity on the northern annular mode: QBO dependence and the Holton-Tan relationship. J. Geophys. Res. 121, 10043–10055.

Marsh, D.R., Solomon, S.C., Reynolds, A.E., 2004. Empirical model of nitric oxide in the lower thermosphere. J. Geophys. Res. 109 (A18), 7301– + .

Matsuno, T., 1971. A dynamical model of the stratospheric sudden warming. J. Atmos. Sci. 28, 1479–1494.
Matthes, K., Funke, B., Andersson, M.E., Barnard, L., Beer, J., Charbonneau, P., et al., 2017. Solar forcing for CMIP6 (v3.2). Geosci. Model Dev. 10, 473–487.
McLandress, C., Scinocca, F., Shepherd, T.G., Reader, M.C., Manney, G.L., 2013. Dynamical control of the mesosphere by orographic and nonorographic gravity wave drag during the extended northern winters of 2006 and 2009. J. Atmos. Sci. 70, 2152–2169.
McPeters, R.D., Jackman, C.H., 1985. The response of ozone to solar proton events during solar cycle 21: the observations. J. Geophys. Res. 90 (D5), 7945–7954.
Meraner, K., Schmidt, H., 2018. Climate impact of idealized winter polar mesospheric and stratospheric ozone loss as caused by particle precipitation. Atmos. Chem. Phys. 18, 1079–1089.
Mironova, I.A., Aplin, K.L., Arnold, F., Bazilevskaya, G.A., Harrison, R.G., Krivolutsky, A.A., et al., 2015. Energetic particle influence on the earth's atmosphere. Space Sci. Rev. 194, 1–96.
Newnham, D.A., Espy, P.J., Clilverd, M.A., Rodger, C.J., Seppälä, A., Maxfield, D.J., et al., 2011. Direct observations of nitric oxide produced by energetic electron precipitation into the Antarctic middle atmosphere. Geophys. Res. Lett. 38, L20104.
Newnham, D.A., Espy, P.J., Clilverd, M.A., Rodger, C.J., Seppälä, A., Maxfield, D.J., et al., 2013. Observations of nitric oxide in the Antarctic middle atmosphere during recurrent geomagnetic storms. J. Geophys. Res. 118, 7874–7885.
Nieder, H., Winkler, H., Marsh, D.R., Sinnhuber, M., 2014. NO_x production due to energetic particle precipitation in the MLT region: results from ion chemistry model studies. J. Geophys. Res. 119, 2137–2148.
Päivärinta, S.-M., Verronen, P.T., Funke, B., Gardini, A., Seppälä, A., Andersson, M.E., 2016. Transport versus energetic particle precipitation: northern polar stratospheric NO_x and ozone in January-March 2012. J. Geophys. Res. 121 (1), 6085–6100.
Pithan, F., Mauritsen, T., 2014. Arctic amplification dominated by temperature feedbacks in contemporary climate models. Nat. Geosci. 7, 181–184.
Porter, H.S., Jackman, C.H., Green, A.E.S., 1976. Efficiencies for production of atomic nitrogen and oxygen by relativistic proton impact in air. J. Chem. Phys. 65, 154–167.
Prasad, S.S., Zipf, E.C., 1981. Atmospheric nitrous oxide produced by solar protons and relativistic electrons. Nature 291, 564–566.
Randall, C.E., Rusch, D.W., Bevilacqua, R.M., Hoppel, K.W., Lumpe, J.D., 1998. Polar ozone and aerosol measurement (POAM) II stratospheric NO_2, 1993–1996. J. Geophys. Res. 103 (D21), 28. 361–28, 371.
Randall, C.E., Siskind, D.E., Bevilacqua, R.M., 2001. Stratospheric NO_x enhancements in the southern hemisphere vortex in winter/spring of 2000. Geophys. Res. Lett. 28 (12), 2385–2388.
Randall, C.E., Harvey, V.L., Singleton, C.S., Bailey, S.M., Bernath, P.F., Codrescu, M., et al., 2007. Energetic particle precipitation effects on the Southern Hemisphere stratosphere in 1992-2005. J. Geophys. Res. 112 (D8). Available from: https://doi.org/10.1029/2006JD007696.
Randall, C.E., Harvey, V.L., Holt, L.A., Marsh, D.R., Kinnison, D., Funke, B., et al., 2015. Simulation of energetic particle precipitation effects during the 2003–2004 Arctic winter. J. Geophys. Res. 120 (6), 5035–5048. 2015JA021196.
Reddmann, T., Ruhnke, R., Versick, S., Kouker, W., 2010. Modeling disturbed stratospheric chemistry during solar-induced NO*x* enhancements observed with MIPAS/ENVISAT. J. Geophys. Res. 115, D00I11.
Reichler, T., Kushner, P.J., Polvani, L.M., 2005. The coupled stratosphere-troposphere response to impulsive forcing from the troposphere. J. Atmos. Sci. 62, 3337–3352.
Rinsland, C.P., Salawitch, R.J., Gunson, M.R., Solomon, S., Zander, R., Mahieu, E., et al., 1999. Polar stratospheric descent of NO_y and CO and Arctic denitrification during winter 1992–1993. J. Geophys. Res. 104 (D1), 1847–1861.
Rinsland, C.P., Boone, C., Nassar, R., Walker, K., Bernath, P., McConnell, J.C., et al., 2005. Atmospheric Chemistry Experiment (ACE) Arctic stratospheric measurements of NO_x during February and March 2004: impact of intense solar flares. Geophys. Res. Lett. 32. Available from: https://doi.org/10.1029/2005GL022425.
Rozanov, E., Callis, L., Schlesinger, M., Yang, F., Andronova, N., Zubov, V., 2005. Atmospheric response to NO_y source due to energetic electron precipitation. Geophys. Res. Lett. 32, L14811.

Rozanov, E., Calisto, M., Egorova, T., Peter, T., Schmutz, W., 2012. Influence of the precipitating energetic particles on atmospheric chemistry and climate. Surv. Geophys 33, 483–501.
Rusch, D.W., Barth, C.A., 1975. Satellite measurements of nitric oxide in the polar region. J. Geophys. Res. 80, 3719–3721.
Rusch, D.W., Gérard, J.-C., Solomon, S., Crutzen, P.J., Reid, G.C., 1981. The effect of particle precipitation events on the neutral and ion chemistry of the middle atmosphere. I—Odd nitrogen. Planet. Space Sci. 29, 767–774.
Russell III, J.M., Solomon, S., Gordley, L.L., Remsberg, E.E., Callis, L.B., 1984. The variability of stratospheric and mesospheric NO_2 in the polar winter night observed by LIMS. J. Geophys. Res. 89 (D5), 7267–7275.
Sætre, C., Stadsnes, J., Nesse, H., Aksnes, A., Petrinec, S., Barth, C., et al., 2004. Energetic electron precipitation and the NO abundance in the upper atmosphere: a direct comparison during a geomagnetic storm. J. Geophys. Res. 109. Available from: https://doi.org/10.1029/2004JA010485.
Salmi, S.-M., Verronen, P.T., Thölix, L., Kyrölä, E., Backman, L., Karpechko, A.Y., et al., 2011. Mesosphere-to-stratosphere descent of odd nitrogen in February-March 2009 after sudden stratospheric warming. Atmos. Chem. Phys. 11 (1), 4645–4655.
Scaife, A.A., Ineson, S., Knight, J.R., Gray, L., Kodera, K., Smith, D.M., 2013. A mechanism for lagged North Atlantic climate response to solar variability. Geophys. Res. Lett. 40, 434–439.
Scaife, A.A., Knight, J.R., Vallis, G.K., Folland, C.K., 2005. A stratospheric influence on the winter NAO and Northern Atlantic surface climate. Geophys. Res. Lett. 32, L18715.
Semeniuk, K., McConnell, J.C., Jin, J.J., Boone, C.D., Bernath, P.F., 2008. N_2O production by high energy auroral electron precipitation. J. Geophys. Res. 113, D16302.
Semeniuk, K., Fomichev, V.I., McConnell, J.C., Fu, C., Melo, S.M.L., Usoskin, I.G., 2011. Middle atmosphere response to the solar cycle in irradiance and ionizing particle precipitation. Atmos. Chem. Phys. 11 (10), 5045–5077.
Seppälä, A., Verronen, P.T., Clilverd, M.A., Randall, C.E., Tamminen, J., Sofieva, V., et al., 2007. Arctic and Antarctic polar winter NO_x and energetic particle precipitation in 2002–2006. Geophys. Res. Lett. 34 (12), L12810.
Seppälä, A., Randall, C.E., Clilverd, M.A., Rozanov, E., Rodger, C.J., 2009. Geomagnetic activity and polar surface air temperature variability. J. Geophys. Res. 114 (A10), 1297–1311.
Seppälä, A., Lu, H., Clilverd, M.A., Rodger, C.J., 2013. Geomagnetic activity signatures in wintertime stratospheric wind, temperature, and wave response. J. Geophys. Res. 118, 2169–2183.
Seppälä, A., Douma, E., Rodger, C.J., Verronen, P.T., Clilverd, M.A., Bortnik, J., 2018. Relativistic electron microburst events: modeling the atmospheric impact. Geophys. Res. Lett. 45, 1141–1147.
Sheese, P.E., Walker, K.A., Boone, C.D., Bernath, P.F., Funke, B., 2016. Nitrous oxide in the atmosphere: first measurements of a lower thermospheric source. Geophys. Res. Lett. 43, 2866–2872.
Sinnhuber, B.-M., von der Gathen, P., Sinnhuber, M., Rex, M., König-Langlo, G., Oltmans, S., 2006. Large decadal scale changes of polar ozone suggest solar influence. Atmos. Chem. Phys. 6, 1835–1841.
Sinnhuber, M., Berger, U., Funke, B., Nieder, H., Reddmann, T., Stiller, G., et al., 2018. NO_y production, ozone loss and changes in net radiative heating due to energetic particle precipitation in 2002–2010. Atmos. Chem. Phys. 18, 1115–1147.
Sinnhuber, M., Kazeminejad, S., Wissing, J.-M., 2011. Interannual variation of NO_x from the lower thermosphere to the upper stratosphere in the years 1991-2005. J. Geophys. Res. 116, A02312. Available from: https://doi.org/10.1029/2010JA015825.
Sinnhuber, M., Friederich, F., Bender, S., Burrows, J.P., 2016. The response of mesospheric NO to geomagnetic forcing in 2002-2012 as seen by SCIAMACHY. J. Geophys. Res. Space Phys. 121, 3603–3620.
Sinnhuber, M., Nieder, H., Wieters, N., 2012. Energetic particle precipitation and the chemistry of the mesosphere/lower thermosphere. Surv. Geophys. 33, 1281–1334.
Siskind, D.E., 2000. On the coupling between middle and upper atmospheric odd nitrogen. In: Atmospheric Science Across the Stratopause, vol. 123 of Geophysical Monograph. American Geophysical Union, pp. 101–116.
Siskind, D.E., Barth, C.A., Russell III, J.M., 1998. A climatology of nitric oxide in the mesosphere and thermosphere. Adv. Space Res. 21, 1353–1362.
Siskind, D.E., Sassi, F., Randall, C.E., Harvey, V.L., Hervig, M.E., Bailey, S.M., 2015. Is a high-altitude meteorological analysis necessary to simulate thermosphere-stratosphere coupling? Geophys. Res. Lett. 42 (19), 8225–8230.

Smith, A.K., 2012. Global dynamics of the MLT. Surv. Geophys. 33 (6), 1177–1230.
Smith-Johnsen, C., Marsh, D., Orsolini, Y., Nesse-Tyssøy, H., Hendrickx, K., Sandanger, M., et al., 2018. Nitric oxide response to the April 2010 electron precipitation event: using WACCM and WACCM-D with and without medium-energy electrons. J. Geophys. Res. 123, 5232–5245.
Smith-Johnsen, C., Nesse Tyssøy, H., Hendrickx, K., Orsolini, Y., Kishore Kumar, G., Glesnes Ødegaard, L.-K., et al., 2017. Direct and indirect electron precipitation effect on nitric oxide in the polar middle atmosphere, using a full-range energy spectrum. J. Geophys. Res. 122, 8670–8693.
Solomon, S., Crutzen, P.J., Roble, R.G., 1982. Photochemical coupling of the thermosphere and the lower atmosphere 1. odd nitrogen from 50 to 120 km. J. Geophys. Res. 87, 7206–7220.
Solomon, S., Rusch, D.W., Gérard, J.-C., Reid, G.C., Crutzen, P.J., 1981. The effect of particle precipitation events on the neutral and ion chemistry of the middle atmosphere. II - Odd hydrogen. Planet. Space Sci. 29, 885–892.
Stiller, G.P., Mengistu Tsidu, G., von Clarmann, T., Glatthor, N., Höpfner, M., Kellmann, S., et al., 2005. An enhanced HNO_3 second maximum in the Antarctic mid–winter upper stratosphere 2003. J. Geophys. Res. 110, D20. Available from: https://doi.org/10.1029/2005JD006011.
Thompson, D.W.J., Solomon, S., Kushner, P.J., England, M.H., Grise, K.M., Karoly, D.J., 2011. Signatures of the Antarctic ozone hole in southern hemisphere surface climate change. Nat. Geosci. 4, 741–749.
Thorne, R.M., 1977. Energetic radiation belt electron precipitation: a natural depletion mechanism for stratospheric ozone. Science 195, 287–289.
Thoudam, S., Rachen, J.P., van Vliet, A., Achterberg, A., Buitink, S., Falcke, H., et al., 2016. Cosmic-ray energy spectrum and composition up to the ankle: the case for a second galactic component. Astron. Astrophys. 595. Available from: https://doi.org/10.1051/0004-6361/201628894.
Tinsley, B.A., Burns, G.B., Zhou, L., 2007. The role of the global electric circuit in solar and internal forcing of clouds and climate. Adv. Space Res. 40, 1126–1139.
Turunen, E., Verronen, P.T., Seppälä, A., Rodger, C.J., Clilverd, M.A., Tamminen, J., et al., 2009. Impact of different precipitation energies on NO_x generation during geomagnetic storms. J. Atmos. Sol. Terr. Phys. 71, 1176–1189.
Verronen, P., Lehmenn, R., 2015. Enhancement of odd nitrogen modifies mesospheric ozone chemistry during polar winter. Geophys. Res. Lett. 42, 10445–10452.
Verronen, P.-T., Andersson, M.E., Marsh, D.R., Kovacs, T., Plane, J.M.C., 2016. WACCM-D – whole atmosphere community climate model with D-region ion chemistry. JAMES 8, 954–975.
Verronen, P.T., Lehmann, R., 2013. Analysis and parameterisation of ionic reactions affecting middle atmospheric HO_x and NO_y during solar proton events. Ann. Geophys. 31, 909–956.
Verronen, P.T., Santee, M.L., Manney, G.L., Lehmann, R., Salmi, S.-M., Seppälä, A., 2011. Nitric acid enhancements in the mesosphere during the January 2005 and December 2006 solar proton events. J. Geophys. Res. 116, D17.
Wagner, R., et al., 2017. The role of ions in new particle formation in the cloud chamber. Atmos. Chem. Phys. 17, 15181–15197.
Weeks, L.H., Cuikay, R.S., Corbin, J.R., 1972. Ozone measurements in the mesosphere during the solar proton event of 2 November 1969. J. Atmos. Sci. 29, 1138–1142.
Winkler, H., Kazeminejad, S., Sinnhuber, M., Kallenrode, M.-B., Notholt, J., 2009. Conversion of mesospheric HCl into active chlorine during the solar proton event in July 2000 in the northern polar region. J. Geophys. Res. 114, D00I03.
World Meteorological Organization, 2014. Scientific Assessment of Ozone Depletion, vol. 55. World Meteorological Organization.
Zel'dovic, Y.B., Raizer, Y.R., 1967. Physics of Shock Waves and High–Temperature Hydrodynamic Phenomena, vol. II. Academic Press.
Zipf, E.C., Borst, W.L., Donahue, T.M., 1970. A mass spectrometer observation of NO in an auroral arc. J. Geophys. Res. 75, 6371–6376.
Zipf, E.C., Prasad, S.S., 1980. Production of nitrous oxide in the auroral D and E regions. Nature 287, 525–526.

This page intentionally left blank

Index

Note: Page numbers followed by "*f*" and "*t*" refer to figures and tables, respectively.

D

E

F

G

H

I

K

L

M

N

S

T

W

X

THE DYNAMIC LOSS OF EARTH'S RADIATION BELTS

From Loss in the Magnetosphere to Particle Precipitation in the Atmosphere

A uniquely interdisciplinary focus on the effects of the Earth's radiation belts from both an atmospheric and planetary science point of view.

- Examines both the causes and effects of particle loss in the magnetosphere from multiple perspectives
- Presents interdisciplinary content, helping to bridge the gap between the magnetospheric and atmospheric communities through communication and collaboration
- Fills a gap in the current literature by focusing on loss in the radiation belts, which is especially timely based on data from the Van Allen Probes, the Magnetospheric Multiscale Mission, and other projects

The Dynamic Loss of Earth's Radiation Belts: From Loss in the Magnetosphere to Particle Precipitation in the Atmosphere presents a timely review of data from various explorative missions, including the Van Allen Probes, MMS, the completion of four BARREL balloon campaigns, and several current and upcoming CubeSat missions focusing on precipitation losses. This is the first book in the area to include a focus on loss, and not just acceleration and radial transport.

Bringing together two communities, the book includes contributions from experts with knowledge in both precipitation mechanisms and the effects on the atmosphere. There is a direct link between the radiation belt losses and the energy deposited in the layers of our atmosphere. *The Dynamic Loss of Earth's Radiation Belts* brings together scientists from space and atmospheric science communities to examine both the causes and the effects of particle loss in the magnetosphere.

Dr. Allison N. Jaynes is an assistant professor in the Department of Physics & Astronomy, The University of Iowa, United States. Her research involves spacecraft data and instrumentation used to investigate the near-Earth space environment. She obtained her PhD from the University of New Hampshire in 2013 after studying the Northern Lights in the specific form of pulsating aurora. She is serving as Co-Investigator on NASA's MMS and Van Allen Probes spaceflight missions.

Dr. Maria E. Usanova is a research scientist at the Laboratory for Atmospheric and Space Physics, University of Colorado Boulder, United States. She graduated with honors from the Department of Physics, Moscow State University, Russia and received her PhD in space physics from the University of Alberta, Canada. Her research interests include the dynamics of energetic particles in the Earth's radiation belts and ring current, mechanisms for particle acceleration and loss in the magnetosphere, inner magnetosphere coupling, and wave–particle interactions.

ELSEVIER elsevier.com/books-and-journals

ISBN 978-0-12-813371-2

9 780128 133712